University of Windsor
Scholarship at UWindsor

Electronic Theses and Dissertations
Theses, Dissertations, and Major Papers

1-1-1987

Physical and numerical modelling of an aerated sump.

David William Machina
University of Windsor

Follow this and additional works at: https://scholar.uwindsor.ca/etd

Recommended Citation

Machina, David William, "Physical and numerical modelling of an aerated sump." (1987). *Electronic Theses and Dissertations*. 6141.
https://scholar.uwindsor.ca/etd/6141

This online database contains the full-text of PhD dissertations and Masters' theses of University of Windsor students from 1954 forward. These documents are made available for personal study and research purposes only, in accordance with the Canadian Copyright Act and the Creative Commons license—CC BY-NC-ND (Attribution, Non-Commercial, No Derivative Works). Under this license, works must always be attributed to the copyright holder (original author), cannot be used for any commercial purposes, and may not be altered. Any other use would require the permission of the copyright holder. Students may inquire about withdrawing their dissertation and/or thesis from this database. For additional inquiries, please contact the repository administrator via email (scholarship@uwindsor.ca) or by telephone at 519-253-3000ext. 3208.

PHYSICAL AND NUMERICAL MODELLING OF AN AERATED SUMP

by

David William Machina, B.A.Sc., M.A.Sc.

A Dissertation
submitted to the Faculty of Graduate Studies
through the Department of
Civil Engineering in Partial Fulfillment
of the requirements for the Degree
of Doctor of Philosophy at
The University of Windsor

Windsor, Ontario, Canada

May, 1987

UMI Number: DC53238

INFORMATION TO USERS

The quality of this reproduction is dependent upon the quality of the copy submitted. Broken or indistinct print, colored or poor quality illustrations and photographs, print bleed-through, substandard margins, and improper alignment can adversely affect reproduction.
In the unlikely event that the author did not send a complete manuscript and there are missing pages, these will be noted. Also, if unauthorized copyright material had to be removed, a note will indicate the deletion.

UMI®

UMI Microform DC53238
Copyright 2009 by ProQuest LLC
All rights reserved. This microform edition is protected against
unauthorized copying under Title 17, United States Code.

ProQuest LLC
789 East Eisenhower Parkway
P.O. Box 1346
Ann Arbor, MI 48106-1346

ABE 8318

ⓒ David William Machina 1987
All Rights Reserved

870566

To Tamye

ABSTRACT

Current problems in the operation of water and wastewater pumping stations include adverse vortex activity and sediment deposition on the floor of the wet well. It has been shown that the practice of designing water and wastewater pumping stations to prevent vortex activity is well advanced, and if conventional design procedures are followed, the system will operate without vortex activity. However, there is wide spread disagreement in designing floor slope, sump geometry and inlet conditions in order to minimize deposition of sediments within the wet well. As a consequence, often the pump(s) must be stopped, the wet well drained, and the sediments and other settled debris removed manually.

This study proposes the use of a compressed air diffuser system in the sump to provide an auxiliary circulation to assist in scouring deposited sediments from the floor. With this scheme, the manual removal of the debris would be eliminated.

A numerical model has been formulated to simulate a wide variety of sump geometry and air diffuser operating schemes. The model couples a drift flux formulation to describe the plume performance with the conservation of linear and angular momentum to describe the overall sump flow. A physical sump model, 1576 mm long, 684 mm wide and 1140 mm deep, was used to obtain velocity profiles, plume width measurements, observe the general performance of the diffuser and to optimize, calibrate and investigate the sensitivity of the numerical model. Refinements to the numerical model were made which allowed for

large scale simulations. Significant restrictions have been noted and a thorough discussion of these limitations has been provided.

Design curves are presented which allow for the investigation of a variety of air flow and sump geometries. In all cases, operating variables are chosen so that the system is kept vortex free.

The numerical model has been shown to be a useful tool for estimating the air flowrate required to scour sediments from the wet well floor and to size the air diffuser equipment. Full-scale testing is required to assess scale effects and for site specific calibration. The model conforms to accepted geometric sump standards so that implementation of the model is not further complicated.

ACKNOWLEDGEMENTS

The author wishes to express his sincere gratitude to Drs. J.K. Bewtra and J.A. McCorquodale for their continued support, constructive criticism and guidance throughout the tenure of this research. It has been my great pleasure to work along side, and under their direction, throughout my academic career.

The suggestions of the comprehensive committee are greatly appreciated. Their input has led to an overall improvement in the scope of the work.

The skill of Mr. F. Kiss during the assembly of the experimental apparatus is gratefully acknowledged. The expertise of the Central Research Shop in fabricating the acrylic bell-mouths is also appreciated.

The author would also like to thank the staff of the West Windsor Pollution Control Plant for their assistance in collecting grit samples.

I am indebted to Mr. G. Chodola for his skill and patience in helping me to collect much of the experimental data.

Miss Anne-Marie Bartlett is to be credited with her expertise in transforming my handwritten manuscript into typed text. Mr. N. Bewtra prepared the inked drawings.

The patience and support of my wife, parents and family cannot be understated. They have proven to be a continual source of motivation for this work.

The financial support of the Natural Sciences and Engineering Research Council of Canada, the Ontario Ministry of Colleges and Universities, the University of Windsor and the Department of Civil Engineering is greatfully acknowledged.

TABLE OF CONTENTS

PAGE

ABSTRACT v

ACKNOWLEDGEMENTS vii

LIST OF TABLES xiii

LIST OF FIGURES xv

CHAPTER 1 INTRODUCTION

- 1.1 Preamble 1
- 1.2 Objective and Scope 3

CHAPTER 2 LITERATURE REVIEW - WET WELL DESIGN

- 2.1 General 4
- 2.2 Current Practice 13
  - 2.2.1 General 13
  - 2.2.2 Wet Well and Dry Well Pumping Stations 14
  - 2.2.3 Bell-Mouth Design 16
  - 2.2.4 Recommended Sump Design 18
  - 2.2.5 Minimum Submergence Requirements 28
- 2.3 Basic Concepts of Vortex Formation 32
- 2.4 Causes and Effects of Swirl Formation 35
- 2.5 Growth of the Boundary Layer and the Effects of Boundary Shear on Vorticity Generation 46
- 2.6 Model Studies of Vortices and Sumps 50
  - 2.6.1 Geometric Similarity 50
  - 2.6.2 Similarity of Gravity Forces 50
  - 2.6.3 Similarity of Viscous Forces 51
  - 2.6.4 Scaling of Surface Tension Forces 51
  - 2.6.5 Boundary Roughness Similarity 52
  - 2.6.6 Additional Modelling Considerations 52
- 2.7 Scale Effects in Modelling Sump and Vortical Flows 56
- 2.8 Dimensional Analysis Considerations 59

CHAPTER 3 LITERATURE REVIEW - THE INITIATION OF PARTICLE MOTION

- 3.1 General 71
- 3.2 White's Analysis of the Equilibrium of Grains on the Bed of a Stream 73
- 3.3 Shields' and Camp's Approach to the Initiation of Particle Motion 78
- 3.4 Other Significant Works on the Initiation of Sediment Transport 84

PAGE

3.5 The Effects of Lift and Drag on Particle Motion 103
3.6 The Effects of Steep Slopes on Particle Motion 116
3.7 Similitude Principles of Sediment Transport 129

CHAPTER 4 DEVELOPMENT OF THE NUMERICAL MODEL

4.1 General 136
4.2 Conceptual Overview 138
4.3 The Diffuser Plume Model 139
4.4 General Sump Model 150
4.5 Formulation of System Elements 154
  4.5.1 Shear Stress on the Inclined Portion of the Wet Well Floor 154
  4.5.2 Shear Stress on the Horizontal Portion of the Wet Well floor 158
  4.5.3 Shear Stress on the Vertical Wall Adjacent to the Diffuser Plume 158
  4.5.4 The Mutual Hydrodynamic Bubble Force 160
  4.5.5 Drag Force on the Pump Columns 161
  4.5.6 Side Wall Shear Stress 168
  4.5.7 Linear Momentum Balance 172
  4.5.8 The ΔP_2 Force 176
  4.5.9 The Force Due to the Mass of Fluid Above the Static Water Level 178
  4.5.10 The Pressure Imbalance Force, ΔP_B 179
  4.5.11 Angular Momentum Crossing the System Boundary 182
4.6 A Note on the Selection of Friction Factors 185

CHAPTER 5 EXPERIMENTAL APPARATUS AND MEASUREMENT EQUIPMENT

5.1 Description of the Physical Model 187
5.2 Errors, Calibration and Operational Procedures 194
  5.2.1 Errors in Length Measurement 195
  5.2.2 Errors in Air Flowrate Measurement 196
  5.2.3 Errors in Velocity Measurement 197

CHAPTER 6 EXPERIMENTAL PROGRAM AND DISCUSSION OF RESULTS

6.1 General 202
6.2 Test Series 1, Critical Submergence 204
6.3 Test Series 2, Baffle Bottom Clearance 211
6.4 Test Series 3, Top Baffle Clearance 218
6.5 Test Series 4, Width of Diffuser Zone 225

PAGE

6.6 Test Series 5, Experimental Particle Characteristics 229
6.7 Test Series 6, Particle Deposition in the Wet Well 234
6.8 Test Series 7, Circulation Studies 237
6.9 Test Series 8, Plume Velocity Studies 241
6.10 Test Series 9, Velocity Profiles Through the Centre of Rotation 243

CHAPTER 7 NUMERICAL CALIBRATION, SENSITIVITY AND DESIGN APPLICATION

7.1 General 249
7.2 Sensitivity to Diffuser Plume Parameters 251
7.3 Calibration of the Friction Factors, f 267
7.4 Sensitivity of the System Dynamics to the Centre of Rotation 269
7.5 Additional Correlation Parameters 278
7.6 C_f, Final Calibration 279
7.7 Comments on the Magnitudes of Various Terms in the Angular Momentum Equation 285
7.8 Momentum Correction Factors 289
7.9 Closure on Sensitivity 290
7.10 Range of Design Parameters 295
7.11 Design Example and Program Application 309
  7.11.1 Statement of the Problem 309
  7.11.2 Design Procedure 310
  7.11.3 Determine the Suction Pipe Diameter 310
  7.11.4 Determine the Minimum Submergence Required 311
  7.11.5 Determine the Sump Volume Required for Peak Flow 312
  7.11.6 Fix the Sump Dimensions 313
  7.11.7 Check Design Variable Ranges 313
  7.11.8 Determine the Particle Requirements 314
  7.11.9 Determine the Range of Operating Conditions 315
  7.11.10 Estimation of the Air Flowrates 316
  7.11.11 Scale Effects 317
  7.11.12 Design Example Results 320

CHAPTER 8 CONCLUSIONS 324

CHAPTER 9 RECOMMENDATIONS 326

APPENDIX 1

A1.1 Numerical Program Flowsheet 328

PAGE

A1.2 Computer Program Nomenclature 334

A1.3 WATFIV Computer Program Listing 342

A1.4 Computer Program Output 380

APPENDIX 2 Computer Program Input 388

NOMENCLATURE 391

REFERENCES 403

VITA AUCTORIS 418

LIST OF TABLES

TABLE PAGE

3.1 Range of Shields-Camp β Values 82

3.2 Critical Bottom Velocities 86

3.3 Critical Mean Velocity in the Cross-Section 88

3.4 Equations for Critical Shear 93

3.5 Distance of Theoretical Bed Level Below the Tops of Roughness Elements 121

3.6 Equivalent Sand Roughness for Various Boundaries 123

4.1 Terminal Velocities of Single Gas Bubbles in Liquids 147

4.2 Summary of Governing Equations for the Diffuser Plume Model 151

4.3 Pump Column Reynolds Numbers and Corresponding Drag Coefficients 167

5.1 Specifications of Experimental Equipment 192

6.1 Pumping Schemes for Model Study 203

6.2 Range of Values for Test Series 1 205

6.3 Range of Test Values for Test Series 2 213

6.4 Range of Variables for Test Series 3 219

6.5 Experimental Particle Characteristics 230

6.6 Test Variables Used in the Observation of Particle Deposition 235

6.7 Range of Test Values for Circulation Studies 239

6.8 Test Variables Used in Determining Vertical Velocity Profiles 244

6.9 Correlation Equations for Velocity Profiles 248

7.1 Range of Calibration Parameters 250

TABLE PAGE

7.2 Friction Factor Calculations 268

7.3 Range of Variables for C_f Determination 281

7.4 Magnitudes of Angular Momentum Terms 286

7.5 Magnitudes of Angular Momentum Terms 287

7.6 Calculation of Momentum Correction Factors 291

7.7 Overall Sensitivity Trends 292

7.8 Design Example Results 323

A2.1 Computer Program Input Cards 389

A2.2 Input Variable Description 390

LIST OF FIGURES

FIGURE PAGE

2.1 Suction Velocity vs. Water Depth for Vortex-Free and Vortex-Forming Region 8

2.2 The Effect of Changing the Angular Momentum on the Critical Submergence 10

2.3 The Effect of Bottom Clearance on Critical Submergence 11

2.4 The Effect of Wall Clearance for Various Suction Pipe Sizes Located Equidistant from Two Adjacent Walls 12

2.5 Wet and Dry Well Pump Installations 15

2.6 Bell-mouth Design 17

2.7 The Main Aspects of a Good Single Cell Sump 19

2.8 General Layout for the Inlet (Zone I) to a Multiple Pump Sump 20

2.9 General Layout for a Multiple Pump Sump (Zone III) 21

2.10 Basic Design for a Single Pump Wet Well with a Vertical Intake 22

2.11 Basic Design for a Single Pump Dry Well Design 23

2.12 Basic Design for a Multiple Pump Wet Well Arrangement 24

2.13 Plan Views of Multiple Pump Sumps, Including the Approach Works to the Sump 25

2.14 Plan and Elevation of Recommended Sump Dimensions 29

2.15 Dimensions A, B, C, H, S and Y Corresponding to Fig. 2.14 30

2.16 Stages in the Development of an Air-Entraining Vortex 36

FIGURE PAGE

2.17 The Effect of Water Depth on Swirling Flow in a Suction Pipe 38

2.18 Approach Flow to a Pump Inlet in a Straight Channel 40

2.19 Indicated Swirl for a 2 inch Diameter Suction Pipe in a Straight Channel 43

2.20 Sump and Baffle Geometries 45

2.21 The Relative Magnitudes of Vorticity Arising from Flow Past a Pipe and a Flat Plate 49

2.22 Plots of Vortex Type for a Pumped Storage Inlet 54

2.23 Vortex Type vs. Core Length and Froude Number 55

2.24 Vortex Severity vs. Froude Number Ratio and Reynolds Number 60

2.25 The Variation of the Viscous Correction Factor, K, with the Viscosity Number, N_ν 66

2.26 Criterion for Vortex Type 68

2.27 The Relationship Between L_R, V_R and H/D for the Onset of Air-Entraining Vortices 69

3.1 Forces on a Sediment Grain on a Sloping Bed 74

3.2 Shields Diagram 79

3.3 Diagram for the Derivation of the Shields-Camp Equation 80

3.4 Critical Bottom Velocity vs. Particle Diameter 96

3.5 Critical Mean Velocity in the Cross-Section vs. Particle Diameter 97

3.6 Critical Tractive Shear Stress vs. Particle Diameter 98

3.7 Relationship of Shear Intensity Parameter and Particle Reynolds Number 100

FIGURE		PAGE
3.8	Lift Factor and Drag Coefficient	107
3.9	Development of Drag and Lift Forces	109
3.10	Variation of Drag and Lift Coefficients	111
3.11	Variation of Drag Coefficient with Reynolds Number for Smooth Boundaries	112
3.12	Variation of Drag Coefficient with Reynolds Number for Rough Boundaries	113
3.13	Comparison of Drag Coefficients for a Rolling Sphere, Stationary Sphere and Falling Sphere	115
3.14	Variation of the Critical Shields Parameter with Relative Roughness and Steep Slopes	118
3.15	Modified Critical Shear Stress vs. Critical Shear Reynolds Number	125
3.16	Modified Critical Shear Stress vs. Critical Depth to Particle Size Ratio	126
3.17	Unified Graphic Sediment Discharge Function for Flume Data	132
3.18	Sediment Transport Function	135
4.1	General Layout of the Sump Model	137
4.2	Defining Diagram for Diffuser Plume Model	140
4.3	Assumed Velocity Profiles	156
4.4	Discretization of the Diffuser Plume	159
4.5	Discretization of the Pump Columns	162
4.6	The Effect of Centre of Rotation Coordinates Tangential Velocities	163
4.7	Elements used to Calculate Side Wall Shear Stress	169
4.8	An Element used to Calculate Side Wall Shear	170

FIGURE PAGE

4.9 Application of Linear Momentum to Control Volume 173

4.10 Added Hydrostatic Pressure Force 177

4.11 Calculation of the Pressure Imbalance 180

4.12 Terminal Rise Velocity of Bubbles 183

4.13 Evaluating the Angular Momentum Crossing the Boundary 184

5.1 Plan of Model Wet Well 188

5.2 Cross-Section of Model Wet Well 189

5.3 Profile of the Bell-Mouth 190

6.1 Critical Submergence for Test PS1 206

6.2 Composite Plot of Critical Submergence-Average for All Pumping Schemes 208

6.3 Envelope of Critical Submergence for All Pumping Schemes and Floor Slopes 209

6.4 Comparison of Critical Submergence Data 210

6.5 Explanation of Reaction Baffle Geometry 212

6.6 Effect of Baffle Bottom Clearance With Horizontal Floor 214

6.7 Effect of Baffle Bottom Clearance With 15° Floor Slope 215

6.8 Effect of Baffle Bottom Clearance With 45° Floor Slope 216

6.9 Effect of Top Baffle Clearance for Horizontal Floor 221

6.10 Effect of Top Baffle Clearance for 45° Floor Slope 222

6.11 Floor Velocity as a Function of Air Flowrate and d_A/D for a Horizontal Floor 223

FIGURE PAGE

6.12 Floor Velocity as a Function of Air Flowrate and d_A/D for a 45° Floor Slope 224

6.13 Diffuser Zone Investigations 226

6.14 The Effect of Various Diffuser Locations 228

6.15 Critical Shields Plot 233

6.16 Coordinate Axis for Locating the Centre of Rotation 240

6.17 Typical Plume Velocity Profiles 242

6.18 Typical Velocity Profile Through Centre of Rotation 246

6.19 Generalized Velocity Profile 247

7.1 The Effect of Bubble Radius on Plume Growth 253

7.2 The Effect of Initial Plume Width on Plume Growth 254

7.3 Relationship Between Air Fraction and Plume Width 255

7.4 Entrainment Coefficient Sensitivity 256

7.5 Sensitivity to the Entrainment Coefficient 257

7.6 Entrainment Coefficient Sensitivity 260

7.7 Friction Factor Sensitivity 261

7.8 Comparison of Measured and Predicted Air Fractions 264

7.9 Sensitivity to the B_o/R_b Ratio 265

7.10 Sensitivity to the B_o/R_b Ratio 266

7.11 Sensitivity to Angular Momentum 272

7.12 Sensitivity to Kinetic Energy 274

FIGURE PAGE

7.13 Dimensionless Shear Stress on Horizontal Portion of Wet Well Floor 276

7.14 Dimensionless Shear Stress on Inclined Portion of Wet Well Floor 277

7.15 C_f Value Predicted from Numerical Model for $L/H = 3.160$ and $H/D = 4.0$ 282

7.16 C_f Value Predicted from Numerical Model for $L/H = 2.107$ and $H/D = 6.0$ 283

7.17 C_f Value Predicted from Numerical Model for $L/H = 1.580$ and $H/D = 8.0$ 284

7.18 β_{TOP} Ratios 293

7.19 β_{BOT} Ratios 294

7.20 Dimensionless Shear Stress Number for Horizontal Portion of Wet Well Floor with $L/H = 1.580$; $H/D = 8.0$; $W/L = 0.475$ 297

7.21 Dimensionless Shear Stress Number for Horizontal Portion of Wet Well Floor with $L/H = 2.107$; $H/D = 6.0$; $W/L = 0.475$ 298

7.22 Dimensionless Shear Stress Number for Horizontal Portion of Wet Well Floor with $L/H = 3.160$; $H/D = 4.0$; $W/L = 0.475$ 299

7.23 Dimensionless Shear Stress Number for Inclined Portion of Wet Well Floor with $L/H = 1.580$; $H/D = 8.0$; $W/L = 0.475$ 300

7.24 Dimensionless Shear Stress Number for Inclined Portion of Wet Well Floor with $L/H = 2.107$; $H/D = 6.0$; $W/L = 0.475$ 301

7.25 Dimensionless Shear Stress Number for Inclined Portion of Wet Well Floor with $L/H = 3.160$; $H/D = 4.0$; $W/L = 0.475$ 302

7.26 $\tau_C - d_S$ Envelope 303

FIGURE PAGE

7.27 Relationship Between Dimensionless Shear Stress and Dimensionless Grain Size for L/H = 1.580, 2.107 and 3.160 305

7.28 Relationship Between C_{fopt} and C_{feqn} 307

7.29 Probable Error in Shear Stress Prediction 308

7.30 Extrapolation of the Ratio of the Torques Associated with the "$T_{\Delta m}$" and "F" Forces 319

7.31 Design Example Results 321

CHAPTER 1

INTRODUCTION

1.1 Preamble

The pumping stations represent a significant fraction of the cost of any water or wastewater treatment scheme. Proper design procedures must be developed to minimize energy and maintenance requirements. This design must also minimize vortex activity, sump volume and sediment deposition.

The slope of the wet well floor determines the ease with which solids and fluids are moved through the pumping station; however, there is little agreement in the literature as to acceptable floor configurations. Some of the commonly used recommendations are quoted below:

> "Although it is generally agreed that proper pump suction conditions should be maintained and that the deposition of solids in the wet well should be minimized, opinions vary greatly on how to accomplish these ends. Probably the most controversial point in the design of wet wells is the bottom slope needed to minimize deposition of solids. A relatively large number of state regulatory agencies call for a minimum bottom slope of 1:1 to the pump inlet". (WPCF, 1981)

> "Wet wells and suction channels should be designed so that dead areas where solids and scum may accumulate are avoided. The bottom should be sloped as steeply as possible in the direction of flow so that deposits and scum accumulations are carried to the pump suctions by the scouring action of the high velocities at low operating levels". (ASCE, 1977(b)).

> "A sump which handles solid matter in suspension needs special care. The slope of the benching is usually not critical between 30° and 60°, but it is important to avoid the sewer discharging directly into a pool of water because a free falling jet would result in air entrainment". (Prosser, 1977).

> "The floor of the wet well should sloped at 1 in 1, or steeper, to a sump at the pump suctions. Many engineers prefer a slope of about 1.75 vertical to 1 horizontal, but on the other hand these steeper slopes are inconvenient for maintenance". (Bartlett, 1974).

Uncertainties and contradiction abound in the literature. "Rules of Thumb" design methods have been in use for the last 30 years, often resulting in severe siltation problems.

No extensive review of sedimentation in sumps has been undertaken. Scattered short discussions and test results are provided in different journals over a period extending back to the 1890's. Most of these articles were concerned with the layout of the pumping equipment. No evidence exists as to tests specifically performed to determine optimum floor slope conditions.

Prior to any experimental work, an extensive literature review of wet well design was carried out and is presented in Chapter 2.

Chapter 3 presents a literature review of significant factors which must be considered when dealing with the initiation of particle motion on the wet well floor.

The formulation of the numerical model is given in Chapter 4. A detailed description of the drift flux formulation to describe the diffuser plume, and the linear and angular momentum approach to describe the main sump flow are presented.

Chapter 5 deals with a description of the physical model employed for calibration purposes, and gives a qualitative description of sources of errors.

Chapter 6 presents and discusses the significance of the physical model experiments. Numerical model calibration and sensitivity is given in Chapter 7. A detailed design example and application is also given in Chapter 7.

Conclusions and recommendations for additional research are given in Chapters 8 and 9, respectively.

The Structured WATFIV program listing, sample input, output and program nomenclature are given in Appendix 1.

1.2 Objective and Scope

The objectives of this dissertation were:

(i) to identify the factors which affect the behaviour of solids on the floor of the wet well,

(ii) to investigate the use of a compressed air diffuser as an auxiliary power source to aid in scouring the particles,

(iii) to develop a numerical model to describe the circulation pattern within the sump under various air diffuser and pump operating conditions,

(iv) to validate and calibrate the numerical model via physical modelling, and

(v) to investigate the validity of the numerical model under large scale conditions.

CHAPTER 2

LITERATURE REVIEW

WET WELL DESIGN

2.1 General

A comprehensive review of pumping station wet well design has been provided previously by Machina (1983) and Machina and Bewtra (1983). Significant developments in sump design are reviewed herein to present the factors which are important in proper wet well design.

In the design of wet wells, the bell-mouth submergence and spacing are of primary importance. Richardson (1941) pointed out that the following considerations should be given when laying out the location of suction bells:

(i) distance between the suction bell and the bottom of the wet well,

(ii) distance between the suction bell and any obstruction,

(iii) the minimum submergence of the suction bell for maximum flow.

Richardson stated that the flow in the region of the suction bell should be free of vortices. Any change in the direction of flow will tend to form vortices, and it is important that ample space between any obstruction, such as columns, other suction bells, walls, etc., be provided to permit dissipation of the vortex before reaching the suction bell entrance. Richardson recommended minimum values of D/2, D and 2D for the bottom clearance, wall clearance and distance between suction bells, respectively, where D is the suction bell diameter. He specified a minimum submergence of D/2 and recommended that this value be increased if strainers were used over the bell-mouth entry. Richardson's guidelines appear to be the earliest specifications for suction bell clearances and submergence.

Brkich (1953) further studied wet well design and made additional recommendations and refinements. A bottom clearance of D/3 as the minimum and D/2 as the maximum was recommended. Rear wall clearance was changed from D, proposed by Richardson, to 0.75D. It was recommended to insert triangular blocking, measuring D/2 on each side, into the corner between the side and rear walls of the wet well to prevent the formation of vortices in corners. Brkich also stated that the approach channel should produce an even distribution of water just upstream of the pump intakes. A plane of 0.75D upstream from the bell-mouth centre line was proposed for reference.

For pumps arranged in a single row in one long channel, Brkich gave the minimum channel width as being

$$W = D + D^2 (4 + 8N)/3H \tag{2.1}$$

where W = channel width, N = number of pumps downstream of the pump under consideration, and H = water depth. It was stressed that, if possible, putting a number of pumps in one long channel should be avoided in order to prevent mutual interference. If a long channel is used, the velocity in the channel should be the same as for single-pump installations. All attempts should be made to eliminate turbulence in the flow as it may pass from one pump to the next.

The work of D.F. Denny and his colleagues at the British Hydromechanics Research Association has been instrumental in advancing the work on wet well design.

Denny (1956) stated two aspects of problems with respect to vortex formation in wet wells. Firstly, swirl in the sump leads to rotation of the water in the suction pipe, which may impair the performance of the pump. Secondly, severe swirl sometimes leads to a fully developed vortex having a hollow core through which air is drawn into the suction inlet. Apart from the effect of the air itself, which tends to lower the delivery of the pump, such vortices are unstable and give rise to unsteady swirl flows in the pipe, and to fluctuating loads on the pump bearings. Denny and Young (1957) observed that the air carried into the intake may easily reach 5% of the water flow, whereas it was known that 1% of air was capable of reducing the efficiency of a centrifugal pump by as much as 15%. The origin of the problem of persistent rotational flow lies in the relation between the position of the intake and the direction of the approaching flow. If, in the oncoming flow there is a resultant angular momentum about a vertical axis at the intake, then rotational flow will result which may develop into an air-entraining vortex. Denny and Young pointed out that it would be erroneous to suppose that such vortices originated at the intake itself, which merely acted as a sink to withdraw water from a particular place at a particular rate. It was determined that even the shape and direction in which the intake faced were very minor factors in this phenomenon because the tail of the vortex could turn through large angles with ease.

Rotation in the approaching flow can arise from a number of causes, and the two most frequently encountered are:

(i) asymmetry of the intake with respect to the boundaries of the approaching flow, and

(ii) change in the direction of the boundaries immediately upsteam of the intake.

Denny and Young observed that it was not always possible to avoid serious rotation in the flow approaching the intake, but fortunately other factors such as depth of water, velocity through the intake, etc., which were usually under the control of the designer, also had a large influence on the formation of vortices and on the swirl at the intake. They developed a curve relating the water depth to the suction pipe velocity for a given set of boundary conditions and approaching flow pattern as shown in Fig. 2.1. It was observed that the boundary between vortex-forming and vortex-free conditions was not very precise. The criterion used was whether, after a reasonable time at steady conditions of depth and flow, any air from the free water surface entered the intake, either continuously or intermittently. The shape of the boundary curve varied with the circumstances but in general the curves had one limb tending to become asymptotic to a constant velocity and another limb tending to become asymptotic to a constant depth. In other words, there was one region at low intake velocities where the submergence was very dependent on the velocity through the intake, and another at high intake velocities where the submergence was not so dependent on velocity.

Denny and Young also studied varying the degree of angular momentum about a vertical axis by varying the width of the sump through which the water was allowed to enter. Rotational flow was

8" pipe in an 8' sump
Bottom Clearance, C/d = 0.90

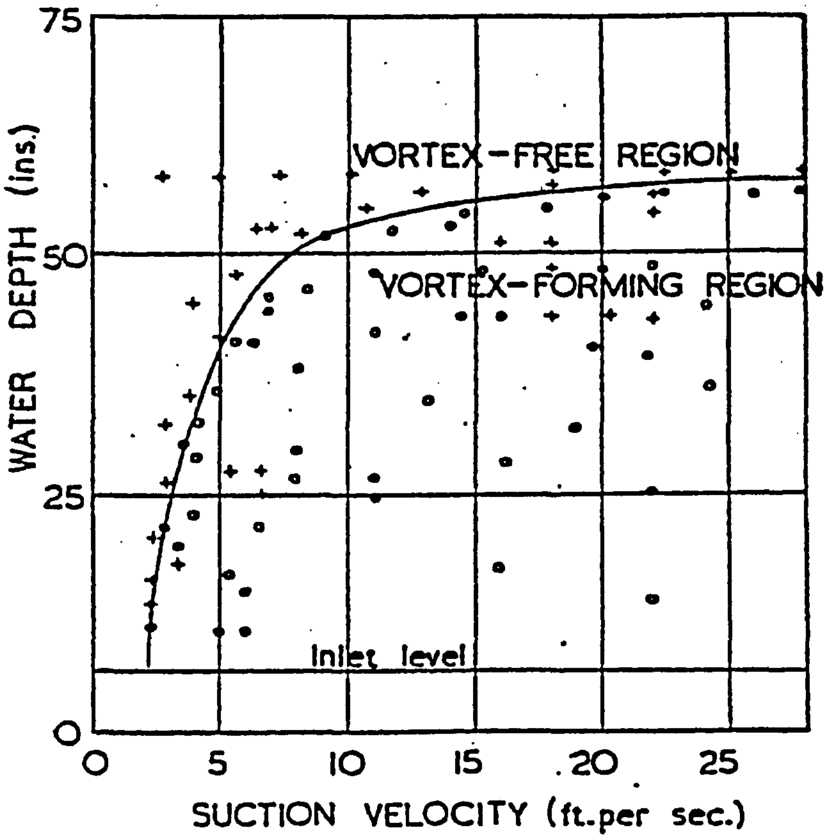

+ Indicates no vortex formed
0 Indicates vortex formed

Fig. 2.1 Suction Velocity vs. Water Depth for Vortex-Free and Vortex-Forming Region (after Denny and Young, 1957)

strongest when the water entered through half the width of the sump and this condition caused the most severe vortices, requiring a critical submergence, S, of 15 bell-mouth diameters to prevent air-entrainment at high velocities, Fig. 2.2. With the water entering over the whole width of the sump, i.e. a nominal zero resultant angular momentum, the critical submergence was only 3.5 diameters at high velocities. Thus a fourfold change in the critical submergence at high velocity was effected merely by varying the angular momentum about the intake in the approaching flow. Denny and Young also investigated the effects of boundaries on the critical submergence. The effects of bottom clearance below a vertical intake pipe with upward flow are shown in Fig. 2.3. The tests were conducted with a 102 mm pipe in a 2.44 m square sump and a 22 mm pipe in a 610 mm square sump with similar entry conditions. The results for the two models were precisely similar and demonstrated that as the bell-mouth was raised from the floor, the critical submergence decreased, although the actual water depth increased considerably. When the intake was moved about the sump it was found that the critical submergence was greater when the intake was nearest the centre of the sump and least when the intake was close to the walls. The critical submergence was smaller for a given size pipe in a smaller sump, and also for a larger pipe in a given size sump. Figure 2.4 shows the correlation of the results, using both different pipes and different sumps in which the rotational flow was nominally the same, and when the suction pipe was equidistant from two adjacent walls. The

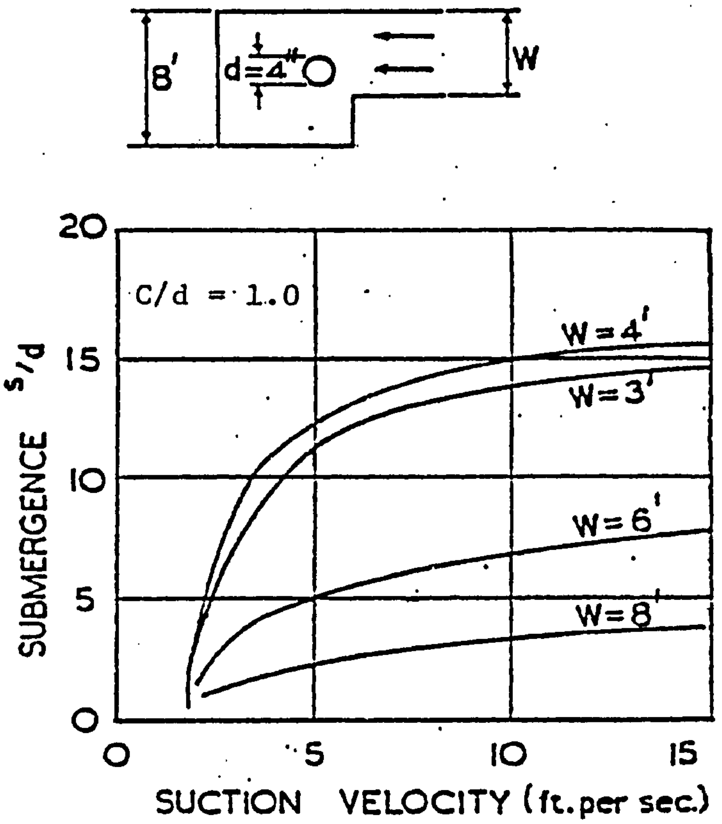

Fig. 2.2 The Effect of Changing the Angular Momentum on the Critical Submergence (after Denny and Young, 1957)

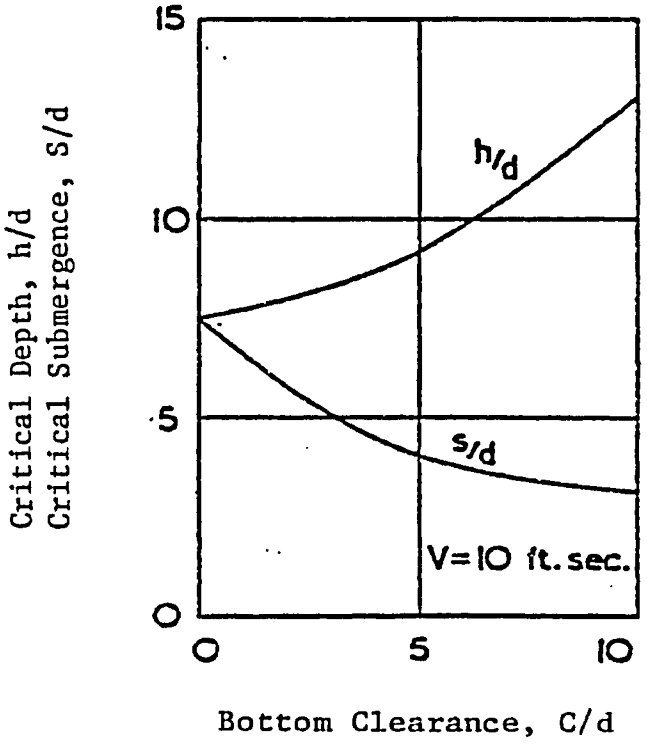

Fig. 2.3 The Effect of Bottom Clearance on Critical Submergence (after Denny and Young, 1957)

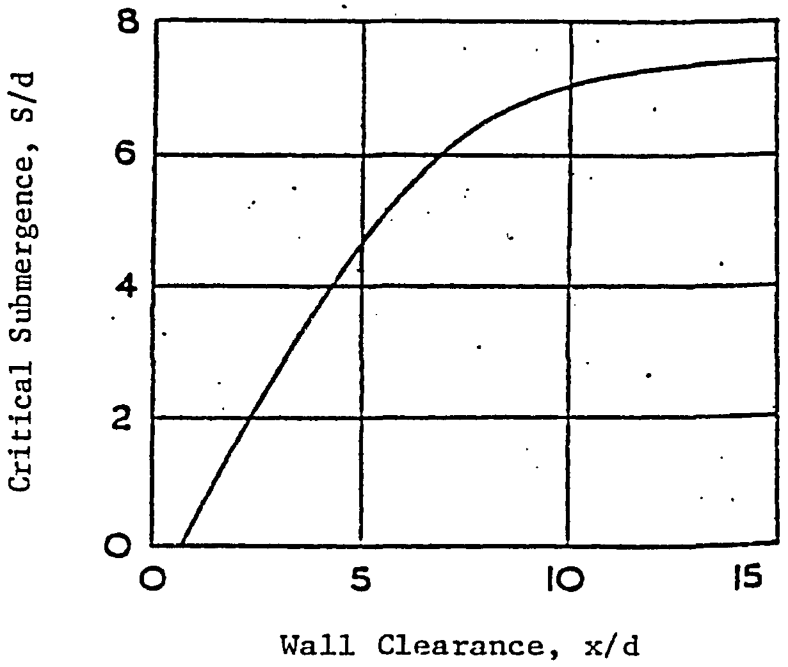

Fig. 2.4 The Effect of Wall Clearance for Various Suction Pipe Sizes Located Equidistant from Two Adjacent Walls (after Denny and Young, 1957)

critical submergence was independent of wall clearance when this exceeded ten pipe diameters and was approximately proportional to wall clearance when this was less than five diameters. The results for an inlet in the wall were very similar to those for a vertical pipe close to the wall. These studies also indicated that the shape of the intake had very little effect on vortex formation. Upward and downward facing vertical intakes behaved very much alike, but with horizontal intakes, the disposition of the intake relative to the vortex zone in the sump appeared to be important.

Research on vortex formation, submergence and sump geometry continued by many researchers who all built upon and refined the fundamental research of Denny and Young. Investigations by Brewer (1957), Dornaus (1958), Shahroody and Davis (1964), Hattersley (1965), Linford (1965), Berge (1966), Paterson and Campbell (1968), Zanker (1968), Bird (1968), Anwar (1968), Gordon (1970), Quick (1970), Messina (1971), Reddy and Pickford (1972), Swainston (1974, 1976), Nakato and Kennedy (1976), and Farell (1976) have all contributed to the increased state of knowledge with respect to vortex-free sump design.

2.2 Current Practice

2.2.1 General

Prosser (1977) and the Hydraulic Institute (1983) analyzed the data and experimental results published in the twenty-year period from 1957 to 1977 and have set forth the design standards for sump well design. Prosser described the desirable flow conditions approaching an intake as being uniform, steady and of single phase:

uniform flow - the velocity, in magnitude and direction, of fluid particles is the same at all points across the section considered

steady flow - the velocity, in magnitude and direction, does not change with time

single phase flow - there is no entrained air, vapour or other gases.

He divided a typical pump intake and sump arrangement into four sections or zones as follows:

Zone I: The water is channelled into the pumping station as free surface flow or as internal flow through an inlet culvert. There may be several inlet channels, or the water may be taken from a natural stream or river. The final entry into Zone II is often through a control structure.

Zone II: This zone contains items such as screens for removing solid matter from the water and division walls to control the flow into the appropriate sump (Zone III).

Zone III: The sump is usually rectangular, and except for sewage applications, has a flat floor. A sump may serve more than one pump. The intake may be a suspended bell-mouth or it may be built, wholly or partly, into a wall. The primary purpose of the sump is to provide stored volume and to damp out any extremely distorted flow patterns arising from Zone II.

Zone IV: This is a short section of pipe between the intake and the pump impeller. In some cases, this section can be fairly long and perhaps contain several bends and changes in cross-section. The flow should always fill this pipe section to ensure that there is no free surface. With a long inlet pipe, the flow patterns at the pump are influenced by the design of the bends and the changes in the pipe cross-section are not influenced much by poor conditions at the intake. Long suction pipes are unusual since they introduce a large pressure drop with the consequent possibility of cavitation at the pump.

2.2.2 Wet Well and Dry Well Pumping Stations

A pump can be installed in a wet or dry well. Figure 2.5 illustrates a vertical suspended pump in a wet well and a similar pump

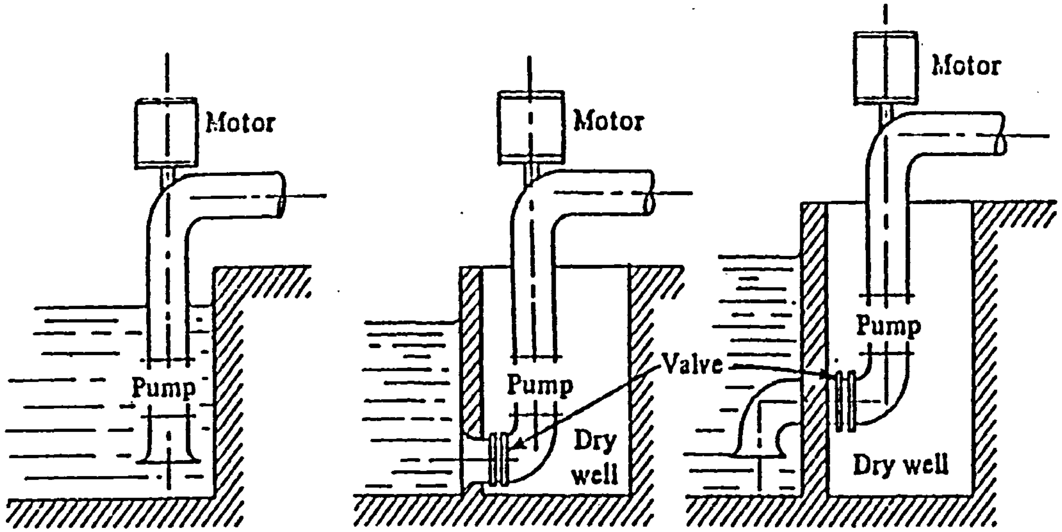
Motor
Pump
Motor
Pump
Valve
Dry well
Motor
Pump
Dry well

(a) Wet well

(b) Dry well – horizontal flow intake

(c) Dry well – turned-down intake

Fig. 2.5 Wet and Dry Well Pump Installations (after Prosser, 1977)

in a dry well. In a dry well, the bell-mouth may be directly in the wall or turned down through an angle of up to 90^o as shown.

The wet well has the great advantage of simplicity, and is widely used. However, maintenance can be a problem as it involves de-watering the sump or lifting the pump unit out of the well. The wet well arrangement is very suitable for intermittent duty such as for pumping storm water where the well will be dry for most of the time.

The dry well configuration is usually used when reliablity is a prime requirement, since the pump can be reached and maintained at all times. The "turned-down" bell-mouth of Fig. 2.5(c) is a popular arrangement in sewage applications since it allows a lower submergence in the sump than a horizontal intake, Fig. 2.5(b), and in general is less prone to vortex action at similar submergences.

2.2.3 Bell-mouth Design

The main pupose of a bell-mouth entry to a circular pipe is to eliminate the flow separation which occurs with a sharp edged inlet, as shown in Fig. 2.6. This ensures that the flow is uniform throughout the intake cross-section (assuming that the approach flow in the sump is reasonably uniform) and that the head losses associated with the intake are minimal.

For an intake in a vertical wall, replacing the sharp edge by a radius equal to about one-tenth of the pipe diameter is the minimum required. A freely suspended bell-mouth would need a larger radius to cater to the flow coming from behind the bell-mouth. In practice,

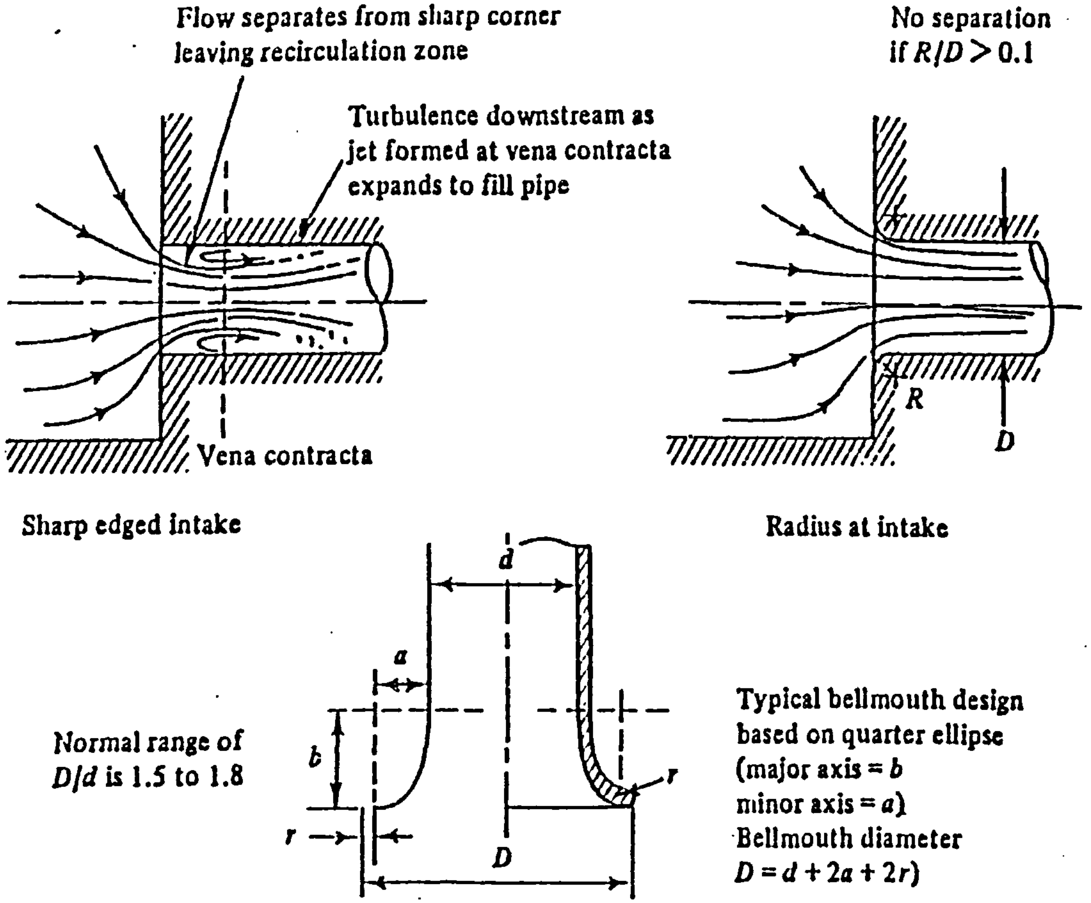
Flow separates from sharp corner leaving recirculation zone
Turbulence downstream as jet formed at vena contracta expands to fill pipe
Vena contracta
Sharp edged intake
No separation if $R/D > 0.1$
R
D
Radius at intake
d
a
b
r
D
Normal range of D/d is 1.5 to 1.8
Typical bellmouth design based on quarter ellipse (major axis = b minor axis = a) Bellmouth diameter $D = d + 2a + 2r$)

Fig. 2.6 Bell-mouth Design (after Prosser, 1977)

most pump manufacturers specify bell-mouth shapes which are usually based on a quarter of an ellipse. The bell-mouth diameter D is usually in the range of 1.5 to 1.8d, where d is the inlet pipe diameter.

2.2.4 Recommended Sump Design

Examples of satisfactory sump design practice, suggested by Prosser (1977), are illustrated in Figs. 2.7 to 2.13. The preferred designs define the basic parameters of good sump design, but the main points to remember when considering the design of the whole sump system, Zones I, II and III are:

(i) The flow approaching the pump intake, whether a horizontal or a vertical bell-mouth, should be uniform across the width of the channel.

(ii) The kinetic energy associated with changes in level, whether down a slope, or over a weir, should be dissipated well away from the final approach to the pump(s).

(iii) Obstructions, such as supporting pillars, should be streamlined to eliminate flow separation near the intake section.

(iv) Areas where stagnant water could occur should be filled in.

(v) Average velocities must be kept low: about 0.6 m/s maximum for flow into the pumping station and 0.3 m/s maximum for the approach flow to the bell-mouth if there are no solids in the water. For sewage, the mean velocity should be greater than 0.7 m/s at all sections.

(vi) Screens used for trash exclusion also act as flow straightening screens. Trashracks and screens must be sited so that they serve this dual function where possible.

The clearance of the bell-mouth from the floor, C, should be in the range of 0.5 to 0.75 times D, the bell-mouth diameter. If C is less than 0.25D, the flow area under the lip of the bell is less than the flow area into the bell and the resulting deceleration causes

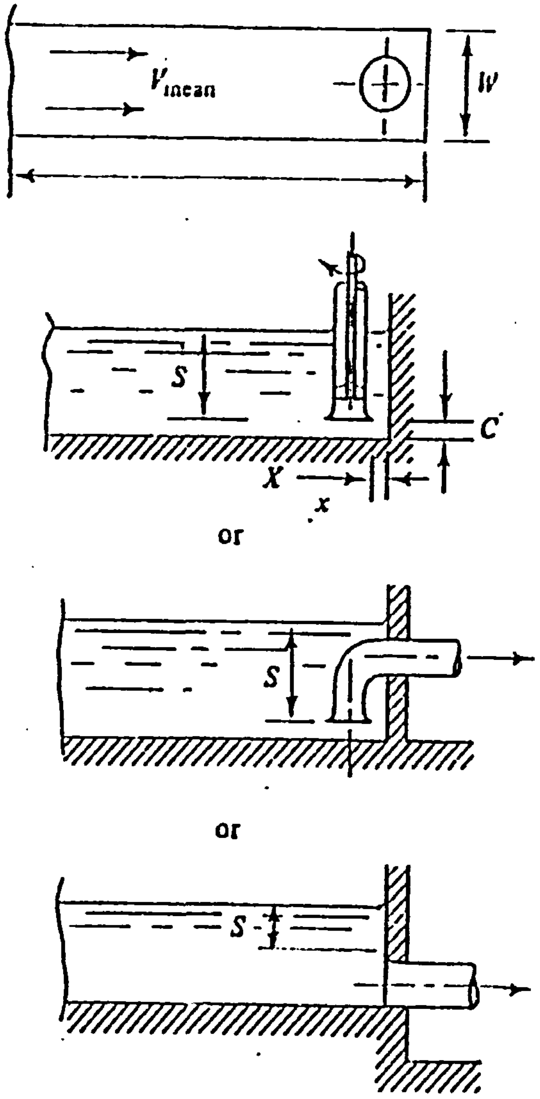

X = Horizontal distance from bellmouth to rear wall
C = Height of bellmouth above sump floor, for vertical intake
S = Height of water surface above bellmouth
D = Bellmouth outer diameter
L = Sump length, with uniform cross-section; measured from rear wall to first major upstream change of cross-section
W = Lateral width of sump
V_n = Mean velocity in sump
Q = Flow rate

Good features

1. Bellmouth near to sump floor; $C \simeq \frac{1}{2}D$
2. Intake close to rear wall; $X \simeq \frac{1}{4}D$
3. Flat sump floor
4. Width about $2D$; up to $3D$ acceptable
5. Deep water, S large and at least greater than $1\frac{1}{2}D$
6. Long approach from upstream obstructions; L large and at least greater than $4D$
7. Mean approach velocity should be low; $V = \dfrac{Q}{W(S+C)}$ should be less than 0.3 m/s

Fig. 2.7 The Main Aspects of a Good Single Cell Sump (after Prosser, 1977)

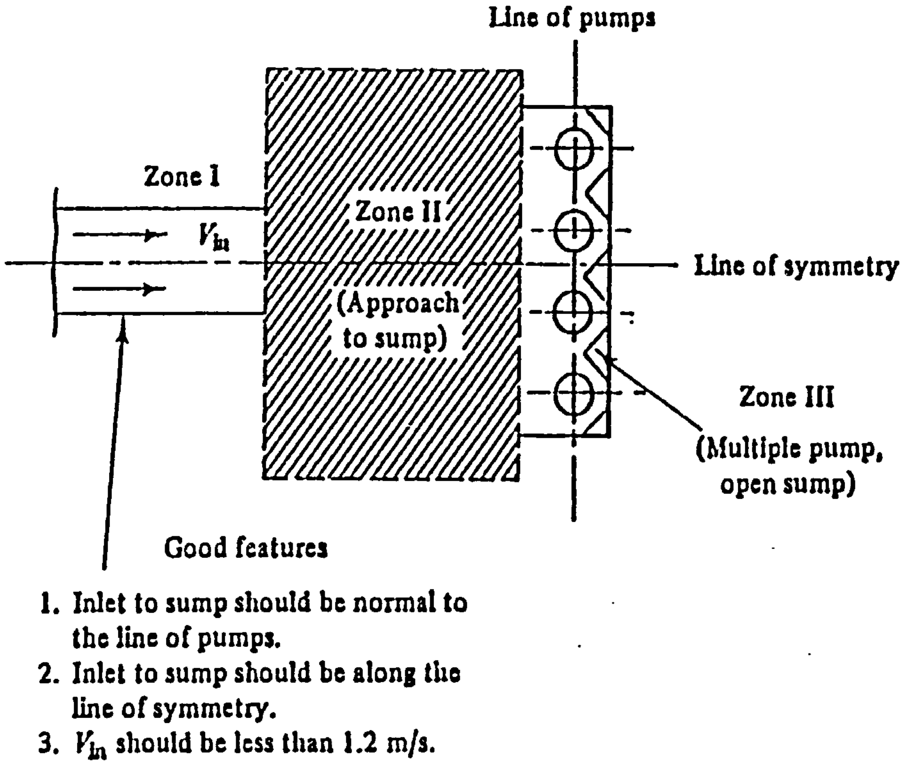
Line of pumps
Zone I
V_{in}
Zone II
(Approach to sump)
Line of symmetry
Zone III
(Multiple pump, open sump)

Good features

1. Inlet to sump should be normal to the line of pumps.
2. Inlet to sump should be along the line of symmetry.
3. V_{in} should be less than 1.2 m/s.

Fig. 2.8 General Layout for the Inlet (Zone I) to a Multiple Pump Sump (after Prosser, 1977)

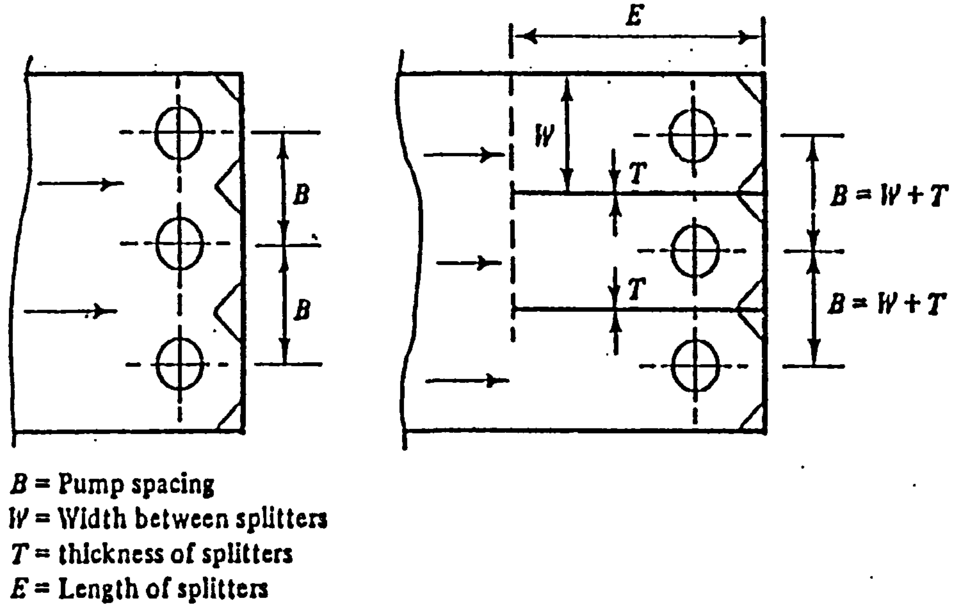
E
W
T
T
B
B
B = W + T
B = W + T
B = Pump spacing
W = Width between splitters
T = thickness of splitters
E = Length of splitters

Fig. 2.9 General Layout for a Multiple Pump Sump (Zone III) (after Prosser, 1977)

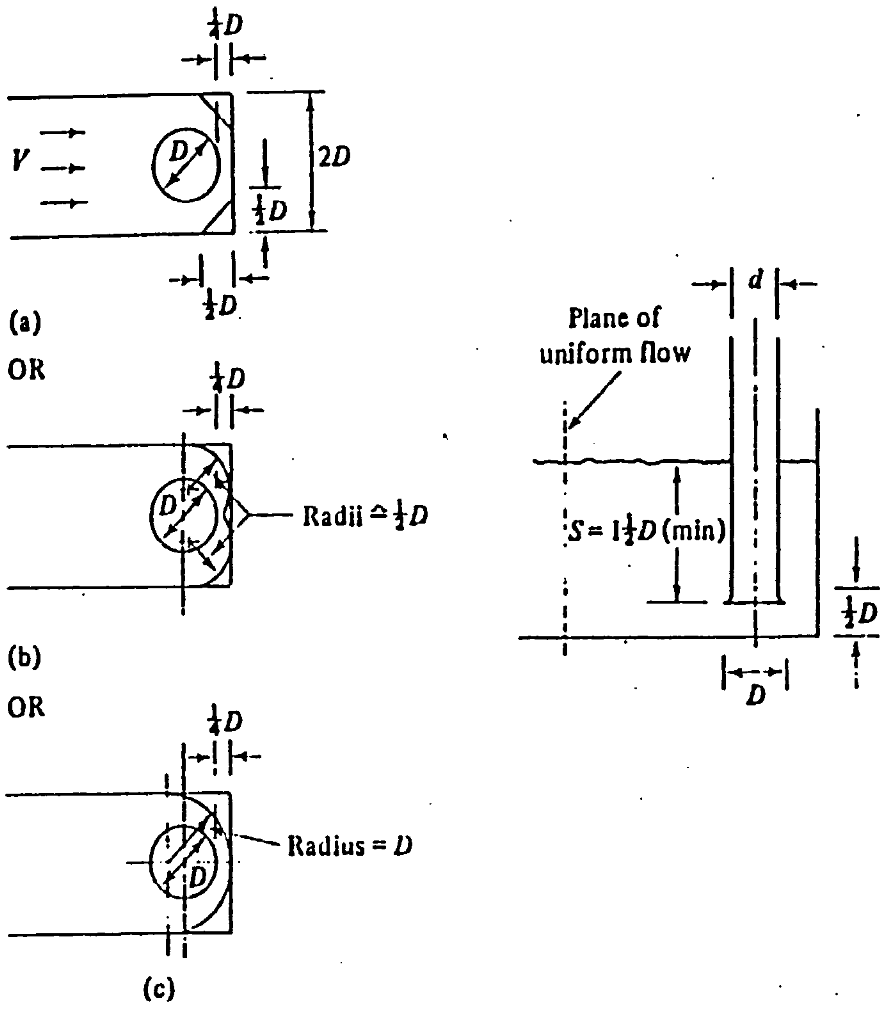
¼D
V
D
2D
½D
¼D
(a)
OR
¼D
D
Radii ≏ ½D
(b)
OR
¼D
Radius = D
D
(c)
d
Plane of
uniform flow
S = 1½D (min)
½D
D

Fig. 2.10 Basic Design for a Single Pump Wet Well Sump with a Vertical Intake (after Prosser, 1977)

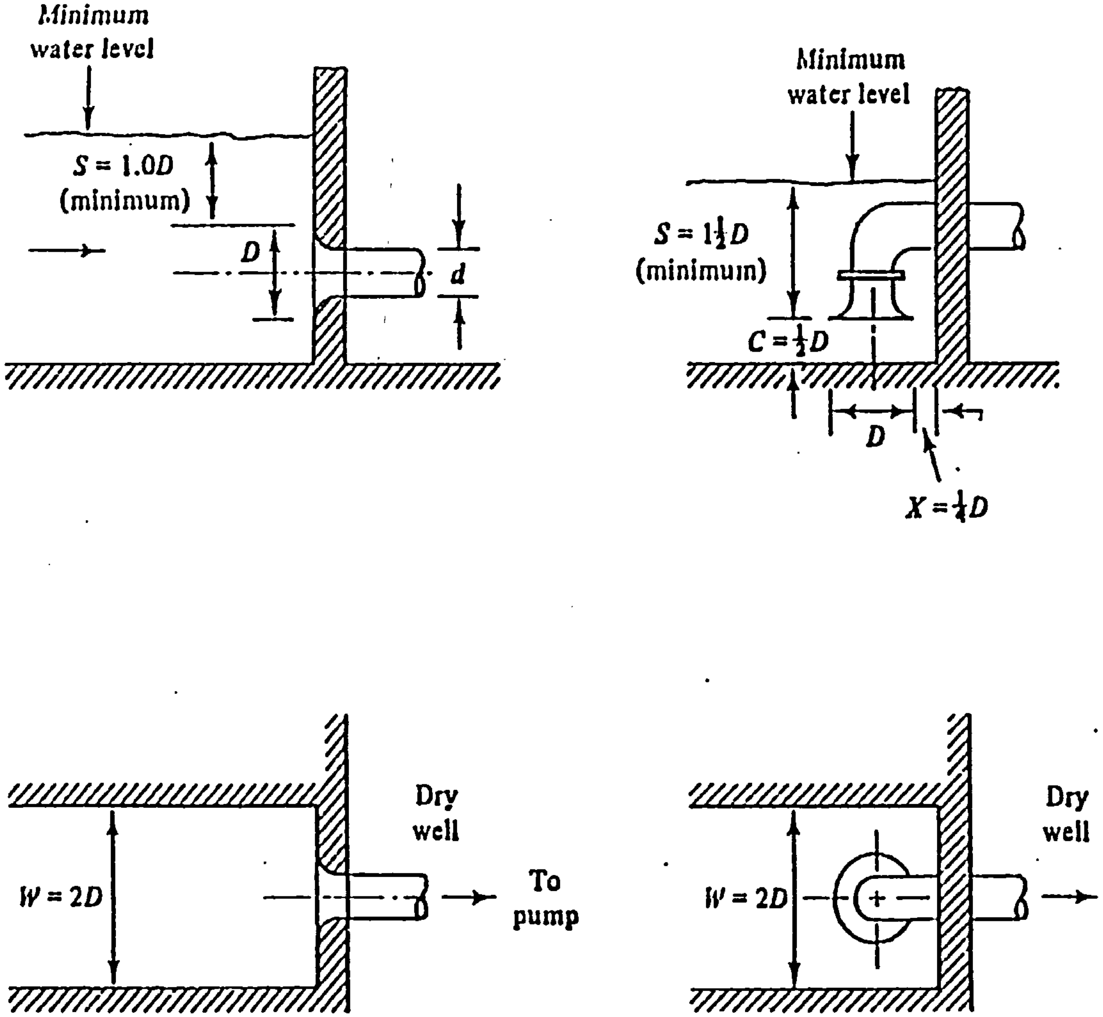
Minimum water level
S = 1.0D (minimum)
D
d
Minimum water level
S = 1½D (minimum)
C = ½D
D
X = ¼D
W = 2D
Dry well
To pump
W = 2D
Dry well

(a) Horizontal intake

(b) Turned-down bellmouth

Fig. 2.11 Basic Design for a Single Pump Dry Well Sump (after Prosser, 1977)

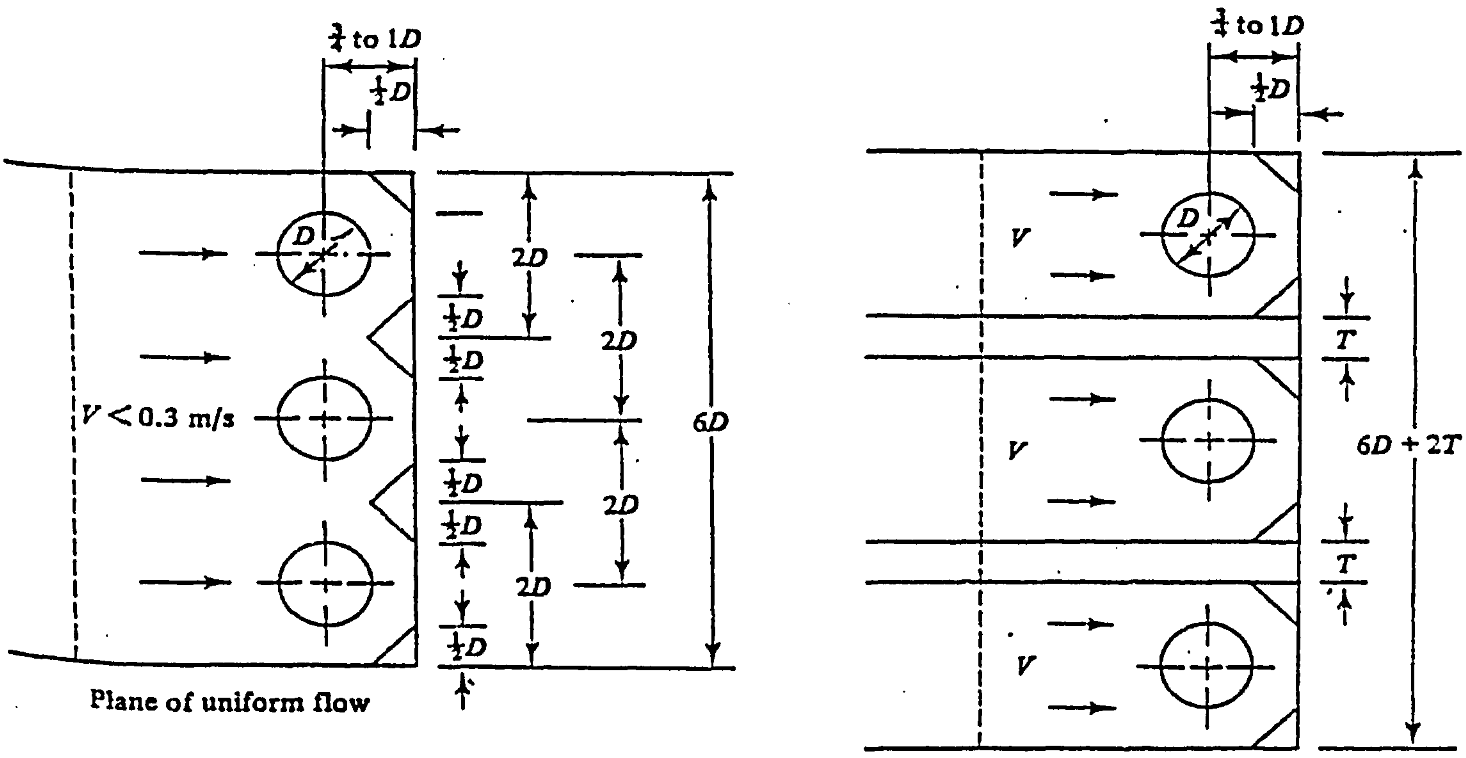

¾ to 1D
½D
D
V < 0.3 m/s
2D
½D
½D
2D
½D
½D
2D
½D
½D
2D
½D
6D
Plane of uniform flow
¾ to 1D
½D
D
V
V
V
T
T
6D + 2T

(a) Open sump

(b) Unitised sump

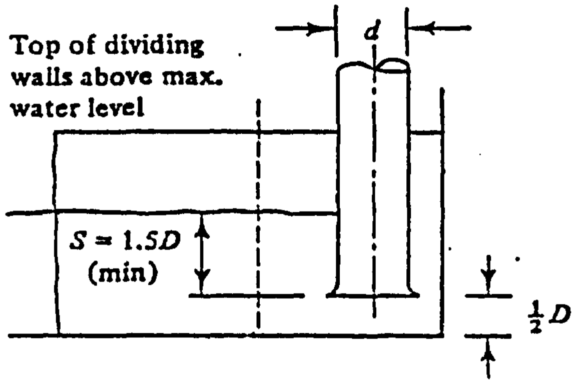

Top of dividing walls above max. water level
d
S = 1.5D (min)
½D

Fig. 2.12 Basic Design for a Multiple Pump Wet Well Arrangement (after Prosser, 1977)

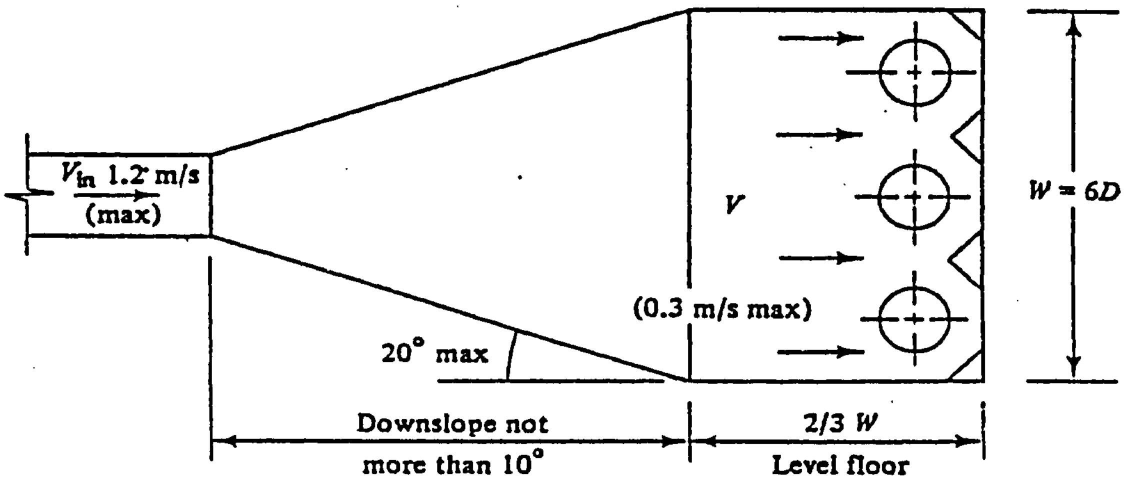
V_{in} 1.2 m/s
(max)
V
(0.3 m/s max)
20° max
Downslope not
more than 10°
2/3 W
Level floor
W = 6D

(a) Example of open sump design

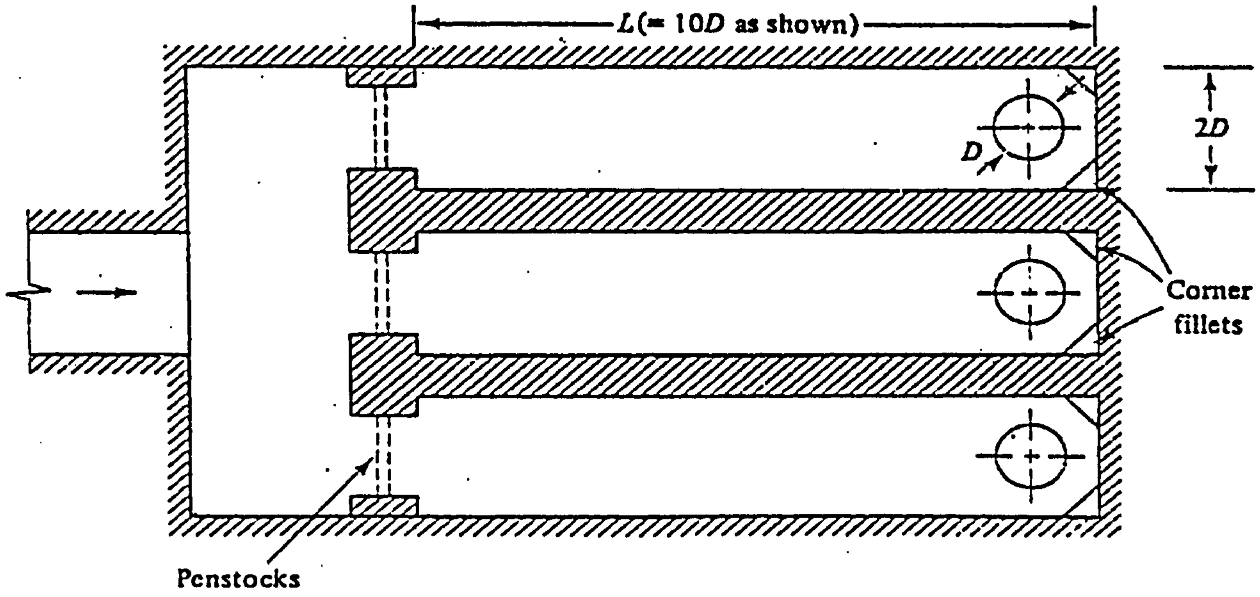
L(= 10D as shown)
2D
D
Corner
fillets
Penstocks

(b) Example of unitised sump design

Fig. 2.13 Plan Views of Multiple Pump Sumps, including the Approach Works to the Sump
(after Prosser, 1977)

unsteady flow in the bell-mouth. If C is greater than D there is a tendency for the upward component of flow into the bell-mouth to become unstable and promote swirling flow. The proximity of the end and side walls to the bell-mouth inhibits the production of swirling flow and vortex formation.

In multiple pump sumps, the pump spacing, B, should be 2 to 2.5D, although satisfactory conditions can be obtained up to 4D if the increased spacing is required for access to the motors. If the flow distribution is skewed or from the side, and when less than the maximum number of pumps are operating, splitters may be necessary. If splitters are to be used, E, the length of the splitters, should not be less than 4D.

The basic design for a simple rectangular sump suitable for a single pump is shown in Figs. 2.10 and 2.11. The dimensions are given in terms of the bell-mouth diameter, D. Tolerances on these recommended dimensions are not critical to about plus or minus 20 percent (Prosser, 1977).

It may be convenient to make the end wall in the form of a circular arc rather than use corner fillets. As long as the principle of 0.25D minimum space between the bell-mouth and the wall is maintained, the design proves satisfactory. Thus, in Fig. 2.10, (b) and (c) are alternatives to the standard shape shown in (a). These designs are applicable if there is uniform, steady, single-phase flow through the channel cross-section upstream of the bell-mouth. The distance of this plane of uniform flow from the bell-mouth centre line is about 3D. When significant variations occur in the velocity and turbulence distribution at this section, problems begin to occur. For mildly non-uniform conditions, which in practice occur in many sumps, remedial measures include increasing the submergence and using structures such as cones, splitters or crosses underneath the bell-mouth.

The designs shown in Fig. 2.12 provide two alternative ways of installing three pumps in a sump where uniform steady flow occurs just upstream of the intakes. These designs give the preferred way of defining the final part of the sump, Zone III. The wet well designs shown in Fig. 2.12 can be easily adapted for dry well installation of the pumps. The plan dimensions should be the same whether the intake is a turned down bell-mouth or a horizontal intake through the end wall. The corner fillets or radii need not be used if the intakes are horizontal.

Examples of multiple sump designs which include the approach to the sump are shown in Fig. 2.13. The problem of providing steady, uniform flow to a multiple sump is made more difficult because, in the majority of cases, the intakes must function satisfactorily with all possible combinations of pumps in operation.

The unitized design shown in Fig. 2.13(b) would function correctly, since the approach length of each unit, L, can be a conservative value based on the single pump design. The open sump design shown in Fig. 2.13(a) may require baffles or splitters or a grid in order to distribute the flow evenly to all pumps. Since the need for these devices and the siting of them depends upon the specific design under consideration, no basic design details can be given. The best way to determine the details is with the aid of hydraulic models.

The design guidelines published by the Hydraulic Institute (1983) are given in Figs. 2.14 and 2.15. These figures were developed for pumps normally operating in the capacity range of 3000 to 300000 USGPM (0.19 to 18.93 m^3/s). All of the dimensions in Fig. 2.14 and Fig. 2.15 are based on the rated capacity of the pump at the design head. If the operation at an increased capacity is to be undertaken for considerable periods of time, the maximum capacity should be used for the design value in obtaining sump dimensions.

2.2.5 Minimum Submergence Requirements

The choice of the minimum submergence of a pump is usually a critical design decision. The minimum water level, MWL, in a pumping station is often defined by external conditions, such as the level of an incoming pipe or culvert, or the net positive suction head requirements of the pump. Thus, the sump floor level, SFL, is defined as

$$\text{SFL} = \text{MWL} - (C + S) \qquad [2.2]$$

As noted earlier, the optimum clearance, C, between the bell-mouth and the sump floor is about 0.5D. Therefore, the submergence, C, should be kept as small as possible to reduce the cost of the structure.

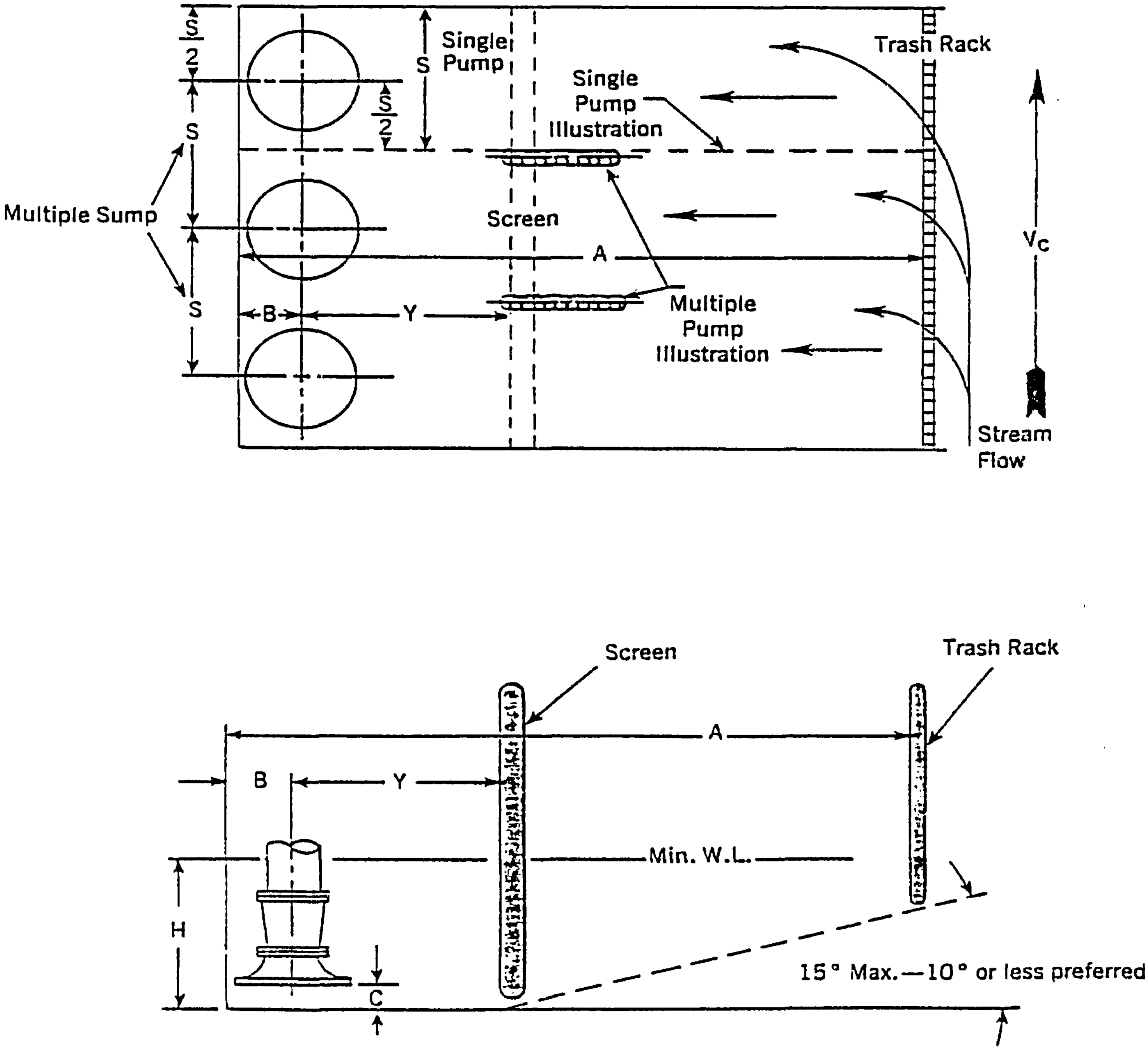
S/2
S
Single Pump
S/2
Single Pump Illustration
Trash Rack
S
Multiple Sump
Screen
A
S
B
Y
Multiple Pump Illustration
Vc
Stream Flow
Screen
Trash Rack
A
B
Y
Min. W.L.
H
C
15° Max.—10° or less preferred

Fig. 2.14 Plan and Elevation of Recommended Sump Dimensions (after Hydraulic Institute, 1983)

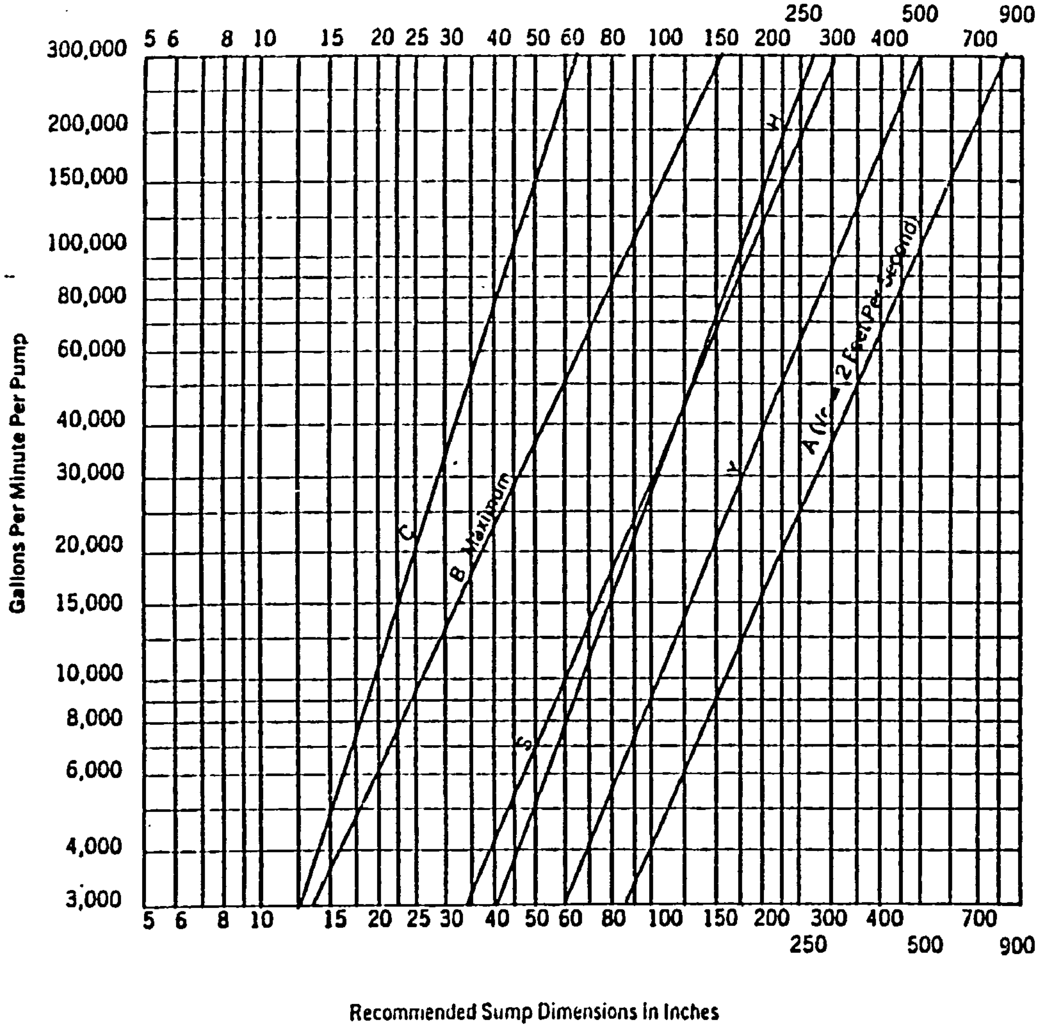

Fig. 2.15 Dimensions A, B, C, H, S and Y Corresponding to Fig. 2.14 (after Hydraulic Institute, 1983)

The minimum submergence, or critical submergence, S_C, is usually defined as the submergence when air-entraining vortices form. The critical submergence was found to depend on the mean velocity in the bell-mouth, V_B, and the bell-mouth size, D. The general trend was that S_C/D increased as V_B increased and that for a given V_B, S_C/D was slightly less for larger intakes than for smaller intakes (Prosser, 1977). Satisfactory values of S_C may be obtained from Fig. 2.15 once the pump capacity is known. For a given flowrate, Q, or the corresponding velocity, V_B, the critical submergence can be calculated from the water depth, H, and the bottom clearance, C, as

$$[2.3] \qquad S_C = H - C$$

Prosser (1977) reported that for most practical applications the range of S_C/D was from 1 to 10 and that V_B was usually similar for all fixed speed pumps, so that the value of S = 1.5D, as shown in Figs. 2.7, 2.10, 2.11 and 2.12, represented a reasonable design value. For variable delivery pumps, where V_B was smaller than normal for some operating conditions, S_C could be less than 1.5D.

In general, the submergence of an intake should be large enough to reduce the possible occurrence of air-entraining vortices, swirling flow and the effects of any surface waves which may arise. Therefore, there is a conflict in that a conservative design with a deeply submerged intake costs more than a design in which the minimum submergence is only just adequate. The minimum submergence value of 1.5D is based on the assumption that the approach flow to the bell-mouth is ideal. Slight departures from this ideal condition can be offset by increasing the minimum submergence, but obviously it would be very expensive to compensate in this way for very poor approach conditions.

2.3 Basic Concepts of Vortex Formation

Prior to the research of Fraser (1953) and Iversen (1953) little consideration had been given to the formation and modelling of vortices in pump intakes.

Fraser studied the flow impinging on the back wall of the sump. He noted that a portion of the incoming flow continued until it struck the back wall of the sump, and owing to this impact, the water level built up and the flow was reversed back toward the pump. The level immediately downstream from the pump was lowered by the wake caused by the diversion of flow around the pump body in addition to the drawdown caused by the reduction in pressure at the pump suction. The difference between levels at the back wall and the wake of the pump may cause severe turbulence which may create or destroy vortices.

As the flow between the pump column and the back wall was highly turbulent, Fraser noted that any quantitative analysis of these conditions was uncertain. An indication of the magnitude of these disturbances may be approximated by determining the impact of water against the upstream side of the pump column and against the back wall. The column and the back wall were stagnation points and the force at these points was proportional to the time rate of change of momentum of that portion of the flow affected. The mass of water,

m_f, affected in one second is

[2.4] $m_f = \rho_f A v_m$

where ρ_f = fluid density, A = area normal to the flow and v_m = mean velocity. Since momentum is mass times velocity, the impact force for the rear wall, F_i, can be expressed as

[2.5] $F_i \approx \rho_f A {v_m}^2$

A drag coefficient, C_d, comparable to the drag coefficient used in aerodynamic studies can be applied with averages of 0.6 to 0.8 for the pump column, and a value close to 2.0 for the back wall (Fox and McDonald, 1973). The Reynolds number encountered in suction intakes usually exceeds 10^6 and thus the boundary layer flow is always turbulent with constant values of C_d. It follows then, that the greater the value of the impact force on the pump column given by

[2.6] $F_i = 0.5\ C_d\ \rho_f A {v_m}^2$

the more severe will be the turbulence in the vicinity of the pump and the greater will be the forces on the pump column.

Iversen (1953) also considered the mechanisms responsible for vortex formation. Iversen classified vortices as being either a "local vortex" or a "column vortex". The local vortex contained a rotating region of liquid with the free surface being drawn down in a localized area. An air core was present which may be pulled into the pump suction if the vortex strength and inflow velocity are sufficient. In a column vortex, the liquid swirled around the pump column with the drawdown around the periphery of the column.

Iversen reasoned that vortices were initiated from an eddy in the sump. When the eddy reached the higher velocity regions of flow near the suction intake, the lower portion of the eddy was constricted and drawn into the intake. Rotational velocities in the lower portion of the eddy were increased, pressures were decreased, and an air core was established. Hence any configuration of sump boundaries, such as sharp corners or piers, or irregular velocity distributions, at which eddies form, were potential sources of a vortex.

Iversen also considered the prerotation of the fluid entering the suction bell due to impeller action as a predominating influence on vortex formation. While the effect undoubtedly was present, prerotation was only a minor cause of vortex formation because in some sumps a vortex was initiated far from the suction bell where any prerotation in the region of the suction bell could not have conceivably been the cause.

Iversen noticed two other effects, in addition to air entering the pump. If the vortex was unstable, i.e. formed, broke and then reformed, the periodic air flow produced velocity fluctuations with a corresponding fluctuation in the impeller thrust, which led to "bouncing" of the impeller and shaft assembly and serious effects on the bearings and supports. The disturbances also affected the pump hydraulic efficiency. If the vortex was stable, the bouncing may not have been evident, but the hydraulic efficiency may still have been affected.

Denny (1956) provided a more detailed description of the vortex formation phenomenon than that of Iversen. Denny noticed five distinct stages in the development of an air-entraining vortex as shown in Fig. 2.16. When the suction inlet was well covered with water, the vortex appeared first as a small dimple in the free surface, Fig. 2.16(a), which gradually deepened to form a cone-shaped hole; air bubbles broke away from time to time and were swept into the bell-mouth, Fig. 2.16(d). With steady flows, this condition appeared to be quite stable and often persisted for long periods. At high velocities, the air-core lengthened and allowed a continuous passage of air up the pipe, Fig. 2.16(e). Such a vortex was located some distance from the pipe; it was very stable and soon reformed if disturbed; its core rotated at great speed and the internal free surface was corrugated by small waves. Flow of air through the core was inaudible except with very high water velocities.

When the mouth of the pipe was less deeply submerged the vortex formed much closer to the pipe and tended to be less stable. It rarely remained in the same position for long, usually revolving slowly around the pipe and then disappearing; during this time another vortex would have formed at the original point and that one would begin to entrain air as soon as the previous one had disappeared. Only rarely did two vortices entrain air simultaneously.

2.4 Causes and Effects of Swirl Formation

Denny (1955(b)) and Bonnington and Denny (1956) during experimental work on vortices in sumps observed that the water in the

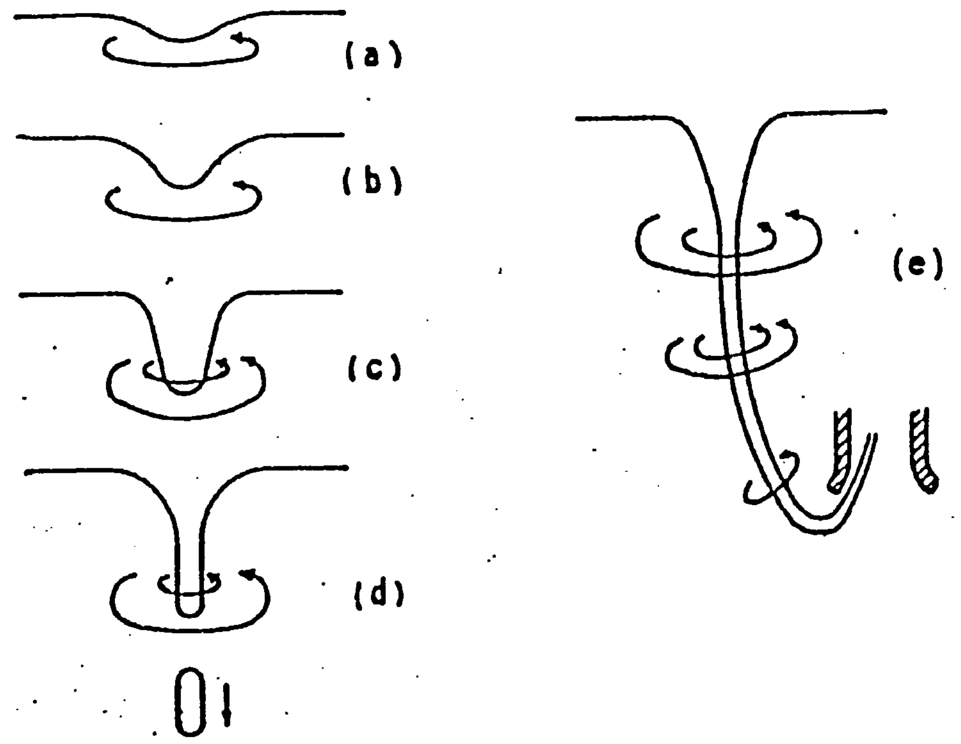

Fig. 2.16 Stages in the Development of an Air-Entraining Vortex (after Denny, 1956)

suction pipe appeared to flow along a spiral path, although centrifugal and axial-flow pumps are designed on the assumption that the flow approaches the impeller in an axial direction. They subsequently performed a series of tests to determine the effects of a number of variables on the severity of the swirling flow in the intake.

Pitot-tube traverses across the pipe indicated that the direction of flow was not always steady, due to turbulence and minor changes in the flow pattern in the sump. It was observed that the distribution of the tangential component of velocity across the pipe inlet approximated a free vortex, wherein velocity was inversely proportional to radius, as in the sump itself, while further along the pipe the swirl corresponded to a solid body rotation, wherein velocity was proportional to radius. Denny and Bonnington also measured the swirl using a vane which was allowed to rotate about the pipe axis. Both the Pitot-tubes and the vanes were located four diameters downstream of the intake.

Swirl angles in the pipe were found to be independent of the flow, but were considerably affected by the depth of water in the sump, as can be seen in Fig. 2.17, where the swirl is expressed non-dimensionally both as the pitch of the spiral, and as the equivalent angle of flow at the pipe wall. In sumps which were nearly symmetrical, the swirl increased abruptly as the water was lowered beyond a particular level, corresponding to a sudden change in the flow pattern in the sump, Fig. 2.17(b). Boundary walls in close

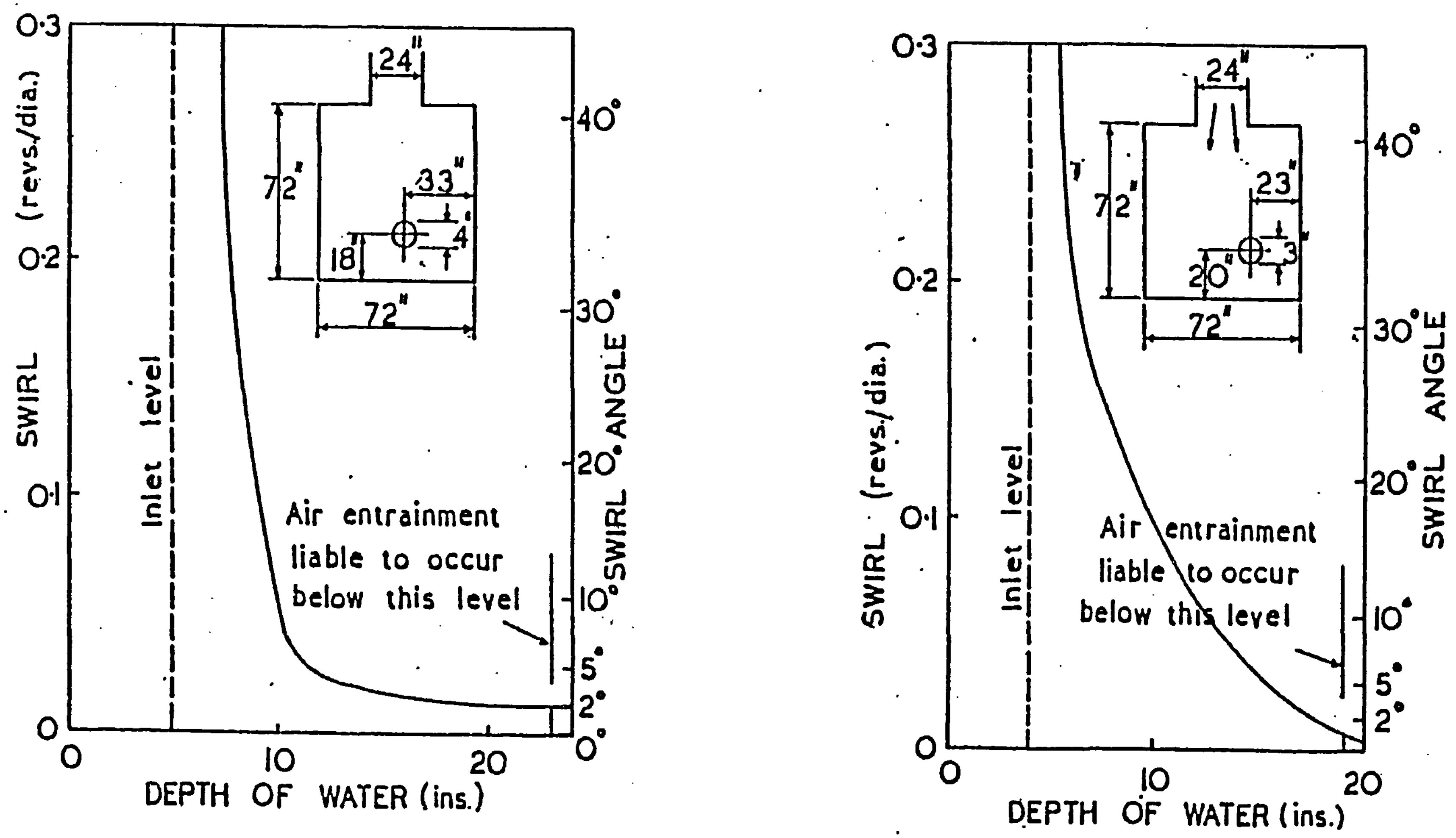

(a)

(b)

Fig. 2.17 The Effect of Water Depth on Swirling Flow in a Suction Pipe (after Denny and Young, 1957)

proximity to the intake improved the flow conditions, and had much the same influence on swirl as on air-entrainment.

Hattersley (1965) also studied swirling flow in pump intakes. It was noticed that in order to control swirl adequately at the bell-mouth entrance, the angular momentum, given by the product of mass, velocity and radius, produced from extraneous sources must be neutralized. The water approaching the bell-mouth arrived by various curved paths, as shown in Fig. 2.18, and the objective was to design an approach channel in which the positive and negative components of angular momentum would have a zero resultant at the entrance to the bell-mouth.

Hattersley reasoned that if the approach channel walls were built with reasonable continuity and if they were sufficiently long, a boundary layer would be established in the flow past the walls. Within the limits of the boundary layer a continuous exchange of momentum occurred, whereas close to the walls, loss of momentum in the water occurred under the action of drag. The distribution of vorticity generated in the boundary layer was illustrated by considering a suction pipe which was placed off centre in a channel in which the depth was greater than the width. As the flow approached the suction pipe, the part of the flow on the near side closest to the suction pipe converged directly to the pipe entrance. The part on the off-side of the channel passed by the suction pipe, lost its forward momentum in the backwater, and was finally drawn downwards towards the suction pipe entrance. In passing the pump column, a boundary layer

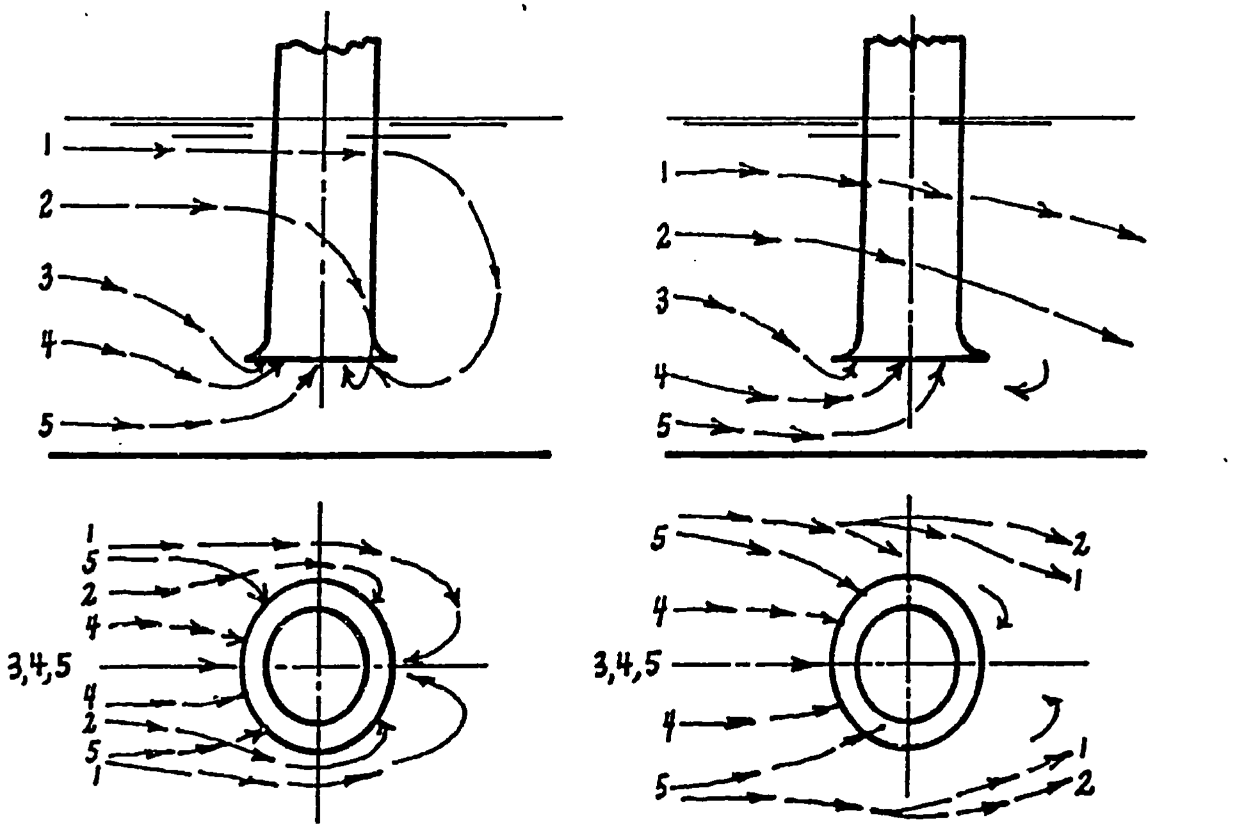
1
2
3
4
5
1
5
2
4
3,4,5
4
2
5
1
1
2
3
4
5
5
2
1
4
3,4,5
4
5
1
2

(a) No Flow Downstream of Pump

(b) Flow in Channel Downstream of Pump

Fig. 2.18 Approach Flow to a Pump Inlet in a Straight Channel (after Hattersley, 1965)

was developed; the part of the flow contained in this boundary layer had vorticity of opposite sign to that against the off-side wall and so it tended to neutralize the vorticity in the off-side wall boundary layer. It was also observed that the downward motion was generally unsteady and was associated with unstable vortices in the backwater region.

Thus, the purpose of Hattersley's research was to investigate the effects of wall drag on vorticity generation and swirl in the intake. Hattersley measured the swirl in the suction pipe using a series of freely pivoted meridional vanes known as a vortometer, as was done by Denny, Bonnington and Young. Swirl measurements depended on the size of the suction pipe itself and upon the revolving speed of the vanes. The following general expression for swirl was found in the terms of the tangent of the angle of indicated swirl measured at the inner wall of the suction pipe

[2.7] $\tan \alpha = \pi n d / v_d$

where α = angle of indicated swirl, n = revolutions per second of the vortometer vanes, d = suction pipe diameter and v_d = average suction pipe axial velocity. The term $\pi n d$ denotes the tangential linear velocity of the tip of the vortometer vane.

Hattersley found that the swirl readings were sensitive to changes in viscosity and accounted for these variations with the following parameters

[2.8] $N_R f^{0.5} = 8^{0.5} U_* d_e / \nu$

[2.9] $U_* / V_m = (f/8)^{0.5}$

and

[2.10] $N_R = V_m d_e/\nu$

where N_R = Reynolds number, f = Darcy-Weisbach friction factor, U_* = friction velocity, d_e = equivalent diameter of the channel cross-section obtained by multiplying the hydraulic radius by four, ν = kinematic viscosity of the fluid and V_m = mean channel velocity.

Hattersley conducted all the experiments at Reynolds numbers less than 10^5 and the channels had practically smooth walls so that the friction factor could be calculated from the Blasius equation

[2.11] $f = 0.316/N_R^{0.25}$

Figure 2.19 shows the results of experiments conducted in a straight walled channel in which the suction pipe was centered at one quarter of the width from the wall. The direction of rotation viewed in plan was observed to be clockwise. When the suction pipe was placed in the middle of the channel, the swirl had zero average rotation and when the pipe was placed on the opposite quarter of the channel width, the direction of the rotation of the swirl was reversed, while the magnitude remained virtually unaltered.

Hattersley recognized three distinct phases in his experimental plots of $N_R f^{0.5}$ vs. $\pi nd/v_d$. In the initial phase, $N_R f^{0.5}$ below about 2000, the swirl values were irregular and random at low Reynolds numbers. In this phase, extraneous influences such as vanes and air movement over the surface of the water upstream of the suction pipe were noted to have a distinctive but transient

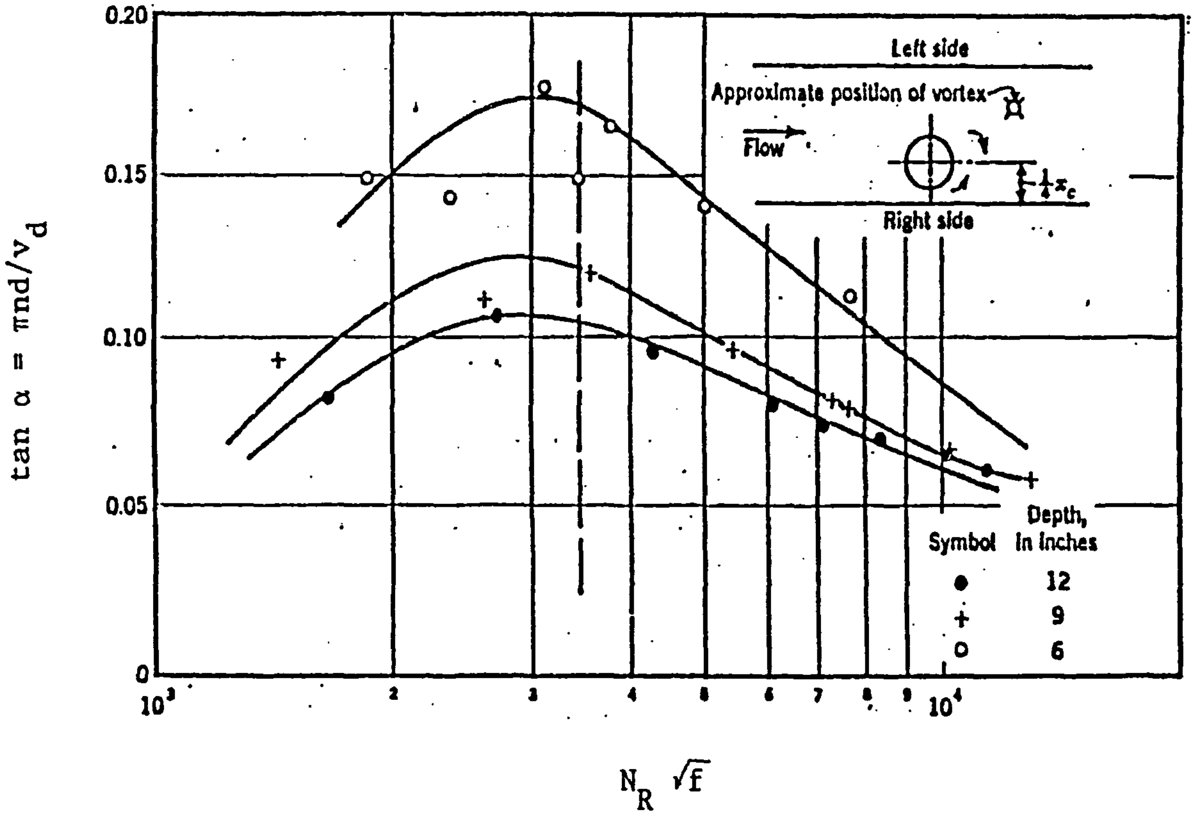

Fig. 2.19 Indicated Swirl for a 2 inch Diameter Suction Pipe in a Straight Channel (after Hattersley, 1965)

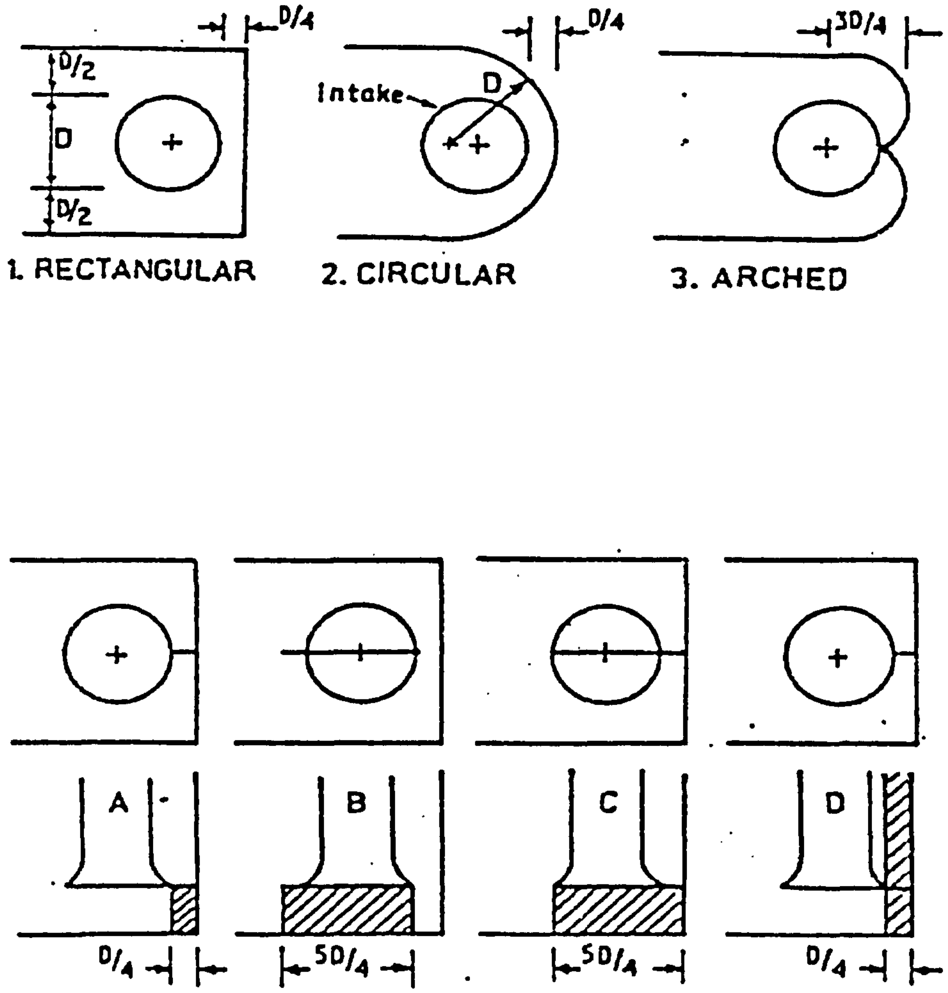
D/4
D/2
D
D/2
1. RECTANGULAR
Intake
D
D/4
2. CIRCULAR
3D/4
3. ARCHED
A
B
C
D
D/4
5D/4
5D/4
D/4

Fig. 2.20 Sump and Baffle Geometries
(after Haradasa and Cox, 1980)

influence on the magnitude of the swirl readings. Beyond the initial phase, the plot was a straight line, indicating that tanα is proportional to log $(N_R f^{0.5})$. Hattersley termed this proportional phase as the "secondary phase". In the secondary phase, the influence of the boundary layer was the predominant cause of swirl. The secondary phase terminated as the swirl parameter reached a minimum value, called the "tertiary phase". This phase corresponded to the formation of a concentric vortex about the suction pipe axis.

If the critical value of $N_R f^{0.5}$ is exceeded, the flow is in the secondary phase, and the drag on the channel walls fully control the swirl at the suction pipe entrance. If a hydraulic model is operated above the critical $N_R f^{0.5}$ value, the approach channel and sump should be shaped by trial to obtain zero swirl at the suction inlet, as measured by the vortometer. Hattersely found good agreement between prototype and model pump inlets when designed using the $N_R f^{0.5}$ and $\pi nd/v_d$ parameters and keeping the $N_R f^{0.5}$ values in the secondary phase.

Haradasa and Cox (1980) investigated the use of baffles to prevent swirl in pump inlets. The sump and baffle geometries used are illustrated in Fig. 2.20. Haradasa and Cox observed a large reduction in the swirl with the use of baffles. Baffle configuration C was found to give the highest reduction in swirl. All four baffles produced swirl counts of less than 30 rpm which was a reduction of more than 70% from that swirl produced in a bare sump. In the rectangular sump, the difference in swirl among baffles was minimal with baffles C and D resulting in marginally less swirl than baffles A and B. The arched sump was found to give the lowest swirl values of all of the sump configurations tested. The difference between the rectangular and circular sumps were minimal with only a marginally higher swirl for the circular sump.

2.5 Growth of the Boundary Layer and the Effects of Boundary Shear on Vorticity Generation

Chang (1979, 1980) reported that when the flow in the main body of fluid was irrotational, the basic mechanism responsible for the generation of vorticity was boundary shear, either at a solid-liquid boundary or between two fluid layers. These shear layers gave rise to velocity gradients within the fluid, often with high local values, and the resulting vorticity if sufficiently organized, caused a vortex to appear. This process was further aided by amplification of vorticity which occurred when a vortex filament was stretched, as in the case of fluid drawn down into the intake. This had the effect of concentrating vorticity which initially had diffused into a relatively small core. The two major sources of boundary layer growth were the walls and the floor of the sump, and the cylindrical surface of the suction pipe.

The flow along the sump boundaries can be approximated to that past a flat plate which is placed parallel to the direction of the main flow. The boundary layer thickness increases as fluid progresses along the plate due to diffusion of vorticity away from the solid boundary. Fox and McDonald (1973) showed that, at a Reynolds number of approximately 120000, a transition from a laminar to a turbulent boundary layer occurred, and the thickness of the boundary layer was given by

[2.12] $\delta_{plate}/X_b = 0.37/N_{Rx}{}^{0.20}$

where δ_{plate} = thickness of the boundary layer, X_b = distance along the plate and N_{Rx} = Reynolds number at the distance X_b.

The Reynolds number is given by

[2.13] $N_{Rx} = v_m X_b/\nu$

The transition to a turbulent boundary layer occurred earlier if the approach flow was unsteady or disturbed by surface roughness.

The flow past the suction pipe was also a source of vorticity, and was similar to steady flow past a cylinder or pipe. In this case, a laminar boundary layer developed starting from the upstream stagnation point and gradually thickened until it was separated from the cylinder and produced vortices downstream of the intake. Assuming a steady flow outside the boundary layer, the laminar boundary layer thickness was expressed as

[2.14] $\delta_{pipe}/d_{ext.} = 2.26/N_{Rd}{}^{0.50}$

where $d_{ext.}$ = external diameter of the suction pipe, and N_{Rd} = the suction pipe Reynolds number. The suction pipe Reynolds number is given by

[2.15] $N_{Rd} = v_m d/\nu$

The transition to a turbulent boundary layer occurred for N_{Rd} greater than 500000, but the corresponding value of δ_{pipe} was

?

not known. After separation from the cylinder, vortices were shed in discrete cells along the length of the cylinder, the length of each cell was called the "correlation length". Gerlach and Dodge (1970) reported that the correlation length was 2d to 3d for $150 < N_{Rd} < 10^5$ and dropped to 0.5d for $N_{Rd} > 10^5$.

Since the velocity at any solid boundary must be zero because of viscosity, velocity gradients are present in the boundary layer which are a source of vorticity, ζ (xi). ? Quick (1970) showed that a boundary layer of thickness δ gave rise to a mean distributed vorticity, ζ_A, over the entire boundary layer as

[2.16] $$\zeta_A = v_m/\delta$$

The equations to describe the vorticity generated by the suction pipe and the walls (plate) can be obtained by substitution of Eqs. [2.16], [2.15] and [2.13] into Eqs. [2.14] and [2.12] to yield

[2.17] $$\zeta_{pipe} = 0.442\, v_m^{1.5}/(\nu d_{ext.})^{0.5}$$

[2.18] $$\zeta_{plate}(turbulent) = v_m^{1.2}/(0.37X_b^{0.8}\,\nu^{0.2})$$

The boundary layer thickness for laminar flow over a flat plate is given by

[2.19] $$\delta_{plate}/X_b = 5.83/N_{Rx}^{0.5}$$

Therefore

[2.20] $$\zeta_{plate}\,(laminar) = v_m^{1.5}/(5.83(\nu X_b)^{0.5})$$

As illustrated in Fig. 2.21, a comparison between the laminar boundary layer on the pump column, and the laminar and turbulent boundary layers on a flat plate was made to identify the major source of vorticity. The figure indicates that for a given pipe size and sump

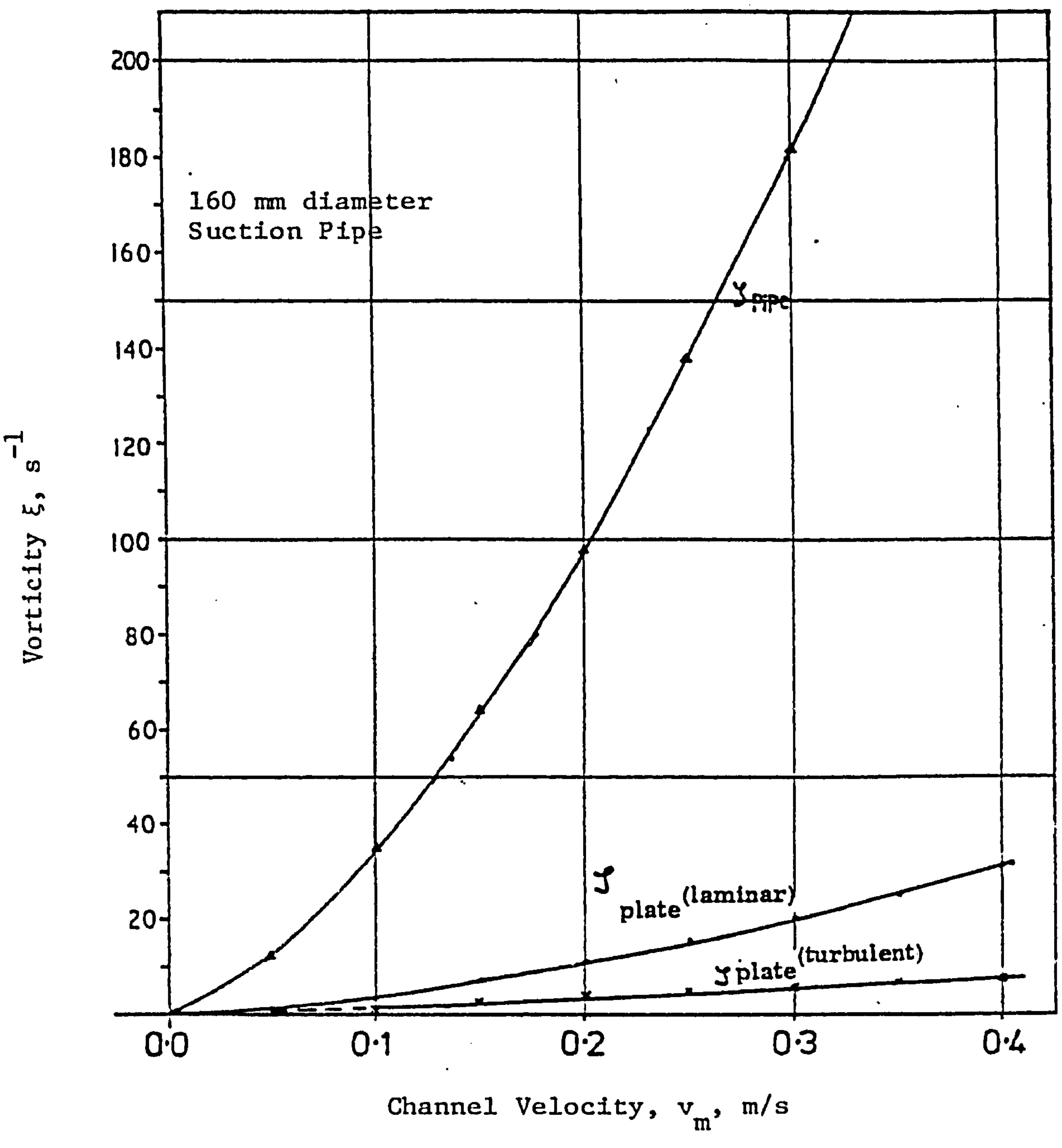

Fig. 2.21 The Relative Magnitudes of Vorticity Arising from Flow Past a Pipe and a Flat Plate (after Chang, 1979, 1980)

geometry the dominant contribution to vorticity arose from the suction pipe column. The contribution from the sidewalls was in the opposite direction and had a relatively small destabilizing effect. Thus, an obvious solution to the vortex problem would be to remove the suction pipe completely and extract the flow through the floor or wall of the sump.

2.6 Model Studies of Vortices and Sumps

The similitude requirements that must be met in a specific model investigation depend on the flow phenomena that are of primary importance. Complete similarity between model and prototype requires geometric, kinematic and dynamic similarity; however, it is practically impossible to achieve dynamic similarity of all forces involved. Therefore, it becomes necessary to determine which forces are dominant in the flow under consideration and to ensure that dynamic similarity is achieved among them.

2.6.1 Geometric Similarity

Geometric similarity requires that the ratios of all corresponding dimensions in the model and prototype be equal. In an undistorted model, the length ratio, L_R, is given by

[2.21] $$L_R = L_p/L_m$$

where L_p = prototype length and L_m = model length.

2.6.2 Similarity of Gravity Forces

In most free surface flows it is important that the prototype ratio of gravity forces to inertial forces be preserved. This is achieved by keeping the same Froude number, N_F, for the model and the prototype, that is

[2.22] $N_{FR} = N_{F_p}/N_{F_m} = 1$

where N_{FR} = Froude number ratio, N_{F_p} = prototype Froude number, N_{F_m} = model Froude number, and

[2.23] $N_F = v_m/(gL)^{0.5}$

where v_m = characteristic mean velocity, g = acceleration due to gravity and L = representative length.

2.6.3 Similarity of Viscous Forces

The ratio of viscous forces to inertial forces in the model and the prototype will be equal if the Reynolds number, N_R, is the same in both the model and the prototype, where

[2.24] $N_R = v_m L/\nu$

Nakato and Kennedy (1976) report that it is impossible to preserve the similarity of both gravity and viscous forces in an undistorted model built to a practical scale using ordinary fluids. However, for turbulent flows it is not necessary that the ratio of Reynolds numbers for the model and prototype be unity. It generally suffices to insure that the flow is turbulent, both in the model and the prototype. This is the case if the Reynolds number is equal to or greater than approximately 1400.

2.6.4 Scaling of Surface Tension Forces

Surface tension forces are correctly reduced in the model if the Weber numbers, N_W, in the model and prototype are equal.

[2.25] $N_W = \rho_f L v_m^2/\sigma$

where ρ_f and σ are the mass density and surface tension of the fluid, respectively. The Weber numbers in most civil engineering structures are generally sufficiently large to insure that the surface tension forces are small compared to the gravitational and/or viscous forces.

2.6.5 Boundary Roughness Similarity

For fully turbulent flow regime, such that the Darcy-Weisbach friction factor is independent of the Reynolds number, the friction factor ratio will be unity in an undistorted model if the boundary roughness is scaled according to the same ratio as the model dimensions. If the Manning's formula is used for the resistance relationship, it can be shown that the Manning roughness ratio, n_R, is given by

$$n_R = L_R^{1/6} \tag{2.26}$$

For an undistorted Froude model, shear stresses and boundary tractive stresses scale in the same ratio as lengths.

2.6.6 Additional Modelling Considerations

Due to the complex flow patterns associated with vortices, and the crucial influence of the boundary geometry on flow circulation, model studies are often conducted to ensure satisfactory performance. Since sump and vortex models involve a free surface, Froude similarity is used and the effects of other forces are assumed insignificant and are labelled "scale effects". Scale effects are discussed further in Section 2.7.

For better comparison of vortex activities between the model and the prototype, Durgin and Hecker (1978) refined the vortex classification system of Iversen (1953) and Denny (1956). They recognized six vortex types as listed below:

Type 1 - Coherent surface swirl
Type 2 - Surface depression
Type 3 - Coherent dye core
Type 4 - Suction of slightly buoyant particles
Type 5 - Air bubbles pulled into intake
Type 6 - Full air core to intake

Since each vortex type is likely to be intermittent, the duration of each type of vortex may be as important as the vortex type itself. Durgin and Hecker developed a curve relating vortex type to the percent time vortices weaker than a given type occurred, as shown in Fig. 2.22. However, they pointed out that it might be more relevant to consider the worst vortex type, and characterize the flow and sump design by this vortex type irrespective of its frequency of occurrence.

Figure 2.23 illustrates a typical plot of vortex type versus the length of the vortex air core relative to the total depth of fluid, Z/H. Durgin and Hecker showed that the length of the air core was related to the maximum tangential velocity, v_t, by

[2.27] $$Z = (v_t^2)/g$$

It follows that the relative core length is given by

[2.28] $$Z/H = v_t^2/gH = F_t^2$$

where F_t is a Froude number based on the maximum tangential velocity and total water depth. The vortex type curve versus F_t is also plotted in Fig. 2.23. For vortices up to Type 4, the vortex

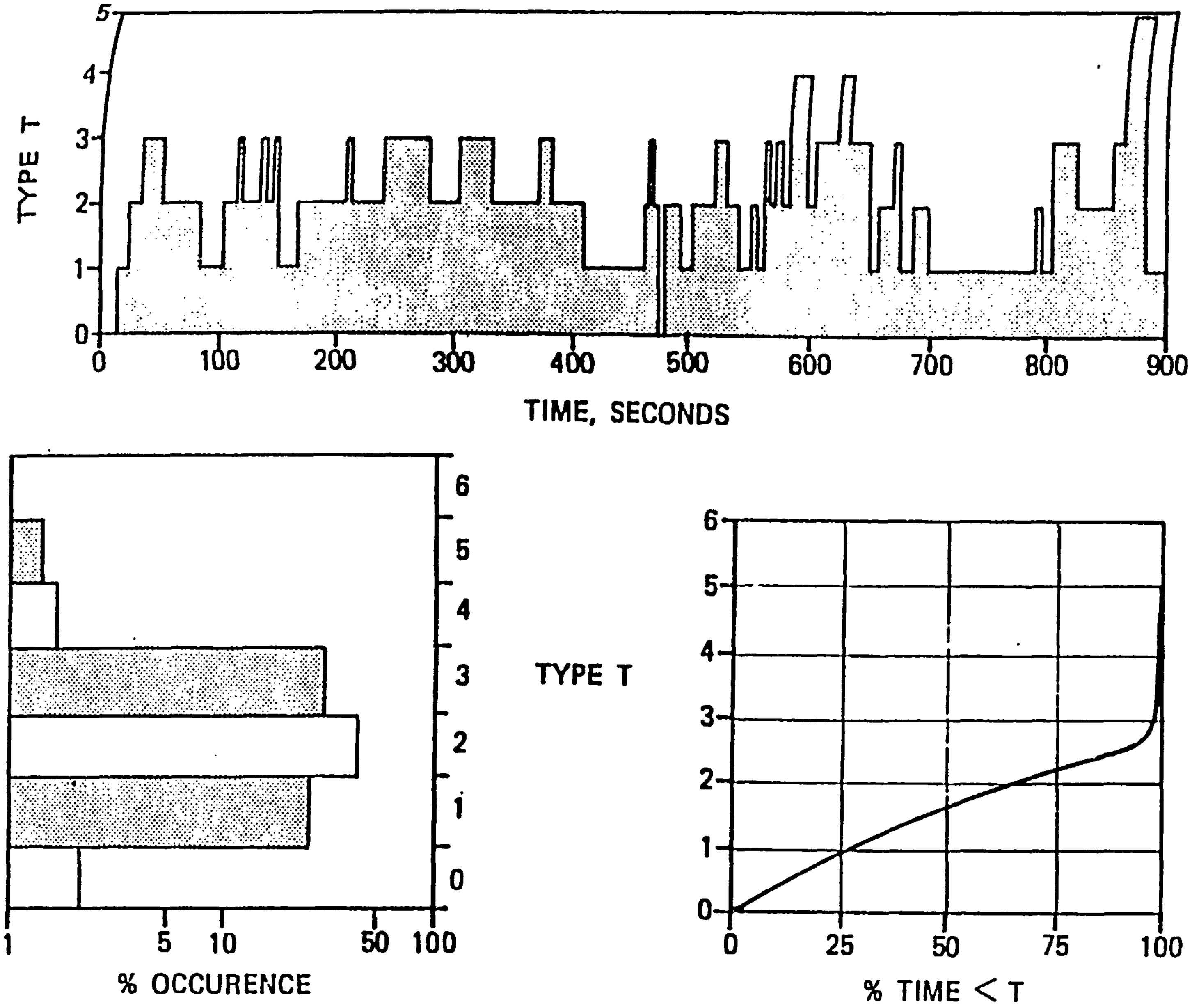

Fig. 2.22 Plots of Vortex Type for a Pumped Storage Inlet
(after Durgin and Hecker, 1978)

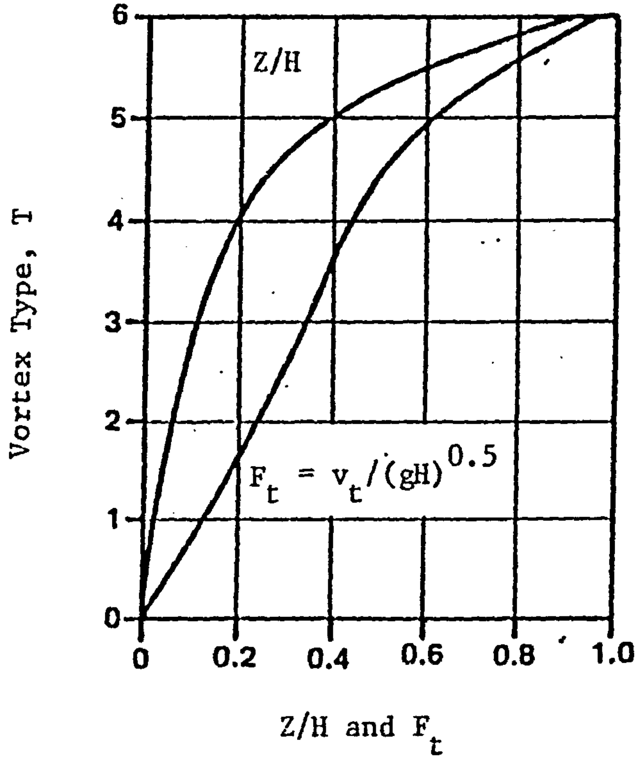

Fig. 2.23 Vortex Type vs. Core Length and Froude Number (after Durgin and Hecker, 1978)

type increases almost linearly with F_t and thus the square root of the rotational energy. Alternatively, the rotational energy increases as the square of the vortex type, indicating a larger energy difference between, for example, Types 3 and 4 than between 1 and 2.

2.7 Scale Effects in Modelling Sump and Vortical Flows

Despite decades of work on sumps and vortices, the present state of knowledge is such that reduced scale hydraulic models are required for each case where it is important that no vortices occur. Although the predominant inertial and gravitational forces are reduced similarly in the Froude-scaled models, viscous and surface tension forces cannot be reduced simultaneously as much, and the extra influence of these forces are called "scale-effects".

Hecker (1981) reviewed the literature on scale effects in modelling vortices and found considerable disagreement among investigators. As with other flow phenomenon subject to viscous scale effects, it is important that the model Reynolds number be sufficiently high. Anwar, et al. (1978) and Daggett and Keulegan (1974) recommended a minimum Reynolds number of 3×10^4, based on inlet flow and submergence, or intake diameter, respectively. A recent study by Dhillon (1979) indicated good model-prototype agreement in vortex strength for a 1:20 scale model satisfying the Reynolds number criteria operated at Froude-scaled flows.

Testing models at higher than Froude-scaled intake velocities, up to prototype intake velocities, to overcome scale effects in modelling air core vortices has been proposed by many investigators including

Haindl (1959), Jain, et al. (1978), Denny (1956), Iversen (1953), Dicmas (1967, 1978), Zajdlik (1977) and Chang (1979b). Their results showed that the required increase in the flow above Froude-scaled value was based on the sump geometry and relative submergence. However, for some scale ratios, Linford (1965), and Dhillon (1979) found that the use of the equal intake velocity concept seriously undermined the primary Froude-scaling criterion used to achieve proper approach flow patterns and the resulting circulation at the intake. Studies indicated that the use of prototype velocities in models produced highly exaggerated vortices which were incompatible with prototype observations. In some circumstances, increased wave action and turbulence at flow rates considerably higher than dictated by Froude scaling were found to dissipate rather than increase vorticity.

Hecker (1981) noted that the concept proposed by Jain, et al. (1978) of correcting the critical submergence predicted by the model to a relatively higher prototype value, had the inherent difficulty that the ambient circulation may change with geometric differences at higher elevations. In addition, the studies of Hattersley (1965) and Quick (1970) had shown that the required correction was a function of the basic geometry involved and of the mechanisms which generated vorticity, in particular, the influence of vorticity generated in the approach flow boundary layer. This mechanism was paramount in cases in which no boundary discontinuities existed.

Daggett and Keulegan (1974) and Jain, et al. (1978) used fluids with various degrees of surface tension but constant viscosity in order to investigate the effects of a change in the Weber number on the vortex air core characteristics. Daggett and Keulegan indicated that the flow characteristics varied little for a threefold variation in surface tension, and Jain, et al., showed that the critical submergence for incipient air entrainment was essentially constant when the surface tension was reduced by about 50% for any given value of intake velocity, outlet diameter, and circulation. However, Yildirim and Jain (1981) concluded that the effect of surface tension on the free-vortex surface profile became significant at low values of circulation and may give rise to some scale effects in model studies on vortex formation.

Irrespective of the relative influence of surface tension and viscous forces on the air core, Hecker concluded that vortices with air cores extending to or into the inlet were more subject to scale effects than surface dimples. Hecker also concluded that the following factors accounted for differences between model and prototype vortices:

(i) A natural tendency for the observer to be impressed with the size and intensity of the prototype vortex. A belief may develop that it is more severe than that predicted by the hydraulic model. This belief is partly due to the increased levels of surface turbulence and noise, which undoubtedly do not scale directly.

(ii) The difference in time scale makes it appear that the prototype vortex is more persistent. However, the prototype may be viewed for a relatively shorter time period compared with the model.

(iii) It is usually difficult to distinguish between various strengths of vortices in the field and the depth of the air core cannot usually be determined.

(iv) Insufficient attention to approach topography and boundary roughness in the model. Vorticity approaching the inlet has a first order effect on the resulting vortex strength.

(v) Viscous scale effects on modelling appurtenant flow devices such as screens, baffles and vortex suppressors.

(vi) Wind induced currents, and

(vii) Ambient density stratification.

Projection of model vortex severity to the prototype, assuming that only inertial and viscous forces dominate, implies that the Reynolds number must be increased without changing the Froude number. Durgin and Hecker (1978) changed the Reynolds number but held the Froude number constant by varying the water temperature, and hence, its viscosity. Additional data points were generated by operating the model at different flow rates, both above and below those indicated by Froude scaling. This technique resulted in a Froude ratio versus Reynolds number graph, as shown in Fig. 2.24. Each solid line represents the changes produced in Froude number ratio and Reynolds number ratio when the model flow rate is increased at a given water temperature. At any given operating point, the parameters related to vortex intensity are recorded and lines of constant vortex severity may be superimposed on this graph. The prototype performance is predicted by noting the vortex severity indicated at the corresponding Reynolds number and properly scaled Froude number, when the Froude number ratio is equal to unity.

2.8 Dimensional Analysis Considerations

In the analysis of vortices, several investigators used a dimensional analysis procedure in an attempt to define the

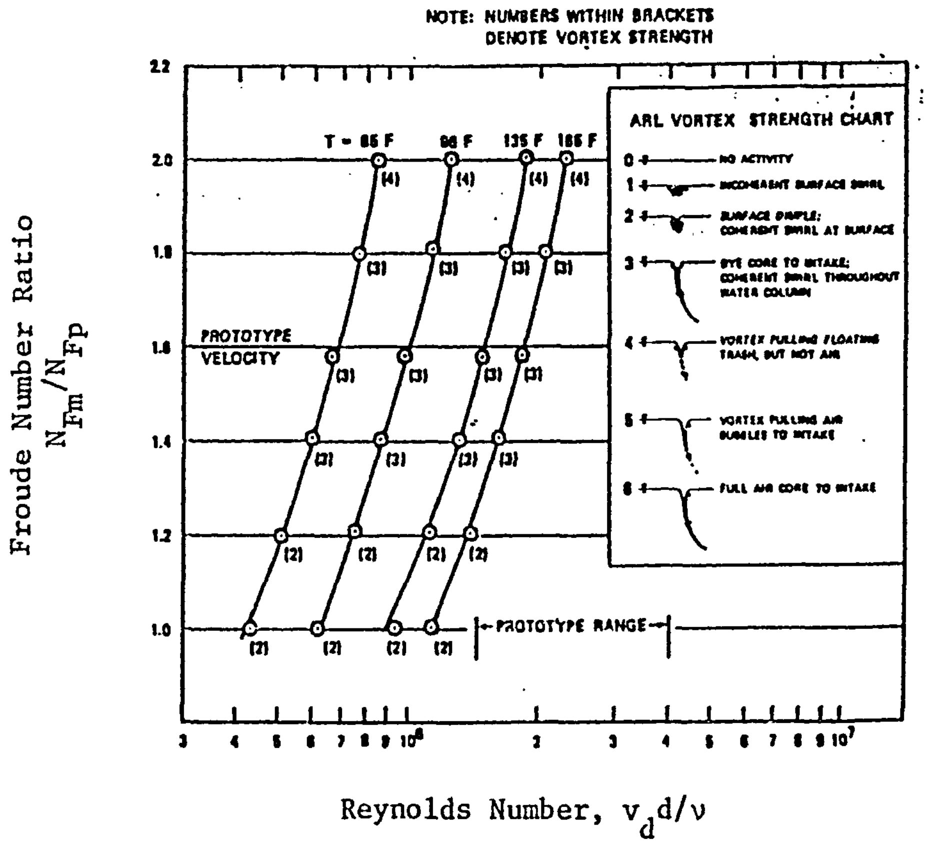

Fig. 2.24 Vortex Severity vs. Froude Number Ratio and Reynolds Number (after Nystrom, Padmanabhan and Hecker, 1982)

inter-relationships between the significant variables.

Anwar (1983) studied the parameters relevant to vortex formation in intakes and expressed the relationships by

[2.29] $f(\Gamma r_o/Q,\ Q/\nu S,\ r_o/S,\ N_W,\ I_\eta,\ S/d,\ C/d,\ X/d) = 0$

where Γ = circulation, r_o = radius of vortex at the free surface, Q = discharge rate, ν = kinematic viscosity of the fluid, S = intake submergence, N_W = Weber number, I_η = intake efficiency or coefficient of discharge, d = inlet pipe diameter, C = height of inlet above sump floor, and X = rear and side wall clearance. The Weber number and intake efficiency are defined as:

[2.30] $N_W = Q^2 S \rho_f / A_i \sigma$, and

[2.31] $I_\eta = (Q/A_i)(2gS)^{0.5}$

where A_i = cross-sectional area of the intake, and σ = surface tension.

Anwar's analysis was based on the assumptions that the steady flow was axisymmetric, the fluid was incompressible, the vortex flow was affected by the viscosity of the fluid alone, and that surface tension acted only when there was a surface depression or an air core. Other researchers, Donaldson and Sullivan (1960), Einstein and Li (1955), Granger (1966), Lewellen (1962), Stevens and Kolf (1957) and Turner (1966), obtained non-dimensional parameters similar to Anwar using the Navier-Stokes equations under laminar flow conditions. The first term in the brackets of Eq. [2.29] describes the circulation, given by

[2.32] $\Gamma = V_\theta r$

where V_θ = tangential velocity component, and r = radius measured from vortex axis. Hecker (1981), Durgin, Neale and Churchill (1977), Einstein and Li (1955), Granger (1966), Turner (1966) and Weller (1975) proved that without the circulation, Γ, a vortex could not form. Anwar found that the depth of the surface depression and the size of the air core increased as the tangential velocity component increased. Levi (1972) found that a local pressure drop could also produce a circulation, and hence, a vortex.

From Eq. [2.29], it can be seen that the first four non-dimensional parameters indicate geometric and dynamic similarity of vortices. The parameters contain viscous forces and surface tension and together with the last three parameters are considered as independent parameters in vortex phenomenon. The variation of all of the parameters will affect the intake efficiency as given by Eq. [2.31], which is thus a dependent parameter.

Based on extensive testing of intakes, Anwar found that the circulation was a function of the vortex radius, submergence, intake pipe diameter, total water depth, and bottom clearance, i.e.

[2.33] $\Gamma = 0.86\ (g/H)^{1/2}\ r_o^{\ 2}$, and

[2.34] $r_o = 0.06S + 0.143\ (C/d) + 0.89$

The units of Eqs. [2.33] and [2.34] are in metres and the experimental constants were obtained for vertical intakes.

Anwar plotted the circulation parameter, $\Gamma r_o/Q$, against "radial Reynolds number", $Q/\nu S$. The results showed that the circulation number rapidly decreased with an increase in the radial

Reynolds number. These changes became slower when radial Reynolds numbers were greater than approximately 3 x 10^4, but the circulation never became fully independent of the radial Reynolds number. Anwar's results confirmed the assumption that if the flow in the vortex was laminar, then the vortex was affected by the viscosity. The test results also showed that the circulation parameter and radial Reynolds number were independent of the intake geometry expressed by X/d and C/d. Thus, it was concluded that the circulation number and radial Reynolds number determined the onset of free surface vortices once the intake geometry had created the necessary circulation.

Anwar also investigated the relationship between the circulation and the Weber number and found that the effect of surface tension on vortices became apparent as soon as a depression occurred at the free surface. The dimple became less sensitive to the Weber number variation when $N_W > 1.5 \times 10^4$, representing the cases in which the free surface curvature became small. It was observed that the relationship between the circulation parameter and the Weber number was dependent upon S/d and r_o/S. The submergence dependency was due to (i) the linear variation of N_W with S, such that an increase in S caused a linear increase in N_W and in S/d for a given d, and (ii) an increase in r_o and Γ, as indicated by Eqs. [2.33] and [2.34] in order to obtain a definite type of vortex. Again, the two parameters, $\Gamma r_o/Q$ and N_W were found to be independent of the intake geometry described by X/d and C/d.

The effect of the circulation parameter on the dependent parameter, I_η, the intake efficiency, was also investigated by Anwar. It was found that the coefficient I_η increased with a decrease in circulation parameter and that both parameters varied with the submergence parameter S/d and to a lesser extent with the intake diameter d. The latter influence was also reported by Chang (1979), Denny and Young (1957), Dhillon (1979) and Iversen (1953). Anwar's measurements showed that for vertical intakes the I_η value decreased with increasing values of X/d and became almost independent of this parameter when X/d > 5. The coefficient I_η also varied with the floor clearance, when the clearance parameter C/d was less than 2 for vertical intakes. Similar results were reported by Chang (1979) and Iversen (1953).

Jain, Raju and Garde (1978) also investigated the effects of surface tension and viscosity on the formation of vortices. They used circular tanks with a bell-mouth placed centrally in the bottom of each tank through which the submergence and flow rate could be controlled. Three fluids of different viscosity and surface tension were used in their tests. Jain et al. found that the significant parameters could be expressed non-dimensionally as

$$[2.35] \qquad f(S_c/d,\ g^{0.5}d^{1.5}/\nu,\ \Gamma S_c/Q,\ v_d/(gd)^{0.5},\ \rho_f v_d^2 d/\sigma) = 0$$

They plotted the effect of surface tension against submergence and intake velocity. It was found that, within the range of Weber numbers $1.2 \times 10^2 < \rho_f v_d^2 d/\sigma < 3.4 \times 10^4$, the surface tension did not affect vortex formation, and accordingly the last term within the brackets of Eq. [2.35] was dropped. They also observed that an increase in the kinematic viscosity decreased the critical submergence for a given inlet pipe velocity. This decrease in critical submergence was attributed to the reduction in the strength of the circulation in the region of the vortex core when the liquid had a higher viscosity.

Equation [2.35] was then reduced to the form

[2.36] $f(S_c/d,\ N_\nu,\ N_\Gamma,\ N_F) = 0$

where N_ν = viscosity number and N_Γ = circulation number. Jain, et al. evaluated the relationship given in Eq. [2.36] and found that it could be described by

[2.37] $K(S_c/d) = 5.6(N_\Gamma^{0.84}\ N_F)^{0.50}$

where K was designated as the viscous correction factor and found to be a function of N_ν, as shown in Fig. 2.25. Plots of S_c/d versus N_F for constant values of N_Γ and different values of N_ν showed that the variation of log (S_c/d) with log (N_F) was linear, given by

[2.38] $K_1(S_c/d) = N_F^{0.50}$ where

K_1 is a function of N_ν and N_Γ. A log-log plot of K_1 versus N_ν revealed that the lines of constant N_Γ were parallel and that K_1 became independent of N_ν at $N_\nu > 5 \times 10^4$ for all values of N_Γ. For each N_Γ value, the ratio of K_1 for any value of N_ν to that for $N_\nu > 5 \times 10^4$ was designated as K. It can be seen from Fig. 2.25 that as N_ν increases, the value of K decreases and

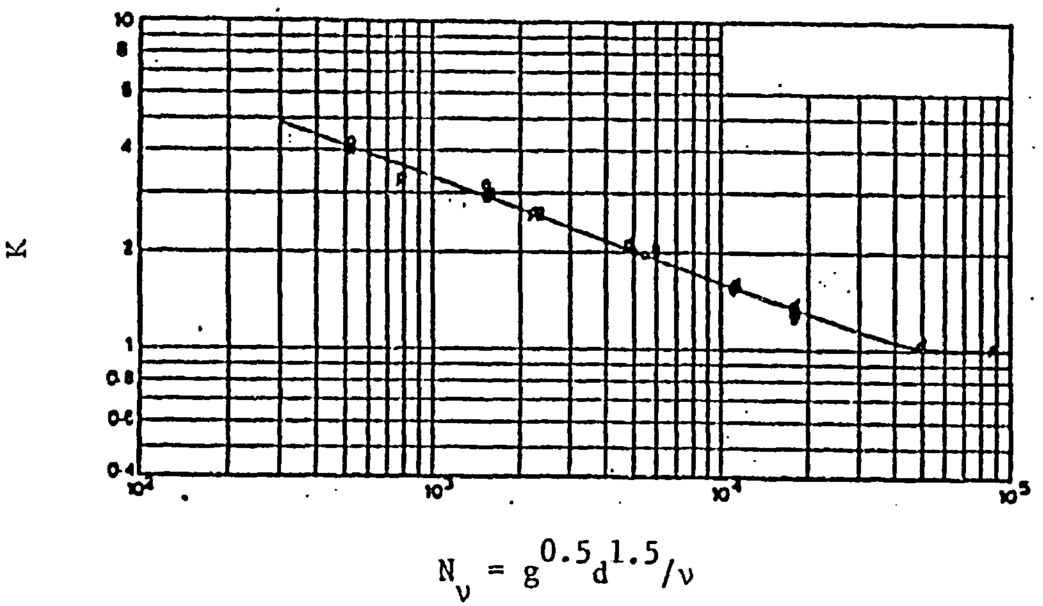

Fig. 2.25 The Variation of the Viscous Correction Factor, K, with the Viscosity Number, N_ν (after Jain, et al., 1978)

becomes unity for $N_\nu > 5 \times 10^4$, indicating no viscous effects at values of N_ν greater than 5×10^4. The relationship between KS/d and $N_\Gamma^{0.84} N_F$ is shown in Fig. 2.26. Daggett and Keulegan's data (1974) was found to be in general agreement with that predicted by Eq. [2.37].

Jain et al., subsequently made use of Fig. 2.25 and Eq. [2.37] to express the relationship between S_c/d, N_R and N_F. The plots of N_F versus S_c/d for various values of N_R showed that for each value of N_F, there was a limiting N_R beyond which viscous effects were negligible. This observation was significant because previous studies by Anwar (1966) and Amphlett (1976) indicated that there was a limit of N_R beyond which viscous effects were negligible. Jain, et al. had shown that the limit was different for each different value of N_F.

Zajdlik (1977) studied the relationship between the length scale ratio, L_R, velocity scale ratio, V_R, water depth, H, and suction bell diameter, D, using five sizes of rectangular sumps and five suction bell diameters. Based on his tests, Zajdlik obtained the relationship given by

[2.39] $V_R = f(L_R, H/D)$

The results of his experiments are shown in Fig. 2.27 which illustrates that the velocity scale for the start of an air-entraining vortex increases with increase in the length scale and also with decrease in water depth in the sump. When the water depth exceeds approximately 4D and when the length scale exceeds approximately 2.7,

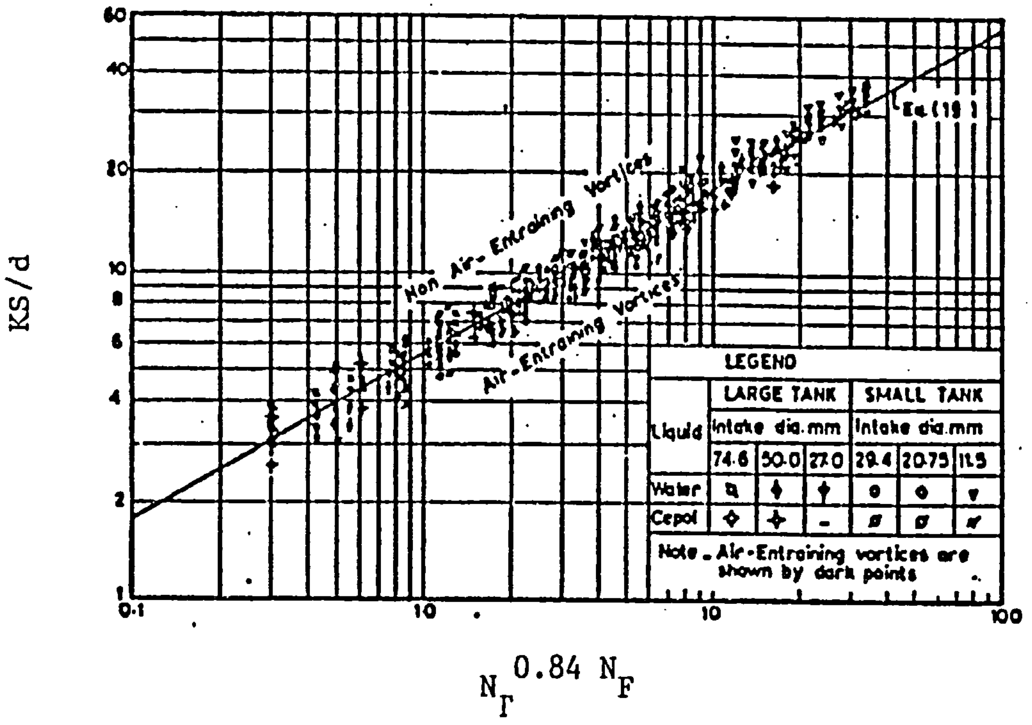

Fig. 2.26 Criterion for Vortex Type
(after Jain, et al., 1978)

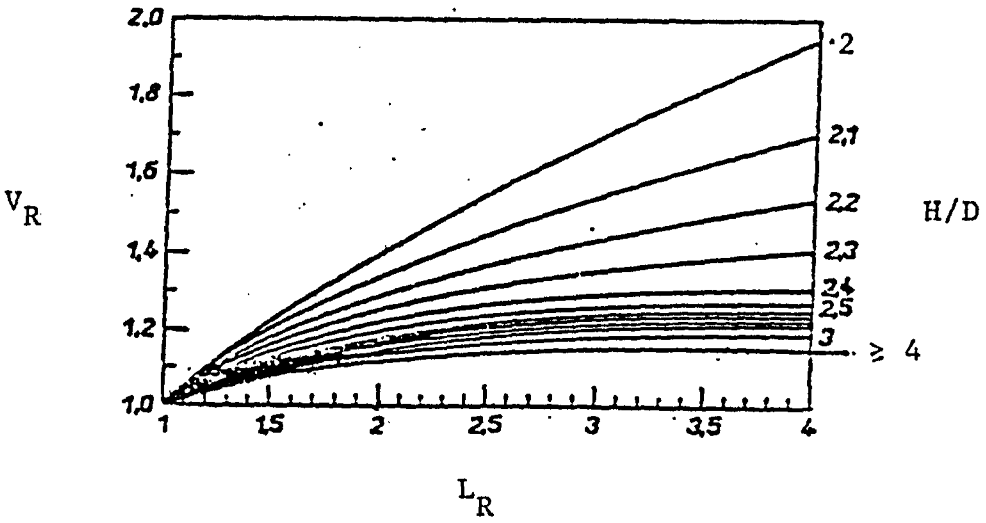

Fig. 2.27 The Relationship Between L_R, V_R and H/D for the Onset of Air-Entraining Vortices (after Zajdlik, 1977)

it can be seen that the velocity scale does not change substantially and is approximately equal to a constant value of $V_R = 1.15$.

Zajdlik's curve of V_R versus L_R may be used to check for the onset of vortices once a relationship between the inlet velocity and H/D is determined for a given size of model. The critical water depth, H, can then be computed for a given model scale and intake pipe velocity.

CHAPTER 3

LITERATURE REVIEW

THE INITIATION OF PARTICLE MOTION

3.1 General

A.A. Kalinske (1947) stated that, in any analysis of movement of particles by a moving liquid, there was some minimum fluid force which would start a particle to move. Since, even for unigranular material, all particles did not rest identically, this force varied for different particles, especially if the particles were angular.

Another concept suggested was that the force to which a particle was subjected was not constant but fluctuated about some mean value. This fluctuation was caused by two conditions. Firstly, even though the general fluid motion was laminar, after certain critical flow conditions around a particle had been reached, small eddies were generated behind the particle, and these caused the fluctuations in the drag force acting on the particle. Secondly, usually the main fluid stream was turbulent, and this relatively larger scale turbulence caused the fluid velocity acting on any individual particle to vary considerably with time. The variation in turbulent fluid velocity should be known, or estimated, before analyzing any bed-load movement.

Einstein (1942) discussed two important considerations with respect to initiation of particle motion. First was the difficulty or impossibility of defining accurately the so-called "critical" values. Second was the possibility of correlating bed-load movement with local fluctuations in water velocity along the bed. Attempts were made to derive an expression for the "initial movement" which was governed by certain definable "critical" conditions used as a first step toward the solution of the transport problem. In interpreting the results of bed-load movement, Einstein concluded that a distinct condition for the beginning of transportation did not exist. Einstein believed that the description of bed-load movement as set forth by Rubey (1938) was a valid approach. A particle on the bed moved when the pushing force or lifting force of the water overcame the weight of the particle. This push or "lift" was expressed in terms of the average flow. The usual concept was that particle transport began when the velocity increased enough to overcome the weight. With further increase in water velocity, the rate of transportation also increased, following a certain empirical law. Einstein suggested that it was misleading to describe the force acting on a particle by means of the average flow alone. If the velocity of the water was increased gradually to a point at which the first particle would just be moving the force acting on all other particles of the same kind and size would also move. Therefore, in a uniform bed with particles of the same size and shape, all particles would start moving together and would be unable to settle again because at all points the water velocity was just sufficient to start movement. Thus, at velocities less than the critical, there would be no transportation, whereas at velocities greater than the critical, the rate of transportation would be limited only by the number of particles available. This not being the case, it was presumed that the rate of bed-load transportation was not a function of the average flow. Instead, Einstein and Rubey believed that the initiation of bed-load movement should be expressed in terms of the _fluctuations_ of the water velocity near the bed.

The two best known and widely accepted investigations on particle motion were conducted by Shields (1936) and White (1940). By considering the forces to be restricted to shear, each author derived an expression for a critical shear stress, which, if exceeded would cause motion.

3.2 White's Analysis of the Equilibrium of Grains on the Bed of a Stream

White (1940) reasoned that a fluid flowing over a loose granular bed tended to move the grains in the direction of the fluid motion. Further, the bed exerted a drag upon the fluid, like any solid boundary, and the accompanying shear stress was transmitted from the bed to the fluid almost wholly by the more prominent grains in the uppermost layer. The forces acting on a grain of non-cohesive sediment lying in a bed of similar grains over which a fluid is flowing are shown in Fig. 3.1.

The forces acting on the sediment were the gravitational forces of weight and buoyancy, hydrodynamic lift normal to the bed, and drag parallel to the bed.

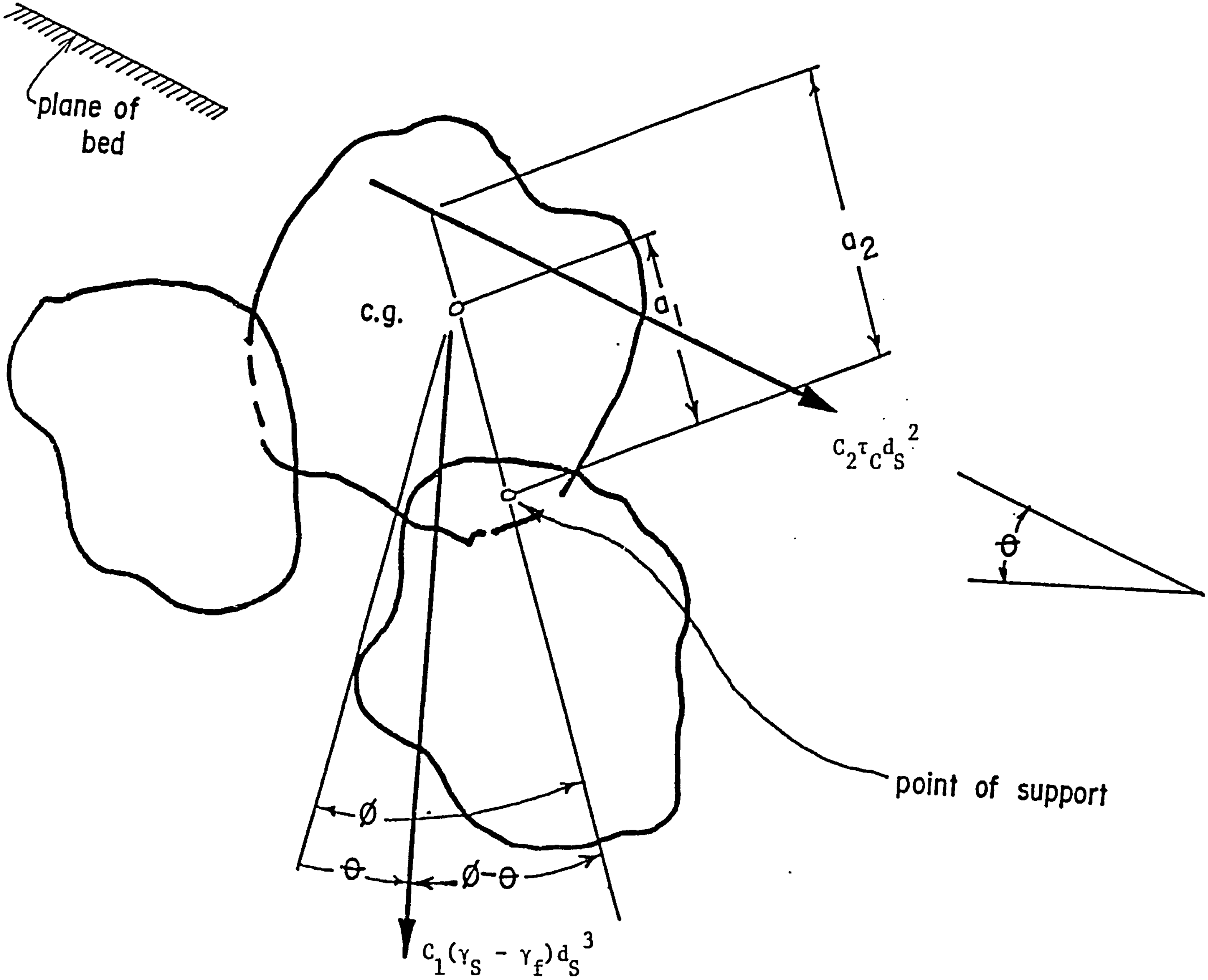
plane of bed
c.g.
a_2
a_1
$C_2\tau_C d_S^2$
θ
point of support
ϕ
θ
$\phi-\theta$
$C_1(\gamma_S - \gamma_f)d_S^3$

Fig. 3.1 Forces on a Sediment Grain on a Sloping Bed

In theoretical analyses of sediment motion, the lift has often been neglected. However, in determining various experimental constants, lift was implicitly included because it depended upon the same variables as the drag. According to White, when particle motion is impending, the bed shear stress attains the critical value of τ_C, and under these conditions the particle is about to move by rolling about its point of support. The gravity or weight force is given by $C_1 (\gamma_S - \gamma_f) d_S^3$ where γ_S and γ_f are the unit weights of the particle and the fluid, respectively, d_S is the mean particle diameter and $C_1 d_S^3$ represents the volume of the particle. The critical drag force is given by $C_2 \tau_C d_S^2$ where $C_2 d_S^2$ is the effective surface surface area of the particle exposed to the critical shear stress τ_C.

Equating the moments of gravity and drag force about the point of support yields

[3.1] $$C_1(\gamma_S - \gamma_f)d_S^3 \; a_1 \sin(\phi - \theta) = C_2 \tau_C d_S^2 a_2 \cos\phi$$

where θ is the bed slope and ϕ is the angle of repose of the sediment submerged in the fluid.

When rearranged, Eq. [3.1] yields the critical shear stress as

[3.2] $$\tau_C = (C_1 a_1 / C_2 a_2)(\gamma_S - \gamma_f) d_S \sin(\phi - \theta)/\cos\phi$$

Equation [3.2] represents a general expression for the critical shear stress in either a uniform or non-uniform channel with or without a horizontal free surface.

When the distances a_1 and a_2 are equal, the forces on the grain act through the centre of gravity and the fluid forces are caused predominantly by pressure. It can also be seen that the critical shear stress on a horizontal bed is greater than on a downward sloping bed, but less than on an upward sloping bed.

Taking τ_C approximately equal to V_{bc}^2, in which V_{bc} is the fluid velocity near the bed under critical conditions, and further, assuming a horizontal bed, $\theta = 0$, and substituting these relationships into Eq. [3.2] shows that V_{bc}^2 is proportional to d_S. Cubing both sides results in V_{bc}^6 being proportional to $d_S{}^3$, which is known as the sixth power law after Rubey (1948) and Lelliavsky (1955). Because the volume or weight of the grain is proportional to $d_S{}^3$, the law states that the weight of the largest particle that a flow will move is proportional to the sixth-power of the velocity in the neighbourhood of the particle. Rubey found that this law applied only when d_S was large compared with the thickness of the laminar sublayer and when the flow about the grain was turbulent. The sixth-power law agreed with the findings of Shields (1936) and Tison (1953).

White observed that when the particle was subjected to turbulent flow, the resultant fluid forces were caused mostly by pressure and tended to pass through the centre of gravity. At high velocities and with large grains, the tangential drag became relatively unimportant compared with the drag due to pressure differences. The pressure distribution was not symmetrical but was less over the downstream half of the grain, so that when integrated it gave rise to a resultant force or form drag whose component resisted motion. However, when viscous effects were important, the fluid velocity was low and the grain size was small, the pressure at the front of the grain did not appreciably exceed that at its rear, and the force applied was the resultant of viscous stresses acting tangentially. The resultant of these forces tended to fall above the centre line of the particle, i.e., a_2 exceeded a_1.

White considered the division line between turbulent flow and viscous flow to be when

[3.3] $(\tau/\rho_f)^{0.5}d_s/\nu > 3.5$

where τ is the bed shear stress and ρ_f, d_s and ν are as previously described.

White found that the constants C_1a_1/C_2a_2 for turbulent boundary layers were 50 to 65% of that when the flow was laminar. He attributed these differences to velocity fluctuations in the turbulent flows which in turn caused fluctuations in the bed shear stress and on the forces acting on the grains. It is clear that, in turbulent flows, the observed mean critical shear stress, τ_c, may not be high enough to entrain the sediment, and that most if not all the motion results from pulsating values of the shear stress that exceed the mean values of τ_c. White concluded that the true critical shear stress required to move a particular grain had a fixed value given by the experiments with laminar flow. He obtained the equation for the critical shear stress on a horizontal bed under laminar flow conditions as

[3.4] $\tau_C = 0.18(\gamma_S - \gamma_f)d_S \tan\phi$

If it is assumed that the initiation of particle motion is represented by τ_C, then τ_C is a function of γ_S, γ_f, d_S, ρ_f and ν. Then dimensional analysis will yield

[3.5] $\tau_C/((\gamma_S - \gamma_f)d_S) = \mathrm{fcn}(U_{*C}d_S/\nu)$

where U_{*C} is the critical shear velocity and is given by

[3.6] $U_{*C} = (\tau_C/\rho_f)^{0.5}$

3.3 Shields' and Camp's Approach to the Initiation of Particle Motion

Shields (1936) obtained a similar expression to Eq. [3.5]. He called the left hand side of Eq. [3.5] as the dimensionless critical shear stress and the variable on the right hand side as the critical boundary Reynolds number. Figure 3.2 shows the data used by Shields to determine the function of Eq. [3.5]. These data were obtained by Shields and several other researchers from experiments in flumes with fully-developed turbulent flows and artificially flattened beds of noncohesive sediments. The curve in Fig. 3.2 is termed as the Shields curve, as first proposed by Rouse (1939).

Shields work has been widely accepted although some researchers have reported slightly different values for the parameters. Egiazaroff (1950), Tison (1953) and Matsunashi (1957) obtained curves having the same general shape as that shown in Fig. 3.2.

Camp (1946), based on the work of Shields and others, developed an equation for the velocity required to initiate sediment motion. Camp considered a sheet of sediment of thickness t_S in a channel under uniform flow conditions, Fig. 3.3. For small angles of the

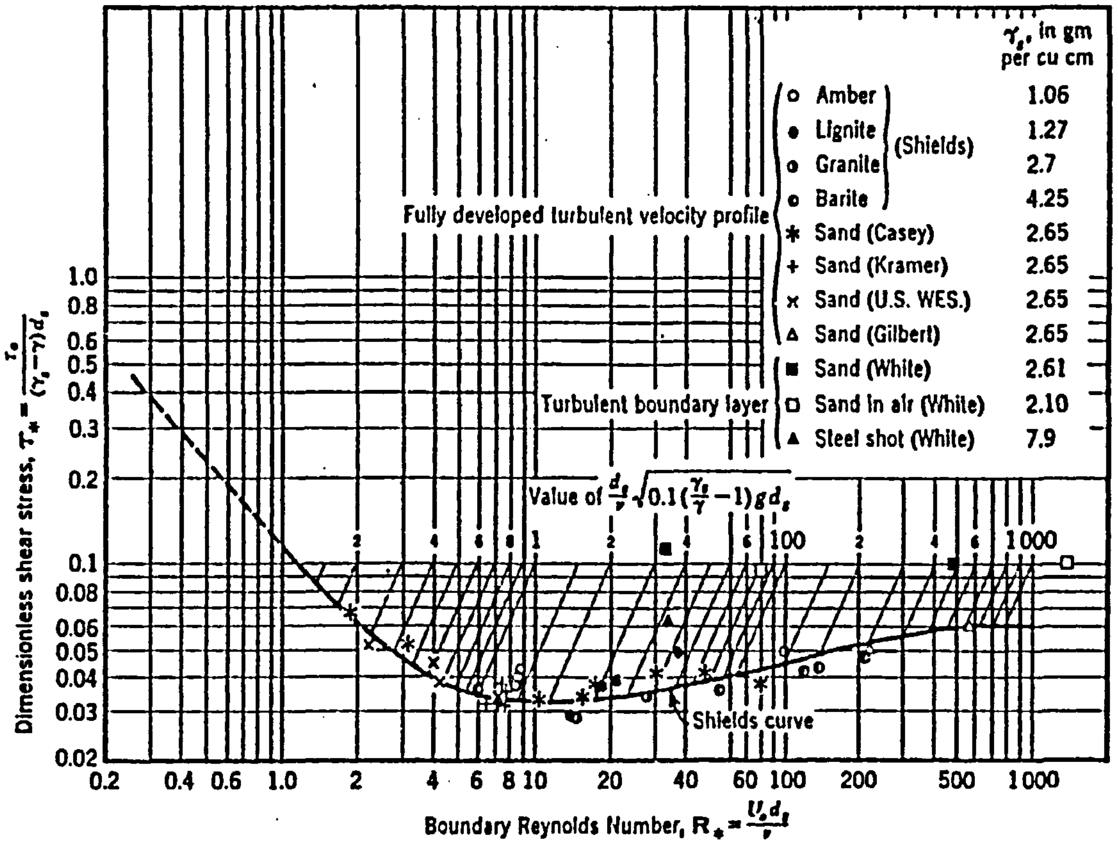

Fig. 3.2 Shields Diagram
(after ASCE, 1977)

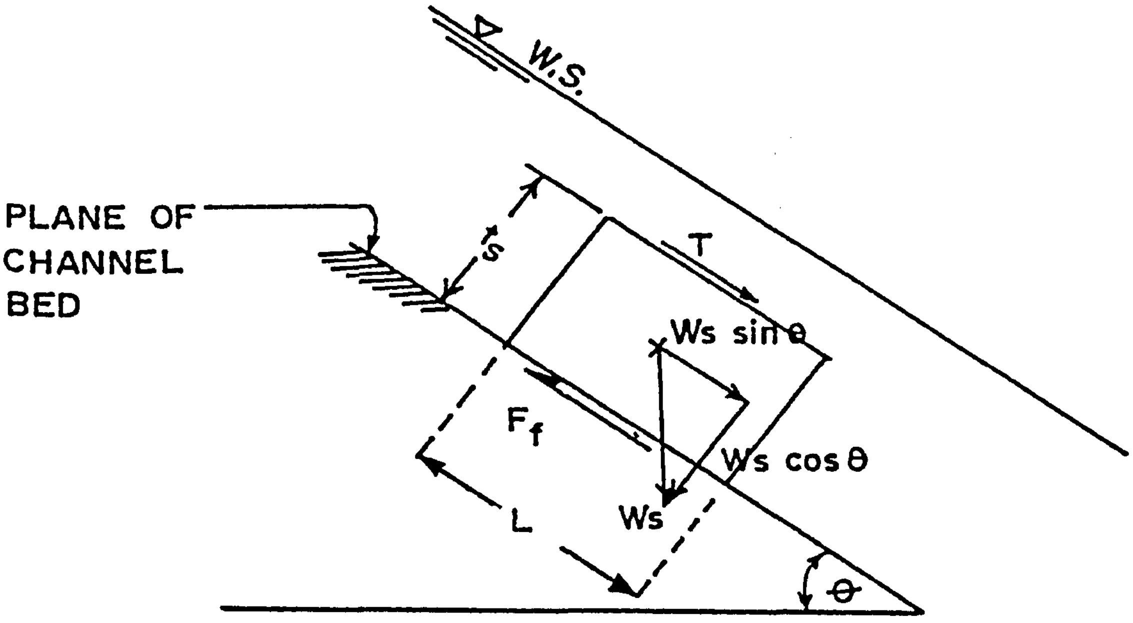
W.S.
PLANE OF CHANNEL BED
t_s
T
Ws sin θ
F_f
Ws cos θ
L
Ws
θ

ELEVATION

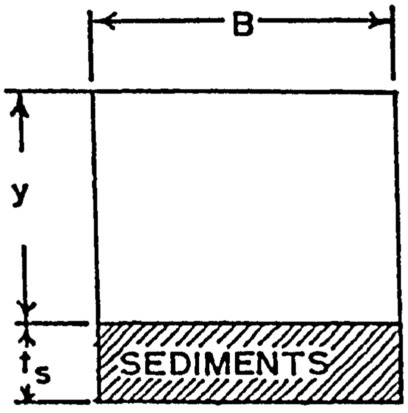
B
y
t_s
SEDIMENTS

CROSS-SECTION

Fig. 3.3 Diagram for the Derivation of the Shields-Camp Equation

channel slope, θ, the intensity of tractive stress, τ, on the sediment layer is equal to the component of the fluid weight along the bed and was expressed as

$$[3.7] \qquad \tau = \gamma_f ByLS/LB$$

where B, y, S and L are the channel width, depth and slope respectively and L is a unit length of the sediment layer. For large angles of θ, $\sin\theta$ should be substituted for S in Eq. [3.7]. As θ approaches zero, $\sin\theta$ approaches S. In wide channels, it is usually assumed that the depth, y, approaches the hydraulic radius, R_h. According to the Darcy-Weisbach formula for uniform flow in open channels, the slope can be expressed as

$$[3.8] \qquad S = fv_m{}^2/(8gR_h)$$

where v_m is the mean channel flow velocity. Substituting [3.8] into [3.7] and assuming a wide channel yields

$$[3.9] \qquad \tau = \gamma_f fv_m{}^2/(8g)$$

Based on the Shields curve, Camp proposed that for the initiation of bed-load movement,

$$[3.10] \qquad \tau = \beta(\gamma_S - \gamma_f)d_S$$

in which β is a constant and a function of d_S/δ, where δ is the thickness of the laminar film adjacent to the boundary. Combining Eqs [3.9] and [3.10] yields the mean channel velocity required for the initiation of particle motion as

$$[3.11] \qquad v_m = (8g\beta d_S(S_S - 1)/f)^{0.5}$$

where S_S is the specific gravity of the particles. Table 3.1 gives the range of β under various sediment conditions.

Table 3.1 Range of Shield-Camp β Values

β	Application	Reference
0.04	initiating the scour of relatively clean grit and unigranular particles	Fair, Geyer and Okun (1966)
0.06	for non-uniform, sticky and interlocking grit particles	Shields (1936)
0.08	for full removal of sticky grit	Fair, Geyer and Okun (1966)
0.10 - 0.25	sand grains	Camp (1946)

Fair and Geyer (1958) also developed Eq. [3.11] by evaluating the forces acting on a sediment layer on a horizontal channel bottom. In 1966, Fair, Geyer and Okun again developed Eq. [3.11]. However, in doing so, they assumed the channel bed slope and the angle of repose of the sediments to be equal, which may not always hold true.

Simons and Sentürk (1977) divided the Shields' diagram into three regions. The first region was identified as

[3.12] $U_* d_S / \nu < 3.63 \sim 5.0$

In this region, d_S was less than 3δ and the boundary was considered hydraulically smooth. Simons and Sentürk reported the limit as 3.63 but it has often been replaced with 3.5, 3.3 or 2.0. The original curve given by Shields ended at around $U_* d_S / \nu$ equal to 1.0. Other researchers have provided the data for $U_* d_S / \nu < 1.0$. According to Shields when

[3.13] $\tau_C / ((\gamma_S - \gamma_f) d_S) \cong 0.1$, then

[3.14] $U_* d_S / \nu \cong 1.0$

The second region of the Shields' diagram was identified by

[3.15] $3.63 \sim 5.0 < U_* d_S / \nu < 68.0 \sim 70.0$

In this region the boundary was considered to be in a transitional state and

[3.16] $\delta/3 < d_S < 6\delta$

The minimum value of the dimensionless shear stress, in this region, was approximately $0.032 \sim 0.033$, and the corresponding value of the Reynolds number was about 10.0 which corresponded to $\delta \sim d_S$ and

d_S = 0.0006 m. The limiting value of d_S has been reported by many authors to range from 0.5 to 0.6 mm.

Region 3 was identified by

[3.17] $U_* d_S/\nu > 70 \sim 500$

In this region the boundary was completely rough and the critical shear stress was independent of the critical Reynolds number. The upper limit in Region 3 has been subject to discussion and some researchers have given values as high as 1000. The value of the dimensionless shear stress, in this region, is 0.06. However, Meyer-Peter and Muller (1948) suggested a value of 0.047 instead of 0.06, but 0.06 is still most generally accepted.

The auxiliary scale on Fig. 3.2 is used to obtain the critical shear stress when the particle and fluid properties are known. The value $(d_S/\nu)(0.1(\gamma_S/\gamma_f - 1)gd_S)^{0.5}$ originates from the fact that the Shields diagram was somewhat inconvenient to use because the dependent variables, critical shear stress and grain diameter, appear in both the ordinate and abscissa parameters. Entering the main diagram and following the correct parallel line one can determine its intersection with the curve and the corresponding value of the dimensionless shear stress.

3.4 Other Significant Works on the Initiation of Sediment Transport

Stelczer (1981) reviewed the literature on bed-load transportation and particle motion and tabulated the significant equations. Tables for the critical bottom velocity, critical mean velocity in a cross-section and critical shear stress are given in Tables 3.2, 3.3 and 3.4 respectively. In these tables, the value V_{bcmin} corresponds to the initial stage of the critical condition corresponding to the displacement of individual particles, whereas V_{bcmax} corresponds to the initiation of "total bed-load movement". Thus the critical bottom velocity, V_{bc}, is obviously the mean value of the velocity range given by the minimum and maximum velocities, V_{bcmin} and V_{bcmax}.

Figure 3.4 illustrates the range of V_{bc} versus particle diameter based on the work listed in Table 3.2. Figure 3.5 illustrates the range of v_m, v_{mmin} and v_{mmax} as given in Table 3.3. Figure 3.6 illustrates the range of critical tractive shear stress for a given particle diameter.

Graf and Acaroglu (1968a, 1968b) developed two parameters to describe the total sediment transport in a conveyance system. Based on the assumptions that (i) the channel has a constant cross-sectional area, (ii) the flow is in a steady and turbulent state, (iii) the particles are cohesionless and have a uniform size distribution and (iv) saltation and suspension are the primary means of transport, they derived a shear intensity parameter and a transport parameter given by

[3.18] $\psi = (S_S - 1)d_S/SR_h$, and

[3.19] $\phi_{GA} = (C_S v_m R_h)/((S_S - 1)gd_S^3)^{0.5}$

where

ψ = the shear intensity parameter

ϕ_{GA} = transport parameter, and

Table 3.2 Critical Bottom Velocities (after Stelczer, 1981)

Author and Year of Publication	Formula	Range of Validity
(A) From Laboratory Data		
Velikhanov, et al. (1931)	$V_{bc} = 37\ d_S^{0.5}$	$d_S > 0.5$ cm
Mavis, et al. (1935)	$V_{bc} = 53.77\ d_S^{0.44}$	$d_S > 0.03$ cm
Mavis and Laushey (1949)	$V_{bc} = 57.88\ d_S^{0.41}$	not specified
Kalmár (1952)	$V_{bc} = 25.18\ d_S^{0.1}$	$0.01 < d_S < 0.1$ cm
Kalmár (1952)	$V_{bc} = 53.83\ d_S^{0.43}$	$0.1 < d_S < 1.0$ cm
(B) From Field Data		
Sainjon (1871)	$V_{bc} = 70.7\ d_S^{0.5}$	not specified
Hjulström (1935)	$V_{bc} = 26.54\ d_S^{0.712}$	not specified
Helley (1969)	$V_{bc} = 15.5\ d_S^{0.5}$	S.F. = 1.0, $\theta = 0^0$
Helley (1969)	$V_{bc} = 30.0\ d_S^{0.5}$	S.F. = 1.0, $\theta = 25^0$
Helley (1969)	$V_{bc} = 33.0\ d_S^{0.5}$	S.F. = 0.25, $\theta = 0^0$
Helley (1969)	$V_{bc} = 41.1\ d_S^{0.5}$	S.F. = 0.25, $\theta = 25^0$
Stelczer (1978)	$V_{bc} = V_{bcmin} + 14.0$	$d_{S_{80}} > 0.5$ cm

Table 3.2 Critical Bottom Velocities (after Stelczer, 1981) continued

Author and Year of Publication	Formula	Range of Validity
(C) From Laboratory and Field Data		
Rossinskiy, et al. (1968)	$V_{bc} = 77.1\ d_S^{0.5}$	$d_S/d_{S_{90}} = 0.30$
(D) V_{bcmin} from Laboratory Data		
Bogárdi and Yen (1938)	$V_{bcmin} = 51.57\ d_S^{0.38}$	$d_S > 0.03$ cm
(E) V_{bcmax} from Laboratory Data		
Mirtshulava (1967)	$V_{bcmax} = 1.41\ V_{bcmin}$	not specified
Stelczer (1978)	$V_{bcmax} = V_{bcmin} + 28.0$	$d_{S_{80}} > 0.5$ cm

Table 3.3 Critical Mean Velocity in the Cross-Section (after Stelczer, 1981)

Author and Year of Publication	Formula	Range of Validity
(A) From Laboratory Data		
Velikhanov, et al. (1931)	$v_m = 0.77g^{0.5}$	$0.001 < d_S < 0.01$ cm
Velikhanov, et al. (1931)	$v_m = 9.9(140d_S + 5.8)^{0.5}$	$0.01 < d_S < 0.5$ cm
Mavis, et al. (1935)	$v_m = 76.77d_S^{0.44}$	$d_S > 0.1$ cm
Kalmár (1952)	$v_m = 45.55d_S^{0.14}$	$0.01 < d_S < 0.1$ cm
Kalmár (1952)	$v_m = 97.4d_S^{0.47}$	$0.1 < d_S < 1.0$ cm
Ivicsics (1959)	$v_m = 73.85d_S^{0.33}$	not specified
Novak-Nalluri (1972)	$v_m = 61.62d_S^{0.38}$	$0.01 < d_S < 1.0$ cm
Novak-Nalluri (1974)	$v_m = 37.95d_S^{0.24}$	rectangular flume
Novak-Nalluri (1974)	$v_m = 29.70d_S^{0.16}$	circular flume
Ghvelisiani (1950)	$v_m = 34d_S^{0.5} \log(A)/\log(B)$ where: $A = 8.8h/d_S$ $B = (12d_{S\max} + d_S)/d_S$	non-uniform sized sediments

Table 3.3 Critical Mean Velocity in the Cross-Section (after Stelczer, 1981) continued

Author and Year of Publication	Formula	Range of Validity
Levi (1948)	$v_m = 56.3h^{0.2}d_S^{0.3}$	$d_S < 0.1$ cm (sand)
Levi (1948)	$v_m = 43.84d_S^{0.5}\ln(h/7d_S)$	$h/d_S > 60$ (uniform size)
Levi (1948)	$v_m = 43.84d_S^{0.5}(1 + \ln(h/7d_S)^{0.5})$	$10 < h/d_S < 60$ (uniform size)
Levi (1948)	$v_m = 43.84d_S^{0.5}\ln(h/7d_S)(d_{Smax}/d_S)^{1/7}$	$h/d_S > 60$ (mixed size)
Levi (1948)	$v_m = 43.84d_S^{0.5}(1 + \ln(h/7d_S)^{0.5})(d_{Smax}/d_S)^{1/7}$	$10 < h/d_S < 60$ (mixed size)
Levi (1957)	$v_m = 43.84d_S^{0.5}\log(12R_h/d_{Smax})$	$R_h/d_{Smax} > 60$ (mixed size)
Levi (1957)	$v_m = 40.7d_S^{0.5}(0.8 + 0.667\log(10R_h/d_{Smax})$	$10 < R_h/d_{Smax} < 60$ (mixed size)
Zamarin (1951)	$v_m = 95(0.01R_h)^{1/(2 + 0.01R_h)}$	$d_S < 0.5$ cm; $50 < R_h < 200$ cm
Zamarin (1951)	$v_m = 105(0.01R_h)^{1/(2 + 0.01R_h)}$	$0.5 < d_S < 1$ cm; $50 < R_h < 200$ cm
Zamarin (1951)	$v_m = 115(0.01R_h)^{1/(2 + 0.01R_h)}$	$1.0 < d_S < 1.5$ cm; $50 < R_h < 200$ cm
Zamarin (1951)	$v_m = 140(0.01R_h)^{1/(2.5 + 0.01R_h)}$	$1.5 < d_S < 5.0$ cm; $50 < R_h < 200$ cm
Zamarin (1951)	$v_m = 175(0.01R_h)^{1/(2.5 + 0.01R_h)}$	$5.0 < d_S < 10.0$ cm; $50 < R_h < 200$ cm
Zamarin (1951)	$v_m = 200(0.01R_h)^{1/(2.5 + 0.01R_h)}$	$10.0 < d_S < 15.0$ cm; $50 < R_h < 200$ cm

Table 3.3 Critical Mean Velocity in the Cross-Section (after Stelczer, 1981) continued

Author and Year of Publication	Formula	Range of Validity
Kumine (1955)	$v_m = 39.2h^{0.2}d_S^{0.3}$	not specified
Sundborg (1956)	$v_m = 123.8d_S^{0.5}\log(0.0302h/d_S)$	not specified
Herheulidze (1958)	$v_m = 54(10d_{S_{70}} + 0.05)^{0.27}0.01^x h^x$	
	$x = 0.45/(10d_{S_{70}} + 0.35)^{0.1}$	
Knoroz (1959)	$v_m = (2.56d_S^{0.05})/(0.0008+0.006/R_h^{0.25})^{0.5}$	hydraulically smooth bed
Knoroz (1959)	$v_m = 25d_S^{0.3}\log(3.6R_h/d_S^{1.6})$	transition range
Knoroz (1959)	$v_m = 40.7\ \log(14.7R_h/d_S^{0.75})d_S^{0.5}$	hydraulically rough bed
Latishenkov (1960)	$v_m = 50.1h^{0.2}d_S^{0.3}$	not specified
Orlov, et al. (1960)	$v_m = 48.8h^{0.17}d_S^{0.33}$	not specified
Garbrecht (1963)	$v_m = 44.5h^{0.17}((0.01d_S+0.8)/d_S^{0.17})$	not specified
Studenitshnikov (1964)	$v_m = 36.5h^{0.25}d_S^{0.25}$	not specified
Neill (1967a)	$v_m = 63.7h^{0.1}d_S^{0.4}$	not specified

Table 3.3 Critical Mean Velocity in the Cross-Section (after Stelczer, 1981) continued

Author and Year of Publication	Formula	Range of Validity
Bodrayashkin as mentioned by Müller (1973)	$v_m = 50.0h^{0.17}d_S^{0.33}$	not specified
Hankó (1968)	$v_m = 56.315\nu^{0.294}d_S^{0.059}/(f)^{0.5}$	$d_S < 0.000145$ m
Hankó (1968)	$v_m = 15.13d_S^{0.5}/(f)^{0.5}$	$d_S > 0.000145$ m
	where:	
	$1/(f)^{0.5} = -2\log[0.0676(d_S/h)(1+0.309\delta'/d_S)]$	
Bogárdi (1971)	$v_m = 0.00138h^{0.5}S^{0.5}(h/d_S)^{1.6}(d_S/(\nu^{2/3}g^{-1/3}))^{1.8}$	$h < 23.5$ cm $d_S < 0.5$ cm
(B) Lowest Critical Mean Velocity in the Cross-Section (from Laboratory Data)		
Meyer-Peter, et al. (1934)	$v_{mmin.} = 10.87d_S^{0.375}$	not specified
Bogárdi and Yen (1938)	$v_{mmin.} = 81.8d_S^{0.44}$	$d_S > 0.03$ cm
Bogárdi and Yen (1938)	$v_{mmin.} = 84.55d_S^{0.45}$	$d_S > 0.03$ cm

Table 3.3 Critical Mean Velocity in the Cross-Section (after Stelczer, 1981) continued

Author and Year of Publication	Formula	Range of Validity
Czechoslovakian Standard Specification mentioned by Ivicsics (1959)	$v_{mmin.} = 155.2h^{0.2}(0.01d_S+0.0014)^{0.3}(d_S/d_{S_{90}})^{0.2}$	$0.01 < d_S < 0.15$ cm
	$v_{mmin.} = 30.41d_S^{0.5}\log(8.8h/d_{S_{90}})$	$0.15 < d_S < 2.0$ cm
	$v_{mmin.} = 26.5d_S^{0.33}h^{0.17}$	$d_S > 2.0$ cm
(C) Highest Critical Mean Velocity in the Cross-Section		
Kharaushev (1977) from Levi's formula	$v_{mmax.} = 100.0\ell n(h/7d_S)d_S^{0.5}$	$h/d_S > 60$
Kharaushev (1977) from Samov's formula	$v_{mmax.} = 28.44h^{0.17}((0.01/0.457d_S^{0.17})+1.08d_S^{0.33})$	not specified
Kharaushev (1977) from Gontsharov's formula	$v_{mmax.} = 270.7h^{0.2}(0.0165d_S+0.0023)^{0.5}(d_S/d_{Smax})^{0.2}$	not specified

Table 3.4 Equations for Critical Shear (after Stelczer, 1981)

Author and Year of Publication	Formula	Range of Validity
(A) Laboratory Data for Hydraulically Smooth Beds		
Schoklitsch (1934)	$\tau_c = 0.18(\gamma_s - \gamma_f)d_s^{1.5}$	$d_s < 0.02$ cm
Kalinske (1947)	$\tau_c = 0.1444(\rho_s - \rho_f)d_s$	$d_s < 0.02$ cm
Laursen (1958)	$\tau_c = 0.0388(\gamma_s - \gamma_f)d_s$	$d_s < 0.02$ cm
Nagy-Karádi (1960)	$\tau_c = 0.0036(\gamma_s - \gamma_f)d_s^{0.4}$	$d_s < 0.1$ cm
Bogárdi (1962)	$\tau_c = 0.0011(\gamma_s - \gamma_f)d_s^{0.118}$	$d_s \leqslant 0.0145$ cm
(B) Laboratory Data for Hydraulically Smooth and Transition Region		
Bogárdi (1968)	$\tau_c = 620.00(h/d_s)^{-2}(\gamma_s-\gamma_f)d_s(d_s/\nu^{2/3}g^{-1/3})^{-2.75}$	$d_s < 1.0$ cm
Bogárdi (1968)	$\tau_c = 57.8\ S^{0.66}(\gamma_s-\gamma_f)d_s(d_s/\nu^{2/3}g^{-1/3})^{-0.89}$	$h < 20$ cm
Bogárdi (1975)	$\tau_c = 4.437 \times 10^{-8}(h/d_s)^{1.767}(\gamma_s-\gamma_f)d_s(d_s/\nu^{2/3}g^{-1/3})^{0.639}$	not specified
Bogárdi (1975)	$\tau_c = 42.788\ S^{1.096}(\gamma_s-\gamma_f)d_s(d_s/\nu^{2/3}g^{-1/3})^{-0.888}$	

Table 3.4 Equations for Critical Shear (after Stelczer, 1981) continued

Author and Year of Publication	Formula	Range of Validity
(C) Laboratory Data for the Transition Region		
Mavis-Liu-Soucek (1936)	$\tau_C = 0.028(\gamma_S - \gamma_f)d_S$	$d_S < 0.5$ cm
Nagy-Karádi (1960)	$\tau_C = 0.04(\gamma_S - \gamma_f)d_S^{1.49}$	$0.1 < d_S < 1.0$ cm
(D) Laboratory Data for Transition Region and Hydraulically Rough Bed		
Meyer-Peter and Müller (1948)	$\tau_C = 0.047(\gamma_S - \gamma_f)d_S$	$d_S > 0.02$ cm
Bogárdi (1962)	$\tau_C = 0.0469(\gamma_S - \gamma_f)d_S$	$d_S > 0.0145$ cm
(E) Laboratory and Field Data for Transition Region and Hydraulically Rough Bed		
Gessler (1965)	$\tau_C = 0.047(\gamma_S - \gamma_f)d_S$	$d_S > 0.6$ cm
(F) Laboratory Data for Hydraulically Rough Bed		
Shields (1936)	$\tau_C = 0.06(\gamma_S - \gamma_f)d_S$	$d_S > 1.0$ cm
Lane (1937)	$\tau_C = 0.0485(\gamma_S - \gamma_f)d_{S_{75}}$	$d_S > 0.5$ cm
Nagy-Karâdi (1960)	$\tau_C = 0.055(\gamma_S - \gamma_f)d_S$	$d_S > 1.0$ cm

Table 3.4 Equations for Critical Shear (after Stelczer, 1981) continued

Author and Year of Publication	Formula	Range of Validity
(G) Field Data for Hydraulically Rough Bed		
Ramette and Heuzel (1962)	$\tau_c = 0.02(\gamma_s - \gamma_f)d_{s_{95}}$	$d_s > 1.0$ cm
Stelczer (1978)	$\tau_c = 0.01(\gamma_s - \gamma_f)d_{s_{80}}$	$d_s > 1.0$ cm

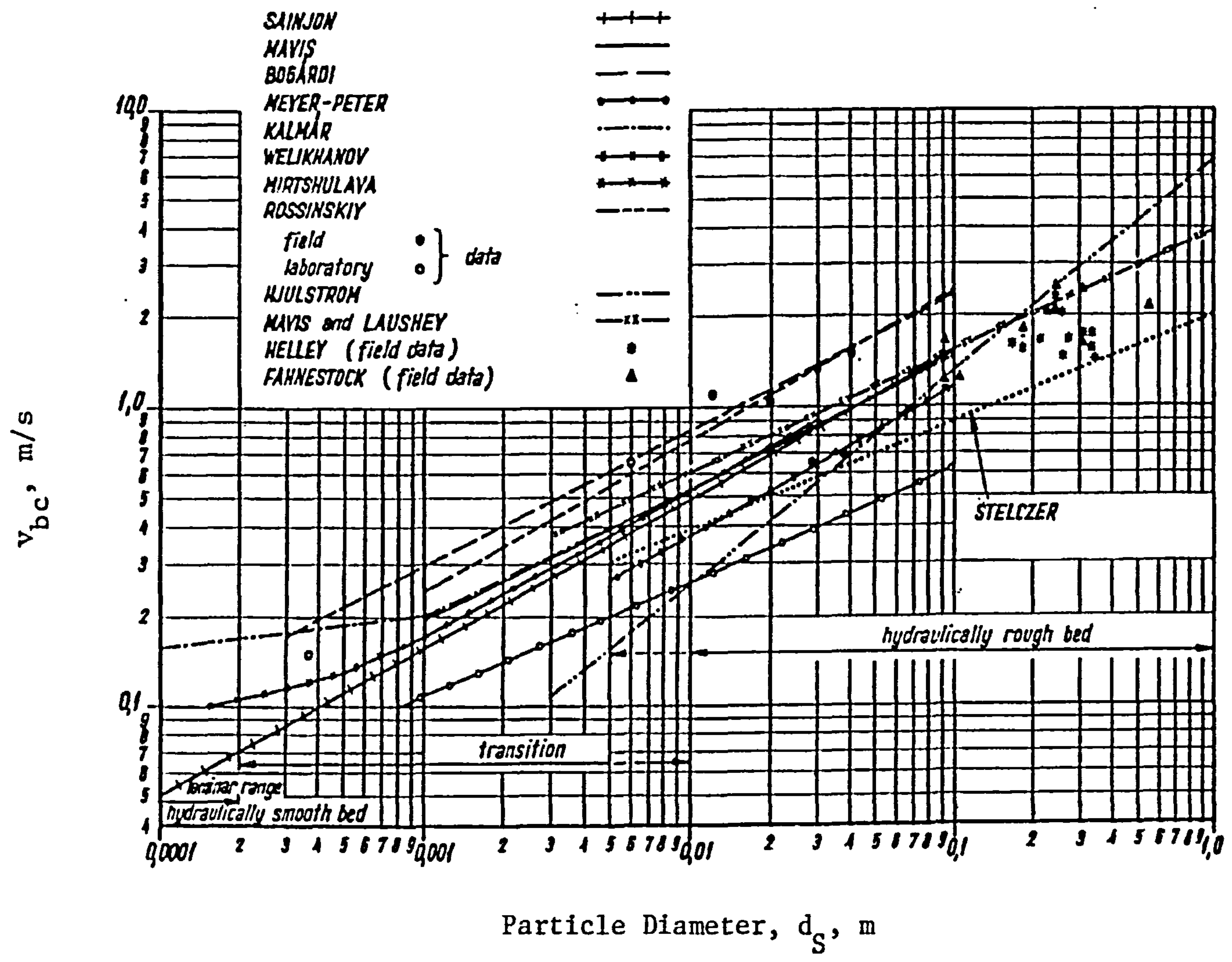

Fig. 3.4 Critical Bottom Velocity vs. Particle Diameter
(after Stelczer, 1981)

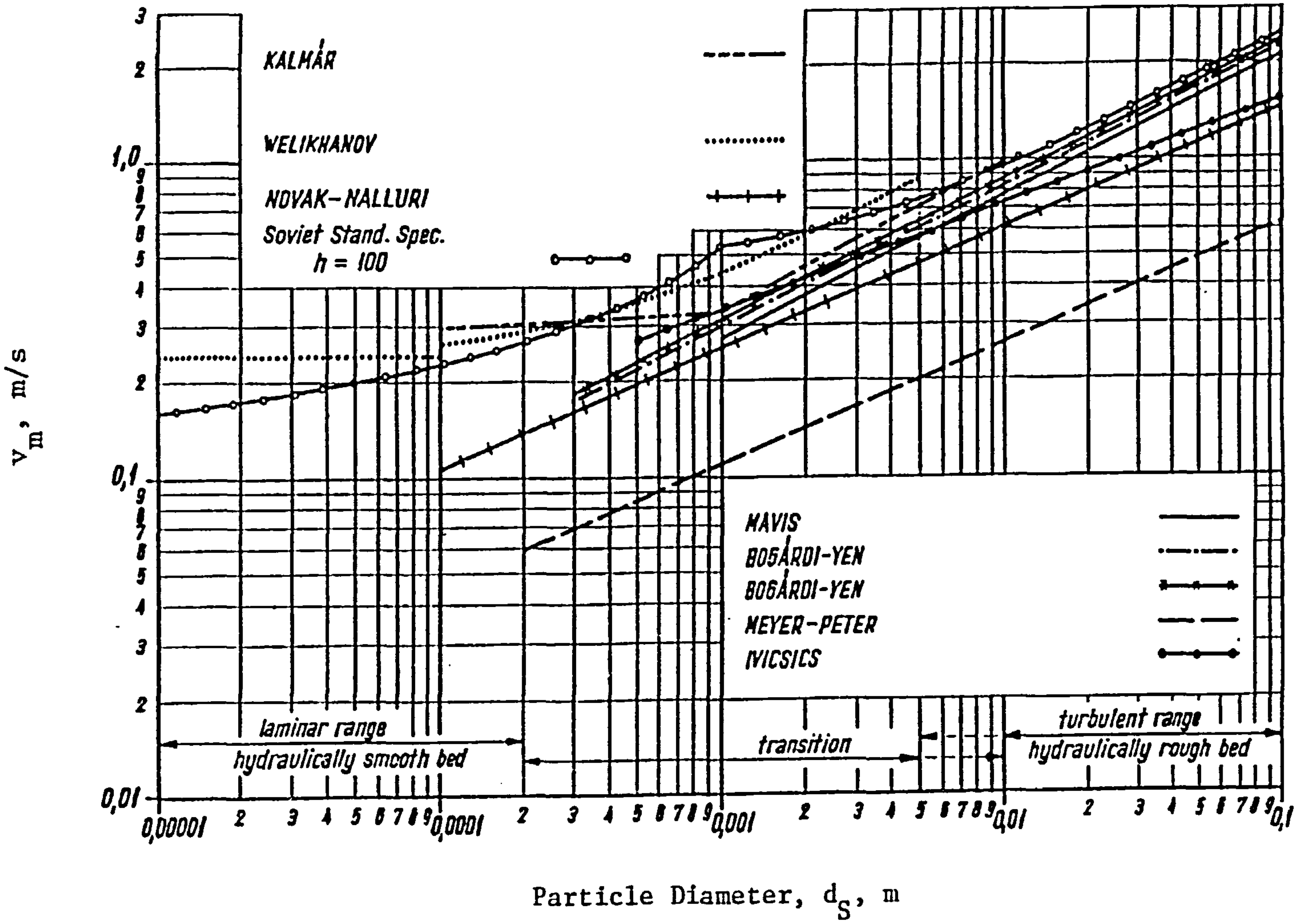

Fig. 3.5 Critical Mean Velocity in the Cross-Section vs. Particle Diameter (after Stelczer, 1981)

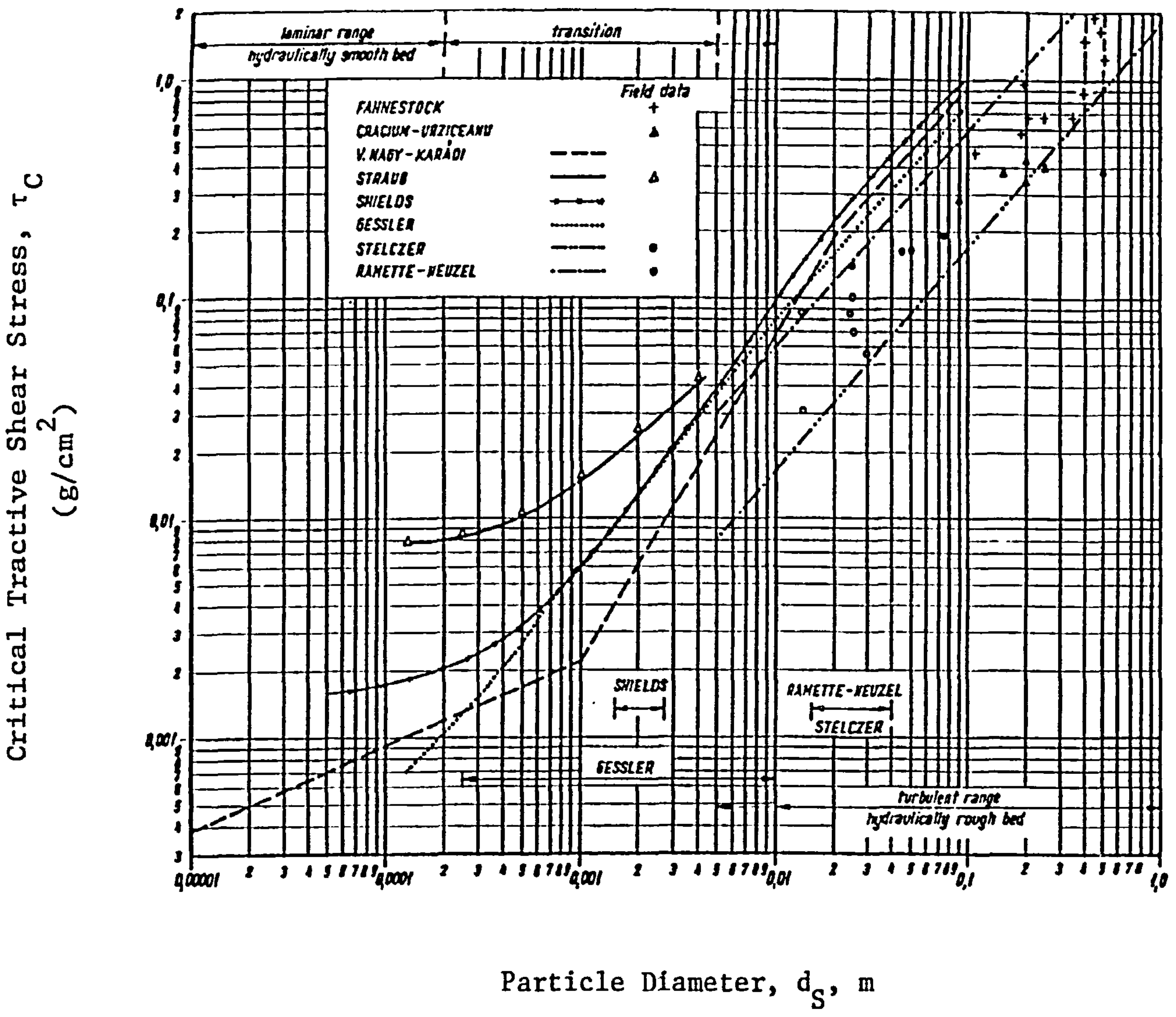

Fig. 3.6 Critical Tractive Shear Stress vs. Particle Diameter (after Stelczer, 1981)

C_S = average volumetric concentration of transported particles

Using both laboratory and field data from closed conduits, flumes and rivers, Graf and Acaroglu determined the relationship between ψ and ϕ_{GA} to be

[3.20] $\phi_{GA} = 10.39\psi^{-2.52}$, or

[3.21] $(C_S v_m R_h)/((S_S - 1)g d_S{}^3)^{0.5} = 10.39((S_S - 1)d_S/SR_h)^{-2.52}$

Hence, Eq. [3.21] gives information on the average liquid-solid mixture velocity and the volumetric concentration of the total load passing through a cross-section of a particular conveyance system for a given value of the shear intensity parameter, ψ. The value of ψ ranged from 0.1 to 100, whereas ϕ_{GA} ranged from 0.01 to 1000.

For particles of diameter 0.091 mm < d_S < 2.78 mm, Graf and Acaroglu were able to relate the shear intensity parameter to the particle settling velocity and shear velocity by

[3.22] $U_*/v_S = (3C_d/4)^{0.5}\ \psi^{-0.5}$

where U_* is the shear velocity given by

[3.23] $U_* = (gR_h S)^{0.5}$, and

v_S is the terminal settling velocity of the particle, given by

[3.24] $v_S = (4g d_S(S_S - 1)/3C_d)^{0.5}$

where C_d is the particle drag coefficient. Liu (1957) defined the ratio of U_*/v_S as the "movability number". The relationship given in Eq. [3.22] delineates the beginning of ripple formation on the bed of the conveyance channel. Figure 3.7 illustrates the relationship between the shear intensity parameter and particle Reynolds number and may be used to determine the critical condition at which motion is initiated.

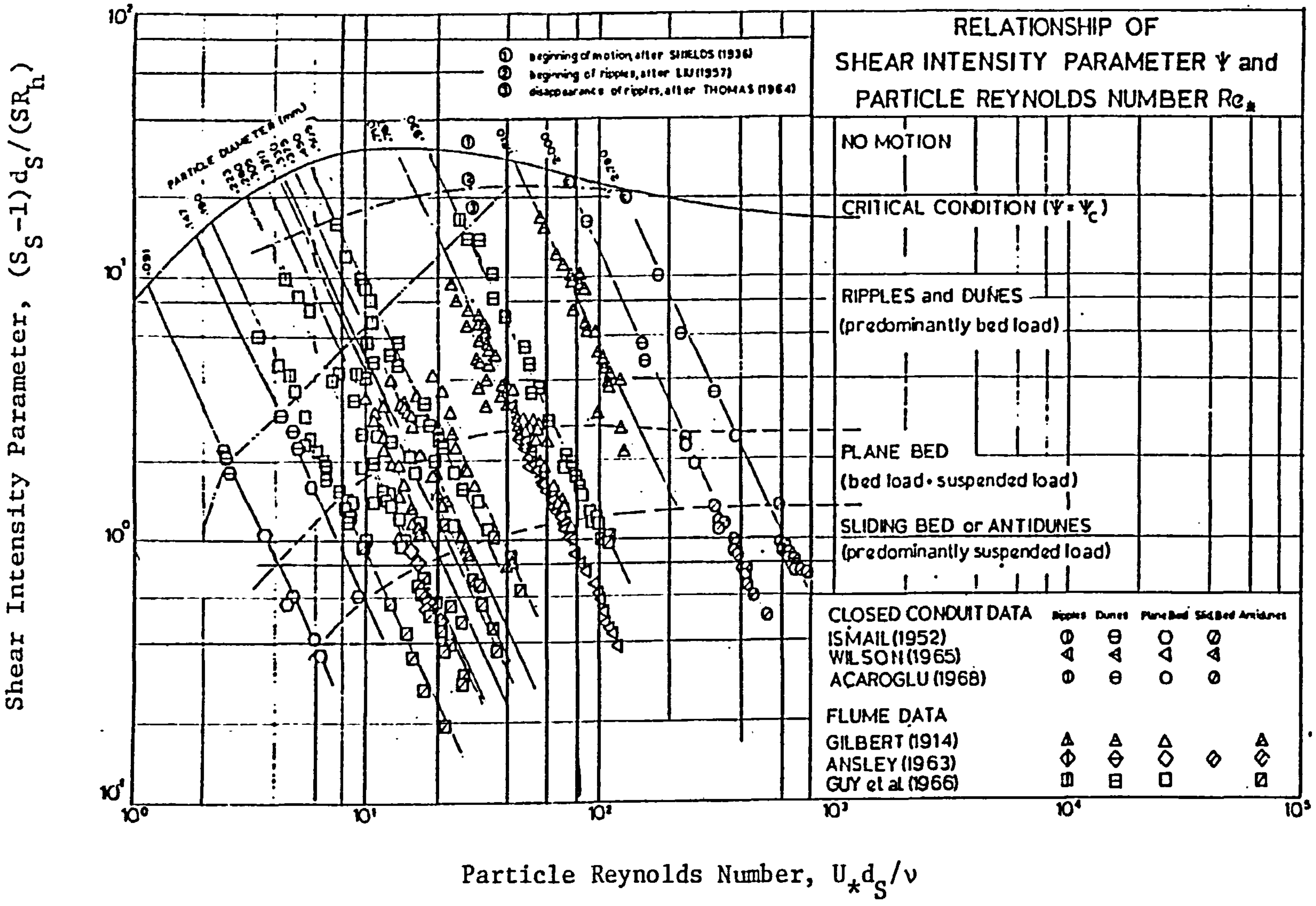

Fig. 3.7 Relationship of Shear Intensity Parameter and Particle Reynolds Number (after Graf and Acaroglu, 1968b)

Neill (1967b, 1968) studied the velocity required to displace particles in a steady, straight, uniform, two-dimensional, wide channel with a fully developed velocity profile. His equation was for uniform-sized material of specific gravity 2.65 and ranging in diameter from 6 to 30 mm. The ratio of flow depth to grain size was between 2 and 100.

Neill's equation can be expressed as

[3.25] $$v_m{}^2 = (2.0\ \gamma_S d_S (d_S/h)^{-0.33})/\rho_f$$

This equation was found to be in good agreement with the results of Mavis and Laushey (1949), Lane (1955) and Sundborg (1956).

Novak and Nalluri (1975, 1978, 1984) studied sediment transport over smooth, fixed bed channels. For rectangular channels, they expressed the Shields dimensionless shear intensity and particle Reynolds number as

[3.26] $$(\tau_C/\rho_f g d_S(S_S - 1))^2 = 0.065\ (U_* d_S \nu^{-1.0})^{-0.52}$$

for particle Reynolds number between 10 and 1000, and

[3.27] $$(\tau_C/\rho_f g d_S(S_S - 1))^2 = 0.060\ (U_* d_S \nu^{-1.0})^{-0.61}$$

for circular cross-sections.

Novak and Nalluri also proposed equations for the velocity required for incipient motion and the critical shear stress as

[3.28] $$V_{bc} = 0.17\ (S_S - 1)^{0.5} d_S{}^{0.24}$$, for rectangular channels,

and

[3.29] $$V_{bc} = 0.16\ (S_S - 1)^{0.5} d_S{}^{0.16}$$ for circular channels,

whereas the critical shear stress was expressed as

[3.30] $\tau_C = 0.128\ (S_S - 1)d_S^{0.4}$, for rectangular channels,

and

[3.31] $\tau_C = 0.104\ (S_S - 1)d_S^{0.4}$, for circular channels,

where τ_c is in N/m^2 and d_S is in mm.

For both rectangular and circular cross-sections, Novak and Nalluri expressed V_{bc} in terms of the relative roughness, d_S/R_h, as

[3.32] $V_{bc} = 0.61(S_S - 1)^{0.5}(d_S/R_h)^{-0.27}(gd_S)^{0.5}$

Equation [3.32] is applicable over the range $0.01 < d_S/R_h < 1$.

Knight (1981) determined the relationship for bed and wall shear in rectangular channels as a function of the percentage of shear force on the walls using artificial strip roughness for the bed and walls. The equations for the mean wall and bed shear stresses are

[3.33] $\tau_W = \rho g S_f(\%SF_W/100)(B/h)$, and

[3.34] $\tau_b = (\rho g h S_f)(1 - 0.1\ \%SF_W)$

where

τ_W = wall shear stress

τ_b = bed shear stress

S_f = energy slope

B = channel width

h = channel depth, and

$\%SF_W$ = the percentage of shear force on the walls and is given by

[3.35] $\%SF_W = e^{\alpha}[\tanh(\pi\beta) - 0.5\ (\tanh(\pi\beta) - \beta)^2]$

where

$\alpha = -3.264 \log(B/h + 3) + 6.211$

$\beta = 1 - \gamma/5$, and

$\gamma = \log(k_{Sb}/k_{Sw})$

where k_{Sb} and k_{Sw} are the mean diameters of the grains making up the roughness of the bed and walls, respectively. The validity ranges for Knight's equations are $1.5 < B/h < 15$, $1 < k_{Sb}/k_{Sw} < 10^4$, $2.1 \times 10^4 < 4v_mR_h/\nu < 3.7 \times 10^5$ and $0.23 < v_m/(gh)^{0.5} < 0.57$.

3.5 The Effects of Lift and Drag on Particle Motion

Lift forces may arise for at least two reasons. Firstly, if the particle is resting on the bottom where the velocity gradients are steepest, a pressure difference is set up which results in lifting the particle. Secondly, the same particle might experience lift because of the upward velocity components adjacent to the bed as a result of turbulence. If the magnitude of the lift becomes equal to the weight, then the smallest drag force would cause an initiation of motion. Therefore, the value of the lift force must be investigated and compared in magnitude to the drag force and the particle's submerged weight. Graf (1971) expressed the lift force as

[3.36] $$F_L = C_L\, k\, d_S^2\, \rho_f\, v_b^2/2$$

where

F_L = the lift force

C_L = the lift coefficient

k = particle shape factor, and

v_b = fluid velocity near the bottom of the channel

The only quantitative observations of lift on sediments on a bed were made by Einstein and El-Samni (1949) and Apperley (1968). Einstein and El-Samni measured the difference in mean static pressure on sediment beds at the bottom level of the top layer of sediments and at the wall of the channel at the top level of the top layer of sediments. The measurements yielded a pressure difference or lift pressure on the grains of

[3.37] $\Delta p = 0.178\ \rho_f\ v^2/2$

where v is the velocity at a distance of $0.35d_{S_{35}}$ above the theoretical bed and $d_{S_{35}}$ is the size of the grains for which 35% by weight of the bed material is finer. The theoretical bed was defined as the position of the origin of y for which the measured velocity profiles conformed to

[3.38] $v/U_* = 8.5 + 5.75 \log(y/k_S)$

where v is the velocity at a distance y above the bed. Equation [3.38] describes the velocity profile for a two-dimensional, free-surface flow over a flat sediment bed. Einstein and El-Samni found that, for gravel beds, the theoretical bed was $0.2d_{S_{67}}$ below the tops of the uppermost grains.

The experimental results reported by Einstein and El-Samni were used by Vanoni (1966) to calculate the ratio $\Delta p/\tau$. This calculation gave values of about 2.5, giving a strong indication that lift forces were of considerable importance in the initial-motion mechanism. However, once a particle was displaced, lift forces tended to diminish and drag forces tended to increase, as pointed out by Chepil (1961).

Apperley (1968) measured the lift and drag forces on a sphere 1/4 inch in diameter in a bed of well-rounded 1/4 inch gravel in a flow 9.25 inches deep with a mean velocity of 3.40 feet per second. When the sphere was in the bed of gravel, the ratio of lift/drag was 0.50. When the sphere was raised a distance equal to 1/4 of its diameter the ratio of lift/drag was 0.78. When the sphere was raised further, the drag continued to increase and the lift decreased sharply and became negative at a distance of 1.5 grain diameters above the bed. The mean drag force with the sphere imbedded with the other particles was nearly equal to the product of the bed shear stress and the cross-sectional area of the sphere. The distribution of the instantaneous lift force observed by Apperley indicated that there was a predominance of negative values, but there were infrequent bursts of large positive lift forces which were apparently responsible for the entrainment of the particles.

Simons and Sentürk (1977) included the lift force in the following equation which is similar to Eq. [3.1] proposed by White (1940).

$$[3.39] \quad C_1(\gamma_S - \gamma_f)d_S^3\, a_1 \sin(\phi - \theta) - a_1 C_L C_3 d_S^2 \rho_f v_b^2 \sin\phi/2 = a_1 C_2 \tau_C d_S^2 \cos\phi$$

where C_3 is the coefficient related to the effective surface area of the particle in the direction of the lift force. When rearranged, Eq. [3.39] yields the critical tractive shear stress as

$$[3.40] \quad \tau_C = (C_1/C_2)(\gamma_S - \gamma_f)d_S \sin(\phi - \theta)/\cos\phi - 0.5(C_3/C_2)C_L \rho_f v_b^2 \tan\phi$$

Coleman (1967) was able to predict the incipient motion of non-cohesive spherical bed particles subjected to certain drag and lift. It was observed that the lift coefficient took on negative values for Reynolds numbers less than about 100, where the Reynolds number was defined as

[3.41] $N_R = v_o \, d_S / \nu$

where v_o is the flow velocity at the particle center-line. Coleman also found that the lift coefficient was zero when d_S/δ' was unity and that the lift coefficient was negative for d_S/δ' less than unity, where δ' is the thickness of the laminar sublayer. Coleman's results indicated that downward-acting "lift" forces existed when the particle was completely enclosed in the layer of laminar flow, so that particle motion was restrained. The equation for the "lift-factor" was given as

[3.42] $K_L = 1 - (2.1169 \, C_d N_R^2 \rho_f \nu^2)/((\gamma_S - \gamma_f)(d_S^3))$

The lift on the particle can be computed from

[3.43] $F_L = (\pi/6)((\gamma_S - \gamma_f)d_S^3 - 2.1169 \, C_d N_R^2 \rho_f \nu^2)$

Coleman's results for the lift factor and drag-coefficient are shown in Fig. 3.8. These equations and figures were shown to apply to quartz spheres ranging in diameter from 0.6 to 20 mm. The kinematic viscosity ranged between 9.3×10^{-7} and 3.7×10^{-5} $m^2 s^{-1}$ and the specific gravity varied between 1.28 and 7.10.

It can be noted in Fig. 3.8 that the C_d data tends to group around the drag coefficient curve for a sphere in free fall. This finding is significant because it verifies Egiazaroff's assumption

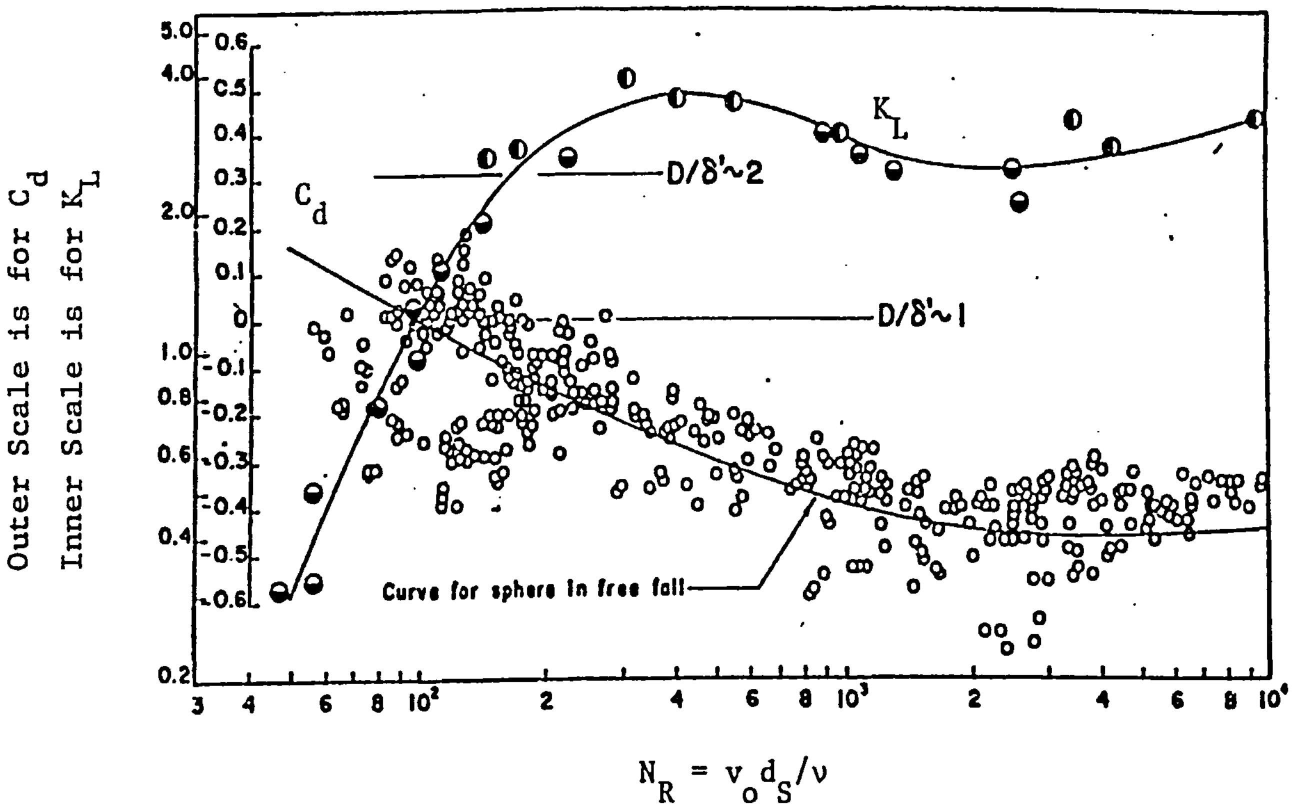

Fig. 3.8 Lift Factor and Drag Coefficient (after Coleman, 1967)

(1957, 1965) that a particle which is near the state of incipient motion experiences drag forces similar to that of a particle in free fall.

Aksoy (1973) also studied fluid forces acting on a sphere near a solid boundary. Aksoy described the formation of lift with the aid of Fig. 3.9. In Fig. 3.9a, the solid boundary was far from the sphere and the velocity distribution was uniform. For low Reynolds numbers, the pressure forces were negligible and the stream-lines came together behind the sphere. When the Reynolds number was increased, the boundary layer separated symmetrically along the surface, and eddies were formed which rotated in opposite directions. In this case, the fluid force was composed of friction and pressure forces. For high Reynolds numbers, the eddies elongated, became unstable and oscillation of the wake could be observed. This produced alternating longitudinal and lateral fluid forces which caused a forced vibration of the sphere.

If, however, the sphere was located near a solid boundary, the upstream velocity was not distributed uniformly but increased with distance from the boundary. The shape of the velocity profile depended upon the character of the flow and the boundary surface. As shown in Fig. 3.9b, the flow did not separate symmetrically. The position of the separation moved to the upper surface and this separation not only produced drag, but also lift. In addition to these two forces, a moment acted on the centre of the sphere. The fluid forces were not constant, but fluctuated about the mean value.

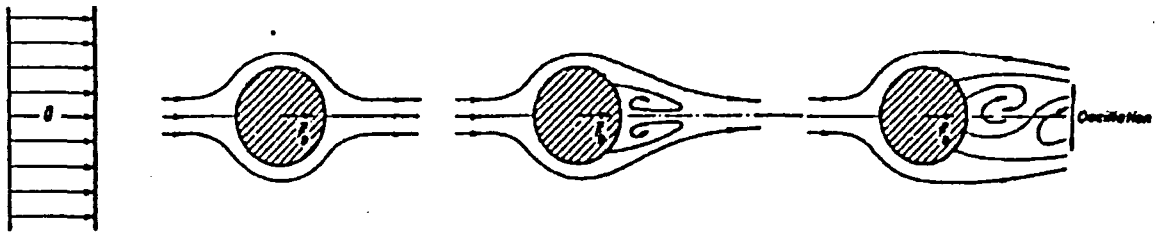
U
Oscillation

a – A sphere in an infinite stream with an uniform upstream velocity

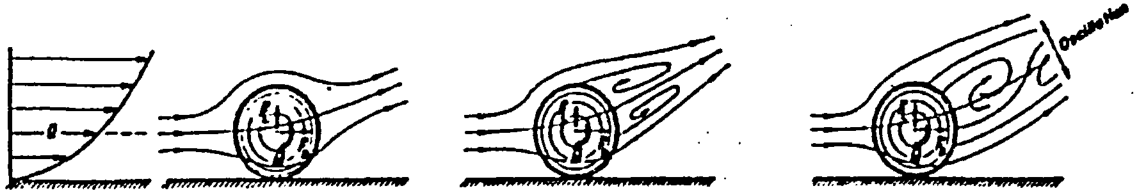
U
Oscillation

b – A sphere near a smooth boundary with an increasing velocity profile

Fig. 3.9 Development of Drag and Lift Forces (after Aksoy, 1973)

The fluctuations arose due to large scale turbulence of the flow and secondly by the wakes which were generated behind the sphere.

Aksoy used transducers mounted on the channel bed to measure instantaneous drag and lift forces and subsequently calculated the drag and lift coefficients. Figure 3.10 shows the drag and lift coefficients over a range of Reynolds numbers from 2700 to 6600. The drag coefficients agree well in the range of measurements with the curve for a sphere rolling down an inclined smooth boundary which was developed by Garde and Sethuraman (1969). Aksoy found that, at a Reynolds number of 6600, the maximum instantaneous lift force was nearly three times the mean lift force.

Garde and Sethuraman (1969) investigated the effects of the boundary on the particle drag coefficient. They considered both smooth and rough surfaces. Garde and Sethuraman, like Carty (1957), assumed that rolling resistance was negligible for smooth boundaries. Equating the drag force to the mass component parallel to the bed yielded

$$[3.44] \qquad C_d = (4d_S g)\sin\theta(\rho_S - \rho_f)/(3\rho_f v_o^2)$$

Garde and Sethuraman studied particle diameters ranging from 9.22 mm to 25.33 mm. The kinematic viscosity ranged from 10^{-6} to 7.15 x 10^{-4} m^2s^{-1}. Glass, steel and plastic spheres were used in this investigation. The results for smooth and rough boundaries are shown in Figs. 3.11 and 3.12 respectively. For smooth boundaries, it was found that, for Reynolds numbers up to 20, the relationship between C_d and N_R obeyed a straight line variation of the form:

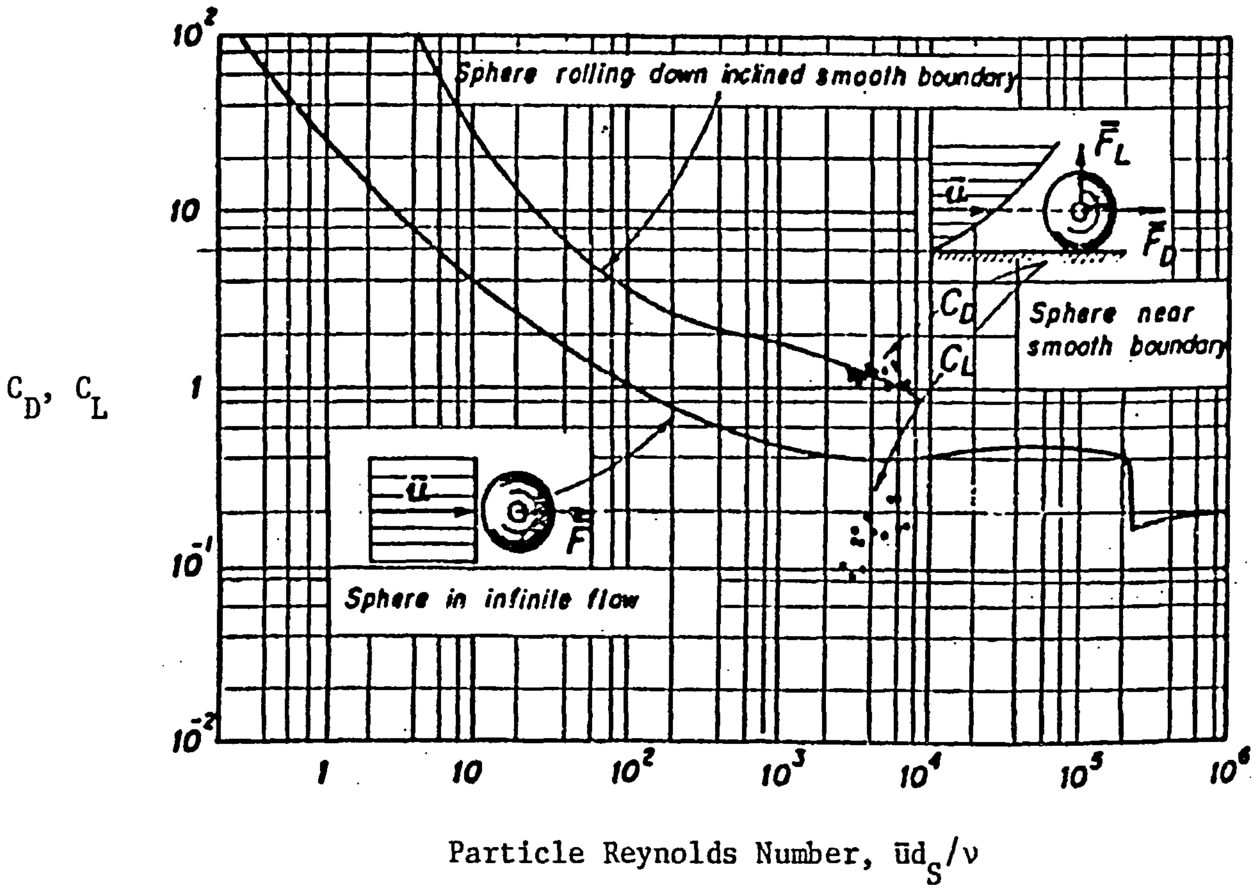

Fig. 3.10 Variation of Drag and Lift Coefficients (after Aksoy, 1973)

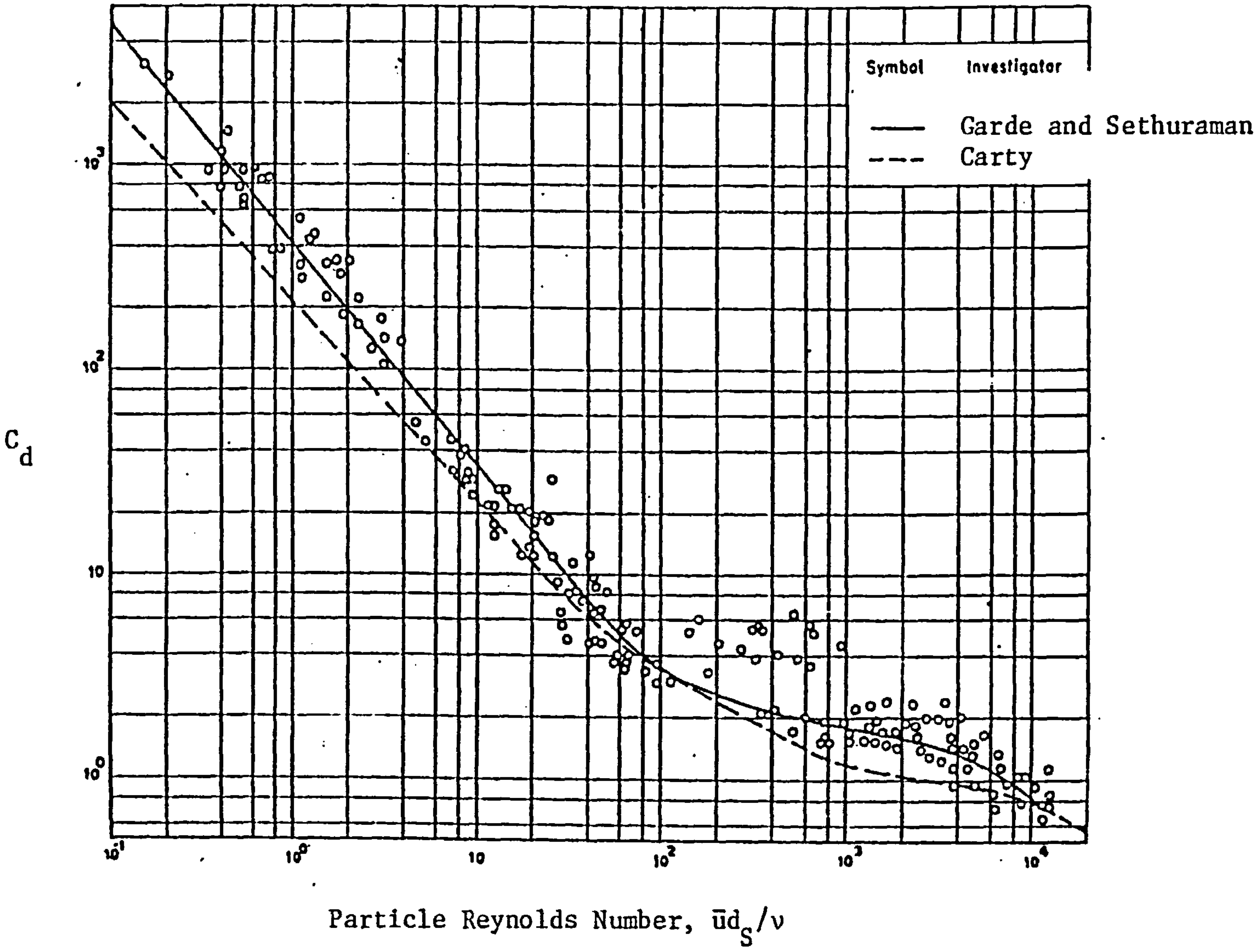

Fig. 3.11 Variation of Drag Coefficient with Reynolds Number for Smooth Boundaries (after Garde and Sethuraman, 1969)

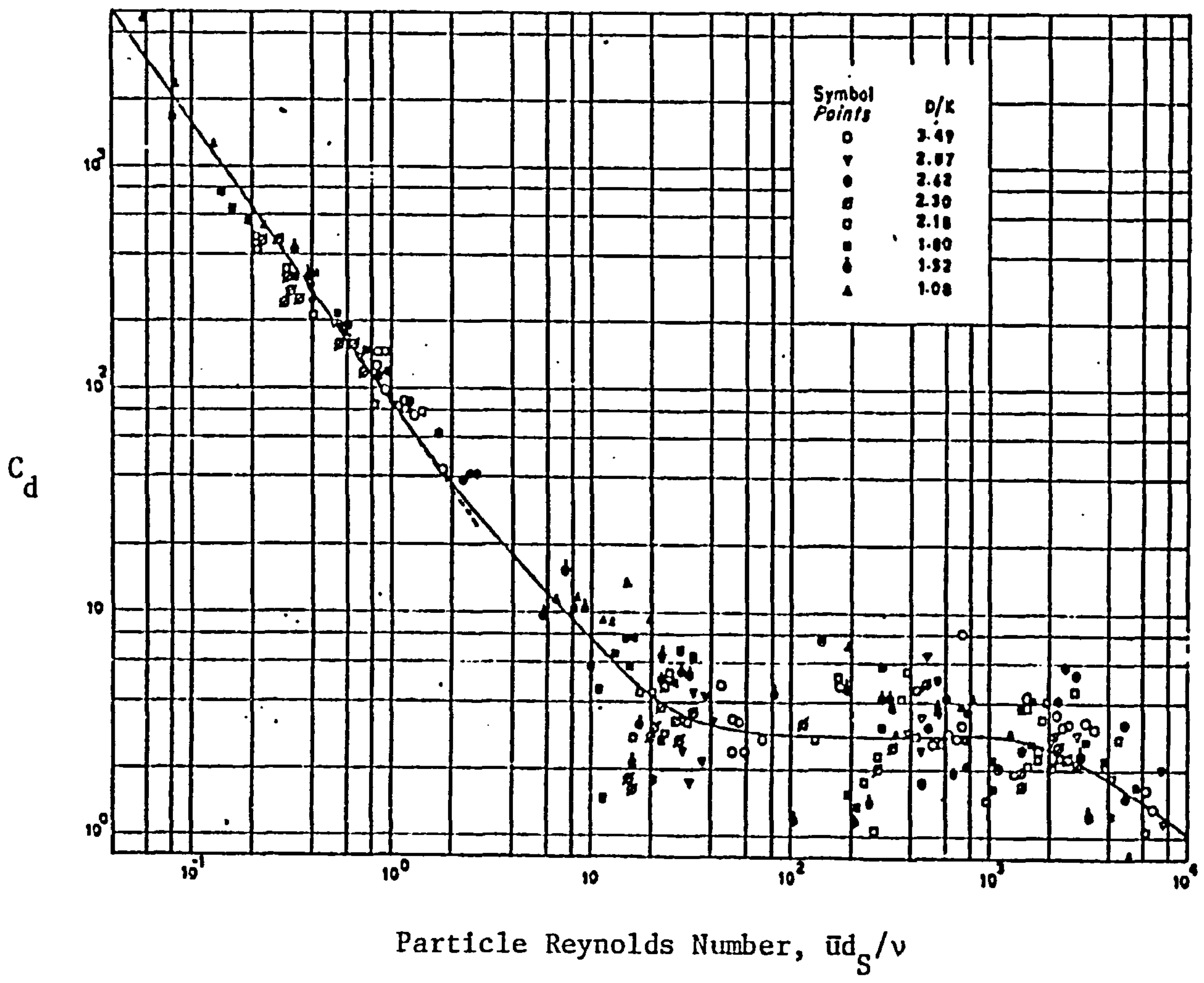

Fig. 3.12 Variation of Drag Coefficient with Reynolds Number for Rough Boundaries (after Garde and Sethuraman, 1969)

[3.45] $C_d = 420/N_R^{1.07}$

For rough boundaries, C_d depended on the relative roughness of the bed, defined by d_S/k, where k is the diameter of the spheres making up the bed roughness elements and d_S is the diameter of the sphere under consideration. The mean curve for all d_S/k values is shown in Fig. 3.12. For Reynolds numbers less than one, the correlation was

[3.46] $C_d = 82.5/N_R^{1.3}$

The results of Garde and Sethuraman indicated that the drag coefficient for a sphere moving on a smooth or rough boundary was significantly different from the drag coefficient of a sphere in an infinite fluid. In their experiments, the fluid was stationary and the slope of the bed was increased until the particle began to roll. The sphere was moving through a fluid that had neither ambient turbulence nor a velocity gradient normal to the boundary and, as Coleman (1972) pointed out, the drag coefficients were higher than those for a sphere moving in an infinite fluid.

As an extension of earlier work, Coleman (1972) studied the drag coefficient of a stationary sphere on a horizontal bed of closely packed identical spheres subjected to a flow that displayed both the ambient turbulence and a velocity gradient normal to the boundary. The purpose was to compare the C_d value for rolling spheres in stationary fluids to the C_d of a stationary sphere in moving fluid. Both Coleman's and Garde and Sethuraman's results are summarized in Fig. 3.13. Coleman's results are for kinematic

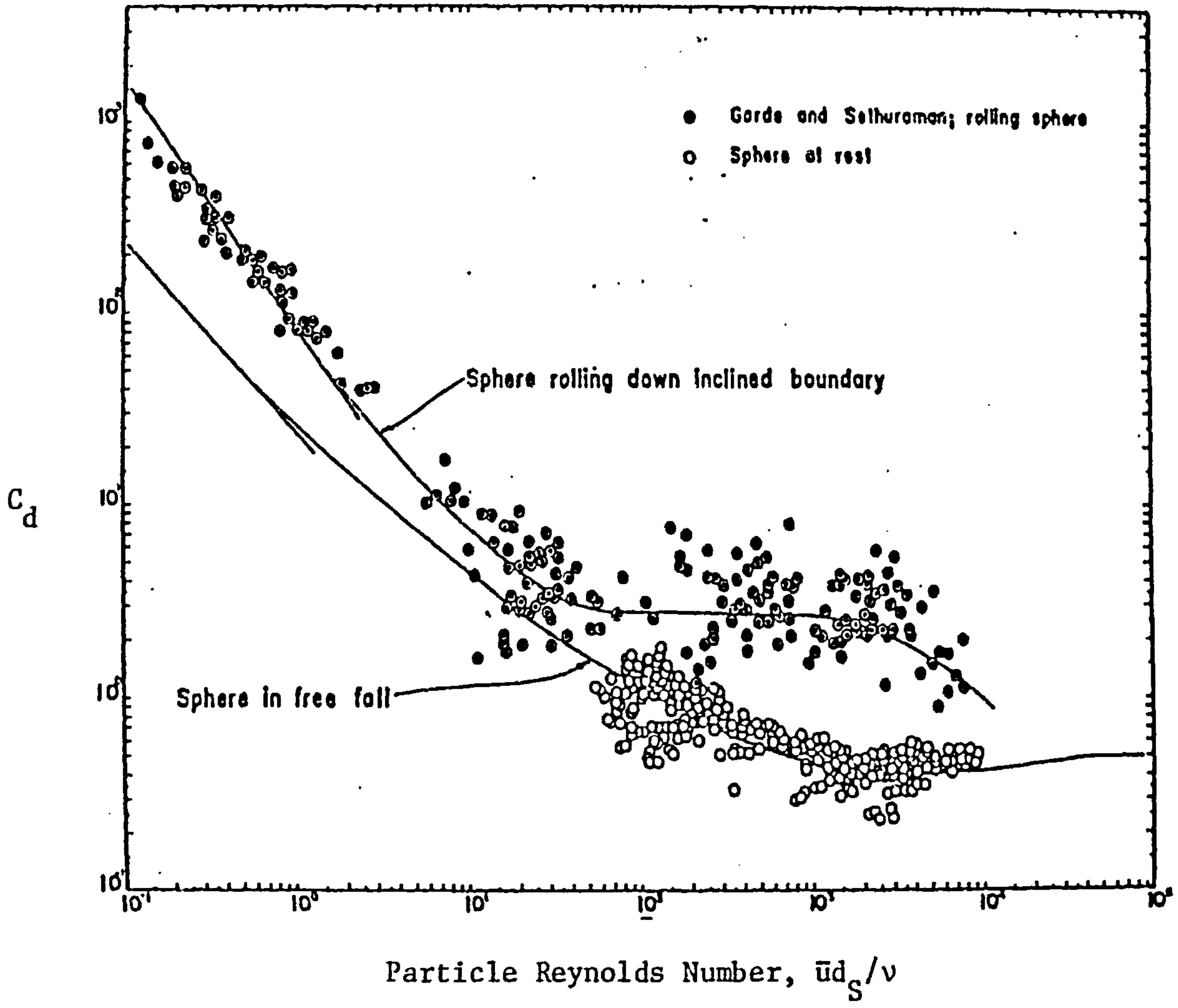

Fig. 3.13 Comparison of Drag Coefficients for a Rolling Sphere, Stationary Sphere and Falling Sphere (after Coleman, 1972)

viscosities from 1×10^{-5} to 40×10^{-5} ft^{2}s^{-1}, and for Reynolds numbers between 50 and 9400.

In the absence of detailed studies on the local flow patterns around the spheres on rough boundaries, Coleman speculated that the marked differences between drag coefficient functions for a rolling sphere and a stationary sphere were a result of the additional circulation induced around the rolling sphere. He also noted that in view of the inherent asymmetry of the flow around a stationary sphere on a boundary, the close correspondence between the drag coefficient function for a sphere in free fall and a stationary sphere was remarkable.

3.6 The Effects of Steep Slopes on Particle Motion

Most of the research conducted on the incipient motion of particles has been concerned with relatively low-sloped channels and flumes. Scheuerlein (1973), Mohanty (1962), Kharrufa (1962), Pe (1975), Ashida and Bayazit (1973), Bathurst, Graf and Cao (1982), and Smart (1984), have shown that the initiation of motion of sediment grains on the bed of steep channels occurs at very shallow depths, corresponding to large values of relative roughness.

In the literature, the effect of relative roughness on the initiation of motion is usually not considered, and some authors, Yalin (1972), are of the opinion that this effect can be neglected. Ashida and Bayazit (1973) subsequently investigated the effect of relative roughness, d_S/h, on the critical Shields' parameter defined by

[3.47] $S_{SC} = \tau_C/((\gamma_S - \gamma_f)d_S)$

Assuming that the sediments moved by sliding, Ashida and Bayazit developed a modified critical Shields parameter for steep slopes

[3.48] $S_{SC} = \tau_C/((\gamma_S - \gamma_f)d_S(\cos\theta\tan\phi - (S_S/(S_S - 1))\sin\theta))$

For small slopes, $\theta \approx 0^o$, it can be seen that Eq. [3.48] becomes the critical Shields parameter divided by tan ϕ. The range of variables used by Ashida and Bayazit were

$6.4 \text{ mm} < d_S < 22.5 \text{ mm}$

$2.49 < S_S < 2.66$

$0.01 < S < 0.20$

$1.15 \text{ cm} < h < 9.75 \text{ cm}$, and

$1.0 < \tan\phi < 1.3$

Graphically, the relationship between d_S/h and S_{SC}, obtained by Ashida and Bayazit, is presented in Fig. 3.14. The figure shows that the critical Shields parameter increases considerably as the flow becomes shallower. For $d_S = 1.5h$, Ashida and Bayazit found that S_{SC} was about 2.5 times larger than its value for milder slopes. Ashida and Bayazit attributed the increase in the Shields parameter for steep slopes to the following factors:

1. As the depth of water is reduced for a constant value of the bed shear stress, energy dissipation in the separation zones downstream of the grains becomes more significant. This results in a reduction of the velocity at a given distance above the bed, and hence the drag force diminishes for a constant shear stress with the increase of the slope. Thus, larger shear stresses are required to start the motion at lower depths.

2. Drag and lift coefficients of a grain may vary as a function of the relative roughness, and

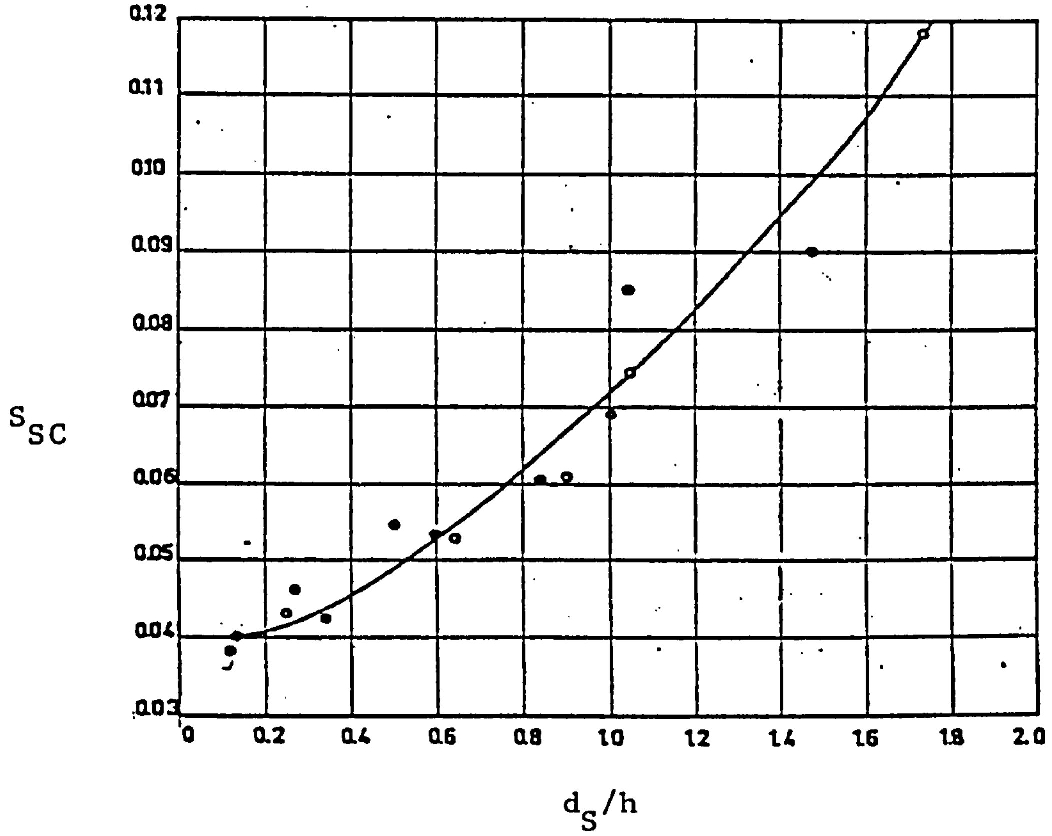

Fig. 3.14 Variation of the Critical Shields' Parameter with Relative Roughness and Steep Slopes (after Ashida and Bayazit, 1973)

3. The turbulence characteristics of the flow may be expected to change.

Pe (1975) defined flows of large roughness and high slopes as "torrential flows". Pe studied the resistance due to cubical elements as well as the incipient motion of these elements, and was able to relate the dimensionless shear stress to the dimensionless Reynolds number for the cubical resistance elements. For a 16% areal concentration of roughness elements, which has been shown by Rouse (1965) to result in the maximum resistance, Pe found the functional relationship

[3.49] $(\gamma_f R_h S)(S_S - 1)^{1.17}/(\gamma_S - \gamma_f)k = 5.6 \times 10^{-11}(k(gR_h S)^{0.5}/\nu^{2.30}$

in which k is the height of the roughness elements.

Pe confined his research to a maximum slope of 0.095 (5.4 degrees), and the Reynolds numbers of the cubes, denoted by $k(\tau/\rho_f)^{0.5}/\nu$, ranged from 6435 to 14438. Values of the dimensionless shear stress, $\tau/(k(\gamma_S - \gamma_f))$, ranged from 0.020 to 0.092. Particle specific gravities ranged from 1.04 to 6.903.

Based on the research of Sayre and Albertson (1961), Mirajgaoker and Charlu (1963), Herbich and Shulits (1964), Powell(3), Mohanty (1962), and Kharrufa (1962), Scheuerlein (1973) determined that the resistance law for flows in steep channels with high relative roughness was given by

[3.50] $C/(g)^{0.5} = (8/f)^{0.5} = -2.30 \log(kB/R_h)/\kappa$

where C is the Chézy friction coefficient, κ is the von Kármán turbulence coefficient, and the coefficient B is given by

[3.51] $B = (0.44 + 3Sk/L)(1 - 1.3S + 0.08R_h/k)$

in which L is the longitudinal spacing of the roughness elements. Scheuerlein found that the von Kármán coefficient ranged from 0.25 to 0.32.

Since the flow along a rough boundary is not uniform for large roughness elements, it is necessary to select a bed level as a reference datum so that uniform flow approximations can be applied. Schlichting (1936) introduced the concept of geometric bed level, which was the level that would arise if all the roughness were melted to form a smooth surface. By using this level as the reference datum, the weight of fluid was distributed evenly along the flow direction to produce an average bed shear stress.

Bayazit (1982) reviewed the literature for different types of roughness elements. Table 3.5 gives the distance of the theoretical bed level below the tops of the roughness elements, expressed as (A)(k), where k is the roughness element height.

In addition to estimating the theoretical bed level, a determination of the equivalent sand roughness, k_s, that will produce the observed energy loss when inserted into the equation for rough open channels is required. Nikuradse (1933) is credited with having defined the term of equivalent sand roughness and he made use of it in the logarithmic velocity equation

[3.52] $(8/f)^{0.5} = (1/\kappa)\ \ell n(h/k_s) + 6$

Bayazit (1982) reported that κ usually was assumed to be equal to 0.40. k_s was not a measure of the physical roughness height but rather the effect of the roughness on the flow, determined

Table 3.5 Distance of Theoretical Bed Level Below the Tops of Roughness Elements (after Bayazit, 1982)

Author	Year	Roughness Element Shape	A
Schlichting	1936	Sphere	0.16
Einstein and El-Samni	1949	Hemisphere	0.20
O'Laughlin and MacDonald	1964	Sand	0.27
Goma and Gelhar	1968	Sphere	0.23
Blinco and Parthenaides	1971	Irregular Particles	0.27
Grass	1971	Gravel	0.18
Cheng and Clyde	1972	Sphere	0.15
Kamphuis	1974	Gravel	0.30
Bayazit	1976	Sphere	0.35
Denker	1980	Cylinder	0.35
Denker	1980	Triangular	0.35

experimentally. For large roughness elements, k_s depended on the size, shape and spacing of roughness elements as well as the relative roughness. Table 3.6 summarizes the work of several researchers in determining the various k_s values. The equivalent sand roughness is expressed as a multiple of a particular particle size.

Bathurst, Graf and Cao (1982) pointed out the errors in using the Shields approach for slopes greater than 0.005. Firstly, for $S \gtrsim 0.005$, and for small ratios of depth to sediment size, $h_{CR}/d_{50} \lesssim 10$, where h_{CR} is the critical flow depth at incipient motion, the critical Shields' factor, $\tau_C/((\rho_S - \rho_f)gd_{50}(\cos\theta \ \tan\phi - \sin \theta))$, increased as h_{CR}/d_{50} decreased. Mizuyama (1977) and Bathurst, et al. (1979) found similar trends. The critical Shields' parameter was also affected by the armouring or paving effects of the surface layer of the bed material where the bed had a non-uniform size distribution; Egiazaroff (1965), Gessler (1971), Andrews (1981) and Parker and Klingman (1982). Bathurst, et al. reported that neither of these processes were adequately catered for in the Shields' approach.

Secondly, the Shields' factor varied essentially with h_{CR}/d_{50} for most natural flows, and the shear Reynolds number varied as $(h_{CR}S)^{0.5}/d_{50}$, so that plotting the critical shear parameter against the shear Reynolds number, or any other flow parameter based on depth, did not provide a useful guide to the critical conditions for initiation of motion; Gessler (1971) and Simons and Sentürk (1977).

Table 3.6 Equivalent Sand Roughness for Various Boundaries** (after Bayazit, 1982)

Author	Year	Roughness Element	k_s
Leopold, Wolman and Miller	1964	Gravel	$3.5\ d_{84}$
Limerinos	1970	Gravel	$3\ d_{84}$
Kamphuis	1974	Gravel	$2\ d_{90}$
Bayazit	1976	Closely Packed Spheres	$2.5\ d_s$
Charlton, _et_ _al_.	1978	Gravel	$3.5\ d_{90}$
Hey	1979	Gravel	$3.5\ d_{84}$
Thompson and Campbell	1979	Gravel	$4.5\ d_{90}$
Gladki	1979	Gravel	$2.5\ d_{80}$
Denker	1980	Closely Packed Cylinders	$2\ d_s$
Bray	1980	Gravel	$3.5\ d_{84}$; $3.1\ d_{90}$
Griffiths	1981	Gravel	$5\ d_{50}$
Denker	1981	Triangular	$8.5\ k$

** d_{90} indicates that 90% of the sediment sample has a diameter smaller than the specified size

Bathurst, et al. developed a new approach based on the Schoklitsch criterion in order to overcome the above mentioned deficiencies. Using the assumption of Flammer, et al. (1970), that the drag and lift coefficients for steep flows and small values of h_{CR}/d_{50} varied with particle Reynolds number, the flow Froude number and h_{CR}/d_{50}, Bathurst, et al. developed a dimensionless discharge factor q_C^*, given by

[3.53] $q_C^* = (V_{bC}\ h_{CR})/[((d_{50}{}^{3/2})(g(S_S - 1)(\cos\theta\ \tan\phi - \sin\theta))^{1/2}]$

where,

[3.54] $q_C^* = \text{fcn.}\ \{N_R,\ S,\ k_1,\ d_{84}/d_{50},\ \text{BPF}\}$

in which d_{84}/d_{50} represented the effect of particle size distribution, k_1 represented the particle shape and BPF was a bed packing factor. The above function is similar to the Schoklitsch (1962) equation for the critical unit flow discharge for gravel-bed rivers.

Using bed slopes between 3 and 9%, and specific gravities of approximately 2.6, Bathurst, et al. plotted their data for steep slopes, as well as other available data for steep slopes, on the traditional Shields diagram.

As can be seen from Fig. 3.15, the data for each bed material fell into a pattern of parallel lines and not along the traditional Shields curve. Bathurst, et al. used Fig. 3.16 to explain the differences between the observed and traditional curves. From Fig. 3.16 it can be noted that the ordinate varies as h_{CR}/d_{50}

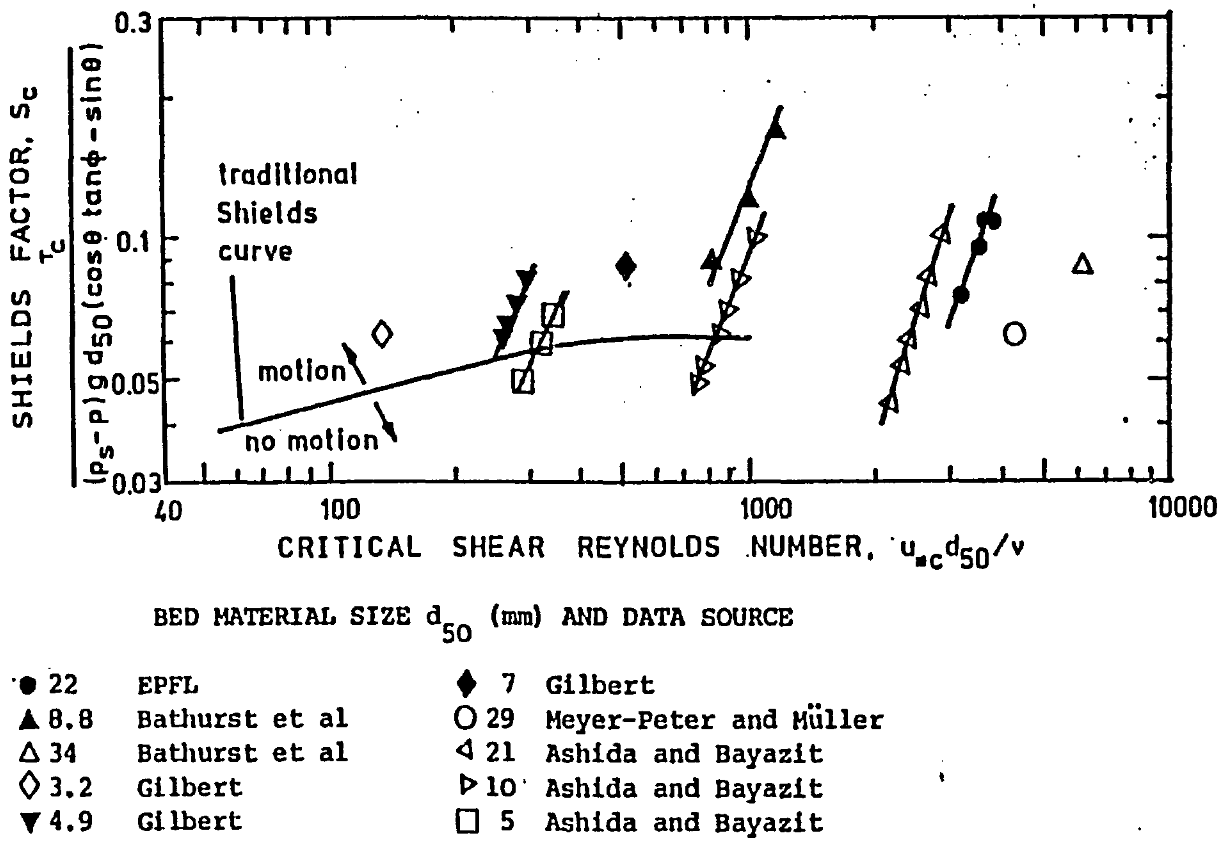

Fig. 3.15 Modified Critical Shear Stress vs. Critical Shear Reynolds Number (after Bathurst, Graf and Cao, 1982)

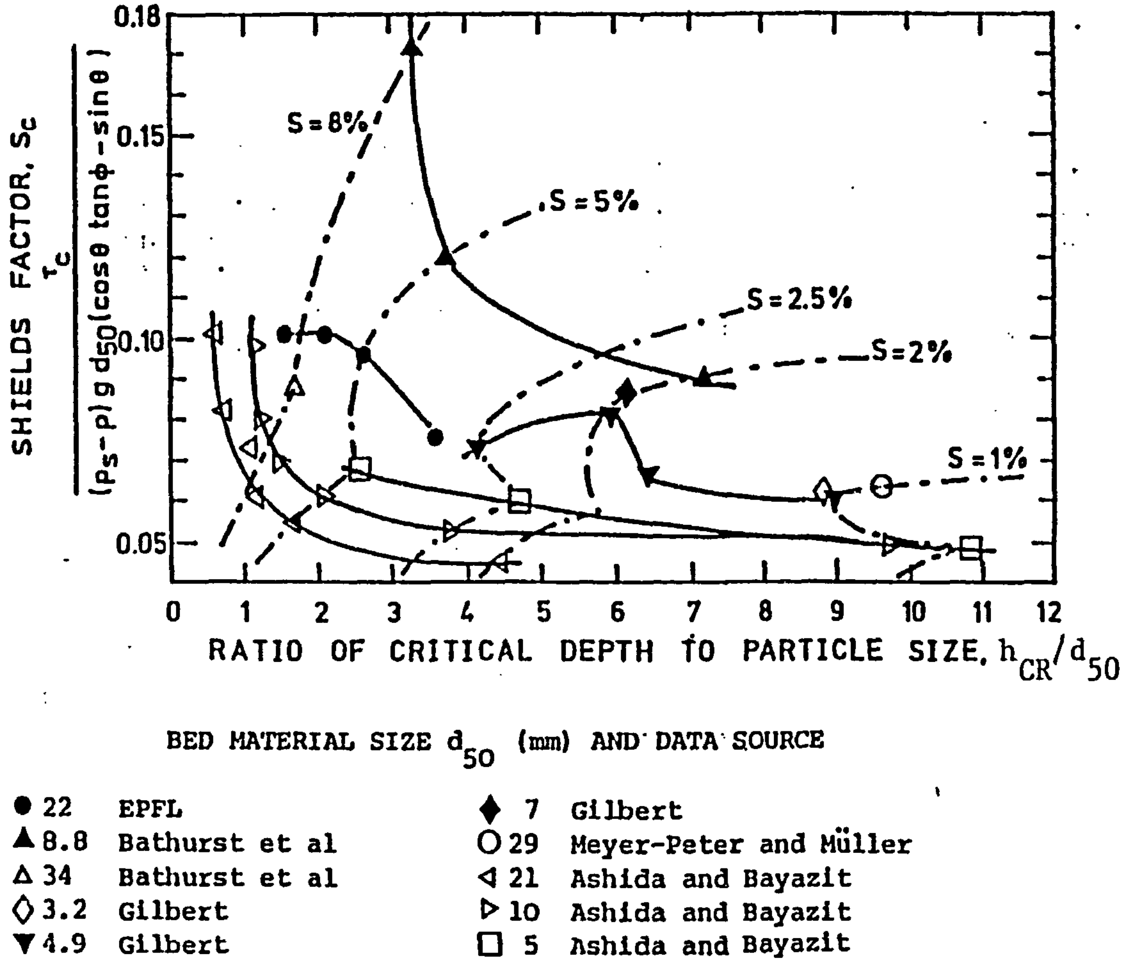

Fig. 3.16 Modified Critical Shear Stress vs. Critical Depth to Particle Size Ratio (after Bathurst, Graf and Cao, 1982)

whereas the abscissa varies essentially as $h_{CR}S/d_{50}$, and that all points of equal channel slope lie on a single line. The lines are not linear and free from discontinuity. Bathurst, et al. attributed the discontinuities to the effect of bed packing and other minor effects which were not included in the analysis. As can be seen from the figure, the lower the channel slope, the lower is the gradient of the lines and less is the change in S_C for a given value of h_{CR}/d_{50}. Thus for flows with $S \lesssim 1\%$, the gradients of these lines are so small that S_C varies only very gradually and is restricted to the traditional Shields range of 0.04 to 0.06. Apparently, earlier studies concerned with evaluating S_C involved only small channel slopes and large values of h_{CR}/d_{50} so that the variations of S_C with the flow and other channel parameters were too small to be commented on. Thus, the Shields diagram does not apply to steep flows.

Before applying their Schoklitsch-type approach, Bathurst, et al. investigated the functional relationship on the right hand side of Eq. [3.54]. For their data, the critical Reynolds number ranged from 1×10^3 to 2.5×10^4, which Flammer, et al. (1970) found had only a secondary effect on the drag coefficient. The bed size distribution was also fairly uniform so that the effect of d_{84}/d_{50} was minimal. They also concluded that the bed material shape had a secondary effect since the bed materials were all natural, cohesionless gravels. Thus, only the bed packing factor was likely to have a significant effect on the critical flow conditions. As mentioned earlier, Bathurst, et al. believed that the effect of bed packing was reflected in the discontinuities in the curves of Fig. 3.16. Thus, in Eq. [3.54], q_C^* varies primarily with the channel slope.

Analyzing the data of several researchers, Bathurst, et al. found that for channel slopes between 0.02 and 0.10, the relationship between the slope and the dimensionless discharge factor was given by

[3.55] $q_C^* = 0.114\ S^{-1.2}$

In all cases, Eq. [3.55] applied only for $h_{CR}/d_{50} \lesssim 6$.

The most recent and extensive study of sediment transport on steep slopes was that of Smart (1984). Smart developed the following equation to predict the transport capacity of a channel with grain sizes greater than 0.4 mm on slopes ranging from 0.04 to 20% (0.023 to 11.3°)

[3.56] $\phi = 4\ \{(d_{S_{90}}/d_{S_{30}})^{0.2}\ S^{0.6}\ C\ \theta^{0.5}\ (\theta - \theta_{Cr})\}$, where

[3.57] $\phi = q_b/(g(S_S - 1)d_S{}^3)^{0.5}$,

[3.58] $C = v_m/(gHS)^{0.5}$,

[3.59] $\theta = HS/((S_S - 1)d_S)$,

[3.60] $\theta_{Cr} = \theta_{0Cr}\ \cos\alpha(1 - \tan\alpha/\tan\beta)$

where S is the channel slope, v_m is the mean channel velocity, H is the flow depth, q_b is the volumetric sediment discharge per unit channel width, θ_{0Cr} = critical Shields' parameter from Shields' diagram, α is the channel slope in degrees and β is the angle of repose of the submerged bed material. The minimum value of $d_{S_{90}}/d_{S_{30}}$ is 8.5.

3.7 Similitude Principles of Sediment Transport

The problem of scale up of sediment transport has been discussed thoroughly in the literature. Yet, there are various theories as to how best extrapolate flume and river data to other operating conditions. In most cases, the proposed equations to predict sediment motion contain dimensionless variables involving shear stress, submerged weight, shape effect, bed slope and channel geometry. A few of the many attempts at unifying sediment transport data are illustrated below. These examples are in no way exhaustive but provide an overview of the variety of techniques currently employed.

Liu and Hwang (1959) considered steady, two-dimensional, uniform flow within a straight alluvial channel and using standard dimensional analysis techniques expressed the significant variables as follows

[3.61] $\mathrm{fcn}[H, q, S, \rho_f, \mu, g, d_{50}, \sigma_S, \Delta\gamma_S, \eta] = 0$

where q is the unit discharge of the flow, σ_S is the standard deviation in the bed material size, $\Delta\gamma_S$ is the difference in specific weight between the bed material and the fluid and η is the shape factor of the sediment. Since $q = Hv_m$, where v_m is the average velocity and because the settling velocity of the particles, v_S, is a function of d_{50}, ρ_f, μ, $\Delta\gamma_S$ and η, Liu and Hwang reduced Eq. [3.61] to

[3.62] $\mathrm{fcn}[H, S, v_m, \rho_f, \mu, g, d_{50}, \sigma_S, \Delta\gamma_S, v_S] = 0$

By selecting H, v_m and ρ_f as the repeating variables, one obtains seven dimensionless parameters; S, $v_m/(gH)^{0.5}$, v_mH/ν, d_{50}/H, σ_S/H,

$v_m^2 \rho_f/(\Delta\gamma_S H)$ and v_m/v_S. Liu and Hwang then introduced the friction velocity, u_*, the bed shear stress, τ, and the hydraulic radius of the channel, R_h, and eliminated the σ/H parameter because it had a secondary effect on the flow depth. Their final dimensionless groupings were

[3.63] $\mathrm{fcn}[v_m/u_*,\ S,\ u_* d_{50}/\nu,\ d_{50}/R_h,\ \tau/(\Delta\gamma_S d_{50}),\ v_S d_{50}/\nu] = 0$

Simons and Richardson (1960) considered the following variables to be of significance in alluvial channel flows

[3.64] $\mathrm{fcn}[H,\ b,\ S_{fC},\ S_{fr},\ v_m,\ S,\ \rho_f,\ \mu,\ \Delta\gamma_A,\ C_f,\ d_{50},\ v_S,\ \sigma,\ \Delta\gamma_S] = 0$

where b is the channel width, S_{fC} and S_{fr} are shape factors for the channel cross-section and channel reach respectively, $\Delta\gamma_A$ is the difference in specific weights between air and water, and C_f is the concentration of fine material. Using the same repeating variables as used by Liu and Hwang, Eq. [3.64] was expressed as

[3.65] $\mathrm{fcn}[b/H,\ S_{fC},\ S_{fr},\ S,\ v_m d_{50} \rho_f/\mu,\ C_f,\ d_{50}/H,\ v_S/v_m,\ \sigma,\ v_m^2/(\Delta\gamma_A H/\rho_f),\ v_m^2/(\Delta\gamma_S H/\rho_f)] = 0$

Assuming that (i) the shape factors could be eliminated because the channel bed was completely alluvial, (ii) the cross-section was uniformly rectangular except for variation due to bed roughness, (iii) the channel was straight, (iv) b/H was of secondary importance for wide channels, and (v) σ was of secondary importance, Eq. [3.65] was reduced to

[3.66] $\mathrm{fcn}[S,\ N_R,\ N_F,\ C_f,\ d_{50}/H,\ v_S/v_m,\ C_D] = 0$

where

[3.67] $N_R = v_m d_{50} \rho_f / \mu$

[3.68] $N_F = v_m/(gH)^{0.5}$,

assuming that $\Delta\gamma_A/\rho_f$ is approximately equal to g, and

[3.69] $C_D = d_{50} \Delta\gamma_S/(\rho_f v_S^2)$

Willis and Coleman (1969) were able to develop four similitude coefficients by transforming the terms of the Reynolds equations and the continuity equation. The coefficients were; $(\rho_S - \rho_f)/\rho_f$, q_S/q, gH/v_m^2 and $\mu_f/(\rho_f H v_m)$ where q_S is the volumetric sediment discharge. They also introduced a particle diameter similitude number given by

[3.70] $N_D = \rho_f^{0.667} g^{0.333} d_{S_{50}} \mu^{-0.667}$

Combining the first two-dimensionless parameters yielded, what they termed as the sediment load similitude number, given by

[3.71] $N_A = (\rho_S - \rho_f) q_S/(\rho_f q)$

Willis and Coleman attempted to correlate N_A, N_D and the Reynolds and Froude numbers, $\mu_f/(\rho_f H v_m)$ and gH/v_m^2 and found that N_A was dependent on the Froude number and N_D only, and not upon the Reynolds number. Their results are shown in Fig. 3.17. The probable reason that the Reynolds number showed no significant effect on N_A was that the gravity forces were dominant and that any viscous effects were adequately accounted for by the particle diameter similitude number, N_D.

Ackers and White (1973) studied sediment transport and developed three-dimensional parameters which described the initiation and

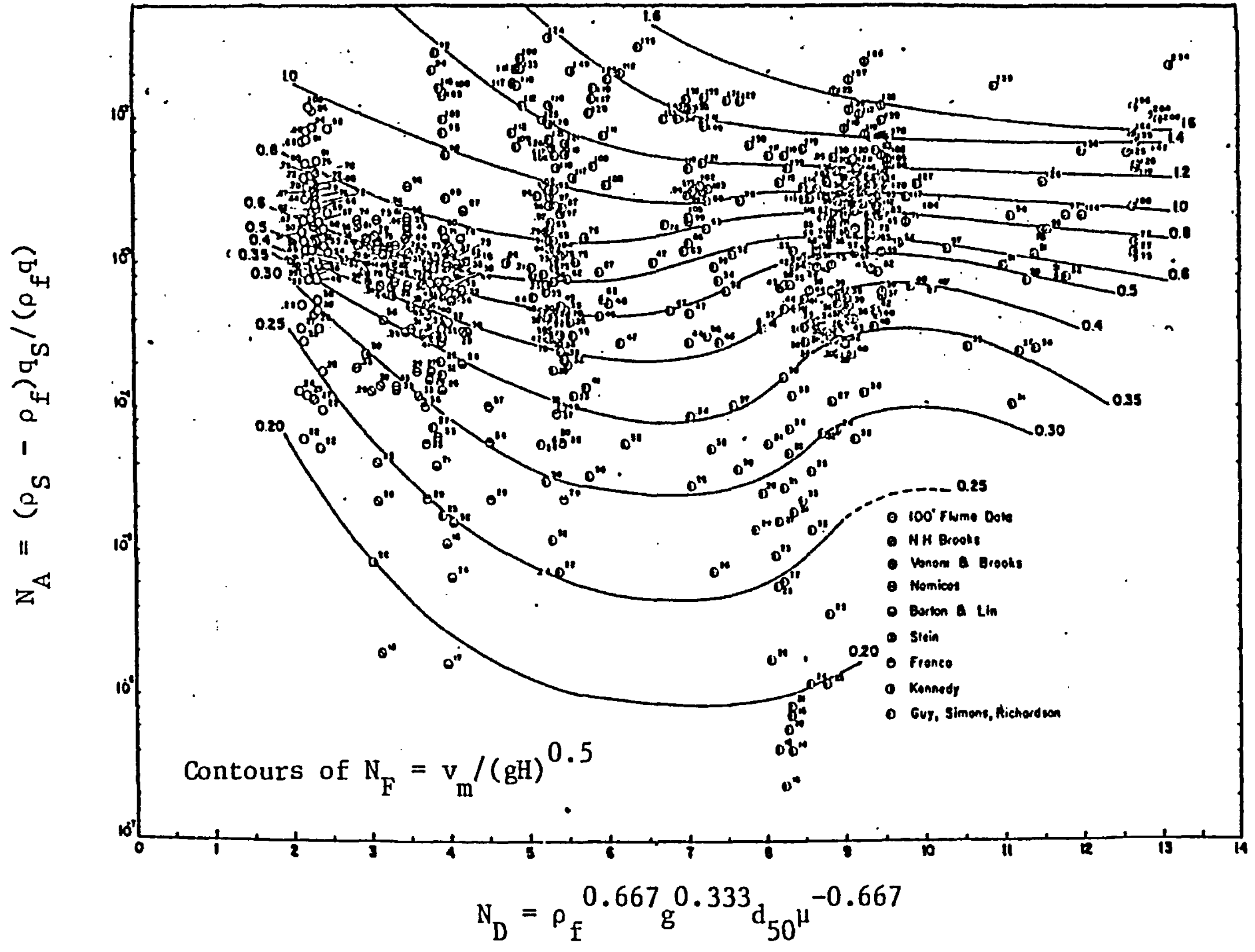

Fig. 3.17 Unified Graphic Sediment Discharge Function for Flume Data (after Willis and Coleman, 1969)

transport of sediment grains with diameters in excess of 0.04 mm. The sediment mobility number, dimensionless grain diameter and transport parameter are given respectively as

[3.72] $F_{gr} = (U_*^n/(gd_S(S_S - 1)^{0.5})(v_m/(32^{0.5} \log (\alpha h/d_S))^{1-n}$

[3.73] $D_{gr} = d_S((g(S_S - 1)/(\nu^2))^{-0.333}$, and

[3.74] $G_{gr} = ((X_b h)/(S_S d_S))(U_*/v_m)^n$

where

F_{gr} = sediment mobility number

D_{gr} = dimensionless grain diameter

G_{gr} = transport parameter

X_b = sediment transport on the bed, mass flux per unit mass flow rate, and

n, and α are experimental constants.

Ackers and White found the correlation between the three parameters as

[3.75] $G_{gr} = C(F_{gr}/A - 1)^m$

where C, A and m are experimental constants. The value of A represents the value of the sediment mobility number, F_{gr}, at which sediment motion is initiated. Ackers and White found that their data could be arranged into two groups, $1.0 < D_{gr} < 60$, and $D_{gr} > 60$. The constants obtained for the group $1.0 < D_{gr} < 60$ were

[3.76a] $n = 1.00 - 0.56 \log D_{gr}$

[3.76b] $\log C = 2.86 \log D_{gr} - (\log D_{gr})^2 - 3.53$

[3.76c] $\alpha = 10.0$

[3.76d] $A = 0.23/(D_{gr})^{0.5} + 0.14$, and

[3.76e] $m = 9.66/D_{gr} + 1.34$,

whereas for $D_{gr} > 60$

[3.77a] $n = 0.00$

[3.77b] $C = 0.025$

[3.77c] $\alpha = 10.0$

[3.77d] $A = 0.17$, and

[3.77e] $m = 1.50$

Making use of Eqs. [3.72] to [3.77e], the mass of sediment transport, the velocity at which motion would initiate and the mean fluid velocity required to maintain a given sediment in supsension may be calculated. The relationship between F_{gr}, D_{gr} and G_{gr} is shown in Fig. 3.18. Subsequent publications in the area of sediment transport seem to indicate a general acceptance for the dimensionless parameters proposed by Ackers and White.

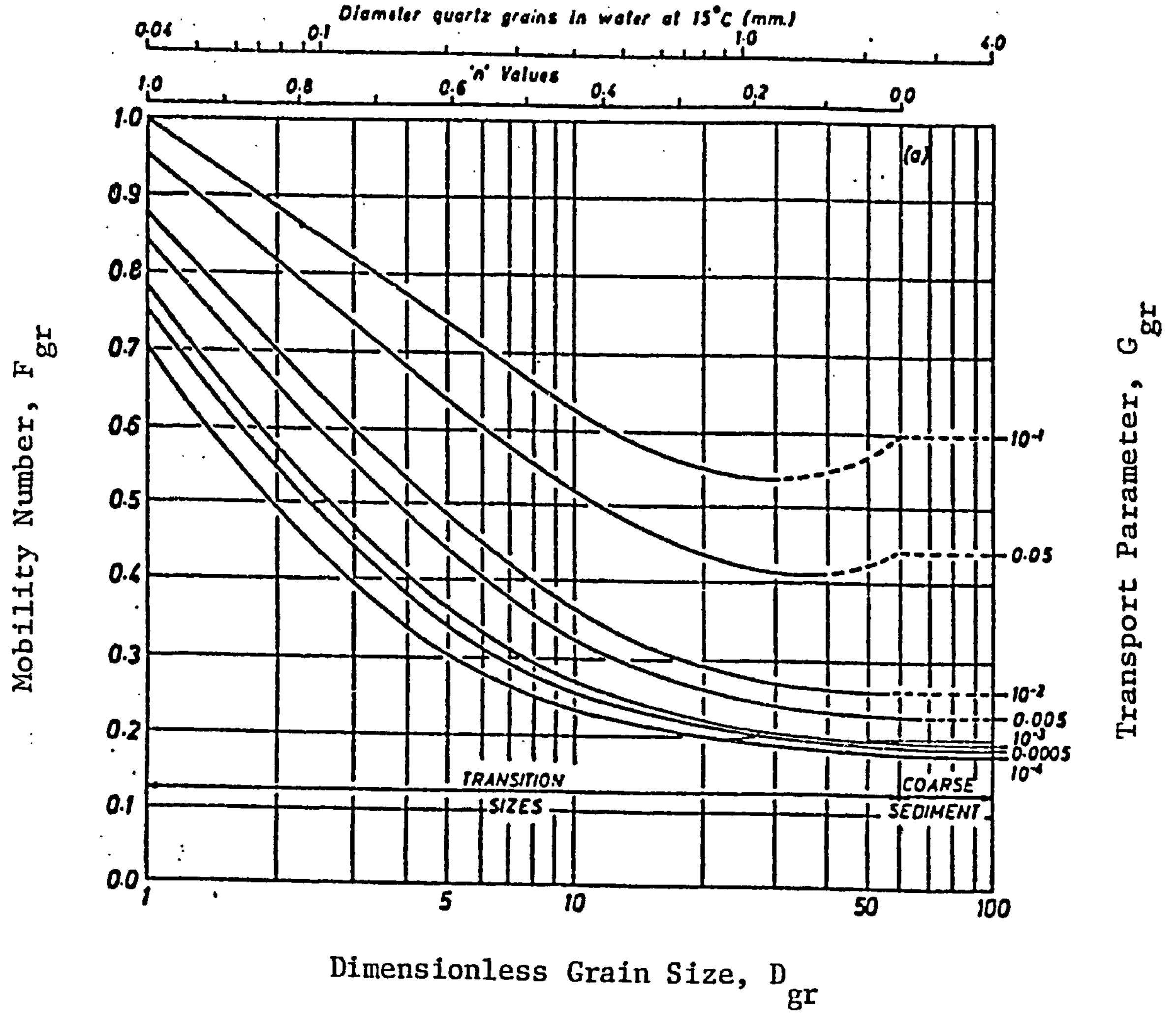

Fig. 3.18 Sediment Transport Function
(after Ackers and White, 1973)

CHAPTER 4

DEVELOPMENT OF THE NUMERICAL MODEL

4.1 General

A cross-sectional view of the wet well considered for numerical analyses is shown in Fig. 4.1. The general layout of the pump intake is in accordance with the recommended sump design as outlined in Chapter 2.2.4. Three parallel intake pipes were used in the system. The diameter of the bell-mouth inlet is denoted as D. The bottom clearance of each bell-mouth was 0.5D; the distance from the centre line of the intakes to the first upstream transition in the floor slope was 3D. The centre-to-centre spacing between intake pipes was 2D. The spacing between the side walls and the centre line of the two outside intakes was D; thus the width of the sump was 6D. The clearance to the back wall of the sump from the intake centre line was 3.5D. The pump discharge was assumed to be uniformly withdrawn from all three intakes; similarily, the inflow to the sump was assumed to be uniform across the entire width of the inlet section. The origin for the X-Y coordinates was in the lower left-hand corner of the sump. The length of the inclined portion of the wet well floor has been denoted as L_i. The total length of the sump considered was 12.6D, i.e. $(6.5D + L_i\cos\theta)$, where θ was the angle of inclination of the sloping portion of the wet well floor; this length was established based on the restrictions due to physical modelling of the sump. The length of the approach channel, $L_i\cos\theta$, was found to be long enough, in the model, so that no abnormal flow conditions occurred

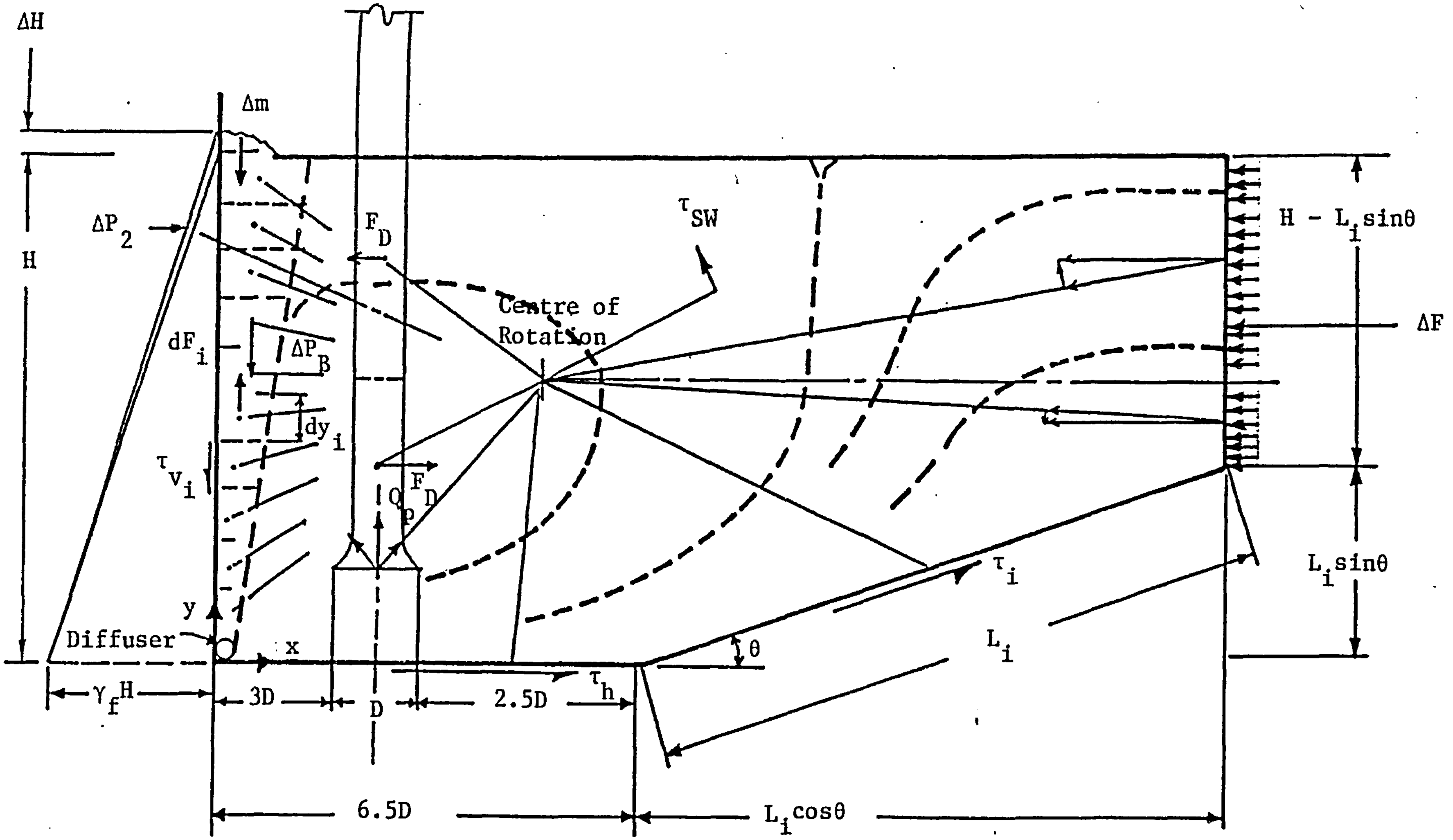
ΔH
Δm
H
ΔP_2
F_D
τ_{SW}
Centre of Rotation
$H - L_i \sin\theta$
ΔF
dF_i
ΔP_B
dy_i
τ_{v_i}
Q_p
F_D
τ_i
$L_i \sin\theta$
y
Diffuser
x
θ
L_i
$\gamma_f H$
3D
D
2.5D
τ_h
6.5D
$L_i \cos\theta$

Fig. 4.1 General Layout of the Sump Model

anywhere within the sump; i.e. the requirements of Chapter 2.2.4 had also been met in the physical model. The maximum flow depth, H, was limited to 8D, which provides for a bell-mouth submergence far greater than that required for vortex free operating conditions.

4.2 Conceptual Overview

The purpose of the numerical model is to establish the sensitivity of the fluid velocities and/or shear stresses along the horizontal and sloping portions of the sump floor to the operating variables. The resultant fluid shear stresses should scour the sediment from the sump floor or prevent deposition of sediment on the sump floor. Manual removal of this sediment, or other debris, would thereby be eliminated.

In order to increase the shear stresses adjacent to the floor, it was decided to use diffused air to increase the fluid velocities within the sump. The air diffuser used was a line source across the entire width of the sump, as shown in Fig. 4.1, and was placed at coordinates (0,0).

As the air leaves the diffuser ports, entrainment and acceleration of the ambient fluid occurs which results in fluid velocities within the sump in excess of that which would otherwise be generated by inflow/outflow alone. The objective of studying the diffused air system was to determine which operating conditions and which diffuser/sump configuration maximized the shear stresses along the sump boundaries. The development of the numerical model is presented in three phases, (i) the development of the equations describing the diffused air plume, (ii) the general formulation of the governing equations for the entire system and (iii) detailed developments of significant forces within the system.

In the proposed model formulation, steady state conditions apply, i.e. the pumping rate is equal to the inflow to the sump, resulting in a constant free surface elevation. The effects of a drawdown condition can be modelled by running the numerical model at various depths. The numerical model can be executed with a zero pumping rate; however, some minimum air flow is required to generate a solution.

4.3 The Diffuser Plume Model

Consider an air diffuser placed at the bottom of the sump of depth H, as shown in Fig. 4.2. The vertical distance above the diffuser, y, is measured with respect to the outlet ports of the diffuser and is assumed to be at coordinates (0,0) with respect to the global coordinate system as shown in Fig. 4.1. At some elevation y above the diffuser there is an element of depth dy, width B and thickness W. In this case, W represents the total sump width, hence,

[4.1] $W = 6D$

The formulation of the plume model was based on a "Drift-flux" theory (Wallis, 1969). In this model, the focus of attention was on the relative motion between the air and water phases rather than on the motion of the individual phases alone. In the homogeneous flow theory, suitable average properties for the multiphase flow are determined and the mixture is subsequently treated as a pseudofluid which obeys the usual fluid mechanics of single-component flows. The

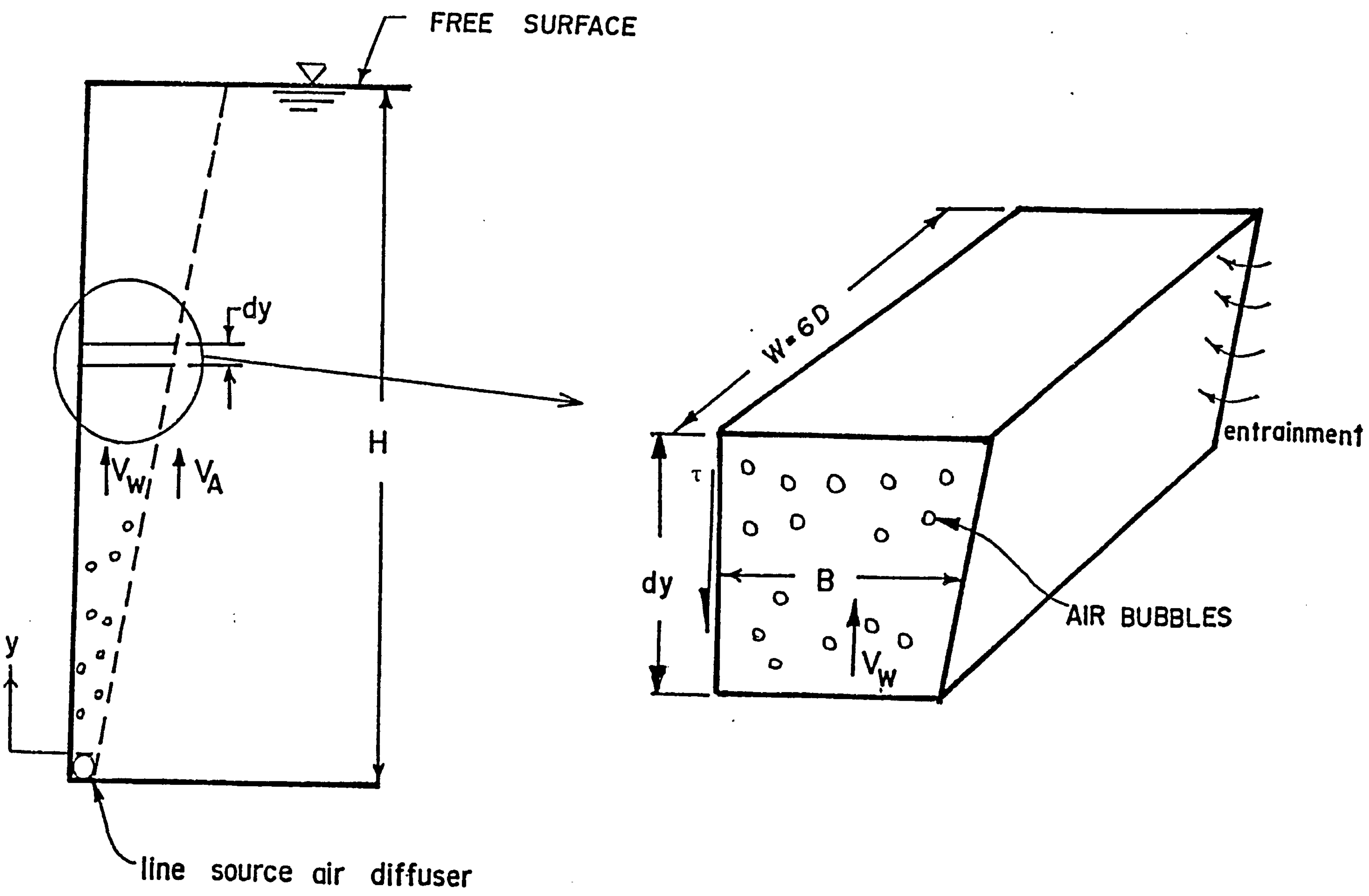
FREE SURFACE
dy
V_W
V_A
H
y
line source air diffuser
W=6D
entrainment
τ
dy
B
AIR BUBBLES
V_W

Fig. 4.2 Defining Diagram for Diffuser Plume Model

drift-flux theory, on the other hand, assumes each phase can have different properties. Wallis (1969) provided a thorough discussion of the drift-flux theory, and indicated that this theory had wide spread application in bubbly and slug, gas-liquid flow regimes. The bubbly flow regime, as in this case, is a pattern characterized by a suspension of discrete bubbles in a continuous liquid. Significant forces in this flow regime are due to surface tension, viscosity, inertia and buoyancy. The resultant forces produce a variety of effects evidenced by different bubble shapes and trajectories. Again, Wallis (1969) provided a detailed description of various equations for bubbly flow.

Consider the fluid element of volume BdyW or Bdy6D, wherein it is assumed that the water velocity and the air are uniformly distributed across the entire element and the ambient velocity, V_A, is vertical. The fluid is entrained from one side of the plume only since the plume is bound on one side by an impervious wall. One obtains the rate of change of water flowrate with depth as

$$[4.2] \qquad \frac{dQ_W}{dy} = \alpha_C(V_W - V_A)(W)$$

where Q_W is the water flowrate, α_C is the entrainment coefficient, V_W is the mean water velocity within the plume, V_A is the ambient water velocity and W = 6D is the width over which entrainment occurs. The entrainment represents the flow which crosses the interface between the plume and main body of flow and is dependent on the differential velocity across the interface. Hence, if both the ambient and plume water velocities were equal, no entrainment would occur.

The momentum flux of the fluid element is given by

[4.3] $\dot{M} = \rho_f \, Q_W \, V_W$

where ρ_f is the fluid density and

[4.4] $Q_W = V_W(B(1 - \alpha)W)$

where α represents the fraction of area occupied by the air. Thus Eq. [4.3] can be written as

[4.5] $\dot{M} = \rho_f \, B \, V_W^2 \, (1 - \alpha)(W)$

The rate of change of momentum of the fluid element, $d\dot{M}/dy$ is given by

[4.6] $d\dot{M}/dy = dF/dy - \tau(W)$

where τ is the shear stress between the fluid element and the confining boundary, and F, is termed the "mutual drag force".

Wallis (1969) derived the mutual drag force per unit volume by expressing the momentum equation for both the air and water phases separately. Assuming that (i) there was no wall shear on the fluid element and that the body force was balanced by the pressure gradient and the forces between the phases, (ii) the flow in the vertical direction was in steady state, and (iii) the fluid element behaved as a perfect fluid, $\mu_f \approx 0$, Wallis showed that the mutual drag force per unit volume, F, was given by

[4.7] $F = g(\rho_f - \rho_{AIR})\alpha(1 - \alpha)$

Thus, in the absence of wall effects, the mutual drag force per unit volume is a function of the phase densities and the void fraction. The incremental change in the mutual force within the element is then given by

[4.8] $dF = B\alpha(1 - \alpha)g(\rho_f - \rho_{AIR})(W)dy$

The shear stress term in Eq. [4.6] is derived from the Darcy-Weisbach formula for pipe flow, and the equation for the tractive shear stress in open channels. The head loss along a length of pipe L is given by

[4.9] $h_L = f\ L\ V_W{}^2/(2Dg)$

and the tractive shear stress in an open channel is

[4.10] $\tau = \gamma_f\ R_h\ S$

Several techniques for evaluating the two phase friction factor have been proposed. For turbulent flows, Wallis (1969) suggests three common alternatives; (i) use a constant value for all two phase flow systems, $f = 0.005$, (ii) use a friction factor calculated from some equivalent single phase flow or (iii) obtain a "virtual viscosity" for the two phase system from which a modified Reynolds number can be obtained, and then use single phase friction factor charts. A friction factor of 0.005 is for high-velocity annular-mist flows. McAdams (1942), Cicchitti (1960) and Duckler (1964) have developed expressions for the virtual viscosity of gas-liquid flows, however, they were only valid at concentrations below 5% for which the change in viscosity was small. In the case of pipe flows, the friction factor has been expressed as a function of the ratio of the pressure drop in a two phase system to the equivalent value for single phase flow of one of the phases alone. The resulting ratio has been termed as a "two phase multiplier". Martinelli and Nelson (1948) developed a "separate cylinders" model to estimate the frictional pressure drop in a horizontal pipe in which a two phase flow is moving. The method assumes that the two phases flow without interaction in two horizontal separate cylinders and that the areas of the cross-sections add up to the cross-sectional area of the actual pipe. The pressure drop in each of the imagined cylinders is the same as in the actual flow, and is due to frictional effects only, and is calculated from single phase flow theory. To the author's knowledge, no correction factors for two phase friction have been developed for vertically discharging plumes bound on one side or both.

For a pipe flowing full, the hydraulic radius is

[4.11] $$R_h = D/4$$

Knowing that the slope, S, is the head loss per unit length, h_L/L, one obtains from Eqs. [4.9], [4.10] and [4.11]

[4.12] $$\tau = \rho_f\ f\ V_W^2/8$$

Equation [4.6] can now be rewritten as

[4.13] $$\begin{aligned}&(d/dy)\{\rho_f B V_W^2(1 - \alpha)(W)\}\\ &= B\alpha(1 - \alpha)g(\rho_f - \rho_{AIR})(W) - \rho_f f V_W^2(W)/8\end{aligned}$$

In terms of the unknown variables, V_W, B and α, Eq. [4.13] can be differentiated and expanded to yield

[4.14] $$\begin{aligned}&(dB/dy)\{\rho_f V_W^2(1 - \alpha)\} + (dV_W/dy)\{2BV_W\rho_f(1 - \alpha)\}\\ &- (d\alpha/dy)\{\rho_f B V_W^2\} - B\alpha(1 - \alpha)g(\rho_f - \rho_{AIR})\\ &+ \rho_f f V_W^2/8 = 0\end{aligned}$$

Equation [4.14] is one of the differential equations required to describe the performance of the plume. Two additional equations will be required to solve for the three unknown parameters.

For the fluid element, in Fig. 4.2, the water discharge is given by

[4.15] $Q_W = BV_W(1 - \alpha)(W)$

Differentiation of Eq. [4.15] with respect to Q_W and subsequently equating this to Eq. [4.2] yields

[4.16] $\alpha_C(V_W - V_A)(W) = BV_W(1 - \alpha)(W)$

Assuming V_A to be constant, the total derivative of Eq. [4.16] with respect to B, V_W and α yields

[4.17] $$(dB/dy)\{V_W - V_W\alpha\} + (dV_W/dy)\{B - B\alpha\}$$
$$- (d\alpha/dy)\{BV_W\} = \alpha_C(V_W - V_A)$$

In order to obtain the third differential equation for the system, it is necessary to examine the general drift flux theory. The water flux and air flux are given respectively as

[4.18] $j_f = Q_W/(WB)$, and

[4.19] $j_{AIR} = Q_{AIR}/(WB)$

If α represents the fraction of the discontinuous phase, i.e., the air, the phase fluxes can be related to the air fraction and component velocities as follows

[4.20] $j_f = (1 - \alpha)V_W$, and

[4.21] $j_{AIR} = \alpha V_{AIR}$

The total local flux, j, is simply the sum of the individual phase fluxes, that is

[4.22] $j = j_f + j_{AIR}$

The total local flux is then interpreted as being the average velocity of the two phase system. The drift flux of either phase is the volumetric flux of that phase relative to some surface or plane of reference which is moving at the average velocity j. Therefore,

[4.23] $j_{AIR,f} = \alpha(V_{AIR} - j)$, and

[4.24] $j_{f,AIR} = (1 - \alpha)(V_W - j)$

Now, the substitution of Eqs. [4.21] and [4.22] into Eq. [4.23] yields

[4.25] $j_{AIR,f} = j_{AIR}(1 - \alpha) - \alpha\, j_f$

Similarily from Eqs. [4.20], [4.22] and [4.24] one obtains

[4.26] $j_{f,AIR} = j_f\alpha - (1 - \alpha)j_{AIR}$, or

[4.27] $j_{f,AIR} = -\, j_{AIR,f}$

For small wall shear stresses, and uniform concentration and velocity profiles, Wallis suggested that the drift flux could be expressed in terms of the air fraction and the terminal rise velocity of the bubbles, i.e.

[4.28] $j_{AIR,f} = v_b\, \alpha(1 - \alpha)^n$

The exponent n is a function of the bubble rise velocity and a bubble Reynolds number as shown in Table 4.1.

When the bubble size exceeded $2(\sigma/g\rho_f)^{0.5}$, the range of applicability for Region 5, Wallis reported that three-dimensional effects became important and there was a significant entrainment of bubbles in each other's wake. At 20°C, this corresponds to a bubble radius of 0.55 cm. At this size of bubble, or larger, there

Table 4.1 Terminal Velocities of Single Gas Bubbles in Liquids (after Peebles and Garber, 1953)

Region	Terminal Velocity	Range of Applicability*	n
1	$v_b = 2R_b^2(\rho_f - \rho_{AIR})g/(9\mu_f)$	$R_{eb} < 2$	2
2	$v_b = 0.33g^{0.76}(\rho_f/\mu_f)^{0.52}R_b^{1.28}$	$2 < R_{eb} < 4.02G_1^{-0.214}$	1.75
3	$v_b = 1.35(\sigma/(\rho_f R_b))^{0.50}$	$4.02G_1^{-0.214} < R_{eb} < 3.10G_1^{-0.25}$	
		or	-
		$16.32G_1^{0.144} < G_2 < 5.75$	
4	$v_b = 1.53(g\sigma/\rho_f)^{0.25}$	$3.10G_1^{-0.25} < R_{eb}$	
		and	1.5
		$5.75 < G_2$	
5	$v_b = (gR_b)^{0.5}$	$R_b \geq 2(\sigma/g\rho_f)^{0.5}$	-

*$R_{eb} = 2\rho_f v_b R_b/\mu_f$; $G_1 = g\mu_f^4/(\rho_f\sigma^3)$; $G_2 = g R_b^4 v_b^4 \rho_f^3/\sigma^3$

was an increase in the relative velocity with an increase in the number of bubbles present and the index n, in Table 4.1 becomes less than unity. This flow regime has been termed "churn-turbulent" by Zuber and Hench (1962), which is characterized by an agitated, unsteady flow regime. Churn-turbulent flow regime is a transition between the "ideal bubbly flow" regime in which the bubbles rise uniformly and steadily and the "slug flow" regime in which the entire cross-section is filled with bubbles which flow entirely in each other's wake. Coalescence is significant in this flow regime since bubbles flowing in the wake of another tend to rise faster than their predecessor. Zuber and Hench give the drift flux for this regime as

[4.29] $$j_{AIR,f} = 1.53\ \alpha(\sigma g(\rho_f - \rho_{AIR})/\rho_f{}^2)^{0.25}$$

in which the value of the exponent n, in Eq. [4.28] is reported to be zero. For simplicity, throughout the remainder of the numerical derivation, a drift flux parameter, ψ_b, will be used, where

[4.30] $$\psi_b = 1.53(\sigma g(\rho_f - \rho_{AIR})/\rho_f{}^2)^{0.25}$$

hence,

[4.31] $$j_{AIR,f} = \psi_b \alpha$$

Assuming the validity of Eq. [4.31], Eq. [4.25] gives

[4.32] $$\psi_b \alpha = j_{AIR}(1 - \alpha) - \alpha j_f$$

Combining Eqs. [4.15] and [4.18] gives another equation for the fluid flux as

[4.33] $$j_f = V_W(1 - \alpha)$$

Substituting Eqs. [4.33] and [4.19] into [4.32] yields an equation in terms of the unknowns α, B and V_W as

[4.34] $$\psi_b \alpha = (1 - \alpha)Q_{AIR}/(WB) - \alpha V_W(1 - \alpha)$$

The total derivative of Eq. [4.34] with respect to y yields

[4.35] $$\begin{aligned}&(d\alpha/dy)\{\psi_b + Q_{AIR}/WB + V_W - 2\alpha V_W\}\\&+ (dB/dy)\{- \alpha Q_{AIR}/(WB^2) + Q_{AIR}/(WB^2)\}\\&+ (dQ_{AIR}/dy)\{\alpha/WB - 1/WB\} + (dV_W/dy)\{\alpha - \alpha^2\} = 0\end{aligned}$$

In the process of differentiating Eq. [4.34] a fourth derivative, dQ_{AIR}/dy, is introduced. Application of the universal gas law and continuity, and assuming isothermal conditions, leads to an expression for this derivative as

[4.36] $$p_o\, Q_{AIR_o} = p_{AIR}\, Q_{AIR}$$

where p_o is the air pressure at the diffuser, Q_{AIR_o} is the air flowrate at the diffuser and p_{AIR} and Q_{AIR} represent the air pressure and flowrate at some elevation, y, above the diffuser. The pressure at the diffuser is given by

[4.37] $$p_o = Z_d + p_{atm}/\gamma_f$$

where Z_d is the diffuser submergence and p_{atm} is the atmospheric pressure at the free surface. The pressure at an elevation y is given by

[4.38] $$p_{AIR} = Z_d - y + p_{atm}/\gamma_f$$

Substitution of Eqs. [4.37] and [4.38] into [4.36] yields

[4.39] $$Q_{AIR} = Q_{AIR_o}\ \{(Z_d + p_{atm}/\gamma_f)/(Z_d - y + p_{atm}/\gamma_f)\}$$

from which one obtains,

[4.40] $$dQ_{AIR}/dy = Q_{AIR_o}\ \{(Z_d + p_{atm}/\gamma_f)/(Z_d - y + p_{atm}/\gamma_f)^2\}$$

Equations [4.40], [4.35], [4.17] and [4.14] can be solved simultaneously to estimate the plume width, B, plume mean water velocity, V_W, and air fraction, α, at any depth, y, above the diffuser once the following are specified:

(i) fluid density
(ii) gas density
(iii) confining wall friction factor
(iv) entrainment coefficient
(v) ambient water velocity
(vi) width of cross-section over which the air is diffused
(vii) air flowrate at the exit ports of the diffuser
(viii) diffuser submergence, and
(ix) unit weight of the fluid.

The four governing equations can be rearranged into a form more suitable for programming. Table 4.2 gives the rearranged form of these equations.

4.4 General Sump Model

The general sump model is a two-dimensional model based upon the conservation of angular momentum. The assumed centre of rotation is shown in Fig. 4.1. As the flow within the plume is accelerated, it approaches the free surface and turns through 90° and proceeds upstream, (in the positive x direction). The diffuser induced circulation is met by the sump inflow which travels in the negative x direction. The two flows impact and are driven downward towards the floor of the sump. The streamlines from the pump suction assist in drawing the flow toward the sump floor and also assist in setting up the clockwise circulation pattern (Fig. 4.1).

Table 4.2 Summary of Governing Equations for the Diffuser Plume Model

$$dQ_{AIR}/dy = Q_{AIR_o}(Z_d + p_{atm}/\gamma_f)/(Z_d - y + p_{atm}/\gamma_f)^2$$

$$dB/dy = \{AA - BB + \{CC(DD) - EE\}\{FF\}\}/GG$$

$$d\alpha/dy = HH + II - JJ$$

$$dV_W/dy = KK + LL - MM$$

where:

$AA = (dQ_{AIR}/dy)/W$

$BB = \alpha\alpha_C(V_W - V_A)/(1 - \alpha)$

$CC = 2/\{(1 - \alpha)V_W\}$

$DD = fV_W/16 + \alpha_C(V_W - V_A)$

$EE = B\alpha g(\rho_f - \rho_{AIR})(V_W^2 \rho_f)$

$FF = \psi_b + Q_{AIR}/(WB) + V_W(1 - \alpha)$

$GG = \psi_b + 2Q_{AIR}/(WB) + V_W(1 - 2\alpha)$

$HH = (dB/dy)\{(1 - \alpha)/B\}$

$II = (1 - \alpha)\alpha g(\rho_f - \rho_{AIR})/(V_W^2 \rho_f)$

$JJ = (2/V_W B)\{fV_W/16 + \alpha_C(V_W - V_A)\}$

$KK = \alpha_C(V_W - V_A)/\{B(1 - \alpha)\}$

$LL = (d\alpha/dy)\{V_W/(1 - \alpha)\}$

$MM = (dB/dy)(V_W/B)$

In its fundamental form, the conservation of angular momentum about the centre of rotation is given by

[4.41] $$\sum \underset{\sim}{r} \times \underset{\sim}{F}_{ext} = \partial / \partial t \int_{CV} \rho_f \underset{\sim}{r} \times \underset{\sim}{v} \, d\forall + \int_{CS} (\rho_f \underset{\sim}{r} \times \underset{\sim}{v})(\underset{\sim}{v} \cdot d\underset{\sim}{A})$$

where $\underset{\sim}{r}$ is a position vector from the centre of rotation to a point on the line of action of the external force $\underset{\sim}{F}_{ext}$. The right hand side of Eq. [4.41] represents the time rate of change of the moment of momentum within the control volume plus the net efflux of moment of momentum through the control surface boundary. The term $\rho_f d\forall$ represents an incremental mass of fluid within the control volume, and $\rho_f \underset{\sim}{v} \cdot d\underset{\sim}{A}$ represents an incremental mass flowrate through the control surface where $d\forall$ and $d\underset{\sim}{A}$ are incremental volumes and areas, respectively. For steady state conditions, the first term on the right hand side of Eq. [4.41] becomes equal to zero. Thus,

[4.42] $$\sum \underset{\sim}{r} \times \underset{\sim}{F}_{ext} = \int_{CS} (\rho_f \underset{\sim}{r} \times \underset{\sim}{v})(\underset{\sim}{v} \cdot d\underset{\sim}{A})$$

It can be seen in Fig. 4.1 that the following external forces create torques about the centre of rotation:

(i) shear on the inclined portion of the wet well floor, τ_i

(ii) shear on the horizontal portion of the wet well floor, τ_h

(iii) shear on the vertical wall adjacent to the diffuser plume τ_v

(iv) drag on the pump columns, F_D

(v) side wall shear (on two sides of the sump), τ_{SW}

(vi) a force, ΔF, required to redirect the flow approaching the inlet and balance linear momentum within the system

(vii) a force, ΔP_2, resulting from an increase in the hydrostatic force along the wall adjacent to the diffuser, as a result of a rise in the free surface due to the momentum of the diffuser air plume

(viii) the mutual hydrodynamic bubble force within the diffuser air plume, F_i

(ix) a force, Δm, due to the mass of fluid above the static water surface in the region where the diffused air plume meets with the free surface, and

(x) a force, ΔP_B, resulting from a pressure imbalance on the wet well floor in the area centred underneath the diffuser air plume. This force is due to the change in effective weight of the column of water which comprises the diffused air plume.

The angular momentum flux, or inertia torques due to fluid crossing the control surface boundary is due to:

(i) flow being extracted by the pump intakes, and

(ii) flow entering the wet well at the upstream end.

The control surface boundary constitutes all of the wetted surfaces of the sump as well as the free surface. In order to extract the flow from the sump, and allow for the flow of angular momentum through the bell-mouths, it is necessary to assume a "hole" in control surface at the plane of the bell-mouths.

The forces τ_i, τ_h, τ_v, F_D, τ_{SW}, ΔF, Δm and ΔP_B all create resistance to circulation, whereas ΔP_2 and F_i are the driving torques. Using the right hand rule, resisting torques are positive (counter-clockwise), and the driving torques are negative (clockwise). The solution to Eq. [4.42] is achieved when the net torques supplied by the inflows and outflows, and the bubble forces, are balanced by shear along the boundaries. The next subsection provides a formulation for each of the torques and momentum fluxes discussed previously.

4.5 Formulation of System Elements

For a given depth of fluid in the wet well, H, and a given inclined floor slope, θ, there is a unique geometric (centroidal) centre for the cross-section. It is assumed that the geometric centre of the cross-section and the centre of rotation of the flow in the sump are coincident. In terms of the length dimensions of the sump, it can be shown that the x and y coordinates with respect to the coordinate axis shown in Fig. 4.1 are respectively

$$[4.43] \qquad \bar{X} = \{3H(6.5D + L_i\cos\theta)^2 - (L_i^2\cos\theta\sin\theta)(19.5D + 2L_i\cos\theta)\}/ \{6H(6.5D + L_i\cos\theta) - 3L_i^2\cos\theta\sin\theta\} \quad , \text{ and}$$

$$[4.44] \qquad \bar{Y} = \{3H^2(6.5D + L_i\cos\theta) - L_i^3\sin^2\theta\cos\theta\}/ \{6H(6.5D + L_i\cos\theta) - 3L_i^2\cos\theta\sin\theta\}$$

The moment arm of all externally applied forces passes through ($\bar{X}$, $\bar{Y}$).

In this formulation of the sump model, the $\bar{X}$ coordinate is maintained to the right of the pump columns, i.e. upstream of the pump columns. It is shown later that if the centre of rotation is to the left of the pump columns, air from the diffuser can be drawn into the pump intakes resulting in a decrease in pumping capacity and an increased risk of cavitation.

4.5.1 Shear Stress on the Inclined Portion of the Wet Well Floor

Regardless of the slope of the incline, including, θ = 0, the inclined floor is considered to extend upstream from a point which is

6.5D from the origin. The shear stress acting on the inclined floor is assumed to be uniformly distributed over the entire area of the incline and is given by

[4.45] $\tau_i = \rho_f \, f \, V_i^2/8$

where V_i is a representative mean velocity adjacent to the inclined boundary. No attempt has been made to correct this velocity for boundary effects. In order to estimate this velocity, it is necessary to assume some form for the velocity distribution, Fig. 4.3, within the wet well. The flow, produced by the diffused air, is assumed to undergo a solid body rotation wherein the velocity increases linearly from zero at the centre to a maximum at the boundary. The flow entering the wet well at the upstream end is assumed to flow in a plug flow distribution wherein the velocity is uniform across the flow section. Assuming the flow undergoing solid body rotation with a constant angular velocity, ω, one can integrate the profile to obtain the discharge through the cross-section as follows

[4.46] $Q_{WD} = W\omega \int_0^{r_o} r dr$

where Q_{WD} represents the total flow of fluid circulating as a result of air diffusion only, and must be greater than or equal to Q_W as given by Eq. [4.15], i.e. the circulating flow must at least satisfy the flow which is entrained by the plume.

Integration of Eq. [4.46] yields

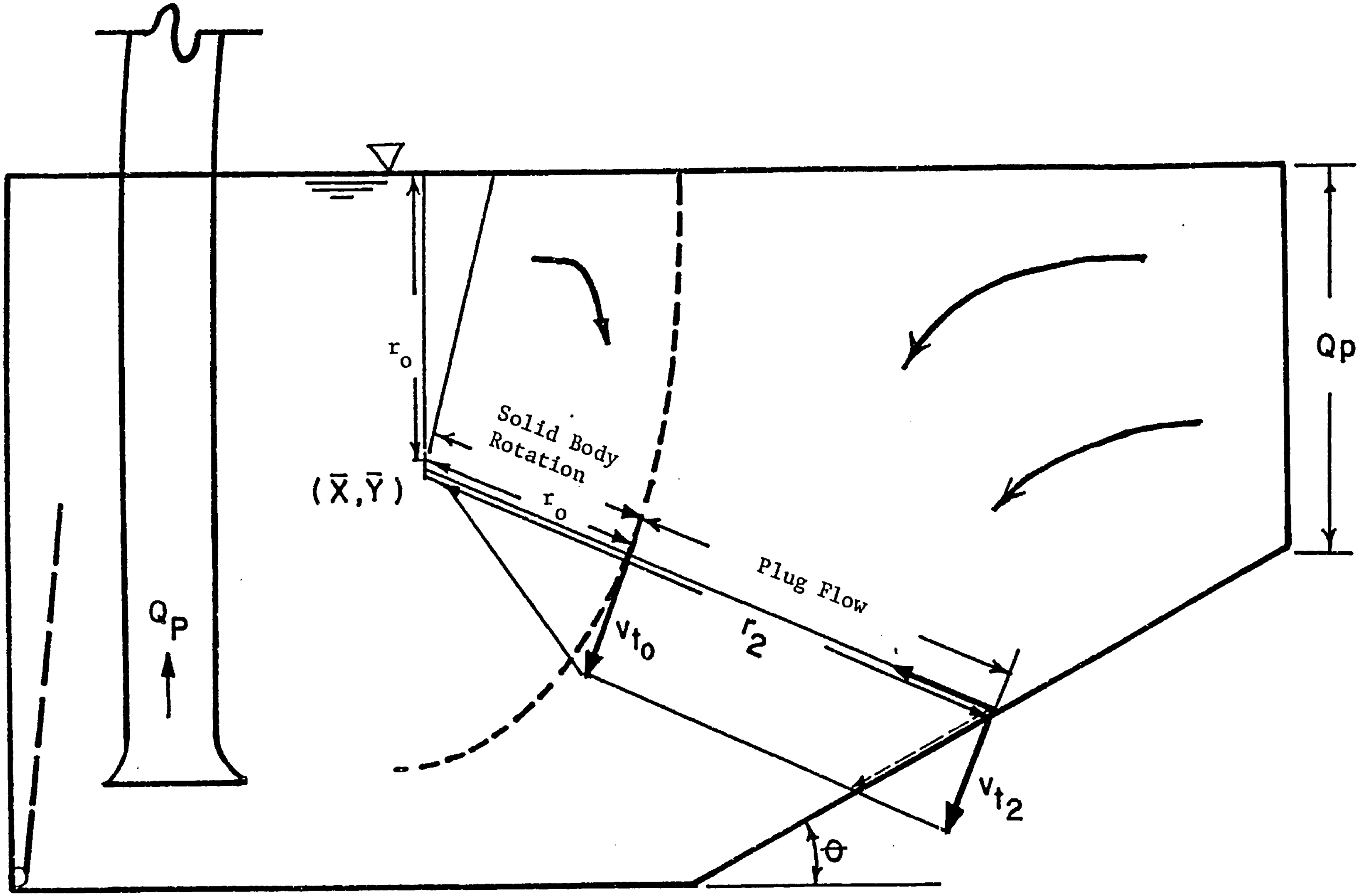
Qp
r_o
Solid Body Rotation
$(\bar{X},\bar{Y})$
r_o
Plug Flow
Q_P
v_{t_0}
r_2
v_{t_2}
θ

Fig. 4.3 Assumed Velocity Profiles

[4.47] $Q_{WD} = \omega r_o^2(W)/2$

At the interface between the solid body flow and the plug flow the velocity is given by

[4.48] $v_{t_o} = \omega r_o$

Combining Eqs. [4.48] and [4.47] yields the tangential velocity at the interface as

[4.49] $v_{t_o} = Q_{WD}/(Wr_o/2)$

The pump discharge is given by

[4.50] $Q_p = v_{t_o}(r_2 - r_o)(W)$

where r_2 is measured from the centre of rotation to the centre of the inclined floor. Combining Eqs. [4.50] and [4.49] gives a ratio for the separation point between the solid body and plug flow regimes as

[4.51] $r_o/r_2 = 1/\{Q_p/(2Q_{WD}) + 1\}$

The pumping rate is generally known, and the circulating flow, Q_{WD}, must be estimated from a velocity traverse extending vertically from the centre of rotation. Q_{WD} is one parameter which will be determined experimentally. Once the circulating flow is estimated, r_o can be determined from Eq. [4.51] and for a known pumping rate, v_{t_o} can be obtained from Eq. [4.50]. This tangential velocity must be resolved into a velocity parallel to the inclined floor, V_i, in order to evaluate the shear stress in Eq. [4.45]. This shear stress is then multiplied by the area of the inclined floor, $L_i(W)$, to estimate the shear force. The shear force, when multiplied by the perpendicular distance between the line of action of this force and the centre of rotation, i.e. the cross product, gives the resisting torque.

4.5.2 Shear Stress on the Horizontal Portion of the Wet Well Floor

Similar to estimating the shear stress produced on the inclined portion of the wet well floor, it is possible to estimate τ_h, the horizontal shear stress. Again, this shear stress is assumed to be uniformly distributed over the entire area of the horizontal floor, (6.5D)(W). For calculating the associated torque, it can be resolved into a force which acts at the centre of the horizontal floor.

4.5.3 Shear Stress on the Vertical Wall Adjacent to the Diffuser Plume

For calculating the shear stress on the wall adjacent to the diffuser air plume, the total depth, H, is divided into ten subsections and the shear stress in each subsection, τ_{v_i}, is calculated as follows

$$[4.52] \qquad \tau_{v_i} = \rho_f \, f \, V_{W_i}{}^2/8$$

where V_{W_i} represents the water velocity adjacent to the wall and is obtained from the drift flux analysis for the plume. Figure 4.4 illustrates the discretization of the plume. During the calculations for the drift flux analysis, the increment in depth, dy, is held constant and equal to 1 mm. Associated with each dy is a dV_{W_i}. The V_{W_i} value used in Eq. [4.52] is the average of the velocities obtained over the distance H/10. The torque, or moment of momentum, associated with each of the ten subsections is given by

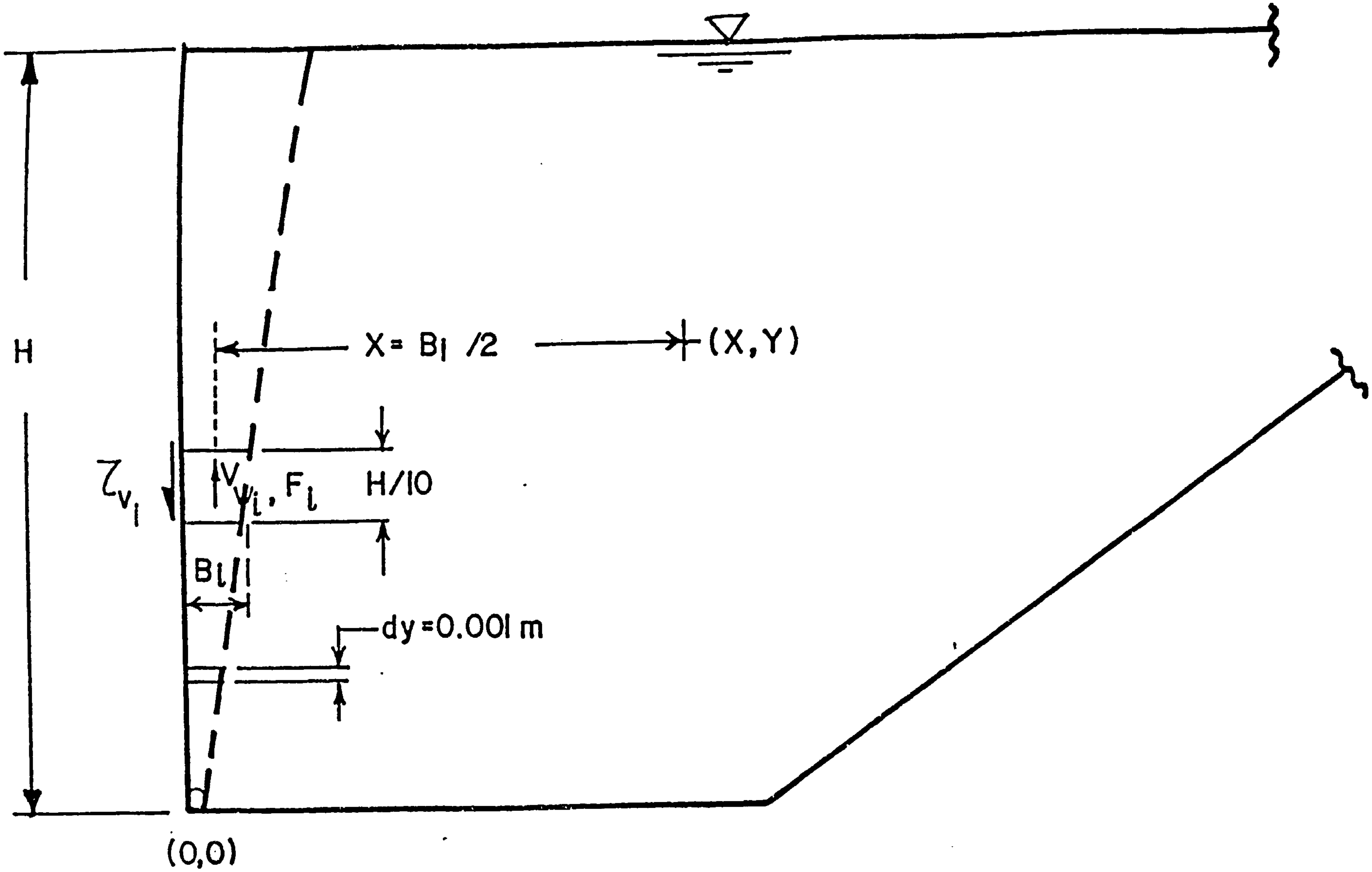
H
X= Bl /2
(X,Y)
ζvl
Vvl, Fl
H/10
Bl/l
dy=0.001 m
(0,0)

Fig. 4.4 Discretization of the Diffuser Plume

[4.53] $r_i x T_i = (\rho_f f V_{W_i}{}^2/8)(W)(H/10)(\bar{X})$

where (W)(H/10) is the wall area of each subsection over which the shear stress acts and $\bar{X}$ is the associated moment arm. The total resisting torque is simply the summation of the torques associated with each subsection.

4.5.4 The Mutual Hydrodynamic Bubble Force

From Eq. [4.8], it is possible to obtain the increment in the mutual force within an element of volume (W)Bdy as

[4.54] $dF/dy = B\alpha g(1 - \alpha)(\rho_f - \rho_{AIR})(W)$

Similar to the shear stress along the vertical wall, the mutual hydrodynamic force has also been calculated and summed up over subsections of depth equal to H/10. The additional force added to the system over a distance dy is given by

[4.55] $dF_i = F_i - F_{i-1}$

where

[4.56] $F_i = F_{i-1} + (dF/dy)(\Delta H)$

For each subsection of depth ΔH = H/10, it is assumed that the total force added to the system by that subsection is the force associated with the mid-point element of the subsection. Remember, that associated with each subsection of depth H/10, there is a number of elements of depth dy. The torque associated with each of the subsections is simply the product of the incremental force added over the subsection and the perpendicular distance from the centre of the subsection to the centre of rotation. From Fig. 4.4, it can be seen that the perpendicular distance is equal to $\bar{X} - 0.5\ B_i$, where B_i is the width of the plume and is also a function of the distance above the diffuser.

4.5.5 Drag Force on the Pump Columns

For calculating the drag forces on the pump columns, the columns were divided into four sections as shown in Fig. 4.5. A horizontal line was projected from the centre of rotation to divide the columns into an upper and lower half. Each half was then evenly divided into two smaller components. Associated with each of the four pump column components is a tangential velocity, v_{t_1}, v_{t_2} etc., which acts at the centre of each. The estimates for the tangential velocities at the pump columns are based on the tangential velocities at the boundaries of the sump along the same line of action. The tangential velocity is assumed to vary linearly along this line. The velocities are denoted as V_{t_1}, V_{t_2} etc., Fig. 4.5. It has been observed, that the tangential velocities V_{t_1} and V_{t_4} can act on either a vertical or horizontal boundary depending on the location of the centre of rotation. Figure 4.6 indicates possible points of application of V_{t_1} and V_{t_4}. If $\bar{X}$ is close to the pump columns then V_{t_1} and V_{t_4} are projected onto the floor of the sump, and the free surface, respectively; whereas, if $\bar{X}$ is farther from the pump columns, V_{t_1} and V_{t_4} are projected onto the rearwall of the sump. V_{t_2} and V_{t_3} were found to always project onto the vertical wall of the sump. The tangential velocities at the boundaries are different depending on whether or not the velocity vector is affected by the

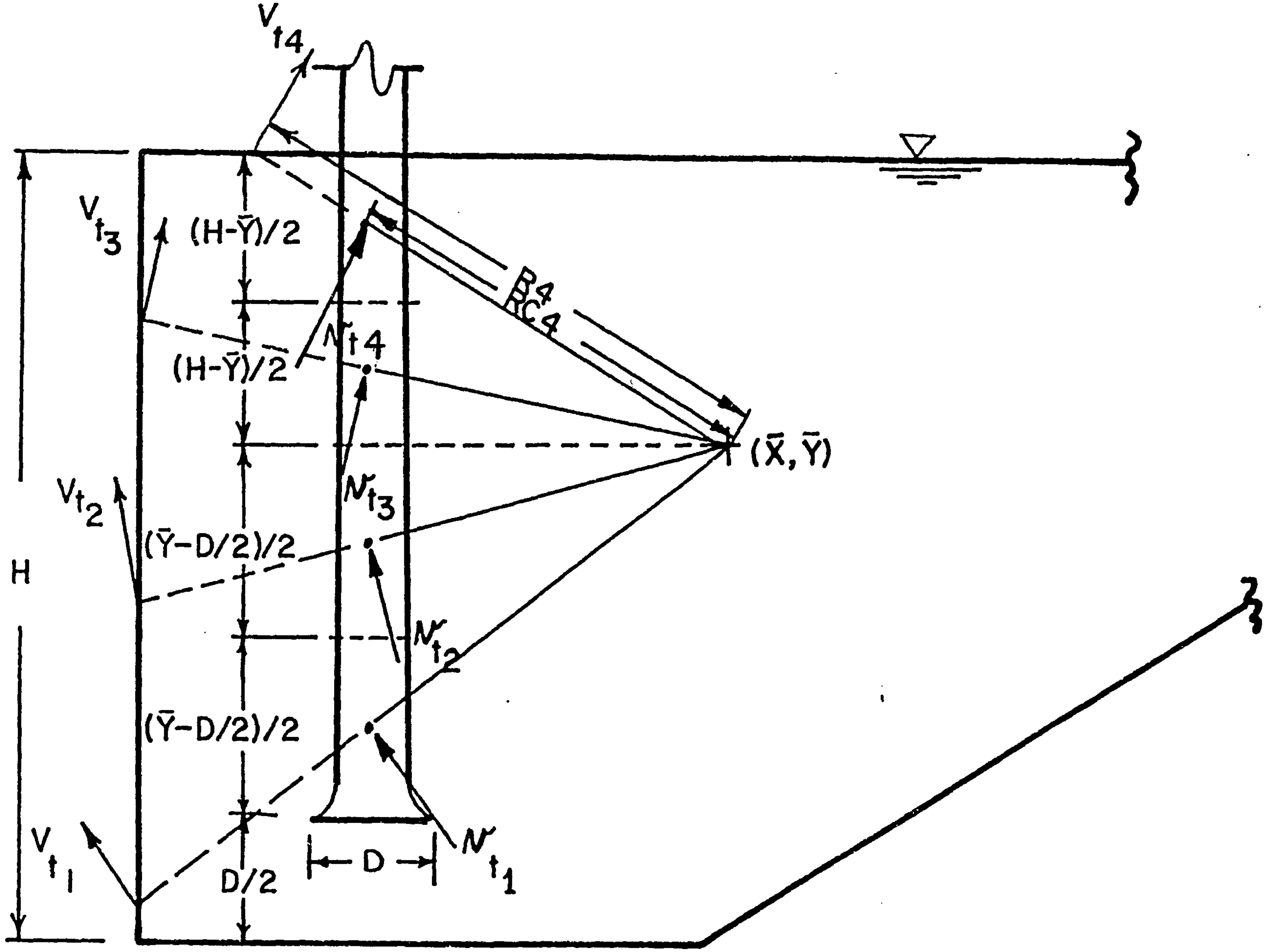
V_{t4}
V_{t3}
$(H-\bar{Y})/2$
$(H-\bar{Y})/2$
B4
RC4
N_{t4}
$(\bar{X},\bar{Y})$
N_{t3}
V_{t2}
$(\bar{Y}-D/2)/2$
H
N_{t2}
$(\bar{Y}-D/2)/2$
V_{t1}
D/2
D
N_{t1}

Fig. 4.5 Discretization of the Pump Columns

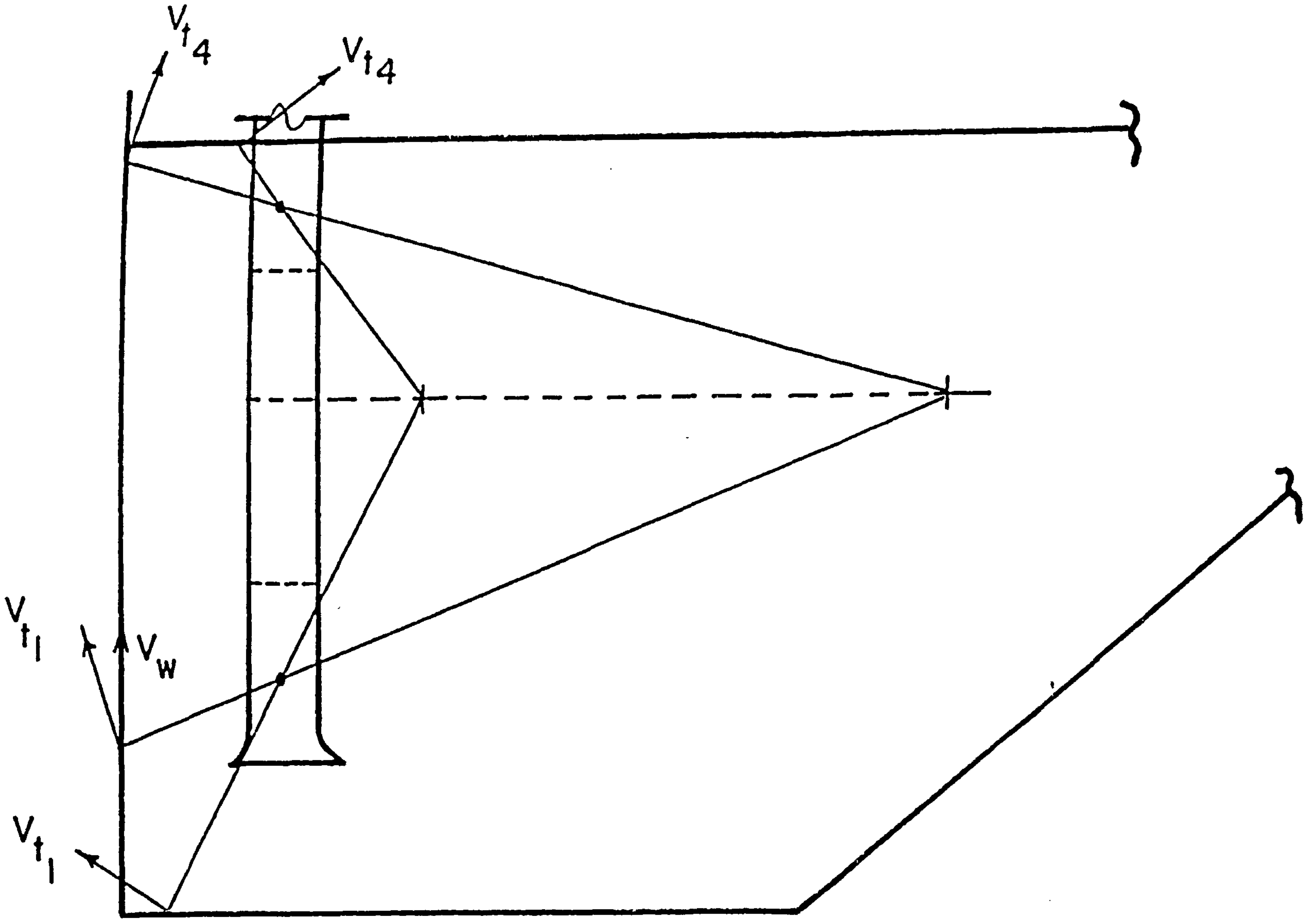
V_{t_4}
V_{t_4}
V_{t_1}
V_w
V_{t_1}

Fig. 4.6 The Effect of Centre of Rotation Coordinates on Tangential Velocities

plume, the floor, or the velocity along the free surface. If the tangential velocity at the boundary is affected by the floor, as is possible for V_{t_1} when $\bar{X}$ is close to the pump columns, then V_{t_1} is estimated assuming that the velocity profile along the line has both solid body and plug flow components, similar to the analysis for the tangential velocity along the inclined floor. The tangential velocity, V_{t_1}, is then calculated by substitution of appropriate quantities in Eqs. [4.51] and [4.50]. Equation [4.50] would yield V_{t_1} for a specific sump configuration, i.e. $\bar{X}$, $\bar{Y}$, depth, air flowrate, pumping rate and floor slope.

If V_{t_1} maps onto the vertical wall, where it is affected by the plume, then V_{t_1} is calculated from the plume water velocity V_W, after applying a cosine correction. The cosine correction is necessary because V_W is vertical, whereas V_{t_1}, and similarly V_{t_2} and V_{t_3}, are at right angles to the line of action from the centre of rotation through the centre of the pump column subsections.

In the case of V_{t_4}, the tangential velocity can be estimated from the plume water velocity, when $\bar{X}$ is far from the pump columns. Otherwise, it can be estimated from physical velocity measurements of the horizontal velocity extending out from the rear wall after the plume flow is turned through 90°. The later case applied when $\bar{X}$ was close to the pump columns. An estimate of the horizontal surface velocity may be obtained by assuming that the plume water velocity at the surface is approximately equal to the horizontal velocity near the plume. It is reasonable to assume a slight reduction in velocity to account for the fact that the flow is turned essentially through 90° at the free surface. Once estimates for the tangential velocities at the boundaries have been made, the tangential velocities at the pump columns can be estimated by assuming that the tangential velocity varies linearly along the line connecting the centre of rotation, the pump column, and the boundary. For example

[4.57] $$v_{t_4} = V_{t_4}(RC_4/R_4)$$

where RC_4 is the distance from the centre of rotation to the pump column, and R_4 is the distance from the centre of rotation to the sump boundary. Figure 4.5 illustrates the locations of RC_4 and R_4.

The drag force acting on each of the pump column subsections is dependent on the velocity which impacts at right angles to it. As such, each of the tangential velocities at the pump column must be resolved into a horizontal velocity. The drag force on each subsection is then calculated as

[4.58] $$F_{D_i} = 0.5\ \rho_f\ C_D\ v_{h_i}^{\ 2}\ A_{p_i}$$

where C_D is the pump column drag coefficient, v_{h_i} is the resolved tangential velocity and A_{p_i} is the projected area of the suction pipes.

The value of the drag coefficient for the pump columns can be estimated by assuming the pump columns to behave as circular cylinders. The drag coefficient then becomes a function of the pump column Reynolds number denoted by

[4.59] $N_{R_p} = v_p d/\nu$

where d = pipe diameter and v_p denotes the average impact velocity and is estimated from the average of the v_{h_i} values. Standard hydraulics and fluid mechanics texts (Fox and McDonald (1973)) give curves for the determination of C_D. Table 4.3 gives the range of C_D values for various N_{R_p} values. The mid-point C_D values are used herein to calculate the drag force.

The impact velocities, v_{h_i}, are corrected by a multiplier which accounts for the fact that the actual velocity experienced by the pump column is higher due to the acceleration of the flow through the contracted area between the pump columns, and the pump columns and the side wall. For a strip width of dy, the gross flow area is (W)(dy). The net area is the gross area minus the area occupied by the three suction pipes, (W - 3d)dy. For continuity to be satisfied

[4.60] $v_C A_C = vA$

where v_C is the velocity through the contracted area; A_C is the contracted area; v is the uncontracted velocity and A is the uncontracted area. Substitution of appropriate areas into Eq. [4.60] yields the contracted velocity as

[4.61] $v_C = (v)(W)/(W - 3d)$

The torque created by the pump column drag forces is the cross product of the force on each subsection and the distance from the centre of rotation to the point of action of the force. For a specific sump geometry, all the distances are known.

Table 4.3 Pump Column Reynolds Numbers and Corresponding Drag Coefficients (after Fox and McDonald, 1973)

N_{R_p}	C_d	Midpoint C_d
1.0	10.0	
		6.35
10.0	2.7	
		2.10
100.0	1.5	
		1.25
1000.0	1.0	
		1.15
10000.0	1.3	
		1.40
100000.0	1.5	

4.5.6 Side Wall Shear Stress

In order to evaluate the effect of side wall shear stress on the circulation, the cross-sectional area of the sump is divided into five sections and each section is further subdivided into three parts. The general scheme is shown in Fig. 4.7. From the centre of rotation, a line is drawn to each of the five corners of the wet well boundary, creating five major divisions within the area. Along the boundary within each of these areas, the three equal divisions are formed and rays extending back to the centre of rotation are constructed. Each ray further subdivides the major area into three smaller subareas. As a result of the selected method of dividing up the cross-section, there results different areas for each subarea; however, the division is simplified due to known coordinate locations along the boundaries.

A small element of the side wall, as shown in Fig. 4.8, is considered to develop the formulation of the torque due to side wall shear. The total torque produced by shear stress τ_{SW} acting over a small element dA is

$$[4.62] \qquad \underset{\sim}{T} = \underset{\sim}{r} \times \underset{\sim}{\tau}_{SW}(r\,dr\,d\theta)$$

Simply stated, the torque produced is equal to the shear stress multiplied by the area over which this stress acts, multiplied by the perpendicular distance between the centre of rotation and the line of action of the resultant shear force. Again, as shown in Fig. 4.8, the velocity profile is made up of a plug flow region and a solid body region. The summation of the contributions of all the dθ's through

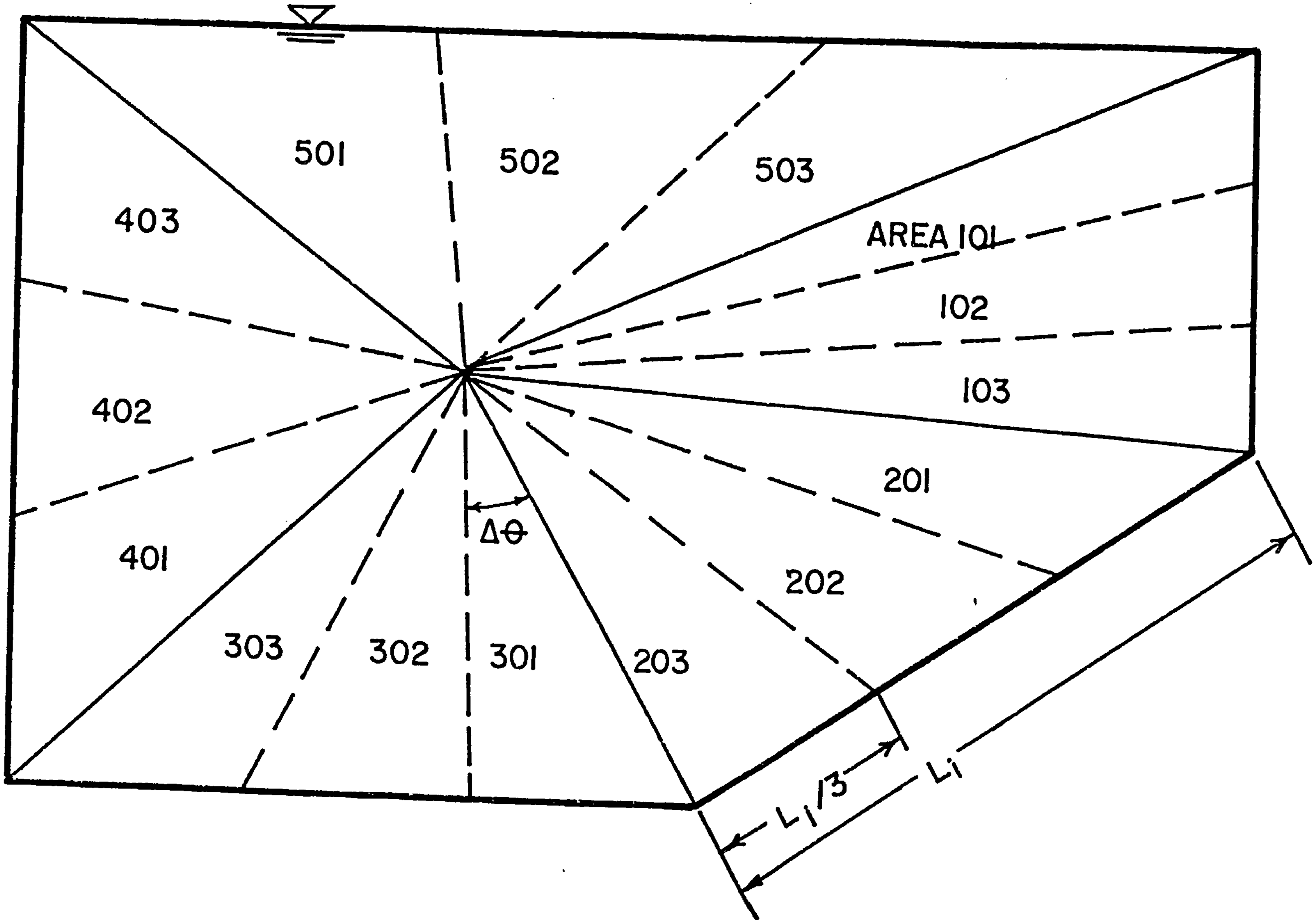
501
502
503
403
AREA 101
102
402
103
201
Δθ
401
202
303
302
301
203
L_i/3
L_i

Fig. 4.7 Elements used to Calculate Side Wall Shear Stress

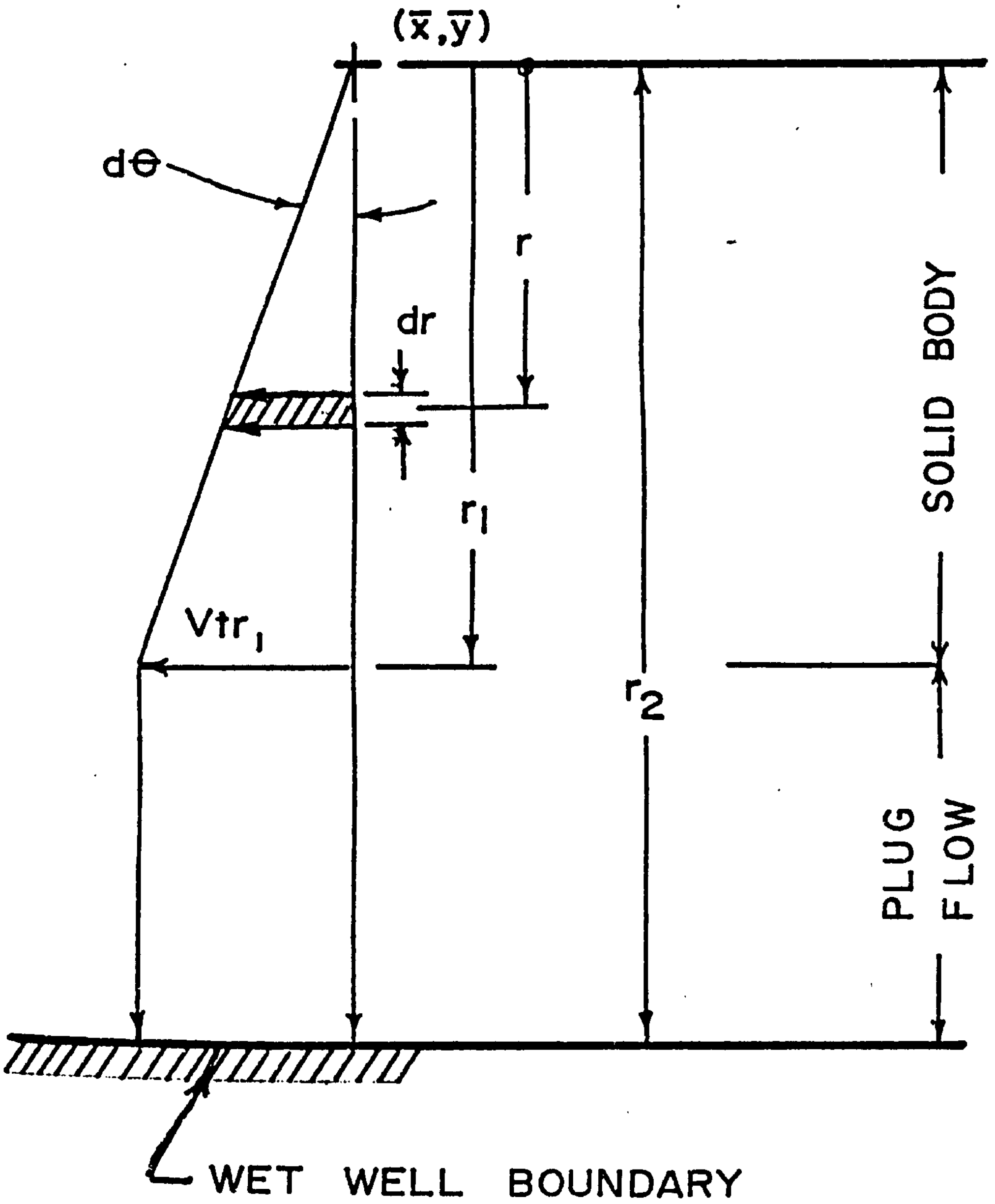
(x̄,ȳ)
dθ
r
dr
r₁
Vtr₁
r₂
SOLID BODY
PLUG FLOW
WET WELL BOUNDARY

Fig. 4.8 An Element used to Calculate Side Wall Shear

one revolution will yield the total resisting torque due to shear. For a finite discretization, Δθ replaces dθ, as shown in Section 301 of Fig. 4.7. The resultant shear torques are summed over the 15 subareas. The total torque due to side wall shear, acting at the centre of rotation is

[4.63] $$T = \sum 2\Delta\theta \left\{ {}_{0}\int^{r_1} rx\tau_{SW} rdr + {}_{r_1}\int^{r_2} rx\tau_{SW} rdr \right\}$$

The total torque is multiplied by two since there are two side walls under consideration. The side wall shear stress can be estimated from the velocity profile and is given by

[4.64] $$\tau_{SW} = \rho_f \; f \; V^2/8$$

In the region from the centre of rotation to a distance r_1, the tangential velocity, V, is given by

[4.65] $$V = V_{tr_1}(r/r_1)$$

and in the plug flow region

[4.66] $$V = V_{tr_1}$$

Substitution of Eqs. [4.66], [4.65] and [4.64] into [4.63] and evaluation of the integrals gives the total torque as

[4.67] $$T = \sum\{(\Delta\theta \; \rho_f \; f \; V_{tr_1}{}^2(r_2{}^3/3 - (2/15)r_1{}^3))/4\}$$

where the summation is carried out over those elements in which the assumptions of plug flow and solid body rotation apply. This two flow regime is assumed for areas 201, 202, 203, 301, 302, 303, 401, 402 and 403 as shown in Fig. 4.7. In areas 101, 102, 103, 501, 502, and 503, it is assumed that only solid body rotation applies. In these cases, r_1 and r_2 are equal and the solution of Eq. [4.63] yields

[4.68] $T = \sum\{\Delta\theta \rho_f f V_{tr_1}{}^2 r_1{}^3/20\}$

In both Eqs. [4.68] and [4.67], r_1 corresponds to the distance away from the centre of rotation. Beyond this distance, the solid body rotation assumption no longer applies. V_{tr_1} corresponds to the tangential velocity at this point.

In Sections 101, 102, and 103, the circulating flow and the incoming flow are impacting on each other and it can be assumed that there is a reduction in the tangential velocities within these subsections. If it is assumed that only 50 percent of the incoming flow contributes to the tangential velocity, and using the assumption of solid body rotation, continuity dictates that the discharge through any cross-section should be equal to the area of the velocity triangle multiplied by the width of the flow section, i.e.

[4.69] $(Q_{WD} + 0.5\ Q_p) = (W)(0.5)r_1\ V_{tr_1}$

where $(Q_{WD} + 0.5\ Q_p)$ represents the discharge through Sections 101, 102 and 103, $(0.5\ r_1\ V_{tr_1})$ represents the area of the velocity profile and W is the width over which the discharge is passing. Equation [4.69] can be rearranged to yield the tangential velocity at the boundary as

[4.70] $V_{tr_1} = (Q_{WD} + 0.5\ Q_p)/(3D\ r_1)$

4.5.7 Linear Momentum Balance

If one applies a linear momentum balance to the system in the horizontal direction, it is possible to estimate the magnitude of the force required to redirect the flow as it impinges on the wall at the inlet section. Figure 4.9 illustrates the forces which must be

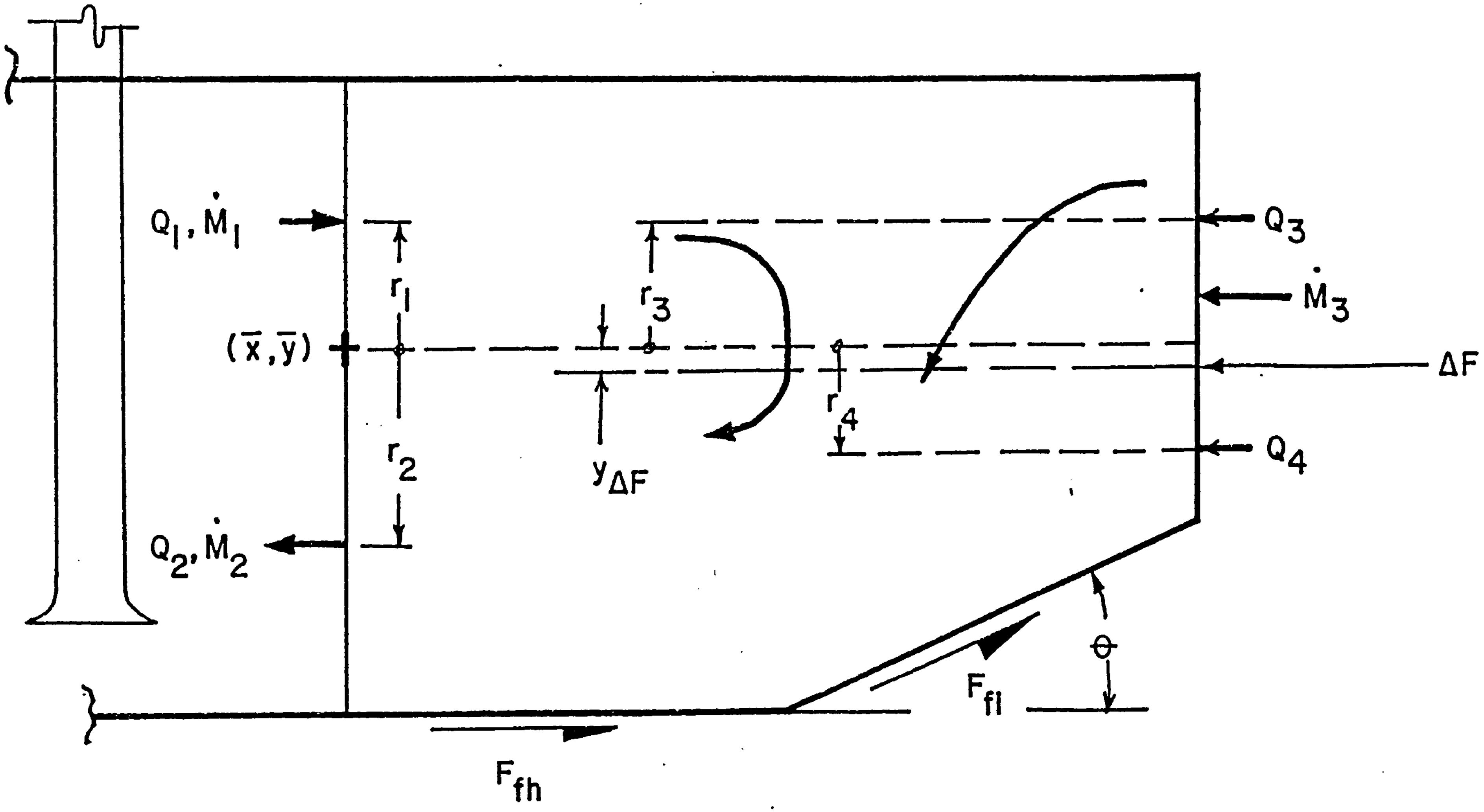
Q$_1$, $\dot{M}_1$
$(\bar{x}, \bar{y})$
Q$_2$, $\dot{M}_2$
r$_1$
r$_2$
r$_3$
y$_{\Delta F}$
r$_4$
Q$_3$
$\dot{M}_3$
ΔF
Q$_4$
θ
F$_{fl}$
F$_{fh}$

Fig. 4.9 Application of Linear Momentum to Control Volume

considered. The control volume for the linear momentum balance includes all of the fluid to the right of the centre of rotation. For steady state conditions, the conservation of linear momentum for steady flow states

[4.71] $\sum \underset{\sim}{F}_{ext} = \int \rho_f \, \underset{\sim}{v}(\underset{\sim}{v} \cdot d\underset{\sim}{A})$

where $\sum \underset{\sim}{F}_{ext}$ is the summation of all external forces acting on the control volume and the right hand side of Eq. [4.71] represents the net efflux of momentum through the system boundaries.

From Fig. 4.9, it can be seen that the solution of Eq. [4.71] is given by

[4.72] $\Delta F = \dot{M}_1 + \dot{M}_2 - \dot{M}_3 + F_{fh} + F_{fi} \cos\theta$

where $\dot{M}_1$, $\dot{M}_2$ and $\dot{M}_3$ are the momentum fluxes crossing the control boundary above the centre of rotation, below the centre of rotation and at the inlet respectively, F_{fh} is the total friction force on the horizontal floor, F_{fi} is the total friction force on the inclined floor and ΔF may be considered as the net pressure force required to redirect the flow. It has been assumed that, except for ΔF, the hydrostatic forces at the left and right hand sides of the control volume cancel each other. In case there is no pumping or inflow, $\dot{M}_3$ is equal to zero.

With pumping, the momentum fluxes are as follows

[4.73] $\dot{M}_1 = \rho_f \, Q_{WD} \, \beta_1 \, v_1$

[4.74] $\dot{M}_2 = \rho_f (Q_{WD} + Q_p) \beta_2 \, v_2$, and

[4.75] $\dot{M}_3 = \rho_f\ Q_p\ \beta_3\ v_3$

With the pumps off and no inflow

[4.76] $\dot{M}_1 = \rho_f\ Q_{WD}\ \beta_1\ v_1$

[4.77] $\dot{M}_2 = \rho_f\ Q_{WD}\ \beta_2\ v_2$, and

[4.78] $\dot{M}_3 = 0.0$

β_1, β_2 and β_3 are the momentum correction factors and v_1, v_2 and v_3 are the mean velocities.

To determine the line of action of the ΔF force, it is necessary to apply the conservation of angular momentum about the centre of rotation. For steady state conditions, Eq. [4.42] gives the formulation for angular momentum. When Eq. [4.42] is applied to the control volume in Fig. 4.9, the vertical distance between the centre of rotation and the line of action of the ΔF force, $y_{\Delta F}$, is given by

[4.79] $$y_{\Delta F} = (\rho_f\{Q_2 r_2 v_2 + Q_4 r_4 v_4 - Q_1 r_1 v_1 - Q_3 r_3 v_3\} - \bar{Y}(F_{fh} + F_{fi}\ \cos\theta))/\Delta F$$

where Q_3 and Q_4 are the flows entering above and below the centre of rotation and are obtained by proportioning the total inflow over the area above and below the centre of rotation. When the pumps are in operation

[4.80] $Q_1 = Q_{WD}$, and

[4.81] $Q_2 = Q_{WD} + Q_p$

and when the pumps are not in operation and there is no inflow

[4.82] $Q_1 = Q_2 = Q_{WD}$, and

[4.83] $Q_3 = Q_4 = 0.0$

The distances r_1, r_2, r_3 and r_4 in Eq. [4.79] are measured from the centre of rotation to the centre of the flow areas.

The torque created by the ΔF force is obtained by multiplying the force by the perpendicular distance between its line of action and the centre of rotation, $y_{\Delta F}$. Attention must be paid to the direction of action of ΔF, and to its line of action, in order to determine the proper sign for the torque i.e. positive or negative torque.

4.5.8 The ΔP_2 Force

In order to estimate the magnitude and point of application of the force due to an increase in hydrostatic pressure, it is necessary to estimate the rise in the free surface due to the momentum of the diffused air plume. Consider the volume of fluid above the static water level in Fig. 4.10. The linear momentum equation for this fluid volume, in the vertical direction, under steady state conditions yields

$$[4.84] \qquad \sum F_y = \Delta(\rho_f Q V_W)_y$$

where Δ represents the rate of change of momentum between the bottom of the fluid control element, which is coincident with the static water level, and the top of the fluid element which is ΔH above the static water level. Equation [4.84] can be expressed in terms of the element properties as

$$[4.85] \qquad -\gamma_f(1-\alpha)(\Delta H)(B_T)(W) = 0 - \rho_f(1-\alpha)V_W(B_T)(W)V_W$$

where B_T is the width of the plume at the static water level. The left hand side of Eq. [4.85] represents the force due to the effective

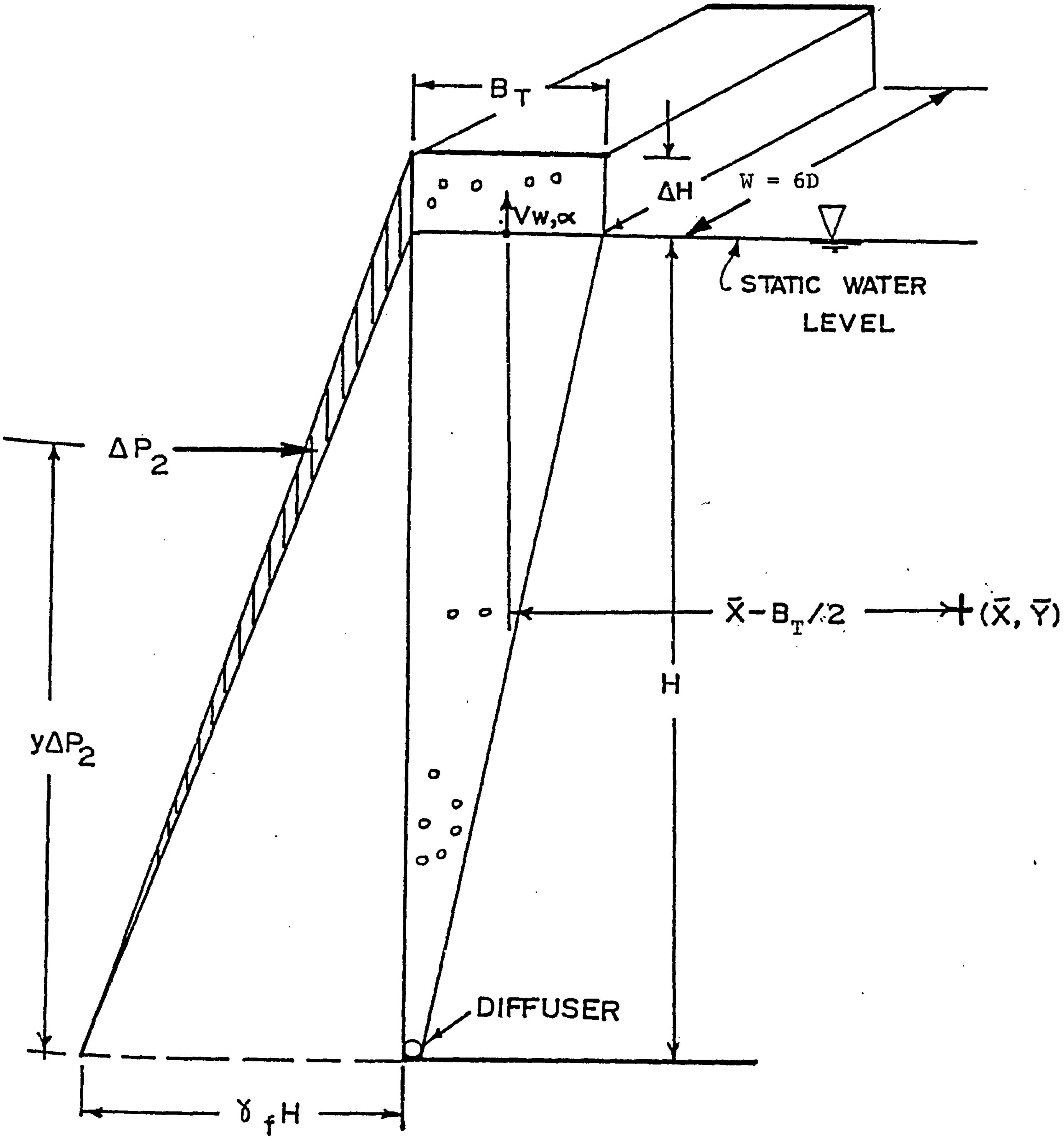

B_T
ΔH
W = 6D
$V_{w,\alpha}$
STATIC WATER LEVEL
ΔP_2
$y\Delta P_2$
$\bar{X}-B_T/2$
$(\bar{X},\bar{Y})$
H
DIFFUSER
$\gamma_f H$

Fig. 4.10 Added Hydrostatic Pressure Force

mass of fluid, whereas on the right hand side of the equation, the zero term represents the momentum leaving the top of the element, and the second term gives the momentum entering at the static water level. Rearranging Eq. [4.85] gives the rise in the free surface, ΔH, as

[4.86] $\Delta H = V_W^2/g$

where V_W can be assumed to be the water velocity obtained for the upper most dy element from the drift flux analysis.

If it is assumed that the increase in the hydrostatic pressure follows the triangular distribution as shown in Fig. 4.10, wherein the effect of the rise in the water level is negligible at the bed; then the total force applied is the volume of the shaded wedge given by

[4.87] $\Delta P_2 = 0.5\ \gamma_f\ H(\Delta H)(W)$.

The line of action of the force is horizontal and passes through the centroid of the wedge. It can be shown that the distance from the floor of the wet well to the line of action, $y_{\Delta P_2}$, is given by

[4.88] $y_{\Delta P_2} = (2H + \Delta H)/3$

The torque associated with the ΔP_2 force is given by the product of ΔP_2 and $y_{\Delta P_2}$. Again, the sign of the torque is dependent on the relative location between the line of action of the force and the centre of rotation.

4.5.9 The Force Due to the Mass of Fluid Above the Static Water Level

In addition to creating an increase in the hydrostatic pressure along the wall of the wet well, the volume of fluid above the free surface also creates a vertical force in the -y direction. This force is due to the mass of the fluid. In Fig. 4.10, the volume of fluid above the free surface is

[4.89] $\forall = (\Delta H)(W)(B_T)(1 - \alpha)$

The force of the fluid is the volume multiplied by the unit weight of the fluid, and the torque is the product of the force and the perpendicular distance between the line of action and the centre of rotation. Assuming that the force acts through the centre of the volume of fluid above the static water level, the torque due to this mass, $T_{\Delta m}$, in Fig. 4.10 is given by

[4.90] $T_{\Delta m} = (\bar{X} - B_T/2)(W)(\Delta H)(1 - \alpha)(\gamma_f)(B_T)$

4.5.10 The Pressure Imbalance Force, ΔP_B

Consider the plume as shown in Fig. 4.11. As the air-water mixture is accelerated and approaches the free surface, a part of this air is released to the atmosphere above the plume. The remaining air is carried by momentum and turned through 90° and proceeds horizontally away from the plume. As a result of the air remaining in the flow that moves horizontally, there is a net reduction in the pressure on the bed. It is assumed that the effect of this pressure reduction takes place over a distance equal to the top width of the plume, B_T, and further, that the depth of the air-water layer is also equal to the top width. An air bubble which enters this zone will travel horizontally at a velocity of V_W, assuming that the water velocity in this zone is equal to the water velocity at the top of the plume. In the vertical direction, the bubble velocity will be approximately equal to its rise velocity, v_b.

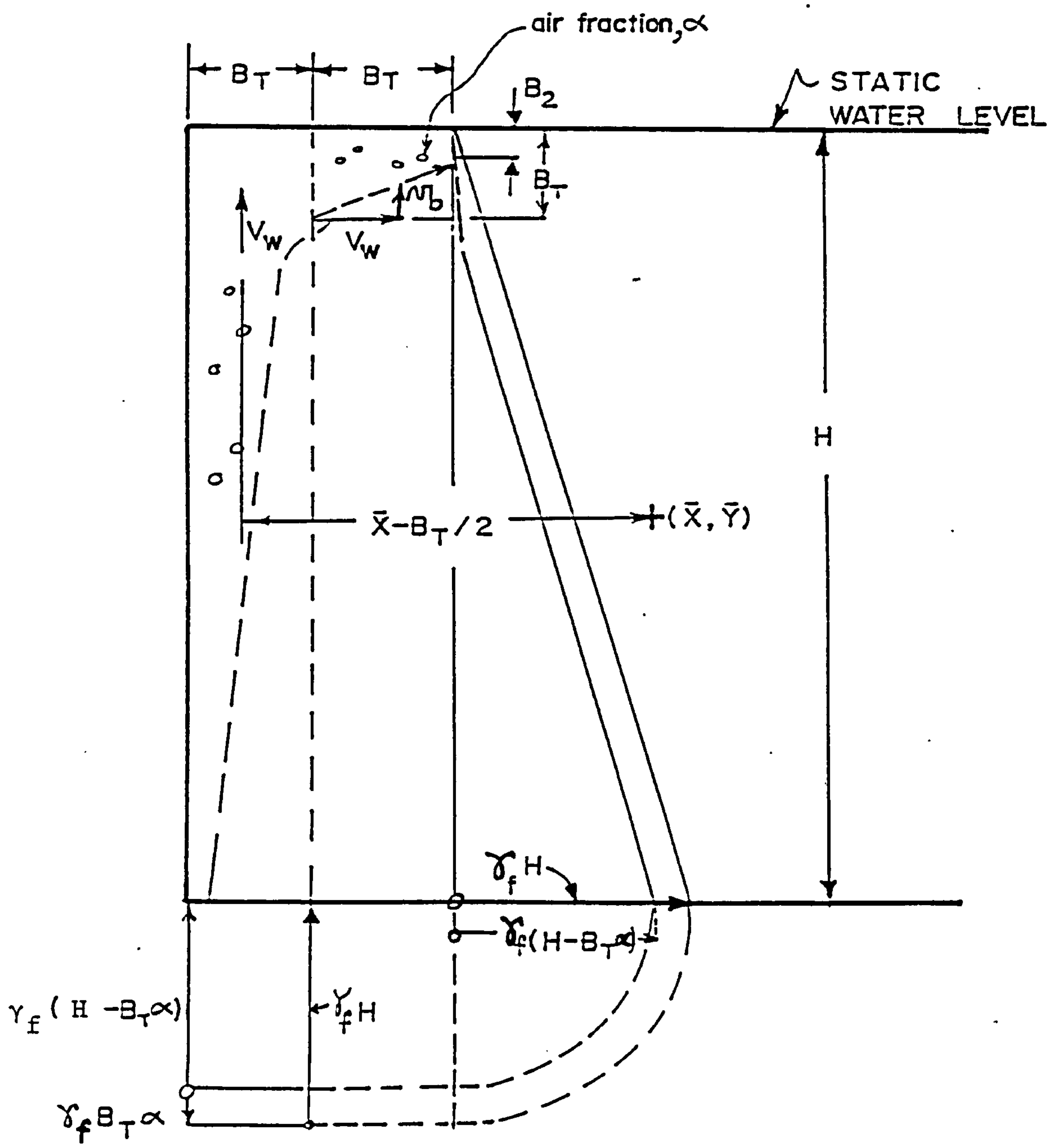
air fraction, α
B_T
B_T
B_2
STATIC WATER LEVEL
B_T
V_w
V_w
w_b
H
X̄−B_T/2
(X̄, Ȳ)
γ_f H
γ_f(H−B_Tα)
γ_f (H −B_Tα)
γ_f H
γ_f B_T α

Fig. 4.11 Calculation of the Pressure Imbalance

In the absence of air, the bed pressure would be the normal hydrostatic pressure, $\gamma_f H$. Due to the presence of air, the bed pressure is given as

[4.91] $p_B = \gamma_f(H - B_T) + \gamma_f(B_T)(1 - \alpha)$

The imbalance in the bed pressure is the difference between the bed pressure in the presence of air and the normal hydrostatic bed pressure, i.e.

[4.92] $\Delta p_B = \gamma_f(H - B_T) + \gamma_f(B_T)(1 - \alpha) - \gamma_f(H)$

or

[4.93] $\Delta p_B = -(B_T\alpha)\gamma_f$

which is acting vertically downward.

Due to the trajectory of the bubble, it can be reasoned that the entire area denoted by $(B_T)(B_T)$ is not filled uniformly with air, and therefore, only part of this volume contributes to a reduction in the bed pressure. A bubble which enters the zone with a horizontal velocity V_W, and vertical velocity v_b, over a horizontal distance B_T will rise to a point B_2 below the free surface. From similar triangles one obtains

[4.94] $(B_T - B_2)/B_T = v_b/V_W$

from which

[4.95] $B_2 = B_T(1 - v_b/V_W)$

If it is assumed that the distance B_2 is effective in creating the pressure imbalance, then B_2 can be substituted for B_T in Eq. [4.93] to yield the estimated pressure imbalance as

[4.96] $\Delta p_B = \gamma_f \alpha B_T(1 - v_b/V_W)$

Assuming this pressure to act over the top width of the plume and along the entire width of the wet well, the force in the vertically downward direction is given by

$$[4.97] \qquad \Delta P_B = \gamma_f \alpha B_T^{\,2}(W)(1 - v_b/V_W)$$

where α can be taken as the air fraction of the upper most dy element of the plume. It is assumed that the line of action of this force is at the mid-point of the plume top width. Thus, the associated moment arm is $(\bar{X} - B_T/2)$.

An estimate of the rise velocity of the bubbles, v_b, may be obtained from Fig. 4.12, in which the rise velocity is shown to be a function of the bubble radius.

4.5.11 Angular Momentum Crossing the System Boundary

Subsections 4.5.1 to 4.5.10 have presented the detailed formulation of the torques due to the external forces included in the summation of terms on the left hand side of Eq. [4.42]. In this subsection, the formulation of the right hand side of Eq. [4.42] is presented. As mentioned, the right hand side of Eq. [4.42] represents the net efflux of the moment of momentum through the control volume boundary. The integral, $\int_{CS} (\rho_f \underset{\sim}{r} x \underset{\sim}{v})(\underset{\sim}{v} \cdot d\underset{\sim}{A})$, is evaluated with the aid of Fig. 4.13.

If a horizontal line is extended from the centre of rotation to the inlet zone, it can be observed that flow enters both above and below this line, resulting in a cancellation of torque. If $\bar{Y}$ is below the top of the sloping portion of the floor, i.e. $\bar{Y} < L_1 \sin\theta$,

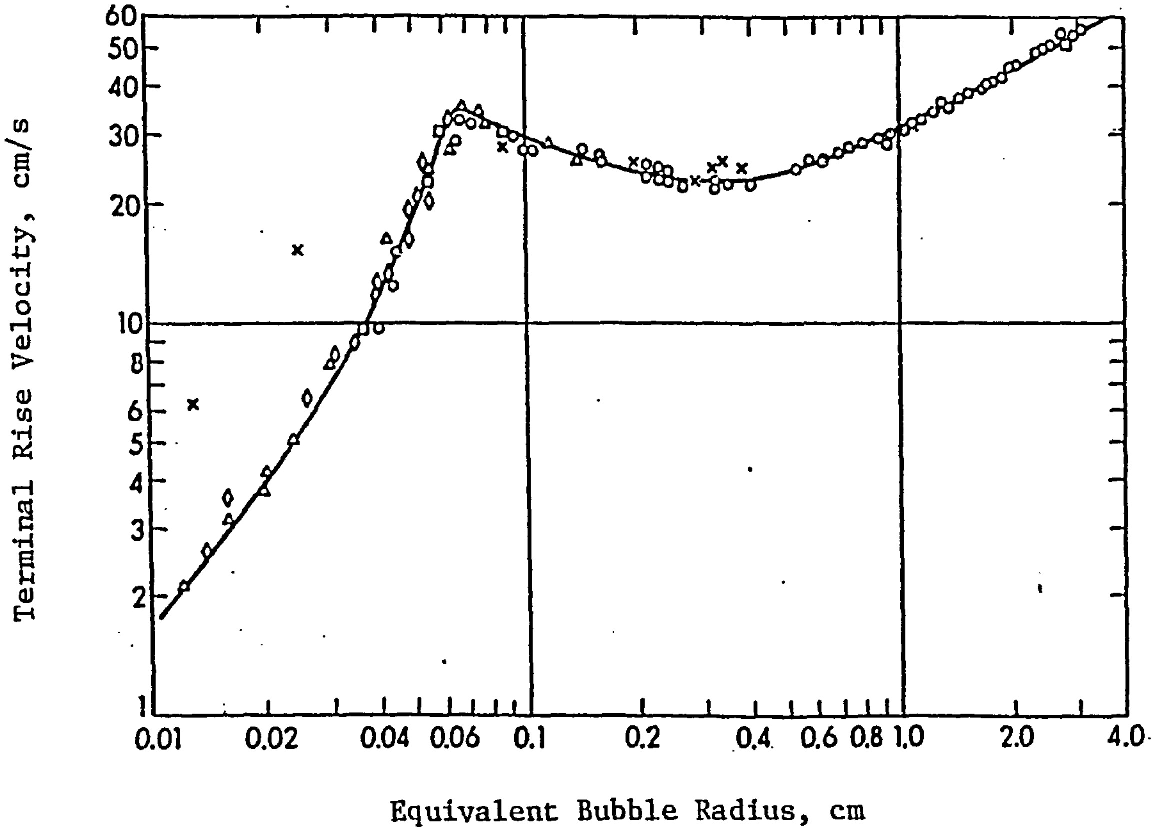

Fig. 4.12 Terminal Rise Velocity of Bubbles
(after Haberman and Morton, 1953)

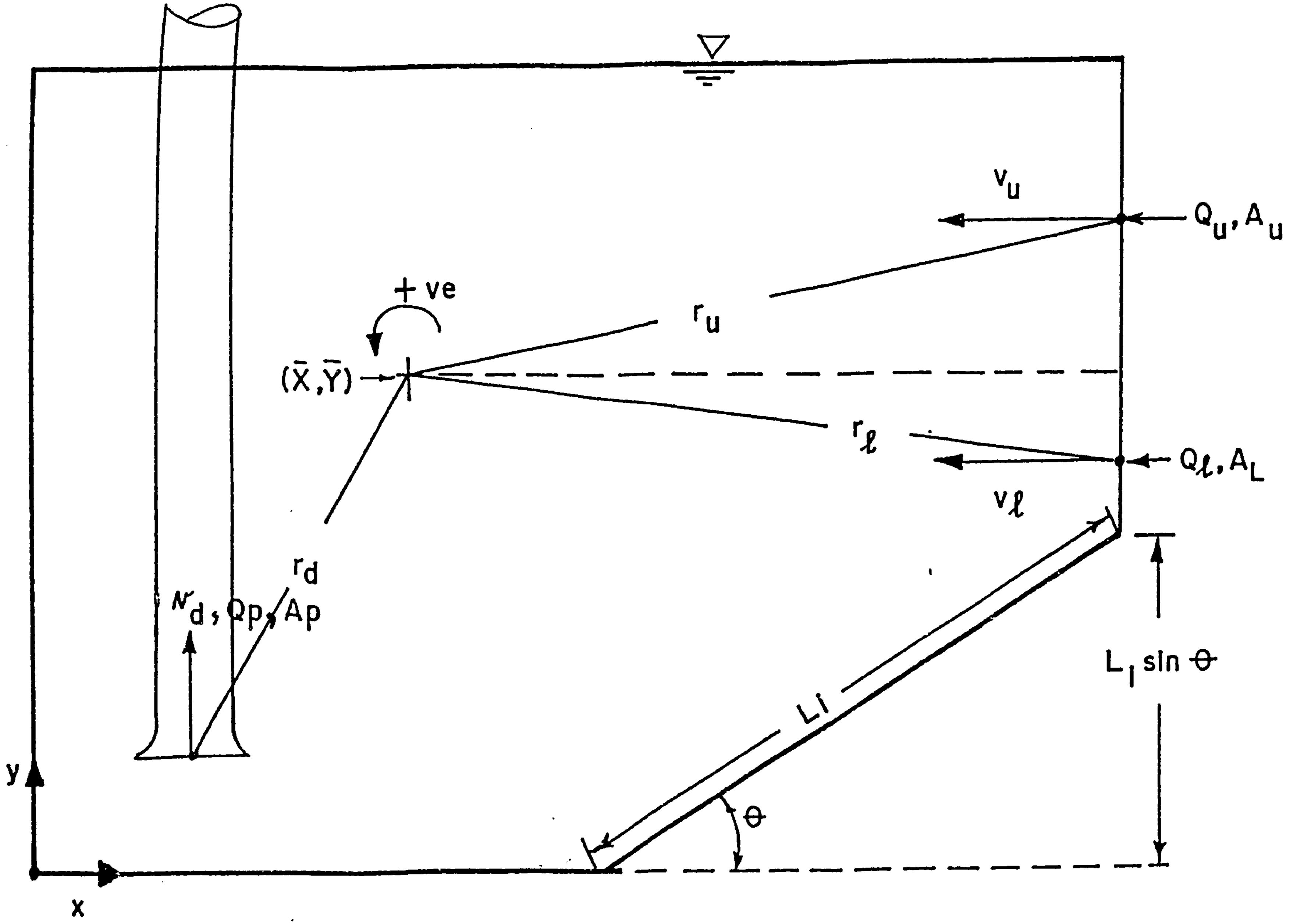
Q_u, A_u
v_u
r_u
+ ve
$(\bar{X},\bar{Y})$
r_ℓ
Q_ℓ, A_L
v_ℓ
r_d
v_d, Qp, Ap
$L_I \sin\theta$
Li
θ
y
x

Fig. 4.13 Evaluating the Angular Momentum Crossing the Boundary

then all the flow entering the system supplies torque of the same sign. For the general case shown in Fig. 4.13, the moment of momentum crossing the boundary is

$$[4.98] \quad \int_{CS} (\rho_f \underset{\sim}{r} x \underset{\sim}{v})(\underset{\sim}{v} \cdot d\underset{\sim}{A}) = \rho_f[Q_\ell(\underset{\sim}{r}_\ell x \underset{\sim}{v}_\ell) - Q_u(\underset{\sim}{r}_u x \underset{\sim}{v}_u) - Q_p(\underset{\sim}{r}_d x \underset{\sim}{v}_d)]$$

where, $\underset{\sim}{r}_u$, $\underset{\sim}{r}_\ell$ and $\underset{\sim}{r}_d$ are the radius arms from the centre of rotation to the upper, lower and outlet zone respectively, and $\underset{\sim}{v}_u$, $\underset{\sim}{v}_\ell$ and $\underset{\sim}{v}_d$ are the average velocities through the cross-sectional areas A_u, A_ℓ and A_p respectively. For a known pumping rate, or inflow, and a known geometry, Q_u and Q_ℓ are proportioned according to the flow areas above and below the line extending horizontally from the centre of rotation.

4.6 A Note on the Selection of Friction Factors

During the calculation of the shear stresses on the horizontal floor, inclined floor, rear wall and side walls, τ_h, τ_i, τ_v and τ_{SW}, the Darcy-Weisbach friction factor, f, is of first order importance. The value of f used in this calculation should be obtained from a relationship between the actual boundary shear stresses developed and the velocity profile which produces the boundary shear stress. During the calibration phase, the actual friction factor was estimated. Prior to calibration, an estimate for f was obtained from the Moody diagram once a suitably defined Reynolds number and relative roughness were computed. The numerical model was found to yield stable solutions for friction factors ranging from 0.02 to 0.05.

CHAPTER 5

EXPERIMENTAL APPARATUS AND MEASUREMENT EQUIPMENT

5.1 Description of the Physical Model

The plan view and cross-section of the physical model are shown in Fig. 5.1 and 5.2 respectively. The overall length, width and depth of the actual sump section are 1576, 684 and 1140 mm. The entire sump was constructed out of 19 mm thick acrylic sheet, with aluminum reinforcing angles at all corners. The sump was bolted to a 13 mm thick steel base. Three pump intake pipes of 75 mm inside diameter and 114 mm bell-mouths were used. As stated in Chapter 4, the entire sump configuration, in terms of wall and floor clearances, as well as clearance between the intakes, conformed to both the Hydraulic Institute Standards (1983) and the British Hydromechanics Research Association Standards, Prosser (1977).

The bell-mouth intakes were machined from a solid block of acrylic and were joined to the copper suction pipes with epoxy. After examining the shapes of bell-mouths, as reported in literature by Markland and Pope (1956), Denny (1956), Denny and Young (1957), Berge (1966) and after consulting the catalogues of several pump manufacturers, elliptical shaped bell-mouths were adopted. Figure 5.3 shows the form and equation used for the bell-mouth inlet.

Separate gate valves were provided on each intake to adjust the flowrate. The three suction pipes were joined into a single 102 mm diameter pipe which was connected to the suction side of the pump. The pump was a single stage, horizontal, centrifugal pump with a

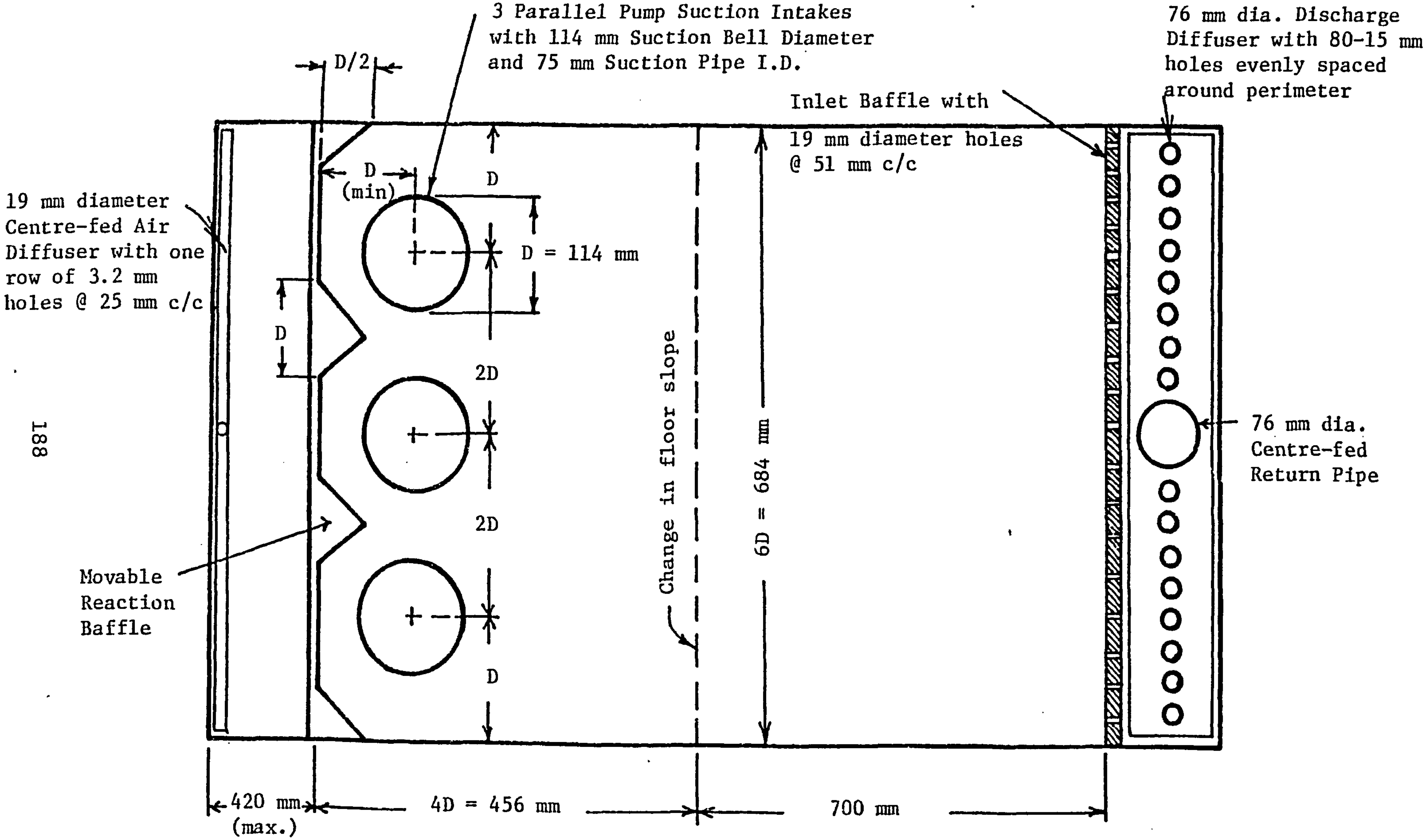
3 Parallel Pump Suction Intakes with 114 mm Suction Bell Diameter and 75 mm Suction Pipe I.D.
76 mm dia. Discharge Diffuser with 80-15 mm holes evenly spaced around perimeter
Inlet Baffle with 19 mm diameter holes @ 51 mm c/c
D/2
D (min)
D
D = 114 mm
19 mm diameter Centre-fed Air Diffuser with one row of 3.2 mm holes @ 25 mm c/c
D
2D
2D
D
Change in floor slope
6D = 684 mm
76 mm dia. Centre-fed Return Pipe
Movable Reaction Baffle
420 mm (max.)
4D = 456 mm
700 mm

Fig. 5.1 Plan of Model Wet Well

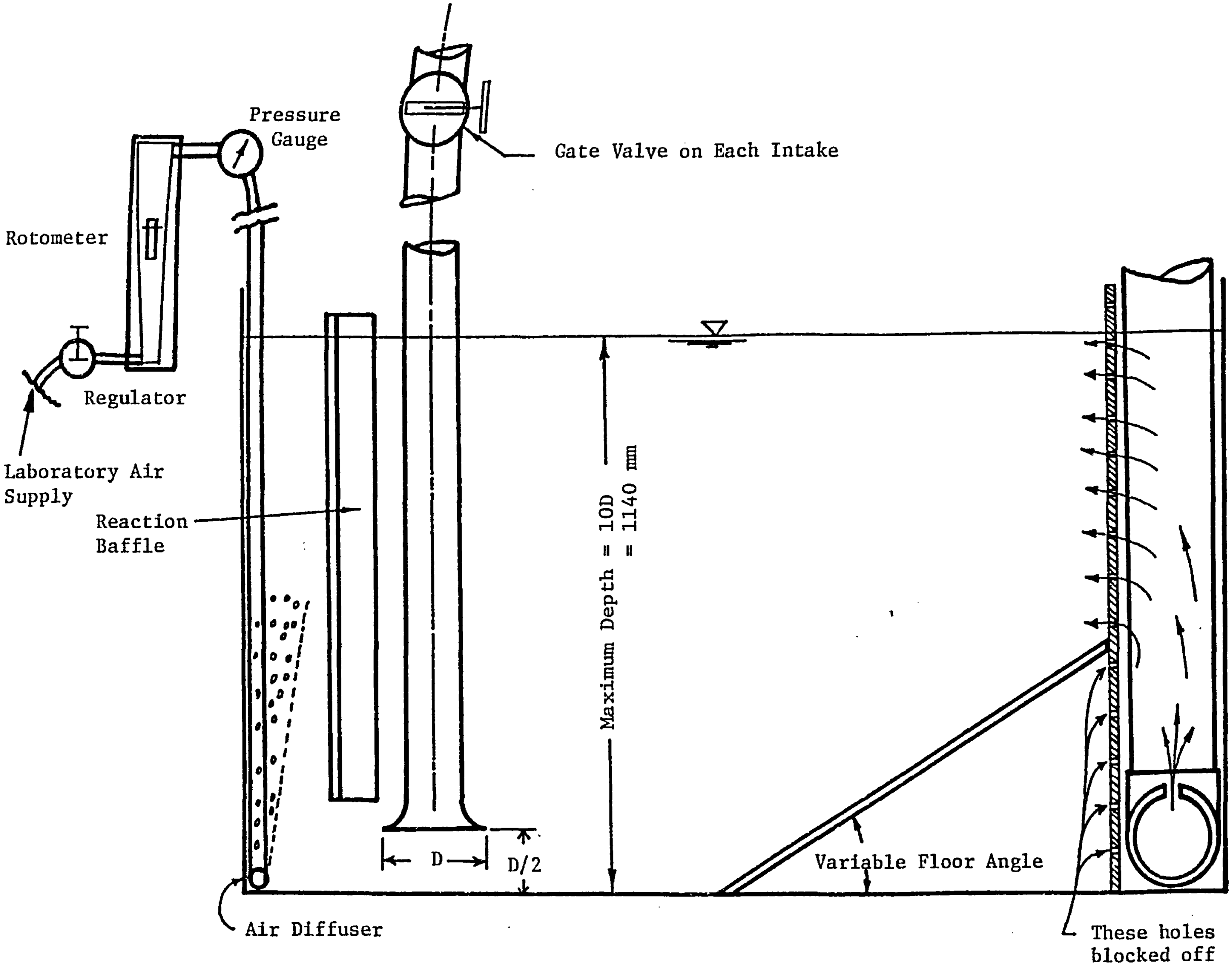
Pressure Gauge
Gate Valve on Each Intake
Rotometer
Regulator
Laboratory Air Supply
Reaction Baffle
Maximum Depth = 10D = 1140 mm
D
D/2
Variable Floor Angle
Air Diffuser
These holes blocked off

Fig. 5.2 Cross-Section of Model Wet Well

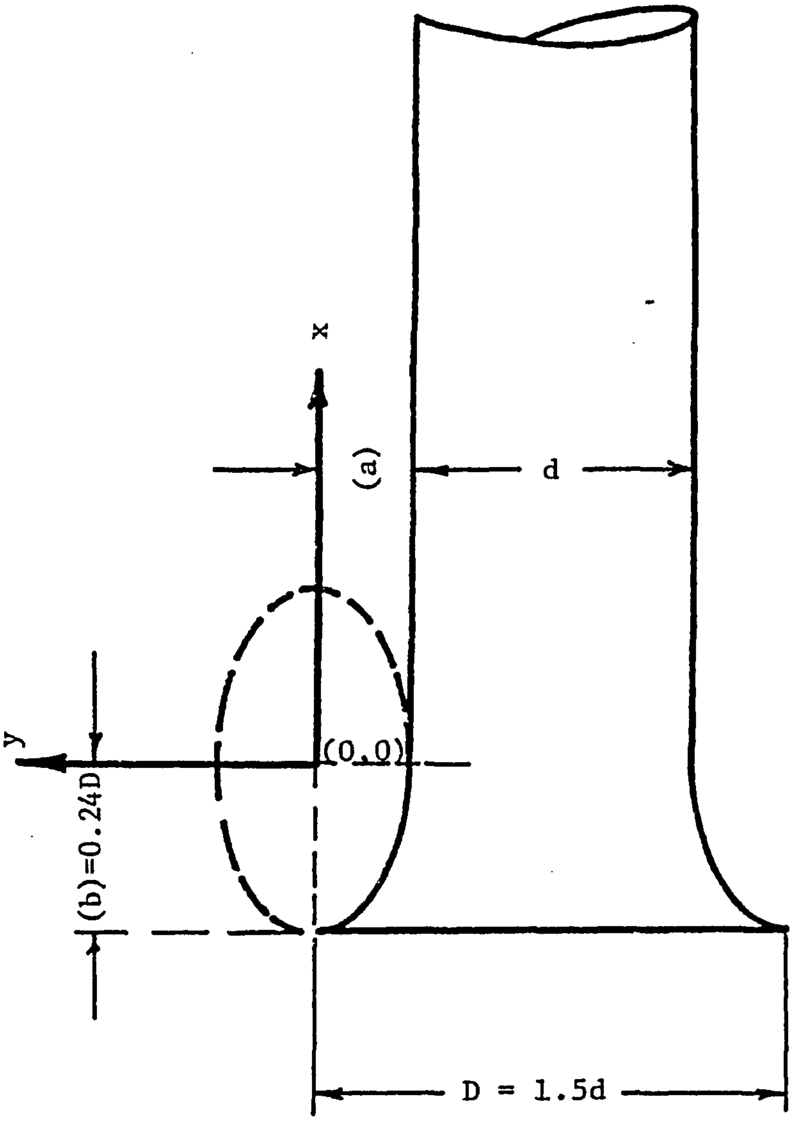
x
(a)
d
y
(0,0)
(b)=0.24D
D = 1.5d

$(x - x_o)/a^2 + (y - y_o)/b^2 = 1.00$; $a = 27.37$ mm ; $b = 17.33$ mm

Fig. 5.3 Profile of the Bell-Mouth

maximum rated capacity of 250 USGPM at 20 feet head (0.0158 m^3s^{-1} @ 6.1 m head) at 1750 rpm. The discharge pipe was 76 mm in diameter and was connected to the discharge diffuser at the inlet zone of the sump. The flow was completely recirculated during the entire period of pump operation. The total discharge of the pump was measured using an ultrasonic flow meter connected to the discharge side of the pump. The specifications for all flow measurement instruments are given in Table 5.1.

Behind the pump columns, a "vee-shaped" movable reaction baffle was inserted in order to vary the width of the diffuser section. This baffle was built in sections, one bell-mouth diameter in height, to vary bottom clearances, baffle heights and top clearances. The air supply to the diffuser was provided with a regulator, rotometer and pressure gauge, Fig. 5.2. The details of these instruments are also given in Table 5.1.

The portion of the sump floor with variable slope was constructed from acrylic sheet and had a tapered base so as to provide a smooth transition for the flow between the inclined and horizontal portions. The inclined plane was connected via two small diameter cables to a crank mechanism which was used to adjust the angle. The angle of incline was measured to an accuracy of 1^{o}. As the floor angle changed, the length of the inclined floor was adjusted by adding or removing bolt on portions of the floor, so that the upstream end always came into contact with the inlet reaction baffle. Holes in the inlet baffle, below the inclined floor, were blocked off so that the entire flow entering the sump was forced through the upper part of the

Table 5.1 Specifications of Experimental Equipment

Description	Use	Specifications*
DET 72L Ultrasonic Flow Meter	Discharge Pipe Velocity	0 to 10 ft/s in 0.10 ft/s divisions accuracy ± 1% of full scale
S.K. Instruments Safeguard Rotometer	Air Flowrate	0 to 25 ft^3/min @ 70°F and 14.7 psi accuracy ± 1% of full scale
Moore Products Co. Pressure Gauge	Air Pressure	0 to 200 inches of water in 5 inch increments
Webster Air Equipment Pressure Regulator	Pressure Regulation	0 to 200 psi in 2 psi divisions
Chaevitz Pressure Transducer Model P3061	Interfaced with pitot-tube, A/D converter and micro-computer to obtain velocity measurements	0 to 5 inches of water column, S/N = 5761 accuracy ± 0.5% of full scale
Fisher Mercury Thermometer 14-983-10B	Fluid Temperature Measurement	-20 to 110°C in 1°C increments
Chesterman Tempered Stainless Steel Rule No. CF967F	Measurement of fluid levels in inclined manometer	0 to 12 inches in 0.01 inch divisions

*All units converted to metric equivalent prior to processing of data.

Table 5.1 Specifications of Experimental Equipment continued

Description	Use	Specification
Marsh, McBirney Electromagnetic Current Meter Model 201D	Velocity Measurements	0 to 20 ft/sec in 0.01 ft/sec increments accuracy ± 2% of reading, S/N = 40330
Inclined U-tube Manometer (Laboratory made)	Pressure Drop across Pitot-tube	0 to 6 inches of fluid with specific gravity = 1.75 smallest division = 0.10 inch
United Sensor Pitot-tube PAD-24-KL	Velocity Measurement	24 inch long probe with 3/16 inch outside tube diameter
Kent Lea Miniflow Low Speed Propeller Meter, Probe 265-3	Velocity Measurement	0 to 150 cm/s accuracy 2% of full scale
Lufkin Ultralok Tape Measure Model Y38CME	Velocity Probe Positioning	8 m in 1 mm divisions, all measurements to within 1 mm

inlet section. No flow could short-circuit underneath the inclined floor. The inlet baffle was totally effective in producing a uniform approach flow in the sump.

Velocities in the sump were measured using four techniques as follows:

(i) pitot-tube with pressure transducer
(ii) pitot-tube with inclined manometer
(iii) magnetic current meter, and
(iv) miniature propeller meter

The specifications of each of these are also given in Table 5.1.

The highest reliability for velocity measurements was placed on the pitot-static probe-pressure transducer - A/D converter system. The transducer was a variable-resistance type transducer and was used to measure the differential pressure between the dynamic and static pressure ports on the pitot-static probe. The transducer was D.C. exited and produced a 0 to 5 volt output signal which was converted into digital signals via a 12 bit A/D converter and subsequently interfaced to an Apple II micro-computer for storage and processing. For each probe location, 1000 pressure measurements were recorded and averaged to make a single estimate of the flow velocity. The sample time for 1000 readings was approximately 76.5 seconds.

5.2 Errors, Calibration and Operational Procedures

Inherent to any experimental observation are three errors; (i) personal error in reading, interpreting and recording an experimental value, (ii) reliability, accuracy and repeatability of the experimental apparatus, and (iii) calibration error. In this subsection, an attempt is made to illustrate, on a descriptive basis, where experimental errors may have been introduced. Table 5.1, indicates that the instrument errors in all the measurements are on the order of one to two percent. The description of errors are dealt with in three divisions; (i) length measurement, (ii) air flowrate measurements, and (iii) velocity measurements.

5.2.1 Errors in Length Measurement

The positioning of all probes, pitot-static, magnetic velocity meter and propeller meter, was measured to an accuracy of ± 1 mm. The greatest source of error in length measurement was introduced when the probe was placed adjacent to a solid boundary and the velocity was measured to estimate the boundary shear stress. The distance above the bed at which the velocity is measured must be known precisely so that accurate estimates of the velocity gradient can be made. In all cases, except when the probes contacted the bed, the positions of the probes were measured to an accuracy of ± 1 mm. When the probe made contact with the bed, the position of the probe above the bed was simply one half the probe diameter.

In measuring the difference in the inclined manometer fluid levels, as well as for estimating the slope of the manometer, a stainless steel ruler accurate to 0.01 inch (0.254 mm) was used. In order to determine the slope of the manometer, a distance of approximately 150 mm along the slope was used. For a manometer with an angle of inclination θ and manometer fluid of specific gravity S_o, the velocity corresponding to a differential manometer reading of X, measured along the slope, is given by

[5.1] $v_m = (2gX\sin\theta(S_o/S - 1))^{0.5}$

where S is the specific gravity of the fluid moving past the tip of the pitot-tube. The inclined manometer was used in conjunction with the pitot-static probe in order to measure the velocity profiles which generated the initiation of particle motion on the bed of a flume. From these velocity profiles, the critical particle Reynolds number and Shields entrainment function values were determined.

5.2.2 Errors in Air Flowrate Measurement

The errors in measurement of the air flowrate, other than calibration errors, are due to; (i) error in reading the flow meter, (ii) error in reading the pressure gauge and (iii) fluctuation in the delivery pressure to the flow meter.

Air flow readings, Q_r, at an operating temperature T_o and operating pressure P_o, were converted to "standard temperature and pressure", STP, as follows

[5.2] $Q_{STP} = Q_r(P_C T_{STP}/T_C P_{STP})(P_o T_C/T_o P_C)^{0.5}$

where P_C and T_C are the pressure and temperature at which the flow meter was calibrated and P_{STP} and T_{STP} are the standard pressure and temperature, respectively. The standard pressure and temperature used for this study are 101.3 kPa and 20°C respectively. It was observed that, in all cases, the adjustment required on the air flowrate was less than 10%. The major part of the adjustment was due to the submergence of the diffuser which altered the operating pressure. In Eq. [5.2], the temperature adjustment was less than 0.61%. A small error in reading the pressure gauge or rotometer would obviously result in an error of far less than the 10% maximum pressure adjustment.

5.2.3 Errors in Velocity Measurement

Of all of the measurements taken in this study, the velocity values probably had the highest errors.

The DET 72L ultrasonic flow meter was used to measure the pump discharge. The effects of small air bubbles, which may have been entrained by the pump, on the velocity readings are not known. Therefore, an attempt was made to prevent air from entering the piping system. In addition, the transducers were located at least 10 pipe diameters from any obstruction or bend. The total flow was calculated by multiplying the flow velocity by the cross-sectional area of the discharge pipe. The pipe diameter was measured to an accuracy of 0.01 mm. The velocity in the pipe during operation was steady and the meter always indicated a strong reading. In order to verify the meter calibration, the discharge pipe was disconnected from the return discharge header and the sump was pumped down. The drawdown in sump volume per unit time was compared to the discharge calculation based on the meter reading. No significant difference was found between the two values. This procedure was carried out several times during this study.

In using the pitot-static probe/transducer set up to estimate velocities, the following errors may have been introduced:

(i) during calibration of the transducer when the output voltage was recorded for a measured water column height

(ii) small air bubbles may have been trapped in the high and low pressure lines leading from the pitot-tube to the transducer

(iii) the pitot-tube may not have been aligned parallel to the flow resulting in an underestimation of the dynamic pressure

(iv) using discrete data rather than continuous data to predict the velocity may have resulted in missing high or low pressure transients being recorded

(v) errors due to the levelling of the transducer base, which would result in some initial pressure drop across the transducer

(vi) errors due to a gradient on the pitot-tube between the dynamic and static pressure ports as a result of curvilinear flow, free surface gradient or a bubble gradient adjacent to the probe, and

(vii) response frequency of the transducer.

The transducer set up was used to measure the velocity profiles in the sump under steady conditions. During calibration, the water column height was measured to an accuracy of 1/64 of an inch (0.40 mm). The equation relating the head to voltage was regressed linearly and the resulting correlation coefficient was 0.99979. The calibration of the transducer was checked periodically throughout the tests and the equation relating head and output voltage was recalculated if the transducer was found to drift. The calibrated equation was incorporated into the data aquisition program directly. The velocity associated with a differential head Δh is given by

$$[5.3] \qquad v_m = (2g\Delta h)^{0.5}$$

Proper attention was paid to purge any small air bubbles from the lines and to properly align the probe. The probe was rigidly fixed to a support frame so that any deflection due to the cantilevering of the probe head was minimized. By rigidly supporting the probe, flow induced vibrations and resulting phase and amplitude errors, when the frequency of the measured pressure wave approached the natural frequency of the transducer, were minimized. The response frequencies of the transducer and the A/D converter were 5 Hz and 50 kHz respectively. Using hot-film anemometry, Giratalla (1977) found that for flows over a ripple bed, the range of macro-scale turbulence was between 19 and 44 Hz. His measurements were recorded in a similar sized flume and were confined to a depth of 3 to 114 mm above the bed. The low response frequency of the transducer would tend to smooth out the data for any turbulence with a frequency of greater than 5 Hz. However, since only the average velocity was recorded in these tests, response frequency introduced no additional errors in the velocity measurements.

The high and low pressure lines were kept as short as possible. Using 1000 samples of discrete data provided a representative value with a high degree of reliability. In addition, several checks were made to ensure the repeatability of transducer data. No problems were encountered in reproducing the velocity estimate for any operating scheme.

The Marsh, McBirney electromagnetic current meter was used to measure the plume water velocities, and to check the pitot-tube measurements. It was found that the probe was affected by the steel base plate supporting the entire sump model. When the probe was within 5 probe diameters away from the steel plate (191 mm), the meter gave an unsteady, rapidly fluctuating output. In these cases, little confidence was placed on the velocity measurements. In addition to any error due the closeness of metal objects, errors may have been introduced due to the presence of air bubbles streaming around the tip of the probe. In the presence of air alone, the probe read -20.00 $\mathrm{ft.s^{-1}}$, indicating that the air reduced the velocity reading. Perhaps the presence of air bubbles introduced errors which were related to the percentage of air passing the probe, that is

[5.4] $$v_{CORRECT} = v_{READING}\ (1 + \text{air fraction at probe tip})$$

No attempt was made to correct the plume velocity measurements for the presence of air because the correction would be purely speculative due to the problem of reliably estimating the local air fraction.

For some velocity measurements, the miniature propeller meter was used. This meter gave the rotational speed of the propeller in Hz. A calibration curve was provided by the manufacturer which gave the flow velocity in $\mathrm{cm.s^{-1}}$ for a given propeller speed. No calibration device was available on the equipment. Under low velocity conditions, $< 30\ \mathrm{cm.s^{-1}}$, the probe readings were very steady; however, at higher velocities, the turbulence in the flow greatly affected the speed of the propeller, and provided sporadic readings with occasional zero readings even when there was obviously some non-zero mean velocity. At times, it was found that the minimum and maximum velocities were up to 50% below or above the observed mean velocity. The meter readings were observed for a period of at least 2 minutes before an average value was estimated.

In order to check the reliability of the pitot-tube, propeller and ultrasonic meters, all three were subjected to the same flow in a small recirculating flume. The probes were positioned along the centre line of a 150 mm wide flume and 100 mm from the bottom. The flow depth was held constant at 250 mm. Under steady state conditions, the maximum difference between all three methods was 4.6% when the mean flow velocity was 0.51 $m.s^{-1}$. As the probes were lowered toward the bed, the difference in readings increased as expected. The highest reliability of velocity measurements near the bed must obviously be placed on the smallest diameter probe. The minimum distance above the bed at which a velocity reading could be obtained for the pitot-tube, propeller meter and ultrasonic meter were 2.4 mm, 7.9 mm and 19.1 mm, respectively.

CHAPTER 6

EXPERIMENTAL PROGRAM AND DISCUSSION OF RESULTS

6.1 General

This chapter outlines the experimental investigations performed on the physical model and discusses the significant trends observed. For the purpose of brevity, only typical data from each test are shown. The remaining experimental data are available in a separately bound copy deposited in the Department of Civil Engineering at the University of Windsor, but, not forming part of this dissertation. Chapter 7 deals with the application of experimental data in the calibration and sensitivity of the numerical model. During the experimental phase, five pumping schemes were adopted as outlined in Table 6.1. It was assumed that the head losses in each of the suction pipes were equal, and therefore, the total pump discharge was equally distributed among the operating suction pipes. A slight error in estimating the discharge through each intake may have occurred when Pumping Scheme 4 was used. Under these conditions, there was an asymmetry in the approach flow resulting in a depression of the free surface near the pump column which was closest to the side wall. This change in head would have resulted in a slight difference in the flowrates carried by different intakes. Generally, in a sump where there are three intakes, only two would be in operation at any one time and the third would be for emergency use or would be alternated with the other two to provide even wear on the pumping equipment. Thus, Pumping Scheme 5 can be considered to be a condition which would

Table 6.1 Pumping Schemes for Model Study

Pumping Scheme Number	Pump(s) in Operation
PS1	Centre pump in operation only
PS2	One outside pump in operation
PS3	Both outside pumps in operation
PS4	The centre and one outside pump in operation
PS5	All three pumps in operation

seldom occur. Pumping Schemes 1, 3 and 5 resulted in symmetrical flow conditions whereas Pumping Schemes 2 and 4 resulted in a skewed flow distribution.

6.2 Test Series No. 1, Critical Submergence

The purpose of this test series was to investigate and determine the critical submergence, S, of the bell-mouth. The critical submergence is defined as the water depth from the free surface to the edge of the bell-mouths at which vortex activity, indicated by the onset of surface swirl near the suction pipe, would just begin. The range of test values for Test Series 1 is given in Table 6.2. For this test series, the "vee" shaped reaction baffle downstream of the intakes extended from the floor to the free surface. The location of the baffle relative to the intake pipes is shown in Fig. 5.1. Figure 6.1 shows typical test results for PS1, with the centre pump in operation. It illustrates that as the inlet Froude number increases, the submergence required to prevent the onset of vortex activity also increases. It also indicates that the submergence is dependent on the floor slope. For a given inlet Froude number, the submergence required first decreases as the angle of the floor slope increases, with the minimum submergence occurring at a floor slope of approximately 10 degrees from the horizontal. As the floor slope is further increased, the submergence required to prevent vortex formation increases. This dependency is due to the fact that the velocity distribution in the region of the bell-mouths is affected by the proximity of the change in floor slope of the approach section of

Table 6.2 Range of Values for Test Series 1

Variable	Range
Pumping Schemes	1, 2, 3, 4, 5
Floor Angle	0, 5, 10, 15, 22.5, 45 degrees from the horizontal
Fluid Depth, H	200 to 600 mm
Suction Pipe Velocity	0.219 to 3.577 m/s
Inlet Froude No., N_{F_i}	0.185 to 1.789
Inlet Reynolds No., N_{R_i}	4.20×10^3 to 2.29×10^4

$N_{F_i} = v_d/(gS)^{0.5}$; $N_{R_i} = v_i H_i/\nu_f$

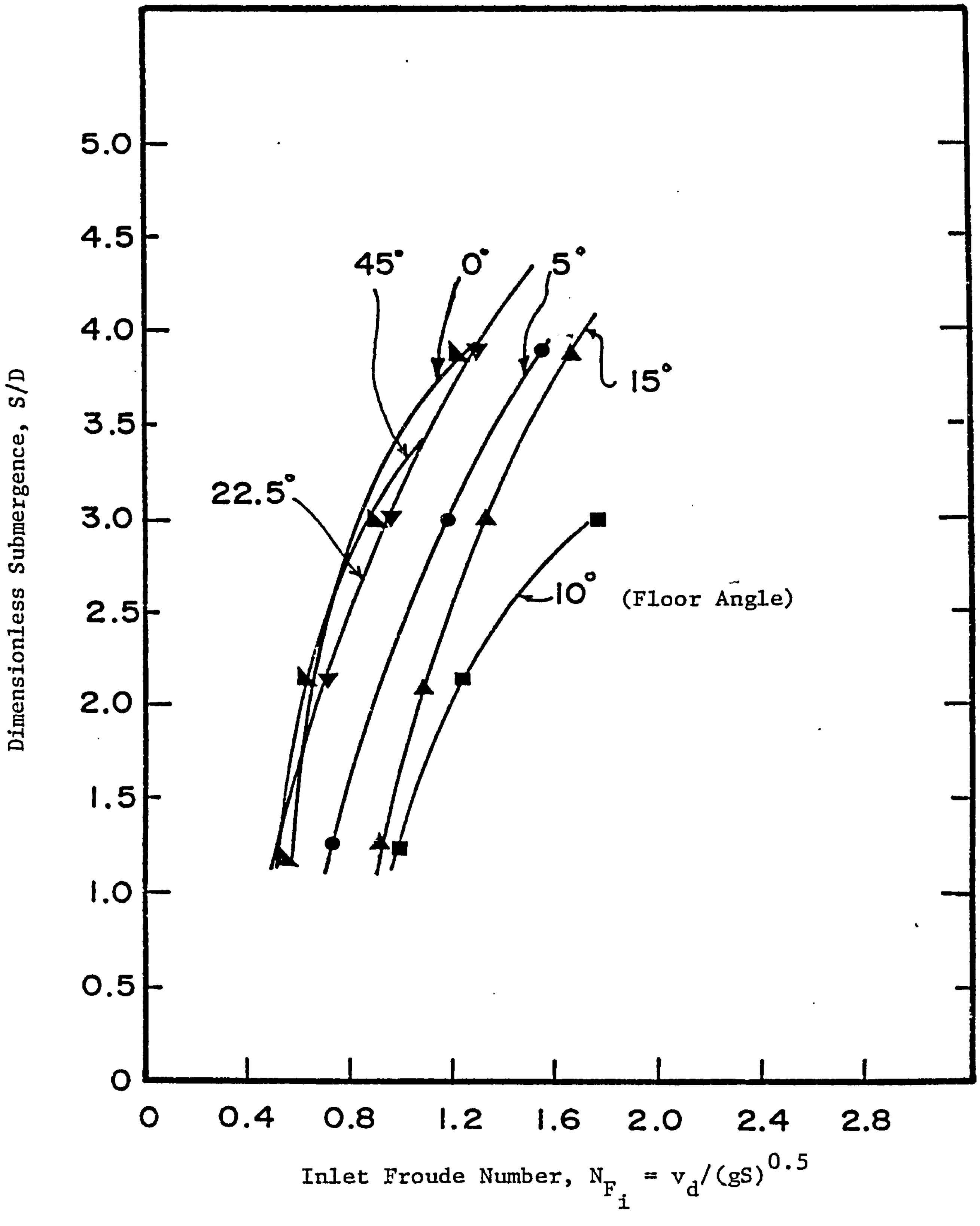

Fig. 6.1 Critical Submergence for Test PS1

the sump. A composite plot of the inlet Froude number versus the dimensionless submergence is shown in Fig. 6.2. This plot represents the average of all pumping schemes, and encompasses the data of 102 observations. The overall trend, as discussed for Fig. 6.1, also applies to the composite data. It can be deduced from Fig. 6.2 that the distance from the centre line of the pump column to the transition in the floor slope should be greater than 3D, as proposed by several researchers, in order to completely eliminate the effect of approach channel floor slope on critical intake submergence.

Figure 6.3 shows the envelope of experimental results obtained for all pumping schemes and for all floor slopes. The Froude number in this figure is expressed as a function of the bell-mouth diameter, and not submergence as in Figs. 6.1 and 6.2. In the literature, both forms of the Froude number are common. The disadvantage in using the submergence in the Froude number is that the estimation of the submergence then becomes a trial and error process. The lowest of the three lines in Fig. 6.3 represents the submergence below which vortex activity will occur for a given inlet Froude number, irrespective of pumping scheme or floor slope. The uppermost curve represents the minimum recommended submergence for design purposes. The centre curve is simply an average of all data obtained.

In Fig. 6.4, the three curves obtained in Fig. 6.3 have been plotted along with the data of ten other researchers.

In Fig. 6.4, two distinct groups of data exist. The lower group of data, which includes the author's results, indicates that the

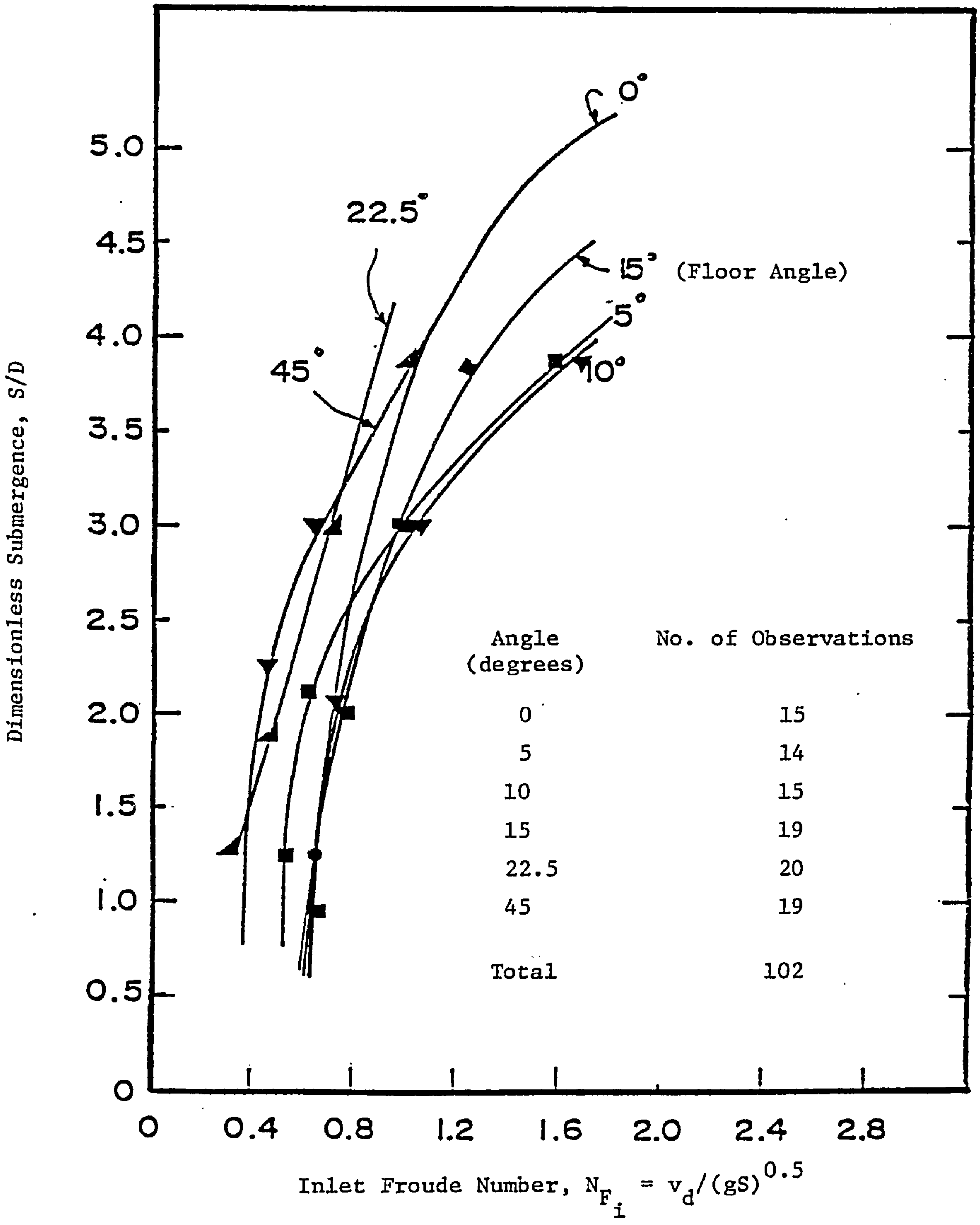

Angle (degrees)	No. of Observations
0	15
5	14
10	15
15	19
22.5	20
45	19
Total	102

Fig. 6.2 Composite Plot of Critical Submergence - Average for all Pumping Schemes

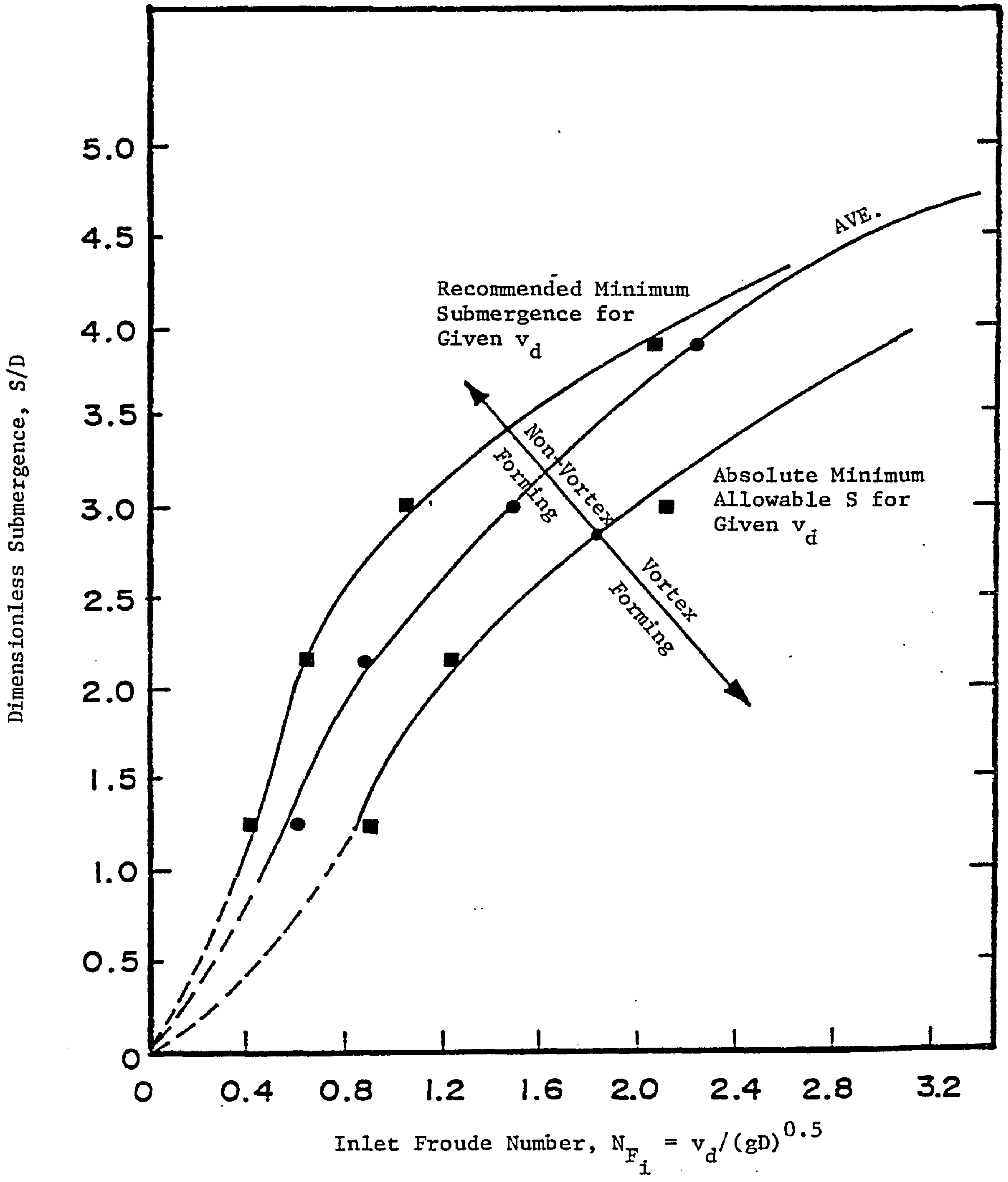

Fig. 6.3 Envelope of Critical Submergence for all Pumping Schemes and Floor Slopes

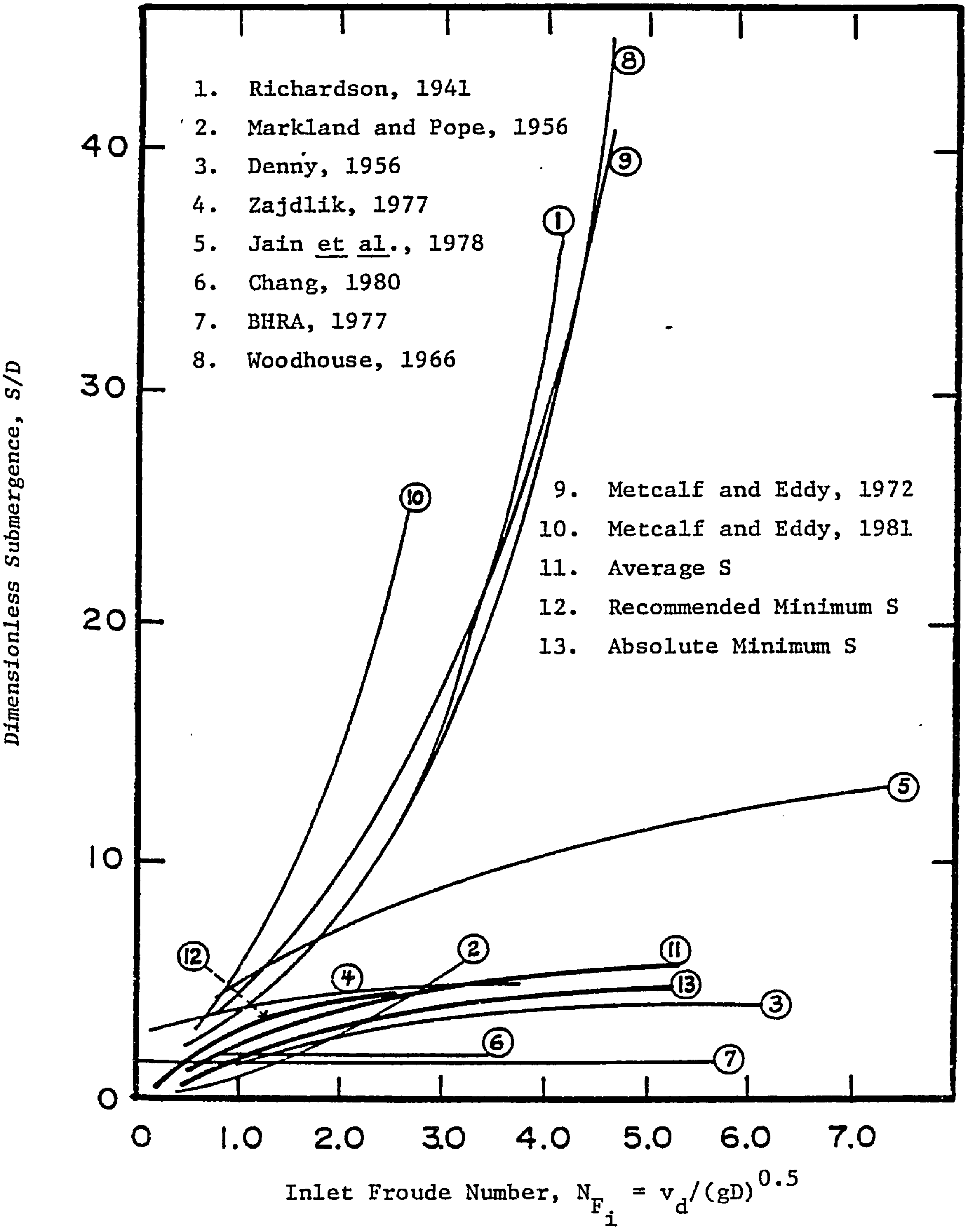

Fig. 6.4 Comparison of Critical Submergence Data

minimum submergence is independent of the Froude number at Froude numbers $N_{F_i} \gtrsim 4$, whereas the upper group of data indicates that the minimum submergence increases exponentially with the Froude number. The wide variations in results are due to (a) some points represent model, while others represent prototype data, (b) different sump configurations and number of suction pipes used in determining the minimum submergence, and (c) different criteria used to define critical submergence. Obviously model studies should be conducted when there is a doubt about the performance of a proposed wet well configuration and operating sequence. The data obtained in this study fit well within the limits of existing design criteria.

6.3 Test Series 2, Baffle Bottom Clearance

The purpose of the second series of tests was to investigate the effect of baffle bottom clearance, d_B, on the critical submergence. The test variables are shown in Fig. 6.5. For this test series, the baffle top clearance, d_A, was equal to zero, i.e. no flow could pass over the top of the baffle. The purpose of this test was to determine (i) the effect of allowing fluid from the area behind the baffle to supply part of the intake flow and thereby influence the velocity distribution, (ii) the interaction between flow and baffle and (iii) the critical submergence. No air was diffused into the system at this point in the experimental program; however, the goal was to optimize the entire reaction baffle and air diffuser system. Table 6.3 gives the range of test variables for this test series. Figures 6.6, 6.7 and 6.8 represent composite plots of the three

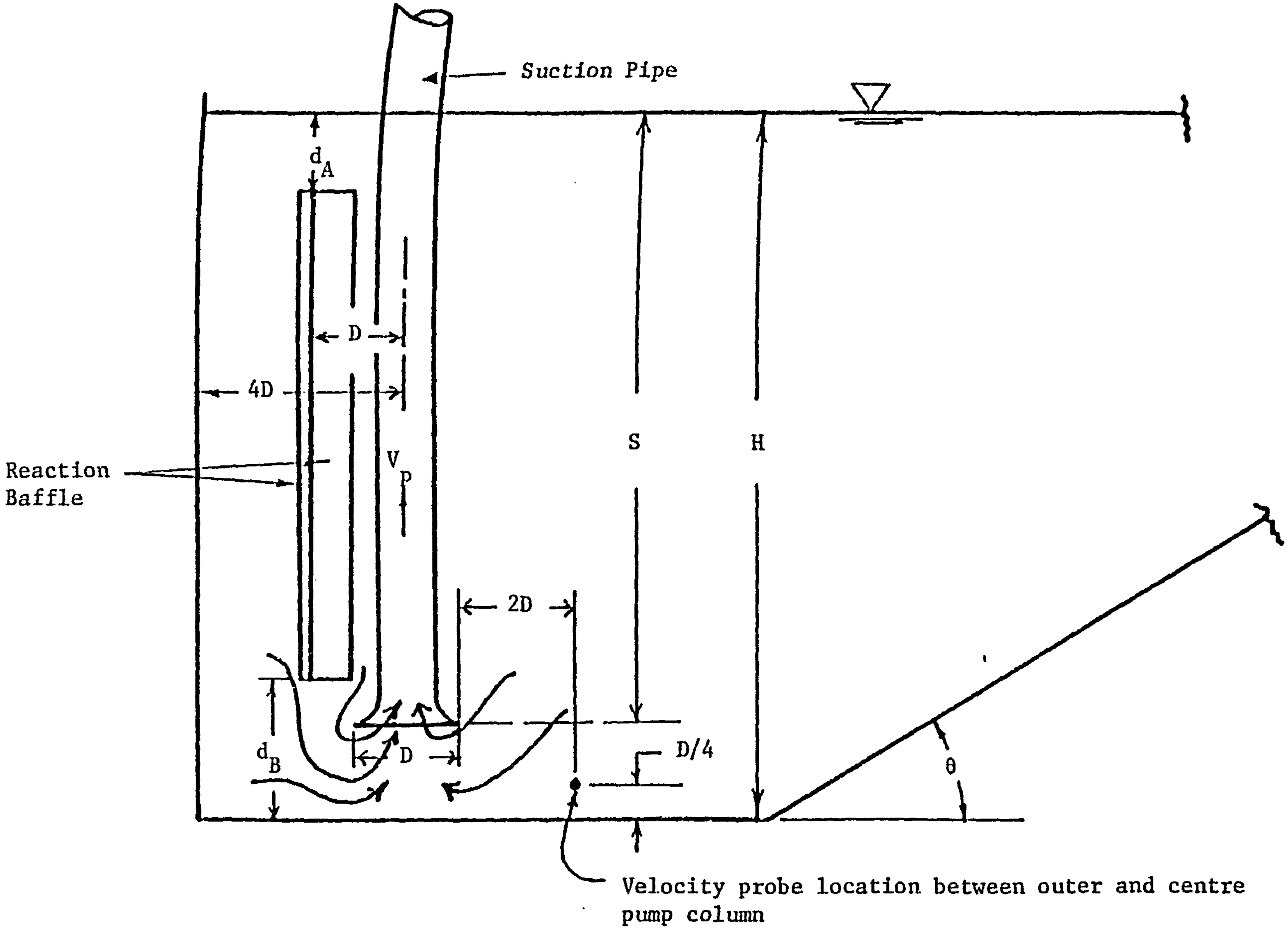
Suction Pipe
d_A
D
4D
Reaction Baffle
V_p
S
H
2D
d_B
D
D/4
θ
Velocity probe location between outer and centre pump column

Fig. 6.5 Explanation of Reaction Baffle Geometry

Table 6.3 Range of Test Values for Test Series 2

Variable	Range
Pumping Schemes	1, 3, 5
Floor Angle	0, 15, 45 degrees from the horizontal
Fluid Depth, H	150 to 500 mm
Bottom Clearance Ratio, d_B/D	0.25, 0.33, 0.5, 0.75, 1.00, 1.50, 2.00, ∞
Inlet Froude No., $v_d/(gD)^{0.5}$	0.186 to 3.010
Sugmergence Ratio, S/D	0.815 to 3.885

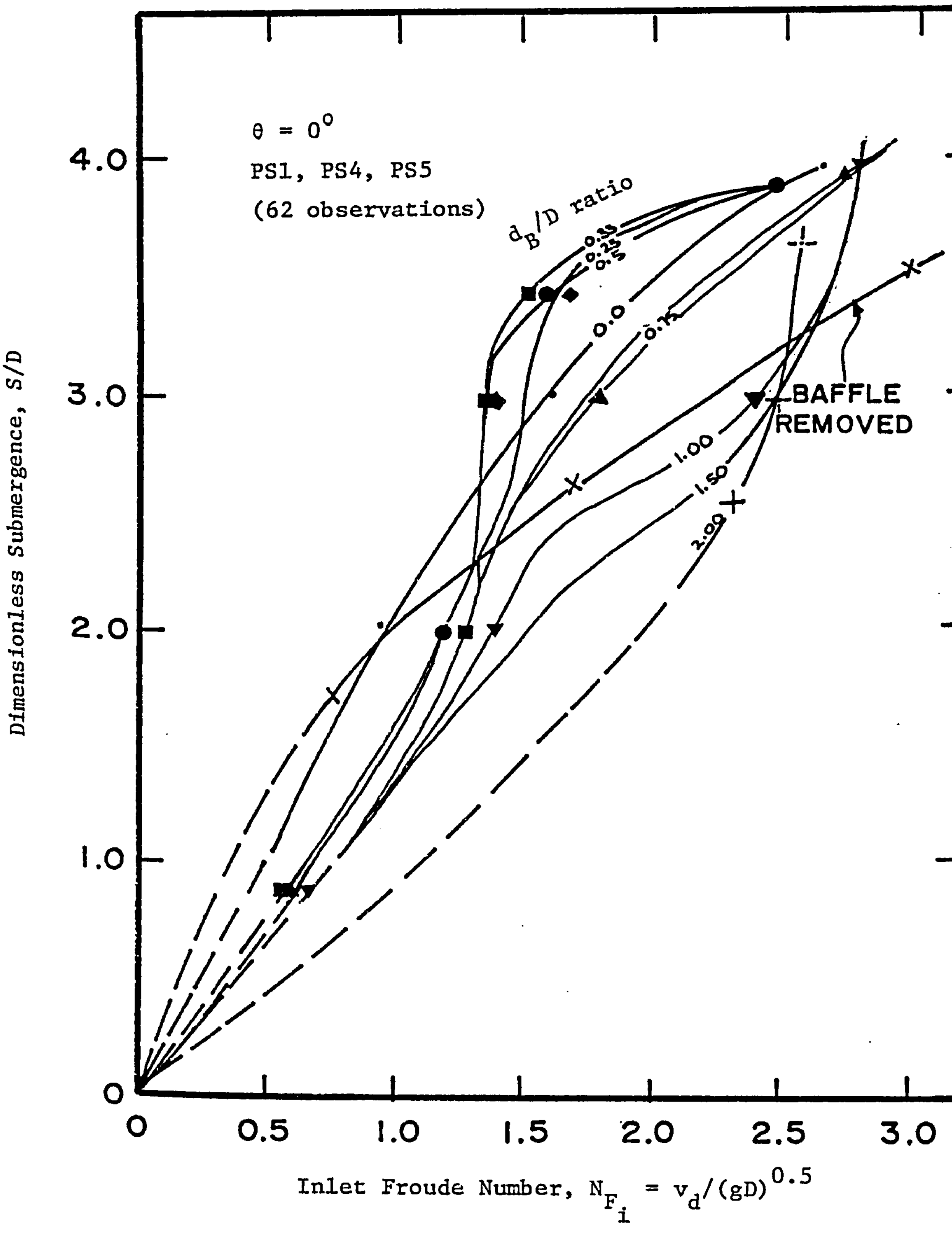

Fig. 6.6 Effect of Baffle Bottom Clearance with Horizontal Floor

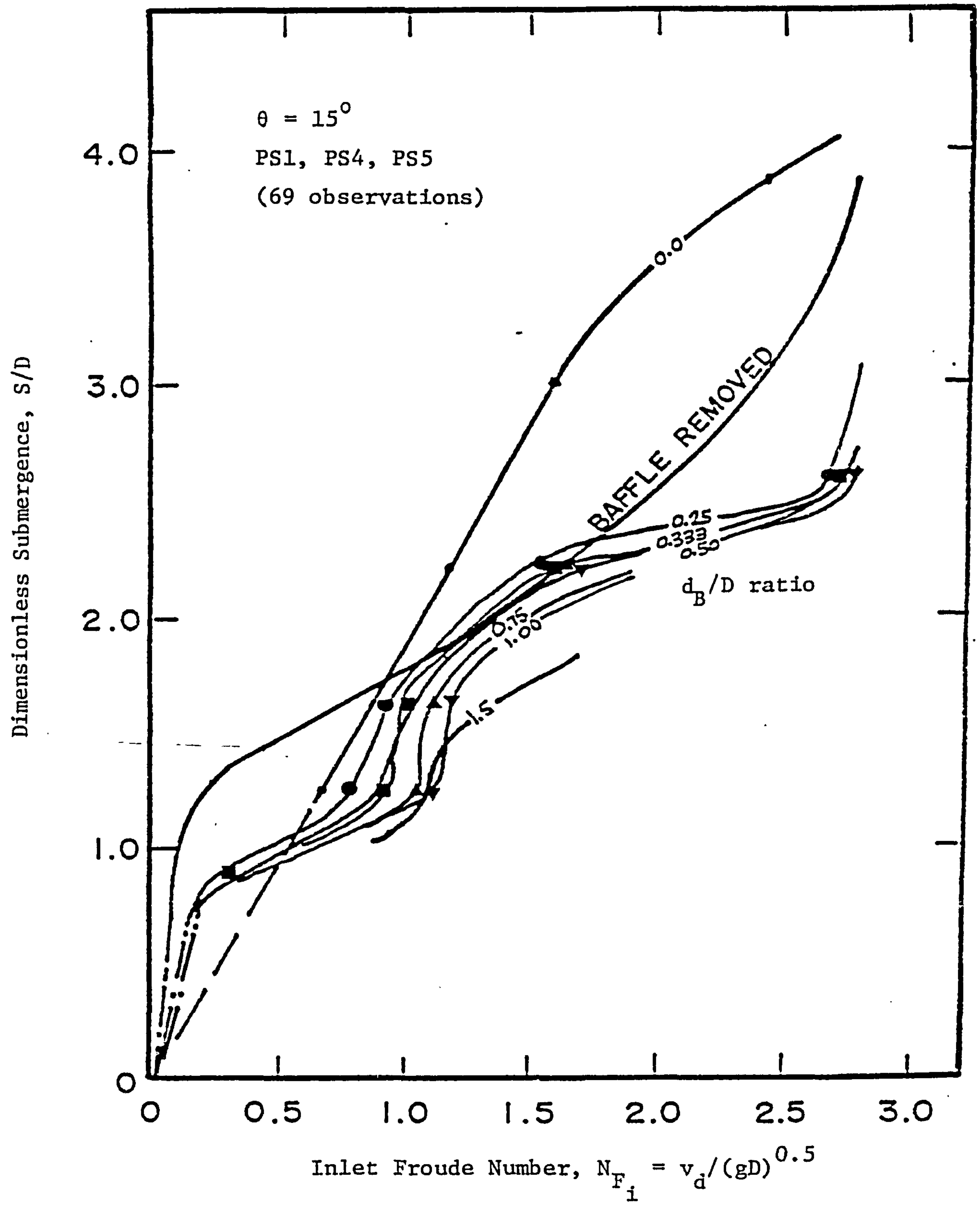

Fig. 6.7 Effect of Baffle Bottom Clearance with 15° Floor Slope

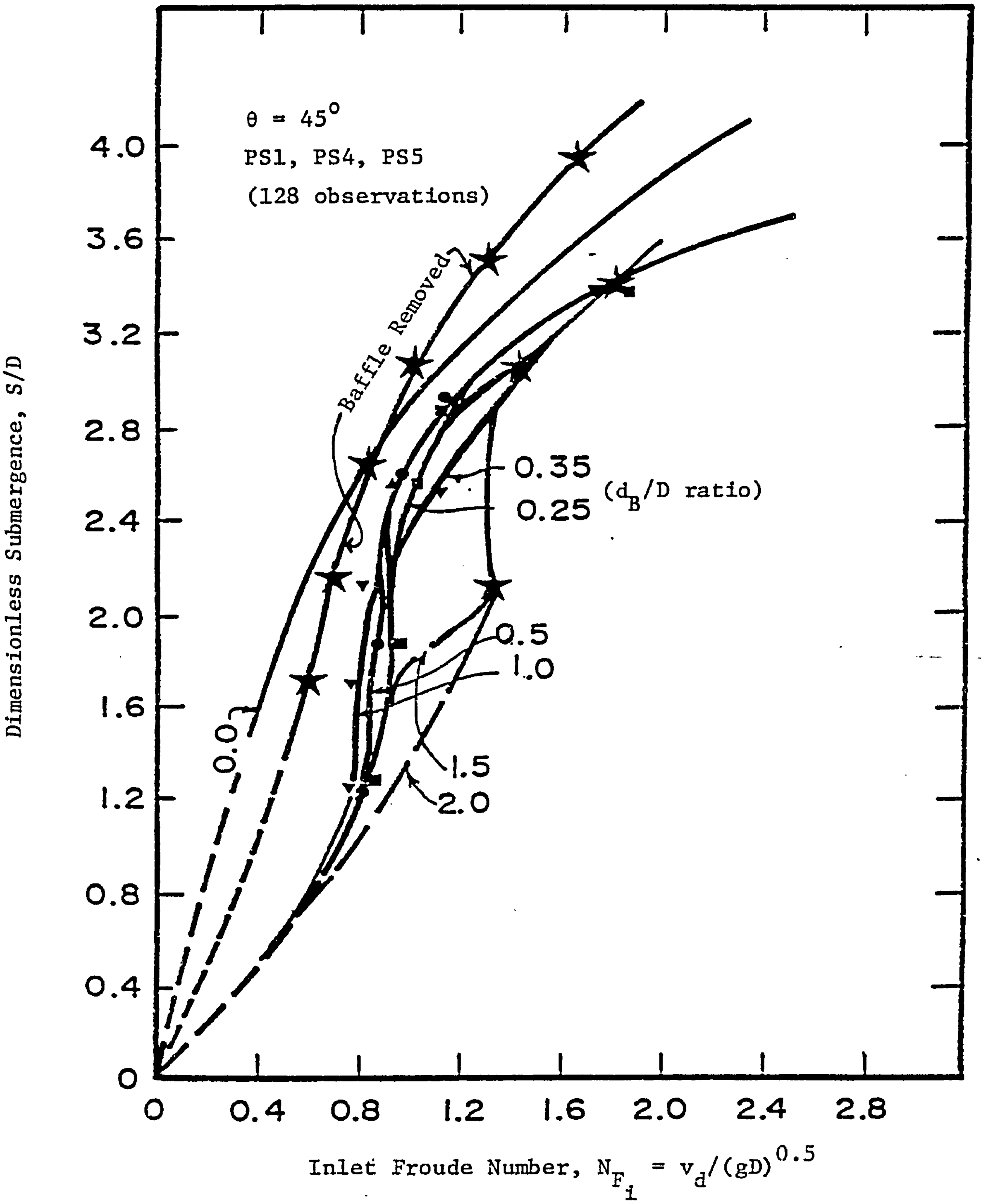

Fig. 6.8 Effect of Baffle Bottom Clearance with 45° Floor Slope

pumping schemes used for 0°, 15° and 45° floor slopes, respectively. In each case, the data for $d_B/D = 0$ was taken from Test Series 1. The following general trends are observed: (a) the critical submergence increases with increasing inlet Froude number, (b) the d_B/D ratio affects the critical submergence, but the trend is random as the floor angle changes, and , (c) the effect of d_B/D equal to infinity, or zero, is not significantly different from the effects of d_B/D ranging from 0.25 to 2.0.

It was also observed that with some baffle bottom clearance, the effect of floor slope, as observed in Test Series 1, was diminished. This was due to the fact that even with a small baffle bottom clearance, the flow distribution around the bell-mouths was affected more by the flow moving in and out of the backwater region behind the baffle, than by the flow disturbed by the transition in the approach channel floor. For subsequent test series, $d_B/D = 1.0$ was selected for the following reasons:

(a) a finite bottom clearance was required to supply the necessary discharge required for entrainment by the diffuser plume,

(b) a large bottom clearance would increase the risk of the pump entraining the air bubbles from the diffuser, resulting in decreased pump performance. It was observed that the influence of the pump suction streamlines extended fully into the diffuser region with $d_B/D > 1.5$, and

(c) $d_B/D = 1.0$ falls within extreme trends observed in Fig. 6.6, 6.7 and 6.8.

6.4 Test Series 3, Top Baffle Clearance

The purpose of this series of tests was to determine the effect of the top baffle clearance, d_A, Fig. 6.5, on the critical submergence and to investigate the flow patterns introduced by the air diffuser. The range of variables used is given in Table 6.4. Test Series 1 and 2 indicated that the most severe case of vortex formation occurred when the flow was asymmetric and the highest degree of asymmetry occurred with Pumping Scheme 2. Therefore, Pumping Scheme 2 was selected for analysis in this test series.

It was observed that, as the diffuser plume rose to the free surface and the flow passed over the top of the baffle and spread horizontally, vortices were shed intermittently from the pump columns and from the side wall of the sump between the wall and the outside two pump columns. The vortices generated from the side wall moved upstream, towards the inlet section, as far as 5 to 6 suction pipe diameters. The wave action on the free surface or the oscillatory nature of the flow then broke apart the vortices.

At high air flow numbers, $Q_{AIR_o}/(g^{0.5}D^{2.5})$ greater than 0.5, it was observed that a strong roller formed in the area behind the baffle where the diffuser was located. This roller kept small air bubbles in suspension. At high pump intake velocities, these small bubbles were "sucked" both over and under the baffle and into the pump. When this occurred, a small floor vortex developed underneath the operating intake.

Table 6.4 Range of Variables for Test Series 3

Variable	Range
Pumping Scheme	2
Floor Angle	0, 45 degrees from the horizontal
Fluid Depth Ratio, H/D	2, 3, 4, 5, 6, 7, 8
Top Baffle Clearance Ratio, d_A/D	0.25, 0.5, 1.0, 1.5, 2.0, no baffle
Inlet Froude No., $v_d/(gD)^{0.5}$	0.186 to 3.290
Air Flow No., $Q_{AIR_o}/(g^{0.5}D^{2.5})$	0.030 to 0.940

In order to determine the critical pump intake velocity for a given top baffle clearance and air flowrate through the diffuser, the air flowrate and top baffle clearance were set to the desired test value and then the pump discharge, and hence the suction pipe velocity, was increased until a small surface swirl was formed. This surface swirl indicated the onset of vortex formation, and this condition was recorded as being the critical submergence condition. Typical test results, as shown in Figs. 6.9 and 6.10, indicate that the critical submergence increases with (a) increasing inlet Froude numbers, and (b) increasing air flow numbers. It was also observed that the effect of d_A/D on the submergence, was minimal.

In order to investigate the effectiveness of the air diffuser in forcing a circulation in the sump, point velocities were measured near the sump floor. The location of the velocity probe is shown in Fig. 6.5. It was centred between the outermost and the middle pump columns at a point D/4 above the floor and 2D upstream of the edge of the bell-mouths. Such velocity measurements indicate the effectiveness of the plume in providing additional shear stress on the particles at rest on the wet well floor. For this part of the test, the pump was not operating so that only the effect of the air induced circulation was studied. Typical results of this investigation are shown in Figs. 6.11 and 6.12. Three trends were noticed in these figures:

(i) the ratio of the velocity along the floor to the air flow rate increases with decreasing air flowrates,

(ii) a maximum velocity for a given air flowrate exists with d_A/D in the range of 0.25 to 1.0, and

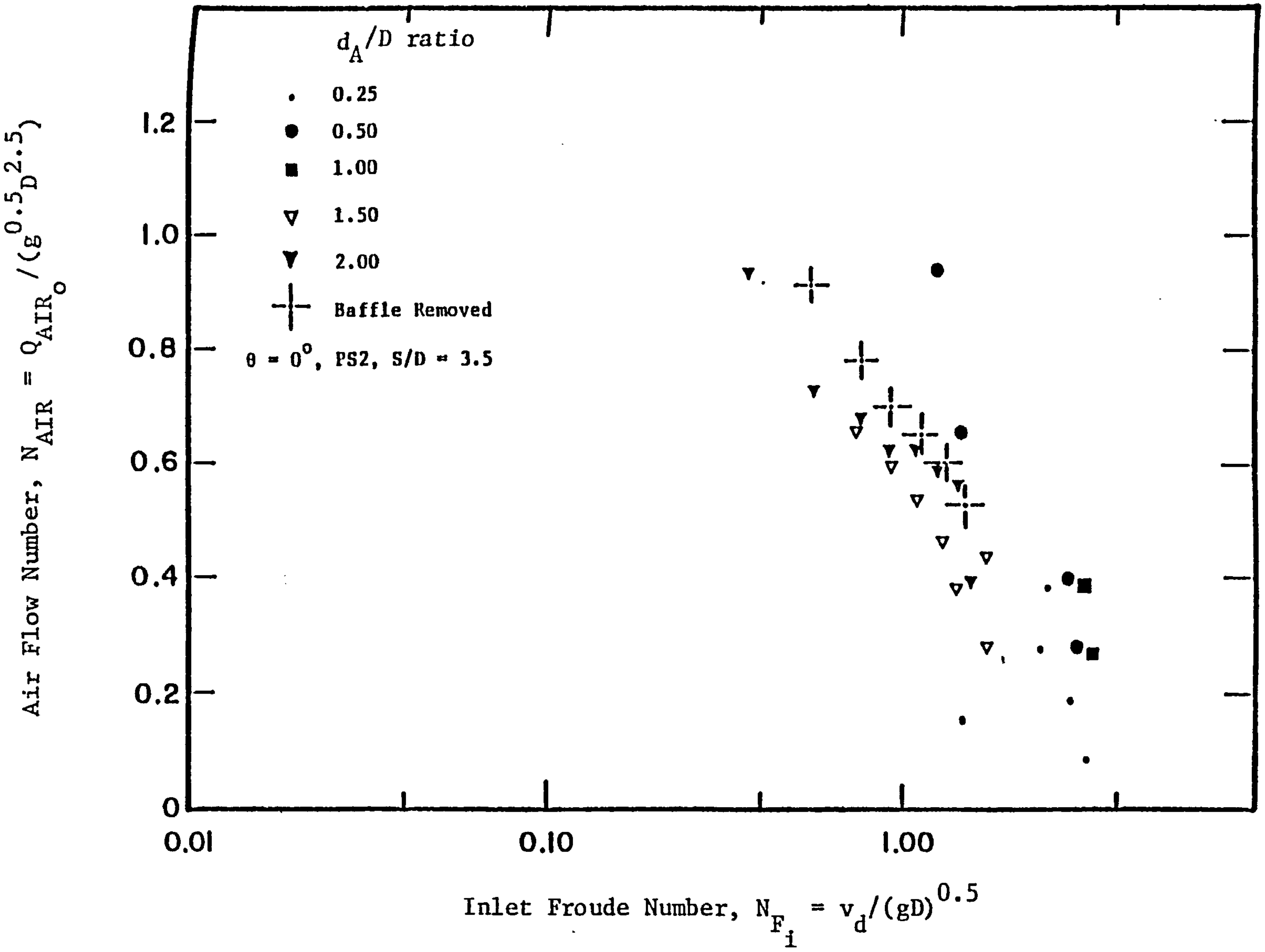

Fig. 6.9 Effect of Top Baffle Clearance for Horizontal Floor

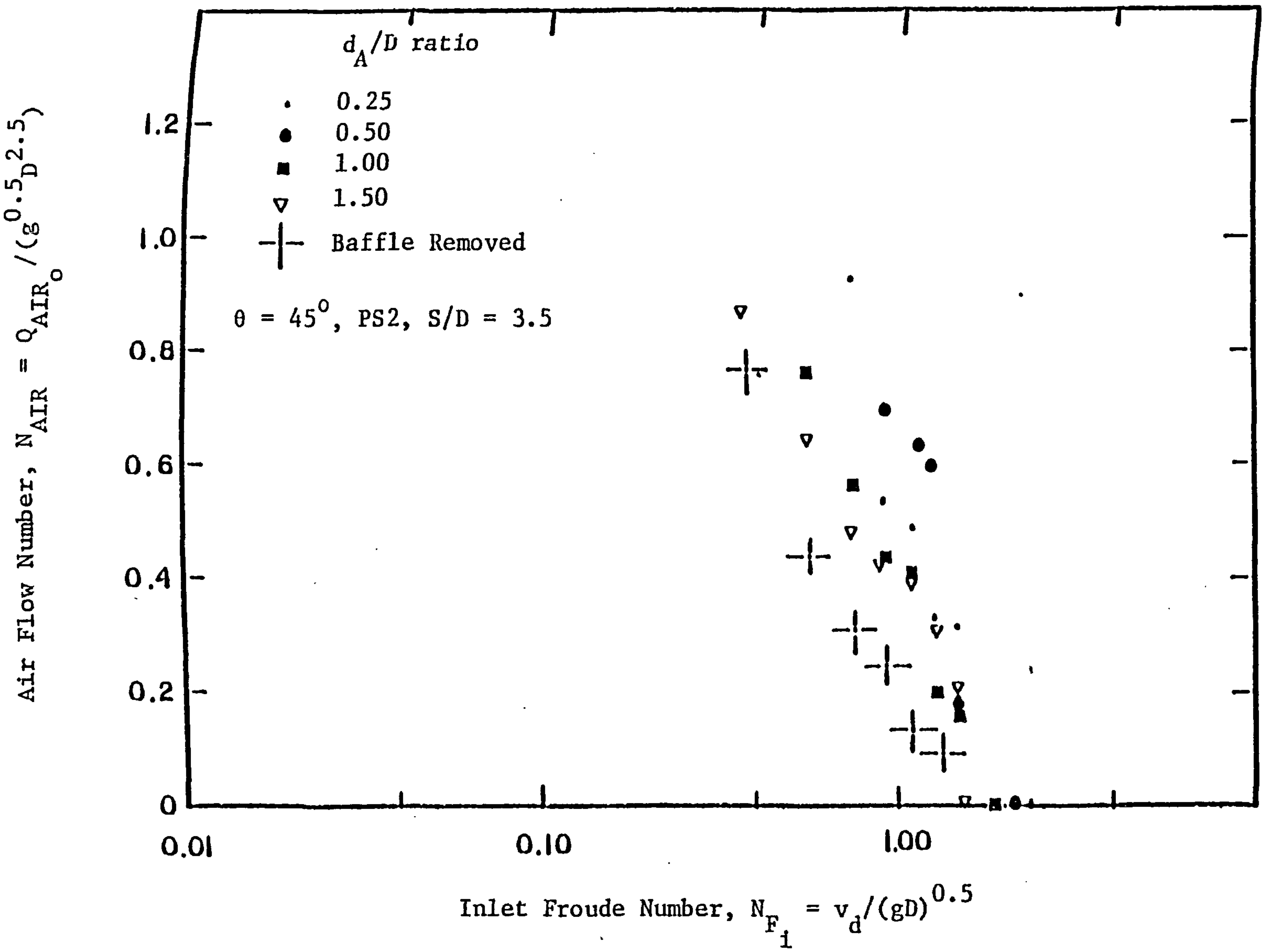

Fig. 6.10 Effect of Top Baffle Clearance for 45^0 Floor Slope

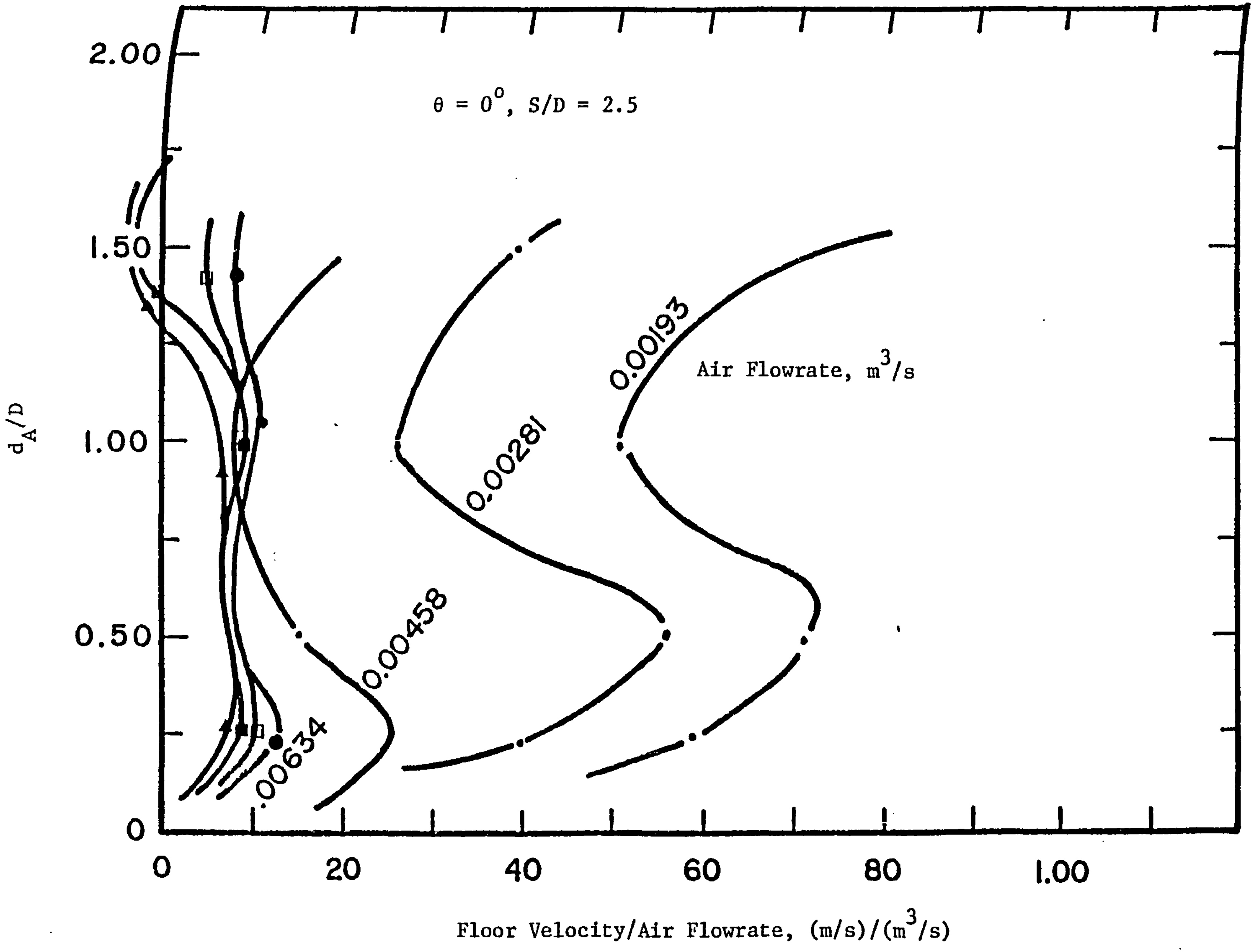

Fig. 6.11 Floor Velocity as a Function of Air Flowrate and d_A/D for a Horizontal Floor

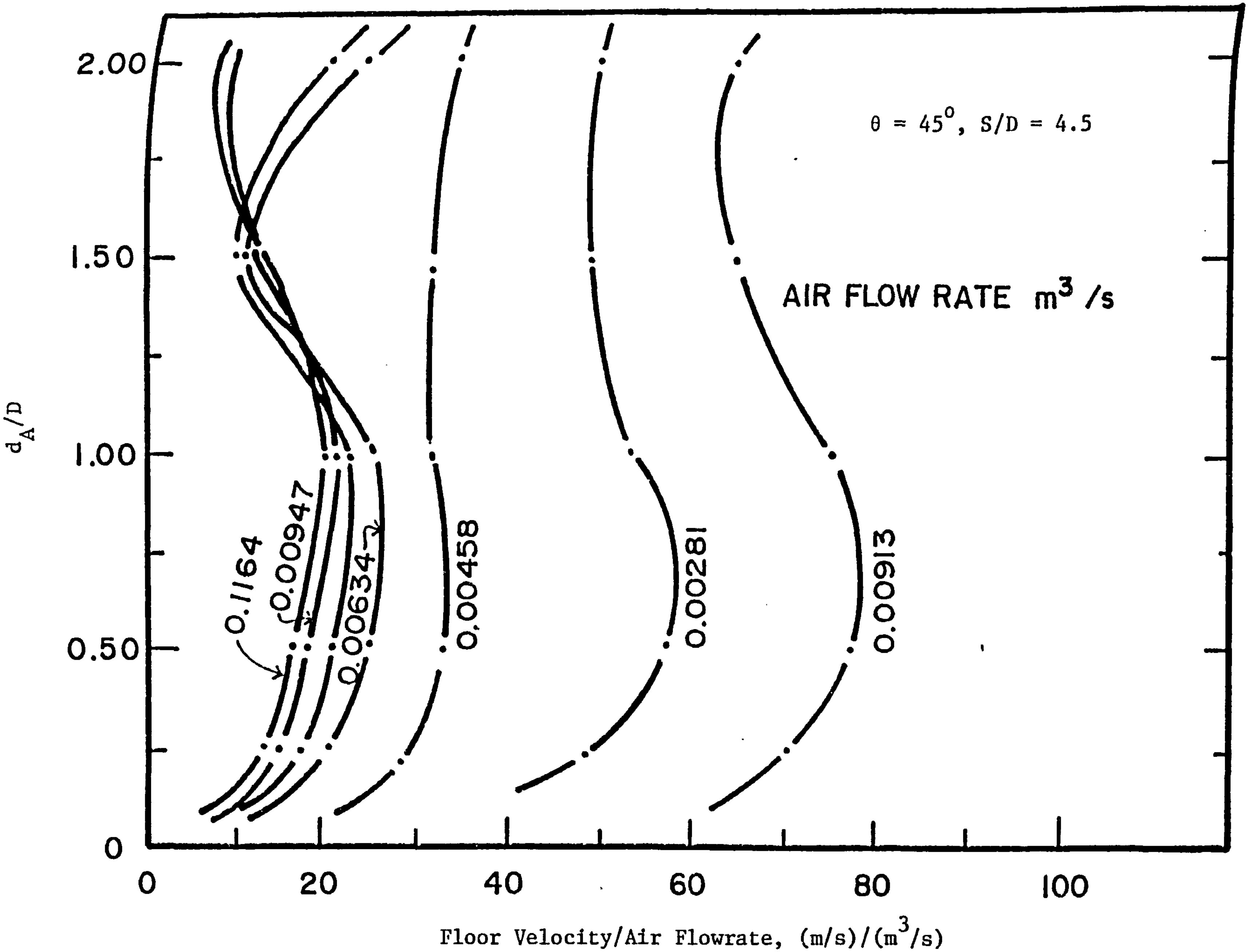

Fig. 6.12 Floor Velocity as a Function of Air Flowrate and d_A/D for a 45° Floor Slope

(iii) at d_A/D greater than 1.75, the velocity to air flowrate ratio again begins to increase.

The optimum air flowrate, which maximizes the velocity along the floor, can be determined for a specific d_A/D by reading the flow velocity to air flowrate ratio corresponding to each air flowrate and calculating the velocity from that ratio. The maximum velocity corresponds to the optimum air flowrate. The study of the top baffle clearance also included the case of no baffle. Under identical operating conditions, it was observed that the velocities along the floor were at least equal to, and often 10 to 50% higher than, the maximum recorded with any other top baffle clearance.

At this point in the research, it was decided to eliminate the reaction baffle for the following reasons:

(a) interaction between the diffuser plume and the baffle, under certain operating conditions, produced unfavourable rollers in the wet well which entrained air bubbles. These air bubbles often were sucked into the pump intake,

(b) under certain operating conditions, the baffle promoted rather than hindered vortex formation,

(c) the baffle did not conclusively produce higher shear stresses along the sump floor, and

(d) the construction and maintenance costs of the baffle would be eliminated.

Development of the numerical model was begun at this stage.

6.5 Test Series 4, Width of Diffuser Zone

In this test series, the location of the diffuser within the diffuser zone and the width of the diffuser zone were studied. Four different combinations as shown in Fig. 6.13 were tested. The width of the diffuser section was kept at D and 3D. The diffuser itself was

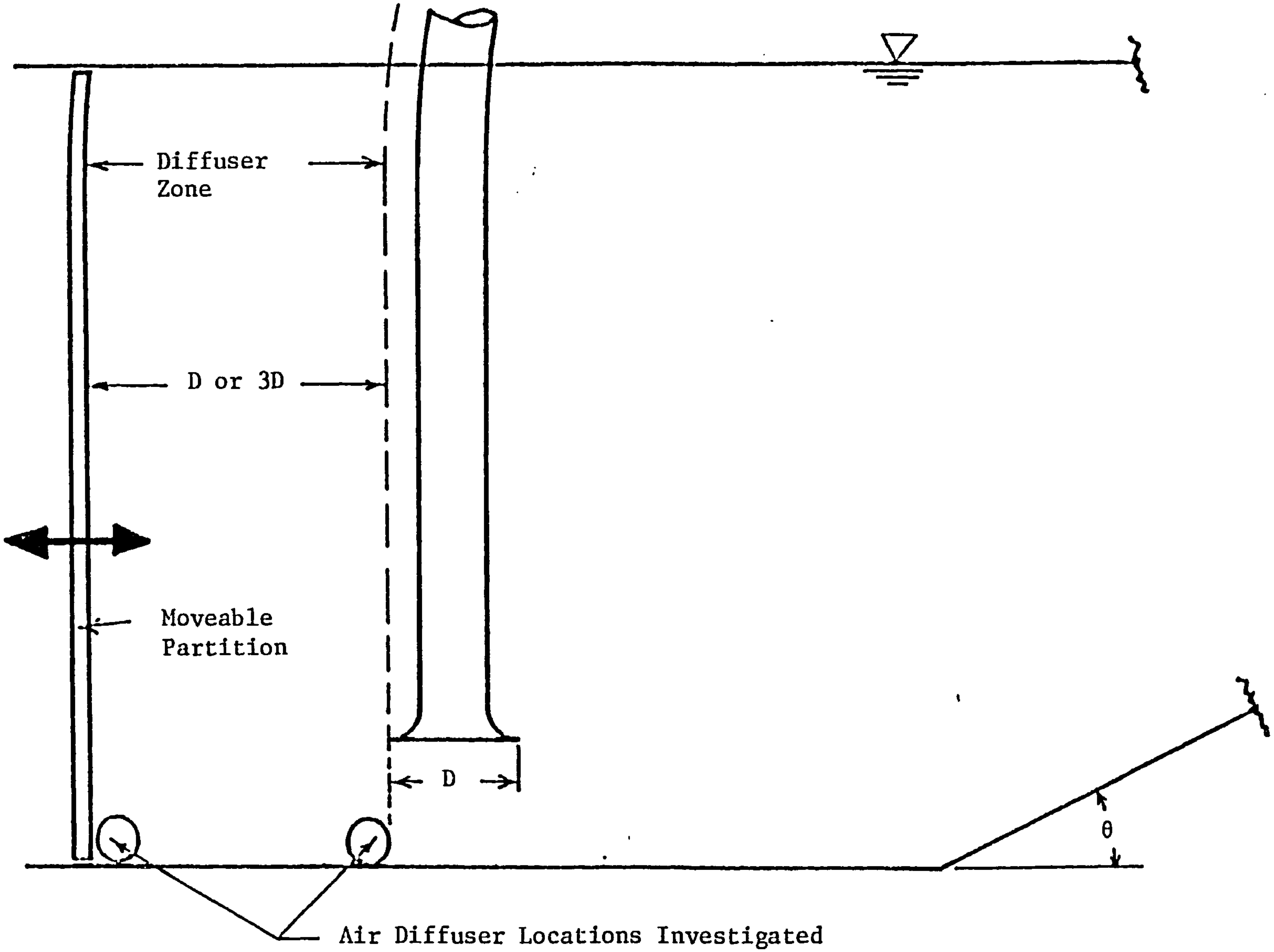
Diffuser Zone
D or 3D
Moveable Partition
D
θ
Air Diffuser Locations Investigated

Fig. 6.13 Diffuser Zone Investigations

placed on the floor of the sump, either along the edge of the bell-mouths or adjacent to the moveable rear wall. In order to determine the effect of the diffuser alone, pumps were not operated. The range of other test variables was the same as in Test Series 3. The point velocities were measured at the same probe location as described previously.

When the diffuser was located adjacent to bell-mouths, two circulations, as shown in Fig. 6.14(a) were set up in the wet well. This phenomenon occurred in both the wide and narrow width diffuser zones. The net effect of the two circulations was a reduction in the velocity along the wet well floor. In some cases, the velocity vector at the probe location was directed away from the bell-mouths. This in effect defeated the purpose of the air diffuser system since it was intended to transport particles towards the intakes. When the diffuser was located adjacent to the rear wall, Fig. 6.14(b), only one circulation was induced.

The width of the diffuser section seemed to have very little effect on the floor velocities. However, when the diffuser was located adjacent to the bell-mouth, small bubbles were drawn into it. It is assumed that when the pumps are operating, more air will be sucked into the intakes. Based on these observations, it was concluded that the optimum width of the diffuser zone was 3D and the best diffuser location was adjacent to the rear wall and at the floor of the sump. All further diffuser studies were carried out with this configuration.

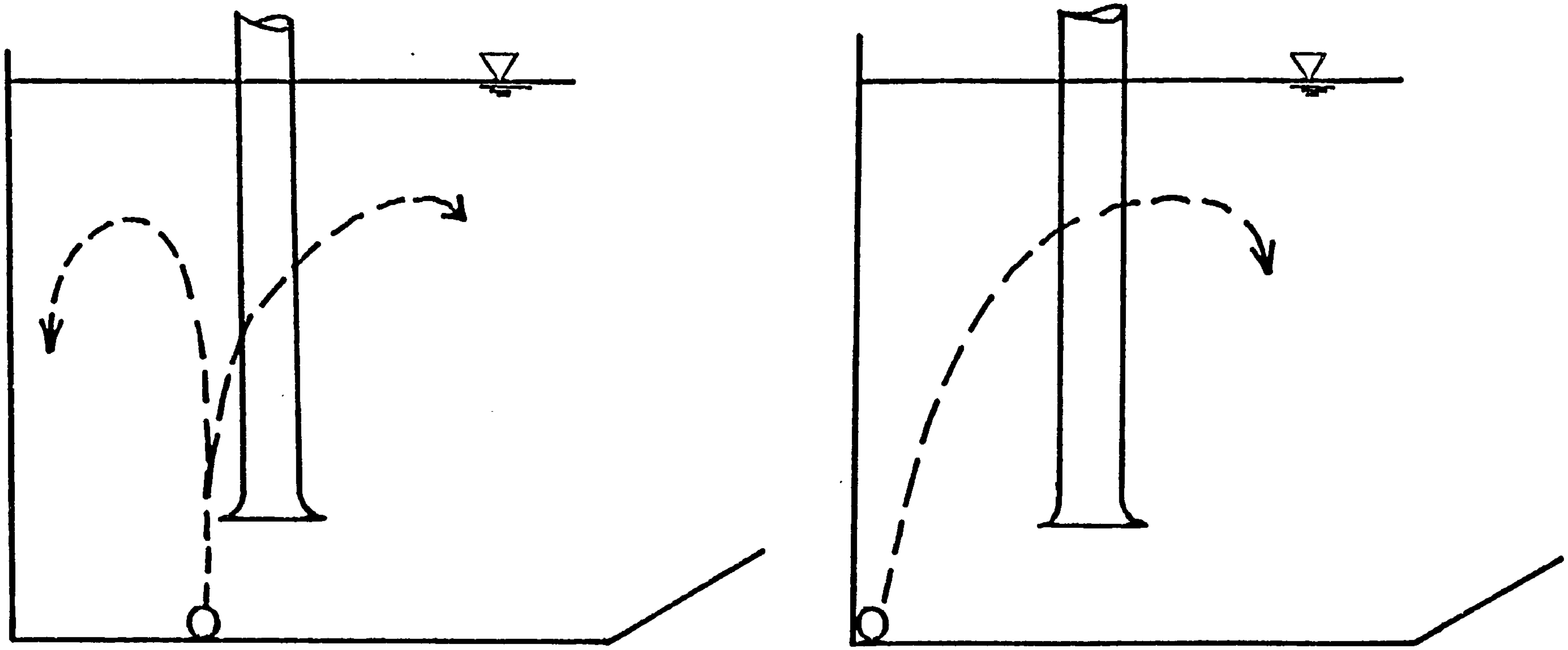

(a) diffuser near bell-mouths

(b) diffuser near rear wall

Fig. 6.14 The Effect of Various Diffuser Locations

6.6 Test Series 5, Experimental Particle Characteristics

The next investigation was to observe the behaviour of particles in the wet well and how the fluid velocities within the wet well assisted or retarded their motion. The selection of particle characteristics and the techniques employed to obtain these characteristics are discussed in this section. The observations of particle motion are described in the next subsection.

Six different types of particles were selected to represent a wide range of characteristics. The description of each type of particle and their significant characteristics are given in Table 6.5. The grain size and particle specific gravity were determined using standard sieve tests and pycnometer tests, respectively. The particle diameter shown in Table 6.5 is the arithmetic mean of the sieve size on which the particle was retained and the next largest sieve size through which the particle passed. The settling velocity was obtained by timing a representative group of particles as they fell through a distance of 3 feet (0.914) in a 6 inch (152 mm) diameter column of water at 20°C. The procedure was repeated ten times for each particle and the average settling velocity was obtained.

The submerged angle of repose of the particles was measured by dropping the particles through a funnel into a 390 mm deep tank. As the particles hit the bottom of the tank, a cone of sediments began to build up. Once a sufficient number of particles had been dropped to form a constant slope on the sides of the cone, the angle of repose was determined from the physical dimensions of the cone. The

Table 6.5 Experimental Particle Characteristics

Particle Description	Particle Diameter (mm)	Specific Gravity	Settling Velocity (m/s)	Submerged Angle of Repose (degrees)	Smooth Bed Case			Rough Bed Case		
					τ_C (N/m^2)	$\frac{U_* d_S}{\nu}$	$\tau_C/((\gamma_S-\gamma_f)d_S)$	τ_C (N/m^2)	$\frac{U_* d_S}{\nu}$	$\tau_C/((\gamma_S-\gamma_f)d_S)$
Very Fine Gravel	2.19	2.54	0.241	41.2	0.514	54.43	0.016	1.483	71.13	0.045
Coarse Sand	0.63	2.54	0.121	33.6	0.186	9.43	0.020	0.421	12.58	0.044
Fine Sand	0.20	2.54	0.040	30.3	0.055	1.52	0.018	0.330	2.82	0.109
Coarse Grit	0.63	2.52	0.122	34.1	0.176	8.95	0.019	0.722	16.88	0.077
Activated Carbon	2.61	1.59	0.141	43.1	0.198	37.02	0.013	1.668	106.07	0.111
Charcoal	0.72	1.13	0.038	37.1	0.067	5.96	0.073	0.531	16.43	0.579

particles were stirred in a beaker of water prior to release into the tank in order to purge any air which was trapped on, or in, the particles. This procedure was repeated three times for each particle size and the average values were reported.

In Table 6.5, the critical shear stress, particle Reynolds number and Shields entrainment function value are recorded for both smooth and rough bed cases. The tests to determine the critical shear stress were carried out in a recirculating flume with 2.8 m length, 0.15 m width and 0.30 m depth. The flow depth at the test section was kept constant at 0.20 m. The shear stress required to initiate particle motion was calculated using the Hwang and Laursen formula (1963)

[6.1] $\tau = (P_{ST} - P_o)/(16.531\{A - (B)(C) + D\})$

where P_{ST} is the stagnation pressure of the pitot-tube, P_o is the static pressure and

[6.2] $A = (\log(30h/k_S))^2$

[6.3] $B = \log(30h/k_S)$

[6.4] $C = 0.25(d_p/2h)^2 + 0.0833(d_p/2h)^4 + 0.00704(d_p/2h)^6$, and

[6.5] $D = 0.25(d_p/2h)^2 + 0.1146(d_p/2h)^4 + 0.0586(d_p/2h)^6$

where h is the distance from the centre of the stagnation tube to the top of the grains, k_S is the sand roughness and d_p is the inside diameter of the stagnation tube. Equation [6.1] is based on the logarithmic Kármán-Prandtl velocity distribution. It also builds on the earlier work of Preston (1954) who interpreted the dynamic pressure reading as a measure of local shear on the wall. The equation has correction factors for the channel roughness and for the transition regime of the flow.

In the smooth bed case, a thin layer of grains was levelled along the entire length of the galvanized floor of the flume and the discharge was gradually increased until the velocity adjacent to the grains was just sufficient to initiate rolling. This condition was considered to be the critical condition and the velocity profile at the test section, 2 m downstream of the inlet section, was recorded. The velocity was obtained with the probe resting just on the top of the grains and at 20 mm intervals above that, up to the free surface.

The pitot-tube was connected to an inclined manometer to give the differential pressure across the probe. The inside diameter of the stagnation tube was 1.788 mm. Measurements with the propeller meter, ultrasonic meter and pitot-tube indicated that at the test section, the influence of the inlet and outlet sections was negligible. For the rough bed case, a layer of the particles was glued to a separate galvanized sheet and it was placed in the flume. A second layer of loose particles was then levelled on top of the glued particles. The flow was then increased until movement of the upper layer began. At this point the velocity profiles were recorded. The increase in shear stress required to move the grains would be a measure of the effect of interlocking of the particles on the bed. For the smooth bed, the value of k_s was assumed to be 0.0005 inches (0.0127 mm) as proposed by Moody (1944) for galvanized iron pipe. For the rough bed, the value of k_s was assumed to be equal to the diameter of the particles under consideration. The results of the critical shear stress measurements are shown in Fig. 6.15 along with Shields'

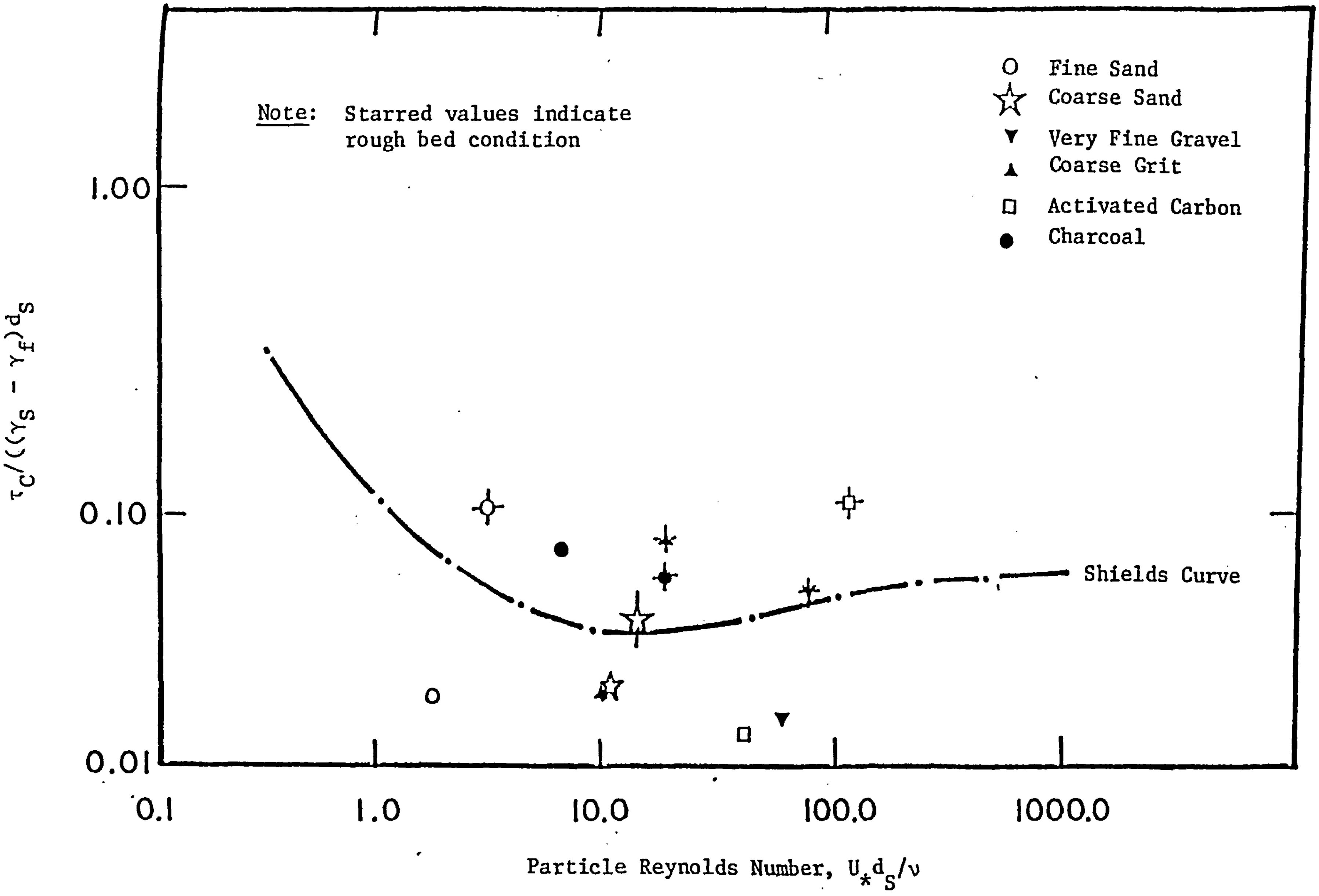

Fig. 6.15 Critical Shields Plot

results. The Shields curve represents the case of a "packed-bed" in which several layers of grains would deflect under a given shear stress. The lower set of data points represents the smooth bed case with low interaction between particles and low interaction between the particles and the galvanized sheets. The upper set of data points represents the rough bed case with high interaction between particles and only the upper layer of particles deflects under a given shear stress. The only anomaly in the data appears in the case of the charcoal particles resting on a smooth bed. The behaviour of these particles was sporadic and the initial motion was both through rolling and saltating. Small air bubbles may have been trapped in the porous structure and this may have altered the motion of the particle. No attempt was made to optimize the k_S value used in Eqs. [6.2] and [6.3] in order to make the data conform to the Shields' curve. The channel slopes, during the determination of the critical shear stress, ranged from 0.0019 to 0.0031. No attempt was made to correct the critical shear stresses for this very low slope.

6.7 Test Series 6, Particle Deposition in the Wet Well

The purpose of these tests was to observe where particles would settle on the wet well floor under various operating schemes. For this series of tests, no air was introduced into the system in order to represent a normal sump condition. The test variables are given in Table 6.6.

A total of 180 observations were made with various particles and under different operating schemes. Prior to starting the pump, the

Table 6.6 Test Variables used in the Observation of Particle Deposition

Variable	Range
Particles	6 particles as per Table 6.5
Floor Angle	0, 5, 15, 30, 45 degrees from the horizontal
Water Depth Ratio, H/D	2, 4, 8
Pumping Schemes	1, 2, 3, 4
Inlet Froude No., $v_d/(gD)^{0.5}$	0.388 to 3.103
Total Pump Discharge	3.61 to 14.42 ℓ/s (47.59 to 190.36 gpm)

desired floor angle and water depth were set. The entire floor of the wet well was then covered with a layer of sediment of thickness 2 to 5 grain diameters. Care was taken to ensure that the sediment layer was as uniform as possible. If the sloping portion of the wet well floor was at an angle greater than the angle of repose of the particle, the sheet of sediment was allowed to slump to the base of the slope. The excess grains were then removed. Once the bed layer was established, the pump was started and gradually brought to the desired flowrate. It was observed that the sediments on the sump floor were scoured and entrained by the inflow to the pump. The sediments passed through the pump and were discharged into the wet well at the inlet zone. Some of the sediments remained permanently suspended in the flow. After a steady state sediment pattern was established on the wet well floor, usually in 20 minutes, the sediment conditions in the sump were recorded. The main observations are summarized below:

(a) A clear zone of approximately 200 to 300 mm in diameter (1.8D to 2.6D) was observed on the floor of the wet well under the operating intake. This pattern was observed for inlet Froude numbers greater than 1.49. At lower inlet Froude numbers, the area below the intake was "thinned down", but the particles on the floor of the wet well were not completely scoured.

(b) For inclined floor slopes of 5° or more, and with inlet Froude numbers greater than 1.49, the entire sloping portion of the wet well floor contained no settled particles.

(c) For a horizontal wet well floor, i.e. floor slope of 0°, the particles on the floor adjacent to the inlet zone of the sump were completely scoured for a distance of 100 to 400 mm (0.9D to 3.5D). As the inlet Froude number increased, the completely scoured area also increased.

(d) "Fillets" of sediments were deposited at the interface between the vertical walls and the floor of the sump. The height of the fillet ranged from 20 to 50 mm, depending on the particle diameter, specific gravity and inlet Froude number.

(e) A fillet also developed at the base of the incline. The shape of the fillet depended on the streamlines of the flow over the transition from the inclined to the horizontal portion of the floor.

(f) When sediments were deposited on the horizontal floor, the thickness of the sediment layer gradually decreased with the decrease in distance to the operating intake.

(g) With low fluid depths and high inlet Froude numbers, and with the formation of surface swirl or floor vortices, the sediments were scoured quickly and a larger percentage of the total sediment load remained in suspension.

(h) The effect of the "thinning" of the sediment layer was barely noticed at inlet Froude numbers less than 0.59.

The major areas for sediment deposition were the horizontal portion of the floor and the transitions between the floor and the walls. Permanent concrete corner fillets, either triangular or curvilinear in shape, would help to improve the flow conditions and reduce deposition. The remainder of sediment would have to be scoured by the additional shear stresses introduced by the air diffuser. The resulting velocities would have to produce shear stresses at least as large as τ_C, for the rough condition given in Table 6.5, to eliminate deposition and to promote resuspension of any solids which may have settled during periods of no pumping.

6.8 Test Series 7, Circulation Studies

The purpose of these tests were:

(a) to locate the centre of rotation of the circulating flow, and

(b) to estimate the maximum rise in the free surface above the diffuser plume.

The range of test variables is given in Table 6.7.

In order to improve the flow visualization, aluminum oxide powder was mixed into the sump fluid. The location of the centre of rotation of the flow was measured with respect to the coordinate axis shown in Fig. 6.16.

It was observed that the location of the centre of rotation correlated with several non-dimensional parameters as well as with the calculated geometric centre of the cross-section. The non-dimensional parameters used were

[6.6] $N_p = Q_p/(H^{2.5}g^{0.5})$

[6.7] $N_{AIR} = Q_{AIR_o}/(H^{2.5}g^{0.5})$

[6.8] $N_H = H^{1.5}g^{0.5}/\nu_f$, and

[6.9] $N_Y = \bar{Y}/H$

The following correlation equations were developed based on 69 observations

[6.10] $(XCR - \bar{X})/\bar{X} = 0.161 - 30.395N_p + 4.042N_{AIR} + \ldots$
$0.00494(\text{Floor slope in degrees}) - 3.619 \times 10^{-8} (N_H)$, and

[6.11] $(YCR - \bar{Y})/\bar{Y} = -1.568 + 3.056(N_Y) - 4.836(N_{AIR}) + \ldots$
$5.815(N_p) + 7.004 \times 10^{-8}(N_H)$
$- 0.00537(\text{Floor slope in degrees})$

Table 6.7 Range of Test Values for Circulation Studies

Variable	Range
Water Depth Ratio, H/D	4, 6, 8
Floor Angle	0, 30, 45 degrees from the horizontal
Pumping Scheme	5
Inlet Froude No., $v_d/(gD)^{0.5}$	0.000 to 1.034
Air Flowrate	1.57 to 12.25 ℓ/s @ 20°C and 101.3 kPa

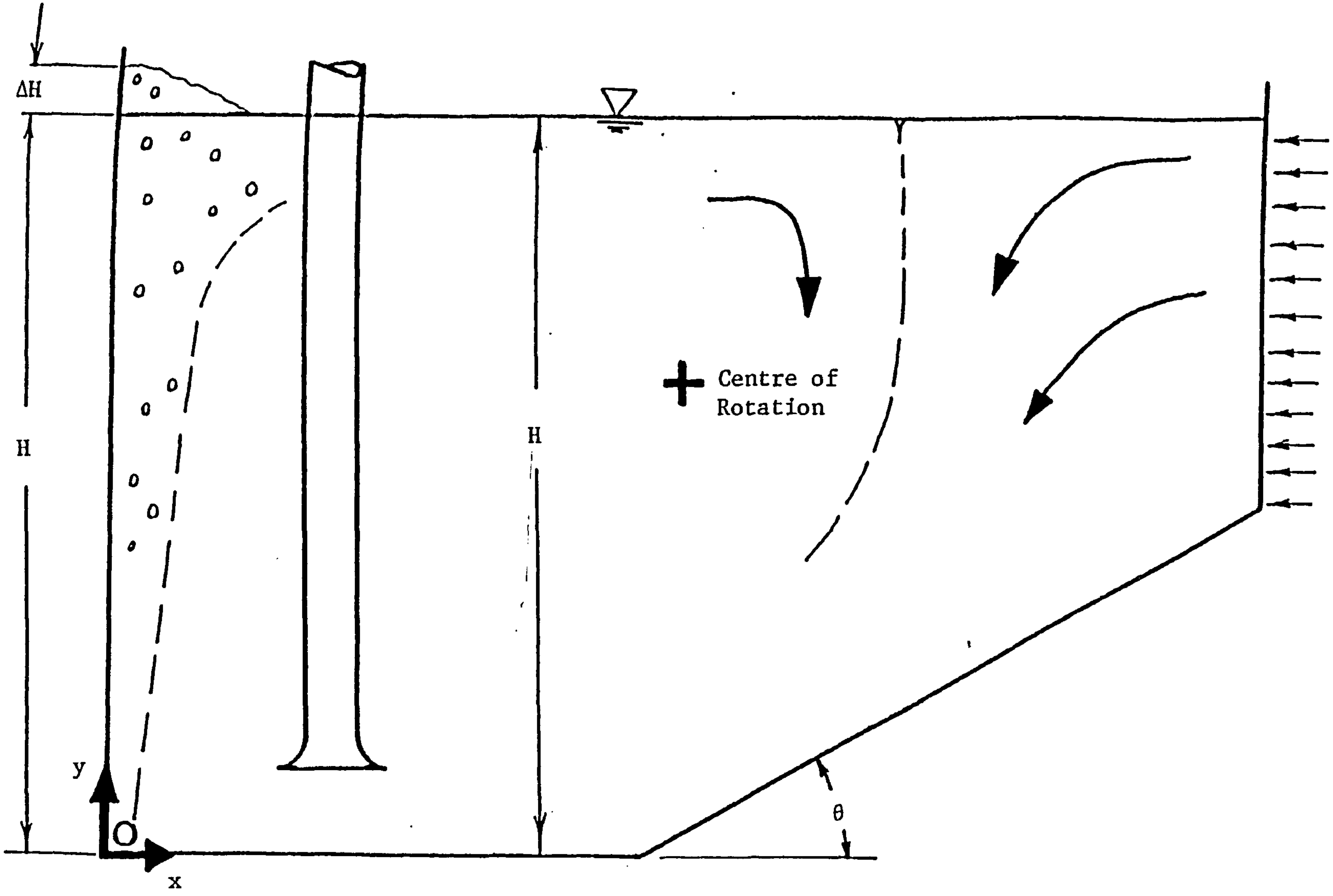
ΔH
H
H
Centre of Rotation
θ
y
O
x

Fig. 6.16 Coordinate Axis for Locating the Centre of Rotation

where XCR and YCR are the measured locations of the x and y components of the centre of rotation and $\bar{X}$ and $\bar{Y}$ are the geometric coordinates for the same floor slope and depth, H. The correlation coefficients for Eqs. [6.10] and [6.11] are 0.911 and 0.769 respectively.

At the same time that the location of the centre of rotation was observed, the maximum rise in the free surface above the plume, ΔH, as shown in Fig. 6.16, was also recorded. The statistical analysis of data resulted in the following correlation

$$[6.12] \qquad \Delta H/H = 0.0334 + 7.816(N_{AIR}) + 1.197 \times 10^{-8} (N_H)$$

with a correlation coefficient of 0.932. The measurements of the centre of rotation and ΔH were used in the calibration of the numerical model, as discussed in Chapter 7.

6.9 Test Series 8, Plume Velocity Studies

The purpose of this test series was to measure the plume water velocities under different air flowrates and water depths. The plume water velocities were measured at three locations across the plume for a specified distance above the diffuser. The probe locations were: (a) directly over the holes in the diffuser, (b) at the outer edge of the bubble plume, and (c) one probe diameter (38 mm) away from the outer edge of the plume. H to D ratios of 4, 6 and 8 were used. The plume velocity data were used to verify the drift flux calculations and to adjust the entrainment coefficient in the numerical model. Typical velocity profiles for H/D = 4 are shown in Fig. 6.17. The upper curve in each pair represents the velocity obtained with a diffuser air flowrate of 9.4 L/s, whereas the lower curves represent

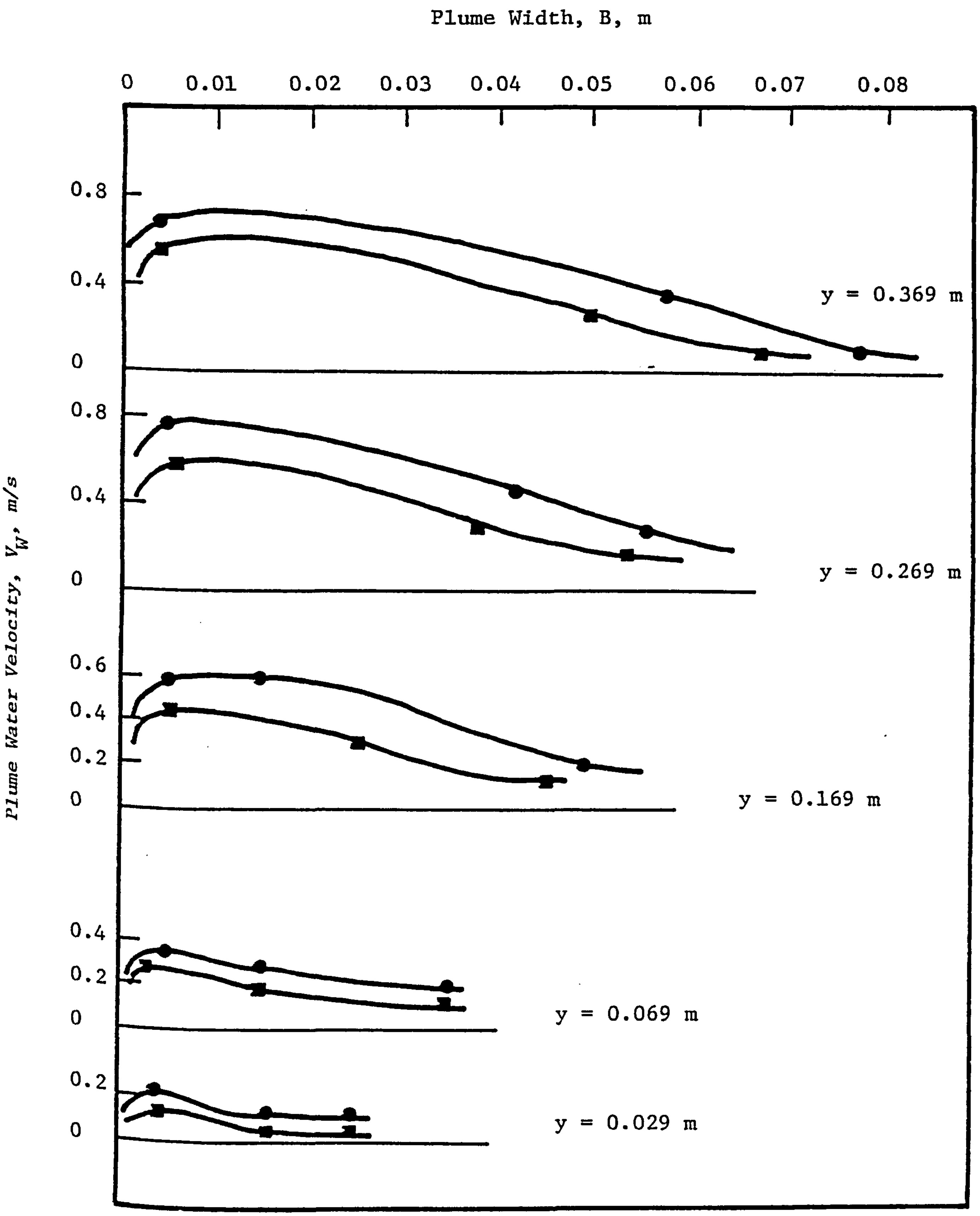

Fig. 6.17 Typical Plume Velocity Profiles

the velocity obtained for an air flowrate of 4.4 L/s. The three data points along each curve represent probe locations (a), (b) and (c), as mentioned above.

A calibration equation was developed for the ambient water velocity at probe location (c), as follows

$$[6.13] \qquad V_A H^2/Q_{AIR_o} = 4.220 - 7.297(Y/H) + 0.214(V_W H^2/Q_{AIR_o})$$

where V_A is the ambient fluid velocity recorded at probe location (c), Y is the distance above the exit ports of the air diffuser and V_W is the plume water velocity measured at probe location (a). The correlation coefficient for Eq. [6.13] was 0.932. The following limits apply to Eq. [6.13]

$$[6.14] \qquad 0.456 < H < 0.912 \text{ (m)}$$

$$[6.15] \qquad 0.01 < V_A < 0.25 \text{ (m/s)}$$

$$[6.16] \qquad 0.00348 < Q_{AIR_o} < 0.00984 \text{ (m}^3\text{/s)}$$

$$[6.17] \qquad 0.029 < Y < 0.869 \text{ (m)}$$

$$[6.18] \qquad 0.07 < V_W < 1.00 \text{ (m/s)}$$

The application of Eq. [6.13] in calibration of the numerical model is discussed in Chapter 7.

6.10 Test Series 9, Velocity Profiles Through the Centre of Rotation

The purpose of these tests was to obtain detailed velocity profiles in a vertical section through the observed centre of rotation. These velocity profiles were used to estimate the shear stresses along the floor of the sump. The range of test variables is given in Table 6.8. For a given flow condition, the velocity was recorded using the pitot-static probe/pressure transducer set up. The

Table 6.8 Test Variables used in Determining Vertical Velocity Profiles

Variable	Range
Water Depth Ratio, H/D	4, 6, 8
Floor Angle	0, 30, 45 degrees from the horizontal
Air Flowrate	3.76 to 10.10 ℓ/s @ 20°C, 101.3 kPa
Pumping Scheme	5
Inlet Froude No., $v_d/(gD)^{0.5}$	0 to 1.06

velocities were measured with the pitot-tube resting on the bed, 10, 30 and 50 mm above the bed and then at 50 mm increments, up to the free surface. A typical velocity profile is shown in Fig. 6.18. It was observed that the shape of the velocity profiles could be generalized to the shape shown in Fig. 6.19. The profile consisted of a uniform bottom velocity, v_b, which extended from the bed to a point BB above the bed. The velocity then decreased linearly to zero at the centre of rotation. Above the centre of rotation the velocity changed direction and increased linearly to a point AA above the bed. The maximum velocity, v_j, occurred at this point. Above AA, the velocity decreased slightly to the surface velocity, $v_{SURFACE}$.

A dimensional analysis on the significant variables led to the formation of ten dimensionless numbers as shown in Table 6.9. The repeating variables were H and g. Correlation equations were developed to describe the shape of the velocity profile. These equations, as well as the correlation coefficient of each equation are also given in Table 6.9. These equations were used in the formulation of the numerical model.

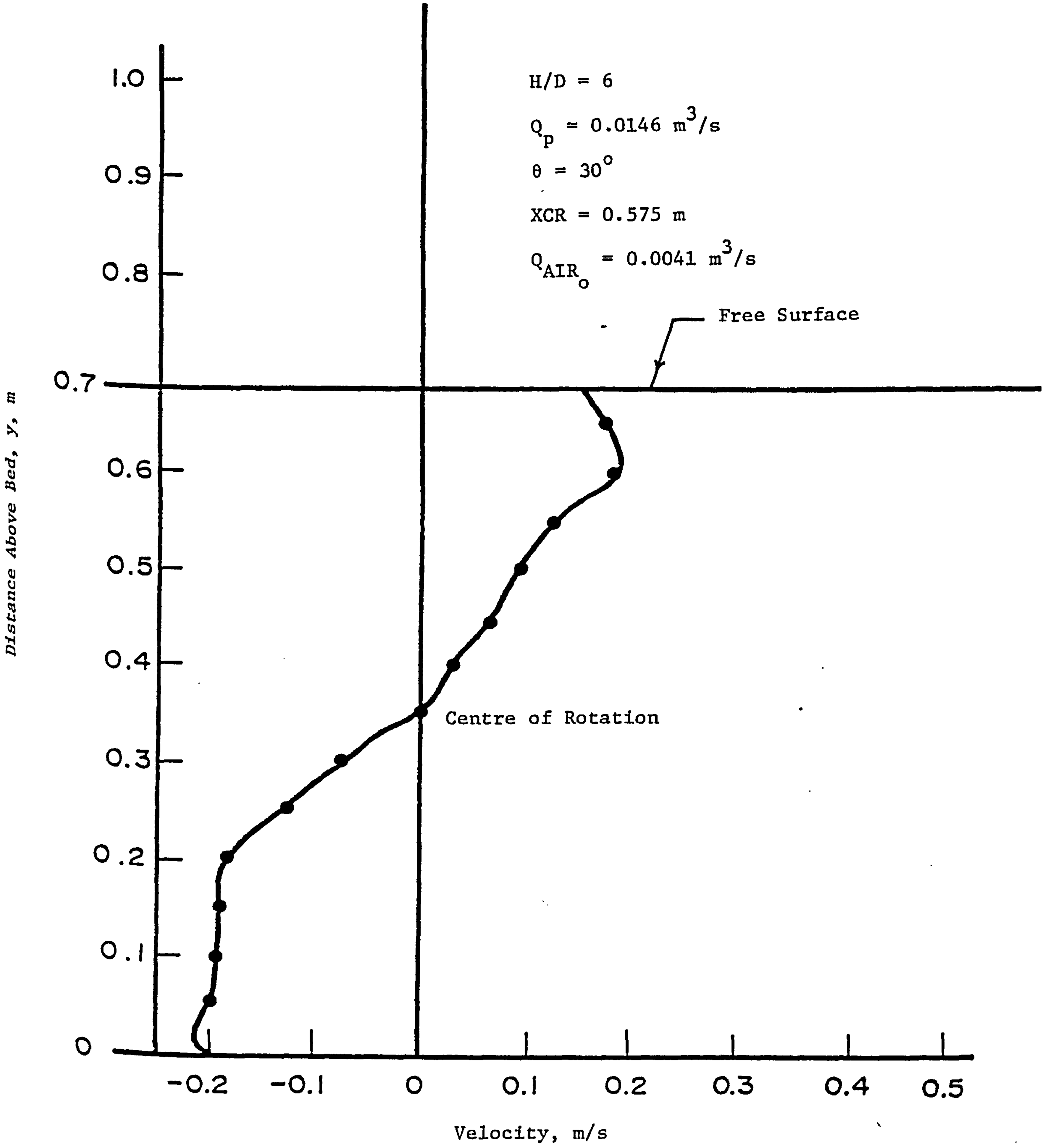

Fig. 6.18 Typical Velocity Profile Through Centre of Rotation

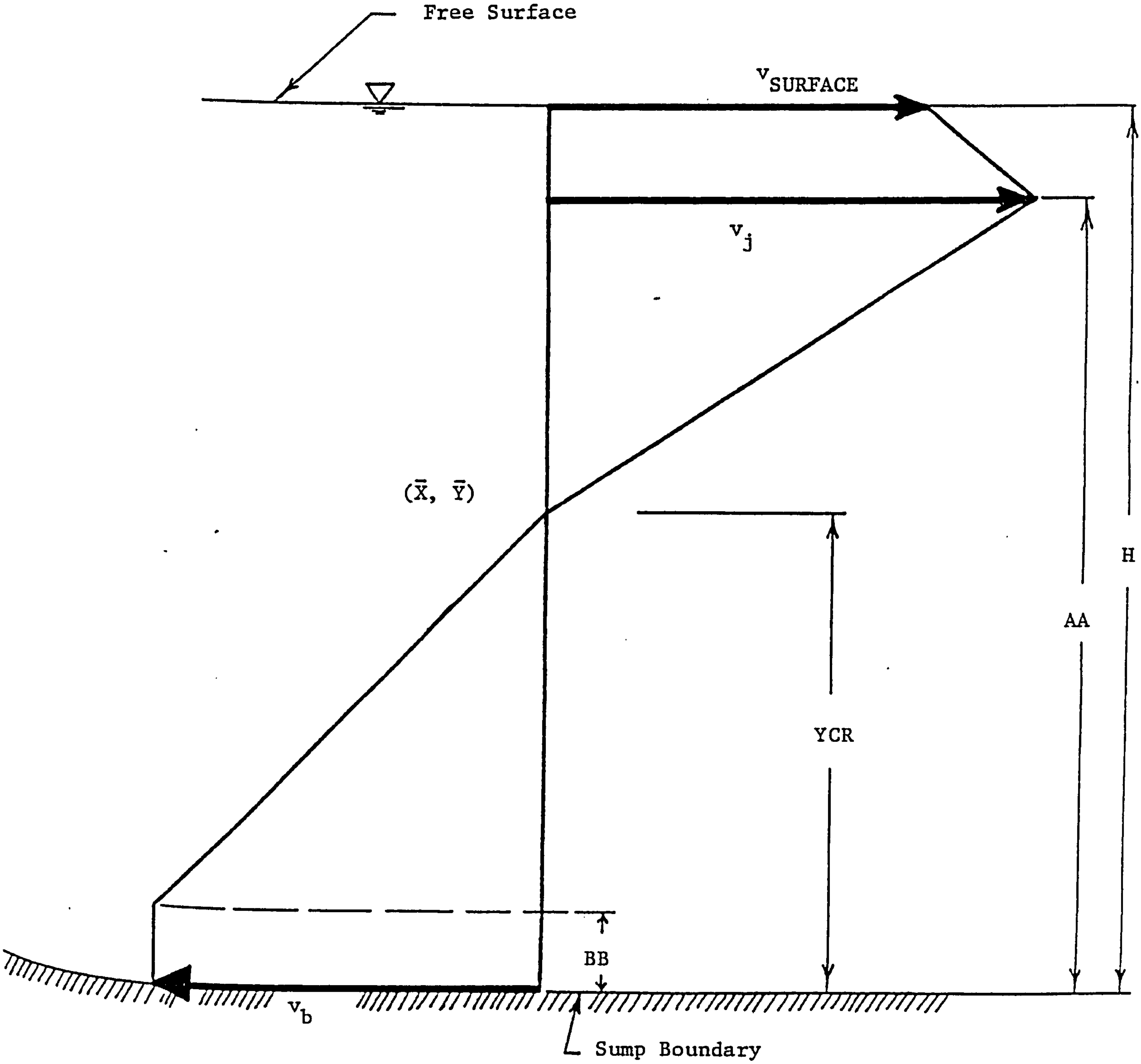
Free Surface
$v_{SURFACE}$
v_j
$(\bar{X}, \bar{Y})$
H
AA
YCR
BB
v_b
Sump Boundary

Fig. 6.19 Generalized Velocity Profile

Table 6.9 Correlation Equations for Velocity Profiles

$N_{AIR} = Q_{AIR_o}/(H^{2.5}g^{0.5})$; $N_p = Q_p/(H^{2.5}g^{0.5})$; $N_H = H^{1.5}g^{0.5}/\nu_f$; $N_j = v_j/(gH)^{0.5}$; $N_b = v_b/(gH)^{0.5}$; N_θ = floor angle, degrees ;

$N_s = v_{SURFACE}/(gH)^{0.5}$; $N_{BB} = BB/H$; $N_{YCR} = YCR/H$; $N_{AA} = AA/H$

Variable	Correlation Equation	Correlation Coefficient
$v_{SURFACE}$	$N_s = -0.2410 + 13.633N_{AIR} - 6.323N_p - 0.00121N_\theta + 0.633N_{YCR} + 1.82 \times 10^{-8}N_H$	0.952
v_j	$N_j = -0.2514 + 14.378N_{AIR} - 7.154N_p - 0.000767N_\theta + 0.618N_{YCR} + 3.027 \times 10^{-8}N_H$	0.909
v_b	$N_b = 0.0389 - 4.246N_{AIR} + 4.269N_p + 0.000269N_\theta - 0.1822N_{BB} + 0.539N_j$	0.895
BB	$N_{BB} = 0.549 - 0.258N_{AIR} - 11.338N_p + 0.00297N_\theta - 1.240 \times 10^{-7}N_H$	0.827
AA	$N_{AA} = 0.589 + 0.385N_{AIR} + 1.534N_p - 0.000945N_\theta + 0.575N_{YCR} + 1.372 \times 10^{-8}N_H$	0.840

CHAPTER 7

NUMERICAL CALIBRATION, SENSITIVITY AND DESIGN APPLICATION

7.1 General

The purpose of this Chapter was to apply the experimental results to calibrate the numerical model and to test the sensitivity of the model to various calibration and design parameters. Design curves and application of the curves are discussed using a comprehensive design example. The program flow chart, complete program listing and a sample output are given in Appendix 1.

The numerical model was calibrated and tested for sensitivity to the following parameters: (a) bubble radius, R_b, (b) initial plume width, B_o, (c) entrainment coefficient, α_C, (d) friction factors, f, (e) pump column drag coefficient, C_d, and (f) the location of the centre of rotation XCR and YCR. The changes in the calibration parameters were used to determine the effect of a change in a given parameter on (a) the total circulating flow within the sump, Q_{WD}, (b) the air fractions at the bottom and top of the diffuser plume, (c) the rate of growth of the plume with depth, and (d) the shear stress along the horizontal portion of the wet well floor. The design variables were (a) the fluid depth, H, (b) floor slope, θ, (c) air flowrate, Q_{AIR_o}, and (d) pumping rate, Q_p. The range of calibration values are given in Table 7.1. The sensitivity tests were carried out with the following variables held constant:

Table 7.1 Range of Calibration Parameters

Calibration Parameter	Values Used in Sensitivity Analysis
Bubble Radius, R_b	0.3, 0.5, 0.75, 1.0, 1.5, 2.0 cm
Initial Plume Width Ratio, B_o/R_b	2.2, 3, 4, 6, 10, 20, 30, 40, 50
Entrainment Coefficient, α_C	0.08, 0.10, 0.12, 0.13, 0.14, 0.145
Friction Factors, f	0.02, 0.03, 0.04, 0.05
Pump Column Drag Coefficient, C_d	0.6, 0.8, 1.0, 1.5, 2.0, 2.5, 3.0, 4.0, 5.0

(a) fluid depth ratio, $H/D = 8$

(b) floor slope, $\theta = 15^{o}$

(c) air number, $N_{AIR} = 0.00402$

(d) pumping number, $N_p = 0.00603$

7.2 Sensitivity to Diffuser Plume Parameters

In order to solve the plume equations given in Table 4.2, it is necessary to provide initialization values for the plume water velocity, plume width, and air fraction adjacent to the diffuser. An estimate for the air fraction adjacent to the diffuser can be obtained by rearranging Eq. [4.34]. The resulting equation is a quadratic equation in α, given by

[7.1] $$\alpha^2 + \alpha(1 - \psi_b/V_W - Q_{AIR_o}/(WBV_W)) + \ldots$$
$$Q_{AIR_o}/(WBV_W) = 0$$

Solution of the above equation depends on estimating the initial plume water velocity and plume width for a given air flowrate. Using the results of Test Series 8, it was possible to obtain a correlation equation for the plume water velocity

[7.2] $$V_W/(gH)^{0.5} = 0.0438 + 0.3728(Y/H) + 3.4153Q_{AIR_o}/(H^{2.5}g^{0.5})$$

where V_W is in m/s, Q_{AIR_o} in m^3/s, H in m and Y in m. The correlation coefficient was 0.922. The distance above the diffuser, Y, where the calculations began was fixed at 0.001 m. In order to estimate the initial plume width, it was assumed that the plume width was proportional to the bubble radius. Obviously, to accommodate a two phase system, it was necessary to assume a plume width greater than $2R_b$. The lowest real positive root between 0.0 and 1.0 obtained from Eq. [7.1] gave the initial estimate of α. Figures 7.1 and 7.2 illustrate the effect of different bubble radii and initial plume widths on the growth of the plume. The ratio $\Delta B/H$ was obtained by dividing the predicted change in plume width between the diffuser and the surface by the total fluid depth. Positive values of $\Delta B/H$ indicate a widening of the plume as it approached the free surface, whereas negative $\Delta B/H$ ratios indicate decreasing plume widths. Negative values of $\Delta B/H$ are inconsistent with experimental observations. Therefore, a maximum bubble radius of 0.009 m can be established from Fig. 7.1. From Fig. 7.2, it can be deduced that the initial plume width should not exceed 0.09 m. This results in a plume width to bubble radius ratio of 10.0. The effect of the initial plume width on the initial estimate of the air fraction near the diffuser, and the resultant air fraction at the surface is shown in Fig. 7.3. The air fraction at the diffuser is strongly dependent on the plume width and decreases with increasing plume widths, i.e. dilution of the air. However, the effect of the initial plume width on the surface air fraction is minimal, indicating that other factors such as entrainment or friction controlled the plume characteristics near the free surface.

The sensitivity to the entrainment coefficient, α_C, is shown in Figs. 7.4 and 7.5. From Fig. 7.4, it is seen that $\Delta B/H$ increased as the entrainment increased. The plume expands as more fluid is entrained. The surface air fraction obviously must decrease

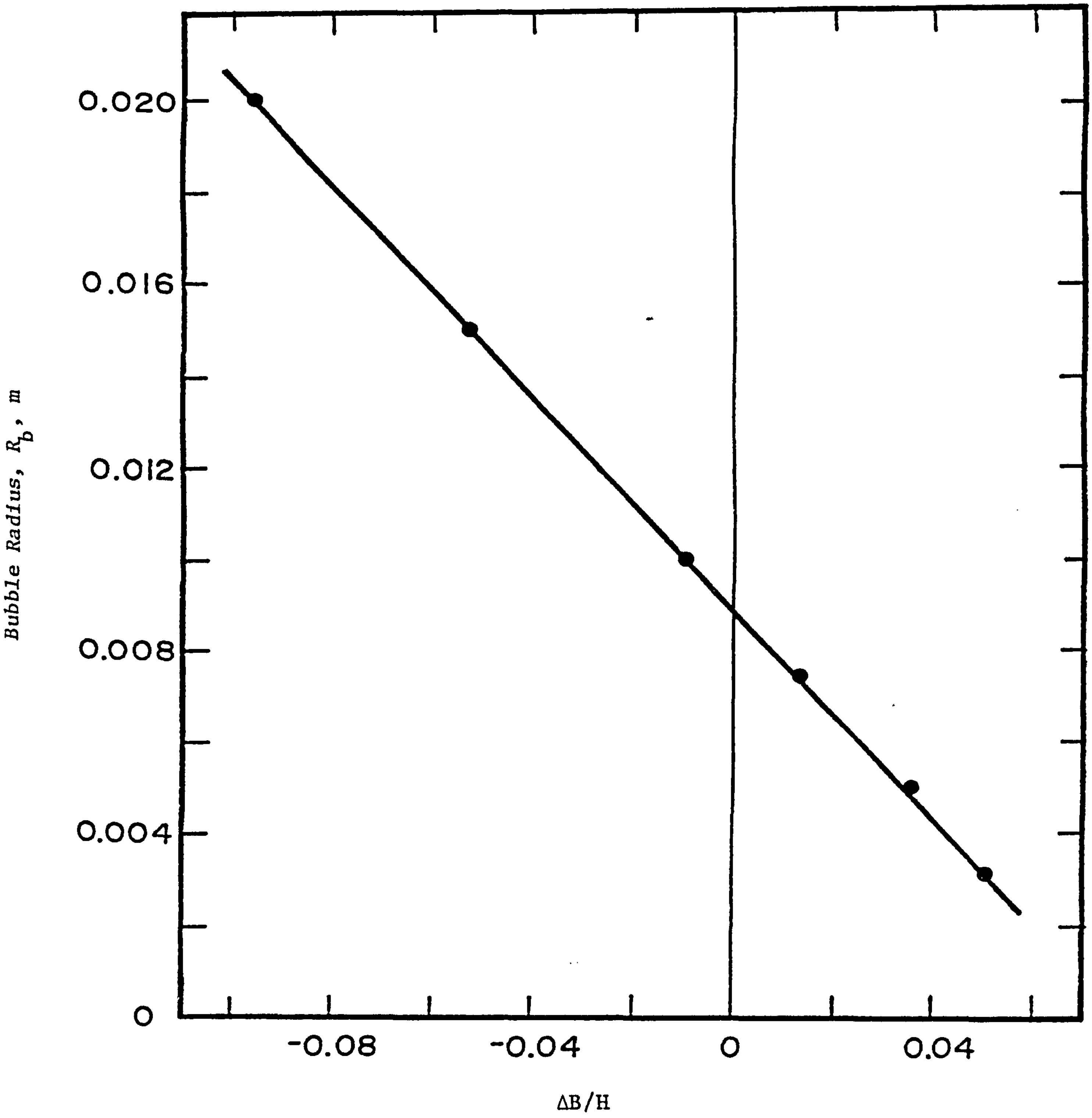

Fig. 7.1 The Effect of Bubble Radius on Plume Growth

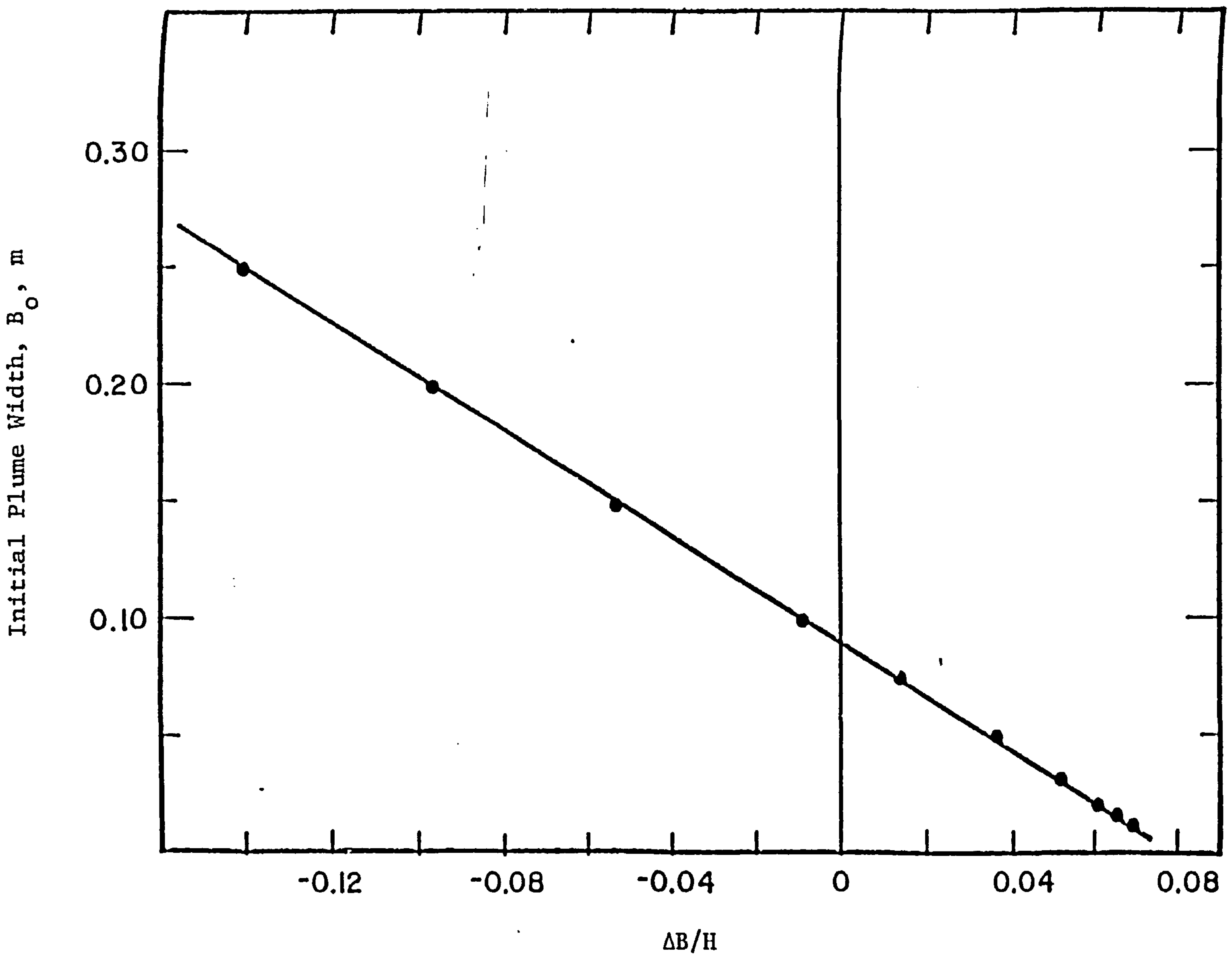

Fig. 7.2 The Effect of Initial Plume Width on Plume Growth

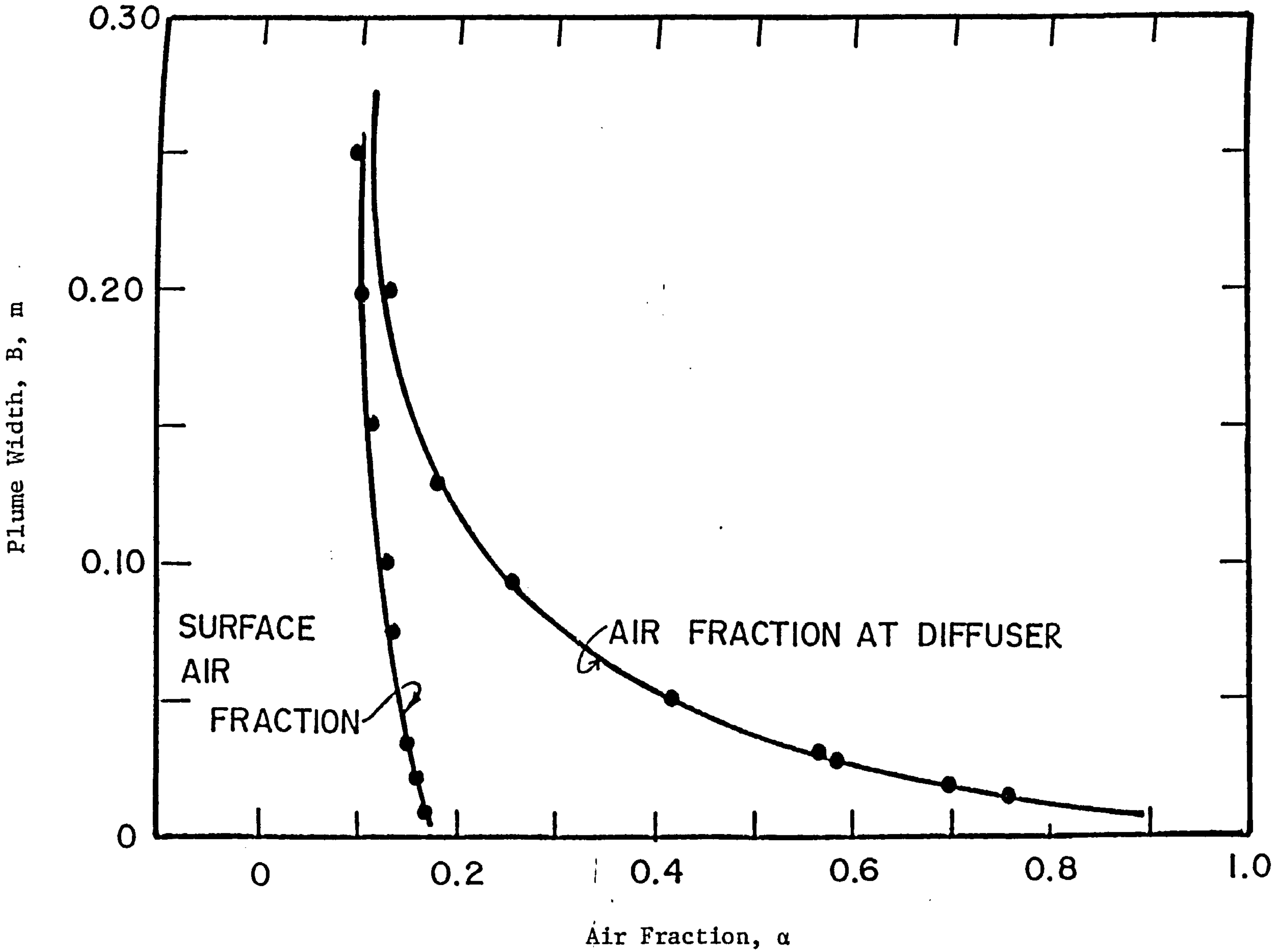

Fig. 7.3 Relationship Between Air Fraction and Plume Width

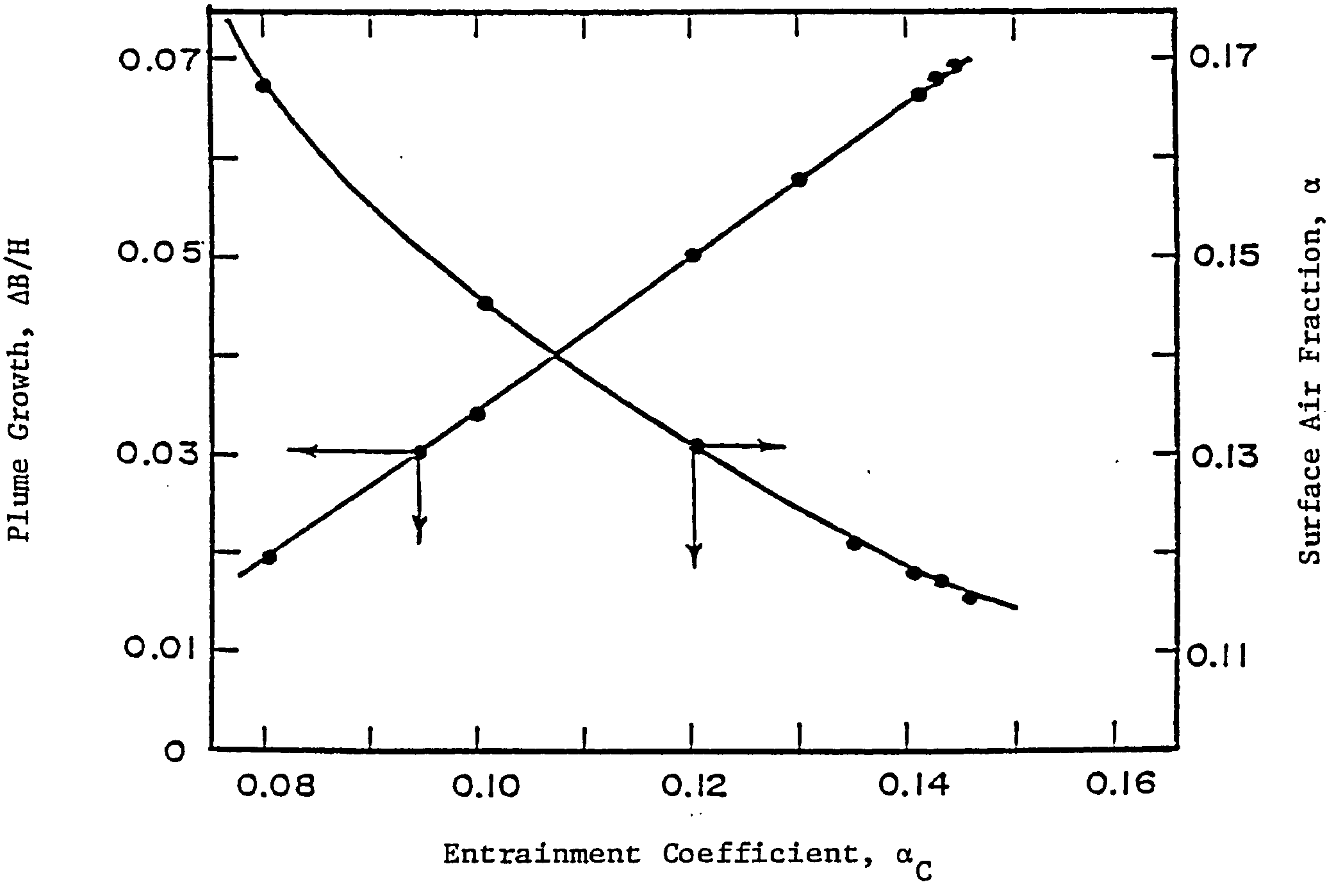

Fig. 7.4 Entrainment Coefficient Sensitivity

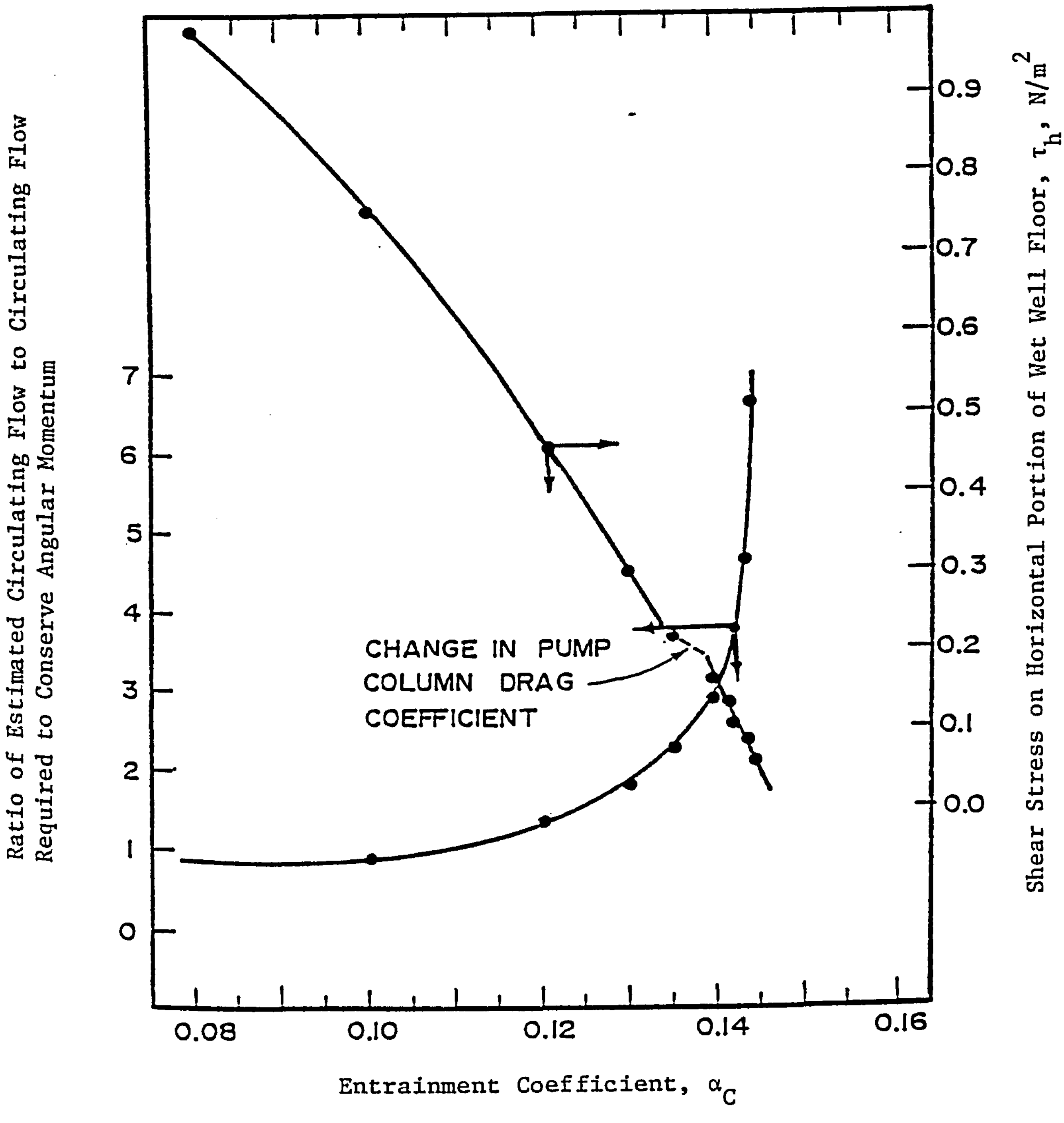

Fig. 7.5 Sensitivity to the Entrainment Coefficient

due to the effect of dilution. The reduction in surface air fraction with increasing entrainment is shown in Fig. 7.4. The effect of increased entrainment on the horizontal boundary shear stress is shown in Fig. 7.5. As the entrainment increased, the circulating flow decreased due to dilution effects, and hence, there was a reduction in boundary shear stress. The discontinuity in the α_C vs. shear stress curve is due to a change in the drag coefficient on the pump columns as the circulating flow changed. As the entrainment increased, the pump column Reynolds number and the C_d of the pump columns decreased. The resultant decrease in pump column drag must be offset by the increase in the boundary shear resistance if equilibrium is to be maintained. The pump column C_d can either increase or decrease depending on the value of the Reynolds number.

The ratio of the estimated circulating flow to the flow required for equilibrium is also plotted as a function of the entrainment coefficient on Fig. 7.5. The estimated circulating flow was calculated from the velocity profiles obtained in Test Series 9. For a specified air flowrate, pumping rate, fluid depth and floor angle, the velocity profile through the centre of rotation was defined using the equations given in Table 6.9. The bottom, surface and jet velocities were adjusted until continuity was satisfied. The flow passing below the centre of rotation was the summation of the circulating flow, Q_{WD}, and the pump discharge, Q_p, whereas above the centre of rotation only the circulating flow, Q_{WD}, passed through the vertical section. This Q_{WD} constituted the estimated circulating flow. For a given test condition, the estimated circulating flow may not balance the conservation of angular momentum. The circulating flow required for equilibrium was obtained by increasing or decreasing the bottom, surface and jet velocities until a sufficient circulating flow was obtained which satisfied the conservation of angular momentum. From Fig. 7.5, it can be seen that for large entrainment coefficients the estimated flow to equilibrium flow ratio is large. Entrainment coefficients in the range of 0.08 to 0.12 appear to give reasonable estimates of the circulating flow required for equilibrium conditions.

The relationship between the entrainment coefficient, pump column drag coefficient and the estimated jet velocity is shown in Fig. 7.6. With increasing entrainment, dilution of the diffuser plume results in lower circulations, and hence, lower jet velocities. Decreasing jet velocities lower the effective pump column Reynolds number, and hence, increase the C_d. Figure 7.7 shows that as C_d increases , the shear stress on the boundary decreases since more resistance is taken up by the pump columns. The boundary resistance must be less to maintain equilibrium. Figure 7.7 also shows that boundary shear stress increases linearly with the friction factor.

In order to select the entrainment coefficient and initial plume width which gave numerical values which coincided with physical measurements, it was necessary to estimate the air flux, j_{AIR}, given by Eq. [4.19] as

[7.3] $$j_{AIR} = Q_{AIR}/(WB)$$

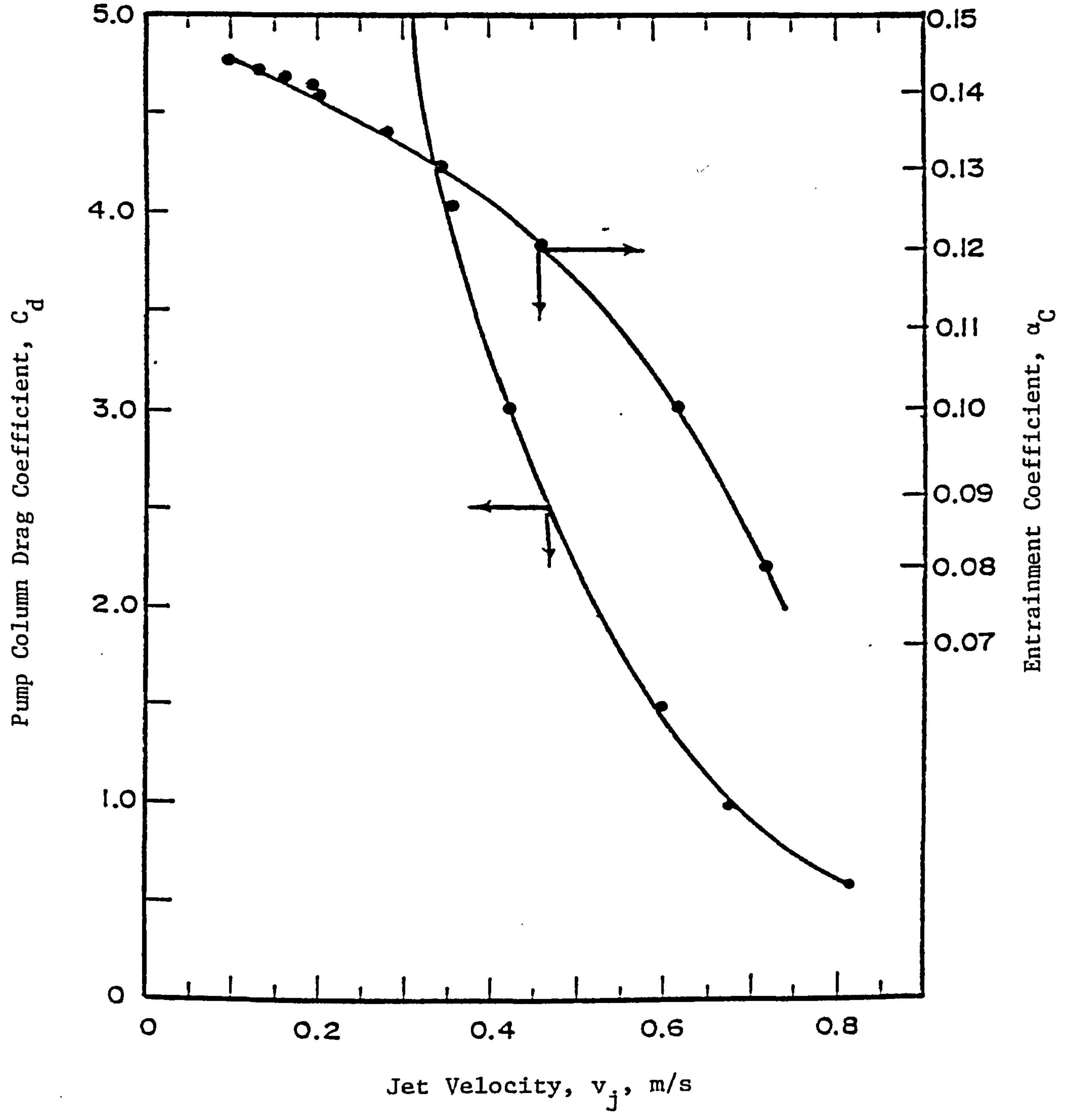

Fig. 7.6 Entrainment Coefficient Sensitivity

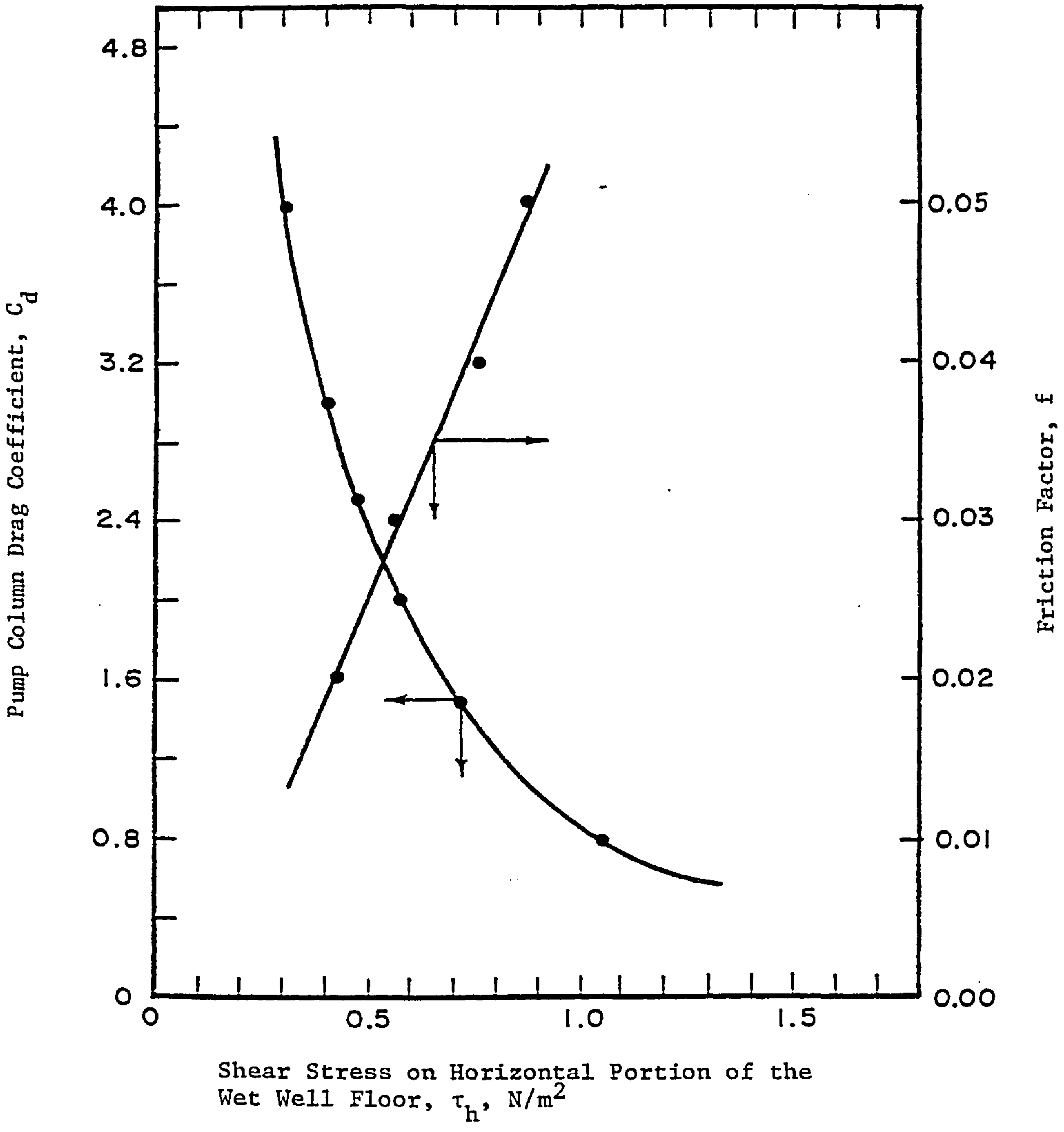

Fig. 7.7 Friction Factor Sensitivity

For the above calculation, Q_{AIR} was taken as the air flowrate at the diffuser, Q_{AIR_o}. Using the plume velocity data of Test Series 8, it was possible to estimate the growth of the plume, dB/dy, by assuming that the plume width at the diffuser was 0.01 m. By using measured plume widths at the free surface, a mean plume growth rate, dB/dy, was obtained. At any elevation, y, above the diffuser, the width B, in Eq. [7.3] was calculated and for a measured air flowrate at the diffuser, the air flux was obtained. The air fraction at an elevation y above the diffuser was estimated from the more general equation for drift flux

$$j_{AIR,f} = \alpha(1 - \alpha)^n (v_b) \tag{7.4}$$

where the exponent n was dependent on the bubble Reynolds number and its terminal velocity, v_b. Equation [4.25] gives

$$j_{AIR,f} = (1 - \alpha) j_{AIR} - \alpha j_f \tag{7.5}$$

where j_{AIR} and j_f are given by Eqs. [4.19] and [4.18]. Equation [7.4] can then be rearranged to yield an expression for α as

$$v_b \, \alpha(1 - \alpha)^{n-1} = Q_{AIR}/(WB) - \alpha V_W \tag{7.6}$$

The first term on the right hand side of the equation is the air flux. The water velocity, V_W, was measured and the terminal rise velocity was assumed to be 0.25 m/s. Equation [7.6] was solved for α for n values of 1.5, 1.75 and 2.0. The procedure for the solution of α was by trial and error in incremental steps of 0.0001 between $0.0 < \alpha < 1.0$. Only one positive root between 0.0 and 1.0 for α was found for each air flux. In addition, the measured water velocity, V_W, was increased by 5% to test the sensitivity of α to a given water velocity. The plume water velocity plots in Fig. 6.17 are not uniform. The measured velocities were increased by 5% to account for the non-uniformity. The 5% increase in V_W had a very small effect on the calculated α value as given by Eq. [7.6].

A comparison plot of the measured air fraction for various air flowrates is given in Fig. 7.8. The numerical results were obtained for entrainment coefficients ranging from 0.08 to 0.14 and for a B_o/R_b ratio of 2.0. The fluid depth ratios, H/D, were varied from 4 to 8. In all cases, it is observed that the measured value was less than the value predicted by the numerical model. An entrainment coefficient, α_C, of 0.12 was selected as the calibration value.

In order to improve the calibration of the model plume performance, a series of computer runs was made in which B_o/R_b was varied, and α_C was held constant at 0.12. The results are shown in Fig. 7.9. The distance between the horizontal slash marks along each curved line represents the range of measured air fractions at a given elevation above the diffuser and for a specified fluid depth. Finally, $B_o/R_b = 6.0$ was selected as the calibrated value. The possible error in the estimated α for a given B_o/R_b and fluid depth, H, is shown in Fig. 7.10. For $B_o/R_b = 6$, the error ranges from +3.5% to −11.5% over the entire range of test depths. A bubble radius of 0.005 m was selected as the calibrated value.

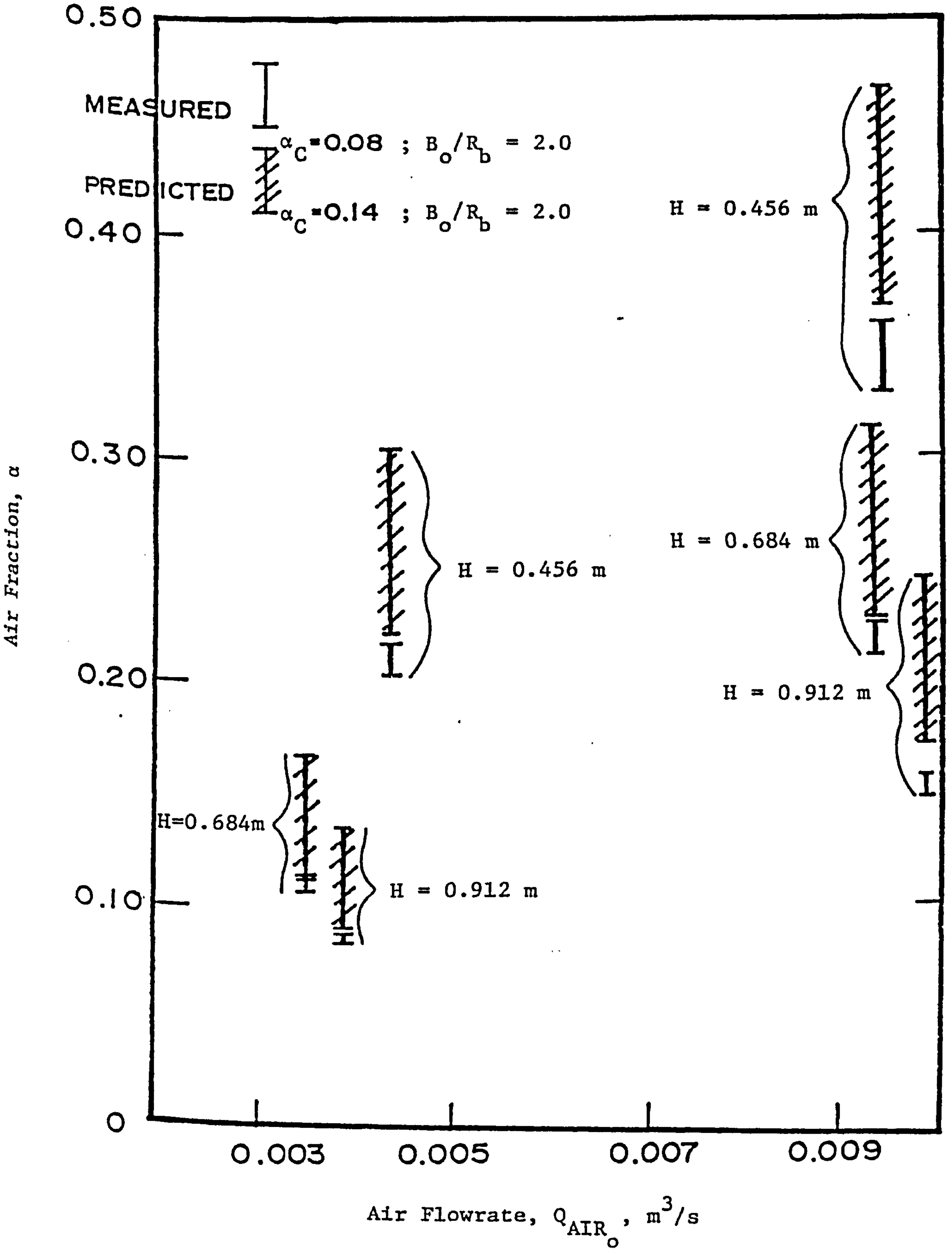

Fig. 7.8 Comparison of Measured and Predicted Air Fractions

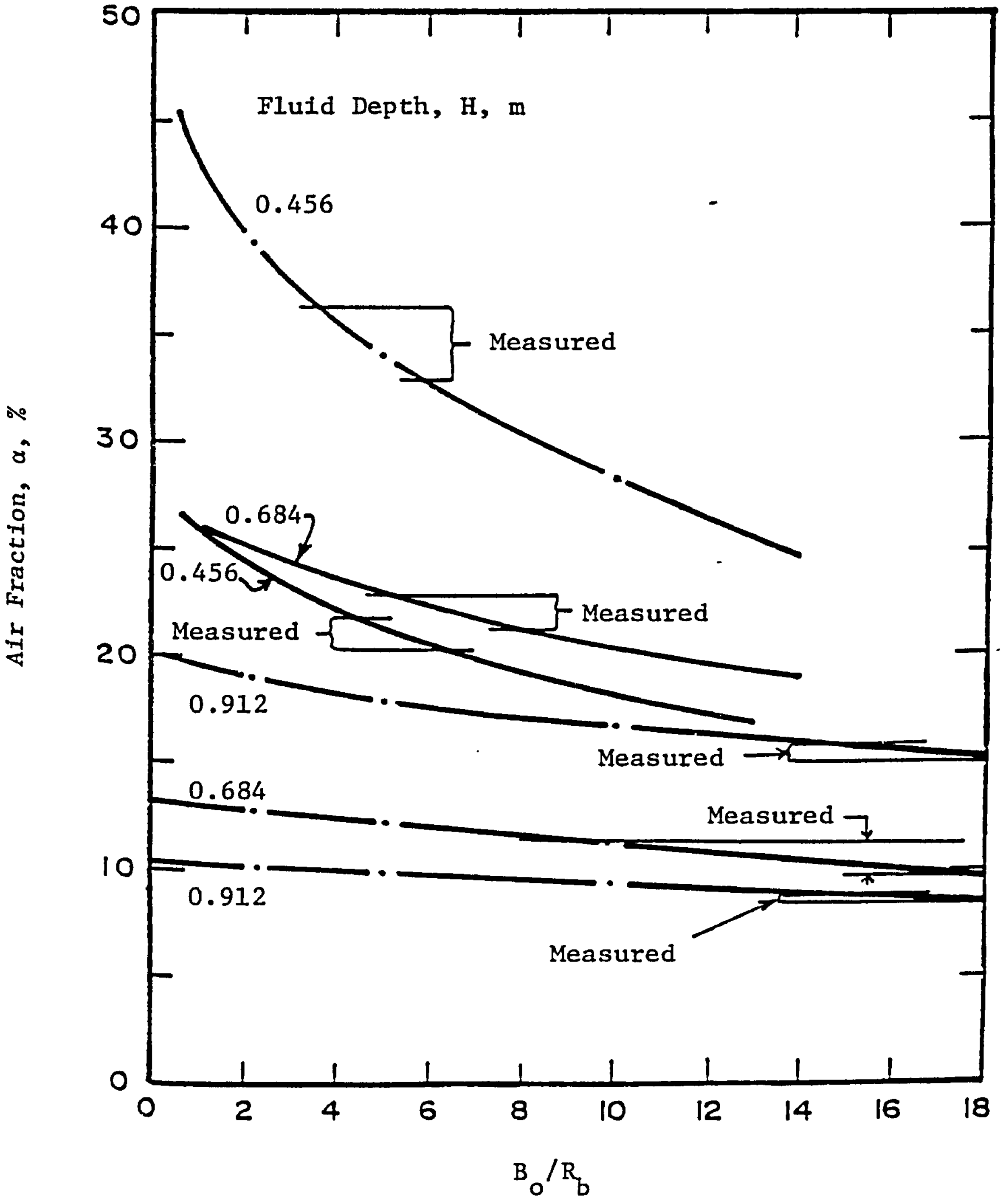

Fig. 7.9 Sensitivity to the B_o/R_b Ratio

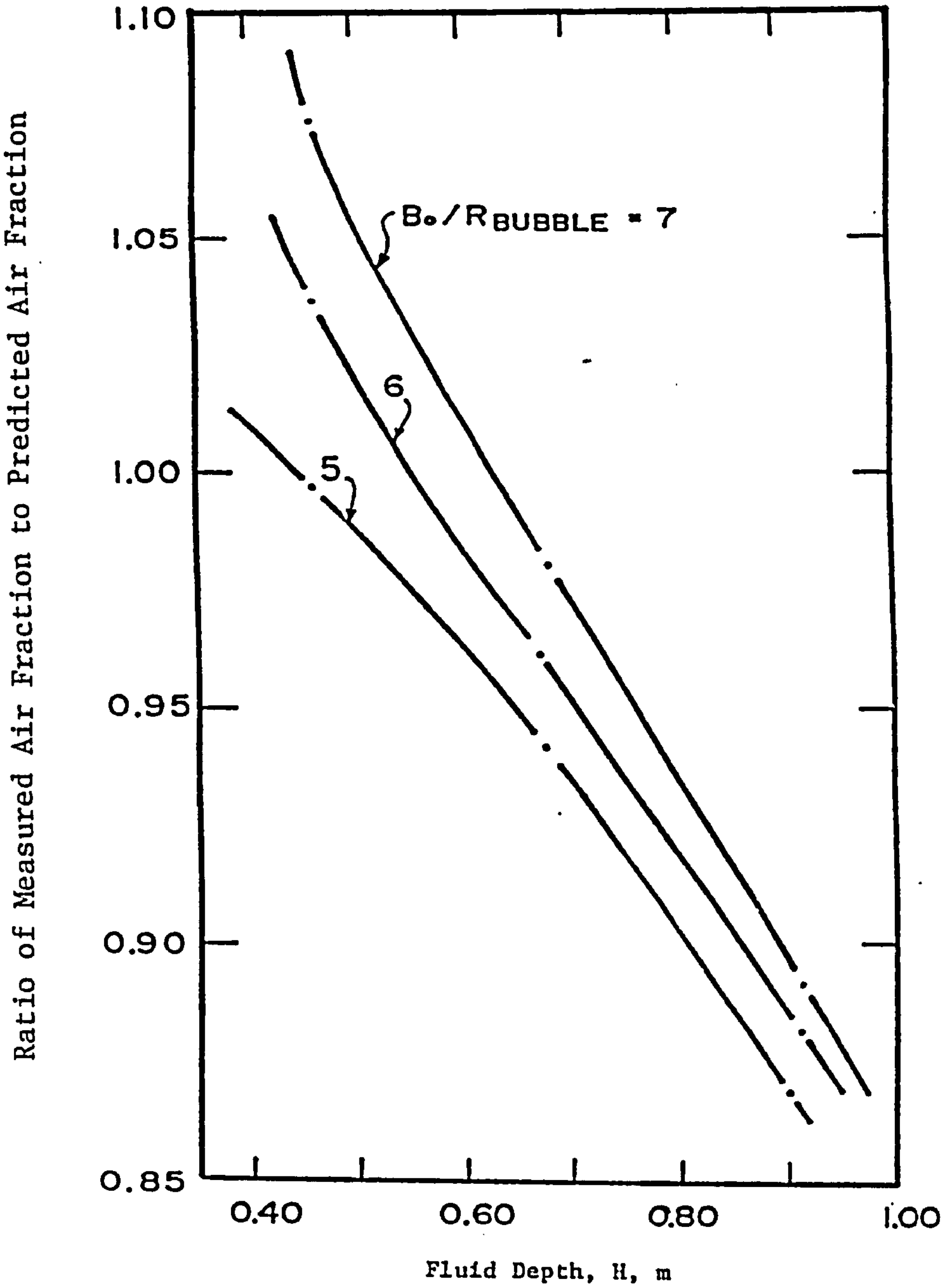

Fig. 7.10 Sensitivity to the B_o/R_b Ratio

7.3 Calibration of the Friction Factors, f

In order to estimate the friction factor of the acrylic floor of the wet well, the velocity profiles obtained from Test Series 9 were used in conjunction with Eq. [6.1]. Since the condition of the bed was not known, i.e. whether smooth or rough, calculations for the bed shear stress were carried out assuming both smooth and rough bed conditions. For the smooth bed case, $30h/k_S$ in Eq. [6.1] was replaced by $9yU_*/\nu_f$ which is Prandtl's constant of integration for flows over smooth walls. For the rough wall case, or quasi-rough wall case, the sand roughness, k_S, was replaced by the thickness of the laminar boundary sublayer

[7.7] $k_S = \delta = 11.6\ \nu_f/U_*$

This provided for an upper limit for the estimation of the shear stress. The difference between the static and dynamic pressures in Eq. [6.1] was replaced with the product of the velocity head and the unit weight of the fluid

[7.8] $P_{ST} - P_o = v_b^2\ \gamma_f/(2g)$

where v_b is the point velocity measured at a distance y above the bed. In all cases, the velocity closest to the bed was measured at y = 0.003 m. Once the boundary shear stress was obtained from the modified form of Eq. [6.1], the friction factor was calculated from

[7.9] $f = 8\ \tau_b/\rho_f v_b^2$

The results of the friction factor calculations for the nine velocity profiles measured in Test Series 9 are given in Table 7.2. The default calibration value for the friction factor was selected as the

Table 7.2 Friction Factor Calculations

Bed Condition	Mean Value for Friction Factor	Standard Deviation	Number of Samples
Smooth	0.023	0.0074	9
Quasi-rough	0.035	0.0109	9
Smooth and Quasi-rough Data Combined	0.029	0.0107	18

mean of the quasi-rough and smooth bed conditions, $f = 0.029$. In the model, the bed conditions were considered to be smooth except for the case when deposited sediments were on the floor.

Using the Moody friction factor diagram, the minimum Reynolds number for fully-turbulent, rough flow, with $f \simeq 0.029$ is approximately 2.7×10^5. If the Reynolds number is defined as a function of the velocity adjacent to the sump floor, v_b, and the total depth, H, i.e.

$$N_R = v_b H/\nu_f \qquad [7.10]$$

then no correction for the friction factor is required if the prototype Reynolds number exceeds 2.7×10^5, since f is no longer a function of N_R. The prototype Reynolds number and relative roughness may increase or decrease the friction factor to be used in the numerical model.

7.4 Sensitivity of the System Dynamics to the Centre of Rotation

The total angular momentum, and kinetic energy of the system were calculated for a specific location of the centre of rotation. In order to investigate the sensitivity of the system dynamics to the location of the centre of rotation, the coordinates of the centre of rotation $(\bar{X}, \bar{Y})$, were changed and the kinetic energy and angular momentum were recalculated for the same air flowrate, pumping rate, depth and floor slope. The change in coordinates were made in steps of 10% of the length x, and 10% of the depth y.

The angular momentum of the system was calculated from

[7.11] $AM = \rho_f \int \underset{\sim}{r} x \underset{\sim}{v}\, d\forall$

where AM is the total angular momentum and

[7.12] $\underset{\sim}{r} x \underset{\sim}{v} = (r)(v_t)$, and

[7.13] $d\forall = r(d\theta)(dr)(W)$

where v_t is the tangential velocity of the flow at a distance r from the centre of rotation. The term r(dθ)(dr)(W) represents an incremental volume of the fluid at a distance r from the centre of rotation. The integration of Eq. [7.11] was carried out over the same 15 elements that were used for the determination of the side wall shear as discussed in Chapter 4.5.6. For volume elements in which both plug flow and solid body rotation apply, the integration of Eq. [7.11] yields

[7.14] $AM_{element} = \rho_f\ W\ \Delta\theta\ v_{t_{r_1}}\ \{r_2{}^3/3 - r_1{}^3/12\}$

For elements in which only solid body rotation applies, integration of Eq. [7.11] yields

[7.15] $AM_{element} = \rho_f\ W\ \Delta\theta\ v_{t_{r_1}}\ (r_1{}^3/4)$

The following parameters were held constant during the angular momentum and kinetic energy sensitivity calculations

(a) $R_b = 0.005$ m

(b) H = 0.912 m (H/D = 8)

(c) $B_o/R_b = 6.0$

(d) $\alpha_C = 0.12$

(e) $\theta = 30^o$

(f) $Q_{AIR_o} = 0.015 \text{ m}^3/\text{s}$

(g) $Q_p = 0.010 \text{ m}^3/\text{s}$, and

(h) $f = 0.029$

The sensitivity to the angular momentum is shown in Fig. 7.11. The numbers are non-dimensionalized by dividing with the angular momentum of the reference centre of rotation. The coordinates of the reference centre of rotation are given by the calibration Eqs [6.10] and [6.11]. The angular momentum increases as the y component of the centre of rotation increases, and conversely, decreases as the y component decreases. There appears to be little change along any line of constant y component of the centre of rotation.

The kinetic energy of an incremental fluid volume with a uniform velocity is given by

[7.16] $$KE = \frac{1}{2} m_f v^2$$

where KE is the kinetic energy of a mass of fluid, m_f, flowing with a uniform velocity v. For a small element of fluid, Eq. [7.16] can be expressed as

[7.17] $$KE_{element} = 0.5 \rho_f W \Delta\theta \int (v_t^2 + v_r^2) r dr$$

where $r(dr)(\Delta\theta)W$ represents an incremental volume and v_t and v_r are the tangential and radial components of the mean velocity v. Integration of Eq. [7.17], similar to the integration of the angular momentum, will yield equations for the same 15 elements used in the calculation of the side wall shear stress. For elements with both plug flow and solid body rotation, integration yields

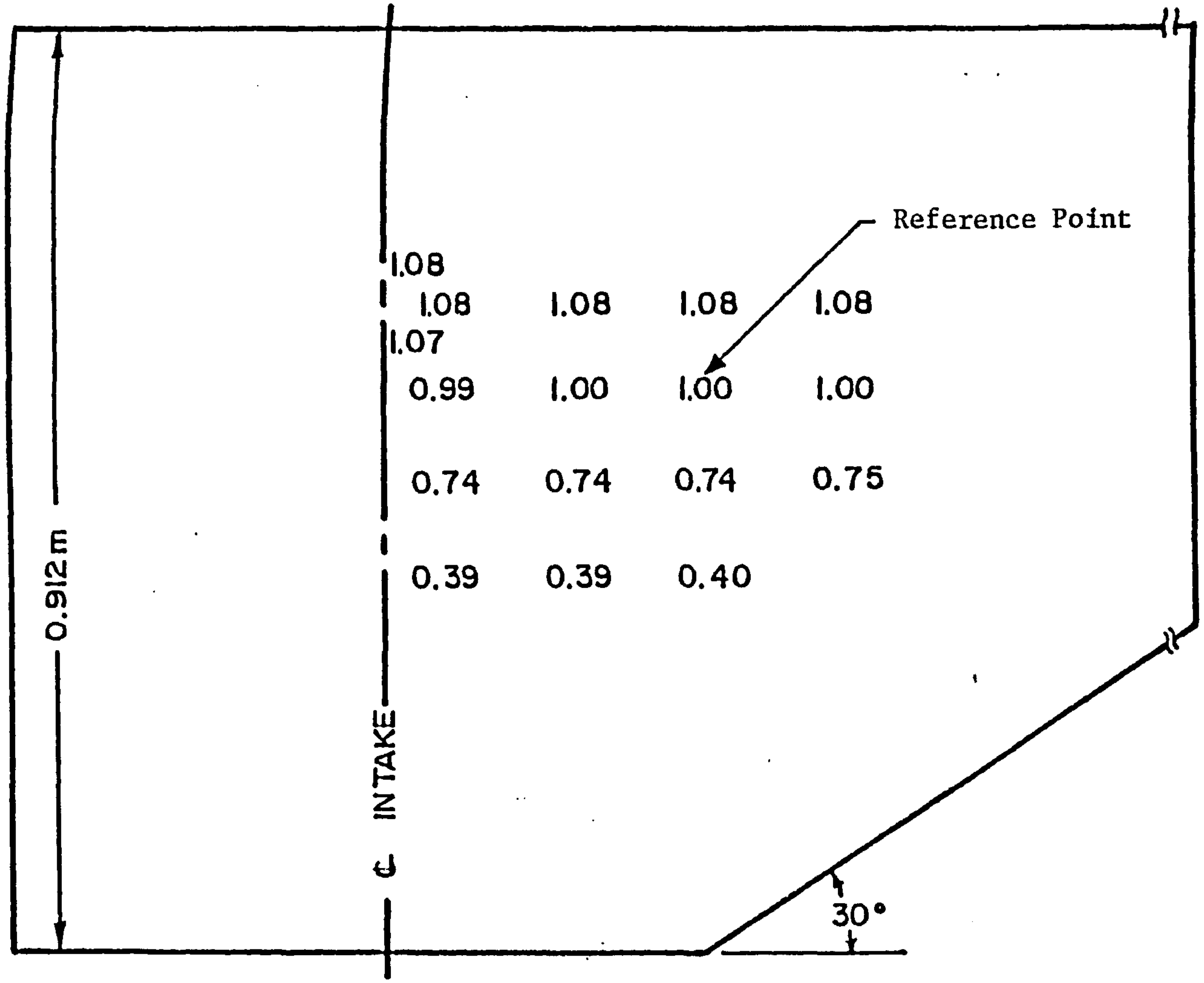
Reference Point
1.08
1.08 1.08 1.08 1.08
1.07
0.99 1.00 1.00 1.00
0.74 0.74 0.74 0.75
0.39 0.39 0.40
0.912 m
℄ INTAKE
30°

Fig. 7.11 Sensitivity to Angular Momentum
(angular momentum of reference point = 103.02 Nms)

$$[7.18] \qquad KE_{element} = \frac{1}{4}\, \rho_f\, W\, \Delta\theta (v_{t_{r_2}}^{\;2}/(\cos\phi)^2)(r_2^{\,2} - \frac{1}{2}\, r_1^{\,2})$$

where ϕ is the angle between the tangential and mean velocity vectors. For elements with solid body rotation only

$$[7.19] \qquad KE_{element} = \frac{1}{8}\, \rho_f\, W\, \Delta\theta\, v_1^{\,2}\, r_1^{\,2}$$

Figure 7.12 shows the dimensionless kinetic energy ratios obtained. As in the case of the angular momentum ratios, the kinetic energy increases with distance above the bed. The kinetic energy also appears to be more sensitive to the x coordinate of the centre of rotation than does the angular momentum. As the x coordinate increases, the kinetic energy of the system increases. The calculations for the angular momentum and kinetic energy of the system were made to investigate if, under given operating conditions, the location of the centre of rotation corresponded to the minimum kinetic energy and/or angular momentum. It appears from Figs. 7.11 and 7.12 that it is not true. The angular momentum appears to increase along a line from the centre of rotation to the upper left hand corner of the sump, whereas minimum kinetic energy appears to be on a line from the centre of rotation to the lower left hand corner, near the diffuser. Both of the lines along which minimization or maximization occur are large radial distances from the centre of rotation, and these large radial distances control the solution of Eqs. [7.14], [7.15], [7.18] and [7.19].

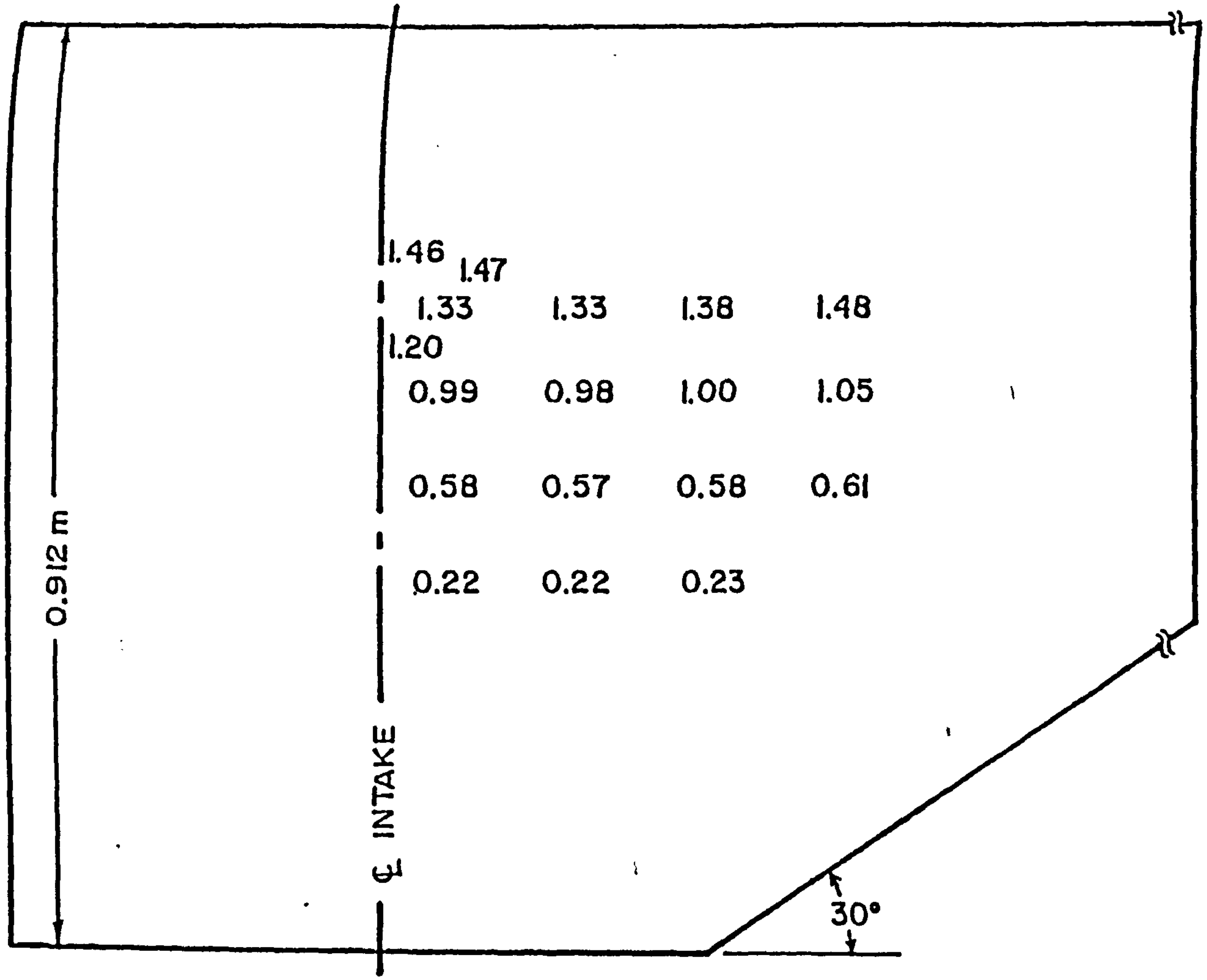
1.46
1.47
1.33 1.33 1.38 1.48
1.20
0.99 0.98 1.00 1.05
0.58 0.57 0.58 0.61
0.22 0.22 0.23
0.912 m
℄ INTAKE
30°

Fig. 7.12 Sensitivity to Kinetic Energy
(kinetic energy of reference point = 50.48 J)

The variations in the shear stress on the horizontal and inclined portions of the wet well floor are shown in Fig. 7.13 and Fig. 7.14, respectively. Figure 7.13 shows that at any point of constant y, the shear stress on the horizontal plane is constant. This is expected since the flow passing below the centre of rotation is constant, and the velocity component parallel to the floor varies inversely with the radial distance to the centre of the floor.

The variation in the shear stress on the inclined part of the wet well floor is not as consistent as the shear stress on the horizontal portion of the floor, as shown in Fig. 7.14. Iso-shear stress lines indicate

(a) for a constant y, the shear stress increases as the x coordinate of the centre of rotation increases, and

(b) for a constant x coordinate, the maximum shear stress decreases as the y coordinate increases or decreases with respect to the default, measured location of the centre of rotation.

Figures 7.13 and 7.14 do not illustrate the exact shear stress experienced by the wet well floor, because each different location for the centre of rotation is the result of a unique air flowrate and pumping rate. The data presented are based on a constant air flowrate and pumping rate for all of the locations shown. It can be concluded from Figs. 7.13 and 7.14 that:

(a) the shear stress exerted on the wet well floor varied with location of the centre of rotation

(b) a 10% change in either the $\bar{Y}$ coordinate or the $\bar{X}$ coordinate had significantly more than 10% effect on the magnitude of the shear stress developed, and

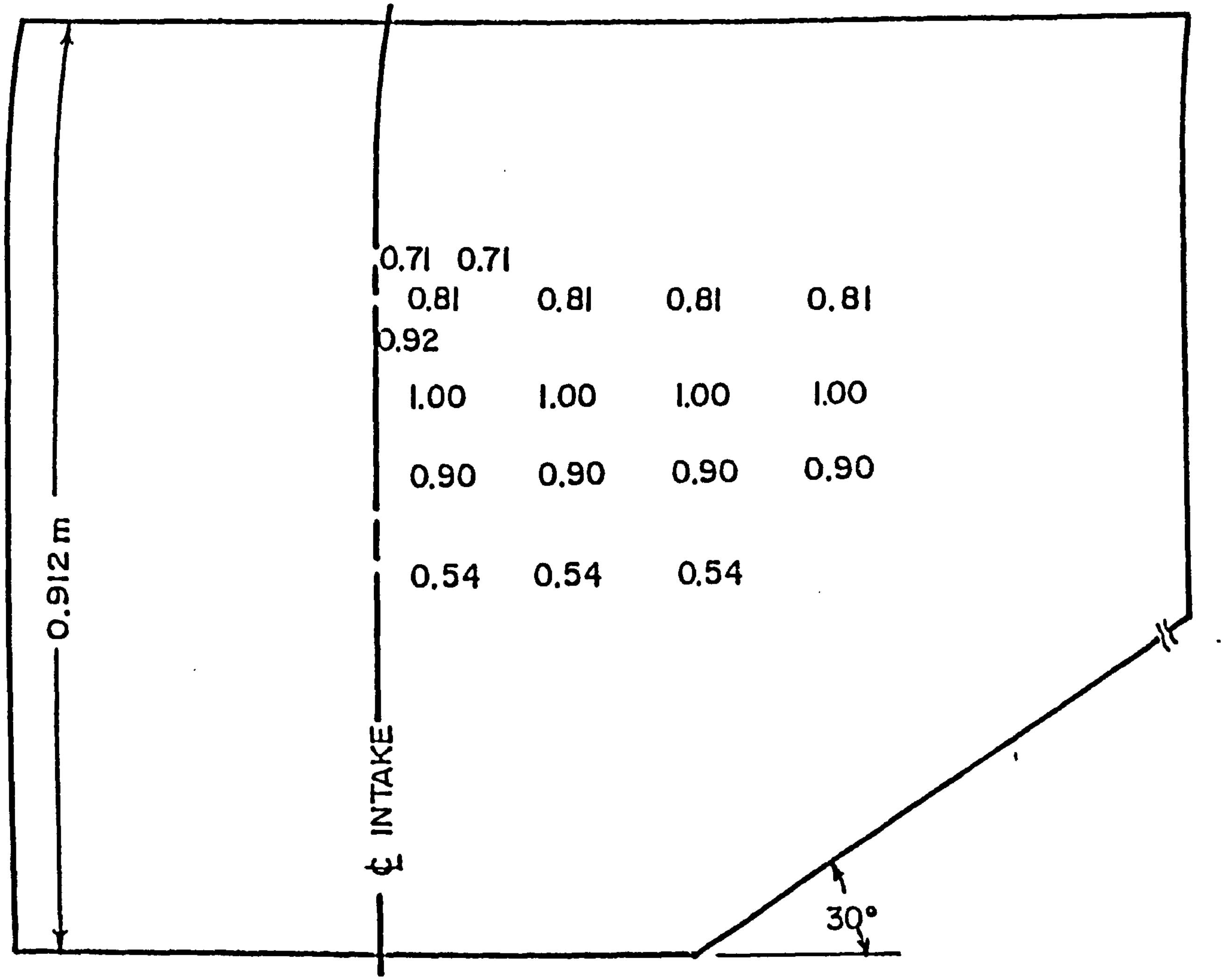
0.71 0.71
0.81 0.81 0.81 0.81
0.92
1.00 1.00 1.00 1.00
0.90 0.90 0.90 0.90
0.54 0.54 0.54
0.912 m
℄ INTAKE
30°

Fig. 7.13 Dimensionless Shear Stress on Horizontal Portion of Wet Well Floor (shear stress associated with reference point = 0.60 N/m^2)

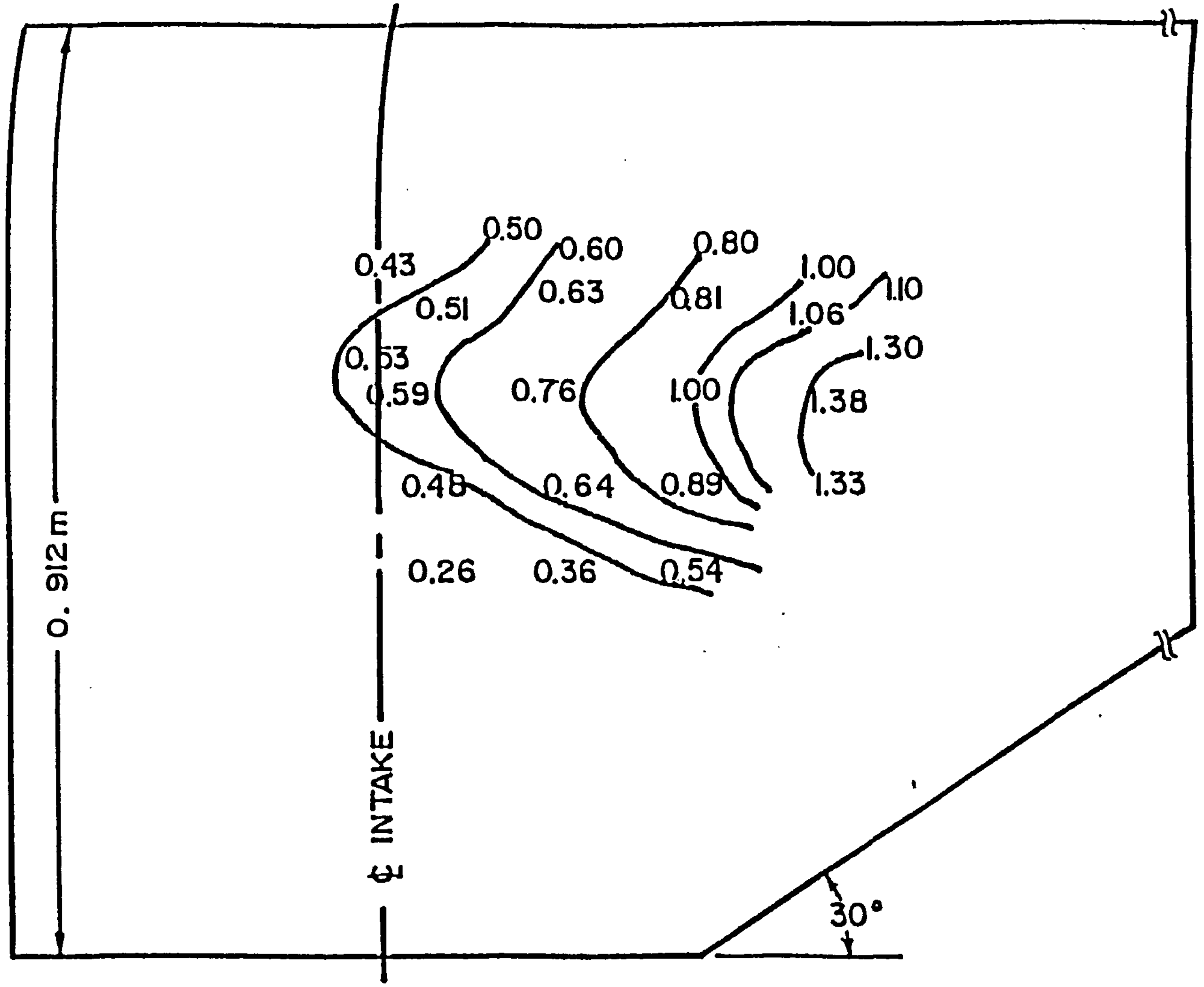
0.43
0.50
0.60
0.80
1.00
1.10
0.51
0.63
0.81
1.06
1.30
0.53
0.59
0.76
1.00
1.38
0.48
0.64
0.89
1.33
0.26
0.36
0.54
0.912 m
℄ INTAKE
30°

Fig. 7.14 Dimensionless Shear Stress on Inclined Portion of Wet Well Floor (shear stress associated with reference point = 0.79 N/m^2)

(c) changes in sump geometry or operating conditions showed greater effects on the shear stress on the inclined portion of the wet well floor than on the horizontal portion.

7.5 Additional Correlation Parameters

After adjusting the diffuser plume variables, R_b, B_o/R_b and α_c, it was observed that the numerical program still did not converge in "one-pass". Convergence was assumed to be satisfied when the driving torques and the resisting torques in the angular momentum equation for the system were within 1% of each other. After one pass of the numerical program, the applied torques generally exceeded the resisting torques, i.e. the resisting forces were being underestimated. All of the terms in the angular momentum equation were subsequently re-examined to determine where deficiencies in the approach or assumptions, could have occurred. The following corrections were subsequently applied:

(a) The friction factor for the rear wall of the sump, adjacent to the diffuser, was increased from 0.029 to 0.035 to account for higher friction which would be generated between the wall and the highly turbulent air/water plume.

(b) The drag coefficient on the upper quarter of the pump columns was increased by 20% and the jet velocity, v_j, was used as an impact velocity over the same area. The jet velocity was increased further by dividing with $(1 - \alpha)$ where α is the air fraction of the uppermost plume element. These corrections account for the higher drag force due to:

  (i) surging of the flow near the surface and adjacent to the pump columns

  (ii) uncertainties due to the effect of the air on C_d

  (iii) non-uniformities in the impact velocity profile

  (iv) constriction and side wall effects, and

  (v) wave resistance effects.

(c) The predicted rise in the free surface above the diffuser was adjusted by dividing with $(1 - \alpha)$ to account for the uncertainties due to air fraction, and air fraction distribution, and also to bring the predicted rise in the free surface into line with the observed rise. The observed rise was correlated to other variables as given below

$$[7.20] \quad \Delta H = H(0.033 + 7.816 Q_{AIR_o} / (H^{2.5} g^{0.5}) + \ldots$$
$$1.197 \times 10^{-8} (H^{1.5} g^{0.5} / \nu))$$

The correlation coefficient for Eq. [7.20] was 0.940.

(d) The predicted shear stress on the horizontal and inclined portions of the wet well floor was increased by 10% to account for surface roughness and turbulence effects.

(e) All other corrections were applied to the torque due to the weight of the fluid which was displaced above the free surface due to the momentum of the plume, as shown in Fig. 4.10. The torque, $T_{\Delta m}$ was multiplied with a correction factor C_f. The range and use of the C_f correction factor factor are discussed in the next subsection.

7.6 C_f, Final Calibration

Several uncertainties exist in the theory and these uncertainties resulted in calibration error. Assuming that the physical measurements introduced no calibration error, a correction factor, C_f, was introduced and applied to the term $T_{\Delta m}$ in the angular momentum equation. This parameter accounted for discrepencies due to:

(a) assuming uniform air fraction and water velocity distributions within the plume,

(b) uncertainties about the forces generated when the plume reached the free surface and turned through a 90° angle to spread out horizontally,

(c) the effect of air fraction on the drag force generated by the pump columns,

(d) forces generated at the point of interaction between the air induced circulating flow and the incoming sump flow,

(e) neglecting the effect of sediment concentration on fluid velocities and fluid properties,

(f) errors in the assumed hydrostatic force distributions, particularly on the rear wall adjacent to the diffuser plume and on the floor of the sump directly below the plume, and

(g) drag on the diffuser.

The above mentioned points indicate that the major uncertainties with respect to the numerical model are generally related to the plume characteristics. Therefore, the correction factor C_f was applied to the term $T_{\Delta m}$.

In order to establish the range of C_f values, the numerical program was executed 81 times under different test conditions. The resulting C_f values that provided equilibrium between the driving and resisting torques were recorded. The range of test conditions was made as large as possible so that all possible operating conditions were analyzed. Table 7.3 gives the range of variables and constants for which C_f values were determined. Figures 7.15, 7.16 and 7.17 show the range of C_f values obtained for H/D ratios of 4, 6 and 8, respectively. Two distinct trends are noticed in the data:

(a) the general shape of the curves is parabolic, i.e. as the air number increases, C_f increases to some maximum, then decreases with continued increase in N_{AIR}, and

(b) for a specific pumping number, N_p, as θ increases, C_f decreases to some minimum C_f, then continues to increase.

The following correlation equation was developed between C_f and other variables:

Table 7.3 Range of Variables for C_f Determination

Variable	Range
Floor Slope (degrees)	0, 15, 30, 40, 45
Air Number, $N_{AIR} = Q_{AIR_o}/(H^{5/2}g^{1/2})$	0.00020 to 0.03411
Pumping Number, $N_p = Q_p/(H^{5/2}g^{1/2})$	0.00 to 0.02274
Wet Well Length to Depth Ratio, L/H	1.580, 2.107, 3.160
Depth Ratio, H/D	4, 6, 8
B_o/R_b	6.0
α_C	0.12
R_b	0.005 m
Width Ratio, W/L	0.475

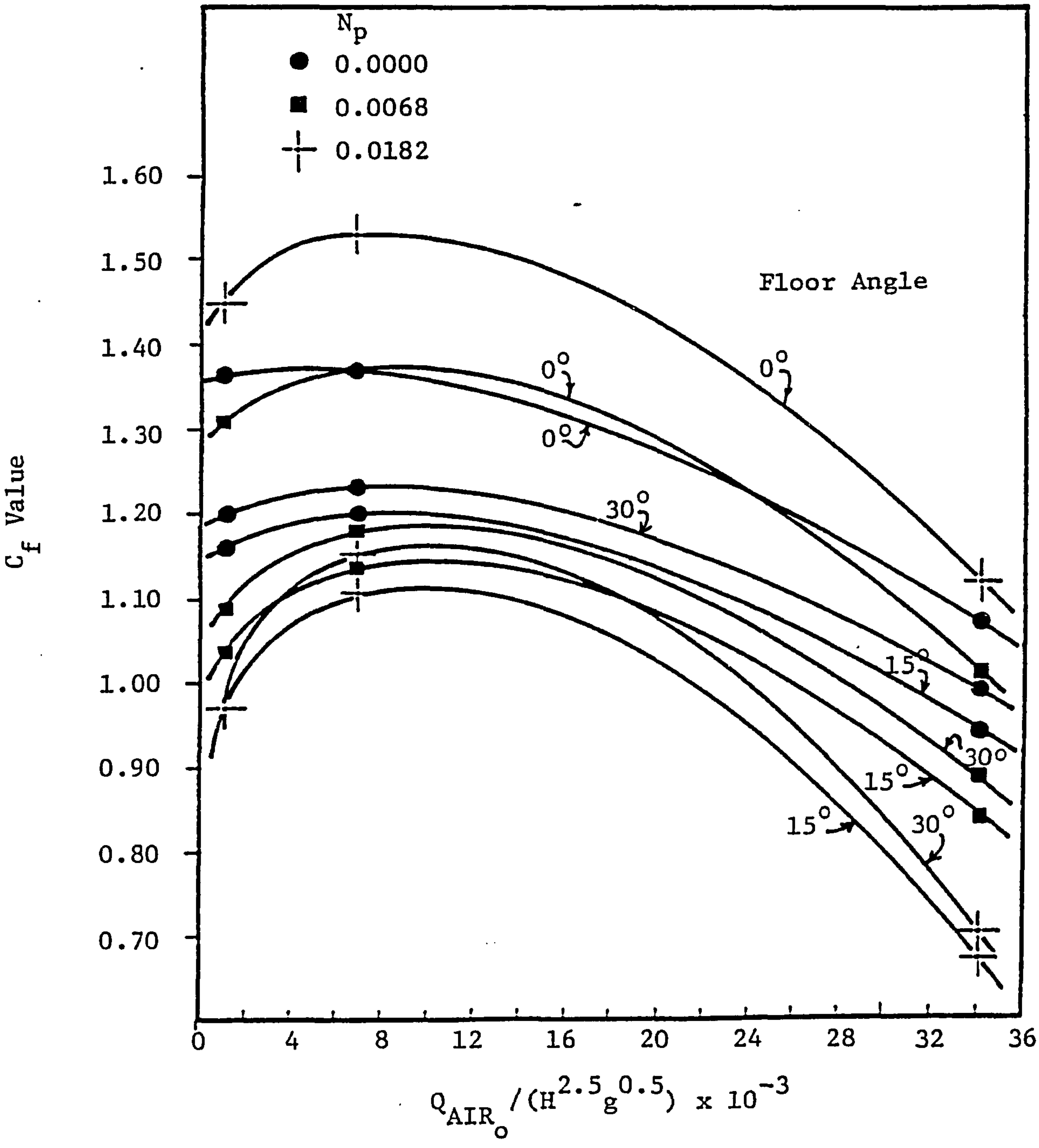

Fig. 7.15 C_f Value Predicted from Numerical Model for L/H = 3.160 and H/D = 4.0

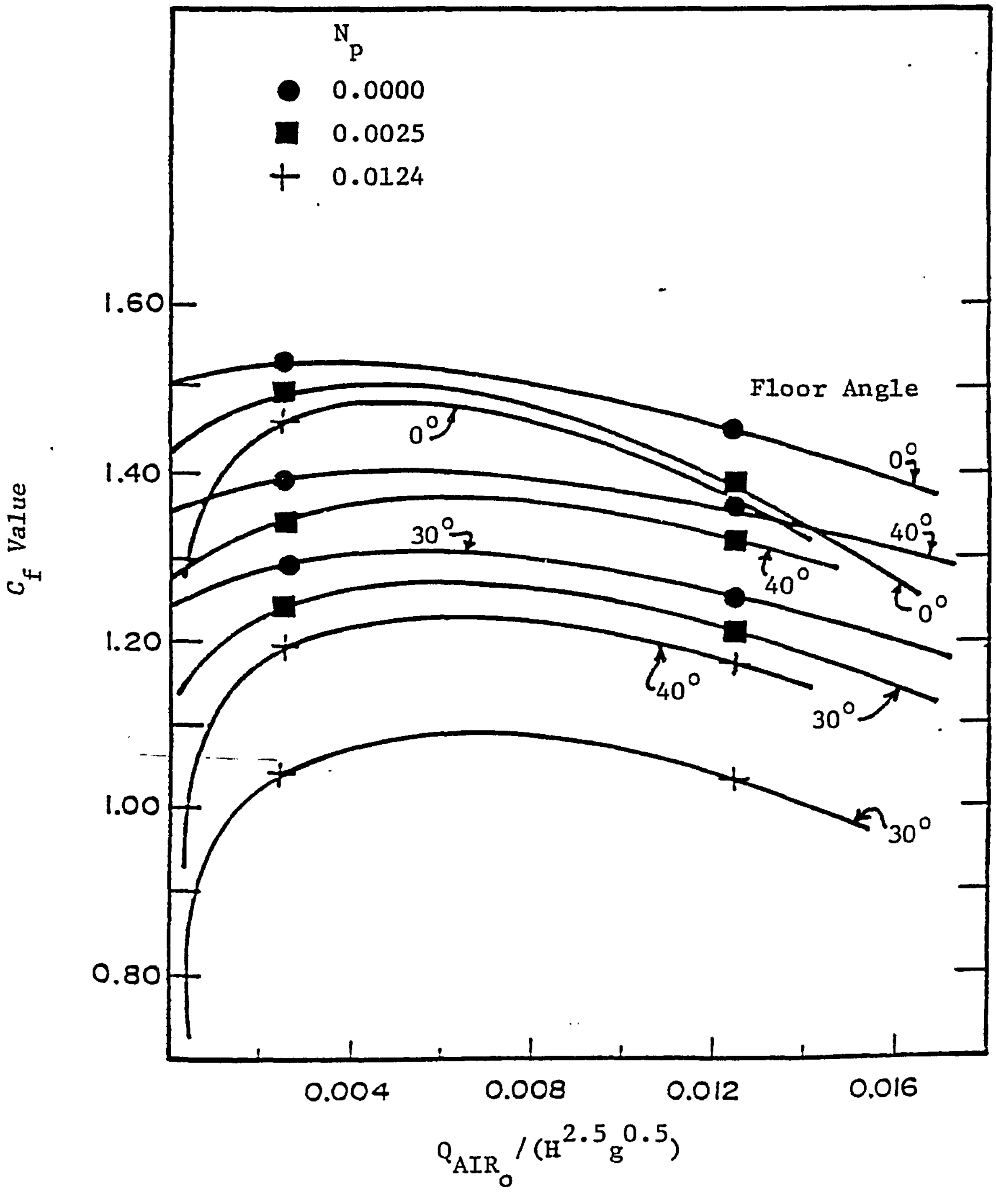

Fig. 7.16 C_f Value Predicted from Numerical Model for $L/H = 2.107$ and $H/D = 6.0$

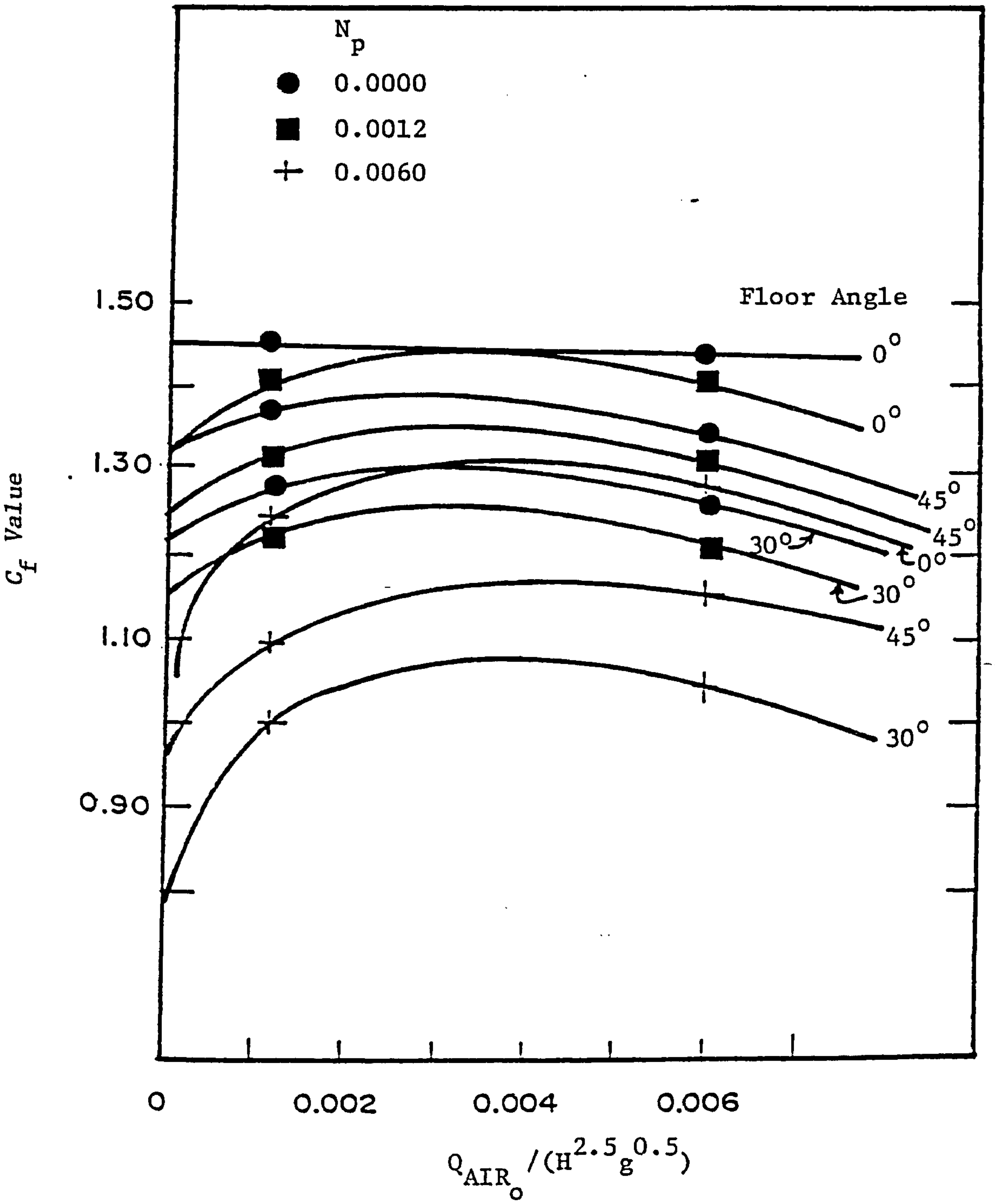

Fig. 7.17 C_f Value Predicted from Numerical Model for L/H = 1.580 and H/D = 8.0

[7.21] $$C_f = C_{f_o} + A(1 + B\pi_2\pi_6 + C\pi_2{}^2\pi_6)(1 - e^{D\pi 1} + Ee^{-F\pi 1}) \ldots (\pi_3{}^G + H)(\pi_6 I)$$

where:

C_{f_o} = 1.705

A = -1.477

B = -11.40

C = 450.0

D = -0.18

E = 0.73

F = 0.04

G = 0.48

H = 0.28

I = -0.08, and

π_1, π_2, π_3 and π_6 are dimensionless variables given by

[7.22] $\pi_1 = \theta$, inclined floor angle, degrees

[7.23] $\pi_2 = N_{AIR} = Q_{AIR_o}/(H^{5/2}g^{1/2})$

[7.24] $\pi_3 = N_p = Q_p/(H^{5/2}g^{1/2})$

[7.25] $\pi_6 = L/H$

The correlation coefficient for Eq. [7.21] was 0.888 and the observed mean value of C_f was 1.21.

7.7 Comments on the Magnitudes of Various Terms in the Angular Momentum Equation

The relative magnitudes of various terms which make up the balance in angular momentum are given in Tables 7.4 and 7.5. For the

Table 7.4 Magnitudes of Angular Momentum Terms

Resisting Torques		Value (Nm)	%
Shear Stress on Inclined Part of Wet Well Floor		0.042	0.21
Shear Stress on Horizontal Part of Wet Well Floor		0.033	0.16
Shear Stress on Rear Wall		0.714	3.60
Pump Column Drag		1.388	7.00
Side Wall Shear Stress		0.050	0.25
ΔF		0.146	0.74
$T_{\Delta m}$		15.225	76.84
ΔP_B		1.575	7.95
Angular Momentum Crossing System Boundary		0.641	3.24
	Σ	19.814	99.99

Table 7.5 Magnitudes of Angular Momentum Terms

Driving Torques		Value (Nm)	%
Hydrodynamic Bubble Force		18.157	92.08
ΔP_2		1.562	7.92
	Σ	19.719	100.00

following test conditions, Table 7.4 shows the values of the resisting torque terms, whereas Table 7.5 shows the values of the driving torque terms.

$H/D = 6$

$L/H = 2.107$

$W/L = 0.475$

$\theta = 30^{\circ}$

$N_{AIR} = 0.00248$

$N_p = 0.00248$

$B_o/R_b = 6.0$

$\alpha_C = 0.12$

$R_b = 0.005$ m

The hydrostatic torque due to the weight of water above the free surface as a result of the momentum of the plume, $T_{\Delta m}$, constitutes approximately 77% of the resisting torque. The total resisting shear from all sump boundaries, floor, side wall and rear wall, constitutes 4.22%, and pump column drag, 7%. Hydrostatic forces, ΔF, $T_{\Delta m}$ and ΔP_B account for 85.53% of all the resistance. Torque due to the net flow of angular momentum across the system boundaries is 3.24%. The significance of the C_f correction factor becomes very apparent when the contribution of each resisting force is considered with respect to the total resisting torque.

The hydrostatic bubble forces constitute approximately 92% of the driving torque in the system. The other 8% is supplied by the hydrostatic force created by the rise in the free surface, ΔH.

7.8 Momentum Correction Factors

During the formulation of the angular momentum equation, the momentum correction factor appears in the linear momentum balance, which is used to estimate the force required to redirect the circulating flow, ΔF. Using the experimental velocity profiles obtained in Test Series 9, it was possible to estimate momentum correction factors for flows both above and below the centre of rotation. The general definition of the momentum correction factor is

[7.26] $$\beta = \int v^2 \, dA / V^2 A$$

where v is the velocity of an element with a flow area of dA, and V is the mean velocity passing through the total flow area A. For discrete flow areas, Eq. [7.26] may be expressed as

[7.27] $$\beta = \sum_{i=1}^{n} v_i^2 A_i / V^2 A$$

where n is the number of discrete fluid tubes. The velocity profiles were discretized into 14, 20 and 21 vertical strips for H/D ratios of 4, 6 and 8 respectively and used in Eq. [7.27]. Correlation equations were derived for the flow areas above and below the centre of rotation, using different dimensionless variables. The equations given below resulted in the highest correlation coefficients. For the flow area above the centre of rotation

[7.28] $$\beta_{TOP} = 1.922 + 6.167N_s - 5.341N_j - 0.997N_H$$

For the flow area below the centre of rotation

[7.29] $$\beta_{BOT} = 1.135 + 15.249N_{AIR} + 0.000699N_\theta \ldots$$
$$-3.204N_b - 0.548N_{BB} + 0.461N_H + 5.891 \times 10^{-8}N_\nu$$

where the dimensionless numbers are described in the Nomenclature. The correlation coefficients for Eqs. [7.28] and [7.29] were 0.867 and 0.941 respectively. The ranges for β_{TOP} and β_{BOT}, obtained from Test Series 9, were

[7.30] $1.17 < \beta_{TOP} < 1.68$, and

[7.31] $1.04 < \beta_{BOT} < 1.25$

Table 7.6 gives the equations for the momentum correction factors for the default velocity profiles as shown in Fig. 6.19. Both the experimental and observed momentum correction factors, as predicted by Eqs. [7.28], [7.29] and from Table 7.6, were calculated in the program. The sensitivity of the momentum correction factor to changes in various design parameters is discussed in Section 7.9.

7.9 Closure on Sensitivity

The general sensitivity trends are summarized in Table 7.7. Based upon all of the numerical runs, the sensitivity of a parameter was judged to be of relatively low sensitivity, medium sensitivity, high sensitivity or no effect. The changes in the numerical values for the parameter are also recorded in this table. The β_{TOP} and β_{BOT} ratios are the ratios of the momentum correction factor for the default velocity profile to the momentum correction factor based on the observed velocity profiles. Figures 7.18 and 7.19 show how β_{TOP} and β_{BOT} were affected by changes in the entrainment coefficient and the pump column drag coefficient. The assumed velocity profile generally underestimated the momentum correction factor for the flow passing above the centre

Table 7.6 Calculation of Momentum Correction Factors

$\beta_{TOP} = \{A + B + (C)(D)(E) + F^2/G\}/H$

where:

$A = R_1 v_j^2/3$

$B = (v_{SURFACE} - v_j)^2(R_2^3 - R_1^3)/\{3(R_2 - R_1)^2\}$

$C = (v_{SURFACE} - v_j)/(R_2 - R_1)^2$

$D = v_j R_2 - v_{SURFACE} R_1$

$E = R_2^2 - R_1^2$

$F = v_j R_2 - v_{SURFACE} R_1$

$G = R_2 - R_1$

$H = V^2 R_2$

$R_1 = AA - H$

$R_2 = H - YCR$

$V = 0.5 v_j + v_{SURFACE} (H - AA)/\{2(H - YCR)\}$

$\beta_{BOT} = (A + B)/C$

where:

$A = v_b^2 R_1/3$

$B = v_b^2 (R_2 - R_1)$

$C = V^2 R_2$

$R_1 = YCR - BB$

$R_2 = YCR$

$V = v_b (BB + YCR)/(2YCR)$

Table 7.7 Overall Sensitivity Trends[1,2]

Variable \ Parameter	Surface Air Fraction	ΔB/H	τ_h	τ_i	$v_{SURFACE}$	v_J	β_{TOP} Ratio	β_{BOT} Ratio
Bubble Radius, R_b	V decr.	V decr.	L decr.	L decr.	L decr.	L decr.	L decr.	L incr.
B_o/R_b	V decr.	V decr.	M decr.	M decr.	M decr.	M decr.	L decr.	L incr.
α_C	V decr.	V incr.	V decr.	V decr.	V decr.	V decr.	V decr.	V incr.
f	L incr.	N/C	V incr.	V incr.	M decr.	M decr.	L decr.	L incr.
Pump Column Drag Coefficient	N/C	N/C	V decr.	V decr.	V decr.	V decr.	V decr.	V incr.

[1] Trend is specified when the variable in the left hand column is increased.

[2] N/C denotes no change; L denotes low sensitivity; M denotes medium sensitivity; V denotes very sensitive; incr. means parameter value increases; decr. means parameter value decreases.

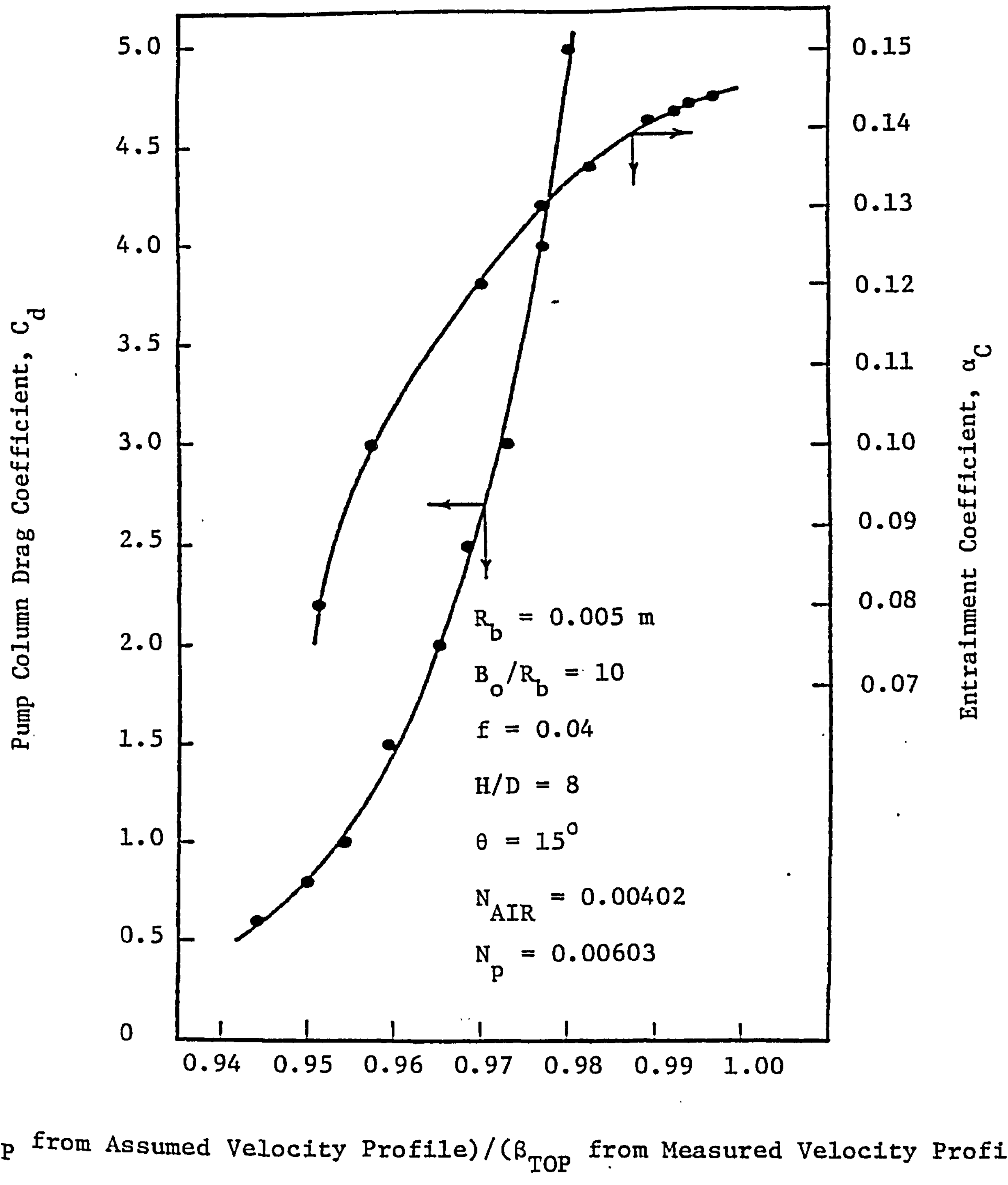

Fig. 7.18 β_{TOP} Ratios

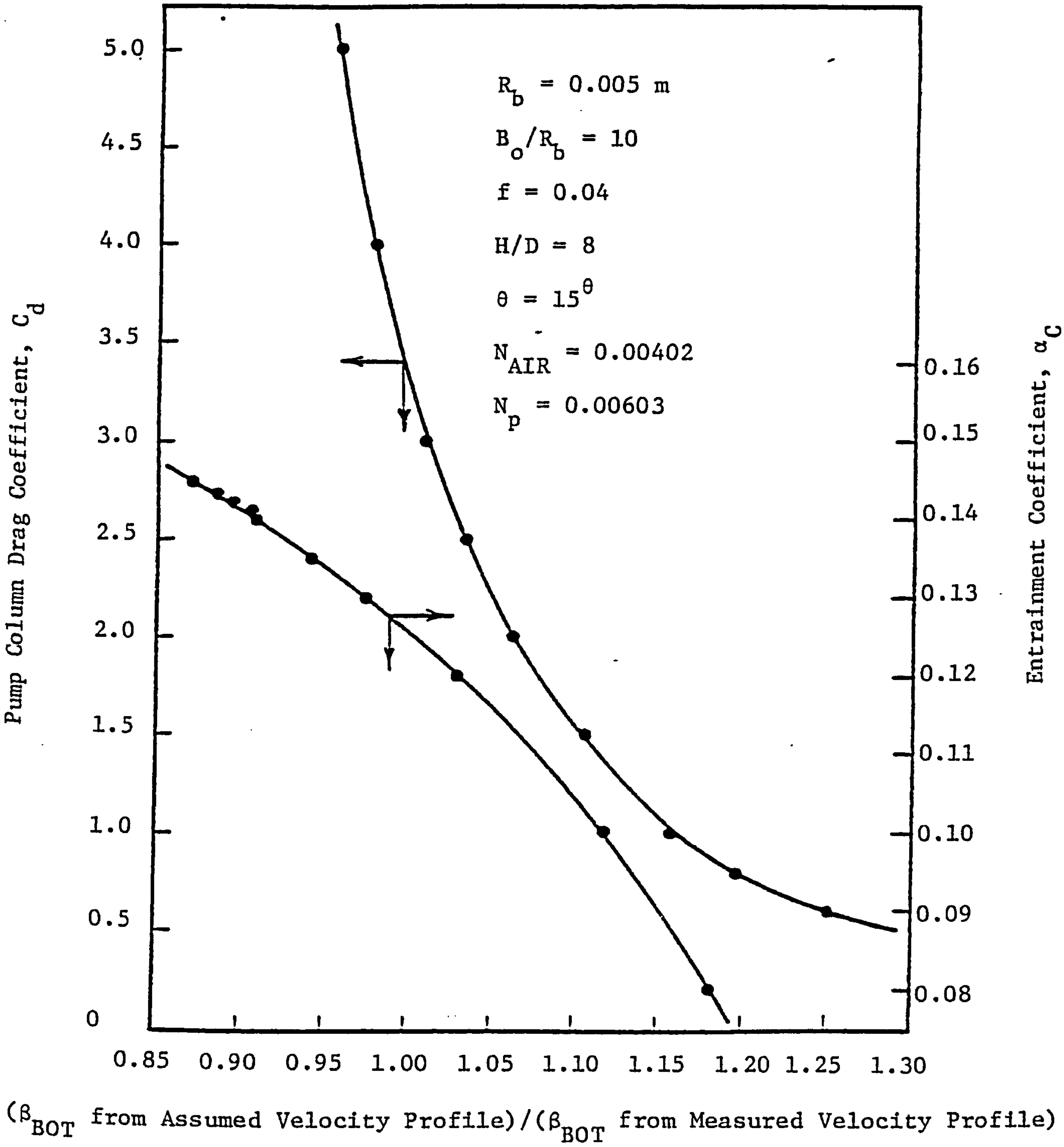

Fig. 7.19 β_{BOT} Ratios

of rotation, whereas the β_{BOT} ratio appears to be uniformly distributed within ± 20% of 1.0. The following ranges were observed for the range of test values given in Table 7.1.

[7.32] $0.944 < \beta_{TOP} \text{ Ratio} < 0.997$

[7.33] $0.871 < \beta_{BOT} \text{ Ratio} < 1.251$

The effect of a change in the momentum correction factor on the overall balance of angular momentum would be very small. The momentum correction factor is included in the ΔF force calculation, and it, as shown in Table 7.4, constitutes only 0.74% of the total resisting torque.

7.10 Range of Design Parameters

The ultimate goal of the numerical model was to prepare a general formulation of the aerated sump model so that a variety of design strategies could be tested without physical modelling of the system. In this subsection, graphs are prepared to generate a number of different sump operating conditions which will produce the necessary boundary shear stresses to scour, resuspend, or prevent the deposition of a specified particle. Application and design methodology will be discussed in Section 7.11.

Using the calibration values discussed in the previous subsections, the numerical program was used to determine the shear stresses produced on the horizontal and inclined portions of the wet well floor for a given floor angle, air flowrate, pumping rate and fluid depth. Design values were generated for the range of operating conditions shown in Table 7.3. Results are plotted in terms of useful dimensionless design parameters, as shown in Figures 7.20, 7.21, 7.22, 7.23, 7.24 and 7.25. The dimensionless design parameters are:

(a) floor slope

(b) air number

(c) pumping number, and

(d) length to depth ratio

When all the above parameters are specified or selected, the dimensionless shear stress number, τ_N, can be obtained from

[7.34] $\tau_N = \tau/(\rho_f gH)$

where τ is the shear stress generated along the horizontal or inclined portion of the floor.

Figures 7.20, 7.21 and 7.22 are the plots for the horizontal shear stress numbers, whereas Figs. 7.23, 7.24 and 7.25 are for the inclined shear stress numbers. For any design values of floor slope, length to depth ratio or pumping number, shear stress numbers can be interpolated between appropriate graphs.

Once the shear stress generated under given operating conditions is known, the behaviour of different types of particles can be investigated. Using the τ_C vs. d_S plot of Stelczer (1981) as shown in Fig. 7.26, it is possible to determine the range of particle diameters which will be scoured for a given shear stress. An envelope of all of the data has been superimposed onto Stelczer's data. This envelope is broad, but gives an indication of the relationship between τ_C and d_S for a wide variety of flume and field data. The curves reflect the degree of uncertainty in

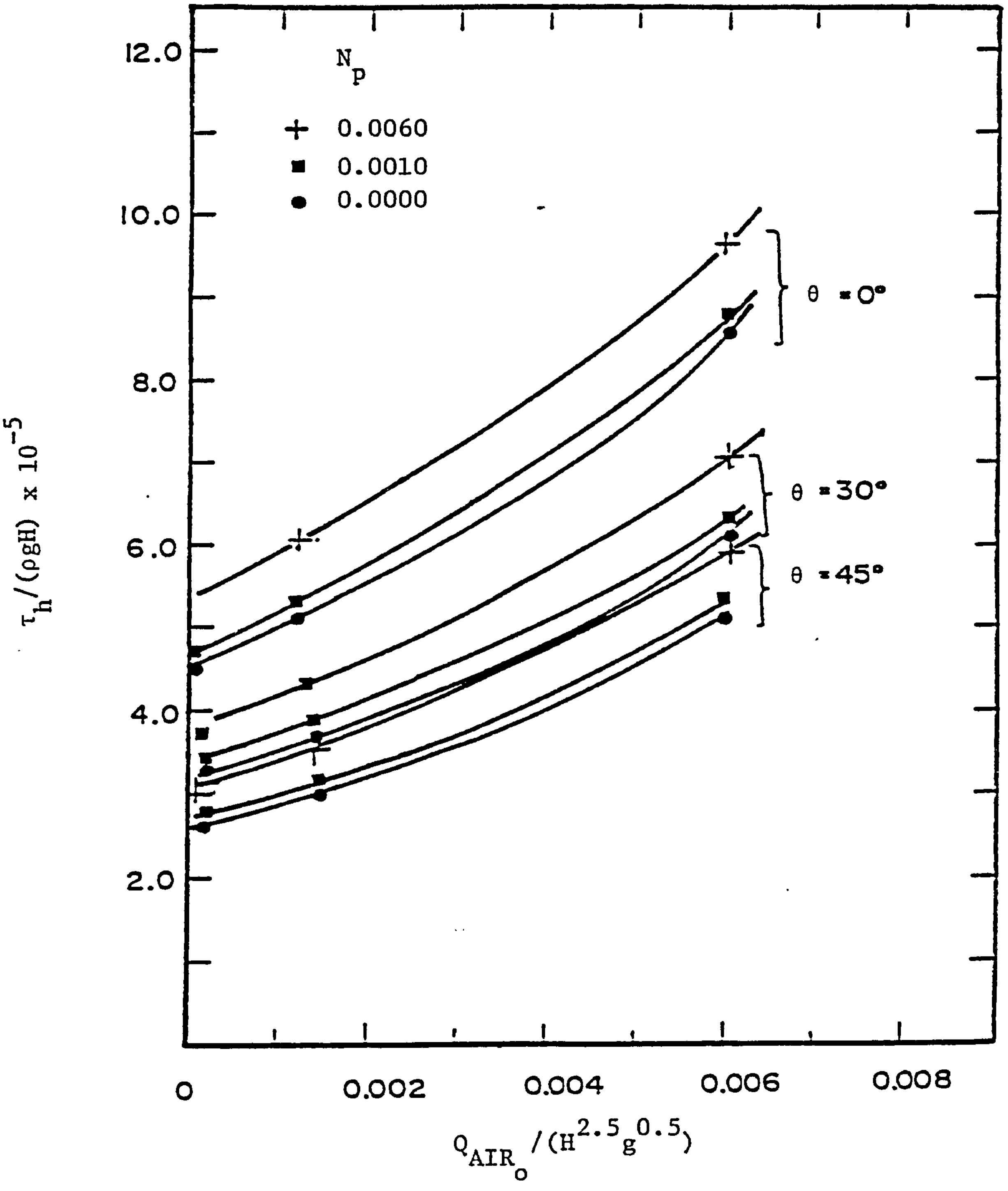

Fig. 7.20 Dimensionless Shear Stress Number for Horizontal Portion of Wet Well Floor with L/H = 1.580; H/D = 8.0; W/L = 0.475

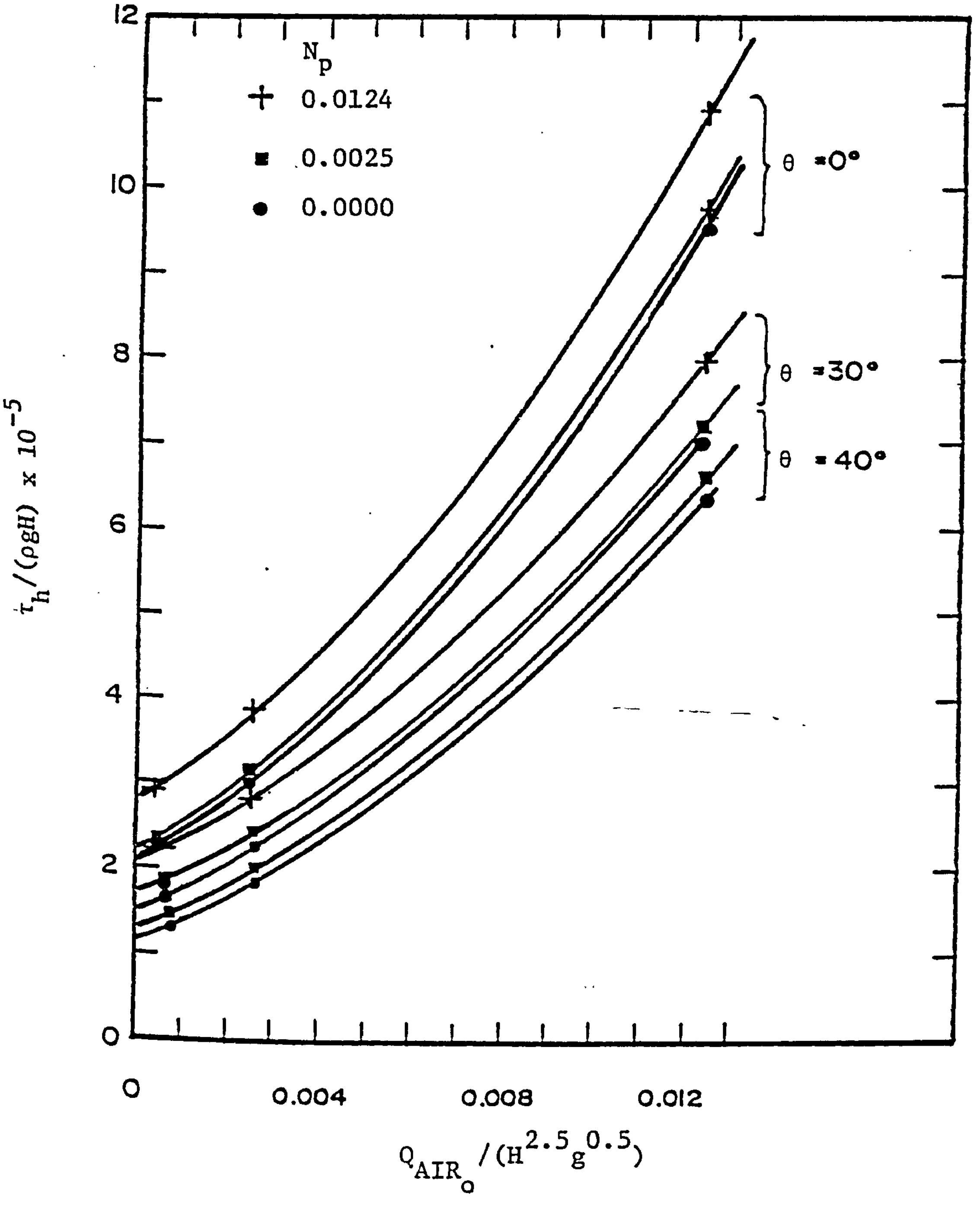

Fig. 7.21 Dimensionless Shear Stress Number for Horizontal Portion of Wet Well Floor with L/H = 2.107; H/D = 6.0; W/L = 0.475

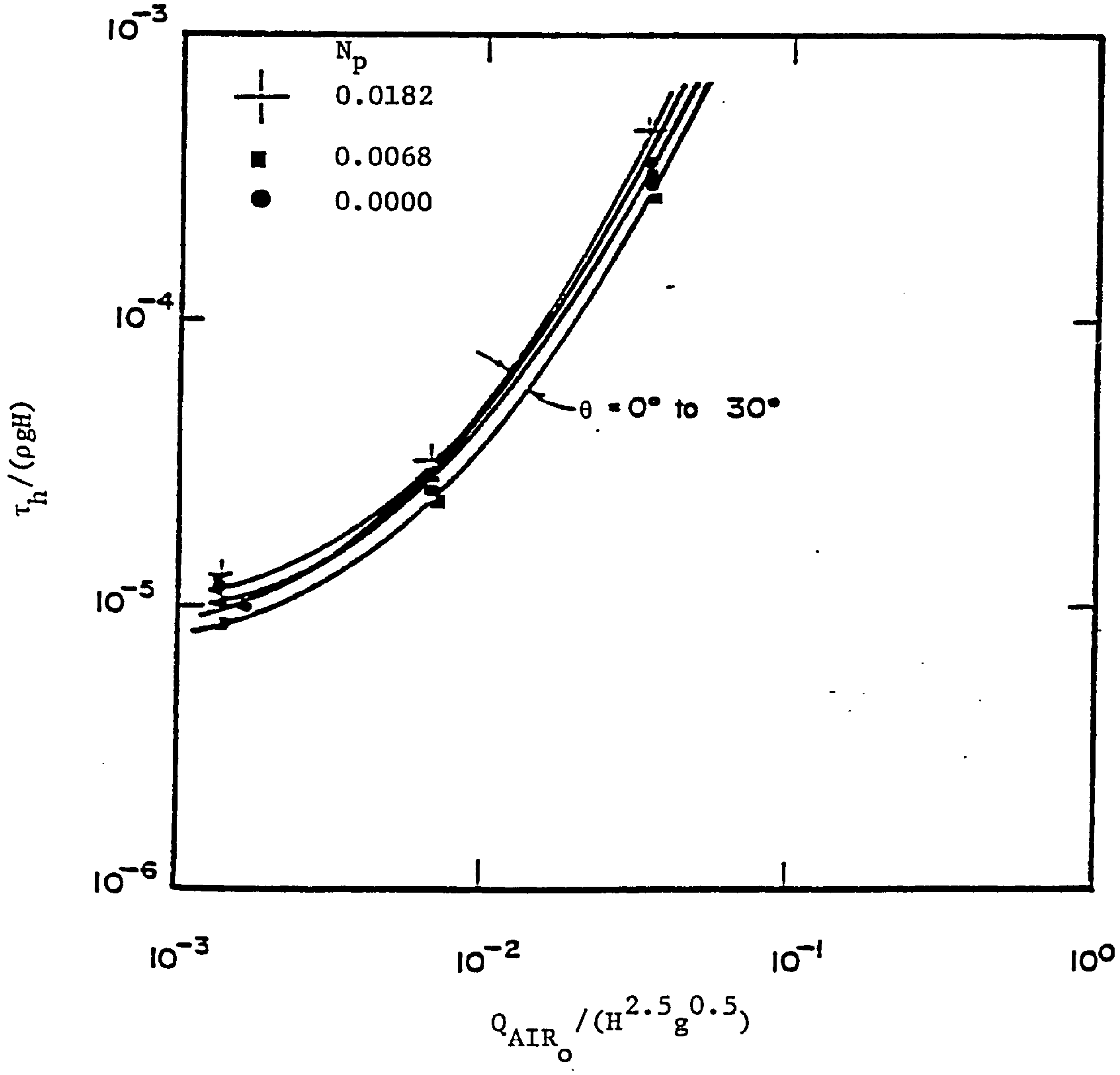

Fig. 7.22 Dimensionless Shear Stress Number for Horizontal Portion of Wet Well Floor with L/H = 3.160; H/D = 4.0; W/L = 0.475

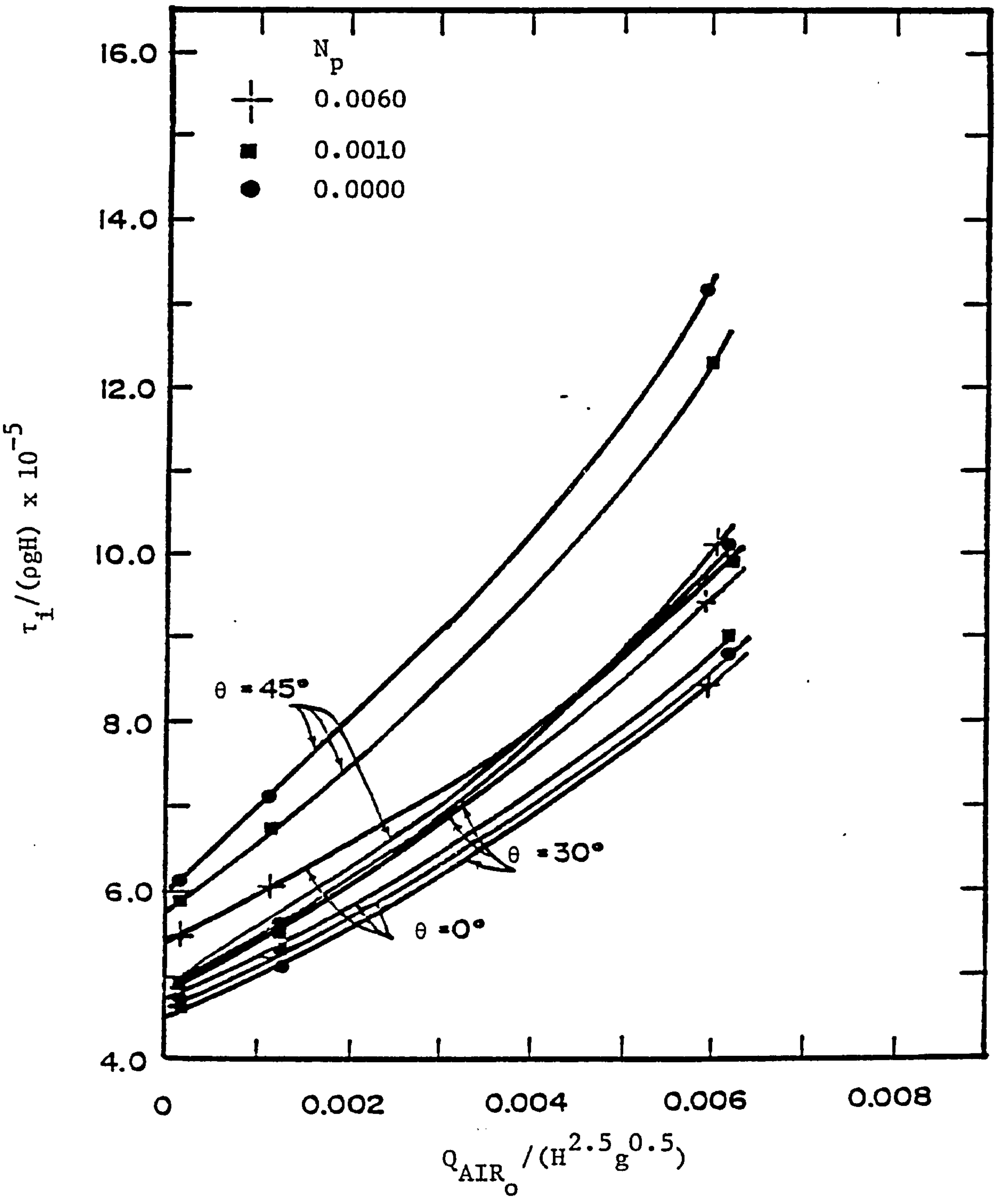

Fig. 7.23 Dimensionless Shear Stress Number for Inclined Portion of Wet Well Floor with L/H = 1.580; H/D = 8.0; W/L = 0.475

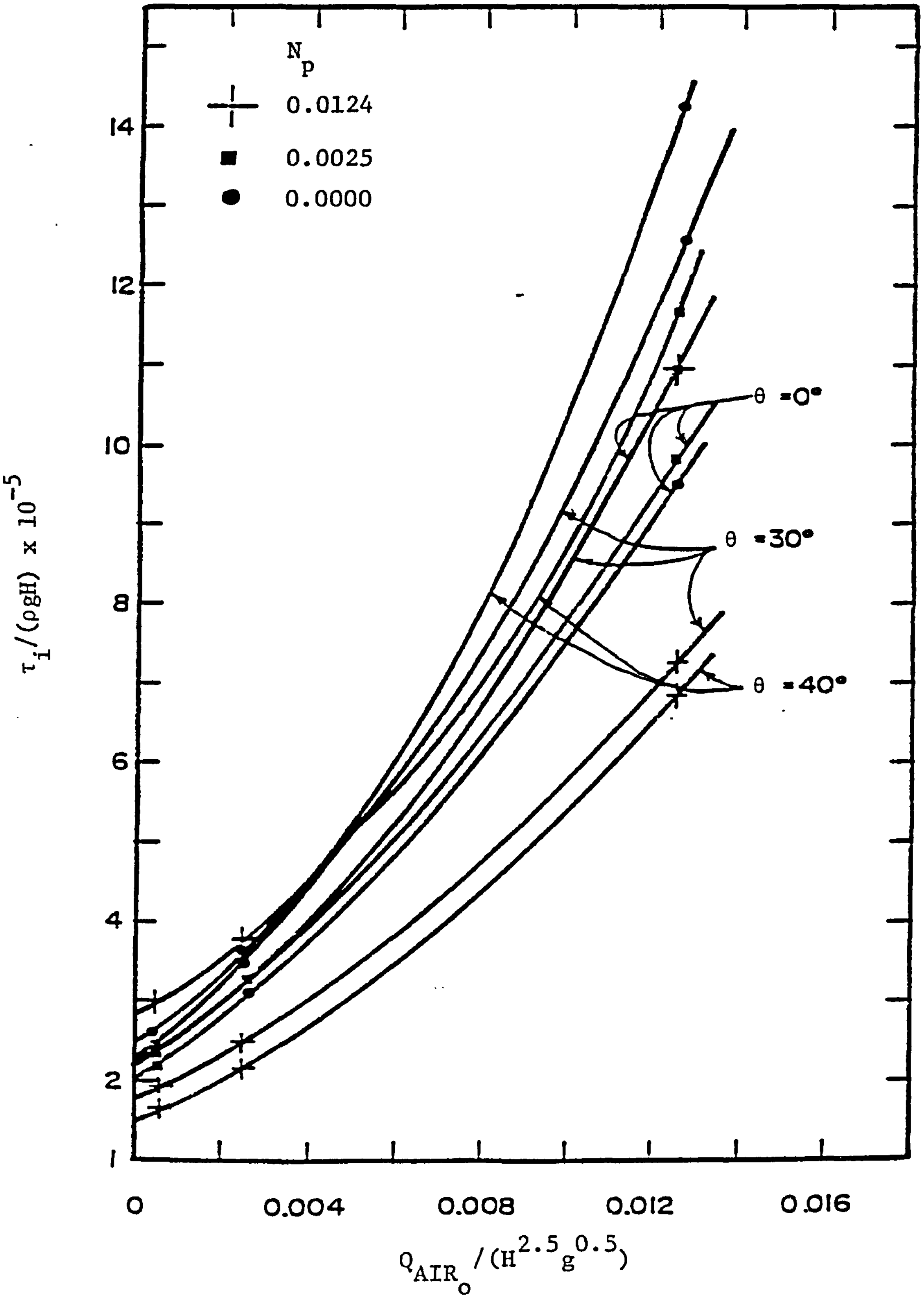

Fig. 7.24 Dimensioness Shear Stress Number for Inclined Portion of Wet Well Floor with L/H = 2.107; H/D = 6.0; W/L = 0.475

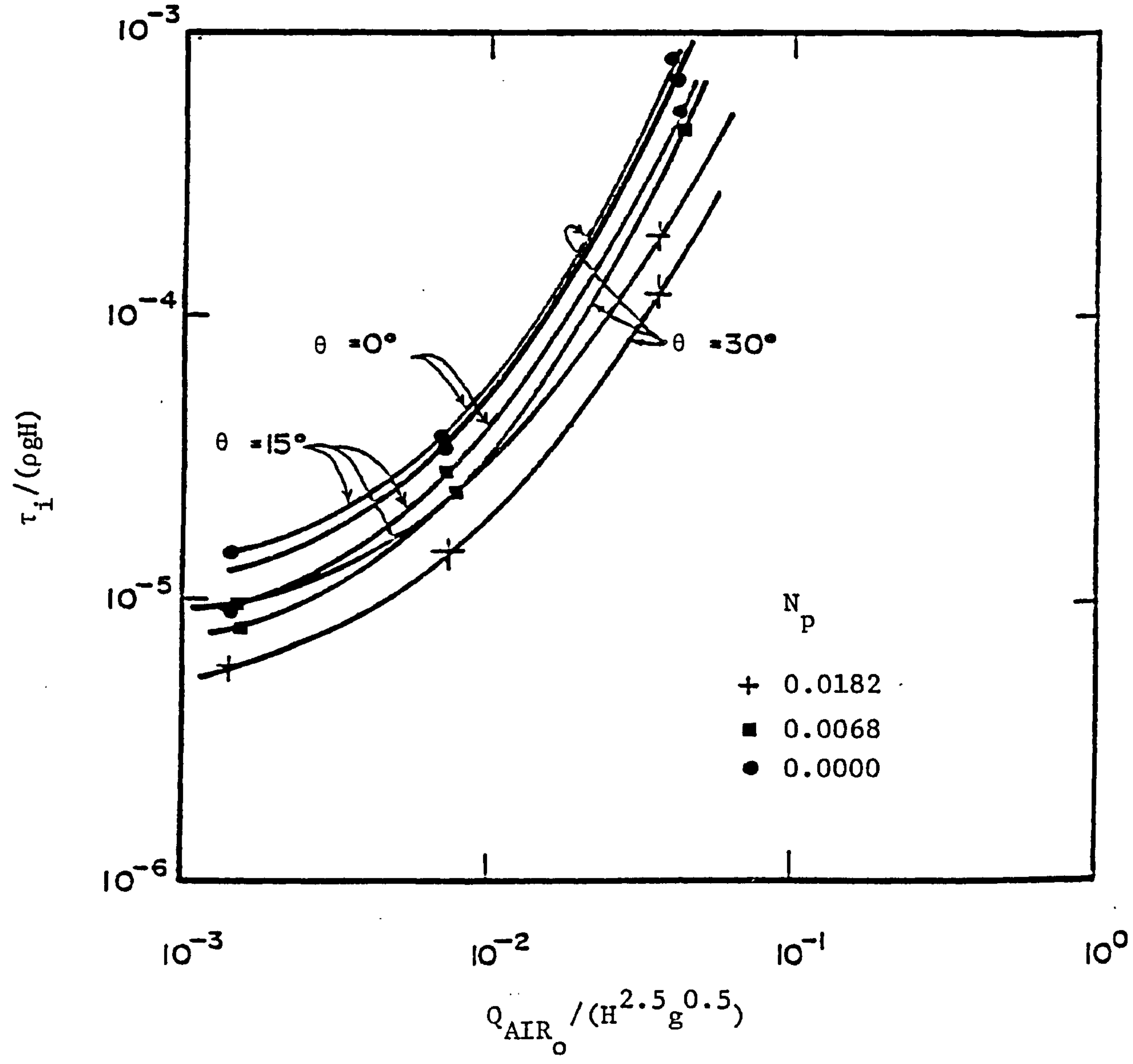

Fig. 7.25 Dimensionless Shear Stress Number for Inclined Portion of Wet Well Floor with L/H = 3.160; H/D = 4.0; W/L = 0.475

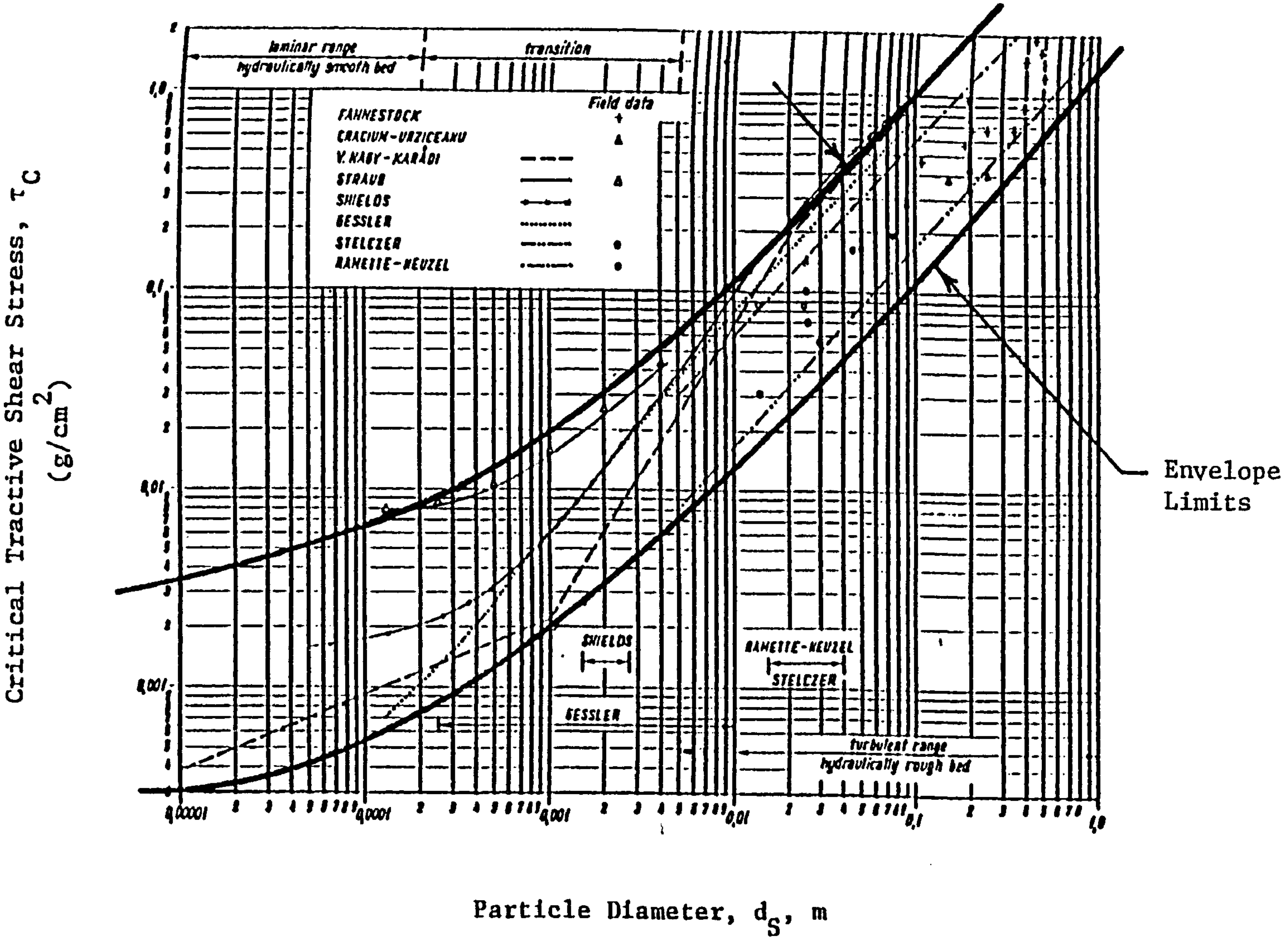

Fig. 7.26 τ_C - d_S Envelope
(adapted from Stelczer, 1981)

critical shear stress determination. For a specified critical shear stress, there exists a range of particle sizes which can be scoured. Conversely, for a specific particle diameter, there is some minimum shear stress which is required to initiate motion and some upper limit beyond which scouring is absolutely certain. For a given particle diameter, the upper and lower shear stress limits were obtained from the envelope in Fig. 7.26. For a known fluid depth, the shear stress number, as given by Eq. [7.34] could be calculated by assuming that τ_C and τ were equal. Then, for a given particle diameter and fluid depth, an upper and lower limit for the shear stress number was obtained. Using the auxiliary scale of Fig. 3.2, (d_S/ν) $(0.1(S_S - 1)\ gd_S)^{0.5}$, and assuming a specific gravity of 2.65, a series of curves for various L/H ratios were generated. These relate the shear stress number to the dimensionless grain size parameter as shown in Fig. 7.27. The dimensionless grain size parameter is plotted on the y-axis and the shear stress number is plotted on the x-axis. Three curves for L/H equal to 1.580, 2.107 and 3.160 are drawn. These curves are based on the shear stress predicted from the Shields curve. The larger outside envelope of data is based on the envelope of shear stress given in Fig. 7.26. Again, it can be noted that there is a broad range of values, even for one specified L/H ratio. It appears that Shields' curve will not result in gross errors, as his curve fits well within the range of known data. The use of Fig. 7.27 is discussed in Section 7.11.

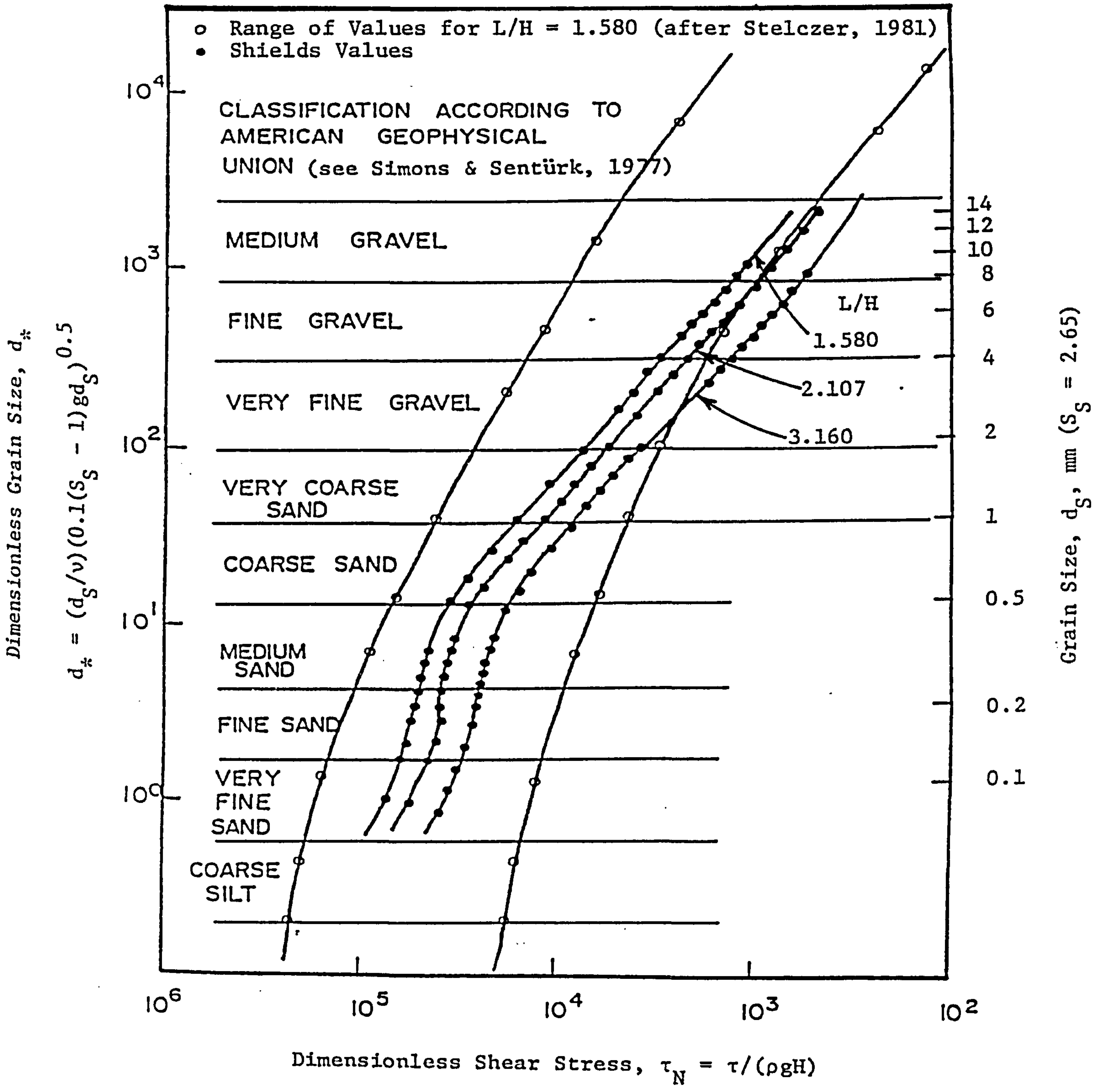

Fig. 7.27 Relationship Between Dimensionless Shear Stress and Dimensionless Grain Size for L/H = 1.580; 2.107 and 3.160

The final uncertainty in the design process exists in the confidence which is placed upon the boundary shear stress predicted by the numerical model. Figure 7.28 illustrates a plot of all the values obtained from numerical runs. The horizontal axis has the C_f correction factor which results in an error in the solution of the angular momentum equation of less than 1%. This C_f value can be considered to be the C_f value which results in a convergence error of less than 1% after one pass of the numerical program. The vertical axis has the C_f factor predicted by Eq. [7.21] for the same operating conditions. The solid 45° line represents a perfect correlation. Obviously, as one moves away from the line, the error in the C_f factor, and hence, the predicted boundary shear stress, increases. Twenty random points, including the maximum outliers, were selected to estimate the level of confidence in the predicted boundary shear stress. The selected points are "starred" in Fig. 7.28. The numerical program was executed to determine the boundary shear stresses using the "convergent" C_f value and the C_f value predicted by Eq. [7.21]. The results are shown in Fig. 7.29. The relationship is plotted nondimensionally in terms of:

(a) C_{fopt}/C_{feqn}, and

(b) τ_{opt}/τ_{eqn}

where

C_{fopt} and τ_{opt} are the C_f and τ values corresponding to the "convergent" solution, and C_{feqn} and τ_{eqn} are the C_f and τ values corresponding to the correlation equation, Eq. [7.21]. The

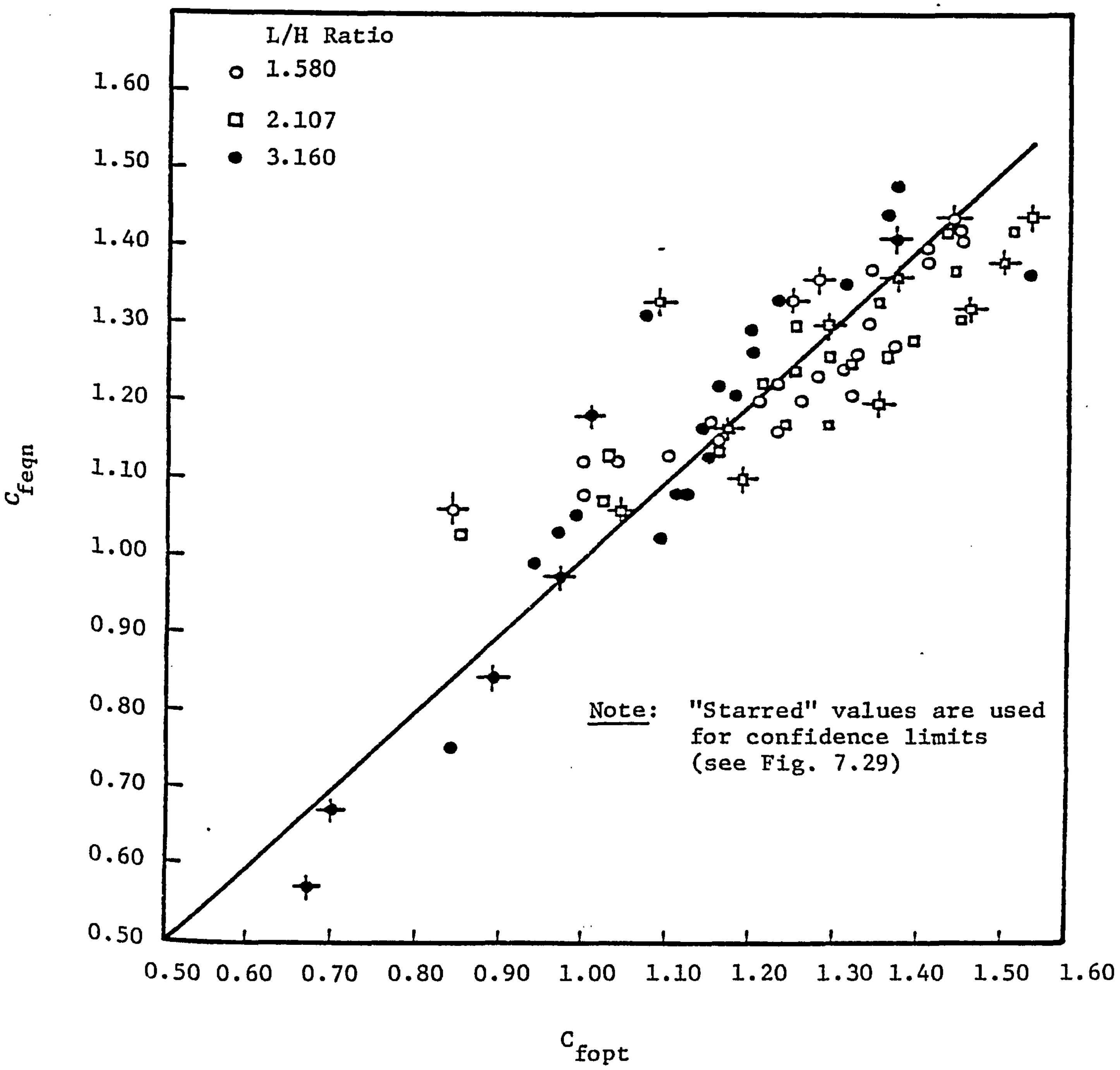

Note: "Starred" values are used for confidence limits (see Fig. 7.29)

Fig. 7.28 Relationship Between C_{fopt} and C_{feqn}

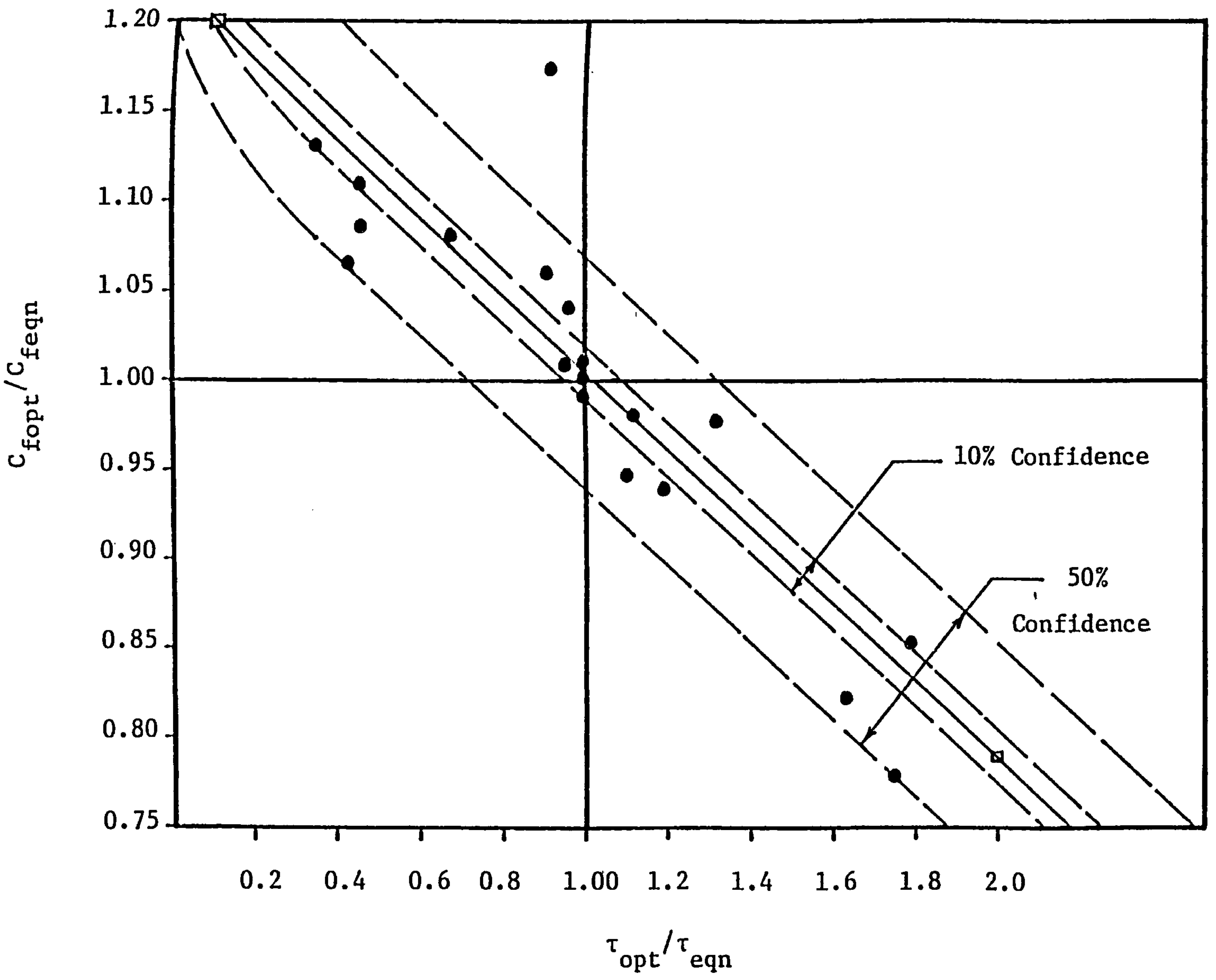

Fig. 7.29 Probable Error in Shear Stress Prediction

data points were analyzed to obtain the line of "best fit" as

[7.35] $C_{fopt}/C_{feqn} = -0.218(\tau_{opt}/\tau_{eqn}) + 1.221$

The standard deviation of C_{fopt}/C_{feqn} was 0.0978. Assuming the randomness to be normally distributed, the 10% and 50% confidence limits were computed. The 50% confidence limit is called the "probable error" and implies that a single observation has an equal chance of falling within or without this range. The horizontal projection of the 50% confidence limit gives an error of approximately ± 30% in the ratio of τ_{opt}/τ_{eqn} for a specified value of C_{fopt}/C_{feqn}. This would represent the largest probable error in the predicted shear stress, since the data in Fig. 7.29 contain the maximum outliers.

7.11 Design Example and Program Application

The purpose of this subsection is to illustrate an example design procedure and to comment on various design aspects where there is room for engineering judgement and flexibility.

7.11.1 Statement of the Problem

Select the air flowrate required to scour particles from the wet well floor for the following conditions:

(a) peak pumping rate = 3.5 MGD (0.184 m^3/s)

(b) use 3 pumps with 1 pump as standby

(c) $d_{95} = 0.1"$ (2.54 mm); $S_S = 2.65$

Use standard sump design procedures, and obtain the air flowrates required for a 30° inclined floor slope. Examine the entire operating range to determine the most severe conditions.

7.11.2 Design Procedure

Obviously, much more information about the maximum pump head, inlet sewer elevations, site conditions and sewage characteristics would be known prior to final design; however, the performance of the air diffuser system is not significantly affected by these additional design restrictions. The design consists of obtaining the sump dimensions necessary to handle the flow, and subsequently, determine what air flowrate will scour the particles for a fixed wet well configuration.

The numerical model can be used to size an aeration system for an existing wet well configuration. Some error may be expected if the geometric shape of the existing sump is significantly different from the geometric shape of the sump used in this formulation.

7.11.3 Determine the Suction Pipe Diameter

As discussed in Chapter 2, the sump geometry is given as a function of the bell-mouth diameter, D, which depends on the suction pipe diameter. All calculations are carried out with S.I. units.

The peak pumping rate is

$$Q_p = 3.5 \text{ MGD} = 0.184 \text{ m}^3/\text{s}$$

Metcalf and Eddy (1981) indicate that this flowrate would classify the pumping station as an "intermediate capacity" pumping station. They recommend the suction pipe velocity to range from 1.2 to 1.8 m/s. Using three pumps, with one for emergency, or for rotation of workload, the effective Q for each pump is $Q_p/2$.

Based on v_d of 1.6 m/s,

$d = ((0.184/2)/((\pi/4)(1.6)))^{0.5} \cong 0.271$ m, and

d = 0.25 m is selected. The range of recommended suction pipe velocities and available suction pipe diameters would vary with each manufacturer as well as the availability of standard pipe sizes. The actual suction pipe velocity is

$v_d = (0.184/2)/((\pi/4)(0.25^2)) = 1.87$ m/s, which is acceptable.

Generally, mixed-flow or axial-flow, centrifugal pumps with suspended pump suction columns and bell-mouths would be suitable. The motor would be housed above the sump, and the pump column and bell-mouth would be suspended into the sump below.

Prosser (1977) recommended the range of bell-mouth diameters as

[7.36] $1.5 < D/d < 1.8$

Selecting a ratio of 1.6, one obtains

$D = 1.6d = (1.6)(0.25) = 0.40$ m

The scale ratio, between the actual design condition and the model sump used in this study can be calculated as

[7.37] $L_R = D_p/D_m = (0.40)/(0.114) \approx 3.5$

The scale ratio is expressed in terms of the bell-mouth diameter which is the significant sump characteristic length.

7.11.4 Determine the Minimum Submergence Required

The minimum submergence required can be obtained from Fig. 6.4 for a known inlet Froude number

$N_{F_i} = v_d/(gD)^{0.5} = 1.87/((9.806)(0.40))^{0.5} \approx 0.94$

For the average condition

$S/D \simeq 2.2$

Therefore,

$S = (2.2)(0.4) = 0.88$ m

This submergence represents the minimum submergence required when the pumps are handling the peak flow.

7.11.5 Determine the Sump Volume Required for Peak Flow

Prosser (1977) had shown that the volume of a wet well between start and stop elevations for a single pump or a single speed control step for multiple-speed operation was given by

[7.38] $\forall = T_p Q/4$

where T_p is the minimum time of one pumping cycle or the time between successive starts or changes in speed of a pump operating over the control range. The above equation will result in equal "on" and "off" times when the flowrate into the sump is exactly one half of the pumping rate. The normal range of cycle times ranges from 5 to 30 minutes (Metcalf and Eddy (1981), Water Pollution Control Federation (1981), Buratto and McCorquodale (1981), ASCE (1977b)). Consideration should be given to start up and shutdown transients and over-heating of the motors. All manufacturers recommend certain minimum cycle times for their pumps. For the worst case scenario, it is assumed that the pumps are single speed and are cycled together between the "cut-in" and "cut-out" levels. Assuming a six minute cycle time, the volume of the sump required above the minimum submergence level is

$\forall = (6)(60)(0.184)/4 \simeq 16.6$ m^3

7.11.6 Fix the Sump Dimensions

The length, L, width, W, and maximum depth, H, can now be established using the same geometric ratios as in the model sump.

[7.39] $W = 6D = 6(0.40) = 2.4$ m

[7.40] $L = 12.64D = (12.64)(0.4) \simeq 5.00$ m

[7.41] $H = D/2 + S + \Delta y$

where $D/2$ is the bottom clearance of the bell-mouths and Δy is the depth required to store $\forall$.

[7.42] $\Delta y = \forall/((W)(L)) = 16.6/((2.4)(5.00) = 1.38$ m

Therefore, the maximum depth is

$$H = 0.40/2 + 0.88 + 1.38 = 2.46 \text{ m}$$

7.11.7 Check Design Variable Ranges

The mean approach velocity in the sump is given by

[7.43] $v = Q_p/(WH) = 0.184/((2.4)(2.46)) \simeq 0.03$ m/s

This velocity is low, and satisfactory for minimizing vortex formation. However, it will not promote the scouring of deposits, nor will it prevent settling of particles. Prosser (1977) recommends a minimum approach velocity of 0.7 m/s for sewage pumping stations, and velocities of 0.3 to 0.6 m/s for water pumping stations. The mean velocity could be increased by making the sump narrower. This would result in a deeper and longer sump, and hence more expensive, in order to satisfy the same volume requirements.

The maximum length to depth ratio in the model was 3.160. The ratio for the design is

$$L/H = 5.0/2.46 = 2.03 \text{ (O.K.)}$$

The design pumping number is

$$N_p = Q_p/(H^{2.5}g^{0.5}) = 0.184/((2.46^{2.5})(9.806)^{0.5}) \approx 0.0062$$

The maximum and minimum pumping numbers in the model were 0.023 and 0 respectively. Therefore, the proposed design is within the model limits.

7.11.8 Determine the Particle Requirements

Once the physical dimensions of the sump have been selected, it is necessary to establish the minimum air flowrate which will scour the deposited sediments. In order to obtain an estimate for the air flowrate, the critical shear stress for the given particle diameter must be obtained from Fig. 7.26 or Fig. 3.2. Using the auxiliary scale of Fig. 3.2, the dimensionless grain size can be obtained from

$$[7.44] \qquad d_* = (d_S/\nu)(0.1(S_S - 1)gd_S)^{0.5}$$

which yields $d_* = 162$ for the design particle. From Fig. 3.2, a dimensionless shear stress, $\tau_C/((\gamma_S - \gamma_f)d_S)$, of 0.046 is obtained. This yields a critical shear stress of 1.89 N/m^2. From Fig. 7.26, upper and lower limits for τ_C of 3.82 N/m^2 and 0.42 N/m^2 are obtained. At this point in the design, a grain size distribution curve of the incoming sediment load would assist the designer in selecting the required τ_c. If the design particle is of large diameter and low in frequency, its behaviour would be that of an isolated particle, and the lower limit of the critical shear stress range would give a reasonable estimate of τ_C. However, if it is a small particle and constitutes a large fraction of the total sediment load, then the upper limit of τ_C would be a better estimate. In selecting the design τ_c, consideration should also be given to the state of the sediments as they would deposit on the sump floor. If the sediments were "sticky", they may behave as a "packed-bed" with a high degree of particle interaction. For clean sediments, a "loose-bed" assumption may be more reasonable. τ_c can be adjusted up or down as necessary.

If the diffuser is to be used in an existing installation, consideration should be given to the wall and floor roughness as well as any discontinuities in the floor or walls which may affect the eventual shear stress produced. For new designs, safeguards against these discontinuities can be built in. Engineering judgement is required in selecting the critical τ_c. In any case, the air flowrate can be adjusted in the field as required.

From Shields′ curve, τ_c is estimated as 1.89 N/m^2. The design curves of Figs. 7.20 through 7.25 can now be used to estimate the required air flowrate. As discussed earlier, the probable error in estimating τ_c with the numerical model is ± 30%. In order to compensate for this error, the design τ_c is increased by 30% to yield a design critical shear stress of (1.89)(1.30) = 2.46 N/m^2.

7.11.9 Determine the Range of Operating Conditions

Prior to selecting the trial air flowrates and executing the program, it is necessary to decide on the operating conditions which are critical for sediment motion, and can be simulated using the numerical model. Three conditions are selected:

Case A: Calibration Condition: in this case, the inflow is made equal to the pumping rate. This condition may be used to check the range of validity of the physical model equations and to examine possible scale effects when the model relationships are applied to larger, prototype applications.

Case B: No Pumping: in this case, the pumps are idle and inflow to the sump is minimal. This allows the prediction of the air flowrate required to keep the sediment in suspension during "no pumping" or "non-peak" conditions.

Case C: Drawdown Condition: for this case, the inflow to the sump is limited to 5% of the pumping rate. It represents a typical operating scheme, wherein the sump would be drawn down during the pumping phase.

In Case C, even though the numerical formulation does not include the case of a varying free surface level, which introduces errors into the predicted velocity distributions and predicted shear stresses, the numerical results still yield estimates for the boundary shear stresses. At a specific free surface elevation, a unique air flowrate is required to scour a particle. As the sump is drawn down, laboratory observations indicate that the changing velocity distributions enhance scouring, and hence reduce the air flow requirement. As such, the air flowrate predicted from the Case (C) condition yields a conservative design.

7.11.10 Estimation of the Air Flowrates

In order to estimate the air flowrate required to scour a given particle, using Figs. 7.20 through 7.25, the inclined floor slope, pumping number and length to depth ratio must be known. In addition, the dimensionless shear stress, $\tau/(\rho g H)$ must be determined. Using the design critical shear stress, 2.46 N/m^2, and the maximum sump depth, 2.46 m, the dimensionless shear stress is calculated as

$\tau/(\rho g H) = 2.46/((998.203)(9.806)(2.46)) = 1.02 \times 10^{-4}$

Figures 7.20 to 7.25 are used to guess the air flowrate requirement. The numerical program is executed at a variety of air flowrates until a curve of Q_{AIR_o} vs. τ is developed, from which the specific Q_{AIR_o} can be obtained for the design τ. Estimates for the air flowrate required to scour a particle on the horizontal and inclined portions of the wet well floor can be made separately. The highest air flowrate would correspond to the most critical condition, and this should be used as the first guess. For a specified air flowrate, the critical shear stress on the horizontal and inclined planes should just be exceeded for all possible operating conditions. Using Fig. 7.21, which is the curve that most closely approximates the design conditions, the following air numbers, N_{AIR}, were obtained

Case A: $Q_{AIR_o}/(H^{2.5}g^{0.5}) \cong 0.0157$, and

Case B: $Q_{AIR_o}/(H^{2.5}g^{0.5}) \cong 0.0166$

For Case C an average value of 0.0162 was assumed. The corresponding air flowrates are

Case A: $Q_{AIR} = 0.47\ m^3/s$

Case B: $Q_{AIR} = 0.49\ m^3/s$

Case C: $Q_{AIR} = 0.48\ m^3/s$

The program is then executed after entering the design variables.

7.11.11 Scale Effects

It was observed that at the design depth, 2.7 times the maximum depth tested in the physical model, the dimensionless calibration equations were predicting total resisting torques 30% to 40% higher than the driving torques after the first pass of the program. Negative values for the circulating discharge, Q_{WD}, would have to occur to converge the program. Obviously, certain scale effects had been overlooked in the theoretical approach or, the numerical model was operating beyond the range of the calibration equations. The torque associated with the weight of water above the free surface as a result of the plume momentum, $T_{\Delta m}$, was suspected to be a function of the fluid depth. From the 81 computer runs made to develop the calibration curves, it was found that there was a relationship between $T_{\Delta m}$, the torque associated with the hydrodynamic bubble force, F, and the fluid depth, H. The relationship is shown in Fig. 7.30. The three curves represent the upper, lower and average limits for the torque ratios at three model depths of 0.456 m, 0.684 m and 0.912 m. With depths greater than 0.912 m, it is assumed that the torque associated with the rise in the free surface would continue to decay with increasing depth. For the upper limit curve, the following decay equation was fitted using the model torque ratios at depths of 0.684 m and 0.912 m

$$F_R = 0.792H^{-0.510} \qquad [7.45]$$

where H is the fluid depth and F_R is the ratio of the torques due to the rise in the free surface and the hydrodynamic bubble force. The use of Eq. [7.45] was invoked in the numerical model whenever the prototype depth exceeded 0.70 m and the predicted ratio of the torques exceeded the ratio given by Eq. [7.45]. At a depth of 0.70 m, it can

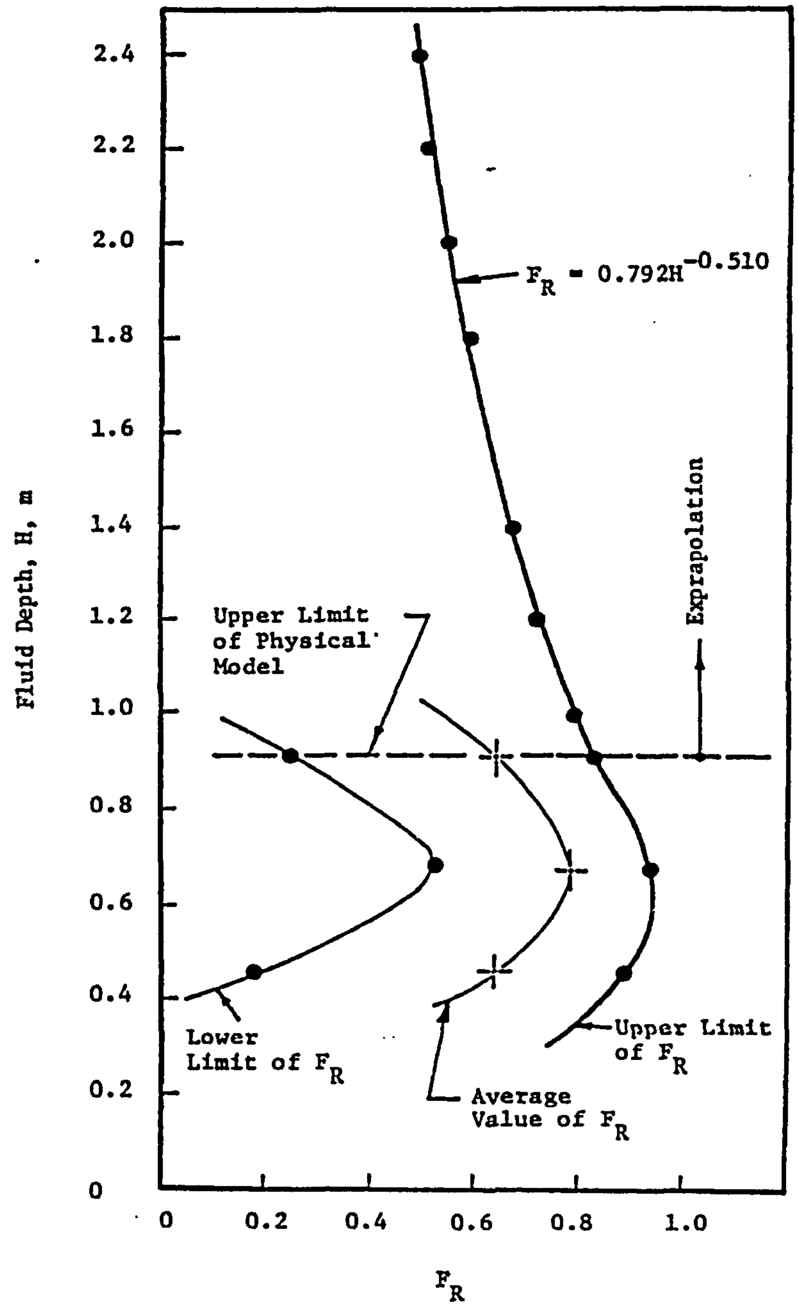

Fig. 7.30 Extrapolation of the Ratio of the Torques Associated with the "$T_{\Delta m}$" and "F" Forces

be seen from Fig. 7.30 that the torque ratio obtains a maximum value of approximately 0.94. When the predicted torque ratio was less than that predicted by Eq. [7.45], no convergence problems were encountered in the program.

7.11.12 Design Example Results

The results for the three test cases are plotted in Fig. 7.31. For the drawdown case, Case C, the plots were prepared for the dimensionless shear stress on both the horizontal and vertical portions of the wet well floor. The air flowrates tested for Case C were extended over a range of 0.01 to 1.40 m^3s^{-1}, in order to observe the response of the system. The curves indicate that there exists an air flowrate which results in a maximum boundary shear stress. Beyond this air flowrate, the boundary shear begins to decrease with increasing air flowrates. The decreasing leg of the air flowrate versus shear stress curve is a result of the calculations being carried out beyond the upper limit of the centre of rotation, and default velocity profile calibration equations. In no case should the curves be used to the right of the upper limit shown in Fig. 7.31. For each design, a series of curves similar to that shown in Fig. 7.31 should be developed so that there is no doubt as to the upper limit of the design.

Using the curves plotted in Fig. 7.31, one can obtain the air flow number required to produce the desired boundary shear stress. A comparison of the original estimates for the air flow number using the design curves, and the results of the design example, are given in

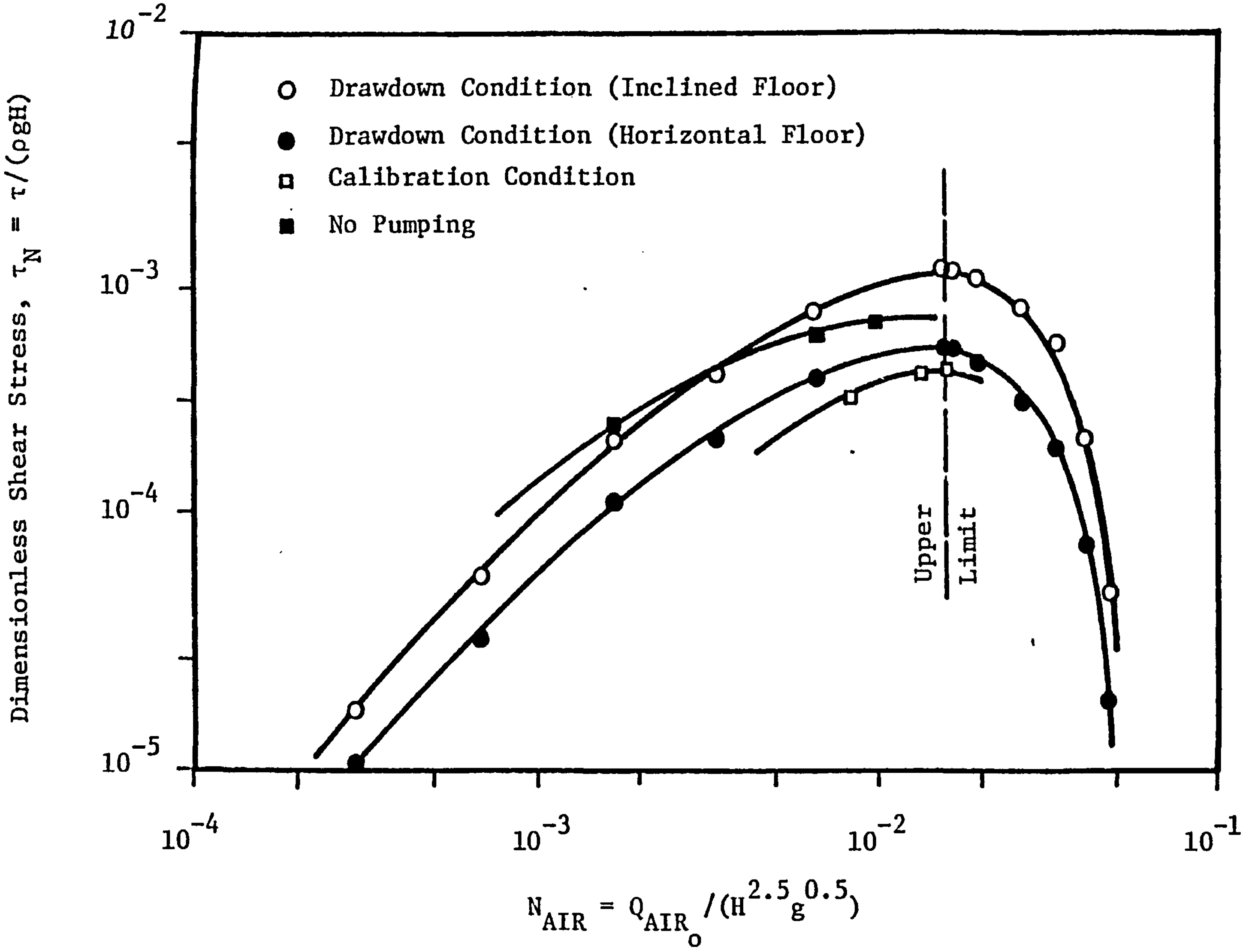

Fig. 7.31 Design Example Results

Table 7.8. Table 7.8 indicates that the air flowrate required for the design condition ranges from 14 to 52% of that predicted from the physical model. This reduction can be attributed to

(a) higher efficiencies with the larger system,

(b) scale effects, and

(c) calibration limitations.

The results of the numerical model can be used to size the aeration equipment. The numerical results, along with a safety factor, can be used as a guide for the operation of the installed system and changes in the air flowrate can be made, as necessary, in the field. Data from the prototype design can be collected to develop site specific calibration adjustments. With site specific data, a variety of operating sequences can be tested numerically and the pumping and diffused air cycles optimized.

Table 7.8 Design Example Results

	Case A Calibration Condition	Case B No Pumping	Case C Drawdown
Estimated N_{AIR}	1.57×10^{-2}	1.66×10^{-2}	1.62×10^{-2}
Estimated Q_{AIR_o} (m^3/s)	0.467	0.493	0.482
Required N_{AIR}	8.1×10^{-3}	2.25×10^{-3}	5.15×10^{-3}
Required Q_{AIR_o} (m^3/s)	0.241	0.067	0.153
Ratio of Required Air Flowrate to Estimated Air Flowrate	0.52	0.14	0.32

CHAPTER 8

CONCLUSIONS

The following conclusions are drawn based on this study:

1. The drift flux formulation is applied to describe the performance of the diffuser plume. The plume width, air fraction and mean water velocity are shown to be sensitive to (i) the initial estimate of the plume width and water velocity, (ii) the entrainment coefficient, (iii) bubble radius, (iv) shear developed by confining boundaries, and (v) surface tension.

2. The conservation of linear and angular momentum has been applied to describe the flow circulation and torque balance within the sump. The two-dimensional model has shown that the significant driving torque is due to the mutual hydrodynamic bubble force, whereas the significant resisting torques are due to hydrostatic forces resulting from the momentum of the diffuser plume and pressure differences resulting from the two phase mixture.

3. The geometric centre of the cross-section (elevation) of the wet well is a reasonable estimate for the centre of rotation. The air flowrate is the major variable responsible for variation in the location of the centre of rotation.

4. Measured velocity profiles indicate that the assumption of part solid body rotation and part plug flow adequately describes the flow distribution within the sump.

5. There is no obvious advantage to using a reaction baffle between the pump columns and the diffuser zone. Plume interaction with the baffle enhances the possibility of air ingestion into the pump intakes.

6. A diffuser zone width of 3D reduces the possibility of air entrainment by the pump intakes, while at the same time, allows for sufficient width to entrain and accelerate the sump flow.

7. The critical locations for sediment deposition are at the interfaces between the walls and floor, and at the base of the inclined portion of the wet well floor. Triangular fillets assist in minimizing the deposition of sediments in these locations.

8. The solution of the numerical model does not correspond to a minimum kinetic energy or maximum angular momentum state for the predicted centre of rotation.

9. The effect of the two phase flow on the boundary pressures, and the resulting torques has been shown to be related to $(1 - \alpha)$. The effects of the two phase system are still not fully understood. Considerable experimental data on boundary pressures is needed to clarify the individual effects.

CHAPTER 9

RECOMMENDATIONS

Based on this study the following recommendations for further research are proposed:

1. In order to quantify the C_f correction factor, it is necessary to investigate a sump in which the air diffuser is operated in the absence of the pump columns. Piezometers placed along the entire boundary of the sump would provide reliable estimates of the boundary pressures when circulation is induced by the air only. A more fundamental understanding of the forces and torques involved would be generated.

2. Based on experimental observations, it appears that there may be three-dimensional effects in the sump flow. The bell-mouth intakes behave as three-dimensional sinks which affect the velocity distributions and boundary shear stresses. The assumption of average shear stress over the sump floor is valid, however, the spatially varying boundary velocity would result in the critical shear stress being generated in some areas, whereas other areas would be in a sub-critical state. Corner conditions and transitions in the walls and floor create additional three-dimensional effects. The numerical model would be enhanced if such three-dimensional effects were included. Critical shear stress would become a function of coordinate location as well as air flowrate, pumping rate and sump geometry.

3. In the formulation of the drift flux model to describe the diffuser plume, average, uniform distributions for the water velocity and air fraction were assumed. Physical plume measurements indicate a well defined, Gaussian velocity profile within the plume. Additional plume water velocity and air fraction distribution measurements are neccessary to refine the estimates for the torque due to the mutual hydrodynamic bubble force. The shear stress generated on the wall adjacent to the diffuser would also be affected by the accuracy of the phase fraction measurements in the plume.

4. The numerical model assumed steady state conditions; as such, all time derivatives were set equal to zero. The reliability of any drawdown simulations are greatly affected by this assumption. Derivative formulations such as dH/dt and $d\tau/dt$, where t is time, are essential for reliable drawdown simulations.

5. In this study the diffuser arrangement was a linear air diffuser placed at the floor of the sump. Additional diffuser configurations such as horizontally directed water jets, placed near the free surface, should also be investigated. Higher circulating velocities and lower energy requirements may be realized. The feed for the water jets may be connected to the discharge side of the pump(s), thereby eliminating compressor requirements. In addition, diffusers near the surface would allow for the system to be implemented not only in sumps where the pump columns are suspended from above, but also in sumps where the suction pipe enters from the side wall of the sump.

6. The air diffuser system has been shown to provide an excellent source of auxiliary power to scour particles; moreover, the oxygen transfer benefits of the system will also be beneficial in reducing septicity and purging odours from the water or wastewater. A variety of diffuser nozzle configurations should be tested to maximize circulation, and oxygen transfer. The possiblity of adding disinfectant or process chemical into the plume of the diffuser should also be studied.

7. Inherent to any physical model study is the problem of scale-up. In order to fully test the validity and range of the calibration parameters and equations, large scale studies are necessary.

8. The use of benching adjacent to the diffuser and coping at the free surface, similar to those used in aeration tanks, would assist in minimizing the energy losses associated with the diffuser plume interacting with the free surface and reduce the "dead" spaces in the corners, and thereby improve the energy transfer efficiency.

9. The pump intakes may be located in the rear wall or floor of the sump. With these suction orientations, the air requirement would be reduced because gravity would assist in particle transport. In the intake configuration used in this study, the particles must be resuspended before entering the intakes.

APPENDIX 1

A1.1 NUMERICAL PROGRAM FLOWSHEET

1. Specify array size and define Common Blocks for communication between the Mainline Program and SUBROUTINE SOLVE which is a fifth order Runge-Kutta subroutine used to solve for the diffuser plume parameters.

2. Define and print the number of simultaneous equations used in SUBROUTINE SOLVE.

3. Specify and print the default constant values at 20°C. The following values are defaulted:

   p_{atm}, γ_f, g, ρ_f, ρ_{AIR}, ψ_b, π, dy, y_o, ν_f

4. Read in and print out the required input variables. The following values are read in:

   D, H, θ, Scale Ratio, R_b, α_C, B_o/R_b, Q_{AIR_o}, Q_p,

   Inflow fraction, friction factors (f) for the inclined floor, horizontal floor, side walls and rear wall; see Appendix 2 for input variable description and format.

5. Calculate the diffuser submergence.

6. Convert the floor slope in degrees to radians.

7. Calculate the length of the inclined portion of the wet well floor and check if the slope is exposed at the specified depth. If so, stop calculations and go to step 54.

8. Calculate the cross-sectional area and velocity head of the intake pipes.

9. Calculate the coordinates of the geometric centre of rotation; $\bar{X}$, $\bar{Y}$.

10. Modify $\bar{X}$ and $\bar{Y}$ to obtain the actual coordinates of the centre of rotation; XCR, YCR. Use calibration equations [6.10] and [6.11] to modify the geometric centre of rotation coordinates. If YCR < D/2, stop calculations and go to step 54.

11. Calculate the radial distances from the centre of rotation to (a) the centre of the inclined portion of the floor, (b) the centre of the horizontal portion of the wet well floor, (c) the plane of the bell-mouths, and (d) the centre of the upper and lower parts of the inlet zone to the sump.

12. Sub-divide the total depth into 10 subsections. Calculate the radial distance from the centre of rotation to the centre of each of these 10 subsections along the wall of the sump adjacent to the diffuser plume.

13. Calculate the angles for the cosine correction for the pump column drag force and to determine the point of application of tangential velocities, V_{t_1} and V_{t_4}.

14. Calculate the x coordinate of the centre line of the pump columns. If the x coordinate is greater than XCR, stop calculations and go to step 54.

15. Calculate the radial distances from the centre of rotation to the centre of the sub-divided pump columns.

16. Calculate the radial distances from the centre of rotation to the point on the sump boundary where velocities V_{t_1}, V_{t_2}, V_{t_3} and V_{t_4} act.

17. Calculate the number of dy steps from the outlet of the diffuser to the centre of each of the (H/10) subsections.

18. Calculate the initial estimates for: B_o, α, V_W, F, and Q_{AIR}

    (a) $B_o = (B_o/R_b)(R_b)$

    (b) solve for α from Eq. [7.1]

    (c) estimate the initial V_W from Eq. [7.2]

    (d) F = 0.0

    (e) $Q_{AIR} = Q_{AIR_o}$ (Q_{AIR_o} is read in)

19. Determine the number of iterations of SUBROUTINE SOLVE. The number of iterations is the integer value of the total depth divided by dy. dy is defaulted to 0.001 m.

20. Call SUBROUTINE SOLVE (see step 56) and print out y, B, α and V_W for each dy element.

21. Using the plume data of step 20, obtain velocities V_{t_2}, V_{t_3} and V_{t_4} and the corresponding plume widths at these sections.

22. Using the plume data of step 20, obtain the water velocity, hydrodynamic bubble force and plume width at the centre of each of the (H/10) subsections.

23. Obtain the air fraction and plume width at the free surface using the data obtained from step 20.

24. Calculate the steady state velocity profile through the centre of rotation.

    (a) Using the calibration equations as given by Table 6.9, estimate $v_{SURFACE}$, v_j, v_b, BB and AA.

    (b) Calculate the velocity profile area above and below the centre of rotation using the data of step 24(a) or the modified velocities of step 24(e) or step 50.

    (c) Calculate the discharge passing above and below the centre of rotation from the velocity profiles given in 24(b).

    (d) For a known pumping rate check for continuity. The discharge passing above the centre of rotation should equal the discharge passing below the centre of rotation, minus the pumping rate. If the difference in discharges is less than 0.5% go to step 25. If the difference in discharge is greater than 0.5% go to step 24(e).

    (e) The velocities $v_{SURFACE}$, v_j and v_b are increased or decreased by 0.0005 m/s, as neccessary, to satisfy continuity. The distances YCR, AA and BB are kept constant as in step 24(a). Go to step 24(b).

25. Calculate the depth, discharge and mean velocity through the upper and lower parts of the inlet zone of the sump.

26. Calculate the circulating discharge, Q_{WD}, by averaging the two discharges which satisfy continuity in step 24(d).

27. Calculate the tangential velocities V_{t_1}, V_{t_2}, V_{t_3} and V_{t_4} as per Chapter 4.5.5.

28. Calculate the tangential velocities v_{t_1}, v_{t_2}, v_{t_3} and v_{t_4}, at the centres of the sub-divided pump columns, using the relationship given by Eq. [4.57].

29. Determine the pump column drag coefficient.

    (a) Calculate the outside diameter of the pump columns; it is a function of the bell-mouth diameter, D.

(b) Obtain the mean impact velocity on the pump columns by averaging the tangential velocities as calculated in step 28. Apply the necessary cosine correction to each v_{t_i} value to resolve it into a velocity acting at right angles to the pump columns.

(c) Calculate the pump column Reynolds number as per Eq. [4.59].

(d) Obtain C_d from the data as given in Table 4.3.

30. Calculate the rise in the free surface above the diffuser plume from Eq. [4.86].

31. Calculate the total depth of fluid above the diffuser by adding the static depth to the rise in the free surface as calculated from step 30.

32. Calculate the line of action of ΔP_2 force from Eq. [4.88].

33. Calculate ΔP_2 from Eq. [4.87].

34. Estimate the C_f correction value from the calibration Eq. [7.20].

35. Calculate the torque due to the shear stress on the inclined portion of the wet well floor as per subsection 4.5.1.

36. Calculate the torque due to shear stress on the horizontal portion of the wet well floor as per subsection 4.5.2.

37. Calculate the torque due to shear stress on the wall adjacent to the diffuser plume as per subsection 4.5.3.

38. Calculate the torque due to drag on the pump columns as per subsection 4.5.5:

(a) on the lower 1/4 of the pump columns,

(b) on the section of the pump columns immediately below the centre of rotation,

(c) on the section of the pump columns immediately above the centre of rotation, and

(d) on the upper 1/4 of the pump columns.

39. Calculate the total angular momentum crossing the control volume boundaries as per subsection 4.5.11.

40. Calculate the torque due to the hydrodynamic bubble force as per subsection 4.5.4.

41. Calculate the torque due to the ΔP_2 force as per subsection 4.5.8.

42. Calculate the torque due to side wall shear as per subsection 4.5.6.

    (a) Calculate the 15 $\Delta\theta$ angles.

    (b) Calculate the length of the 15 radial arms from the centre of rotation to the sump boundary.

    (c) Calculate the tangential velocity associated with each $\Delta\theta$ as given by Eq. [4.65] or Eq. [4.66].

    (d) Calculate the torque associated with each $\Delta\theta$ element as per Eq. [4.67] or Eq. [4.68], depending on whether or not the element is assumed to have both solid body and plug flow regions, or just solid body flow.

43. Calculate the momentum fluxes and the magnitude of the ΔF force as per subsection 4.5.7.

44. Apply the conservation of angular momentum to the control volume to calculate the line of action of the ΔF force using Eq. [4.79]. Calculate the torque associated with the ΔF force by taking the cross product of $y_{\Delta F}$ and ΔF as per Eq. [4.79] and Eq. [4.72].

45. Calculate the torque associated with the mass of water above the diffuser, $T_{\Delta m}$ as per subsection 4.5.9.

    (a) Calculate the volume of water above the free surface as per Eq. [4.89].

    (b) Calculate the associated torque as per Eq. [4.90].

    (c) Calculate the ratio of the torque due to the mass of fluid above the free surface to the torque due to the hydrodynamic bubble force.

    (d) Calculate the maximum torque ratio as per Eq. [7.45].

    (e) If the ratio of the torques calculated in step 45(c) exceeds that calculated in step 45(d), correct the $T_{\Delta m}$ torque using the ratio given by Eq. [7.45].

46. Calculate the torque due to the pressure balance, ΔP_B, as per subsection 4.5.10.

47. Calculate the total resisting torques by summing up the torques calculated in steps 35, 36, 37, 38, 42, 44, 45 and 46.

48. Calculate the total driving torques by summing up the torques calculated in steps 39, 40 and 41.

49. Calculate the difference between the driving and resisting torques and if the difference is less than 2% go to step 51. If the difference is greater than 2% go to step 50.

50. Iterate solution until convergence is obtained. If the resisting torques exceed the driving torques, then reduce $v_{SURFACE}$, v_j and v_b by 0.02 m/s; and vice-versa, if the driving torques exceed the resisting torques. Return to step 24(b) and repeat steps 24(b) through 49 until convergence is achieved.

51. Calculate the momentum correction factors as per Eq. [7.28], Eq. [7.29] and Table 7.6.

52. Calculate the total kinetic energy of the system as per Eq. [7.18] and Eq. [7.19].

53. Calculate the angular momentum of the system as per Eq. [7.14] and Eq. [7.15].

54. Print out suitable error and caution statements as required by steps 7, 10 and 14.

55. SUBROUTINE VECTOR

    This subroutine sets up the equations to be solved for using the fifth order Runge-Kutta SUBROUTINE SOLVE given in step 56.

    (a) Set up the equation to estimate the ambient water velocity given by Eq. [6.13].

    (b) Set up the equation to estimate dQ_{AIR}/dy given by Eq. [4.40].

    (c) Calculate dB/dy, $d\alpha/dy$, dV_W/dy and dF/dy as per equations given in Table 4.2 and Eq. [4.8].

    (d) Return to SUBROUTINE SOLVE.

56. SUBROUTINE SOLVE

    This subroutine solves the equations specified in SUBROUTINE VECTOR via a fifth order Runge-Kutta technique.

    (a) Specify SUBROUTINE VECTOR as an external subroutine.

    (b) Initialize constants and specify array sizes.

    (c) Solve equations.

A1.2 COMPUTER PROGRAM NOMENCLATURE

```
C     HYDRODYNAMIC MODEL TO DESCRIBE THE FLOW CONDITIONS WITHIN A
C     WETWELL UNDER VARIOUS OPERATING CONDITIONS.
C
C     METRIC UNITS USED THROUGHOUT
C*****DEFINITION OF TERMINOLOGY*************************************
C
C     AGINLO       DENOMINATOR OF A TERM USED IN CALCUL'TG FACTOR(1)
C     AGINUP       NUMERATOR OF A TERM USED IN CALCUL'TG FACTOR(1)
C     AIRFCN       AIR FRACTION AT THE FREE SURFACE
C     AIRNO        IS A FUNCTION OF QAIRO, DEPTH AND G AND IS USED
C                  TO ADJUST XCENRO AND YCENRO
C     ALPHAC       ENTRAINMENT COEFFICIENT
C     AM...        IS THE ANGULAR MOMENTUM ASSOCIATED WITH FLUID
C                  VOLUME "...", N.M.S.
C     AMTOT        IS THE TOTAL ANGULAR MOMENTUM OF THE SYSTEM,
C                  N.M.S.
C     ANGHOR(I)    ANGLES COMPUTED FOR FACTOR(2),DEGREES
C     ANGHRR(I)    ANGLES COMPUTED FOR FACTOR(2),RADIANS
C     ANGINC(I)    ANGLE COMPUTED FOR FACTOR(1),DEGREES
C     ANGINR(I)    ANGLE COMPUTED FOR FACTOR(1),RADIANS
C     ANGL2(I)D    ANGLE USED IN CALCULATING TANGENTIAL AND RADIAL
C                  VELOCITIES,DEGREES
C     ANGL(I)R     ANGLE USED IN CALCULATING TANGENTIAL AND RADIAL
C                  VELOCITIES,RADIANS
C     ANGPHI(I)    ANGLE USED IN CALCULATING THE PUMP COLUMN
C                  DRAG,DEGREES
C     ANGPHR(I)    ANGLE USED IN CALCULATING THE PUMP COLUMN
C                  DRAG,RADIANS
C     ANGSWS(I) &  ARE THE INTERNAL ANGLES OF THE SUB-DIVIDED CROSS-
C     ANGSS(I)  &  SECTION USED IN CALCULATING THE SIDE-WALL SHEAR
C     ANGSD(I)  &
C     ANGSWD(I)
C     APIPE        AREA OF SUCTION PIPE,M**2
C     ARGU(I)      ARE THE COEFFICIENTS OF THE SOLUTION OF THE
C                  QUADRATIC EQUATION FOR THE INITIAL AIRFRACTION
C     AVELJT       IS THE DISTANCE ABOVE THE FLOOR TO THE LINE OF
C                  ACTION OF VELJET,M.
C     BBOB5        IS THE MOMENTUM CORRECTION FACTOR FOR THE FLOW
C                  PASSING BELOW THE CENTRE OF ROTATION; BASED ON
C                  THE ASSUMED VELOCITY PROFILE
C     BBOTVL       IS THE DISTANCE ABOVE THE FLOOR OVER WHICH BOTVEL
C                  IS ASSUMED TO BE CONSTANT,M.
C     BBTH         IS THE MOMENTUM CORRECTION FACTOR FOR THE FLOW
C                  PASSING BELOW THE CENTRE OF ROTATION; BASED ON
C                  THE OBSERVED VELOCITY PROFILES.
C     BETDEG(I)    ANGLE USED IN CALCULATING THE PUMP COLUMN
C                  DRAG,DEGREES
C     BETRAD(I)    ANGLE USED IN CALCULATING THE PUMP COLUMN
C                  DRAG,RADIANS
```

```
C      BOTAR        IS THE VELOCITY PROFILE AREA BELOW THE CENTRE OF
C                   ROTATION,M**2/S
C      BOTVEL       IS THE VELOCITY ADJACENT TO THE FLOOR IN A
C                   VERTICAL CROSS SECTION PASSING THROUGH THE CENTRE
C                   OF ROTATION,M/S
C      BPLUM2       PLUME WIDTH USED IN CALCULATING THE PUMP COLUMN
C                   DRAG,M
C      BPLUM3       PLUME WIDTH USED IN CALCULATING THE PUMP COLUMN
C                   DRAG,M
C      BTOB         IS THE MOMENTUM CORRECTION FACTOR FOR THE FLOW
C                   PASSING ABOVE THE CENTRE OF ROTATION; BASED ON
C                   THE ASSUMED VELOCITY PROFILE
C      BTOP         IS THE PLUME WIDTH AT THE FREE SURFACE,M.
C      BTTH         IS THE MOMENTUM CORRECTION FACTOR FOR THE FLOW
C                   PASSING ABOVE THE CENTRE OF ROTATION; BASED ON
C                   THE OBSERVED VELOCITY PROFILES.
C      CALRAT       IS THE RATIO OF FACTOR(14)/FACTOR(10)
C      CDRAG        PUMP COLUMN DRAG COEFFICIENT
C      CF           IS THE CALIBRATION CORRECTION FACTOR APPLIED TO
C                   THE MASS OF WATER ABOVE THE FREE SURFACE, (SEE
C                   FACTOR(14))
C      CHECK        A FUNCTION OF THE LENGTH OF THE INLINED FLOOR,M
C      CORRN        INCREASE IN FLUID DEPTH DUE TO DIFFUSED AIR,M
C      DBELL        BELL-MOUTH DIAMETER,M
C      DCFF         CORRECTION FACTORS USED TO ADJUST THE IMPACT
C                   VELOCITY ON THE PUMP COLUMNS; THE FACTORS CORRECT
C                   FOR FLOW CONSTRICTION
C      DELP2        PRESSURE FORCE DUE TO ELEVATED FREE SURFACE
C                   ABOVE THE DIFFUSER,N
C      DELTAF       EXTERNAL FORCE APPLIED AS CALCULATED BY THE
C                   LINEAR MOMENTUM EQUATION,N.
C      DEPTH        FLUID DEPTH IN THE WET-WELL,M
C      DEPTNO       IS A FUNCTION OF DEPTH,THE KINEMATIC VISCOSITY OF
C                   THE FLUID AND G AND IS USED TO ADJUST XCENRO AND
C                   YCENRO
C      DF           INCREMENTAL CHANGE IN THE HYDRODYNAMIC BUBBLE
C                   FORCE OVER A DISTANCE DY,N
C      DIFFER       THE DIFFERENCE BETWEEN THE L.H.S AND THE R.H.S.
C                   OF THE ANGULAR MOMENTUM EQUATION,N.M.
C      DIFSUB       DIFFUSER SUBMERGENCE,M
C      DOCOL        OUTER DIAMETER OF THE SUCTION PIPES,M
C      DQARDY       RATE OF CHANGE OF AIRFLOWRATE WITH RESPECT TO
C                   DEPTH,(M**3/S)/M
C      DY           INCREMENT IN FLUID DEPTH,M
C      DYP          INCREMENT IN FLUID DEPTH,M
C      FACTOR(I)    THE TERMS WHICH MAKE UP THE ANGULAR MOMENTUM
C                   EQUATION
C      FCROSR(I)    ARE THE "F" CROSS "R" TERMS OF FACTOR(10),N.M
C      FFH          FRICTION FORCE ON THE HORIZONTAL FLOOR,N.
C      FFI          FRICTION FORCE ON THE INCLINED FLOOR,N.
C      FHORIZ       THE FRICTION FACTOR OF THE HORIZONTAL FLOOR
```

```
C      FINCL        THE FRICTION FACTOR OF THE INCLINED FLOOR
C      FORCE        THE HYDRODYNAMIC BUBBLE FORCE,N
C      FRRWAL       THE FRICTION FACTOR OF THE WET WELL WALL ADJACENT
C                   TO THE DIFFUSER
C      FSWS         IS THE FRICTION FACTOR OF THE SIDE WALLS
C      G            ACCELERATION DUE TO GRAVITY,M/S**2
C      GAMFLU       UNIT WEIGHT OF FLUID,N/M**3
C      GAMMA        BUBBLE RADIUS PROPORTIONALITY FACTOR
C      H(I)         ELEVATION ABOVE THE WET-WELL FLOOR,M
C      HENTR        FLUID DEPTH AT THE INLET SECTION,M
C      HLOWER       FLUID DEPTH OF LOWER PART OF INLET SECTION,M
C      HPRIME       TOTAL FLUID DEPTH IN DIFFUSER PLUME CENTRELINE,M
C      HUPPER       FLUID DEPTH OF UPPER PART OF INLET SECTION,M
C      HVEL         VELOCITY HEAD OF INTAKE PIPES,M
C      LAMBDD(I)    ANGLE USED IN CALCULATING THE PUMP COLUMN DRAG,
C                   DEGREES
C      LAMBDR(I)    ANGLE USED IN CALCULATING THE PUMP COLUMN
C                   DRAG,RADIANS
C      LENGTH       LENGTH OF INCLINED FLOOR,M
C      LENGT1       LENGTH OF INCLINED FLOOR,M
C      MCF.         IS THE DEFAULT MOMENTUM CORRECTION AT FLOW CROSS-
C                   SECTION "."
C      MDOT1,2,3    MOMENTUM FLUXES CALCULATED BY THE LINEAR MOMENTUM
C                   EQUATION,N.
C      NN           THE NUMBER OF DIFFERENTIAL EQUATIONS TO BE
C                   SOLVED FOR USING THE RUNGA-KUTTA SUBROUTINE
C                   "SOLVE"
C      PATMOS       ATMOSPHERIC PRESSURE,PA,N/M**2
C      PERERR       THE % DIFFERENCE BETWEEN THE L.H.S & THE R.H.S.
C                   OF THE ANGULAR MOMENTUM EQUATION
C      PHISTD(I)    ANGLE USED IN CALCULATING THE PUMP COLUMN
C                   DRAG,DEGREES
C      PHISTR(I)    ANGLE USED IN CALCULATING THE PUMP COLUMN
C                   DRAG,RADIANS
C      PIE          3.141592654
C      PLUWID(I)    ARE THE DIFFUSER WIDTHS AT THE MID-POINT OF
C                   EACH OF THE DIFFUSER PLUME SUB-SECTIONS
C      PMPGNO       IS A FUNCTION OF THE PUMPING RATE,DEPTH AND G AND
C                   IS USED TO ADJUST XCENRO AND YCENRO
C      PMPRN        IS THE PUMP COLUMN REYNOLDS NUMBER
C      PSI          A FUNCTION INVOLVING SURFACE TENSION,M/S
C      QAIR         AIR FLOW RATE,M**3/S
C      QAIRO        DIFFUSER AIR FLOW RATE,M**3/S
C      QCIRC1       IS THE ESTIMATED CIRCULATING FLOW BASED ON BOTAR,
C                   M**3/S
C      QCIRC2       IS THE ESTIMATED CIRCULATING FLOW BASED ON TOPAR,
C                   M**3/S
C      QIQPR        IS THE FRACTION OF THE TOTAL PUMPING CAPACITY
C                   WHICH IS ASSUMED TO BE ENTERING THE INLET ZONE
C                   TO THE SUMP; IT IS USED TO SIMULATE A DRAWDOWN
C                   CONDITION
```

```
C     QLOWER      DISCHARGE OF LOWER PART OF INLET SECTION,M**3/S
C     QPUMP       PUMPING RATE,M**3/S
C     QUPPER      DISCHARGE OF UPPER PART OF INLET SECTION,M**3/S
C     QWATDF      WATER DISCHARGE WITHIN THE PLUME AT THE FREE
C                 SURFACE,M**3/S
C     R1(I)       ARE THE DISTANCES FROM THE CENTRE OF ROTATION TO
C                 THE LINE OF DIVISION BETWEEN THE PLUG FLOW AND THE
C                 LINEAR FLOW ZONES; USED TO CALCULATE THE SIDE WALL
C                 SHEAR,M.
C     R(I)        RADIAL DISTANCE FROM CENTRE OF ROTATION TO
C                 DIFFUSER PLUME SUB-SECTIONS,M
C     RAY(I)      ARE THE LENGTHS OF THE SIDES OF THE TRIANGULAR
C                 SHAPED WEDGES USED IN CALCULATING THE SIDE WALL
C                 SHEAR,M.
C     RBUBLE      BUBBLE RADIUS,M
C     RCOL(I)     RADIAL DISTANCES FROM CENTRE OF ROTATION TO THE
C                 PUMP COLUMN SUB-SECTIONS
C     RDELTF      MOMENT ARM CORRESPONDING TO FORCE DELTAF,M.
C     RDISCH      RADIAL DISTANCE TO CENTROID OF PUMP INTAKE,M
C     RDIVH       THE RADIAL DISTANCE FROM THE CENTRE OF ROTATION
C                 TO THE DIVISION LINE BETWEEN THE DIFFUSER AND THE
C                 INLET INFLUENCED FLOWS ABOVE THE HORIZONTAL
C                 PORTION OF THE WET-WELL FLOOR,M
C     RDIVN(I)    THE RADIAL DISTANCE TO THE DIVIDING LINE BETWEEN
C                 THE FLOW INFLUENCED BY THE DIFFUSER AND THE FLOW
C                 INFLUENCED BY THE INLET CONDITIONS,M
C     REXTRM(I)   RADIAL DISTANCE TO THE CENTROID OF THE EXTREME
C                 SURFACES,M
C     RHOFLU      FLUID DENSITY,KG/M**3
C     RHOGAS      GAS DENSITY,KG/M**3
C     RHORIZ      RADIAL DISTANCE TO CENTROID OF HORIZONTAL FLOOR,M
C     RINCDV      THE RADIAL DISTANCE FROM THE CENTRE OF ROTATION
C                 TO THE DIVISION LINE BETWEEN THE DIFFUSER AND
C                 INLET INFLUENCED FLOWS ABOVE THE INCLINED PART
C                 OF THE WET-WELL FLOOR,M
C     RINCL       RADIAL DISTANCE TO CENTROID OF INCLINED FLOOR,M
C     RKE...      IS THE KINETIC ENERGY OF FLUID VOLUME "...",J
C     RKETOT      IS THE TOTAL KINETIC ENERGY OF THE SYSTEM,J.
C     RLOWER      RADIAL DISTANCE TO CENTROID OF LOWER PART OF
C                 INLET SECTION,M
C     RPAR        A COMPONENT OF RINCL PARALLEL TO THE INCLINED
C                 PORTION OF THE WET-WELL FLOOR,M.
C     RPERPI      THE PERPENDICULAR DISTANCE FROM THE CENTRE OF
C                 ROTATION TO THE INCLINED PLANE,M
C     RU,RL       RADIAL DISTANCE FROM THE CENTRE OF ROTATION;
C                 USED IN LINEAR MOMENTUM BALANCE,M.
C     RUPPER      RADIAL DISTANCE TO CENTROID OF UPPER PART OF
C                 INLET SECTION,M
C     SCALE       IS THE RATIO OF THE DESIGN BELL-MOUTH DIAMETER TO
C                 THE PHYSICAL MODEL BELL-MOUTH DIAMETER
C     SUBINT      THE SUBMERGENCE OF THE INTAKE PIPES,M.
```

```
C      SURFVL        IS THE HORIZONTAL WATER VELOCITY AT THE FREE
C                    SURFACE AT A VERTICAL CROSS SECTION THROUGH THE
C                    CENTRE OF ROTATION,M/S.
C      SWSTOT        IS THE TOTAL SIDE WALL SHEAR TORQUE,N.M.
C      TARLAC        IS THE DECAY RELATIONSHIP FOR THE "CALRAT" RATIO
C                    AND IS GIVEN AS: TARLAC=0.792/(DEPTH**0.510)
C      TAUHOR        IS THE SHEAR STRESS ON THE HORIZONTAL PART OF THE
C                    WET WELL FLOOR,N/M**2
C      TAUINC        IS THE SHEAR STRESS ON THE INCLINED PART OF THE
C                    WET WELL FLOOR,N/M**2
C      TCROSR(I)     ARE THE "T" CROSS "R" TERMS OF FACTOR(3),N.M
C      THETAD        FLOOR SLOPE,DEGREES
C      THETAR        FLOOR SLOPE,RADIANS
C      TOPAR         IS THE VELOCITY PROFILE AREA ABOVE THE CENTRE OF
C                    ROTATION,M**2/S
C      TORQUE(I)     ARE THE ASSOCIATED TORQUES FOR EACH OF THE SIDE
C                    WALL SUB-AREAS,N.M.
C      VA...         FLOW VELOCITIES USED IN CALCULATING THE KINETIC
C                    ENERGY OF THE SYSTEM,M/S.
C      VACT(I)       FLUID VELOCITIES AT THE PUMP COLUMNS,M/S
C      VACTUL(I)     THE FLUID VELOCITIES AT THE EXTREME SURFACES,
C                    USED IN CALCULATING THE PUMP COLUMN DRAG,M/S
C      VAMBNT        THE AMBIANT VERTICAL FLUID VELOCITY ADJACENT TO
C                    THE DIFFUSER PLUME,M/S
C      VAR1 &        CALIBRATION PARAMETERS USED IN ESTIMATING THE
C      VAR2          AMBIENT PLUME VELOCITY
C      VCD           IS THE MEAN IMPACT VELOCITY ON THE PUMP COLUMNS;
C                    USED TO ESTIMATE THE PUMP COLUMN REYNOLDS NUMBER,
C                    M/S
C      VCD.          VELOCITIES USED TO OBTAIN THE MEAN PUMP COLUMN
C                    IMPACT VELOCITY
C      VDISCH        IS THE VELOCITY IN THE SUCTION PIPE,M/S
C      VDOT1,2,3     VELOCITIES USED IN CALCULATING THE EXTERNALLY
C      VDOT11,22,33  APPLIED FORCES AS CALCULATED BY THE LINEAR
C                    MOMENTUM EQUATION,M/S.
C      VELJET        IS THE MAXIMUM VELOCITY IN A VERTICAL PROFILE
C                    PASSING THROUGH THE CENTRE OF ROTATION,M/S.
C      VER           RADIAL VELOCITY, USED IN CALCULATING THE KINETIC
C                    ENERGY OF THE SYSTEM,M/S
C      VERT(I)       VERTICAL DISTANCE BETWEEN THE CENTRE OF ROTATION
C                    AND THE CENTRE OF THE DIFFUSER PLUME SUB-SECTIONS
C                    ,M
C      VET           TANGENTIAL VELOCITY, USED IN CALCULATING THE
C                    KINETIC ENERGY OF THE SYSTEM,M/S
C      VHORIZ(I)     HORIZONTAL FLUID VELOCITIES AT THE PUMP COLUMNS,
C                    M/S
C      VINCL         IS THE FLUID VELOCITY PARALLEL TO THE INCLINED
C                    PART OF THE WET-WELL FLOOR,M/S.
C      VISKIN        IS THE KINEMATIC VISCOSITY OF THE FLUID,M**2/S.
C      VLOWER        FLUID VELOCITY OF LOWER PART OF INLET SECTION,M/S
```

```
C     VPARH        FLUID VELOCITY PARALLEL AND ADJACENT TO THE
C                  THE HORIZONTAL FLOOR,M/S
C     VR(I)        RADIAL FLUID VELOCITIES AT THE PUMP COLUMNS,M/S
C     VRAD2(I)     RADIAL FLUID VELOCITIES AT THE EXTREM SURFACES,
C                  M/S
C     VT(I)        TANGENTIAL VELOCITIES AT THE PUMP COLUMNS,M/S
C     VTANH        THE TANGENTIAL VELOCITY COMPONENT OF THE FLUID
C                  ADJACENT TO THE HORIZONTAL FLOOR,M/S
C     VTANIC       THE TANGENTIAL VELOCITY OF THE FLUID ADJACENT
C                  TO THE INCLINED FLOOR,M/S.
C     VTAN2(I)     TANGENTIAL FLUID VELOCITIES AT THE EXTREME
C                  SURFACES,M/S
C     VTR(I)       ARE THE TANGENTIAL VELOCITIES USED TO CALCULATE
C                  THE SIDE WALL SHEAR TORQUE,M/S.
C     VU,VL        MEAN VELOCITY; USED IN CALCULATING THE LINEAR
C                  MOMENTUM BALANCE,M/S.
C     VUPPER       FLUID VELOCITY OF UPPER PART OF INLET SECTION,M/S
C     VVERT(I)     THE VERTICAL AMBIANT FLUID VELOCITIES WHICH ARE
C                  AVERAGED TO OBTAIN VAMBNT,M/S
C     VW           IS THE WATER VELOCITY AT THE DIFFUSER,M/S
C     WATVEL(I)    WATER VELOCITY IN THE PLUME,M/S
C     WIDTH        PLUME WIDTH AT THE FREE SURFACE,M
C     WW(I)        THE DIFFERENTIAL EQUATIONS CORRESPONDING TO Y(I)
C     XCENRO       X COORDINATE OF CENTRE OF ROTATION,M
C     XGEOM        IS THE X COORDINATE OF THE GEOMETRIC CENTRE OF
C                  THE SUMP,M.
C     XRHS         IS THE EQUATION WHICH CALIBRATES THE GEOMETRIC
C                  TO THE MEASURED X COMPONENT OF THE CENTRE OF
C                  ROTATION
C     XSP          X COORDINTE OF SUCTION PIPES,M
C     XXTRM(I)     X COORDINATE OF THE EXTREME SURFACES,M
C     Y            IS THE DISTANCE ABOVE THE DIFFUSER,M
C     Y(1)         PLUME WIDTH,M
C     Y(2)         PLUME AIR FRACTION
C     Y(3)         PLUME WATER VELOCITY,M/S
C     Y(4)         HYDRODYNAMIC BUBBLE FORCE,N
C     YBARP        Y COORDINATE OF CENTROID OF PRESSURE FORCE,M
C     YCENRO       Y COORDINATE OF CENTRE OF ROTATION,M
C     YDF          IS THE VERTICAL DISTANCE BETWEEN THE CENTRE OF
C                  ROTATION AND THE LINE OF ACTION OF THE DELTAF
C                  FORCE,M.
C     YGEOM        IS THE Y COORDINATE OF THE GEOMETRIC CENTRE OF
C                  THE SUMP,M.
C     YLM          DISTANCE USED TO CALCULATE VDOT2 WHEN PUMPING IS
C                  OCCURRING;USED IN APPLYING THE LINEAR MOMENTUM
C                  EQUATION TO THE CROSS-SECTION,M.
```

```
C      YP            DISTANCE ABOVE THE DIFFUSER AT WHICH THE SOLUTION
C                    OF THE DIFFERENTIAL EQUATIONS BEGINS
C      YRHS          IS THE EQUATION WHICH CALIBRATES THE GEOMETRIC
C                    TO THE MEASURED Y COMPONENT OF THE CENTRE OF
C                    ROTATION
C      YVAL(I)       A DISTANCE ABOVE THE DIFFUSER USED IN CALCULATING
C                    THE PUMP COLUMN DRAG,M
C      YXTRM(I)      Y COORDINATE OF THE EXTREME SURFACES,M
?
```

A1.3 WATFIV COMPUTER PROGRAM LISTING

The following program listing is written in Structured WATFIV for execution on an IBM 3031 computer. The pertinent information about the program, is given below:

1. Core Usage
    (a) object code = 80336 bytes
    (b) array area = 90280 bytes
2. Compile Time = 1.3 seconds
3. Execution Time = 23.5 seconds
4. Statements Executed = 1054900

```
//MODEL JOB   (R040,GF9,1,10),'D. MACHINA',CLASS=Z
// EXEC  WATFIV
//GO.SYSIN  DD  *
$JOB   WATFIV  R040 MACHINA
C
C
C     HYDRODYNAMIC MODEL TO DESCRIBE THE FLOW CONDITIONS WITHIN A
C     WETWELL UNDER VARIOUS OPERATING CONDITIONS.
C
C     METRIC UNITS USED THROUGHOUT
C
C     PRECISION SPECIFICATION AND ARRAY DIMENSIONING
C
      EXTERNAL VECTOR
      DIMENSION H(10),VERT(10),R(10),PHISTR(3),PHISTD(3)
      DIMENSION YVAL(4),NUMIT(4),VACTUL(4),RDIVN(4),VTAN2(4)
      DIMENSION VRAD2(4),ITERF(10),DF(10)
      DIMENSION RCOL(4),XXTRM(4),YXTRM(4),REXTRM(4)
      DIMENSION VR(4),VT(4),VACT(4),ANGPHI(4),ANGPHR(4)
      DIMENSION BETDEG(4),BETRAD(4),VHORIZ(4)
      DIMENSION ITERAN(10),WATVEL(10),FORCE(10)
      DIMENSION ANGINR(3),ANGINC(3),FACTOR(15),ANGHRR(2),ANGHOR(2)
      DIMENSION TCROSR(10),FCROSR(10),PLUWID(10)
      DIMENSION VVERT(4)
      DIMENSION DIFFER(20000)
      DIMENSION ANGSWS(550),TORQUE(550),ANGSWD(550)
      REAL LAMBDR(4)
      REAL LAMBDD(4)
      REAL MCF1,MCF2,MCF3,MDOT1,MDOT2,MDOT3
      REAL*8 Y(25),WW(25),DY(25)
      REAL*8 A,DIFSUB,PATMOS,GAMFLU,QAIRO,B,DQARDY
      REAL*8 AA,DBELL,BB,ALPHAC,CC,FRRWAL,DD,RHOFLU,RHOGAS
      REAL*8 FF,PSI,QAIR,GG,HH,G,PP,QQ,RR,SS,TT
      COMMON/XYZ1/A,DIFSUB,PATMOS,GAMFLU,QAIRO
      COMMON/XYZ2/B,DQARDY,AA,DBELL,BB
      COMMON/XYZ3/ALPHAC,CC,FRRWAL,DD,RHOFLU
      COMMON/XYZ4/RHOGAS,FF,PSI,QAIR,GG
      COMMON/XYZ5/HH,G,PP,QQ,RR
      COMMON/XYZ6/SS,TT,SCALE
      COMMON/XYZ7/DEPTH,VAMBNT,VAR1,VAR2
      REAL*8 LENGTH,LENGT1
      NN=5
      PRINT,'NN=',NN
C
```

```
C
C     SPECIFICATION OF DEFAULT VALUES AT 20 DEGREES CENTIGRADE
C
C
      PATMOS=101300.0
      GAMFLU=9788.3786
      G=9.806
      RHOFLU=998.203
      RHOGAS=1.2047
      PSI=0.2500845266
      PIE=3.141592654
      DYP=0.001
      YP=0.001
      VISKIN=0.0000010038038
      PRINT,'THE KINEMATIC VISCOSITY OF THE FLUID IS=',VISKIN
      PRINT,'PATMOS=',PATMOS
      PRINT,'GAMFLU=',GAMFLU
      PRINT,'G=',G
      PRINT,'RHOFLU=',RHOFLU
      PRINT,'RHOGAS=',RHOGAS
      PRINT,'PSI=',PSI
      PRINT,'PIE=',PIE
      PRINT,'DYP=',DYP
      PRINT,'YP=',YP
C
C
C     READ IN THE REQUIRED INPUT INFORMATION
C
C
      READ,DBELL,DEPTH,THETAD,SCALE
      READ,RBUBLE,ALPHAC,GAMMA,QAIRO,QPUMP,QIQPR
      READ,FINCL,FHORIZ,FSWS,FRRWAL
      PRINT,'DBELL=',DBELL
      PRINT,'RBUBLE=',RBUBLE
      PRINT,'DEPTH=',DEPTH
      PRINT,'GAMMA=',GAMMA
      PRINT,'ALPHAC=',ALPHAC
      PRINT,'THETAD=',THETAD
      PRINT,'QAIRO=',QAIRO
      PRINT,'QPUMP=',QPUMP
      PRINT,'THE INFLOW TO PUMPING RATIO=',QIQPR
      PRINT,'THE SCALE RATIO=',SCALE
C
C
      DIFSUB=DEPTH-(0.01905*SCALE)
      PRINT,'DIFSUB=',DIFSUB
      THETAR=THETAD*PIE/180.0
C
```

```
C
C     DETERMINE THE LENGTH OF THE INCLINED PORTION OF THE WETWELL
C     FLOOR
C
C
      LENGT1=(6.138*DBELL)/(COS(THETAR))
      CHECK=LENGT1*SIN(THETAR)
      IF(CHECK.GE.DEPTH)THEN DO
      LENGTH=DEPTH/(SIN(THETAR))
      ELSE DO
      LENGTH=LENGT1
      END IF
      IF(CHECK.GE.DEPTH)GO TO 900
      PRINT,'LENGTH=',LENGTH
C
C
C     CALCULATION OF THE VELOCITY HEAD FOR EACH INTAKE
C
C
      APIPE=0.337952*DBELL*DBELL
      HVEL=((QPUMP/3.0)**2)/(2.0*G*APIPE*APIPE)
      PRINT,'APIPE=',APIPE
      PRINT,'HVEL=',HVEL
C
C
C     LOCATE THE ASSUMED CENTRE OF ROTATION
C
C
      T1=(3.0*DEPTH)*((6.5*DBELL+LENGTH*COS(THETAR))**2)
      T2=LENGTH*LENGTH*COS(THETAR)*SIN(THETAR)
      T3=19.5*DBELL+2.0*LENGTH*COS(THETAR)
      T4=6.0*DEPTH*(6.5*DBELL+LENGTH*COS(THETAR))
      T5=3.0*LENGTH*LENGTH*COS(THETAR)*SIN(THETAR)
      T6=(6.5*DBELL+LENGTH*COS(THETAR))*3.0*DEPTH*DEPTH
      T7=LENGTH*LENGTH*LENGTH*SIN(THETAR)*SIN(THETAR)*COS(THETAR)
      T8=(6.5*DBELL+LENGTH*COS(THETAR))*6.0*DEPTH
      T9=3.0*LENGTH*LENGTH*COS(THETAR)*SIN(THETAR)
      XGEOM=(T1-T2*T3)/(T4-T5)
      YGEOM=(T6-T7)/(T8-T9)
      PRINT,'XGEOM=',XGEOM
      PRINT,'YGEOM=',YGEOM
C
```

```
C
C     MODIFY THE COORDINATES OF THE GEOMETRIC CENTRE OF ROTATION
C     USING EXPERIMENTAL OBSERVATIONS
C
C
      PMPGNO=QPUMP/(DEPTH**2.5*G**0.5)*QIQPR
      IF(PMPGNO.GE.0.023)PMPGNO=0.023
      AIRNO=QAIRO/(DEPTH**2.5*G**0.5)
      IF(AIRNO.GE.0.034)AIRNO=0.034
      DEPTNO=DEPTH**1.5*G**0.5/VISKIN
      IF(DEPTNO.GE.2.72E06)DEPTNO=2.72E06
      XRHS=0.161-30.395*PMPGNO+4.042*AIRNO+0.00494*THETAD-
     &((3.619E-08)*(DEPTNO))
      YRHS=-1.568+3.056*YGEOM/DEPTH-4.836*AIRNO+5.815*PMPGNO+
     &((7.004E-08)*(DEPTNO))-0.00537*THETAD
      XCENRO=XGEOM*(1.0+XRHS)
      YCENRO=YGEOM*(1.0+YRHS)
      IF(YCENRO.LT.(0.5*DBELL))GO TO 908
      PRINT,'PMPGNO=',PMPGNO
      PRINT,'AIRNO=',AIRNO
      PRINT,'DEPTNO=',DEPTNO
      PRINT,'XCENRO=',XCENRO
      PRINT,'YCENRO=',YCENRO
C
C
C     CALCULATION OF RADIAL DISTANCES FROM THE CENTRE-OF-ROTATION
C
C
      AAA=(6.5*DBELL+LENGTH*COS(THETAR)*0.5)-XCENRO
      AAAA=ABS(AAA)
      AAAAA=AAAA**2
      BBBBB=(YCENRO-0.5*LENGTH*SIN(THETAR))
      BBBB=ABS(BBBBB)
      BBB=BBBB**2
      RINCL=(AAAAA+BBB)**0.50
      CCC=XCENRO-5.25*DBELL
      DDD=ABS(CCC)
      RHORIZ=(DDD**2+YCENRO**2)**0.50
      EEE=(YCENRO-0.5*DBELL)**2
      FFF=(XCENRO-3.5*DBELL)**2
      RDISCH=(EEE+FFF)**0.5
      IF(YCENRO.GT.CHECK)GO TO 50
      IF(YCENRO.LT.CHECK)GO TO 51
   50 GGG=(0.5*(DEPTH-YCENRO))**2
      HHH=(12.638*DBELL-XCENRO)**2
      PPP=(0.5*(YCENRO-LENGTH*SIN(THETAR)))**2
      QQQ=(12.638*DBELL-XCENRO)**2.0
      RUPPER=(GGG+HHH)**0.50
      RLOWER=(PPP+QQQ)**0.50
      GO TO 52
   51 CONTINUE
```

```
      RLOWER=0.0
      PPP=0.0
      QQQ=0.0
      GGG=(0.5*DEPTH+0.5*LENGTH*SIN(THETAR)-YCENRO)**2
      HHH=(12.638*DBELL-XCENRO)**2
      RUPPER=(GGG+HHH)**0.50
   52 CONTINUE
      PRINT,'RINCL=',RINCL
      PRINT,'RHORIZ=',RHORIZ
      PRINT,'RDISCH=',RDISCH
      PRINT,'RUPPER=',RUPPER
      PRINT,'RLOWER=',RLOWER
C
C
C     CALCULATION OF THE RADIAL DISTANCE TO THE SUB-DIVIDED
C     DIFFUSER PLUME
C
C
      H(1)=0.05*DEPTH
      H(2)=0.15*DEPTH
      H(3)=0.25*DEPTH
      H(4)=0.35*DEPTH
      H(5)=0.45*DEPTH
      H(6)=0.55*DEPTH
      H(7)=0.65*DEPTH
      H(8)=0.75*DEPTH
      H(9)=0.85*DEPTH
      H(10)=0.95*DEPTH
      DO 1 I=1,10
      VERT(I)=ABS(YCENRO-H(I))
    1 CONTINUE
      DO 2 I=1,10
      R(I)=(XCENRO**2+VERT(I)**2)**0.5
    2 CONTINUE
C
C
C     CALCULATION OF PHISTAR ANGLES FOR DETERMINATION OF THE PUMP
C     COLUMN DRAG FORCES
C
C
      PHISTR(1)=ATAN(XCENRO/YCENRO)
      PHISTD(1)=PHISTR(1)*180.0/PIE
      PHISTR(2)=ATAN(XCENRO/(DEPTH-YCENRO))
      PHISTD(2)=PHISTR(2)*180.0/PIE
      PHISTD(3)=180.0-PHISTD(2)
      PHISTR(3)=PHISTD(3)*PIE/180.0
C
C
C     CALCULATION OF THE LAMBDA ANGLES FOR THE DETERMINATION
C     OF THE PUMP COLUMN DRAG FORCES
C
```

```
C
C     XSP IS THE "X" COORDINATE OF THE CENTRE-LINE OF THE PUMP
C     COLUMNS
C
C
      XSP=3.50*DBELL
      IF(XCENRO.LE.XSP)GO TO 907
C
C
      Z1=XCENRO-XSP
      Z2=0.75*(YCENRO-0.5*DBELL)
      LAMBDR(1)=ATAN2(Z1,Z2)
      LAMBDD(1)=LAMBDR(1)*180.0/PIE
      Z3=0.25*(YCENRO-0.5*DBELL)
      LAMBDR(2)=ATAN2(Z1,Z3)
      LAMBDD(2)=LAMBDR(2)*180.0/PIE
      Z4=0.25*(DEPTH-YCENRO)
      Z5=ATAN2(Z4,Z1)
      Z6=Z5*180.0/PIE
      LAMBDD(3)=90.0+Z6
      LAMBDR(3)=LAMBDD(3)*PIE/180.0
      Z7=0.75*(DEPTH-YCENRO)
      Z8=ATAN2(Z1,Z7)
      Z9=Z8*180.0/PIE
      LAMBDD(4)=180.0-Z9
      LAMBDR(4)=LAMBDD(4)*PIE/180.0
C
C
C     CALCULATION OF THE DISTANCES FROM THE CENTRE OF ROTATION TO
C     THE CENTROIDS OF THE SUB-DIVIDED PUMP COLUMNS
C
C
      RCOL(1)=(Z1**2+Z2**2)**0.50
      RCOL(2)=(Z1**2+Z3**2)**0.50
      RCOL(3)=(Z1**2+Z4**2)**0.50
      RCOL(4)=(Z1**2+Z7**2)**0.50
C
C
C     CALCULATION OF THE RADIAL DISTANCES TO THE EXTREME SURFACES
C     TO CALCULATE THE RADIAL AND TANGENTIAL VELOCITY COMPONENTS
C     AT THE OUTSIDE BOUNDARIES
C
      XXTRM(1)=(YCENRO*(XCENRO-XSP))/(0.75*(YCENRO-0.5*DBELL))
      YXTRM(2)=(0.25*XCENRO*(YCENRO-0.5*DBELL))/(XCENRO-XSP)
      YXTRM(3)=(0.25*XCENRO*(DEPTH-YCENRO))/(XCENRO-XSP)
      XXTRM(4)=(XCENRO-XSP)/0.75
      REXTRM(1)=SQRT(YCENRO*YCENRO+XXTRM(1)*XXTRM(1))
      REXTRM(2)=SQRT(YXTRM(2)*YXTRM(2)+XCENRO*XCENRO)
      REXTRM(3)=SQRT(XCENRO*XCENRO+YXTRM(3)*YXTRM(3))
      REXTRM(4)=SQRT((DEPTH-YCENRO)**2+XXTRM(4)**2)
C
```

```
C
C     CALCULATE THE DISTANCE ABOVE THE DIFFUSER WHERE REXTRM(2)
C     AND REXTRM(3) INTERCEPT THE WALL
C
C
      YVAL(2)=YCENRO-YXTRM(2)
      YVAL(3)=YCENRO+YXTRM(3)
      NUMIT(1)=YCENRO/DYP
      NUMIT(2)=YVAL(2)/DYP
      NUMIT(3)=YVAL(3)/DYP
C
C
C
C     BREAKING DOWN THE DIFFUSER PLUME INTO TEN SUB-SECTIONS TO
C     ASSIST IN CALCULATING THE SHEAR RESISTANCE TO, AND THE
C     HYDRODYNAMIC FORCE OF THE BUBBLES ON THE FLUID
C
C
      DO 6 J=1,10
      ITERAN(J)=H(J)/DYP
    6 CONTINUE
C     DEFAULT NUMIT(2) AND NUMIT(3) IF THEY ARE OUT OF RANGE
      IF(NUMIT(2).LE.0.0)NUMIT(2)=ITERAN(1)
      IF(NUMIT(3).GE.DEPTH)NUMIT(3)=ITERAN(10)
C
C
C
C     INITIALIZATION OF DATA FOR THE RUNGA-KUTTA SUBROUTINE "SOLVE"
C
C
      EST1=0.0438+(0.3728*SCALE*0.001)/DEPTH
      EST2=3.415*AIRNO
      EST3=SQRT(9.806*DEPTH)
      Y(3)=EST3*(EST1+EST2)
      IF(Y(3).LE.0.0)Y(3)=0.005
      Y(1)=GAMMA*RBUBLE*SCALE
      ARGU1=0.5+PSI/(2.0*Y(3))+QAIRO/(12.0*DBELL*GAMMA*SCALE*
     &RBUBLE*Y(3))
      ARGU2=-1.0-PSI/Y(3)-QAIRO/(6.0*DBELL*GAMMA*RBUBLE*SCALE*
     &Y(3))
      ARGU3=(ARGU2**2)*0.25
      ARGU4=ARGU3-QAIRO/(6.0*DBELL*GAMMA*RBUBLE*SCALE*Y(3))
      ARGU5=SQRT(ARGU4)
      ARGU6=ARGU1+ARGU5
      ARGU7=ARGU1-ARGU5
      IF(ARGU6.GT.1.0.OR.ARGU6.LT.0.0)Y(2)=ARGU7
      IF(ARGU7.GT.1.0.OR.ARGU7.LT.0.0)Y(2)=ARGU6
      IF(ARGU6.LT.1.0.AND.ARGU6.GT.0.0.AND.ARGU7.LT.1.0.AND.ARGU7.
     &GT.0.0)Y(2)=AMIN1(ARGU6,ARGU7)
      Y(4)=0.0
      Y(5)=QAIRO
      IT=1
      VW=Y(3)
  700 CONTINUE
C
C     DYP IS THE INCREMENT IN THE DEPTH AND IS GIVEN IN THE DEFAULT
C     VALUE SECTION OF THE PROGRAM.......=0.001 M.
C
C     YP IS THE FINITE DISTANCE AWAY FROM THE DIFFUSER AT WHICH THE
C     CALCULATIONS BEGIN.................=0.001 M.
C
C
C
C     CALL RUNGA-KUTTA SUBROUTINE AND SOLVE FOR Y(1),Y(2) AND Y(3)
C
C
      NOITER=DEPTH/DYP
      PRINT 480
  480 FORMAT(' '.1X,'Y(M)'.6X,'B(M)',4X,'AIR FRCN',4X,'VW(M/S)')
      PRINT 490,YP,Y(1),Y(2),Y(3)
  490 FORMAT(' ',F5.3,2X,F9.4,2X,F10.8,2X,F7.4)
      DO 4 I=1,NOITER
      CALL SOLVE(YP,Y,DY,DYP,NN,VECTOR)
      IF(Y(1).LE.(3.0*RBUBLE*SCALE))Y(1)=3.0*RBUBLE*SCALE
      PRINT 490,YP,Y(1),Y(2),Y(3)
C
C
C     CALCULATION OF THE FLUID VELOCITIES AT THE EXTREME SURFACES
C     WITHIN THE DIFFUSER PLUME REGION
C
C
      IF(I.EQ.NUMIT(2))THEN DO
      VACTUL(2)=Y(3)
      END IF
      IF(I.EQ.NUMIT(3))THEN DO
      VACTUL(3)=Y(3)
      END IF
      IF(I.EQ.NOITER)THEN DO
      VACTUL(4)=Y(3)
      END IF
      IF(I.EQ.NUMIT(2))THEN DO
      BPLUM2=Y(1)
      END IF
      IF(I.EQ.NUMIT(3))THEN DO
      BPLUM3=Y(1)
      END IF
      IF(I.EQ.NOITER)THEN DO
      WIDTH=Y(1)
      END IF
```

```
C
C
C     SELECT THE APPROPRIATE WATER VELOCITY
C
C
      IF(I.EQ.ITERAN(1))WATVEL(1)=Y(3)
      IF(I.EQ.ITERAN(2))WATVEL(2)=Y(3)
      IF(I.EQ.ITERAN(3))WATVEL(3)=Y(3)
      IF(I.EQ.ITERAN(4))WATVEL(4)=Y(3)
      IF(I.EQ.ITERAN(5))WATVEL(5)=Y(3)
      IF(I.EQ.ITERAN(6))WATVEL(6)=Y(3)
      IF(I.EQ.ITERAN(7))WATVEL(7)=Y(3)
      IF(I.EQ.ITERAN(8))WATVEL(8)=Y(3)
      IF(I.EQ.ITERAN(9))WATVEL(9)=Y(3)
      IF(I.EQ.ITERAN(10))WATVEL(10)=Y(3)
C
C
C     SELECT THE APPROPRIATE HYDRODYNAMIC BUBBLE FORCE
C
C
      ITERF(1)=0.10*DEPTH/DYP
      ITERF(2)=0.20*DEPTH/DYP
      ITERF(3)=0.30*DEPTH/DYP
      ITERF(4)=0.40*DEPTH/DYP
      ITERF(5)=0.50*DEPTH/DYP
      ITERF(6)=0.60*DEPTH/DYP
      ITERF(7)=0.70*DEPTH/DYP
      ITERF(8)=0.80*DEPTH/DYP
      ITERF(9)=0.90*DEPTH/DYP
      ITERF(10)=NOITER
      IF(I.EQ.ITERF(1))FORCE(1)=Y(4)
      IF(I.EQ.ITERF(2))FORCE(2)=Y(4)
      IF(I.EQ.ITERF(3))FORCE(3)=Y(4)
      IF(I.EQ.ITERF(4))FORCE(4)=Y(4)
      IF(I.EQ.ITERF(5))FORCE(5)=Y(4)
      IF(I.EQ.ITERF(6))FORCE(6)=Y(4)
      IF(I.EQ.ITERF(7))FORCE(7)=Y(4)
      IF(I.EQ.ITERF(8))FORCE(8)=Y(4)
      IF(I.EQ.ITERF(9))FORCE(9)=Y(4)
      IF(I.EQ.ITERF(10))FORCE(10)=Y(4)
C
C
```

```
C     SELECT THE APPROPRIATE PLUME WIDTH
C
C
      IF(I.EQ.ITERAN(1))PLUWID(1)=Y(1)
      IF(I.EQ.ITERAN(2))PLUWID(2)=Y(1)
      IF(I.EQ.ITERAN(3))PLUWID(3)=Y(1)
      IF(I.EQ.ITERAN(4))PLUWID(4)=Y(1)
      IF(I.EQ.ITERAN(5))PLUWID(5)=Y(1)
      IF(I.EQ.ITERAN(6))PLUWID(6)=Y(1)
      IF(I.EQ.ITERAN(7))PLUWID(7)=Y(1)
      IF(I.EQ.ITERAN(8))PLUWID(8)=Y(1)
      IF(I.EQ.ITERAN(9))PLUWID(9)=Y(1)
      IF(I.EQ.ITERAN(10))PLUWID(10)=Y(1)
      IF(I.EQ.NOITER)THEN DO
      AIRFCN=Y(2)
      BTOP=Y(1)
      END IF
    4 CONTINUE
C
C
C     OBTAIN THE VELOCITY PROFILE THRU THE CENTRE OF ROTATION
C     BASED ON THE EXPERIMENTAL OBSERVATIONS
C
C
      KRUN=1
      VP1=QAIRO/(DEPTH**2.5*G**0.5)
      IF(VP1.GE.0.034)VP1=0.034
      VP2=QPUMP/(DEPTH**2.5*G**0.5)*QIQPR
      IF(VP2.GE.0.023)VP2=0.023
      VP3=THETAD
      VP8=YCENRO/DEPTH
      VP10=(G**0.5*DEPTH**1.5)/VISKIN
      IF(VP10.GE.2.72E06)VP10=2.72E06
      VP4=-0.2410+13.633*VP1-6.323*VP2-0.00121*VP3+0.633*VP8
     &+(1.820E-08)*(VP10)
      VP5=-0.2514+14.378*VP1-7.154*VP2-0.000767*VP3+0.618*VP8
     &+(3.027E-08)*(VP10)
      VP7=0.549-0.258*VP1-11.338*VP2+0.00297*VP3-(1.240E-07)*
     &(VP10)
      VP9=0.589+0.385*VP1+1.534*VP2-0.000945*VP3+0.575*VP8+
     &(1.372E-08)*(VP10)
      VP6=0.0389-4.246*VP1+4.269*VP2+0.000269*VP3-0.1822*VP7
     &+0.539*VP5
      SURFVL=(VP4*(G*DEPTH)**0.5)
      VELJET=(VP5*(G*DEPTH)**0.5)
      BOTVEL=(VP6*(G*DEPTH)**0.5)
      BBOTVL=VP7*DEPTH
      IF(BBOTVL.GE.YCENRO)BBOTVL=YCENRO
      IF(BBOTVL.LE.0.0)BBOTVL=0.0
      AVELJT=VP9*DEPTH
      IF(AVELJT.GE.DEPTH)AVELJT=DEPTH
      ICOUNT=1
      307 CONTINUE
          TOPAR=0.5*(SURFVL*(DEPTH-AVELJT)+VELJET*(DEPTH-YCENRO))
          BOTAR=0.5*BOTVEL*(YCENRO+BBOTVL)
          QCIRC1=BOTAR*6.0*DBELL-QPUMP
          QCIRC2=TOPAR*6.0*DBELL
          DELQCI=QCIRC1-QCIRC2
          DELQC2=ABS(DELQCI)
          DELQC3=(DELQC2/QCIRC1)*100.00
          IF(DELQC3.LE.0.5)GO TO 300
          IF(QCIRC1.GT.QCIRC2)GO TO 305
          IF(QCIRC2.GT.QCIRC1)GO TO 310
      305 CONTINUE
          BOTVEL=BOTVEL-0.0005
          SURFVL=SURFVL+0.0005
          VELJET=VELJET+0.0005
          GO TO 315
      310 SURFVL=SURFVL-0.0005
          VELJET=VELJET-0.0005
          BOTVEL=BOTVEL+0.0005
      315 CONTINUE
          ICOUNT=ICOUNT+1
          IF(ICOUNT.EQ.10000)GO TO 300
          IF(ICOUNT.NE.10000)GO TO 307
      300 CONTINUE
C
C
C         CALCULATION OF QUPPER,VUPPER,QLOWER,VLOWER
C
C
          HENTR=DEPTH-LENGTH*SIN(THETAR)
          IF(YCENRO.GT.CHECK)GO TO 55
          IF(YCENRO.LT.CHECK)GO TO 56
       55 HUPPER=DEPTH-YCENRO
          HLOWER=HENTR-HUPPER
          QUPPER=HUPPER*QPUMP/HENTR*QIQPR
          QLOWER=HLOWER*QPUMP/HENTR*QIQPR
          VUPPER=QUPPER/(6.0*DBELL*HUPPER)
          VLOWER=QLOWER/(6.0*DBELL*HLOWER)
          GO TO 57
       56 CONTINUE
          HUPPER=HENTR
          HLOWER=0.0
          QUPPER=QPUMP*QIQPR
          QLOWER=0.0
          VLOWER=0.0
          VUPPER=QUPPER/(6.0*DBELL*HUPPER)
       57 CONTINUE
C
```

```
C
C     CALCULATION OF THE AIR INDUCED WATER FLOWRATE
C
C
      QWATDF=(QCIRC1+QCIRC2)/2.0
      RDIVN(1)=REXTRM(1)*(1.0-BBOTVL/YCENRO)
C
C
C     CALCULATION OF THE RADIAL AND TANGENTIAL VELOCITY
C     COMPONENTS AT THE EXTREME SURFACES
C     VTAN2(I) ARE THE TANGENTIAL VELOCITIES AT THE EXTREME
C     SURFACES
C
C
      VTAN2(1)=BOTAR/(REXTRM(1)-0.5*RDIVN(1))
C
C
C     VRAD2(I) ARE THE RADIAL VELOCITIES AT THE EXTREME SURFACES
C
C
      VRAD2(1)=SQRT((VTAN2(1)/(COS(LAMBDR(1))))**2-(VTAN2(1)*
     &VTAN2(1)))
      ANGL2D=90.0-LAMBDD(2)
      ANGL2R=ANGL2D*PIE/180.0
      VTAN2(2)=VACTUL(2)*COS(ANGL2R)
      VRAD2(2)=VACTUL(2)*SIN(ANGL2R)
      ANGL3D=LAMBDD(3)-90.0
      ANGL3R=ANGL3D*PIE/180.0
      VTAN2(3)=VACTUL(3)*COS(ANGL3R)
      VRAD2(3)=VACTUL(3)*SIN(ANGL3R)
      ANGL4D=LAMBDD(4)-90.0
      ANGL4R=ANGL4D*PIE/180.0
      VTAN2(4)=SURFVL*(DEPTH-YCENRO)/REXTRM(4)
      VRAD2(4)=TAN(ANGL4R)*VTAN2(4)
C
C
C     CALCULATION OF THE RADIAL VELOCITY COMPONENTS AT THE CENTROIDS
C     OF THE SUB-DIVIDED PUMP COLUMNS
C
C
      IF(RCOL(1).LT.RDIVN(1))THEN DO
      VR(1)=VRAD2(1)*RCOL(1)/(RDIVN(1))
      ELSE DO
      VR(1)=VRAD2(1)
      END IF
      VR(2)=(RCOL(2)*VRAD2(2))/(REXTRM(2)-BPLUM2)
      VR(3)=(RCOL(3)*VRAD2(3))/(REXTRM(3)-BPLUM3)
      VR(4)=(RCOL(4)*VRAD2(4))/REXTRM(4)
C
```

```
C
C     CALCULATION OF THE TANGENTIAL VELOCITY COMPONENTS AT THE
C     CENTROIDS OF THE SUB-DIVIDED PUMP COLUMNS
C
C
      IF(RCOL(1).LT.RDIVN(1))THEN DO
      VT(1)=VTAN2(1)*RCOL(1)/(RDIVN(1))
      ELSE DO
      VT(1)=VTAN2(1)
      END IF
      VT(2)=(RCOL(2)*VTAN2(2))/(REXTRM(2)-BPLUM2)
      VT(3)=(RCOL(3)*VTAN2(3))/(REXTRM(3)-BPLUM3)
      VT(4)=(RCOL(4)*VTAN2(4))/REXTRM(4)
C
C
C     DETERMINATION OF THE PUMP COLUMN DRAG COEFFICIENT
C
C
      DOCOL=0.696061*DBELL
      VCD1=VT(1)*COS(LAMBDR(1))
      VCD2=VT(2)*COS(LAMBDR(2))
      TCD3=PIE-LAMBDR(3)
      VCD3=VT(3)*COS(TCD3)
      TCD4=PIE-LAMBDR(4)
      VCD4=VT(4)*COS(TCD4)
      VCD=(VCD1+VCD2+VCD3+VCD4)*0.25
      PMPRN=VCD*DOCOL/VISKIN
      IF(PMPRN.LT.1.0)CDRAG=10.0
      IF(PMPRN.GE.1.0.AND.PMPRN.LT.10.0)CDRAG=6.35
      IF(PMPRN.GE.10.0.AND.PMPRN.LT.100.0)CDRAG=2.10
      IF(PMPRN.GE.100.0.AND.PMPRN.LT.1000.0)CDRAG=1.25
      IF(PMPRN.GE.1000.0.AND.PMPRN.LT.10000.0)CDRAG=1.15
      IF(PMPRN.GE.10000.0.AND.PMPRN.LT.100000.0)CDRAG=1.40
      IF(PMPRN.GE.100000.0)CDRAG=0.80
C
C
C     LOCATING THE CENTROID OF THE PRESSURE FORCE TERM
C     THE RISE IN THE FREE SURFACE IS MODIFIED AS PER EXPERIMENTAL
C     RESULTS
C
C
      CORRN=VACTUL(4)*VACTUL(4)/G*(1.0-AIRFCN)
      HPRIME=DEPTH+CORRN
      YBARP=(2.0*DEPTH+CORRN)/3.0
C
C
C     DETERMINE THE MAGNITUDE OF THE PRESSURE FORCE TERM
C
C
      DELP2=0.5*GAMFLU*DEPTH*CORRN*6.0*DBELL
C
```

```
C
C     PREPARE FOR THE SOLUTION OF THE ANGULAR MOMENTUM EQUATION
C
      CFT1=THETAD
      CFT2=AIRNO
      CFT3=PMPGNO*QIQPR
      CFT4=12.638*DBELL/DEPTH
      IF(CFT4.GE.3.160)CFT4=3.160
      CFT5=1.0-11.40*CFT2*CFT4+450.0*CFT2*CFT2*CFT4
      CFT6=(-0.18)*CFT1
      CFT7=(-0.04)*CFT1
      CFT8=1.0-2.71828**CFT6+0.73*(2.71828**CFT7)
      CFT9=CFT3**0.48+0.28
      CFT10=CFT4*(-0.08)
      CFT11=(-1.477)*CFT5*CFT8*CFT9*CFT10
      CF=1.705+CFT11
      CFT20=(12.638*DBELL)/DEPTH
      IF(CFT20.LE.2.107.AND.CF.GE.1.450)CF=1.450
      IF(CFT20.GT.2.107.AND.CF.GE.1.530)CF=1.530
C
C     CALCULATION OF FACTOR(1)
C
C
      YCHECK=0.5*LENGTH*SIN(THETAR)
      XCHECK=6.5*DBELL+0.5*LENGTH*COS(THETAR)
      IF(YCENRO.GE.YCHECK.AND.XCENRO.LE.XCHECK)GO TO 58
      IF(YCENRO.LT.CHECK)GO TO 59
      IF(XCENRO.GT.XCHECK)GO TO 61
   58 AGINUP=6.5*DBELL+0.5*LENGTH*COS(THETAR)-XCENRO
      AGINLO=YCENRO-0.5*LENGTH*SIN(THETAR)
      ANGINR(1)=ATAN2(AGINUP,AGINLO)
      ANGINC(1)=ANGINR(1)*180.0/PIE
      ANGINC(2)=90.0+THETAD-ANGINC(1)
      GO TO 60
   59 AGINUP=0.5*LENGTH*SIN(THETAR)-YCENRO
      AGINLO=6.5*DBELL+0.5*LENGTH*COS(THETAR)-XCENRO
      X=AGINUP/AGINLO
      AGINP=ATAN(X)
      ANGINR(1)=AGINP+0.5*PIE
      ANGINC(1)=ANGINR(1)*180.0/PIE
      ANGINC(2)=90.0+THETAD-ANGINC(1)
      GO TO 60
   61 AGINUP=XCENRO-6.5*DBELL-0.5*LENGTH*COS(THETAR)
      AGINLO=YCENRO-0.5*LENGTH*SIN(THETAR)
      ANGINR(1)=ATAN2(AGINUP,AGINLO)
      ANGINC(1)=ANGINR(1)*180.0/PIE
      ANGINC(2)=90.0-THETAD-ANGINC(1)
      GO TO 60
   60 CONTINUE
```

```
      ANGINC(3)=90.0-ANGINC(2)
      ANGINR(3)=ANGINC(3)*PIE/180.0
      RPERPI=RINCL*COS(ANGINR(3))
      RPAR=RINCL*SIN(ANGINR(3))
      RINCDV=RINCL*(1.0-BBOTVL/YCENRO)
      VTANIC=BOTAR/(RINCL-0.5*RINCDV)
      VINCL=VTANIC/(COS(ANGINR(3)))
      FACTOR(1)=RHOFLU*FINCL*ABS(VINCL)*VINCL*6.0*DBELL*LENGTH*
     &RPERPI/8.0*1.10
      TAUINC=FACTOR(1)/(6.0*DBELL*LENGTH*RPERPI)
C
C
C     CALCULATION OF FACTOR(2)
C
C
      RDIVH=RHORIZ*(1.0-BBOTVL/YCENRO)
      VTANH=BOTAR/(RHORIZ-0.5*RDIVH)
      ANGHRR(1)=ARSIN(YCENRO/RHORIZ)
      ANGHOR(1)=ANGHRR(1)*180.0/PIE
      ANGHOR(2)=90.0-ANGHOR(1)
      ANGHRR(2)=ANGHOR(2)*PIE/180.0
      IF(XCENRO.GT.(5.25*DBELL))THEN DO
      VPARH=VTANH/(SIN(ANGHRR(1)))
      END IF
      IF(XCENRO.LT.(5.25*DBELL))THEN DO
      VPARH=VTANH/(COS(ANGHRR(2)))
      END IF
      IF(XCENRO.EQ.(5.25*DBELL))THEN DO
      VPARH=VTANH
      END IF
      FACTOR(2)=RHOFLU*FHORIZ*ABS(VPARH)*VPARH*6.0*DBELL*6.5*DBELL
     &*YCENRO/8.0*1.10
      TAUHOR=FACTOR(2)/(YCENRO*6.0*DBELL*6.5*DBELL)
C
C
C     CALCULATION OF FACTOR(3)
C
C
      TFACT3=RHOFLU*FRRWAL*6.0*DBELL*DEPTH*XCENRO/80.0
      DO 10 I=1,10
      TCROSR(I)=TFACT3*ABS(WATVEL(I))*WATVEL(I)
   10 CONTINUE
      FACTOR(3)=TCROSR(1)+TCROSR(2)+TCROSR(3)+TCROSR(4)+TCROSR(5)
     &+TCROSR(6)+TCROSR(7)+TCROSR(8)+TCROSR(9)+TCROSR(10)
C
```

```
C
C     CALCULATION OF FACTOR(5)
C
C
      DOCOL=0.696061*DBELL
      DCF=(6.0*DBELL)/(6.0*DBELL-3.0*DOCOL)
      DCFF=DCF*DCF
      TFACT5=COS(LAMBDR(1))
      TF51=(YCENRO-0.5*DBELL)*0.5*DOCOL
      TF52=0.75*(YCENRO-0.5*DBELL)
      TF53=VT(1)*TFACT5
      FACTOR(5)=RHOFLU*CDRAG*TF53*TF53*0.5*3.0*TF51*TF52*DCFF
C
C
C     CALCULATION OF FACTOR(6)
C
C
      TFACT6=COS(LAMBDR(2))
      TF61=TF51
      TF62=0.25*(YCENRO-0.5*DBELL)
      TF63=VT(2)*TFACT6
      FACTOR(6)=RHOFLU*CDRAG*TF63*TF63*0.5*3.0*TF61*TF62*DCFF
C
C
C     CALCULATION OF FACTOR(7)
C
C
      TFACT7=PIE-LAMBDR(3)
      TFAC77=COS(TFACT7)
      TF70=VT(3)*TFAC77
      TF71=(DEPTH-YCENRO-BTOP)*DOCOL
      TF72=0.25*(DEPTH-YCENRO)
      FACTOR(7)=RHOFLU*CDRAG*TF70*TF70*0.5*3.0*TF71*TF72*DCFF
C
C
C     CALCULATION OF FACTOR(8)
C
C
      TF80=VELJET/(1.0-AIRFCN)
      TF82=DEPTH-YCENRO-0.5*BTOP
      FACTOR(8)=RHOFLU*CDRAG*TF80*TF80*0.5*3.0*(BTOP*DOCOL)*
     &TF82*DCFF*1.2
C
C
C     CALCULATION OF FACTOR(9)
C
C
      IF(YCENRO.GT.CHECK)GO TO 68
      IF(YCENRO.LT.CHECK)GO TO 62
   68 TFAC91=QLOWER*VLOWER*0.5*(YCENRO-LENGTH*SIN(THETAR))
```

```
      TFAC92=QUPPER*VUPPER*0.5*(DEPTH-YCENRO)
      GO TO 63
   62 CONTINUE
      TFAC91=0.0
      TFAC92=QUPPER*VUPPER*(0.5*DEPTH+0.5*LENGTH*SIN(THETAR)-YCENRO)
   63 CONTINUE
      VDISCH=QPUMP/(3.0*APIPE)
      TFAC93=QPUMP*BOTVEL*ABS(XCENRO-XSP)*3.0
      FACTOR(9)=RHOFLU*(TFAC91-TFAC92-TFAC93)
C
C
C     CALCULATION OF FACTOR(10)
C
C
      DF(1)=FORCE(1)
      DO 20 I=2,10
   20 DF(I)=FORCE(I)-FORCE(I-1)
      DO 21 I=1,10
   21 FCROSR(I)=DF(I)*ABS(XCENRO-0.5*PLUWID(I))
      FACTOR(10)=FCROSR(1)+FCROSR(2)+FCROSR(3)+FCROSR(4)+FCROSR(5)
     &+FCROSR(6)+FCROSR(7)+FCROSR(8)+FCROSR(9)+FCROSR(10)
C
C
C     CALCULATION OF FACTOR(11)
C
C
      IF(YBARP.GT.YCENRO)FACTOR(11)=DELP2*ABS(YCENRO-YBARP)
      IF(YBARP.LT.YCENRO)FACTOR(11)=(-1.0)*DELP2*ABS(YCENRO-YBARP)
      IF(YBARP.EQ.YCENRO)FACTOR(11)=0.0
C
C
C     CORRECTION FOR THE SIDE WALL SHEAR
C
C
      IF(YCENRO.GT.CHECK)THEN DO
      SWST1=(YCENRO-LENGTH*SIN(THETAR))/(12.638*DBELL-XCENRO)
      SWST2=(DEPTH-YCENRO)/(12.638*DBELL-XCENRO)
      ANGSWS(1)=ATAN(SWST1)+ATAN(SWST2)
      ELSE DO
      SWST1=(DEPTH-YCENRO)/(12.638*DBELL-XCENRO)
      SWST2=(LENGTH*SIN(THETAR)-YCENRO)/(12.638*DBELL-XCENRO)
      ANGSWS(1)=ATAN(SWST1)-ATAN(SWST2)
      END IF
      XCHECK=6.5*DBELL
      YCHECK=LENGTH*SIN(THETAR)
      IF(XCENRO.LT.XCHECK.AND.YCENRO.GT.YCHECK)GO TO 70
      IF(XCENRO.LT.XCHECK.AND.YCENRO.LT.YCHECK)GO TO 71
      IF(XCENRO.GE.XCHECK.AND.YCENRO.GE.YCHECK)GO TO 72
      IF(XCENRO.GE.XCHECK.AND.YCENRO.LE.YCHECK)GO TO 73
   70 SWST3=(6.5*DBELL-XCENRO)/YCENRO
   SWST4=(YCENRO-LENGTH*SIN(THETAR))/(12.638*DBELL-XCENRO)
   ANGSWS(2)=PIE/2.0-ATAN(SWST3)-ATAN(SWST4)
   GO TO 74
71 SWST3=(6.5*DBELL-XCENRO)/YCENRO
   SWST4=(12.638*DBELL-XCENRO)/(LENGTH*SIN(THETAR)-YCENRO)
   ANGSWS(2)=PIE-ATAN(SWST3)-ATAN(SWST4)
   GO TO 74
72 SWST3=YCENRO/(XCENRO-6.5*DBELL)
   SWST4=(YCENRO-LENGTH*SIN(THETAR))/(12.638*DBELL-XCENRO)
   ANGSWS(2)=PIE-ATAN(SWST3)-ATAN(SWST4)
   GO TO 74
73 SWST3=YCENRO/(XCENRO-6.5*DBELL)
   SWST4=(LENGTH*SIN(THETAR)-YCENRO)/(12.638*DBELL-XCENRO)
   ANGSWS(2)=PIE-ATAN(SWST3)+ATAN(SWST4)
   GO TO 74
74 CONTINUE
   IF(XCENRO.LT.(6.5*DBELL))THEN DO
   SWST5=XCENRO/YCENRO
   SWST6=(6.5*DBELL-XCENRO)/YCENRO
   ANGSWS(3)=ATAN(SWST5)+ATAN(SWST6)
   ELSE DO
   SWST5=(XCENRO-6.5*DBELL)/YCENRO
   SWST6=YCENRO/XCENRO
   ANGSWS(3)=0.5*PIE-ATAN(SWST5)-ATAN(SWST6)
   END IF
   SWST7=XCENRO/YCENRO
   SWST8=XCENRO/(DEPTH-YCENRO)
   ANGSWS(4)=PIE-ATAN(SWST7)-ATAN(SWST8)
   SWST9=(DEPTH-YCENRO)/XCENRO
   SWST10=(DEPTH-YCENRO)/(12.638*DBELL-XCENRO)
   ANGSWS(5)=PIE-ATAN(SWST9)-ATAN(SWST10)
   RAYT1=(DEPTH-YCENRO)**2+(12.638*DBELL-XCENRO)**2
   RAY1=SQRT(RAYT1)
   RAYT2=(12.638*DBELL-XCENRO)**2
   RAYT33=(DEPTH-YCENRO)-0.333*(DEPTH-LENGTH*SIN(THETAR))
   RAYT34=ABS(RAYT33)
   RAYT35=RAYT34**2
   RAYT4=RAYT2+RAYT35
   RAY2=SQRT(RAYT4)
   RAYT5=(12.638*DBELL-XCENRO)**2
   RAYT36=(DEPTH-YCENRO)-0.667*(DEPTH-LENGTH*SIN(THETAR))
   RAYT37=ABS(RAYT36)
   RAYT38=RAYT37**2
   RAYT7=RAYT5+RAYT38
   RAY3=SQRT(RAYT7)
   DELXR4=12.638*DBELL-XCENRO
   DELYR4=YCENRO-LENGTH*SIN(THETAR)
   DELYR4=ABS(DELYR4)
   RAY4=SQRT(DELXR4**2+DELYR4**2)
```

```
      DELXR5=6.5*DBELL+0.6667*LENGTH*COS(THETAR)-XCENRO
      DELXR5=ABS(DELXR5)
      DELYR5=YCENRO-0.6667*LENGTH*SIN(THETAR)
      DELYR5=ABS(DELYR5)
      RAY5=SQRT(DELXR5**2+DELYR5**2)
      DELXR6=6.5*DBELL+0.3333*LENGTH*COS(THETAR)-XCENRO
      DELXR6=ABS(DELXR6)
      DELYR6=YCENRO-0.3333*LENGTH*SIN(THETAR)
      DELYR6=ABS(DELYR6)
      RAY6=SQRT(DELXR6**2+DELYR6**2)
      DELXR7=6.5*DBELL-XCENRO
      DELXR7=ABS(DELXR7)
      RAY7=SQRT(DELXR7**2+YCENRO**2)
      DELXR8=XCENRO-0.6667*6.5*DBELL
      DELXR8=ABS(DELXR8)
      RAY8=SQRT(DELXR8**2+YCENRO**2)
      DELXR9=XCENRO-0.3333*6.5*DBELL
      DELXR9=ABS(DELXR9)
      RAY9=SQRT(DELXR9**2+YCENRO**2)
      RAYT20=XCENRO**2+YCENRO**2
      RAY10=SQRT(RAYT20)
      RAYT45=YCENRO-0.333*DEPTH
      RAYT46=ABS(RAYT45)
      RAYT47=RAYT46**2
      RAYT22=XCENRO**2+RAYT47
      RAY11=SQRT(RAYT22)
      RAYT48=0.667*DEPTH-YCENRO
      RAYT49=ABS(RAYT48)
      RAYT50=RAYT49**2
      RAYT24=XCENRO**2+RAYT50
      RAY12=SQRT(RAYT24)
      RAYT25=XCENRO**2+(DEPTH-YCENRO)**2
      RAY13=SQRT(RAYT25)
      RAYT26=(DEPTH-YCENRO)**2
      RAYT51=XCENRO-0.333*12.638*DBELL
      RAYT52=ABS(RAYT51)
      RAYT53=RAYT52**2
      RAYT28=RAYT26+RAYT53
      RAY14=SQRT(RAYT28)
      RAYT29=(DEPTH-YCENRO)**2
      RAYT54=0.667*12.638*DBELL-XCENRO
      RAYT55=ABS(RAYT54)
      RAYT56=RAYT55**2
      RAYT31=RAYT29+RAYT56
      RAY15=SQRT(RAYT31)
      RAY101=0.5*(RAY1+RAY2)
      RAY102=0.5*(RAY2+RAY3)
      RAY103=0.5*(RAY3+RAY4)
      RAY201=0.5*(RAY4+RAY5)
      RAY202=0.5*(RAY5+RAY6)
```

```
RAY203=0.5*(RAY6+RAY7)
RAY301=0.5*(RAY7+RAY8)
RAY302=0.5*(RAY8+RAY9)
RAY303=0.5*(RAY9+RAY10)
RAY401=0.5*(RAY10+RAY11)
RAY402=0.5*(RAY11+RAY12)
RAY403=0.5*(RAY12+RAY13)
RAY501=0.5*(RAY13+RAY14)
RAY502=0.5*(RAY14+RAY15)
RAY503=0.5*(RAY15+RAY1)
SS2T1=(12.638*DBELL-XCENRO)/(DEPTH-YCENRO)
ANGSS2=ATAN(SS2T1)
ANGSS1=PIE/2.0-ANGSS2
SS5T1=YCENRO/XCENRO
ANGSS5=ATAN(SS5T1)
ANGSS6=PIE/2.0-ANGSS5
IF(XCENRO.LT.(6.5*DBELL))THEN DO
SS3T1=YCENRO/(6.5*DBELL-XCENRO)
ANGSS3=ATAN(SS3T1)
ANGSS4=PIE-THETAR-ANGSS3
ELSE DO
SS3T1=(XCENRO-6.5*DBELL)/YCENRO
ANGSS3=0.5*PIE+ATAN(SS3T1)
ANGSS4=PIE-THETAR-ANGSS3
END IF
SS7T1=(DEPTH-YCENRO)/XCENRO
ANGSS7=ATAN(SS7T1)
SS8T1=XCENRO/(DEPTH-YCENRO)
ANGSS8=ATAN(SS8T1)
IF(YCENRO.GT.CHECK)THEN DO
SS9T1=(YCENRO-LENGTH*SIN(THETAR))/(12.638*DBELL-XCENRO)
ANGSS9=ATAN(SS9T1)+THETAR
ELSE DO
SS9T1=(LENGTH*SIN(THETAR)-YCENRO)/(12.638*DBELL-XCENRO)
ANGSS9=THETAR-ATAN(SS9T1)
END IF
ANSS10=PIE/2.0+THETAR-ANGSS9
ASI101=0.333*(DEPTH-LENGTH*SIN(THETAR))*SIN(ANGSS2)/RAY2
ANGSWS(101)=ARSIN(ASI101)
ASI103=0.333*(DEPTH-LENGTH*SIN(THETAR))*SIN(ANSS10)/RAY3
ANGSWS(103)=ARSIN(ASI103)
ANGSWS(102)=ANGSWS(1)-ANGSWS(101)-ANGSWS(103)
ASI201=0.333*LENGTH*SIN(ANGSS9)/RAY5
ANGSWS(201)=ARSIN(ASI201)
ASI203=0.333*LENGTH*SIN(ANGSS4)/RAY6
ANGSWS(203)=ARSIN(ASI203)
ANGSWS(202)=ANGSWS(2)-ANGSWS(201)-ANGSWS(203)
ASI301=0.333*6.5*DBELL*SIN(ANGSS3)/RAY8
ANGSWS(301)=ARSIN(ASI301)
ASI303=0.333*6.5*DBELL*SIN(ANGSS5)/RAY9
```

```
      ANGSWS(303)=ARSIN(ASI303)
      ANGSWS(302)=ANGSWS(3)-ANGSWS(301)-ANGSWS(303)
      ASI403=0.333*DEPTH*SIN(ANGSS8)/RAY12
      ANGSWS(403)=ARSIN(ASI403)
      ASI401=0.333*DEPTH*SIN(ANGSS6)/RAY11
      ANGSWS(401)=ARSIN(ASI401)
      ANGSWS(402)=ANGSWS(4)-ANGSWS(403)-ANGSWS(401)
      ASI501=0.333*12.638*DBELL*SIN(ANGSS7)/RAY14
      ANGSWS(501)=ARSIN(ASI501)
      ASI503=0.333*12.638*DBELL*SIN(ANGSS1)/RAY15
      ANGSWS(503)=ARSIN(ASI503)
      ANGSWS(502)=ANGSWS(5)-ANGSWS(501)-ANGSWS(503)
      VTR101=(2.0/RAY1)*((QWATDF+0.5*QPUMP*QIQPR)/(6.0*DBELL))
      VTR102=(2.0/RAY2)*((QWATDF+0.5*QPUMP*QIQPR)/(6.0*DBELL))
      VTR103=(2.0/RAY3)*((QWATDF+0.5*QPUMP*QIQPR)/(6.0*DBELL))
      SWSRAT=1.0-BBOTVL/YCENRO
      R1201=RAY201*SWSRAT
      R1202=RAY202*SWSRAT
      R1203=RAY203*SWSRAT
      R1301=RAY301*SWSRAT
      R1302=RAY302*SWSRAT
      R1303=RAY303*SWSRAT
      R1401=RAY401*SWSRAT
      R1402=RAY402*SWSRAT
      R1403=RAY403*SWSRAT
      VTR201=BOTAR/(RAY201-0.5*R1201)
      VTR202=BOTAR/(RAY202-0.5*R1202)
      VTR203=BOTAR/(RAY203-0.5*R1203)
      VTR301=BOTAR/(RAY301-0.5*R1301)
      VTR302=BOTAR/(RAY302-0.5*R1302)
      VTR303=BOTAR/(RAY303-0.5*R1303)
      VTSWSU=QWATDF/(6.0*DBELL)
      VTR401=VTSWSU/(RAY401-0.5*R1401)
      VTR402=VTSWSU/(RAY402-0.5*R1402)
      VTR403=VTSWSU/(RAY403-0.5*R1403)
      VTR501=SURFVL*(DEPTH-YCENRO)/RAY501
      VTR502=SURFVL*(DEPTH-YCENRO)/RAY502
      VTR503=SURFVL*(DEPTH-YCENRO)/RAY503
      TORQUE(101)=ANGSWS(101)*RHOFLU*FSWS*VTR101*VTR101*(RAY101
     &**3)/20.0
      TORQUE(102)=ANGSWS(102)*RHOFLU*FSWS*VTR102*VTR102*(RAY102
     &**3)/20.0
      TORQUE(103)=ANGSWS(103)*RHOFLU*FSWS*VTR103*VTR103*(RAY103
     &**3)/20.0
      TORQUE(201)=ANGSWS(201)*RHOFLU*FSWS*(VTR201**2)*((RAY201**3
     &)/3-(2.0/15)*(R1201**3))/4.0
      TORQUE(202)=ANGSWS(202)*RHOFLU*FSWS*(VTR202**2)*((RAY202**3
     &)/3-(2.0/15)*(R1202**3))/4.0
      TORQUE(203)=ANGSWS(203)*RHOFLU*FSWS*(VTR203**2)*((RAY203**3
     &)/3-(2.0/15)*(R1203**3))/4.0
```

```
      TORQUE(301)=ANGSWS(301)*RHOFLU*FSWS*(VTR301**2)*((RAY301**3
     &)/3-(2.0/15)*(R1301**3))/4.0
      TORQUE(302)=ANGSWS(302)*RHOFLU*FSWS*(VTR302**2)*((RAY302**3
     &)/3-(2.0/15)*(R1302**3))/4.0
      TORQUE(303)=ANGSWS(303)*RHOFLU*FSWS*(VTR303**2)*((RAY303**3
     &)/3-(2.0/15)*(R1303**3))/4.0
      TORQUE(401)=ANGSWS(401)*RHOFLU*FSWS*(VTR401**2)*((RAY401**3
     &)/3-(2.0/15)*(R1401**3))/4.0
      TORQUE(402)=ANGSWS(402)*RHOFLU*FSWS*(VTR402**2)*((RAY402**3
     &)/3-(2.0/15)*(R1402**3))/4.0
      TORQUE(403)=ANGSWS(403)*RHOFLU*FSWS*(VTR403**2)*((RAY403**3
     &)/3-(2.0/15)*(R1403**3))/4.0
      TORQUE(501)=ANGSWS(501)*RHOFLU*FSWS*(VTR501**2)*(RAY501**3)
     &/20.0
      TORQUE(502)=ANGSWS(502)*RHOFLU*FSWS*(VTR502**2)*(RAY502**3)
     &/20.0
      TORQUE(503)=ANGSWS(503)*RHOFLU*FSWS*(VTR503**2)*(RAY503**3)
     &/20.0
      SWSTOT=TORQUE(101)+TORQUE(102)+TORQUE(103)+TORQUE(201)+
     &TORQUE(202)+TORQUE(203)+TORQUE(301)+TORQUE(302)+TORQUE(303)
     &+TORQUE(401)+TORQUE(402)+TORQUE(403)+TORQUE(501)+TORQUE(502)+
     &TORQUE(503)
      ANGSWD(1)=ANGSWS(1)*180.0/PIE
      ANGSWD(2)=ANGSWS(2)*180.0/PIE
      ANGSWD(3)=ANGSWS(3)*180.0/PIE
      ANGSWD(4)=ANGSWS(4)*180.0/PIE
      ANGSWD(5)=ANGSWS(5)*180.0/PIE
      ANGSWD(101)=ANGSWS(101)*180.0/PIE
      ANGSWD(102)=ANGSWS(102)*180.0/PIE
      ANGSWD(103)=ANGSWS(103)*180.0/PIE
      ANGSWD(201)=ANGSWS(201)*180.0/PIE
      ANGSWD(202)=ANGSWS(202)*180.0/PIE
      ANGSWD(203)=ANGSWS(203)*180.0/PIE
      ANGSWD(301)=ANGSWS(301)*180.0/PIE
      ANGSWD(302)=ANGSWS(302)*180.0/PIE
      ANGSWD(303)=ANGSWS(303)*180.0/PIE
      ANGSWD(401)=ANGSWS(401)*180.0/PIE
      ANGSWD(402)=ANGSWS(402)*180.0/PIE
      ANGSWD(403)=ANGSWS(403)*180.0/PIE
      ANGSWD(501)=ANGSWS(501)*180.0/PIE
      ANGSWD(502)=ANGSWS(502)*180.0/PIE
      ANGSWD(503)=ANGSWS(503)*180.0/PIE
      ANGSD1=ANGSS1*180.0/PIE
      ANGSD2=ANGSS2*180.0/PIE
      ANGSD3=ANGSS3*180.0/PIE
      ANGSD4=ANGSS4*180.0/PIE
      ANGSD5=ANGSS5*180.0/PIE
      ANGSD6=ANGSS6*180.0/PIE
      ANGSD7=ANGSS7*180.0/PIE
      ANGSD8=ANGSS8*180.0/PIE
      ANGSD9=ANGSS9*180.0/PIE
      ANSD10=ANSS10*180.0/PIE
```

```
C
C
C     LINEAR MOMENTUM BALANCE
C
C
      MCF1=1.0
      MCF2=1.0
      MCF3=1.0
      IF(QPUMP.EQ.0.0)GO TO 777
      IF(QPUMP.NE.0.0)GO TO 778
  777 VDOT1=SURFVL
      VDOT2=BOTVEL
      VDOT11=QWATDF/(6.0*DBELL*(DEPTH-YCENRO))
      VDOT22=QWATDF/(YCENRO*6.0*DBELL)
      FFI=FACTOR(1)/RPERPI
      IF(XCENRO.GE.(6.5*DBELL))THEN DO
      FFH=0.0
      ELSE DO
      FFH=RHOFLU*FHORIZ*ABS(VPARH)*VPARH*6.0*DBELL*(6.5*DBELL-
     &XCENRO)/8.0
      END IF
      MDOT1=RHOFLU*QWATDF*MCF1*VDOT11
      MDOT2=RHOFLU*QWATDF*MCF2*VDOT22
      DELTAF=RHOFLU*QWATDF*(MCF2*VDOT22+MCF1*VDOT11)+FFI*COS(THETAR)
     &+FFH
      GO TO 779
  778 VDOT1=SURFVL
      VDOT11=QWATDF/(6.0*DBELL*(DEPTH-YCENRO))
      YLM=YCENRO-BBOTVL
      VDOT2=BOTVEL
      VDOT22=(QPUMP+QWATDF)/(6.0*DBELL*YCENRO)
      MDOT1=RHOFLU*VDOT11*QWATDF*MCF1
      MDOT2=RHOFLU*VDOT22*(QWATDF+QPUMP)*MCF2
      VDOT33=QPUMP*QIQPR/(HENTR*6.0*DBELL)
      MDOT3=RHOFLU*VDOT33*QPUMP*MCF3*QIQPR
      FFI=FACTOR(1)/RPERPI
      IF(XCENRO.GE.(6.5*DBELL))THEN DO
      FFH=0.0
      ELSE DO
      FFH=RHOFLU*FHORIZ*ABS(VPARH)*VPARH*6.0*DBELL*(6.5*DBELL-XCENRO
     &)/8.0
      END IF
      DELTAF=MDOT1+MDOT2-MDOT3+FFH+FFI*COS(THETAR)
  779 CONTINUE
C
C
```

```
C     LOCATE THE OFFSET OF THE "DELTA F" FORCE
C
C
      IF(QPUMP.EQ.0.0)GO TO 880
      IF(QPUMP.NE.0.0)GO TO 881
  880 RL=0.5*YCENRO
      RU=0.5*(DEPTH-YCENRO)
      VL=VDOT22
      VU=VDOT11
      Y1T1=RHOFLU*QWATDF*((RL*VL)-(RU*VU))
      Y1T2=YCENRO*(FFH+FFI*COS(THETAR))
      YDF=(Y1T1-Y1T2)/DELTAF
      GO TO 882
  881 RU1=0.5*(DEPTH-YCENRO)
      RL2=0.5*YCENRO
      IF(YCENRO.GE.CHECK)THEN DO
      RU3=0.5*(DEPTH-YCENRO)
      RL4=0.5*(YCENRO-LENGTH*SIN(THETAR))
      ELSE DO
      RU3=0.5*DEPTH+0.5*LENGTH*SIN(THETAR)-YCENRO
      RL4=0.0
      END IF
      Y1T1=(QPUMP+QWATDF)*(RL2*VDOT22)
      Y1T2=QLOWER*RL4*VLOWER
      Y1T3=QWATDF*RU1*VDOT11
      Y1T4=QUPPER*RU3*VUPPER
      Y1T5=RHOFLU*(Y1T1+Y1T2-Y1T3-Y1T4)
      Y1T6=YCENRO*(FFH+FFI*COS(THETAR))
      YDF=(Y1T5-Y1T6)/DELTAF
  882 CONTINUE
      IF(YDF.LT.0.0)GO TO 883
      IF(YDF.GT.0.0)GO TO 884
  883 AYDF=ABS(YDF)
      IF(AYDF.GE.YCENRO)YDF=YCENRO*(-1.0)
      GO TO 885
  884 IF(YDF.GE.(DEPTH-YCENRO))YDF=DEPTH-YCENRO
  885 CONTINUE
      FACTOR(13)=DELTAF*YDF
C
C
C     CALCULATION OF FACTOR(14)
C
C
      TF141=CORRN*WIDTH*6.0*DBELL*CF
      TF142=TF141*GAMFLU
      FACTOR(14)=TF142*(XCENRO-PLUWID(5))
      CALRAT=FACTOR(14)/FACTOR(10)
      TARLAC=0.792/(DEPTH**0.510)
      IF(DEPTH.GE.0.70.AND.CALRAT.GE.0.820)GO TO 444
      IF(DEPTH.GE.0.70.AND.CALRAT.LT.0.820)GO TO 445
      IF(DEPTH.LT.0.70.AND.CALRAT.GE.0.820)GO TO 446
      IF(DEPTH.LT.0.70.AND.CALRAT.LT.0.820)GO TO 447
      GO TO 448
  444 FACTOR(14)=FACTOR(14)*TARLAC
      GO TO 448
  445 FACTOR(14)=FACTOR(14)
      GO TO 448
  446 FACTOR(14)=0.820*FACTOR(10)
      GO TO 448
  447 FACTOR(14)=FACTOR(14)
  448 CONTINUE
C
C
C     CALCULATION OF FACTOR(15)
C
C
      TF151=GAMFLU*AIRFCN*BTOP*BTOP
      TF152=1.0-0.3/VACTUL(4)
      TF153=6.0*DBELL
      TF154=TF151*TF152*TF153
      FACTOR(15)=TF154*(XCENRO-PLUWID(5))
C
C
C     FORMULATION OF THE ANGULAR MOMENTUM EQUATION
C
C
      TRMLFT=FACTOR(1)+FACTOR(2)+FACTOR(3)+FACTOR(5)+FACTOR(14)+
     &FACTOR(6)+FACTOR(7)+FACTOR(8)+SWSTOT+FACTOR(13)+FACTOR(15)
      TRMRGT=FACTOR(9)+FACTOR(11)+FACTOR(10)
      DIFFER(KRUN)=ABS(TRMRGT-TRMLFT)
      PERERR=ABS(DIFFER(KRUN)/TRMRGT)*100.0
      IF(ABS(PERERR).LE.2.0)THEN DO
      GO TO 905
      ELSE DO
      CONTINUE
      END IF
      IF(TRMLFT.GT.TRMRGT)GO TO 825
      IF(TRMLFT.LT.TRMRGT)GO TO 826
  825 SURFVL=SURFVL-0.02
      VELJET=VELJET-0.02
      BOTVEL=BOTVEL-0.02
      GO TO 827
  826 SURFVL=SURFVL+0.02
      VELJET=VELJET+0.02
      BOTVEL=BOTVEL+0.02
  827 KRUN=KRUN+1
      GO TO 307
  905 CONTINUE
C
C
C     CHECK MOMENTUM CORRECTION FACTOR SENSITIVITY
C
C
```

```
      BTR1=AVELJT-YCENRO
      BTR2=DEPTH-YCENRO
      BTVJ=VELJET
      BTVS=SURFVL
      BTT1=BTR1*BTVJ*BTVJ/3.0
      BTT2=(BTVS-BTVJ)*(BTVS-BTVJ)/3.0
      IF(AVELJT.GE.DEPTH)THEN DO
      BTT3=0.0
      ELSE DO
      BTT3=(BTR2**3-BTR1**3)/((BTR2-BTR1)*(BTR2-BTR1))
      END IF
      BTT4=BTT2*BTT3
      IF(AVELJT.GE.DEPTH)THEN DO
      BTT5=0.0
      ELSE DO
      BTT5=(BTVS-BTVJ)/((BTR2-BTR1)*(BTR2-BTR1))
      END IF
      IF(AVELJT.GE.DEPTH)THEN DO
      BTT6=0.0
      ELSE DO
      BTT6=(BTVJ*BTR2-BTVS*BTR1)*(BTR2**2.0-BTR1**2.0)
      END IF
      BTT7=BTT5*BTT6
      IF(AVELJT.GE.DEPTH)THEN DO
      BTT8=0.0
      ELSE DO
      BTT8=(BTVJ*BTR2-BTVS*BTR1)*(BTVJ*BTR2-BTVS*BTR1)/(BTR2-BTR1)
      END IF
      BTT9=BTT1+BTT4+BTT7+BTT8
      BBR1=YCENRO-BBOTVL
      BBR2=YCENRO
      BBVB=BOTVEL
      BBT1=BBVB*BBVB*BBR1/3.0
      BBT2=BBVB*BBVB*(BBR2-BBR1)
      BBT3=BBT1+BBT2
      BTVT=0.5*VELJET+SURFVL*(DEPTH-AVELJT)/(2.0*(DEPTH-YCENRO))
      BBVB=BOTVEL*(BBOTVL+YCENRO)/(2.0*YCENRO)
      BTTH=BTT9/(BTVT*BTVT*BTR2)
      BBTH=BBT3/(BBVB*BBVB*BBR2)
C
C
C     CALCULATION OF MOMENTUM CORRECTION FACTOR BASED ON
C     OBSERVED VELOCITY PROFILES
C
C
      BTOB=1.922+6.167*SURFVL*(G*DEPTH)**(-0.5)-5.341*VELJET*
     &(G*DEPTH)**(-0.5)-0.997*YCENRO/DEPTH
      BBOBT1=QAIRO/(DEPTH**2.5*G**0.5)
      BBOBT2=THETAD
      BBOBT3=BOTVEL/((G*DEPTH)**0.5)
      BBOBT4=BBOTVL/DEPTH
      BBOBT5=YCENRO/DEPTH
      BBOBT6=(G**0.5*DEPTH**1.5)/VISKIN
      BBOB1=1.135+15.249*BBOBT1+0.000699*BBOBT2-3.204*BBOBT3-
     &0.548*BBOBT4+0.461*BBOBT5+(5.891E-08)*BBOBT6
      BBOB2=1.137+15.619*BBOBT1-3.472*BBOBT3-0.442*BBOBT4+0.402*
     &BBOBT5+(7.908E-08)*BBOBT6
      BBOB3=1.341+16.937*BBOBT1+0.000558*BBOBT2-3.333*BBOBT3-0.406
     &*BBOBT4+(7.257E-08)*BBOBT6
      BBOB4=1.321+17.063*BBOBT1-3.539*BBOBT3-0.334*BBOBT4+
     &(8.766E-08)*BBOBT6
      BBOB5=AMAX1(BBOB1,BBOB2,BBOB3,BBOB4)
C
C
      PRINT,'UPPER MOMENTUM CORRECTION FACTOR(ASSUMED)=',BTTH
      PRINT,'LOWER MOMENTUM CORRECTION FACTOR(ASSUMED)=',BBTH
      PRINT,'UPPER MOMENTUM CORRECTION FACTOR(OBSERVED)=',BTOB
      PRINT,'LOWER MOMENTUM CORRECTION FACTOR(OBSERVED)=',BBOB5
      PRINT,'HENTR=',HENTR
      PRINT,'HUPPER=',HUPPER
      PRINT,'HLOWER=',HLOWER
      PRINT,'QUPPER=',QUPPER
      PRINT,'QLOWER=',QLOWER
      PRINT,'VUPPER=',VUPPER
      PRINT,'VLOWER=',VLOWER
      PRINT,'STABLE CIRCULATING FLOW=',QWATDF
      PRINT,'VR(1)=',VR(1)
      PRINT,'VR(2)=',VR(2)
      PRINT,'VR(3)=',VR(3)
      PRINT,'VR(4)=',VR(4)
      PRINT,'VT(1)=',VT(1)
      PRINT,'VT(2)=',VT(2)
      PRINT,'VT(3)=',VT(3)
      PRINT,'VT(4)=',VT(4)
      PRINT,'VACT(1)=',VACT(1)
      PRINT,'VACT(2)=',VACT(2)
      PRINT,'VACT(3)=',VACT(3)
      PRINT,'VACT(4)=',VACT(4)
      PRINT,'CORRN=',CORRN
      PRINT,'HPRIME=',HPRIME
      PRINT,'YBARP=',YBARP
      PRINT,'DELP2=',DELP2
      PRINT,'RPERPI=',RPERPI
      PRINT,'RPAR=',RPAR
      PRINT,'RINCDV=',RINCDV
      PRINT,'VTANIC=',VTANIC
      PRINT,'VINCL=',VINCL
      PRINT,'FINCL=',FINCL
      PRINT,'RDIVH=',RDIVH
      PRINT,'VTANH=',VTANH
      PRINT,'VPARH=',VPARH
      PRINT,'FHORIZ=',FHORIZ
      PRINT,'TFACT3=',TFACT3
      PRINT,'FRRWAL=',FRRWAL
      PRINT,'DOCOL=',DOCOL
      PRINT,'ANGSWD(101)=',ANGSWD(101)
      PRINT,'ANGSWD(102)=',ANGSWD(102)
      PRINT,'ANGSWD(103)=',ANGSWD(103)
      PRINT,'ANGSWD(201)=',ANGSWD(201)
      PRINT,'ANGSWD(202)=',ANGSWD(202)
      PRINT,'ANGSWD(203)=',ANGSWD(203)
      PRINT,'ANGSWD(301)=',ANGSWD(301)
      PRINT,'ANGSWD(302)=',ANGSWD(302)
      PRINT,'ANGSWD(303)=',ANGSWD(303)
      PRINT,'ANGSWD(401)=',ANGSWD(401)
      PRINT,'ANGSWD(402)=',ANGSWD(402)
      PRINT,'ANGSWD(403)=',ANGSWD(403)
      PRINT,'ANGSWD(501)=',ANGSWD(501)
      PRINT,'ANGSWD(502)=',ANGSWD(502)
      PRINT,'ANGSWD(503)=',ANGSWD(503)
      PRINT,'VTR101=',VTR101
      PRINT,'VTR102=',VTR102
      PRINT,'VTR103=',VTR103
      PRINT,'VTR201=',VTR201
      PRINT,'VTR202=',VTR202
      PRINT,'VTR203=',VTR203
      PRINT,'VTR301=',VTR301
      PRINT,'VTR302=',VTR302
      PRINT,'VTR303=',VTR303
      PRINT,'VTR401=',VTR401
      PRINT,'VTR402=',VTR402
      PRINT,'VTR403=',VTR403
      PRINT,'VTR501=',VTR501
      PRINT,'VTR502=',VTR502
      PRINT,'VTR503=',VTR503
      PRINT,'FSWS=',FSWS
      PRINT,'TORQUE(101)=',TORQUE(101)
      PRINT,'TORQUE(102)=',TORQUE(102)
      PRINT,'TORQUE(103)=',TORQUE(103)
      PRINT,'TORQUE(201)=',TORQUE(201)
      PRINT,'TORQUE(202)=',TORQUE(202)
      PRINT,'TORQUE(203)=',TORQUE(203)
      PRINT,'TORQUE(301)=',TORQUE(301)
      PRINT,'TORQUE(302)=',TORQUE(302)
      PRINT,'TORQUE(303)=',TORQUE(303)
      PRINT,'TORQUE(401)=',TORQUE(401)
      PRINT,'TORQUE(402)=',TORQUE(402)
      PRINT,'TORQUE(403)=',TORQUE(403)
      PRINT,'TORQUE(501)=',TORQUE(501)
      PRINT,'TORQUE(502)=',TORQUE(502)
      PRINT,'TORQUE(503)=',TORQUE(503)
      PRINT,'SWSTOT=',SWSTOT
      PRINT,'YDF=',YDF
      PRINT,'THE RATIO OF FACTOR(14) TO FACTOR(10)=',CALRAT
      PRINT,'THE MODIFIED RATIO OF FACTOR(14) TO FACTOR(10)=',
     &TARLAC
      PRINT,'CF=',CF
      PRINT,'TRMLFT=',TRMLFT
      PRINT,'TRMRGT=',TRMRGT
      PRINT,'DIFFER=',DIFFER(KRUN)
      PRINT,'PERERR=',PERERR
      PRINT,'MCF1=',MCF1
      PRINT,'MCF2=',MCF2
      PRINT,'MCF3=',MCF3
      PRINT,'MDOT1=',MDOT1
      PRINT,'MDOT2=',MDOT2
      PRINT,'FFI=',FFI
      PRINT,'FFH=',FFH
      PRINT,'DELTAF=',DELTAF
      IF(QPUMP.NE.0.0)THEN DO
      PRINT,'MDOT3=',MDOT3
      PRINT,'YLM=',YLM
      ELSE DO
      CONTINUE
      END IF
      GO TO 910
  910 CONTINUE
      PRINT,'XSP=',XSP
      PRINT,'RCOL(1)=',RCOL(1)
      PRINT,'RCOL(2)=',RCOL(2)
      PRINT,'RCOL(3)=',RCOL(3)
      PRINT,'RCOL(4)=',RCOL(4)
      PRINT,'VP1=',VP1
      PRINT,'VP2=',VP2
      PRINT,'VP3=',VP3
      PRINT,'VP4=',VP4
      PRINT,'VP5=',VP5
      PRINT,'VP6=',VP6
      PRINT,'VP7=',VP7
      PRINT,'VP8=',VP8
      PRINT,'VP9=',VP9
      PRINT,'VP10=',VP10
      PRINT,'BBOTVL=',BBOTVL
      PRINT,'AVELJT=',AVELJT
      PRINT,'TOPAR=',TOPAR
      PRINT,'BOTAR=',BOTAR
      PRINT,'BOTVEL=',BOTVEL
      PRINT,'SURFVL=',SURFVL
      PRINT,'VELJET=',VELJET
      PRINT,'VCD=',VCD
      PRINT,'PMPRN=',PMPRN
      PRINT,'CDRAG=',CDRAG
      PRINT,'SUMMARY OUTPUT OF RESULTANT TORQUES'
      PRINT,'FACTOR(1)=',FACTOR(1)
      PRINT,'FACTOR(2)=',FACTOR(2)
      PRINT,'FACTOR(3)=',FACTOR(3)
      PRINT,'FACTOR(5)=',FACTOR(5)
      PRINT,'FACTOR(6)=',FACTOR(6)
      PRINT,'FACTOR(7)=',FACTOR(7)
      PRINT,'FACTOR(8)=',FACTOR(8)
      PRINT,'FACTOR(9)=',FACTOR(9)
      PRINT,'FACTOR(10)=',FACTOR(10)
      PRINT,'FACTOR(11)=',FACTOR(11)
      PRINT,'FACTOR(13)=',FACTOR(13)
      PRINT,'FACTOR(14)=',FACTOR(14)
      PRINT,'FACTOR(15)=',FACTOR(15)
      PRINT,'SWSTOT=',SWSTOT
      PRINT,'SHEAR STRESS ON INCLINED PLANE=',TAUINC
      PRINT,'SHEAR STRESS ON HORIZONTAL PLANE =',TAUHOR
C
C
C     CALCULATE THE TOTAL KINETIC ENERGY OF THE SYSTEM
C
C
      HENTR=DEPTH-LENGTH*SIN(THETAR)
      VENT=QPUMP/(6.0*DBELL*HENTR)*QIQPR
C     SECTION 101
      VTT=SURFVL*(DEPTH-YCENRO)/RAY1
      VER=VENT*COS(ANGSS1)
      VET=VENT*SIN(ANGSS1)
      VT101=VTT-VET
      VR101=VER
      VA101=SQRT(VT101**2+VR101**2)
      RKE101=0.5*RHOFLU*6.0*DBELL*ANGSWS(101)*VA101*VA101*RAY1*
     &RAY1*0.25
C     SECTION 102
      VTT=SURFVL*(DEPTH-YCENRO)/RAY2
      PHI21=PIE-ANGSWS(101)-ANGSS2
      IF(PHI21.GE.(0.5*PIE))THEN DO
      PHI22=PHI21-0.5*PIE
      VET=VENT*SIN(PHI22)
      VER=VENT*COS(PHI22)
      VT102=VTT-VET
      VT102=ABS(VT102)
      VR102=VER
      VA102=SQRT(VT102**2+VR102**2)
      ELSE DO
      PHI22=0.5*PIE-PHI21
      VET=VENT*SIN(PHI22)
      VER=VENT*COS(PHI22)
      PHI23=0.5*PIE-PHI21
      VT102=VET+VTT
      VA102=SQRT(VER**2+VT102**2)
      END IF
      RKE102=0.5*RHOFLU*6.0*DBELL*ANGSWS(102)*VA102*VA102*RAY2*
     &RAY2*0.25
C     SECTION 103
      VTT=SURFVL*(DEPTH-YCENRO)/RAY3
      PHI31=PIE-ANGSWS(101)-ANGSWS(102)-ANGSS2
      IF(PHI31.GE.(0.5*PIE))THEN DO
      PHI32=PHI31-0.5*PIE
      VER=VENT*COS(PHI32)
      VET=VENT*SIN(PHI32)
      VT103=VTT-VET
      VT103=ABS(VT103)
      VR103=VER
      VA103=SQRT(VT103**2+VR103**2)
      ELSE DO
      PHI32=0.5*PIE-PHI31
      PHI33=PHI32
      VER=VENT*COS(PHI32)
      VET=VENT*SIN(PHI32)
      VT103=VTT+VET
      VA103=SQRT(VER**2+VT103**2)
      END IF
      RKE103=0.5*RHOFLU*6.0*DBELL*ANGSWS(103)*VA103*VA103*RAY3*
     &RAY3*0.25
C     SECTION 201
      IF(ANSS10.LE.(0.5*PIE))THEN DO
      PHI41=0.5*PIE-ANSS10
      PHI43=0.5*PIE-PHI41-THETAR
      ELSE DO
      PHI41=ANSS10-0.5*PIE
      PHI43=THETAR-PHI41
      PHI44=ABS(PHI43)
      PHI45=0.5*PIE-PHI44
      END IF
      IF(ANSS10.LE.(0.5*PIE))PHI46=PHI43
      IF(ANSS10.GT.(0.5*PIE))PHI46=PHI45
      R1201=RAY4*(1.0-BBOTVL/YCENRO)
      VT201=BOTAR/(RAY4-0.5*R1201)
      RKE201=0.50*RHOFLU*6.0*DBELL*ANGSWS(201)*VT201*VT201*
     &(0.5*RAY4*RAY4-0.25*R1201*R1201)/(COS(PHI46)*COS(PHI46))
C     SECTION 202
      PHI51=PIE-ANGSWS(201)-ANGSS9
      R1202=RAY5*(1.0-BBOTVL/YCENRO)
      VT202=BOTAR/(RAY5-0.5*R1202)
      IF((PHI51+THETAR).LE.PIE)THEN DO
      PHI52=PIE-PHI51-THETAR
      PHI53=0.5*PIE-PHI52-THETAR
      ELSE DO
      PHI52=PIE-PHI51
      PHI53=0.5*PIE-PHI52
      END IF
      RKE202=0.5*RHOFLU*6.0*DBELL*ANGSWS(202)*VT202*VT202*(0.5*
     &RAY5*RAY5-0.25*R1202*R1202)/(COS(PHI53)*COS(PHI53))
C     SECTION 203
      PHI61=PIE-ANGSS9-ANGSWS(201)-ANGSWS(202)
      R1203=RAY6*(1.0-BBOTVL/YCENRO)
      VT203=BOTAR/(RAY6-0.5*R1203)
      IF((PHI61+THETAR).LE.PIE)THEN DO
      PHI62=PIE-PHI61-THETAR
      PHI63=0.5*PIE-PHI62-THETAR
      ELSE DO
      PHI62=PIE-PHI61
      PHI63=0.5*PIE-PHI62
      END IF
      RKE203=0.50*RHOFLU*6.0*DBELL*ANGSWS(203)*VT203*VT203*(0.5*
     &RAY6*RAY6-0.25*R1203*R1203)/(COS(PHI63)*COS(PHI63))
C     SECTION 301
      R1301=RAY7*(1.0-BBOTVL/YCENRO)
      VT301=BOTAR/(RAY7-0.5*R1301)
      IF(ANGSS3.LE.(0.5*PIE))PHI71=0.5*PIE-ANGSS3
      IF(ANGSS3.GT.(0.5*PIE))PHI71=ANGSS3-0.5*PIE
      RKE301=0.50*RHOFLU*6.0*DBELL*ANGSWS(301)*VT301*VT301*(0.5*
     &RAY7*RAY7-0.25*R1301*R1301)/(COS(PHI71)*COS(PHI71))
C     SECTION 302
      R1302=RAY8*(1.0-BBOTVL/YCENRO)
      VT302=BOTAR/(RAY8-0.5*R1302)
      PHI81=PIE-ANGSS5-ANGSWS(303)-ANGSWS(302)
      IF(PHI81.GE.(0.5*PIE))PHI82=PHI81-0.5*PIE
      IF(PHI81.LT.(0.5*PIE))PHI82=0.5*PIE-PHI81
      RKE302=0.50*RHOFLU*6.0*DBELL*ANGSWS(302)*VT302*VT302*(0.5*
     &RAY8*RAY8-0.25*R1302*R1302)/(COS(PHI82)*COS(PHI82))
C     SECTION 303
      R1303=RAY9*(1.0-BBOTVL/YCENRO)
      VT303=BOTAR/(RAY9-0.5*R1303)
      PHI91=PIE-ANGSS5-ANGSWS(303)
      IF(PHI91.GE.(0.5*PIE))PHI92=PHI91-0.5*PIE
      IF(PHI91.LT.(0.5*PIE))PHI92=0.5*PIE-PHI91
      RKE303=0.50*RHOFLU*6.0*DBELL*ANGSWS(303)*VT303*VT303*(0.5*
     &RAY9*RAY9-0.25*R1303*R1303)/(COS(PHI92)*COS(PHI92))
C     SECTION 401
      R1401=RAY10*(1.0-BBOTVL/YCENRO)
      VT401=(QWATDF/(6.0*DBELL))/(RAY10-0.5*R1401)
      PHI101=0.5*PIE-ANGSS6
      RKE401=0.50*RHOFLU*6.0*DBELL*ANGSWS(401)*VT401*VT401*(0.5*
     &RAY10*RAY10-0.25*R1401*R1401)/(COS(PHI101)*COS(PHI101))
C     SECTION 402
      R1402=RAY11*(1.0-BBOTVL/YCENRO)
      PHI111=PIE-ANGSS6-ANGSWS(401)
      IF(PHI111.LE.(0.5*PIE))THEN DO
      PHI112=PIE-0.5*PIE-PHI111
      PHI113=PHI112
      ELSE DO
      PHI112=PIE-PHI111
      PHI113=0.5*PIE-PHI112
      END IF
      VT402=(QWATDF/(6.0*DBELL))/(RAY11-0.5*R1402)
      RKE402=0.50*RHOFLU*6.0*DBELL*ANGSWS(402)*VT402*VT402*(0.5*
     &RAY11*RAY11-0.25*R1402*R1402)/(COS(PHI113)*COS(PHI113))
C     SECTION 403
      R1403=RAY12*(1.0-BBOTVL/YCENRO)
      PHI121=PIE-ANGSS8-ANGSWS(403)
      IF(PHI121.GE.(0.5*PIE))THEN DO
      PHI122=PHI121-0.5*PIE
      ELSE DO
      PHI122=0.5*PIE-PHI121
      END IF
      VT403=(QWATDF/(6.0*DBELL))/(RAY12-0.5*R1403)
      RKE403=0.50*RHOFLU*6.0*DBELL*ANGSWS(403)*VT403*VT403*(0.5*
     &RAY12*RAY12-0.25*R1403*R1403)/(COS(PHI122)*COS(PHI122))
C     SECTION 501
      VT501=SURFVL*(DEPTH-YCENRO)/RAY13
      PHI131=0.5*PIE-ANGSS7
      VA501=VT501/COS(PHI131)
      RKE501=0.5*RHOFLU*6.0*DBELL*ANGSWS(501)*VA501*VA501*RAY13*
     &RAY13*0.25
C     SECTION 502
      VT502=SURFVL*(DEPTH-YCENRO)/RAY14
      PHI141=PIE-ANGSS7-ANGSWS(501)
      PHI142=PIE-PHI141
      IF(PHI142.LE.(0.5*PIE))THEN DO
      PHI143=0.5*PIE-PHI142
      ELSE DO
      PHI143=PHI142-0.5*PIE
      END IF
      VA502=VT502/COS(PHI143)
      RKE502=0.5*RHOFLU*6.0*DBELL*ANGSWS(502)*VA502*VA502*RAY14*
     &RAY14*0.25
C     SECTION 503
      VT503=SURFVL*(DEPTH-YCENRO)/RAY15
      PHI151=PIE-ANGSS7-ANGSWS(501)-ANGSWS(502)
      PHI152=PIE-PHI151
      IF(PHI151.GE.(0.5*PIE)) THEN DO
      PHI153=0.5*PIE-PHI152
      ELSE DO
      PHI153=PHI152-0.5*PIE
      END IF
      VA503=VT503/COS(PHI153)
      RKE503=0.5*RHOFLU*6.0*DBELL*ANGSWS(503)*VA503*VA503*RAY15*
     &RAY15*0.25
C     TOTAL KINETIC ENERGY
      RKETOT=RKE101+RKE102+RKE103+RKE201+RKE202+RKE203+
     &RKE301+RKE302+RKE303+RKE401+RKE402+RKE403+RKE501+
     &RKE502+RKE503
C
```

```
C
C     CALCULATION OF THE TOTAL ANGULAR MOMENTUM IN THE SYSTEM
C
C
      AM101=RHOFLU*6.0*DBELL*ANGSWS(101)*VT101*0.25*(RAY101**3)
      AM102=RHOFLU*6.0*DBELL*ANGSWS(102)*VT102*0.25*(RAY102**3)
      AM103=RHOFLU*6.0*DBELL*ANGSWS(103)*VT103*0.25*(RAY103**3)
      AM201=RHOFLU*6.0*DBELL*ANGSWS(201)*(0.3333*RAY201**3-
     &(1.0/12.0)*R1201**3)*VTR201
      AM202=RHOFLU*6.0*DBELL*ANGSWS(202)*(0.3333*RAY202**3-
     &(1.0/12.0)*R1202**3)*VTR202
      AM203=RHOFLU*6.0*DBELL*ANGSWS(203)*(0.3333*RAY203**3-
     &(1.0/12.0)*R1203**3)*VTR203
      AM301=RHOFLU*6.0*DBELL*ANGSWS(301)*VTR301*(0.3333*RAY301**
     &3-(1.0/12.0)*R1301**3)
      AM302=RHOFLU*6.0*DBELL*ANGSWS(302)*VTR302*(0.3333*RAY302**
     &3-(1.0/12.0)*R1302**3)
      AM303=RHOFLU*6.0*DBELL*ANGSWS(303)*VTR303*(0.3333*RAY303**
     &3-(1.0/12.0)*R1303**3)
      AM401=RHOFLU*6.0*DBELL*ANGSWS(401)*VTR401*(0.3333*RAY401**
     &3-(1.0/12.0)*R1401**3)
      AM402=RHOFLU*6.0*DBELL*ANGSWS(402)*VTR402*(0.3333*RAY402**
     &3-(1.0/12.0)*R1402**3)
      AM403=RHOFLU*6.0*DBELL*ANGSWS(403)*VTR403*(0.3333*RAY403**
     &3-(1.0/12.0)*R1403**3)
      AM501=RHOFLU*6.0*DBELL*ANGSWS(501)*VTR501*0.25*RAY501**3
      AM502=RHOFLU*6.0*DBELL*ANGSWS(502)*VTR502*0.25*RAY502**3
      AM503=RHOFLU*6.0*DBELL*ANGSWS(503)*VTR503*0.25*RAY503**3
C     CALCULATE THE TOTAL ANGULAR MOMENTUM
      AMTOT=AM101+AM102+AM103+AM201+AM202+AM203+AM301+AM302+
     &AM303+AM401+AM402+AM403+AM501+AM502+AM503
      PRINT,'RKE101=',RKE101
      PRINT,'RKE102=',RKE102
      PRINT,'RKE103=',RKE103
      PRINT,'RKE201=',RKE201
      PRINT,'RKE202=',RKE202
      PRINT,'RKE203=',RKE203
      PRINT,'RKE301=',RKE301
      PRINT,'RKE302=',RKE302
      PRINT,'RKE303=',RKE303
      PRINT,'RKE401=',RKE401
      PRINT,'RKE402=',RKE402
      PRINT,'RKE403=',RKE403
      PRINT,'RKE501=',RKE501
      PRINT,'RKE502=',RKE502
      PRINT,'RKE503=',RKE503
      PRINT,'RKETOT=',RKETOT
      PRINT,'AM101=',AM101
      PRINT,'AM102=',AM102
      PRINT,'AM103=',AM103
      PRINT,'AM201=',AM201
      PRINT,'AM202=',AM202
      PRINT,'AM203=',AM203
      PRINT,'AM301=',AM301
      PRINT,'AM302=',AM302
      PRINT,'AM303=',AM303
      PRINT,'AM401=',AM401
      PRINT,'AM402=',AM402
      PRINT,'AM403=',AM403
      PRINT,'AM501=',AM501
      PRINT,'AM502=',AM502
      PRINT,'AM503=',AM503
      PRINT,'AMTOT=',AMTOT
  907 PRINT,'XCENRO.LE.XSP:PROGRAM TERMINATED'
      GO TO 911
  908 PRINT,'YCENRO.LT.(0.5*DBELL):PROGRAM TERMINATED'
      GO TO 911
  900 PRINT,'DESIGN NOT RECOMMENDED:SLOPING FLOOR EXPOSED'
      GO TO 911
  911 CONTINUE
      STOP
      END
C
C     THIS SUB-ROUTINE SPECIFIES THE EQUATIONS FOR THE FIFTH-ORDER
C     RUNGA-KUTTA SUBROUTINE "SOLVE"
C
C
      SUBROUTINE VECTOR(YP,Y,WW,NN)
      REAL*8 YP,Y(25),WW(25)
      REAL*8 A,DIFSUB,PATMOS,GAMFLU,QAIRO,B,DQARDY
      REAL*8 AA,DBELL,BB,ALPHAC,CC,FRRWAL,DD,RHOFLU,RHOGAS
      REAL*8 FF,PSI,QAIR,GG,HH,G,PP,QQ,RR,SS,TT
      COMMON/XYZ1/A,DIFSUB,PATMOS,GAMFLU,QAIRO
      COMMON/XYZ2/B,DQARDY,AA,DBELL,BB
      COMMON/XYZ3/ALPHAC,CC,FRRWAL,DD,RHOFLU
      COMMON/XYZ4/RHOGAS,FF,PSI,QAIR,GG
      COMMON/XYZ5/HH,G,PP,QQ,RR
      COMMON/XYZ6/SS,TT,SCALE
      COMMON/XYZ7/DEPTH,VAMBNT,VAR1,VAR2
C
C
C     CALCULATION OF THE RATE OF CHANGE OF THE AIRFLOWRATE WITH
C     DEPTH, (DQARDY) AND THE AMBIANT FLUID VELOCITY
C
C
      VAR1=4.220*QAIRO/(DEPTH*DEPTH)
      VAR2=7.297*QAIRO/(DEPTH**3.0)
      VAMBNT=(VAR1-VAR2*YP+0.214*Y(3))
      IF(VAMBNT.GT.Y(3))VAMBNT=0.0
      A=(DIFSUB+(PATMOS/GAMFLU))*QAIRO
      B=(DIFSUB-YP+(PATMOS/GAMFLU))**2
      WW(5)=A/B
C
C
C     INITIALIZATION OF THE WORK VECTORS FOR THE 5TH ORDER RUNGA-
C     KUTTA SUBROUTINE "SOLVE"
C
C
      AA=(1./(6.0*DBELL))*WW(5)
      BB=(Y(2)*ALPHAC*(Y(3)-VAMBNT))/(1.0-Y(2))
      CC=(2.0/Y(3))*(FRRWAL*Y(3)/16.0+ALPHAC*(Y(3)-VAMBNT))/(1.0
     &-Y(2))
      DD=Y(1)*Y(2)*G*(RHOFLU-RHOGAS)/(Y(3)*Y(3)*RHOFLU*(DABS(Y(3))
     &/Y(3)))
      FF=PSI+Y(5)/(6.0*DBELL*Y(1))+Y(3)*(1.0-Y(2))
      GG=PSI+Y(5)/(3.0*DBELL*Y(1))+Y(3)*(1.0-2.0*Y(2))
      HH=(1.0-Y(2))/Y(1)
      PP=(1.0-Y(2))*Y(2)*G*(RHOFLU-RHOGAS)/(Y(3)*Y(3)*RHOFLU*(DABS
     &(Y(3))/Y(3)))
      QQ=(2.0/(Y(3)*Y(1)))*(FRRWAL*Y(3)/16.0+ALPHAC*(Y(3)-VAMBNT))
      RR=(ALPHAC*(Y(3)-VAMBNT))/(Y(1)*(1.0-Y(2)))
      SS=Y(3)/(1.0-Y(2))
      TT=Y(3)/Y(1)
C
C
      WW(1)=(AA-BB+(CC-DD)*FF)/GG
      WW(2)=HH*WW(1)+PP-QQ
      WW(3)=RR+SS*WW(2)-TT*WW(1)
      WW(4)=Y(1)*Y(2)*(1.0-Y(2))*G*(RHOFLU-RHOGAS)*6.0*DBELL
C
C
      RETURN
      END
C
C
C
      SUBROUTINESOLVE(TO,Y,DY,HO,N,VECTOR)
      EXTERNALVECTOR
      REAL*8DY(25),Y
     *(25),W(25),G(6,25),Z(25),T,T1,H,BI,A(6,5)/0.DO,.5DO,.1875DO,2*0
.DO
     *,.1428571428571429,2*0.DO,.0625DO,0.DO,-.1875DO,.57142857142857
14,
     *3*0.DO,.5DO,.375DO,.8571428571428571,4*0.DO,.5625DO,-1.71428571
428
     *5714,5*0.DO,1.142857142857143/,B(6)/.7777777777777778D-1,0.DO,.
355
     *5555555555556,.1333333333333333,.3555555555555556,.777777777777
777
     *8D-1/,C(6)/0.DO,.5DO,.25DO,.5DO,.75DO,1.DO/
```

```
      T1=T0
      H=H0
      T=T1
      CALLVECTOR(T,Y,W,N)
      BI=B(1)
      DO2I=1,N
      G(1,I)=H*W(I)
    2 DY(I)=G(1,I)*BI
      DO3I=2,6
      IM=I-1
      T=T1+C(I)*H
      DO4K=1,N
      Z(K)=Y(K)
      DO4J=1,IM
    4 Z(K)=Z(K)+A(I,J)*G(J,K)
      CALLVECTOR(T,Z,W,N)
      BI=B(I)
      DO3J=1,N
      G(I,J)=H*W(J)
    3 DY(J)=DY(J)+G(I,J)*BI
      DO5I=1,N
    5 Y(I)=Y(I)+DY(I)
      T0=T1+H
      RETURN
      END
$ENTRY
0.400  2.460  30.0  3.50
0.005  0.12   6.00  0.100  0.184  0.05
0.029  0.029  0.029 0.035
$IBSYS
```

?

A1.4 COMPUTER PROGRAM OUTPUT

```
NN=              5
THE KINEMATIC VISCOSITY OF THE FLUID IS=              0.0000010
PATMOS=        0.1013000000000000D 06
GAMFLU=        0.9788378600000000D 04
G=     0.9805999755859374D 01
RHOFLU=        0.9982028808593749D 03
RHOGAS=        0.1204700469970703D 01
PSI=      0.2500845266000000D 00
PIE=             3.1415920
DYP=             0.0010000
YP=             0.0010000
DBELL=        0.4000000000000000D 00
RBUBLE=               0.0050000
DEPTH=               2.4600000
GAMMA=               6.0000000
ALPHAC=        0.1200000000000000D 00
THETAD=              30.0000000
QAIRO=        0.5000000000000000D-01
QPUMP=               0.1840000
THE INFLOW TO PUMPING RATIO=                0.0500000
THE SCALE RATIO=             3.5000000
DIFSUB=        0.2393324851989746D 01
LENGTH=        0.2835020402634751D 01
APIPE=               0.0540723
HVEL=              0.0656026
XGEOM=               2.2495200
YGEOM=               1.3532400
PMPGNO=               0.0003095
AIRNO=               0.0016822
DEPTNO=        2720000.0000000
XCENRO=                2.7177650
YCENRO=                1.5375140
RINCL=               1.3851250
RHORIZ=                1.6569800
RDISCH=                1.8776170
RUPPER=                2.3825070
RLOWER=                2.3382030
 Y(M)        B(M)    AIR FRCN     VW(M/S)
0.001      0.1050  0.32256699    0.2459
0.002      0.1009  0.32773018    0.2583
0.003      0.0972  0.33241546    0.2702
0.004      0.0940  0.33668829    0.2817
0.005      0.0910  0.34060170    0.2928
0.006      0.0884  0.34419924    0.3037
0.007      0.0860  0.34751708    0.3142
0.008      0.0838  0.35058560    0.3244
0.009      0.0818  0.35343052    0.3343
0.010      0.0799  0.35607381    0.3440
0.011      0.0782  0.35853439    0.3534
```

50.	0.012	0.0766	0.36082866	0.3627
51.	0.013	0.0752	0.36297094	0.3716
52.	0.014	0.0738	0.36497375	0.3804
53.	0.015	0.0725	0.36684819	0.3890
54.	0.016	0.0713	0.36860406	0.3974
55.	0.017	0.0702	0.37025011	0.4056
56.	0.018	0.0691	0.37179415	0.4137
57.	0.019	0.0681	0.37324320	0.4215
58.	0.020	0.0672	0.37460360	0.4293
59.	0.021	0.0663	0.37588107	0.4368
60.	0.022	0.0654	0.37708080	0.4442
61.	0.023	0.0646	0.37820753	0.4515
62.	0.024	0.0639	0.37926557	0.4586
63.	0.025	0.0632	0.38025888	0.4656
64.	0.026	0.0625	0.38119108	0.4725
65.	0.027	0.0618	0.38206553	0.4792
66.	0.028	0.0612	0.38288529	0.4858
67.	0.029	0.0606	0.38365323	0.4923
68.	0.030	0.0600	0.38437196	0.4987
69.	0.031	0.0595	0.38504396	0.5050
70.	0.032	0.0590	0.38567148	0.5112
71.	0.033	0.0585	0.38625667	0.5172
72.	0.034	0.0580	0.38680149	0.5232
73.	0.035	0.0575	0.38730780	0.5290
74.	0.036	0.0571	0.38777734	0.5348
75.	0.037	0.0567	0.38821173	0.5404
76.	0.038	0.0563	0.38861250	0.5460
77.	0.039	0.0559	0.38898109	0.5515
78.	0.040	0.0555	0.38931885	0.5569
79.	0.041	0.0552	0.38962706	0.5622
80.	0.042	0.0548	0.38990693	0.5674
81.	0.043	0.0545	0.39015958	0.5725
82.	0.044	0.0542	0.39038611	0.5776
83.	0.045	0.0539	0.39058754	0.5826
84.	0.046	0.0536	0.39076483	0.5875
85.	0.047	0.0533	0.39091890	0.5923
86.	0.048	0.0531	0.39105063	0.5971
87.	0.049	0.0528	0.39116085	0.6017
88.	0.050	0.0526	0.39125035	0.6064
89.	0.051	0.0525	0.39131989	0.6109
90.	0.052	0.0525	0.39136977	0.6154
91.	0.053	0.0525	0.39140072	0.6198
92.	0.054	0.0525	0.39141355	0.6242
93.	0.055	0.0525	0.39140905	0.6285
94.	0.056	0.0525	0.39138794	0.6327
95.	0.057	0.0525	0.39135092	0.6369
96.	0.058	0.0525	0.39129864	0.6411
97.	0.059	0.0525	0.39123174	0.6452
98.	0.060	0.0525	0.39115081	0.6492
99.	0.061	0.0525	0.39105643	0.6532
100.	0.062	0.0525	0.39094911	0.6571

```
101.     0.063     0.0525  0.39082940   0.6610
102.     0.064     0.0525  0.39069776   0.6649
103.     0.065     0.0525  0.39055467   0.6687
104.     0.066     0.0525  0.39040058   0.6724
105.     0.067     0.0525  0.39023591   0.6762
106.     0.068     0.0525  0.39006106   0.6798
107.     0.069     0.0525  0.38987642   0.6835
108.     0.070     0.0525  0.38968237   0.6870
109.     0.071     0.0525  0.38947925   0.6906
110.     0.072     0.0525  0.38926741   0.6941
111.     0.073     0.0525  0.38904716   0.6975
112.     0.074     0.0525  0.38881882   0.7009
113.     0.075     0.0525  0.38858269   0.7043
114.     0.076     0.0525  0.38833905   0.7077
115.     0.077     0.0525  0.38808816   0.7110
116.     0.078     0.0525  0.38783030   0.7142
117.                       .
118.                       .
119.                       .
120.                       .
121.           PRINTOUT CONTINUES FOR EACH dy
122.                       .
123.                       .
124.                       .
125.                       .
126.     2.421     0.2383  0.09253662   1.3174
127.     2.422     0.2384  0.09251392   1.3174
128.     2.423     0.2385  0.09249125   1.3175
129.     2.424     0.2385  0.09246859   1.3176
130.     2.425     0.2386  0.09244595   1.3177
131.     2.426     0.2387  0.09242332   1.3177
132.     2.427     0.2388  0.09240072   1.3178
133.     2.428     0.2389  0.09237813   1.3179
134.     2.429     0.2390  0.09235555   1.3180
135.     2.430     0.2391  0.09233300   1.3180
136.     2.431     0.2392  0.09231046   1.3181
137.     2.432     0.2392  0.09228794   1.3182
138.     2.433     0.2393  0.09226543   1.3182
139.     2.434     0.2394  0.09224295   1.3183
140.     2.435     0.2395  0.09222048   1.3184
141.     2.436     0.2396  0.09219803   1.3185
142.     2.437     0.2397  0.09217559   1.3185
143.     2.438     0.2398  0.09215317   1.3186
144.     2.439     0.2398  0.09213077   1.3187
145.     2.440     0.2399  0.09210839   1.3188
146.     2.441     0.2400  0.09208602   1.3188
147.     2.442     0.2401  0.09206367   1.3189
148.     2.443     0.2402  0.09204133   1.3190
149.     2.444     0.2403  0.09201902   1.3190
150.     2.445     0.2404  0.09199672   1.3191
151.     2.446     0.2405  0.09197443   1.3192
152.     2.447     0.2405  0.09195217   1.3193
```

```
153.       2.448     0.2406  0.09192992    1.3193
154.       2.449     0.2407  0.09190769    1.3194
155.       2.450     0.2408  0.09188547    1.3195
156.       2.451     0.2409  0.09186327    1.3196
157.       2.452     0.2410  0.09184109    1.3196
158.       2.453     0.2411  0.09181892    1.3197
159.       2.454     0.2412  0.09179678    1.3198
160.       2.455     0.2412  0.09177464    1.3198
161.       2.456     0.2413  0.09175253    1.3199
162.       2.457     0.2414  0.09173043    1.3200
163.       2.458     0.2415  0.09170835    1.3201
164.       2.459     0.2416  0.09168628    1.3201
165.       2.460     0.2417  0.09166423    1.3202
166.       UPPER MOMENTUM CORRECTION FACTOR(ASSUMED)=            1.3098750
167.       LOWER MOMENTUM CORRECTION FACTOR(ASSUMED)=            1.1950590
168.       UPPER MOMENTUM CORRECTION FACTOR(OBSERVED)=            1.3186750
169.       LOWER MOMENTUM CORRECTION FACTOR(OBSERVED)=            1.8948440
170.       HENTR=              1.0424900
171.       HUPPER=              0.9224854
172.       HLOWER=              0.1200047
173.       QUPPER=              0.0081410
174.       QLOWER=              0.0010590
175.       VUPPER=              0.0036771
176.       VLOWER=              0.0036771
177.       STABLE CIRCULATING FLOW=          1.3641820
178.       VR(1)=              0.4536579
179.       VR(2)=              0.1440679
180.       VR(3)=              0.1196092
181.       VR(4)=              0.1804527
182.       VT(1)=              0.3453424
183.       VT(2)=              0.5677627
184.       VT(3)=              0.6834455
185.       VT(4)=              0.3437012
186.       CORRN=              0.1614514
187.       HPRIME=              2.6214510
188.       YBARP=              1.6938170
189.       DELP2=           4665.1830000
190.       RPERPI=              1.2726430
191.       RPAR=              0.5467637
192.       RINCDV=              0.7271937
193.       VTANIC=              0.6328728
194.       VINCL=              0.6888088
195.       FINCL=              0.0290000
196.       RDIVH=              0.8699183
197.       VTANH=              0.5290394
198.       VPARH=              0.5701463
199.       FHORIZ=              0.0290000
200.       TFACT3=              7.0073720
201.       FRRWAL=         0.35000000000000000D-01
202.       DOCOL=              0.2784244
```

```
203.     ANGSWD(101)=           7.7091210
204.     ANGSWD(102)=           8.2775100
205.     ANGSWD(103)=           8.4894020
206.     ANGSWD(201)=          18.3498300
207.     ANGSWD(202)=          35.4155800
208.     ANGSWD(203)=          37.6754600
209.     ANGSWD(301)=          28.2203900
210.     ANGSWD(302)=          17.6973100
211.     ANGSWD(303)=          10.2042100
212.     ANGSWD(401)=          14.6927000
213.     ANGSWD(402)=          16.9821700
214.     ANGSWD(403)=          16.5718000
215.     ANGSWD(501)=          22.9786000
216.     ANGSWD(502)=          83.6096600
217.     ANGSWD(503)=          33.1259700
218.     VTR101=          0.4539218
219.     VTR102=          0.4738502
220.     VTR103=          0.4857053
221.     VTR201=          0.4414971
222.     VTR202=          0.6034423
223.     VTR203=          0.6224101
224.     VTR301=          0.5206074
225.     VTR302=          0.4142726
226.     VTR303=          0.3170977
227.     VTR401=          0.2597824
228.     VTR402=          0.2787021
229.     VTR403=          0.2757622
230.     VTR501=          0.4273547
231.     VTR502=          0.7226781
232.     VTR503=          0.4991720
233.     FSWS=          0.0290000
234.     TORQUE(101)=           0.5973896
235.     TORQUE(102)=           0.6312242
236.     TORQUE(103)=           0.6519663
237.     TORQUE(201)=           1.1105510
238.     TORQUE(202)=           1.5681710
239.     TORQUE(203)=           1.6173960
240.     TORQUE(301)=           1.4483950
241.     TORQUE(302)=           1.1414460
242.     TORQUE(303)=           0.8598468
243.     TORQUE(401)=           1.0270910
244.     TORQUE(402)=           1.1065480
245.     TORQUE(403)=           1.0913200
246.     TORQUE(501)=           1.0216180
247.     TORQUE(502)=           2.1981890
248.     TORQUE(503)=           1.2608750
249.     SWSTOT=          17.3320100
250.     YDF=          0.0629393
251.     THE RATIO OF FACTOR(14) TO FACTOR(10)=          1.3914620
252.     THE MODIFIED RATIO OF FACTOR(14) TO FACTOR(10)=          0.5004358
```

```
253.     CF=            1.4499990
254.     TRMLFT=          2749.5790000
255.     TRMRGT=          2792.2450000
256.     DIFFER=            42.6662500
257.     PERERR=             1.5280250
258.     MCF1=            1.0000000
259.     MCF2=            1.0000000
260.     MCF3=            1.0000000
261.     MDOT1=         839.0598000
262.     MDOT2=         648.3842000
263.     FFI=          12.8494400
264.     FFH=           0.0000000
265.     DELTAF=        1498.5380000
266.     MDOT3=            0.0337685
267.     YLM=           0.8071985
268.     XSP=           1.3999990
269.     RCOL(1)=            1.6561360
270.     RCOL(2)=            1.3595270
271.     RCOL(3)=            1.3377930
272.     RCOL(4)=            1.4883480
273.     VP1=           0.0016822
274.     VP2=           0.0003095
275.     VP3=          30.0000000
276.     VP4=           0.1888095
277.     VP5=           0.2161509
278.     VP6=           0.1035630
279.     VP7=           0.2968765
280.     VP8=           0.6250059
281.     VP9=           0.9584690
282.     VP10=   2720000.0000000
283.     BBOTVL=           0.7303162
284.     AVELJT=           2.3578320
285.     TOPAR=          0.5669889
286.     BOTAR=          0.6464974
287.     BOTVEL=           0.5701461
288.     SURFVL=           0.9858341
289.     VELJET=           1.1200810
290.     VCD=           0.1566018
291.     PMPRN=      43436.5800000
292.     CDRAG=          1.3999990
```

```
SUMMARY OUTPUT OF RESULTANT TORQUES
FACTOR(1)=            16.3527500
FACTOR(2)=            12.4135500
FACTOR(3)=            97.5562800
FACTOR(5)=            40.3036900
FACTOR(6)=             5.9873210
FACTOR(7)=             2.9924920
FACTOR(8)=           485.4025000
FACTOR(9)=          -413.9960000
FACTOR(10)=         2477.0620000
FACTOR(11)=          729.1794000
FACTOR(13)=           94.3169000
FACTOR(14)=         1724.8720000
FACTOR(15)=          252.0505000
SWSTOT=          17.3320100
SHEAR STRESS ON INCLINED PLANE=                  1.8884980
SHEAR STRESS ON HORIZONTAL PLANE =                  1.2938730
RKE101=          33.0781800
RKE102=          35.6171500
RKE103=          36.6320600
RKE201=         429.8300000
RKE202=         402.8271000
RKE203=         261.7912000
RKE301=         196.5906000
RKE302=         172.6948000
RKE303=         173.1851000
RKE401=         103.8340000
RKE402=          97.2677300
RKE403=          88.8474200
RKE501=         961.4543000
RKE502=         815.8161000
RKE503=         215.1704000
RKETOT=        4024.6360000
AM101=         432.5607000
AM102=         438.4543000
AM103=         442.4321000
AM201=         831.3898000
AM202=         866.3095000
AM203=         888.4916000
AM301=         950.3041000
AM302=         945.5488000
AM303=         929.9567000
AM401=        1330.4770000
AM402=        1341.9270000
AM403=        1344.0540000
AM501=         989.1997000
AM502=        1258.6460000
AM503=        1045.2140000
AMTOT=       14034.9400000
```

APPENDIX 2

COMPUTER PROGRAM INPUT

Table A2.1 Computer Program Input Cards*

Card No.	Variables	Format
1	D, H, θ, SCALE	All Real
2	R_b, α_C, B_o/R_b, Q_{AIR_o}, Q_p, QIQPR	All Real
3	FINCL, FHORIZ, FSWS, FRRWAL	All Real

*See Table A2.2 for variable description

Table A2.2 Input Variable Description

Variable	Description	Units
D	Bell-Mouth Diameter	m
H	Fluid Depth in Sump	m
θ	Inclined Floor Slope	degrees
SCALE	Ratio of Prototype to Model Bell Mouth Diameters	-
R_b	Bubble Radius	m
α_C	Entrainment Coefficient	-
B_o/R_b	Initial Plume Width to Bubble Radius Ratio	-
Q_{AIR_o}	Diffuser Air Flowrate	m^3/s
Q_p	Maximum Pumping Rate	m^3/s
QIQPR	Inflow to Sump as a Fraction of Total Pumping Capacity	-
FINCL FHORIZ FSWS FRRWAL	Darcy-Weisbach Friction Factors for: inclined portion of floor, horizontal portion of floor, side walls and rear wall	- - - -

NOMENCLATURE

A = area

AA = distance above the bed to the line of action of v_j

A_C = contracted area between suction pipes

A_i = cross-sectional area of the intake

AM = angular momentum

A_{p_i} = projected area of the suction pipes

B = pump spacing; width of conveyance channel

B = plume width (in diffuser plume model)

ΔB = change in plume width over depth H

BB = distance above the bed over which v_b is assumed to be constant

B_o = initial plume width adjacent to diffuser

BPF = bed packing factor

B_T = width of plume at static water level

b = channel width

C = height of bell-mouth above sump floor

C = Chezy friction coefficient

C_d = drag coefficient

C_f = concentration of fine material in the channel

C_f = correction factor applied to $T_{\Delta m}$

C_{feqn} = C_f correction factor estimated from calibration equation

C_{fopt} = C_f correction factor estimated from convergent numerical solution

C_L = particle lift coefficient (see Eq. [3.36])

C_S = average volumetric concentration of transported particles

D = suction bell diameter

D_{gr} = Ackers' and White's dimensionless grain diameter (see Eq. [3.73])

d = inlet pipe diameter

d_A = top clearance of reaction baffle

d_B = bottom clearance of reaction baffle

d_e = equivalent diameter of channel cross-section obtained by multiplying the hydraulic radius by 4

$d_{ext.}$ = external diameter of the suction pipe

d_p = inside diameter of the stagnation tube

d_{Smax} = diameter of largest sand grain in a non-uniform sediment mixture, units of cm. for Table 3.3

d_{S_x} = mean particle diameter; units of cm. for Tables 3.2, 3.3, 3.4; subscript x refers to percent finer than by weight

d_* = dimensionless grain size = $(d_S/\nu)(0.1(S_S - 1)gd_S)^{0.5}$

E = length of splitters in pump sump

F = mutual hydrodynamic drag force

ΔF = external force applied to redirect flow in wet well (based on linear momentum calculation)

F_D = drag force on pump columns

F_{ext} = external force applied to a control volume

F_f = friction force

F_{fh} = friction force on horizontal floor

F_{fi} = friction force on inclined floor

F_{gr} = Ackers' and White's sediment mobility number (see Eq. [3.72])

F_i = impact force

F_L = particle lift force (see Eq. [3.36])

F_R = torque ratio associated with the $T_{\Delta m}$ and F forces

F_t = Froude number based on the maximum tangential velocity and total water depth (see Eq. [2.28])

f = Darcy-Weisbach friction factor

G_{gr} = Ackers' and White's transport parameter (see Eq. [3.74])

g = acceleration due to gravity, units of $cm.s^{-2}$ for Table 3.3 and 3.4

H = water depth

H_i = depth of inlet zone of sump

ΔH = rise in water level above the static water level due to the momentum of the plume

h = flow depth, units of cm. for Table 3.3 and 3.4

h = distance from the centre of the stagnation tube to the top of the grains (see Eqs. [6.2] to [6.5])

Δh = difference between the static and dynamic heads of a pitot-tube

h_{cr} = critical flow depth at incipient motion

h_L = head loss

I_η = intake efficiency or coefficient of discharge (see Eq. [2.31])

j = total local flux

j_{air} = air flux

$j_{air,f}$ = drift flux

j_f = fluid flux

$j_{f,air}$ = drift flux

K = viscous correction factor

KE = kinetic energy

K_L = N.L. Coleman's lift factor (see Eq. [3.42])

k = diameter of bed roughness elements

k_S = equivalent sand roughness

k_{Sb} = mean diameter of the grains making up the roughness of the bed of the conveyance channel

k_{SW} = mean diameter of the grains making up the roughness of the walls of the conveyance channel

L = approach channel length

L_i = length of inclined portion of wet well floor

L_m = model length

L_p = prototype length

L_R = length ratio

M = momentum of plume fluid element

MWL = minimum water level

m_f = mass of fluid

Δm = force due to mass of fluid above the free surface, above the diffuser (calculated based on the momentum of the fluid in the plume at the free surface)

N = number of pumps downstream of the pump under consideration

N_A = sediment load similitude number(see Eq. [3.71])

N_{AA} = AA/H

N_{AIR} = air number = $Q_{AIR_o}/(H^{2.5}g^{0.5})$ or $Q_{AIR_o}/(D^{2.5}g^{0.5})$

N_{BB} = BB/H

N_b = bottom velocity number = $v_b/(gH)^{0.5}$

N_D = particle diameter similitude number (see Eq. 3.70])

N_F = Froude number

N_{F_i} = inlet Froude number; $N_{F_i} = v_d/(gH)^{0.5}$ or $v_d/(gS)^{0.5}$

N_{F_m} = model Froude number

N_{F_p} = prototype Froude number

N_{FR} = Froude number ratio

N_H = depth number = $H^{1.5}g^{0.5}\nu_f^{-1.0}$

N_j = jet number = $v_j/(gH)^{0.5}$

N_p = pumping number = $Q_p/(H^{2.5}g^{0.5})$

N_R = Reynolds number

N_{Rd} = suction pipe Reynolds number (see Eq. [2.15])

N_{R_p} = pump column Reynolds number = $v_p d/\nu_f$

N_{Rx} = Reynolds number at some distance x along the plate (see Eq. [2.13])

N_s = surface velocity number = $v_{SURFACE}/(gH)^{0.5}$

N_W = Weber number (see Eq. [2.25])

N_Y = vertical location number = $\bar{Y}/H$

N_{YCR} = centre of rotation number = YCR/H

N_Γ = circulation number = $\Gamma S_C/Q$

N_θ = floor angle number = floor angle in degrees

N_ν = viscosity number = $H^{1.5}g^{0.5}\nu^{-1.0}$

n = revolutions per second of the vortometer vanes

n_R = Manning roughness ratio

P_C = airflow meter calibration pressure

PS = pumping scheme

P_{ST} = stagnation pressure

P_{STP} = standard pressure

P_o = airflow meter operating pressure

P_o = static pressure

ΔP_B = force resulting from pressure imbalance on floor of wet well underneath diffuser plume

ΔP_2 = force due to increased hydrostatic pressure on wall adjacent to diffuser plume

Δ_p = pressure difference or lift pressure on sediment grains (see Eq. [3.37])

Δ_{p_B} = imbalance in bed pressure due to presence of air

p_{AIR} = air pressure at elevation y above the diffuser

p_{atm} = atmospheric pressure

p_B = bed pressure

p_o = air pressure at the diffuser port

Q = flowrate

Q_{AIR} = air flowrate within the plume at elevation y above the diffuser

Q_{AIR_o} = air flowrate being discharged from the diffuser

Q_p = pump discharge

Q_{STP} = airflow rate at standard temperature and pressure

Q_W = water flowrate within the plume

Q_{WD} = total circulating flow produced as a result of air diffusion

q = unit discharge of the flow

q_b = volumetric sediment discharge per unit channel width

q_C^* = dimensionless discharge coefficient (see Eq. [3.53])

q_s = volumetric sediment discharge

R_b = bubble radius

R_{eb} = bubble Reynolds number = $2 \rho_f v_b R_b/\mu_f$

R_h = hydraulic radius of the conveyance channel, units of cm for Table 3.3

r = radial distance

r = radius measured from vortex axis

r_o = radius of the vortex at the free surface

S = submergence; height of water surface above bell-mouth; conveyance channel slope

S = specific gravity of water

S/N = signal to noise ratio

S_C = critical submergence; the submergence when air-entraining vortices first begin to form

SF = particle shape factor

S_f = energy slope

S_{f_C} = shape factor for channel cross-section

SFL = sump floor level

S_{fr} = shape factor for channel reach

S_S = specific weight of particles

S_{SC} = critical value of the modified Sheilds' parameter for steep slopes

S_o = specific gravity of the manometer fluid

T = thickness of splitters in sump well; tractive force

T_C = airflow meter calibration temperature

$T_{\Delta m}$ = torque due to the mass of fluid above the static water level resulting from the momentum of the diffuser plume

T_o = airflow meter operating temperature

T_p = minimum time of one pumping cycle or the time between successive starts or changes in speed of a pump operating over the control range

T_{STP} = standard temperature

t_S = thickness of the sediment layer

U_* = friction velocity

U_{*C} = critical shear velocity

$\bar{u}$ = mean velocity

$\forall$ = volume

V_A = ambient fluid velocity

V_{AIR} = air velocity

V_B = bell-mouth velocity

V_{bC} = fluid velocity near the bed under critical conditions, units of cm.s^{-1}, (see Table 3.2)

V_{bCmax} = maximium fluid velocity near the bed under critical conditions resulting in the initiation of total bed-load movement, units of cm., (see Table 3.2)

V_{bCmin} = minimum fluid velocity near the bed under critical conditions resulting in the initiation of motion of individual particles, units of cm. (see Table 3.2)

V_i = velocity adjacent to inclined floor

V_{in} = velocity of incoming flow in pumping station inlet structure

V_R = velocity scale ratio

$V_{t_{1,2,3,4}}$ = tangential velocities at the sump boundaries used to calculate pump column drag

V_W = plume water velocity

V_θ = tangential velocity component

v_b = terminal bubble rise velocity

v_b = velocity near the bottom of the channel

v_C = velocity through contracted area

v_d = average suction pipe axial velocity

v_i = mean velocity of flow through inlet zone of sump

v_j = jet velocity

v_m = mean velocity, units of cm/s for Table 3.3

v_{mmax} = highest critical mean velocity in the cross-section initiating total bed-load movement, units of cm/s for Table 3.3

v_{mmin} = lowest critical mean velocity in the cross-section initiating particle motion, units of cm/s for Table 3.3

v_o = flow velocity at the particle center-line

v_s = particle settling velocity

$v_{SURFACE}$ = surface velocity

v_t = maximum tangential velocity

v_{t_o} = tangential velocity at the interface between the solid body and plug flow sections

$v_{t_{1,2,3,4}}$ = tangential velocities acting on the pump column subsections

W = approach channel width at suction bell centre line

W_S = submerged weight of sediments

$\bar{X}$ = x coordinate of the geometric centre of the wet well cross-section

X_b = sediment transport on the bed, mass flux per unit mass flow rate

X = rear and side wall clearance between sump wall and edge of inlet

XCR = x coordinate of the centre of rotation

X_b = distance along a boundary

Y = vertical distance above the diffuser

$\bar{Y}$ = y coordinate of the geometric centre of the wet well cross-section

YCR = y coordinate of the centre of rotation

y = conveyance channel depth; distance above the diffuser

$y_{\Delta F}$ = distance between the line of action of the ΔF force and the centre of rotation

$y_{\Delta P_2}$ = distance from floor of wet well to line of action of the hydrostatic force ΔP_2

Z_d = air diffuser submergence

Z = length of vortex air core

α = angle of indicated swirl

α = air fraction within the diffuser plume

α_C = entrainment coefficient

β = constant in Shields-Camp scouring velocity equation

$\beta_{1,2,3}$ = momentum correction factors

β_{BOT} = momentum correction factor for flow passing below the centre of rotation

β_{TOP} = momentum correction factor for flow passing above the centre of rotation

Γ = circulation (see Eq. [2.32])

$\Delta\gamma_A$ = difference in specific weights between the fluid and the air

γ_f = unit weight of fluid

γ_S = unit weight of solid

$\Delta\gamma_S$ = difference in specific weights between the fluid and the solid

δ = boundary layer thickness

δ' = thickness of the laminar boundary layer (units of cm. for Table 3.3)

η = shape factor of the sediments

θ = bed slope

$\Delta\theta$ = change in angular measurement

κ = von Kármán turbulence coefficient

μ_f = dynamic viscosity of the fluid

ν, ν_f = kinematic viscosity of the fluid

ξ = vorticity

ξ_A = mean vorticity distributed over the entire boundary layer

ρ_{AIR} = density of air

ρ_f = fluid density

ρ_S = density of solid particles

σ = surface tension of the fluid

σ_S = standard deviation of the size of the bed material

τ = shear stress

τ_b = bed shear stress

τ_C = critical shear stress, units of g.cm^{-2} for Table 3.4

τ_{eqn} = boundary shear stress obtained using $C_f = C_{feqn}$ in the numerical solution

τ_h = shear stress on the horizontal portion of the wet well floor

τ_i = shear stress on inclined portion of the wet well floor

τ_N = dimensionless shear stress number; $\tau_N = \tau/(\rho_f gH)$

τ_{opt} = boundary shear stress estimated from convergent numerical solution

τ_{SW} = shear stress on the side walls of the wet well

τ_v = shear stress on the vertical sump wall adjacent to the air diffuser

τ_W = wall shear stress

ϕ = submerged angle of repose of the sediment

ϕ_{GA} = transport parameter proposed by Graf and Acaroglu (see Eq. [3.19])

ψ = shear intensity parameter proposed by Graf and Acaroglu (see Eq. [3.18])

ψ_b = $1.53\ (\sigma g(\rho_f - \rho_{AIR})/\rho_f^{\,2})^{0.25}$

ω = angular velocity of the circulating flow

REFERENCES

ACKERS, P. and WHITE, W.R. 1973. Sediment Transport: New Approach and Analysis. Proc. ASCE, J. of Hyd. Div., Vol. 99, HY11, pp. 2041-2060.

AKSOY, S. 1973. Fluid Force Acting on a Sphere Near a Solid Boundary. Proc. 15th Congress, IAHR, Vol. 1, Paper No. A29, Istanbul, Turkey, pp. 217-224.

AMERICAN SOCIETY OF CIVIL ENGINEERS. 1977. Sedimentation Engineering. ASCE Manuals and Reports on Engineering Practice No. 54, V.A. Vanoni, ed., Prepared by the ASCE Task Committee for the Preparation of the "Manual on Sedimentation" of the Sedimentation Committee of the Hydraulics Division, New York, New York, 745 pp.

AMERICAN SOCIETY OF CIVIL ENGINEERS. 1977(b). Wastewater Treatment Plant Design, Manual and Report on Engineering Practice, No. 36, New York, 560 p.

AMPHLETT, M.B. 1976. Air-Entraining Vortices at a Horizontal Intake. Hydraulics Research Station Report No. OD/7, Wallingford, Oxfordshire, England.

ANDREWS, E.D. 1981. Entrainment of Gravel and Cobbles from a Non-Uniform Streambed, EOS. Trans. Am. Geo. Phys. Union, Vol. 62, No. 45, pp. 858.

ANWAR, H.O. 1966. Formation of a Weak Vortex. Journal of Hydraulic Research, Vol. 4, No. 1, pp. 1-16.

ANWAR, H.O. 1968. Prevention of Vortices at Intakes. Water Power, Vol. 20, No. 10, pp. 393-401.

ANWAR, H.O., WELLER, J.A. and AMPHLETT, M.B. 1978. Similarity of Free-Vortex at Horizontal Intake. Journal of Hydraulic Research, Vol. 16, No. 2, pp. 95-105.

ANWAR, H.O. 1983. The Non-Dimensional Parameters of Free-Surface Vortices Measured for Horizontal and Vertically Inverted Intakes. La Houille Blanche, No. 1, pp. 11-25.

APPERLY, L.W. 1968. Effect of Turbulence on Sediment Entrainment. Thesis presented to the University of Auckland, Auckland, New Zealand, in partial fulfillment of the requirements for the degree of Doctor of Philosophy.

ASHIDA, K. and BAYAZIT, M. 1973. Initiation of Motion and Roughness of Flows in Steep Channels. Proc. 15th Congress, IAHR, Vol. 1, Paper No. A58, Istanbul, Turkey, pp. 475-484.

BARTLETT, R.E. 1974. Pumping Stations for Water and Sewage. John Wiley and Sons, Barking, Essex, England 149 p.

BATHURST, J.C., LI, R.M. and SIMONS, D.B. 1979. Hydraulics of Mountain Rivers. Report CER78-79JCB-RML-DBS55, Department of Civil Engineering, Colorado State University, Fort Collins, Colorado.

BATHURST, J.C., GRAF, W.H. and CAO, H.H. 1982. Initiation of Sediment Transport in Steep Channels with Coarse Bed Material. Proc. of Euromech 156, Mechanics of Sediment Transport, Istanbul, Turkey, pp. 207-213.

BAYAZIT, M. 1976. Free Surface Flow in a Channel of Large Relative Roughness. IAHR, J. of Hydraulic Research, Vol. 14, No. 2, pp. 115-126.

BAYAZIT, M. 1982. Flow Structures and Sediment Transport Mechanics in Steep Channels. Proc. of Euromech 156, Mechanics of Sediment Transport, Istanbul, Turkey, pp. 197-206.

BERG, J.P. 1966. A Study of Vortex Formation and Other Abnormal Flow in a Tank With and Without a Free Surface. La Houille Blanche, Vol. 21, No. 1, pp. 13-40.

BIRD, R.H. 1968. Sump Design for Optimum Pump Performance. Water and Wastes Engineering, Vol. 5, No. 3, pp. 52-53.

BLINCO, P.H. and PARTHENAIDES, E. 1971. Turbulence Characteristics in Free Surface Flows Over Smooth and Rough Boundaries. IAHR, J. of Hydraulic Research, Vol. 9, No. 1, pp. 43-69.

BOGÁRDI, J. and YEN, C.H. 1938. Traction of Pebbles by Flowing Water, Iowa City.

BOGÁRDI, J. 1962. Estimation of the Bed-Load Transporting Capacity of Streams (in Hungarian). Hidrológiai Közlöny, 4.

BOGÁRDI, J. 1968. Incipient Sediment Motion in Terms of the Critical Mean Velocity. Acta Technica Ac. Sci. Hung. Tom., 62, Budapest.

BONNINGTON, S.T. and DENNY, D.F. 1956. Some Measurements of Swirl in Pump Suction Pipes. British Hydromechanics Research Association, Publication No. RR. 526, 23 p.

BRADY, D.I. 1980. Evaluation of Effective Boundary Roughness for Gravel-Bed Rivers. Can. J. of Civ. Eng., Vol. 7, No. 2, pp. 392-397.

BREWER, D. 1957. Air-Entraining Vortices in Pump Sumps. Commonwealth Engineer, Vol. 45, No. 2, pp. 50-55.

BRKICH, A. 1953. Rid Vertical-Pump Intake Design of Guess with Model Tests. Power, Vol. 97, No. 3, McGraw-Hill Publishing Co., New York, pp. 90, 91, 192, 194.

BURATTO, D.A. and McCORQUODALE, J.A. 1981. The Hydraulics of Pumping Stations and Forcemains. Proc. Conf. on Application of Hydraulics in Municipal Engineering, The Canadian Society of Civil Engineering, Ontario Region, Windsor, Ontario, pp. 51-103.

CAMP, T.R. 1946. Sedimentation and the Design of Settling Tanks. Trans. ASCE, Vol. 111, Paper No. 2285, New York, pp. 895-936.

CARTY, J.J. 1957. Resistance Coefficients for Spheres on Plane Boundary. B.S. Thesis, Massachusetts Institute of Technology.

CHANG, E. 1979. Experimental Data on the Hydraulic Design of Intakes and Rectangular Pump Sumps. British Hydromechanics Research Association, Report RR1518, Cranfield, Bedford, England, 42 pp.

CHANG, E. 1979b. Scaling Laws for Air-Entraining Vortices. BHRA Report No. RR1519, Cranfield, Bedford, England.

CHANG, E. 1980. An Investigation Into Vortex Formation in Rectangular Channels. Proc. ASME Winter Annual Meeting, Chicago, Nov. 16-21, 1980, pp. 77-86, published by ASME, New York, W.L. Swift, P.S. Barna and C. Dalton (editors).

CHARLTON, F.G., BROWN, P.M. and BENSON, R.W. 1978. The Hydraulic Geometry of Some Gravel Rivers in Britain. Hyd. Res. St. Report NO. IT 180, Wallingford, United Kingdom.

CHENG, E.D.H. and CLYDE, C.G. 1972. Instantaneous Hydrodynamic Lift and Drag Forces on Large Roughness Elements in Turbulent Open Channel Flow. Sedimentation (Einstein), H.W. Shen (editor) Chapter 3.

CHAPIL, W.S. 1961. The Use of Spheres to Measure Lift and Drag on Wind-Eroded Soil Grains. Proc. Soil Sci. Soc. Am., Vol. 25, No. 5.

CICCHITTI, A. 1960. Two-Phase Cooling Experiments - Pressure Drop, Heat Transfer and Burnout Measurements, Energi Nucl., Vol. 7, No. 6, pp. 407-425.

COLEMAN, N.L. 1967. A Theoretical and Experimental Study of Drag and Lift Forces Acting on a Sphere Resting on a Hypothetical Streambed. Proc. IAHR, 12th Congress, Vol. 3, Paper No. C22, Fort Collins, Colorado, pp. 185-192.

COLEMAN, N.L. 1972. The Drag Coefficient of a Stationary Sphere on a Boundary of Similar Spheres. La Houille Blanche, Vol. 27, No. 1, pp. 17-21.

DAGGETT, L.L. and KEULEGAN, G.H. 1974. Similitude in Free-Surface Vortex Formations. Proc. ASCE, J. Hyd. Div., Vol. 100, No. HY11, New York, pp. 1565-1581.

DENKER, H. 1980. Icing in Open Channels and Structure of Turbulent Flow Between Two Parallel Plates of Infinite Length. Ph.D. Thesis, Tech. Univ. of Istanbul (in Turkish).

DENKER, H. 1981. Personal Communications to M. Bayazit. See reference for M. Bayazit (1982), Proc. of Euromech 156.

DENNY, D.F. 1955(b). Note on Measurements of Swirl in Pump Suction Pipes. British Hydromechanics Research Association, Publication No. RR. 519, 12 p.

DENNY, D.F. 1956. An Experimental Study of Air-Entraining Vortices in Pump Sumps. Proc. The Institution of Mechanical Engineers, Vol. 170, London, pp. 106-116.

DENNY, D.F. and YOUNG, G.A.J. 1957. The Prevention of Vortices and Swirl at Intakes. Proc. IAHR 7th General Meeting, Vol. 1, Paper No. C1, Lisbon, Portugal, pp. C1-1 to C1-18.

DHILLON, G.S. 1979. Vortex Formation at Pipe Intakes and Its Prediction - A Status Report. Irrigation and Power Research Institute Report No. HY/R/4/79, Punjab, India.

DICMAS, J.L. 1967. Development of an Optimum Sump Design for Propeller and Mixed-Flow Pumps. Proc. Conf. on Fluids Engineering, ASME Paper No. 67-FE-26.

DICMAS, J.L. 1978. Effect of Intake Structure Modifications on the Hydraulic Performance of a Mixed Flow Pump. Proc. Joint Symposium on Design and Operation of Fluid Machinery, Vol. 1, IAHR, ASME, ASCE, Fort Collins, Colorado, pp. 403-412.

DONALDSON, C.D. and SULLIVAN, R.D. 1960. Behaviour of Solution of the Navier-Stokes Equations for a Complete Class of Three-Dimensional Viscous Vortices. Proc. Heat Transfer and Fluid Mech. Inst., Standford U. Press, pp. 16-30.

DORNAUS, W.L. 1958. Flow Characteristics of a Multiple-Cell Pump Basin. Trans. ASME, Vol. 80, No. 5, pp. 1129-1137.

DUCKLER, A.E. 1964. Pressure Drop and Hold-up in Two-Phase Flow. American Institute of Chemical Engineers Journal, Vol. 10, No. 1, pp. 38-51.

DURGIN, W.W., NEALE, L.C. and CHURCHILL, R.L. 1977. Hydrodynamics of Vortex Suppression in the Reactor Building Sump Decay Heat Removal System, Three Mile Island Nuclear St., Unit "2". Alden Research Laboratory Report No. 46-77/M202FF, 50 p.

DURGIN, W.W. and HECKER, G.E. 1978. The Modelling of Vortices at Intake Strucutres. Proc. Joint Symposium on Design and Operation of Fluid Machinery, Vol. 1, IAHR, ASME, ASCE, Fort Collins, Colorado, pp. 381-391.

EGIAZAROFF, I.V. 1950. Coefficient f de la force d'entrainment critique des materiau par charriage. Proc. Academy of Sciences, Armenian Soviet Socialist Republic, Translation No. 499, Electricité de France Service des Etudes et Récherches Hydrauliques, Paris, France.

EGIAZAROFF, I.V. 1957. L'Equation generale du transport des alluvions non cohesives par un courent fluide. Proc. 7th Congress, IAHR, Paper No. D43, Lisbon, Portugal, pp. 1-10.

EGIAZOROFF, I.V. 1965. Calculation of Nonuniform Sediment Concentrations. ASCE, J. of Hyd. Div., Vol. 91, No. HY4, Proc. Paper 4417, pp. 225-247.

EINSTEIN, H.A. 1942. Formulas for the Transportation of Bed Load. Trans. ASCE, Vol. 107, Paper No. 2140, pp. 561-597.

EINSTEIN, H.A. and EL-SAMNI, E.A. 1949. Hydrodynamic Forces on a Rough Wall. Reviews of Modern Physics, Vol. 21, No. 3, pp. 520-524.

EINSTEIN, H.A. and LI, H. 1955. Steady Vortex Flow in a Real Fluid. La Houille Blanche, Vol. 10, No. 4, pp. 483-496.

FAIR, G.M. and GEYER, J.C. 1958. Elements of Water Supply and Waste Water Disposal. John Wiley and Sons, Inc., New York, 615 p.

FAIR, G.M., GEYER, J.C. and OKUN, D.O. 1966. Water and Wastewater Engineering, Vol. 1, Water Supply and Wastewater Removal. John Wiley and Sons, Inc., New York.

FARELL, G. 1976. Model Study of the Inlet and Sump of the Clinton First Avenue Pump Station. IIHR Report No. 196, Iowa City, Iowa, 89 p.

FLAMMER, G.H., TULLIS, J.P. and MASON, E.S. 1970. Free Surface, Velocity Gradient Flow Past Hemisphere. Proc. ASCE, J. of Hyd. Div., Vol. 96, No. HY7, pp. 1485-1502.

FOX, R.W. and McDONALD, A.T. 1973. Introduction to Fluid Mechanics. 2nd ed., John Wiley and Sons, Inc., New York, 684 p.

FRASER, W.H. 1953. Hydraulic Problems Encountered in Intake Structures of Vertical Wet-Pit Pumps and Methods Leading to Their Solution. Trans. ASME, Vol. 75, New York, pp. 643-652.

GARBRECHT, G. 1963. Erfahrungswerte über die Zulässigen Strömungsgeschwindigkeiten in Flüssen und Kanälen. Wasser und Boden, No. 13.

GARDE, R.J. and SETHURAMAN, S. 1969. Variation of the Drag Coefficient of a Sphere Rolling Along a Boundary. La Houille Blanche, Vol. 7, No. 7, pp. 727-732.

GERLACH, C.R. and DODGE, F.T. 1970. An Engineering Approach to Tube Flow-Induced Vibrations. Proc. Conf. on Flow-Induced Vibrations in Reactor System Components, Argonne National Laboratory, pp. 205-224.

GESSLER, J. 1965. Der Geschiebetriebbeginn bei Mischungen untersucht an natürlichen Abpflästerungs erscheinungen in Kanälen. Eidgenössischen Technischen Hochschule in Zurich, Prom. Nr. 3711.

GESSLER, J. 1971. Beginning and Ceasing of Sediment Motion. In H.W. Shen (editor), River Mechanics, Vol. 1, Fort Collins, Colorado.

GHVELISIANI, L.G. 1950. Sediment Regime in the Rion River (in Russian). Izvesztija TNII, CGEI, Tbiliszi n. -i in-ta szoruzs i Gidroenerg.t.III.

GIRATALLA, M.K. 1977. Turbulent Characteristics of Flow Over Ripples. Ph.D. Thesis, Department of Civil Engineering, University of Windsor, Windsor, Ontario, Canada, 396 p.

GLADKI, H. 1979. Resistance to Flow in Alluvial Channels with Coarse Bed Materials. IAHR, J. of Hyd. Res., Vol. 17, No. 2, pp. 121-128.

GOMA, M.R.J. and GELHAR, L.W. 1968. Turbulent Pipe Flow with Rough and Porous Walls. Report No. 109, Hydrodynamics Laboratory, Dept. of Civil Engineering, Massachusetts Institute of Technology.

GORDON, J.L. 1970. Vortices at Intakes. Water Power, Vol. 22, No. 4, pp. 137-138.

GRAF, W.H. and ACAROGLU, E.R. 1968a. Sediment Transport in Conveyance Systems, Part 1, A Physical Model for Sediment Transport in Conveyance Systems. International Association of Scientific Hydrology, Vol. 13, No. 2, pp. 20-39.

GRAF, W.H. and ACAROGLU, E.R. 1968b. Sediment Transport in Conveyance Systems, Part 2, The Modes of Sediment Transport and Their Related Bed Forms in Conveyance Systems. International Association of Scientific Hydrology, Vol. 13, No. 3, pp. 123-135.

GRAF, W.H. 1971. Hydraulics of Sediment Transport. McGraw-Hill Book Co., New York, 513 p.

GRANGER, R. 1966. Steady Three-dimensional Vortex Flow. J. Fluid Mech., Vol. 25, Pt. 3, pp. 557-576.

GRASS, A.J. 1971. Structural Features of Turbulent Flow Over Smooth and Rough Boundaries. J. of Fluid Mechanics, Vol. 50, No. 2, pp. 233-255.

GRIFFITHS, G.A. 1981. Flow Resistance in Coarse Gravel Bed Rivers. ASCE, J. of Hyd. Div., Vol. 107, No. HY7, pp. 899-918.

HABERMAN, W.L. and MORTON, R.K. 1953. David W. Taylor Model Basin Report No. 802.

HAINDL, K. 1959. Contribution to Air Entrainment by a Vortex. Proc. 8th Congress, IAHR, Vol. 2, Paper No. 16-D, Montreal, pp. 16-D-1 to 16-D-17.

HANKO, Z. 1968. Über die das Geschiebe in Bewegung setzenden kritische mittlere Geschwindigkeit. Folyöszabályozás és hordalékmozgás idószerü kérdései Symposium, Budapest.

HARADASA, D.K.C. and COX, R.J. 1980. Flow Improvement at Pump Intakes by the Use of Baffles. Proc. 7th Australasian Conf. on Hydraulics and Fluid Mechanics, Brisbane, Australia, Aug. 18-20, pp. 561-564.

HATTERSLEY, R.T. 1965. Hydraulic Design of Pump Intakes. Proc. ASCE, J. of Hyd. Div., Vol. 91, No. HY2, Part 1, pp. 223-249.

HECKER, G.E. 1981. Model-Prototype Comparison of Free Surface Vortices. Proc. ASCE, J. of Hyd. Div., Vol. 107, No. HY10, New York, pp. 1243-1259

HELLEY, E.I. 1969. Field Measurements of the Initiation of Large Bed Particle Motion in Blue Creek Near Klamath California. U.S. Geological Survey, Proc. Paper No. 562-G, Washington, D.C.

HERBICH, J.B. and SHULITS, S. 1964. Large-Scale Roughness in Open-Channel Flow. Proc. ASCE, J. of Hyd. Div., Nov., 1964.

HERHEULIDZE, I.I. 1958. Hydrologic an d Hydraulic Problems of River Crossing (in Russian). Sbornik I. Tbilisi, Izd. HTO.

HEY, R.D. 1979. Flow Resistance in Gravel-Bed Rivers. Proc. ASCE, J. of Hyd. Div., Vol. 105, No. HY4, pp. 365-379.

HJULSTRÖM, F. 1935. Studies of the Morphological Activity of Rivers as Illustrated by the River Fyris, Geological Inst. of Upsala, Vol. 25, Upsala, Sweden.

HWANG, L-S. and LAURSEN, E.M. 1963. Shear Measurement Technique for Rough Surfaces. Proc. ASCE, J. of the Hyd. Div., Vol. 89, No. HY2, New York, pp. 19-37.

HYDRAULIC INSTITUTE. 1983. Hydraulic Institute Standards for Centrifugal, Rotary and Reciprocating Pumps. 14th ed., Hydraulic Institute, Cleveland, Ohio, 360 p.

IVERSEN, H.W. 1953. Studies of Submergence Requirements of High-Specific-Speed Pumps. Trans. ASME, Vol. 75, New York, pp. 635-641.

IVICSICS, L. 1959. Incipient Bed Load Movement Described by Invariant Groups (in Hungarian). Hidrológiai Közlöny, No. 6.

JAIN, A.K., RAJU, K.G.R. and GARDE, R.J. 1978. Vortex Formation at Vertical Pipe Intakes. Proc. ASCE, J. of Hyd. Div., Vol. 104, No. HY10, New York, pp. 1429-1445.

KALINSKE, A.A. 1947. Movement of Sediment as Bed Load in Rivers. Trans. American Geophysical Union, Vol. 28, No. 4, pp. 615-620.

KALMÁR, G. 1952. Experimental Study into Sediment Transport (in Hungarian). Budapest University of Technology.

KAMPHUIS, J.W. 1974. Determination of Sand Roughness For Fixed Beds. IAHR, J. of Hydraulic Research, Vol. 12, No. 2, pp. 193-203.

KARAUSHEV, A.V. 1977. Theory and Methods of Estimating Sediment in Streams (in Russian). Gidrometeoizdat, Leningrad.

KHARRUFA, N.S. 1962. Flume Study of Steep Flow with Large Graded Natural Roughness Elements, Ph.D. Thesis, Utah State University, Logan, Utah.

KNIGHT, D.W. 1981. Boundary Shear in Smooth and Rough Channels. Proc. ASCE, J. of Hyd. Div., Vol. 107, No. HY7, pp. 839-851.

KNOROZ, V.C. 1959. Non-scouring Velocities in Loose Soils and the Factors Affecting Them (in Russian). Izv. VNIIG. T.59, Leningrad.

KUMINE, D. 1955. Hydraulic Dimensioning of Linings in the Tail-water of Structures (in Russian). Gosenergoizdat.

LANE, E.W. 1937. Stable Channels in Erodible Material. Trans. ASCE, Vol. 102.

LANE, E.W. 1955. Design of Stable Channels, Trans. ASCE, Vol. 120, Paper No. 2776, pp. 1234-1279.

LATISHENKOV, A.M. 1960. Hydraulics of Flow in Artificially Restricted Channels (in Russian). Gostroizdat.

LAURSEN, E.M. 1958. The Total Sediment Load of Streams, Proc. ASCE, J. of Hyd. Div., Vol. 84, No. HY1.

LELLIAVSKY, S. 1955. An Introduction to Fluvial Hydraulics, Constable and Co., Ltd., London, England.

LEOPOLD, L.B., WOLMAN, M.G. AND MILLER, J.F. 1964. Fluvial Processes in Geomorphology. Freemand and Co., San Fransisco.

LEVI, I.I. 1948. Streamflow Dynamics (in Russian). Gosenergoizdat. Leningrad, Moscow.

LEVI, E. 1972. Experiments on Unstable Vortices. Proc. ASCE, J. Eng. Mech. Div., Vol. 98, No. EM3, New York, pp. 539-559.

LEWELLEN, W.S. 1962. A Solution for Three-dimensional Vortex Flows with Strong Circulation. J. Fluid Mech., Vol. 14, Pt. 3, pp. 420-432.

LIMERINOS, J.T. 1970. Determination of the Manning Coefficient from Measured Bed Roughness in Natural Channels. USGS, Water Supply Paper 1898-B.

LINFORD, A. 1965. The Application of Models to Hydraulic Engineering, Part 2: Air-Entraining Vortices. Water and Water Engineering, Vol. 69, No. 828, pp. 105-110.

LIU, H.K. 1957. Mechanics of Sediment Ripple Formation. Proc. ASCE, J. of Hyd. Div., Vol. 83, No. HY2, pp. 1-23.

LIU, H-S. and HWANG, S-Y. 1959. Discharge Formula for Straight Alluvial Channels. J. of Hyd. Div., Proc. ASCE, Vol. 85, No. HY11, November 1959, pp. 65-97.

MACHINA, D.W. 1983. An Investigation of the Scouring of Particles on Pumping Station Wet Well Floors. M.A.Sc. Thesis, Department of Civil Engineering, University of Windsor, Windsor, Ontario, Canada, 229 p.

MACHINA, D.W. and BEWTRA, J.K. 1983. Hydraulic Design of Wet Well Floors In Pumping Stations. Proc. 6th Canadian Hydrotechnical Conference, Vol. 1, Ottawa, Ont., pp. 241-265.

MARKLAND, E. and POPE, J.A. 1956. Experiments on a Small Pump Suction Well with Particular Reference to Vortex Formations. Proc. The Institution of Mechanical Engineers, Vol. 170, London, pp. 95-105.

MARTINELLI, R.C. and NELSON, D.B. 1948. Trans. ASME, Vol. 70, p. 695.

MATSUNASHI, J. 1957. Researches on Bed-Load Transportation Under The Tractive Force Near the Critical Limit, Memoirs of the Faculty of Engineering, No. 4, Kobe University, Kobe, Japan, March 1957, pp. 24-42.

MAVIS, F.T., CHITTY, H. and YEUNG-CHEN, T. 1935. The Transportation of Detritus by Flowing Water. University of Iowa Studies No. 294, Bulletin No. 5.

MAVIS, F.T., LIU, T.Y. and SOUCEK, E. 1936. The Transportation of Detritus by Flowing Water. University of Iowa Studies Bulletin No. 11.

MAVIS, F.T. and LAUSHEY, L.M. 1949. Formula for Velocity at Beginning of Bed-Load Movement is Reappraised. Civil Engineering, Vol. 19, No. 1, pp. 1, 39, 72.

McADAMS, W.H. 1942. Vaporisation Inside Horizontal Tubes. II. Benzene Oil Mixtures, Trans. ASME, Vol. 64, p. 193.

MESSINA, J.P. 1971. Periodic Noise in Circulating Water Pumps Traced to Underwater Vortices at Inlet. Power, Vol. 115, No. 9, pp. 70-71.

METCALF and EDDY, INC. 1972. Wastewater Engineering, McGraw-Hill Book Company, New York.

METCALF and EDDY, INC. 1981. Wastewater Engineering: Collection and Pumping of Wastewater. G. Tchobanoglous, Ed., McGraw-Hill Book Company, New York, 432 p.

MEYER-PETER, E., MÜLLER, R. and EINSTEIN, H.A. 1934. Neure Versuchsresultate über den Geschiebetrieb. Shweizenische Bauzeitung. Vol. 103, No. 13, Zurich.

MEYER-PETER, E. and MÜLLER, R. 1948. Formulas for Bed-Load Transport, Proc. 2nd Congress, IAHR, Stockholm, pp. 39-64.

MIRAJGAOKER, A. and CHARLU, K. 1963. Natural Roughness Effects in Rigid Open Channels. Proc. ASCE, J. of Hyd. Div., Sept., 1963.

MIRTSHULAVA, C.E. 1967. Method for Appraising Channel Scouring and Stability (in Russian). Moscow.

MIZUYAMA, T. 1977. Bedload Transport in Steep Channels. Ph.D. Kyoto Univ., Kyoto, Japan.

MOHANTY, P.K. 1962. The Dynamics of Flow in Steep, Rough, Open Channels. Ph.D. Thesis, Utah State University, Logan, Utah.

MOODY, L.F. 1944. Friction Factors for Pipe Flow. Trans. ASME, Vol. 6, No. 8, pp. 671-684.

MÜLLER, G. 1973. Ausführungen über die Erosionsbeständigkeit von Lockergesteinen in Wasserlaufbetten W.W.T. 23, Jahrgang, Heft, 3-4.

NAGY-KARÁDI, V. 1960. Recent Results of Bed Load Movement Studies (in Hungarian). Hidrológiai Közlöny, 3.

NAKATO, T. and KENNEDY, J.F. 1976. Model Study of the Lake Chicot Pumping Plant. IIHR Report No. 188, Iowa City, Iowa, 125 p.

NEILL, C.R. 1967a. Stability of Coarse Bed-Material in Open Channel Flow. Edmonton, reference cited by K. Stelczer, 1981, pp. 267.

NEILL, C.R. 1967b. Mean-Velocity Criteria for Scour of Coarse Uniform Bed-Material. Proc. IAHR 12th Congress, Vol. 3, Paper C3, pp. 46-54.

NEILL, C.R. 1968. Note on Initial Movement of Coarse Uniform Bed-Material. J. of Hydraulic Research, Vol. 6, No. 2, pp. 173-176.

NIKURADSE, J. 1933. Stromungsgesetze in rauhen Rohren. Forschg. Geb. d. Ing.-Wesens, Heft 361.

NOVAK, P. and NALLURI, C. 1972, 1974. A Study into the Correlation of Sediment Motion in Pipe and Open Channel Flow. Hydrotransport 2 and 3, Papers D4 and E4, Cranfield, England.

NOVAK, P. and NALLURI, C. 1975. Sediment Transport in Smooth Fixed Bed Channels. Proc. ASCE, J. of Hyd. Div., Vol. 101, No. HY9, New York, pp. 1139-1154.

NOVAK, P. and NALLURI, C. 1978. Sewer Design for No-Sediment Deposition. Proc. Instn. Civ. Engrs., Part 2, Vol. 65, pp. 669-674.

NOVAK, P. and NALLURI, C. 1984. Incipient Motion of Sediment Particles Over Fixed Beds. Journal of Hydraulic Research, Vol. 22, No. 3, pp. 181-197.

NYSTROM, J.B., PADMANABHAN, M. and HECKER, G.E. 1982. Modelling Flow Characteristics of Reactor Sumps. Proc. ASCE, J. Energy Div., Vol. 108, No. EY3, New York, pp. 169-184.

O'LOUGHLIN, E.M. and MacDONALD, E.C. 1964. Some Roughness Concentration Effects on Boundary Roughness. La Houille Blanche, Vol. 19, No. 7, pp. 773-783.

ORLOV, K.K. and FIDMAN, V.A. 1960. Perfection of Suspended Sediment Formulae (in Russian). Dokladi an CCCR, No. 5.

PARKER, G. and KLINGEMAN, P.C. 1982. On Why Gravel Streams are Paved. Proc. ASCE, J. of Hyd. Div., Vol. 108.

PATERSON, I.S. and CAMPBELL, G. 1968. Pump Intake Design Investigations. Proc. IME, Vol. 182, Part 3M, London, Paper No. 1, pp. 1-10.

PE, J.A. 1975. Incipient Erosion in High Gradient Open Channel Flow with Artificial Roughness Elements. Proc. 16th Congress, IAHR, Vol. 2, Paper B22, Sao Paulo, Brazil, pp. 173-180.

PEEBLES, F.N. and GARBER, H.J. 1953. Chem. Eng. Progr., Vol. 49, pp. 88-97.

POWELL, R.W. 1946. Flow in Channel of Definite Roughness, Trans. ASCE, Paper No. 2276.

PRESTON, J.H. 1954. The Determination of Turbulent Skin Friction By Means of Pitot Tubes. J. of the Royal Aeronautical Soc., Vol. 54.

PROSSER, M.J. 1977. The Hydraulic Design of Pump Sumps and Intakes. BHRA, Cranfield, Bedford, England, 48 p.

QUICK, M.C. 1970. Efficiency of Air-Entraining Vortex Formation at Water Intake. Proc. ASCE, J. of Hyd. Div., Vol. 96, No. HY7, pp. 1403-1416.

RAMETTE, M.M. and HEUZEL, M.M. 1962. Rhône á Lyon Etude de l'entrainement des galets ál' aide de traceurs radio-actifs. La Houille Blanche, Grenoble.

REDDY, Y.R. and PICKFORD, J.A. 1972. Vortices at Intakes in Conventional Sumps. Water Power, Vol. 24, No. 3, pp. 108-109.

RICHARDSON, C.A. 1941. Submergence and Spacing of Suction Bells. Water Works and Sewerage, Vol. 88, No. 6, Reference and Data Section, Water Supply, pp. 25.

ROSSINSKYI, K.I., SAVIN, V.G. and SEVELYEVA, G.G. 1968. Laboratory Study on the Settling of Hydraulic Scouring of Sediment in Settling Basins (in Russian). Problemy regulirovania szcoka i iszpol′ zovanija G.G.I Trudii viip 1960, Leningrad.

ROUSE, H. 1939. An Analysis of Sediment Transportation in the Light of Fluid Turbulence. U.S.D.A., Soil Conservation Service Report No. SCS-TP-25, Washington, D.C.

ROUSE, H. 1965. Critical Analysis of Open Channel Resistance. J. of the Hyd. Div., ASCE, Vol. 91, No. HY4, pp. 1-25.

RUBEY, W.W. 1938. The Force Required to Move Particles on a Stream Bed. U.S. Geological Survey, Washington, D.C., Professional Paper No. 189-E.

RUBEY, W.W. 1948. The Forces Required to Move Particles on a Stream Bed. U.S. Geological Survey, Washington, D.C., Professional Paper No. 189-B.

SAYRE, W. and ALBERTSON, M. 1961. Roughness Spacing in Rigid Open Channels. Proc. ASCE, J. of the Hyd. Div., May, 1961.

SCHEUERLEIN, H. 1973. The Mechanics of Flow in Steep, Rough, Open Channels. Proc. 15th Congress, IAHR, Vol. 1, Paper No. A56, Istanbul, Turkey, pp. 457-465.

SCHLICHTING, H. 1936. Experimentelle untersuchungen zum Raukigkeitsproblem. Ing. Arch., 7, pp. 1-34.

SCHOKLITSCH, A. 1934. Der Geschiebebetrieb und die Geschiebefracht. Wasserkraft und Wasserwirtschaft, 4.

SCHOKLITSCH, A. 1962. Handbuch des Wasserbaues. Vienna, Springer-Verlag.

SHAHROODY, A.M. and DAVIS, J.R. 1964. Efficiency of Pumping From Small Circular Sumps. Proc. ASCE, J. Irr. and Drain. Div., Vol. 90, No. IR1, pp. 1-8.

SHIELDS, A. 1936. Application of Similarity Principles and Turbulence Research to Bed-Load Movement. Translated from: Anwendung der Aehnlichkeitsmechanik und der Turbulenzforschung auf die Geschiebebewegung, by: W.P. Ott and J.C. van Uchelen. Mitteilungen der Preussischen Versuchsanstalt fur Wasserbau und Schiffbau, Berlin, 44 pp.

SIMONS, D.B. and RICHARDSON, E.V. 1960. Resistance to Flow in Alluvial Channels. J. of Hyd. Div., Proc. ASCE, Vol. 86, No. HY5, May 1960, pp. 73-99.

SIMONS, D.B. and SENTÜRK, F. 1977. Sediment Transport Technology. Water Resources Publications, Fort Collins, Colorado, 807 p.

SMART, G.M. 1984. Sediment Transport Formula for Steep Channels. J. of the Hyd. Div., Proc. ASCE, Vol. 110, No. 3, pp. 267-276.

STELCZER, K. 1981. Bed-Load Transport Theory and Practice. Water Resources Publications, Littleton, Colorado, 295 pp.

STEVENS, J.C. and KOLF, R.C. 1957. Vortex Flow Through Horizontal Orifices. Proc. ASCE, J. San. Eng. Div., Vol. 83, No. SA6, pp. 1461-1 to 1461-22.

STUDENITSHNIKOV, B.I. 1964. Scouring Capacity of Flow and Methods of Channel Analysis (in Russian). Stroizdat VODGEO, Moscow.

SUNDBORG, A. 1956. The River Klaralven Study of Fluvial Processes, Geografiska Analler 38, Stockholm, Sweden, Bulletin No. 52, Royal Inst. of Technology.

SWAINSTON, M.J.C. 1974. Vortex Formation Near the Intakes to Turbomachinery and Duct Systems. Proc. IME, Vol. 188, pp. 597-605, D133.

SWAINSTON, M.J.C. 1976. Experimental and Theoretical Identification of Air Ingestion Regimes in Pump Sumps. Proc. IME, Vol. 190, pp. 671-678, D177-D180.

THOMPSON, S.M. and CAMPBELL, P.L. 1979. Hydraulics of a Large Channel Paved with Boulders. IAHR, J. of Hyd. Res., Vol. 17, No. 4, pp. 341-354.

TISON, L.J. 1953. Studies of the Critical Tractive Force for the Entrainment of Bed Materials. Proc. Minnesota International Hydraulics Conference, Minneapolis, Minn., pp. 21-35.

TURNER, J.S. 1966. The Constraints Imposed on Tornado-like Vortices by the Top and Bottom Boundary Conditions. J. Fluid Mech., Vol. 25, Pt. 2, pp. 377-400.

VANONI, V. 1966. Sediment Transportation Mechanics: Initiation of Motion (Progress Report of Task Committee). Proc. ASCE, Vol. 92, No. HY2.

VELIKHANOV, M.A., BOTSHKOW, N.N. and SHWEYKOVSKYI, N.T. 1931. Research on Scouring Velocities. Collection of papers (in Russian).

WALLIS, G.B. 1969. One-dimensional Two-phase Flow. McGraw-Hill, Inc., New York, 408 pp.

WATER POLLUTION CONTROL FEDERATION. 1981. Design of Wastewater and Stormwater Pumping Station, Manual of Practice, No. FD-4, Facilities Development, Washington, D.C., 152 p.

WELLER, J.A. 1975. Discussion of Similitude in Free-Surface Vortex Formations, by L.L. Daggett and G.H. Keulegen. Proc. ASCE, J. of Hyd. Div., Vol. 101, No. HY11, New York, pp. 1449-1451.

WHITE, C.M. 1940. The Equilibrium of Grains on the Bed of a Stream. Proc., Royal Soc. of London, Series A, No. 958, Vol. 174, pp. 322-338.

WILLIS, J.C. and COLEMAN, N.L. 1969. Unification of Data on Sediment Transport in Flumes by Similitude Principles. Water Resources Research, Vol. 6, No. 6, pp. 1330-1336.

WOODHOUSE, H. 1966. The Suction Side of Centrifugal Pumps. Power, Vol. 110, No. 5, McGraw-Hill Inc., New York, pp. 71-73.

YALIN, M.S. 1972. Mechanics of Sediment Transport. Pergamon Press, Oxford, 290 pp.

YILDIRIM, N. and JAIN, S.C. 1981. Surface Tension Effect on Profile of a Free Vortex. Proc. ASCE, J. of Hyd. Div., Vol. 107, No. HY1, New York, pp. 132-136.

ZAJDLIK, M. 1977. New Checking Mode of Model Parameters for Vortex Formation in Pump Tanks. Proc. 17th Congress, IAHR, Vol. 5, Paper No. D49, Baden-Baden, West Germany, pp. 379-386.

ZAMARIN, E.A. 1951. Transport Capacity and Allowable Velocities in Canals (in Russian). Gostroizdat 2, Leningrad, Moscow.

ZANKER, K.J. 1968. Some Hydraulic Modelling Techniques. Proc. IME, Vol. 182, Part 3M, London, Paper No. 8, pp. 54-63.

ZUBER, H. and HENCH, J. 1962. Report No. 62GL100, General Electric Company, Schenectady, New York.

VITA AUCTORIS

David William Machina was born on October 13, 1959 in Windsor, Ontario, Canada.

He graduated from W.D. Lowe Secondary School in June, 1978 and entered the University of Windsor, graduating in June, 1982 with a Bachelor of Applied Science degree in Civil Engineering.

In October of 1983, he received his Master of Applied Science degree in Civil Engineering from the same university.

Immediately thereafter, he was accepted into the Faculty of Graduate Studies at the University of Windsor in a program leading to the degree of Doctor of Philosophy in Civil Engineering.